

Controlled Radical Polymerization: Materials

Publication Date (Web): May 1, 2015 | doi: 10.1021/bk-2015-1188.fw001

ACS SYMPOSIUM SERIES **1188**

Controlled Radical Polymerization: Materials

Krzysztof Matyjaszewski, Editor

*Carnegie Mellon University
Pittsburgh, Pennsylvania*

Brent S. Sumerlin, Editor

*University of Florida
Gainesville, Florida*

Nicolay V. Tsarevsky, Editor

*Southern Methodist University
Dallas, Texas*

John Chiefari, Editor

*CSIRO
Melbourne, Victoria, Australia*

Sponsored by the
ACS Division of Polymer Chemistry



American Chemical Society, Washington, DC

Distributed in print by Oxford University Press



Library of Congress Cataloging-in-Publication Data

Controlled radical polymerization / Krzysztof Matyjaszewski, editor, Carnegie Mellon University, Pittsburgh, Pennsylvania, Brent S. Sumerlin, editor, University of Florida, Gainesville, Florida, Nicolay V. Tsarevsky, editor, Southern Methodist University, Dallas, Texas, John Chiefari, editor, CSIRO, Melbourne, Victoria, Australia ; sponsored by the ACS Division of Polymer Chemistry.

volumes cm. -- (ACS symposium series ; 1187, 1188)

Includes bibliographical references and index.

Contents: volume 1. Mechanisms -- volume 2. Materials

ISBN 978-0-8412-3048-4 (v. 1) -- ISBN 978-0-8412-3050-7 (v. 2) 1. Polymerization. 2.

Free radical reactions. I. Matyjaszewski, K. (Krzysztof) II. Sumerlin, Brent S. III.

Tsarevsky, Nicolay V. IV. Chiefari, John, 1964- V. American Chemical Society. Division of Polymer Chemistry.

QD281.P6C664 2015

547'.28--dc23

2015015377

The paper used in this publication meets the minimum requirements of American National Standard for Information Sciences—Permanence of Paper for Printed Library Materials, ANSI Z39.48n1984.

Copyright © 2015 American Chemical Society

Distributed in print by Oxford University Press

All Rights Reserved. Reprographic copying beyond that permitted by Sections 107 or 108 of the U.S. Copyright Act is allowed for internal use only, provided that a per-chapter fee of \$40.25 plus \$0.75 per page is paid to the Copyright Clearance Center, Inc., 222 Rosewood Drive, Danvers, MA 01923, USA. Republication or reproduction for sale of pages in this book is permitted only under license from ACS. Direct these and other permission requests to ACS Copyright Office, Publications Division, 1155 16th Street, N.W., Washington, DC 20036.

The citation of trade names and/or names of manufacturers in this publication is not to be construed as an endorsement or as approval by ACS of the commercial products or services referenced herein; nor should the mere reference herein to any drawing, specification, chemical process, or other data be regarded as a license or as a conveyance of any right or permission to the holder, reader, or any other person or corporation, to manufacture, reproduce, use, or sell any patented invention or copyrighted work that may in any way be related thereto. Registered names, trademarks, etc., used in this publication, even without specific indication thereof, are not to be considered unprotected by law.

PRINTED IN THE UNITED STATES OF AMERICA

Foreword

The ACS Symposium Series was first published in 1974 to provide a mechanism for publishing symposia quickly in book form. The purpose of the series is to publish timely, comprehensive books developed from the ACS sponsored symposia based on current scientific research. Occasionally, books are developed from symposia sponsored by other organizations when the topic is of keen interest to the chemistry audience.

Before agreeing to publish a book, the proposed table of contents is reviewed for appropriate and comprehensive coverage and for interest to the audience. Some papers may be excluded to better focus the book; others may be added to provide comprehensiveness. When appropriate, overview or introductory chapters are added. Drafts of chapters are peer-reviewed prior to final acceptance or rejection, and manuscripts are prepared in camera-ready format.

As a rule, only original research papers and original review papers are included in the volumes. Verbatim reproductions of previous published papers are not accepted.

ACS Books Department

Preface

This book and the preceding volume are addressed to chemists and polymer scientists interested in radical processes, and especially in controlled/living radical polymerization. They summarize the most recent accomplishments in the field.

The two volumes comprise the topical reviews and specialists' contributions presented at the American Chemical Society (ACS) Symposium on *Controlled Radical Polymerization* that was held in San Francisco, CA, August 10-14, 2014, which was the meeting place of the very first symposium of the series that took place in 1997. The most recent San Francisco meeting was a sequel to several previous ACS Symposia on controlled/living radical polymerization held in San Francisco, California (1997), New Orleans, Louisiana (1999), Boston, Massachusetts (2002), Washington, DC (2005), Philadelphia, Pennsylvania (2008), and Denver, Colorado (2011). The work presented at those symposia was summarized in the ACS Symposium Series Volume 685: *Controlled Radical Polymerization*, Volume 768: *Controlled/Living Radical Polymerization: Progress in ATRP, NMP and RAFT*, Volume 854: *Advances in Controlled/Living Radical Polymerization*, Volume 944: *Controlled/Living Radical Polymerization: From Synthesis to Materials*, Volume 1023: *Controlled/Living Radical Polymerization: Progress in ATRP*, Volume 1024: *Controlled/Living Radical Polymerization: Progress in RAFT, DT, NMP and OMRP*, Volume 1100: *Progress in Controlled Radical Polymerization: Mechanisms and Techniques*, and Volume 1101: *Progress in Controlled Radical Polymerization: Materials and Applications*. The San Francisco 2014 meeting was very successful with 93 lectures and a similar number of posters presented. This level of participation illustrates a continuous growth in comparison to the San Francisco meeting (32 lectures), the New Orleans meeting (50 lectures), the Boston meeting (80 lectures), the Washington meeting (77 lectures), the Philadelphia meeting (90 lectures) and the Denver meeting (96 lectures).

The 37 chapters submitted for publication in the ACS Symposium series could not fit into one volume, and therefore we were asked by ACS to divide the contents into two volumes. Similar to the volumes originating from the Denver Meeting, these two volumes are dedicated to mechanisms and techniques (17 chapters and 358 pages), and materials and applications (20 chapters and 345 pages).

The chapters in this volume are focused on control over macromolecular architecture and functionality, as well as on the synthesis of well-defined polymers in heterogeneous systems, and the preparation and applications of hybrid materials and biomaterials. In addition, one chapter is dedicated to polymer characterization. Substantial progress has been made in these areas since the last symposium in Denver, and as a result, this volume is an excellent resource.

The accompanying volume contains four chapters on general aspects of radical polymerization, five chapters on ATRP, and eight chapters on degenerative transfer and more complex mechanisms.

Thirty-seven chapters published in two volumes show that there have been significant developments in CRP over the last fifteen years. New systems have been discovered; substantial progress has been achieved in understanding the mechanism and kinetics of reactions involved in all CRP systems. As a result of these advances, significant progress has been made toward developing a comprehensive relationship between molecular structure and macroscopic properties. Several commercial applications of CRP were announced at the San Francisco meeting, and it is anticipated that new products made by CRP will soon be on the market.

The financial support for the symposium is acknowledged from the following organizations: ACS Division of Polymer Chemistry, Inc., Bridgestone-Firestone, CSIRO, DSM, Kaneka, Kuraray, the National Science Foundation, PPG, Royal Chemical Society, and Wiley-VCH.

Krzysztof Matyjaszewski

Department of Chemistry
Carnegie Mellon University
4400 Fifth Avenue
Pittsburgh, PA 15213

Brent S. Sumerlin

George & Josephine Butler Polymer Research Laboratory
Center for Macromolecular Science & Engineering
Department of Chemistry
University of Florida
Gainesville, FL 32605-7200

Nicolay V. Tsarevsky

Department of Chemistry and Center for Drug Discovery, Design, and Delivery in
Dedman College
Southern Methodist University
3215 Daniel Avenue
Dallas, TX 75275

John Chiefari

Commonwealth Scientific and Industrial Research Organisation (CSIRO)
Manufacturing Flagship
Private Bag 10
Clayton South, Victoria, 3169
Australia

Editors' Biographies

Krzysztof Matyjaszewski

Krzysztof Matyjaszewski is the J.C. Warner University Professor of Natural Sciences at Carnegie Mellon University. He developed Cu-based atom transfer radical polymerization and other controlled radical polymerization processes that were commercialized in the U.S., Europe, and Japan (17 signed licenses). He has co-authored 880 publications, co-edited 17 books, and holds 51 U.S. patents as well as 132 international patents. Matyjaszewski received the 2013 Inaugural AkzoNobel North America Science Award, the 2011 Wolf Prize in Chemistry, and the 2009 Presidential Green Chemistry Award in addition to seven honorary degrees.

Brent S. Sumerlin

Brent Sumerlin is an associate professor in the department of chemistry at the University of Florida. His research interests include stimuli-responsive polymers, dynamic-covalent materials, and biological applications of synthetic polymers. He has been named a Kavli Fellow (Frontiers of Science, National Academies of Sciences), an Alfred P. Sloan Research Fellow, and a Gerald J. Ford Research Fellow. He has received an NSF CAREER Award, the ACS Leadership Development Award, and the Journal of Polymer Science Innovation Award. He is also a Fellow of the Royal Society of Chemistry.

Nicolay V. Tsarevsky

Nicolay V. Tsarevsky is an assistant professor of chemistry at Southern Methodist University in Dallas, TX. His interests include polymerization techniques, catalysis, functional materials, the chemistry of hypervalent iodine compounds, as well as the history of science and science education. He has published 78 peer-reviewed papers and book chapters, co-authored one textbook and co-edited three books, and is the co-inventor on several patents.

John Chiefari

John Chiefari is a research leader in CSIRO's Manufacturing Flagship. He is a co-inventor and co-developer of the RAFT process, which has been commercialized with products in the U.S., Europe, Australia, and Japan. He is currently managing CSIRO's research activities to extend the utility of the RAFT

process and to explore new application areas in the biomedical, agricultural, personal care, and industrial chemical fields.

Chapter 1

Periodic Introduction of Water-Tolerant Titanatrane Complex to Poly(NIPAM) Prepared by Simultaneous Step-Growth and Living Radical Polymerization

Kotaro Satoh,* Daisuke Ito, and Masami Kamigaito*

Department of Applied Chemistry, Graduate School of Engineering,
Nagoya University, Furo-cho, Chikusa-ku, Nagoya 464-8603, Japan
*E-mail: satoh@apchem.nagoya-u.ac.jp; kamigait@apchem.nagoya-u.ac.jp

This study was directed to the synthesis of periodically titanium-containing organometallic polymer, which is stable in an aqueous solution, by transition metal-catalyzed simultaneous chain- and step-growth radical polymerization and post-polymerization reaction. The simultaneous radical polymerization of three component system, i.e., *N*-isopropylacrylamide (NIPAM), a dihalide with multidentate ligand for organotitanium, and unconjugated diene, was examined with the CuCl/Me₆TREN system in DMF/H₂O = 1/1 at 20 °C to result in the periodically functionalized poly(NIPAM). The periodically-introduced multidentate ligands originating from the dihalide were subsequently reacted with Cp*TiCl₃, the organotitanium part of which was introduced periodically into the poly(NIPAM) as the titanatrane complex. Since the Cp*-titanatrane structure was stable in water, the thermoresponsive behavior of the periodically titanatrane-containing poly(NIPAM) could also be evaluated in an aqueous solution.

Introduction

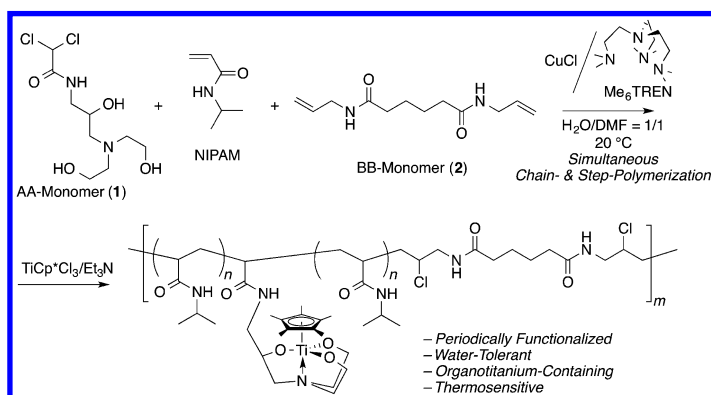
A fusion of organic macromolecule with inorganic metal will provide additional functions to the original materials, as observed in metallopolymers, organized polymer/inorganic composite, supported catalysts, and metalloenzymes, and so forth (1–9). As for the preparation of metal-containing macromolecules, the judicious designs of parent polymers are inevitable for the construction of well-defined metal-containing polymers, such as monomers, metals ligating sites, and metals (1–4). In particular, organometallic compounds bearing early-transition metal-carbon bonds are generally labile toward water or oxygen, so that special handling has been required under rigorously dried and inert atmosphere (10–12).

We have recently found that well-defined organotitanium-containing copolymers could be prepared using the polymerization of glycidyl methacrylate followed by amination of the epoxy group with diethanolamine to form a triethanolamine-pendent ligand, which reacted with CpTiCl_3 or Cp^*TiCl_3 (Cp: cyclopentadienyl; Cp^* : pentamethylcyclopentadienyl) to load titanium complex (13). The obtained titanium-containing unit possessed an atrane structure, i.e. titanatrane (14, 15), which contributed to the solubility in organic solvents as well as the high stability to water with Cp^* derivatives, whereas Cp analogues were easily decomposed by contact with water (13). Since glycidyl methacrylate can be radically polymerized in conjunction with ruthenium catalysts in a living fashion, various types of well-defined macromolecular structures containing stable organometallic segments, such as random, block, and end-functional copolymers, were also successfully obtained by the living radical polymerization of glycidyl methacrylate and post-reactions with diethanolamine and Cp^*TiCl_3 .

N-Isopropylacrylamide (NIPAM) is one of the most attractive radically polymerizable monomers, which affords a water-soluble polymer that exhibits thermal stimuli-responsive character in its aqueous solution (16–19). The aqueous solution of poly(NIPAM) is well-known to show a lower critical solution temperature (LCST) reversibly between 31–35 °C. Owing to the thermoresponsive property, this material has been intensively studied in the interdisciplinary fields, such as bioengineering and nanotechnology. In addition, well-defined poly(NIPAM) has recently been prepared by the development of controlled/living chain-growth radical polymerization (20). In particular, Cu-catalyzed atom transfer radical polymerization (ATRP) or single-electron transfer (SET) polymerization of NIPAM in conjunction with tris[2-(dimethylamino)ethyl]amine (Me_6TREN) as the ligand effectively produced well-defined polymers even at ambient temperature (21–25). Recently, we also applied the $\text{CuCl}/\text{Me}_6\text{TRN}$ system for simultaneous chain- and step-growth radical polymerization (26), in which the living chain-growth radical polymerization was concurrently combined with step-growth polymerization both catalyzed by the transition metal catalyst, such as Cu and Ru (27–30). As for the step-growth reaction, the monomers were well-designed to possess an unconjugated carbon-carbon double ($\text{C}=\text{C}$) and an active carbon-chlorine ($\text{C}-\text{Cl}$) bonds in a molecule, i.e. AB-type monomer. We reported that the simultaneous polymerization of NIPAM and AB-monomer afforded the dual control in degradability and thermoresponsivity of the resultant

polymer, owing to the periodically introduced amide- or ester-linkage derived from the step-growth monomers (26).

In this paper, we intended to synthesize titanium-containing organometallic polymers, which are water-soluble and stable in an aqueous solution, by transition metal-catalyzed simultaneous chain- and step-growth radical polymerization of well-deigned monomers. In particular, since the step-growth radical polymerization proceeded not only for AB-type monomers but also between AA- and BB-type monomers (29), the simultaneous radical polymerization was investigated for the ternary system consisting of NIPAM, dichloride as the AA-monomer, and unconjugated diene as the BB-monomer (Scheme 1). This ternary system provides a facile and highly efficient strategy for the introduction of periodic functional units in the polymer chain.

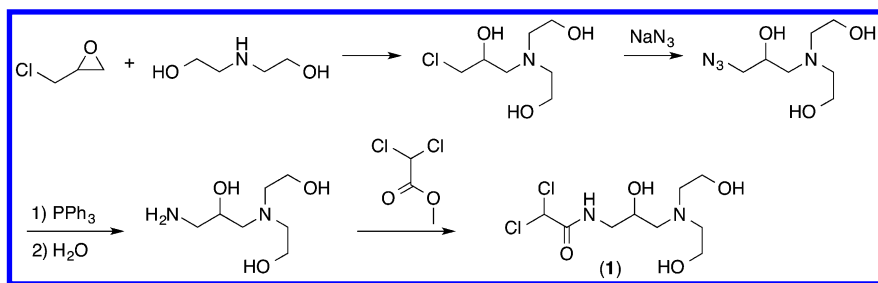


Scheme 1. Synthesis of Periodically Titanatrans-Functionalized Poly(NIPAM) by Simultaneous Chain- and Step-Growth Radical Polymerization.

Results and Discussion

1. Synthesis of Triethanolamine-Bearing Dichloroacetamide (1)

To introduce the multidentate triethanolamine ligand in a precursor polymer, triethanolamine-bearing dichloroacetamide (**1**) was designed as a difunctional compound for the transition metal catalysis, in which both of the two C–Cl bonds will be activated to generate the initiating carbon radicals. As shown in Scheme 2, the synthesis of **1** relied on the ring-opening of the epoxide with diethanolamine: It commenced with the preparation of triethanolamine-bearing chloride by ring-opening of epichlorohydrin, followed by the transformation of chloride into primary amine and the amidation of methyl dichloroacetate to yield the dichloroacetamide derivative (**1**) bearing a triethanolamine pendent group (see also Experimental Section).



Scheme 2. Synthesis of Triethanolamine-Bearing Dichloroacetamide (**1**).

2. Periodically Functionalized Poly(NIPAM) by Simultaneous Chain- and Step-Growth Radical Polymerization

The radical polymerization of NIPAM was then examined using CuCl/Me₆TREN as the catalyst in conjunction with **1** in the absence and presence of an unconjugated amide-linked diene (*N,N'*-diallyladipamide: **2**) in the mixture of DMF and water (1/1) at 20 °C (Figure 1). The polymerization was performed at the initial feed ratio as follows: [NIPAM]₀ = 4000 mM, [**1**]₀ = 80 mM, and [**2**]₀ = 0 or 80 mM (50:1:0 or 50:1:1 molar ratio). In the absence of **2**, the triethanolamine-bearing dichloroacetamide **1** acted as the difunctional initiator for the chain-growth living radical polymerization of NIPAM, in which the NIPAM monomer was completely consumed within 10 min (Figure 1A). On the other hand, **1** and the resulting telechelic polymer can be difunctional AA-monomer and oligomers for step-growth radical polymerization in the combination with **2** as the BB-monomer, in which the reactive C–Cl and unconjugated C=C bonds form new C–C bonds in the main chain. During the polymerization of the three components, i.e. **1**, **2**, and NIPAM, the monomers were simultaneously consumed. Although the consumption rate of unconjugated C=C double bonds in **2** was much slower than the others, the C=C bonds consumption did not cease even after the quantitative consumption of NIPAM and C–Cl bonds in **1** (Figure 1B), which is almost the same tendency with the previously shown results in the binary system of AB-monomer and NIPAM (26). This result indicates that the simultaneous chain- and step-growth radical polymerization also proceeded for the three components system of AA-, BB-monomer, and NIPAM.

The molecular weight and polydispersity of the polymer thus obtained were evaluated. Figure 2 illustrates the SEC curves obtained in the chain-growth living radical polymerization of NIPAM with **1** (A) and the simultaneous chain- and step-growth radical polymerization of NIPAM with **1** and **2** (B), while the number-average molecular weights (*M_n*) of the resulting polymers were plotted as the function of the NIPAM conversions in Figure 3. The SEC curves of the

polymer obtained in the absence of **2** shifted to the higher molecular weight region as the reaction proceeded, retaining very narrow molecular weight distribution. The M_n values by SEC based on a PMMA standard calibration increased in direct proportion to the NIPAM conversion, although they were higher than the calculated values, assuming that one dichloroacetamide **1** molecule generates one poly(NIPAM) chain, due to the difference in their hydrodynamic volumes. This indicates that a difunctional living chain-growth radical polymerization proceeded well with the **1**/CuCl/Me₆TREN system to form poly(NIPAM) ($DP_n = 50$) with telechelic Cl functionalities at both chain ends and a triethanolamine moiety derived from **1** in the middle of chain.

In contrast, the M_n values of the polymers obtained in the presence of **2** proportionally increased with the NIPAM conversion retaining a relatively narrow distribution curves in SEC only at the initial stage of the reaction, and then progressively increased with the SEC curves getting broader and somehow multimodal after the complete consumption of NIPAM. These results suggest that during the initial stage of the polymerization **1** was consumed to induce the NIPAM living polymerization as the difunctional initiator to give the chlorine-end telechelic poly(NIPAM) and that the step-growth propagation between the two C–Cl bonds at chain ends of poly(NIPAM) and the C=C double bonds in unconjugated diene **2** followed to result in the multiblock polymers consisting of poly(NIPAM) segments with approximately $DP_n = 50$ and a central triethanolamine moiety connected by the amide linkages. Thus, the periodic triethanolamine functionality was introduced every 50 NIPAM units.

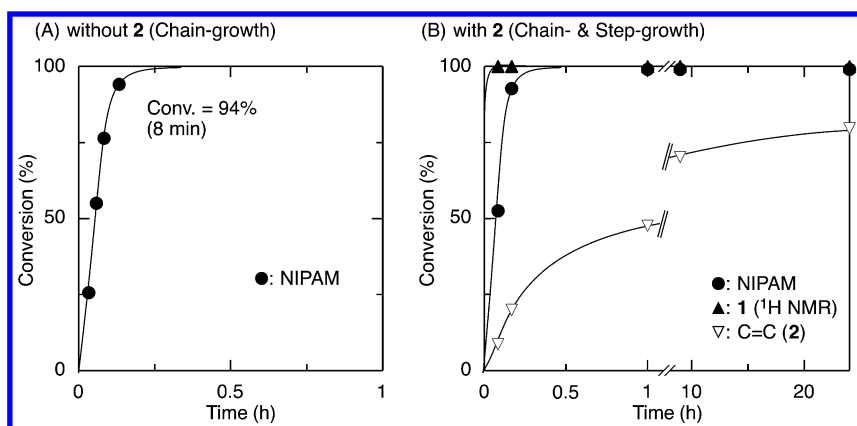


Figure 1. Time-conversion curves for Cu-catalyzed radical polymerization of NIPAM with **1** in the presence (A: chain-growth living) or absence of **2** (B: simultaneous step- & chain-growth) in DMF/H₂O = 1/1 at 20 °C: [NIPAM]₀ = 4.0 M, [**1**]₀ = 80 mM, [**2**]₀ = 0 or 80 mM, [CuCl]₀ = 80 mM, [Me₆TREN]₀ = 80 mM.

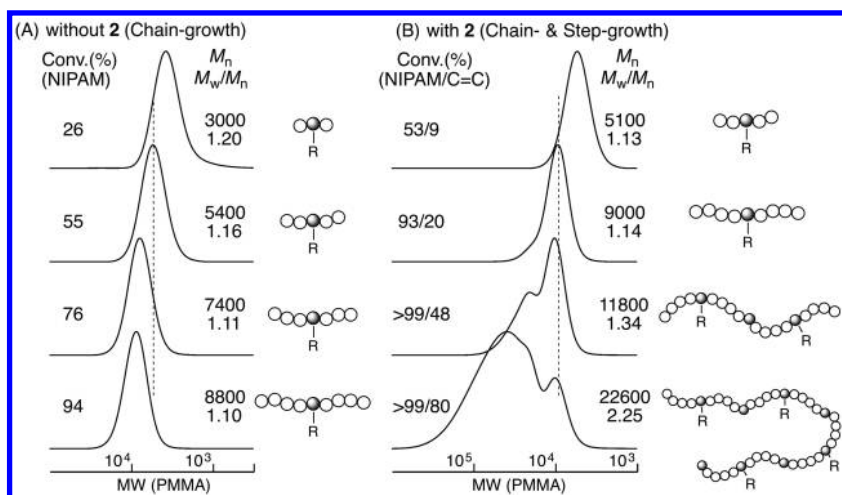


Figure 2. Size-exclusion chromatograms of poly(NIPAM) obtained in the chain-growth living (A) and simultaneous step- & chain-growth radical polymerization (B): $[NIPAM]_0 = 4.0 M$, $[1]_0 = 80 mM$, $[2]_0 = 0$ or $80 mM$, $[CuCl]_0 = 80 mM$, $[Me_6TREN]_0 = 80 mM$ in $DMF/H_2O = 1/1$ at $20^\circ C$.

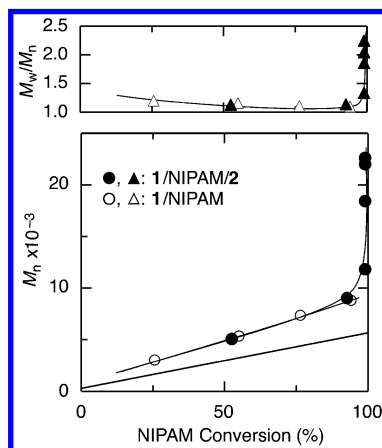


Figure 3. M_n curves of poly(NIPAM) obtained in the chain-growth living and simultaneous step- & chain-growth radical polymerization as the function of NIPAM conversion: $[NIPAM]_0 = 4.0 M$, $[1]_0 = 80 mM$, $[2]_0 = 0$ or $80 mM$, $[CuCl]_0 = 80 mM$, $[Me_6TREN]_0 = 80 mM$ in $DMF/H_2O = 1/1$ at $20^\circ C$. The diagonal bold line indicates the calculated M_n assuming the formation of one living polymer per one **1** molecule.

By changing the initial feed ratio of the three components, the interval of the functionalities can be tuned along with the poly(NIPAM) main chain. The polymerization was also conducted using larger amounts of step-growth monomers **1** and **2** with the initial feed ratio: $[NIPAM]_0 = 4000 mM$, $[1]_0 = [2]_0$

= 160 mM (25:1:1 molar ratio). The three monomers were similarly consumed via simultaneous chain- and step-growth polymerization to give the polymers with periodic triethanolamine functionality every 25 NIPAM units, where the M_n initially increased in direct proportion to the NIPAM conversions with the slope of line almost half to that with 50 NIPAM units in the early stage (Figure 4). However, the final molecular weights of the polymer with 25 units was not so different from that with 50 units. The average number of the functional groups in polymer chains of the final products can be calculated by the final molecular weights to be 2.5 and 3.7 per polymer chain for the polymers with every 50 and 25 NIPAM units, respectively.

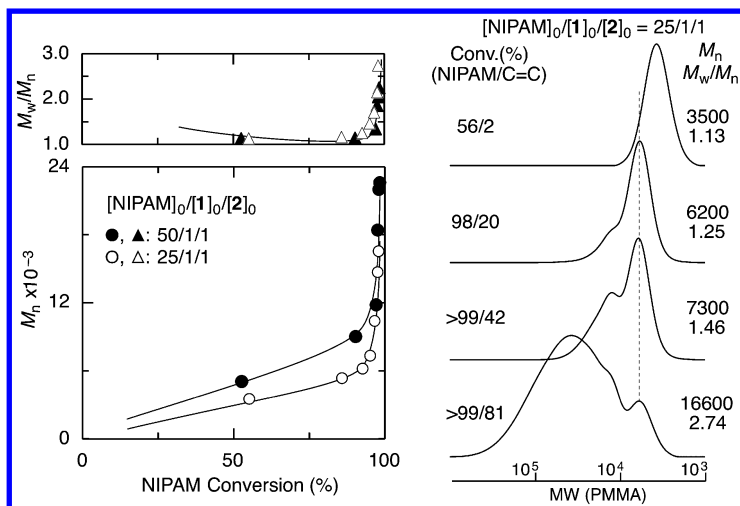


Figure 4. Effect of the initial feed ratio in the simultaneous step- & chain-growth radical polymerization of NIPAM, **1**, and **2**: $[NIPAM]_0 = 4.0$ M, $[1]_0 = [2]_0 = [CuCl]_0 = [Me_6TREN]_0$, $[NIPAM]_0/[1]_0/[2]_0 = 50/1/1$ or $25/1/1$ in DMF/H₂O = 1/1 at 20 °C.

3. Titanatrane Introduction to Periodically-Functionalized Poly(NIPAM)

On the basis of the success in preparing periodically triethanolamine-functionalized poly(NIPAM)s, the loading of titanatrane was investigated with Cp*TiCl₃ using the triethanolamine moiety as the multidentate ligand (13). The reaction was performed with an incremental addition of the Cp*TiCl₃ solution in the presence of Et₃N in CHCl₃, at 0 °C, where the feed ratio was $[triethanolamine]_0/[Cp^*TiCl_3]_0 = 1/2$, and was completed by stirring for another 24 h at ambient temperature. The polymers produced via post-reactions with TiCp*Cl₃ were analyzed by ¹H NMR spectroscopy. Figure 5 shows the ¹H NMR spectra of poly(NIPAM) with periodic functionality every 50 NIPAM units before (A) and after Ti loading (B). In addition to the broad signals of main-chain NIPAM units (*a–e*), small peaks attributed to the unconjugated olefin at chain ends (*k* and *l*) were observed in both spectra, although those attributed to the active C–Cl could not be detected due to overlapping with the main chain peaks.

This again indicates that simultaneous metal-catalyzed chain- and step-growth polymerizations proceeded to form periodically functionalized poly(NIPAM). After the reaction with Cp^*TiCl_3 , a series of characteristic peaks appeared that can be assigned to discrete titanatrane structures. The sharp peak of methyl groups in Cp^* (x) at 1.8 ppm clearly indicates that the conversion from triethanolamine ligand to titanatrane took place, although its quantitative introduction cannot be confirmed due to the broad and overlapped peaks.

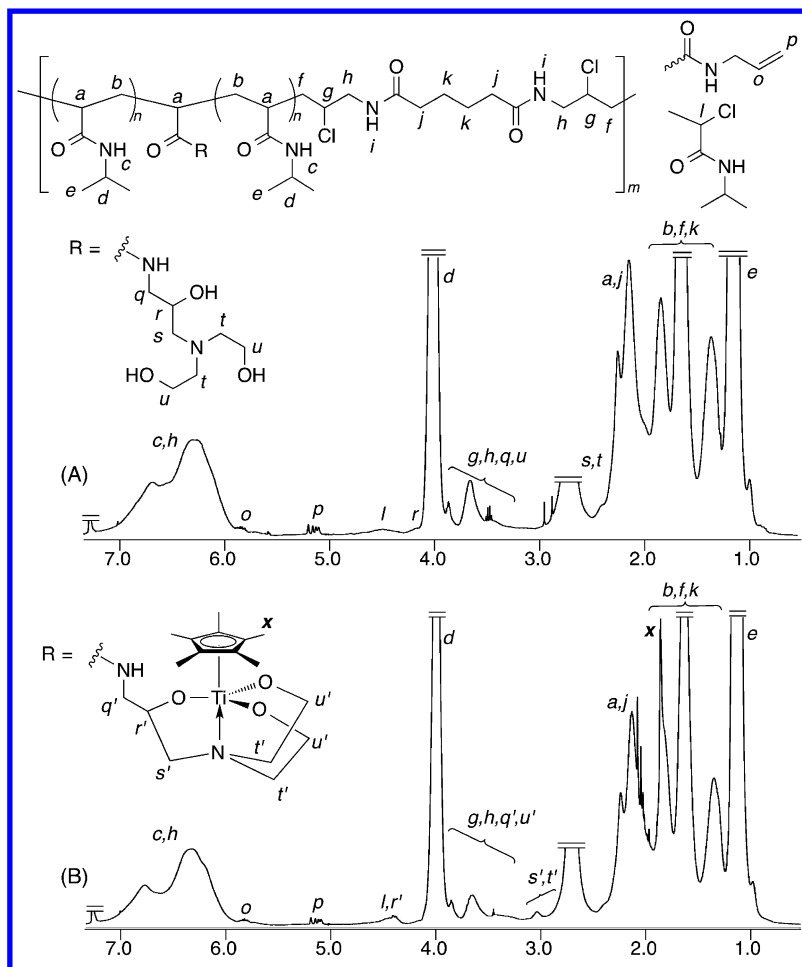


Figure 5. ^1H NMR spectra (400 MHz, CDCl_3 , 55 $^\circ\text{C}$) of poly(NIPAM) obtained in the simultaneous chain- and step-growth radical polymerization of NIPAM, **1**, and **2** ($[\text{NIPAM}]_0/[\mathbf{1}]_0/[\mathbf{2}]_0 = 50/1/1$) before (A) and after post-polymerization reaction (B) with TiCp^*Cl_3 .

The obtained organotitanium-containing poly(NIPAM)s were also analyzed by UV-vis spectroscopy in aqueous solutions at ambient temperature, of which the periodic functionalities were introduced every 50 (A) and 25 NIPAM units

(B) in Figure 6. Before the loading of titanium element, the UV-vis spectra of the aqueous solutions showed only absorbance by the C=O bonds in the NIPAM units. After the reaction with Cp*TiCl₃, the absorbance of titanatrane appeared most probably due to the aromatic Cp* and Ti–O bonds. In addition, the peak intensity increased as the interval of the functional groups shortened and the concentration of the titanatrane increased. These results indicate not only the successful introduction of organotitanium complex to the periodically functionalized poly(NIPAM), but also the stability of the introduced Cp*-titanatrane complex toward water, as in the case that introduced into the hydrophobic segments in the previous work (13).

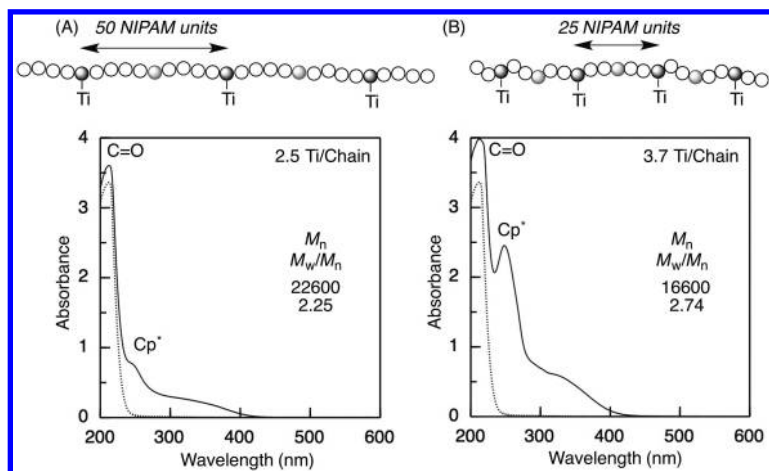
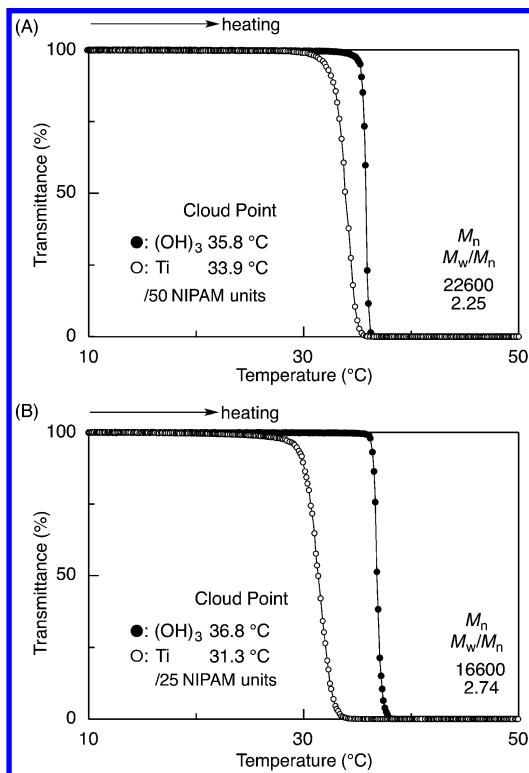


Figure 6. UV-vis absorption spectra of the aqueous solution (1.0 wt%) of poly(NIPAM) obtained in the simultaneous chain- and step-growth radical polymerization of NIPAM, **1**, and **2** ($[NIPAM]_0/[1]_0/[2]_0 = 50/1/1$ (A) or $25/1/1$ (B)) before (dotted line) and after (solid line) post-polymerization reaction to titanatrane.

4. Thermoresponsive Property of Ti-Loaded Poly(NIPAM)

The thermoresponsive properties in aqueous solutions were analyzed for the organotitanium-containing poly(NIPAM)s and their triethanolamine-functionalized precursors obtained by the simultaneous polymerization. Figure 7 shows cloud-point curves for the transmittances of visible light as a function of temperature for the aqueous solutions of the polymers with the periodic functionalities every 50 (A) and 25 NIPAM units (B). Despite of the interval of functionality, the introduction of hydrophobic titanatrane lowered the LCST. More specifically, before the introduction of titanatrane (filled circles in Figures 7A and 7B), the LCST of the polymer with the functionality every 25 units (36.8 °C, Figure 7B) was slightly higher than that with 50 units (35.8 °C, Figure 7A) because the hydrophilic triethanolamine contents were higher for the former. After the titanium loading, however, the LCST temperature decreased to 31.3 °C

and 33.9 °C, respectively. The former was lower due to the higher content of the hydrophobic titanatrane (open circles), although the transition also became broader as increase of the titanatrane contents. These results again indicate that the titanium elements were successfully introduced in the polymer pendant as the titanatrane structures and the resultant organotitanium was stable even in the aqueous solution to show specific thermoresponsivity of the NIPAM polymers.



*Figure 7. Cloud point curves for the aqueous solutions of poly(NIPAM) obtained in the simultaneous chain- and step-growth radical polymerization of NIPAM, **1**, and **2** ($[NIPAM]_0/[1]_0/[2]_0 = 50/1/1$ (A) or $25/1/1$ (B)) before and after post-polymerization reaction to titanatrane. Conditions: concentration = 10 mg/mL, heating rate = 1.0 °C/min, cloud point was determined by the temperature at which the transmittance ($\lambda = 500$ nm) of aqueous solution reach 50%.*

In conclusion, the periodically organotitanium-functionalized poly(NIPAM) was successfully prepared by quantitative simultaneous chain- and step-growth radical polymerization of NIPAM, dichloroacetamide (**1**), and unconjugated diene (**2**) with CuCl/Me₆TREN system, which was followed by the reaction with Cp*TiCl₃ to form a titanatrane structure. The obtained polymer showed water-tolerance and specific thermoresponsivity by tuning the loading ratio, which is potentially applied as smart materials, such as stimuli-responsive catalyst in organic chemistry or drug delivery and imaging agent in biomedical field.

This methodology will provide various types of organometal-containing and water-soluble fusion materials.

Experimental

Materials

N-Isopropylacrylamide (NIPAM) (TCI, > 98%) was recrystallized from hexane and toluene (10/1 v/v). *N,N'*-Diallyladipamide (**2**) was synthesized from adipoyl chloride (TCI, > 98%) and allylamine (TCI, > 99%). CuCl (Aldrich, 99.99%) was used as received. CuCl was handled in a glovebox (MBRAUN LABmaster sp) under a moisture- and oxygen-free argon atmosphere (O₂, < 1 ppm). Methyl dichloroacetate (TCI, > 99%), epichlorohydrin (TCI, > 99%), diethanolamine (Tokyo Kasei, >99%), and triethylamine (Tokyo Kasei, >99%) were distilled from calcium hydride before use. TiCp*Cl₃ (Tokyo Kasei, >97%) and sodium azide (KANTO, >97%) were used as received. DMF was distilled from calcium hydride under reduced pressure and bubbled with dry nitrogen for 15 min just before use. Distilled water was bubbled with dry nitrogen for 15 min just before use.

Synthesis of Triethanolamine-Bearing Dichloroacetamide (**1**)

The triethanolamine-bearing dichloroacetamide (**1**: *N*-(3-(bis(2-hydroxyethyl)amino)-2-hydroxypropyl)-2,2-dichloroacetamide) was synthesized as follows. The reaction was carried out by the use of a syringe technique under dry argon atmosphere in an oven-dried glass tube equipped with three-way stopcocks. Epichlorohydrin (50.0 mL, 0.619 mol) was added dropwise with vigorous stirring to a solution of diethanolamine (48.8 mL, 0.509 mol) in dry THF (220 mL) at 0 °C. The mixture was heated to 50 °C and kept stirred for 12 h to form white solid of (1-chloromethyl)triethanolamine. After filtration, the solid was washed with acetone and dried in vacuo. In another 200 mL flask, the (1-chloromethyl)triethanolamine (20.0 g, 0.101 mol) and NaN₃ (19.8 g, 0.305 mol) were dissolved in 105 mL of DMF. For nucleophilic substitution of the C–Cl bond with NaN₃, the flask was immersed in thermostatic oil bath at 45 °C, and the solution was stirred for 48 h. The solution was filtrated to remove NaCl and concentrated under reduced pressure to afford the azide-analogue (16.2 g, 0.080 mol). The product was dissolved again in 105 mL of DMF and added by triphenylphosphine (45.0 g, 0.172 mol) as the reducing agent. The solution was stirred for another 48 h at ambient temperature, and then 400 mL of water was added to the reaction mixture for hydrolysis. The solution was filtrated and concentrated under reduced pressure to afford a primary amine analogue of (1-aminomethyl)triethanolamine (14.5 g, 0.080 mol). The amine was dissolved in 50 mL of methanol, and to the solution was added dropwise 20 mL of methyl dichloroacetate (0.193 mol) at 0 °C for 10 min. The solution was stirred for another 48 h at ambient temperature, and then under dried under reduced pressure to afford the triethanolamine-bearing dichloroacetamide (**1**). The product was

further purified by column chromatography to yield pure **1** as clear and colorless viscous oil (5.50 g, 0.019 mol).

Simultaneous Chain- and Step-Growth Radical Polymerization

The simultaneous polymerization was carried under dry argon in baked 25 mL glass tubes equipped with a three-way stopcock. A typical example for the polymerization procedure is given below. CuCl (63.4 mg, 0.640 mmol) was put in the glass tube, and Me₆TREN (0.185 mL, 0.640 mmol) and water (1.36 mL) were added. The solution was stirred for 1 h to become a heterogeneous system composed by blue solution and brownish metal powder, which indicates disproportionation of Cu(I)Cl into Cu(II)Cl₂ and Cu(0). The polymerization was initiated by adding the monomer solution (6.40 mL), containing NIPAM (3.62 g, 32.0 mmol), triethanolamine-bearing dichloroacetamide **1** (184 mg, 0.640 mmol), and unconjugated diene **2** (144 mg, 0.640 mmol) in DMF (1.38 mL) and water (0.590 mL) at 20 °C. The total volume of the reaction mixture was thus 8.0 mL. The polymerization reaction was sampled in predetermined intervals. The monomer conversions of NIPAM and the functional groups (C–Cl in **1** and C=C in **2**) were determined from the concentration of residual NIPAM, C–Cl, and C=C by ¹H NMR spectroscopy (conversions for 24 h: >99 %, >99%, 80% for NIPAM, C–Cl, and C=C, respectively). The samples were dissolved in THF and passed through a short silica column to remove the catalyst. The M_n and M_w/M_n values were determined by GPC with PMMA standards ($M_n = 22,600$, $M_w/M_n = 2.25$).

Synthesis of Titanium-Containing Polymer

The periodically functionalized poly(NIPAM) with the multidentate triethanolamine ligands was then treated with titanium compounds. The polymer (0.30 g), 0.038 g of TiCp*Cl₃ (2 eq. to triethanolamine units), and 0.14 mL of triethylamine was dissolved in CHCl₃ (4.0 mL) and stirred at room temperature for 22 h. The reaction mixture was evaporated to dryness, and the product was redissolved in CHCl₃, washed with hot water 3 times, dried on MgSO₄, concentrated under reduced pressure, and precipitated from *n*-hexane to afford periodically titanium-containing polymer as slightly yellowish solid.

Measurements

¹H NMR spectra were recorded in CDCl₃ at 25 °C on a JEOL ECS-400 spectrometer, operating at 400 MHz. The number-average molecular weight (M_n), weight-average molecular weight (M_w), and the molecular weight distribution (M_w/M_n) of the product polymers were determined by size-exclusion chromatography (SEC) in DMF containing 100 mM LiCl at 40 °C on two polystyrene gel columns [Shodex K-805L (pore size: 20–1000 Å; 8.0 mm i.d. × 30 cm); flow rate 1.0 mL/min] connected to Jasco PU-980 precision pump and a Jasco 930-RI refractive index detector. The columns were calibrated against 7 standard poly(MMA) samples (Shodex; $M_p = 1850$ – 1950000 ; $M_w/M_n = 1.02$ – 1.09). The transmittance and UV/vis absorption spectra were recorded using

a JASCO V-550 UV/vis spectrometer equipped with a Peltier-type ETC-505 thermostatic cell holder. The transmittance of a 10 mg/mL aqueous solution of the samples was measured by monitoring the transmittance of a 500 nm light beam through a 1 cm quartz sample cell at the rate of 1.0 °C/min during the heating scans. The LCST is defined as the temperature at which the transmittance of the aqueous solution for the samples is reduced to 50%.

Acknowledgments

This work was supported in part by a Grant-in-Aid for Scientific Research on Innovative Areas “Fusion Materials (Creative Development of Materials and Exploration of their Function through Molecular Control; Area No. 2203)” (No. 25107714) for K.S. from the Ministry of Education, Culture, Sports, Science and Technology, Japan, and Program for Leading Graduate Schools “Integrative Graduate Education and Research Program in Green Natural Sciences”.

References

1. *Frontiers in Transition Metal-Containing Polymers*; Abd-El-Aziz, A. S., Manners, I., Eds.; Wiley-Interscience: Hoboken, NJ, 2007.
2. Whittell, G. R.; Manners, I. *Adv. Mater.* **2007**, *19*, 3439–3468.
3. Abd-El-Aziz, A. S. *Macromol. Rapid Commun.* **2002**, *23*, 995–1031.
4. Grubbs, R. B. *J. Polym. Sci., Part A: Polym. Chem.* **2005**, *43*, 4323–4336.
5. Kato, T. *Adv. Mater.* **2000**, *12*, 1543–1546.
6. Kato, T.; Sugawara, A.; Hosoda, N. *Adv. Mater.* **2000**, *14*, 869–877.
7. Wasser, I. M.; de Vries, S.; Moenne-Loccoz, P.; Schroder, I.; Karlin, K. D. *Chem. Rev.* **2002**, *102*, 1201–1234.
8. Bellas, V.; Rehahn, M. *Angew. Chem., Int. Ed.* **2007**, *46*, 5082–5104.
9. Kamigaito, M. In *Redox Systems under Nano-Space Control*; Hirao, T., Ed.; Springer: Heiderberg, Germany, 2006, pp 233–247.
10. Macomber, D. W.; Hart, W. P.; Rausch, M. D. *J. Am. Chem. Soc.* **1982**, *104*, 884–886.
11. Branham, K. E.; Mays, J. W.; Gray, G. M.; Sanner, R. D.; Overturf, G. E., III; Cook, R. *Appl. Organomet. Chem.* **1997**, *11*, 213–221.
12. Tomita, I.; Ueda, M. *J. Inorg. Organomet. Polym. Mater.* **2006**, *15*, 511–518.
13. Tsujimoto, Y.; Satoh, K.; Sugimori, H.; Jinnai, H.; Kamigaito, M. *Macromolecules* **2014**, *47*, 944–953.
14. Verkade, J. G. *Acc. Chem. Res.* **1993**, *26*, 483–489.
15. Verkade, J. G. *Coord. Chem. Rev.* **1994**, *137*, 233–295.
16. Schild, H. G. *Prog. Polym. Sci.* **1992**, *17*, 163–249.
17. Hsu, S.-H.; Yu, T.-L. *Macromol. Rapid Commun.* **2000**, *21*, 476–480.
18. Bergbreiter, D. E. *Chem. Rev.* **2002**, *102*, 3345–3384.
19. Bergbreiter, D. E.; Tian, J.; Hngfa, C. *Chem. Rev.* **2009**, *109*, 530–582.
20. Aoshima, S.; Kanaoka, S. *Adv. Polym. Sci.* **2008**, *210*, 169–208.
21. Teodorescu, M.; Matyjaszewski, K. *Macromol. Rapid Commun.* **2000**, *21*, 190–194.

22. Masci, G.; Giacomelli, L.; Crescenzi, V. *Macromol. Rapid Commun.* **2004**, *25*, 559–564.
23. Millard, P. E.; Mougin, N. C.; Böker, A.; Müller, A. H. E. *ACS Symp. Ser.* **2009**, *1023*, 127–137.
24. Nguyen, N. A.; Rosen, B. M.; Percec, V. *J. Polym. Sci., Part A: Polym. Chem.* **2010**, *48*, 1752–1763.
25. Han, Y.; Nishimura, T.; Kato, T. *Polym. J.* **2014**, *46*, 499–504.
26. Mizutani, M.; Satoh, K.; Kamigaito, M. *Macromolecules* **2011**, *44*, 2382–2386.
27. Mizutani, M.; Satoh, K.; Kamigaito, M. *J. Am. Chem. Soc.* **2010**, *132*, 7498–7507.
28. Mizutani, M.; Satoh, K.; Kamigaito, M. *Aust. J. Chem.* **2014**, *67*, 544–554.
29. Mizutani, M.; Palermo, E.; Thoma, L.; Satoh, K.; Kamigaito, M.; Kuroda, K. *Biomacromolecules* **2012**, *13*, 1544–1563.
30. Satoh, K.; Abe, T.; Kamigaito, M. *ACS Symp. Ser.* **2012**, *1100*, 133–144.

Chapter 2

Side-Chain Cobaltocenium-Containing Polymers: Controlled Polymerization and Applications

Yi Yan, Jiuyang Zhang, and Chuanbing Tang*

Department of Chemistry and Biochemistry, University of South Carolina,
631 Sumter Street, Columbia, South Carolina 29208, United States

*E-mail: tang4@mailbox.sc.edu

Due to the cationic nature, cobaltocenium-containing polymers are novel metal-containing polyelectrolytes, which could find applications in the fields of magnetic materials, stimuli-responsive materials, chemical/bio sensors and antimicrobials. More interestingly, these polymers show counterion-dependent solubility and hereinafter unique properties. Functional cobaltocenium-containing polymers can be prepared through either direct polymerization of cobaltocenium-functionalized monomers or post-polymerization modification of precursor polymers. This chapter summarizes the most recent progress of side-chain cobaltocenium-containing polymers via controlled polymerization methods, such as ATRP, RAFT, and ROMP. Different methods involving the synthesis of cobaltocenium-containing monomers are discussed. Furthermore, self-assembly and biomedical applications of these metallopolymers in the field of antimicrobials are introduced.

Introduction

During the past several decades, metallopolymers have been widely studied due to their diverse applications as optic, electronic, and magnetic materials, catalysts, and ceramic precursors (1, 2). By incorporation of functional sandwich-structured metallocenes into polymer materials, metallocene-based polymers represent classical metallopolymers (3–5). Different from conventional

neutral ferrocene-containing polymers (6), cobaltocenium-containing polymers are unique due to their charged state and highly stable chemical property, in other words, a novel metal-containing polyelectrolyte (7, 8). However, because of the charged state, there has been a considerable challenge to synthesize mono-substituted cobaltocenium, which is the first step to prepare side-chain cobaltocenium-containing polymers (9).

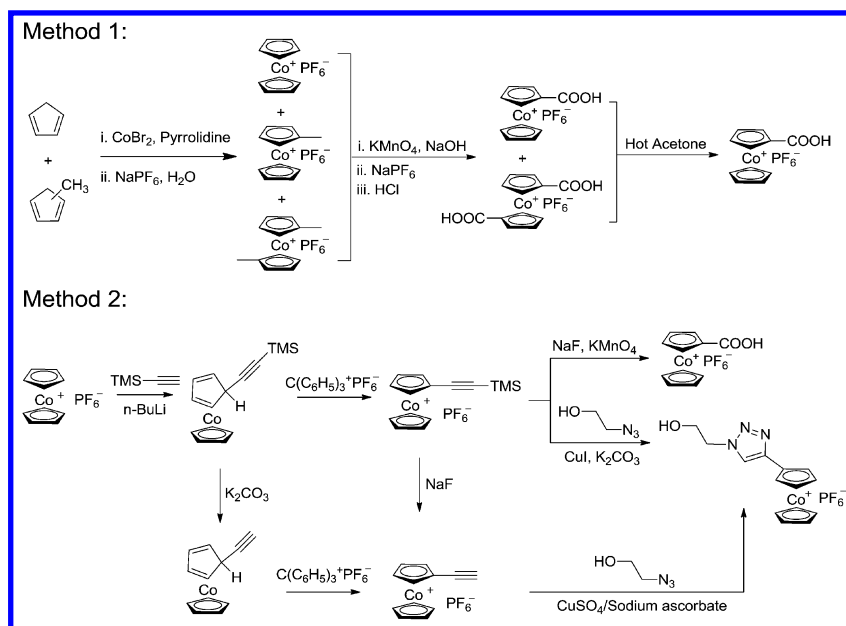
From the view of synthetic chemistry, there are two aspects for consideration to obtain cobaltocenium-containing polymers: (i) synthesis of mono-substituted cobaltocenium, which can be further converted to polymerizable monomers. Although metallocene chemistry has a long history, the chemistry of cobaltocenium is still much less understood and developed; (ii) control over the polymer structure. Controlled polymerization techniques such as atom transfer radical polymerization (ATRP), reversible addition-fragmentation chain transfer polymerization (RAFT) and ring-opening metathesis polymerization (ROMP) could offer a good control on molecular weight, architecture and functionality as well as low dispersity (10–17). They can be used to create functional metal-containing block copolymers (18). Meanwhile, post-polymerization modification of precursor polymers can also give cobaltocenium-containing polymers with pre-existing well-defined structures.

In this contribution, we discuss our recent work on the synthesis of functional side-chain cobaltocenium-containing polymers and their self-assembly into nanostructures, as well as their applications. For main-chain cobaltocenium-containing polymers, the readers should refer to recent work carried out by the Manners group (7, 8, 19, 20).

Results and Discussion

Synthesis of Mono-Substituted Cobaltocenium Derivatives and Their Monomers

Different from neutral metallocenes (e.g. ferrocene), it is very challenging to carry out direct electrophilic substitution on the charged cobaltocenium, which is a key hurdle in cobaltocenium chemistry (9). Basically, two approaches have been established to synthesize mono-substituted cobaltocenium, as shown in Scheme 1: (i) a statistical reaction between methyl cyclopentadiene, cyclopentadiene and cobalt bromide, followed by further oxidation and exhausted separation to give cobaltocenium monoacid, which can be further converted into vinyl monomers (**method 1** in Scheme 1) (9); (ii) reaction between un-substituted cobaltocenium and a nucleophile based on organolithium reagents, followed by hydride abstraction to give mono-substituted cobaltocenium (**method 2** in Scheme 1) (21–23). Due to the nature of the statistical reaction, the first method (**method 1**) is very tedious and produces low yield (ca. 7-14%), while with the facile nucleophilic addition (almost 100% yield) and selective hydride abstraction of the endo-proton, **method 2** is more efficient and can give ethynylcobaltocenium with a total yield of ~30% (23).

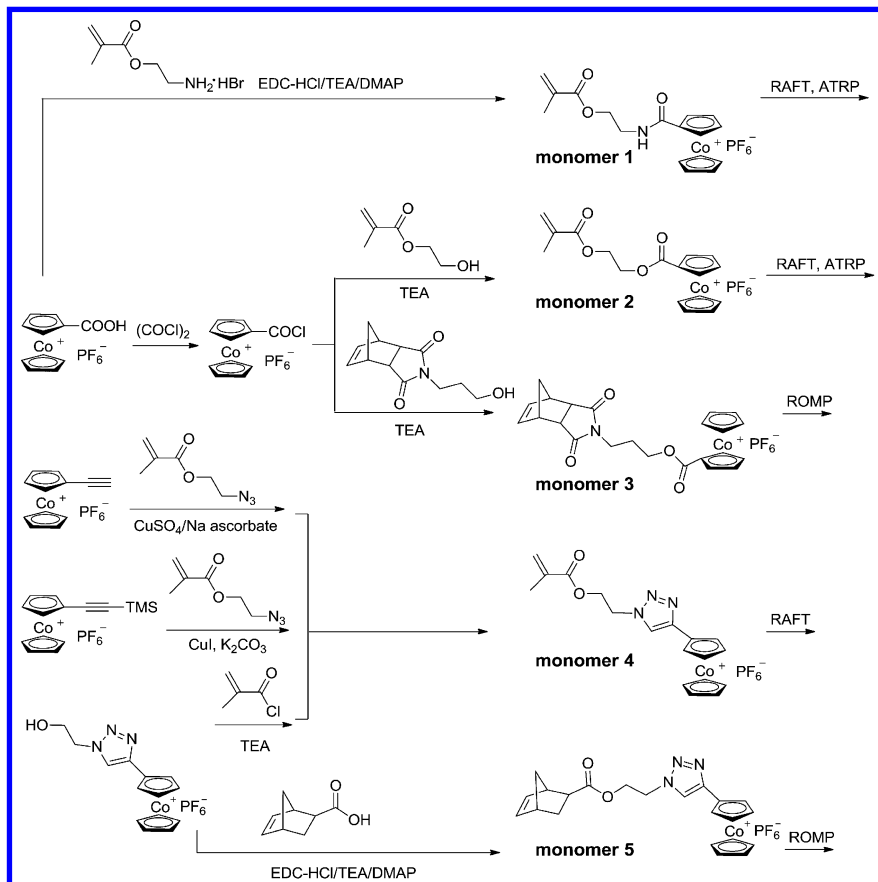


Scheme 1. Two different methods to synthesize mono-substituted cobaltocenium with different functional groups.

Furthermore, ethynylcobaltocenium can react with different azides through a copper-catalyzed azide-alkyne cycloaddition (CuAAC) to give mono-substituted cobaltocenium with different functional groups. To simplify this reaction and avoid purification by column chromatography, we find the easily synthesized TMS-protected ethynylcobaltocenium can be directly used in the CuAAC reaction catalyzed by copper iodide with an in-situ deprotection of TMS group by potassium carbonate. By using azide compounds with different functional groups (hydroxyl-, amine-, carboxyl-, etc.), mono-substituted cobaltocenium can be prepared in a total yield of ~80% without any column purification. Interestingly, in an independent study reported by Herwig Schottenberger and coworkers a few months later after our work, they found a similar and efficient pathway to deprotect the TMS-ethynylcobaltocenium (as shown in Scheme 1, **method 2**) (24). Meanwhile, they also developed direct oxidation of TMS-protected cobaltocenium to synthesize cobaltocenium monoacid with a yield as high as 95% and purity >97%, which could be used to prepare cobaltocenium-containing monomers with an ester bond linker.

As shown in Scheme 2, with the functional mono-substituted cobaltocenium, different cobaltocenium-containing monomers can be prepared. Generally, starting from cobaltocenium monoacid or its acyl chloride, cobaltocenium monomers **1**, **2** and **3** can be synthesized through either amidation or esterification with different amines or alcohols respectively (25). Meanwhile, taking advantage of the facile CuAAC reaction of TMS-protected ethynylcobaltocenium or ethynylcobaltocenium, cobaltocenium monomers **4** and **5** with a triazole linker can be prepared (21). For these monomers, we can find: (i) methacrylate

monomers **1** and **2** with an amide or an ester bond as a linker can be polymerized through either RAFT or ATRP; (ii) norbornene monomers **3** and **5** with either an ester bond or a triazole as a linker can be polymerized through ROMP; (iii) methacrylate monomer **4** with a triazole as a linker can be polymerized through RAFT process.



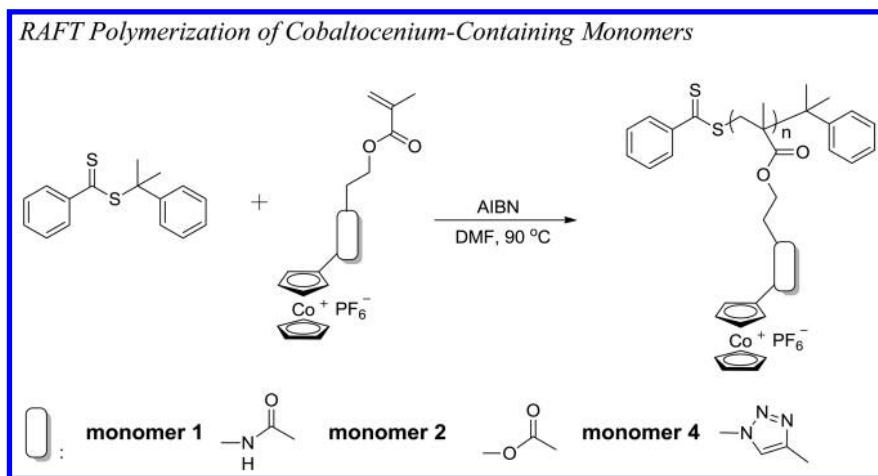
Scheme 2. Synthesis of different cobaltocenium-containing monomers.

Controlled Polymerization of Cobaltocenium-Containing Monomers

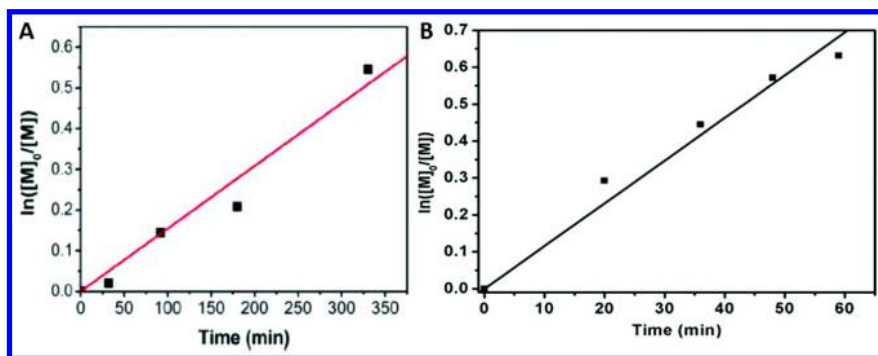
RAFT Polymerization of Cobaltocenium-Containing Monomers

As shown in Scheme 3, methacrylate monomers **1**, **2**, and **4** with different linkers can be polymerized through RAFT process (15, 21, 26, 27). The polymerizations were typically carried out in DMF at 90 °C with a feed ratio of monomer:CDB:AIBN = 200:1:0.3. As shown in Figure 1, linear kinetic plots of $\ln([M_0]/[M])$ vs. time demonstrated the controlled “living” characteristics of the RAFT process. Meanwhile, the low dispersity ($\bar{D} = 1.25$) of final polymers also indicated the good control of the RAFT process. Furthermore,

using the cobaltocenium-containing homopolymer as a macroinitiator, different second monomers, such as *tert*-butyl acrylate, methyl methacrylate and a ferrocene-containing methacrylate, can be chain-extended to give different diblock copolymers. Kinetic studies showed that all chain extension followed a controlled/“living” process under relatively low conversions. Interestingly, the heterobimetallic diblock copolymer can self-assemble into nanoscale micelles in selective solvents. While the ferrocene units are susceptible to oxidation toward decomposition, the cobaltocenium moiety exhibits extraordinary stability to maintain its structure integrity (26). It should be mentioned that **monomer 1** with an amide linker is more active than the other two monomers, as it can be polymerized at 70 °C, while the other two monomers showed nearly no polymerization at this temperature.



Scheme 3. RAFT polymerization of cobaltocenium-containing monomers.

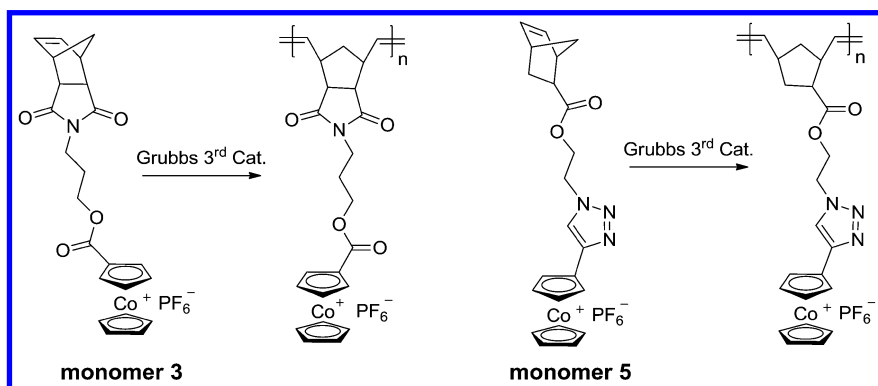


*Figure 1. Representative kinetic plots of RAFT polymerization of different cobaltocenium-containing monomers: A) **monomer 1**; B) **monomer 4**. Figure 1A adapted with permission from reference (26). Copyright 2012 American Chemical Society. Figure 1B adapted with permission from reference (21). Copyright 2014 Wiley-VCH Verlag GmbH & Co. KGaA.*

To tune the amphiphilicity of these cobaltocenium-containing polymers, we developed a strategy for facile counterion exchange by using tetrabutylammonium salts as a phase transfer agent. Different from the PF_6^- -paired polymer, halide-paired cobaltocenium-containing polymers are very soluble in water and show very interesting antimicrobial properties against different bacteria that are resistant to conventional antibiotics. Furthermore, these cobaltocenium-containing polymers can also form bioconjugates with classic antibiotics (penicillin, amoxicillin, and etc.) through electrostatic interactions. The polymer-antibiotic bioconjugates can regenerate the vitality of antibiotics to kill drug-resistant bacteria (28), which will be discussed in a later section. This is a very promising application for cationic metallocenium polyelectrolytes.

ROMP of Cobaltocenium-Containing Monomers

As a powerful controlled polymerization method, ROMP has been broadly used to synthesize well-defined macromolecules (17, 29). Our group reported the first cobaltocenium-containing polymers through ROMP (30). As shown in Scheme 4, polymerization of cobaltocenium-containing norbornene monomers (**monomers 3** and **5**) was carried out in DMF at room temperature with the aid of Grubbs 3rd catalyst. The polymerization was very fast, and can achieve almost 100% conversion within 10 min. According to the corresponding kinetic study, the polymerization showed controlled/“living” nature with a linear relationship between $\ln[M]_0/[M]$ and reaction time (Figure 2). The molecular weight also increased linearly with monomer conversion. Meanwhile, the chain end was still “living” and can be used to further polymerize the second monomers. For example, after the first monomer was completely consumed, addition of second monomers (cobaltocenium-containing norbornene monomers with different counterions (BPh_4^- , Cl^-) and other norbornene monomers) can construct cobaltocenium-containing block copolymers with tunable amphiphilicity.



Scheme 4. ROMP of cobaltocenium norbornene monomers.

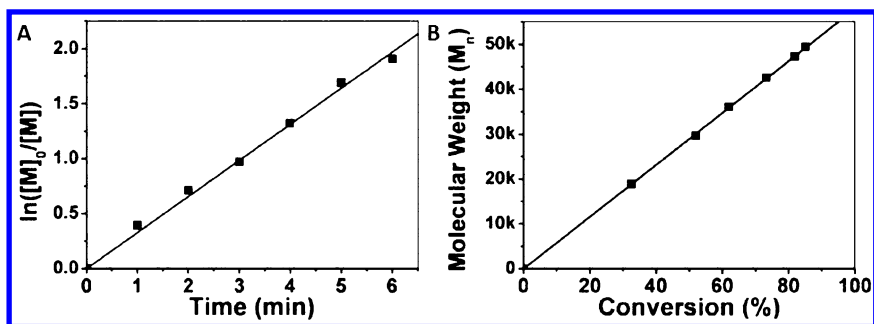


Figure 2. Kinetic plots of ROMP process of *monomer 3* with the aid of Grubbs 3rd catalyst. Adapted with permission from reference (30). Copyright 2012 Royal Society of Chemistry.

Due to the partial hydrophilicity of the PF_6^- -paired polymer (limited solubility in water), the obtained block copolymers were capable of forming micelles, though the micelles were not very stable and would precipitate within hours. This was probably attributed to the ability of ion-exchange between counterions in two cobaltocenium-containing blocks. However, as the Cl^- -paired block is very hydrophilic and the BPh_4^- -paired block is hydrophobic, block copolymer formed micelles that were stable for several days. As expected, micelles resulting from block copolymers could be converted into inorganic nanoparticles upon exposure to UV/ozonolysis or thermal pyrolysis. X-ray diffraction (XRD) and X-ray photoelectron spectroscopy (XPS) analysis of the inorganic nanoparticles resulting from these polymeric micelles confirmed that they consisted of Co_3O_4 and $\text{Co}_2\text{PO}_4\text{F}$. Initial magnetic test revealed that both cobalt oxide species were anti-ferromagnetic (31).

To remove contamination of phosphorous in these nanomaterials, we used a convenient anion-exchange strategy to change the counterion from PF_6^- to different anions (chloride, bromide, iodide and nitrate anions). These polymers could be utilized as universal precursors to prepare diverse advanced cobalt materials such as cobalt metal, cobalt phosphide, cobalt monoxide, cobalt-iron alloy and cobalt ferrite with different nanostructures (Figure 3) (32).

By combining facile ROMP and RAFT, our group reported the first bottle-brush polymers from cobaltocenium-containing monomers using a “grafting from” strategy. As shown in Figure 4, the backbone of this polymer brush was first constructed through the ROMP of dithioester-functionalized norbornene. Further RAFT polymerization of cobaltocenium-containing monomers by the macro-RAFT agent gave the final polymer brush (33). Owing to the solubility change after changing the counterion from PF_6^- to BPh_4^- in acetonitrile, the polymer brush displayed interesting responsiveness and changed from wormlike cylinders to collapsed nanoparticles.

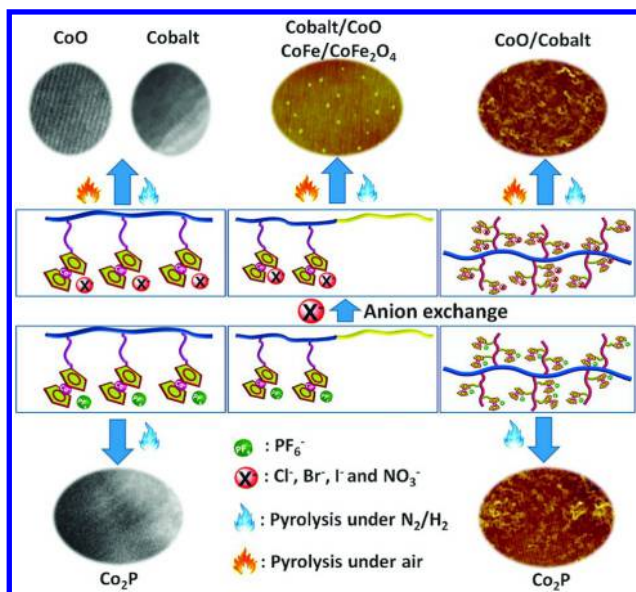


Figure 3. Different cobalt-based nanomaterials made from cobaltocenium polymers. Adapted with permission from reference (32). Copyright 2013 Wiley-VCH Verlag GmbH & Co. KGaA.

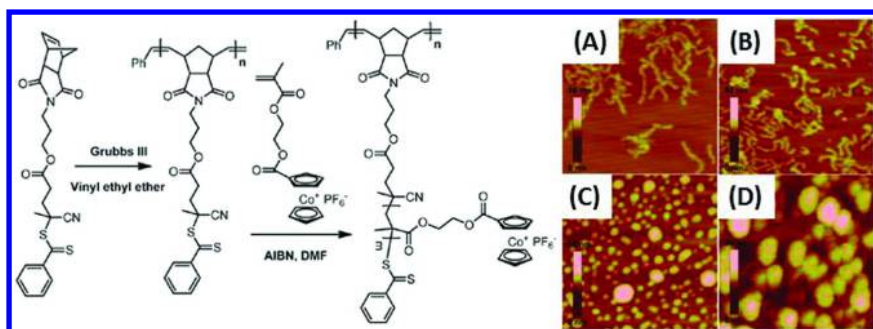


Figure 4. Synthesis of cobaltocenium-containing polymer brush, and AFM images of its response to different ratios of BPh₄⁻/PF₆⁻ (BPh₄⁻ molar ratio gradually increasing from 0:1 (A) to 1:1 (D)). Adapted with permission from reference (33). Copyright 2013 American Chemical Society.

ATRP of Cobaltocenium-Containing Monomers

By combining ATRP (34, 35) and post-polymerization modification, our group reported the first side-chain cobaltocenium block copolymers (Figure 5) (36). The precursor diblock copolymer P⁴BA-*b*-PHEA with hydroxyl

group can be prepared through ATRP by using EBiB/CuBr/PMDETA system. The post-polymerization modification was carried out through esterification between cobaltocenium acyl chloride and hydroxyl group of PHEA block of the PBA-*b*-PHEA diblock copolymer. However, such post-polymerization modification procedure only resulted in ~70% hydroxyl group conversion to cobaltocenium. Nonetheless, the resultant diblock copolymer self-assembled into tubular structures in an acetone/chloroform solvent system. The nanotubes displayed a uniform diameter, ca. 45–55 nm, with an average of wall thickness of 10–14 nm and an average cavity width of 23–29 nm.

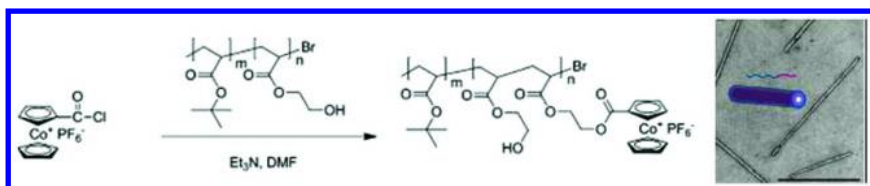
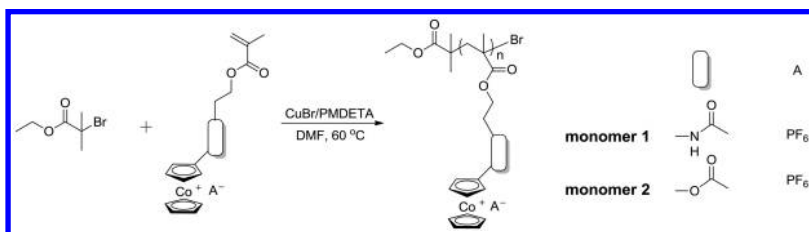


Figure 5. Synthesis of side chain cobaltocenium-containing block copolymer through ATRP and post-polymerization modification, and its nanotubular self-assembled structure in the mixture of acetone and chloroform. Adapted with permission from reference (36). Copyright 2010 American Chemical Society.

By using cobaltocenium-containing EBiB initiator, ATRP of styrene, tert-butyl acrylate, and methyl methacrylate monomers can give cobaltocenium-labeled polymers. Kinetic studies showed that most polymerizations followed a controlled/“living” manner, except that polymerization of methyl methacrylate with displayed significant termination (37).

As shown in Scheme 5, tentative direct ATRP polymerization of cobaltocenium-containing monomers (**monomers 1** and **2**) were carried out by using EBiB as initiator and CuBr/PMDETA as a catalyst system at 90 °C. Kinetic study (Figure 6) shows there was significant termination reactions. If we used the more active monomer **1**, the polymerization can achieve up to 20% conversion even at temperature as low as 60 °C.



Scheme 5. ATRP of cobaltocenium-containing monomers.

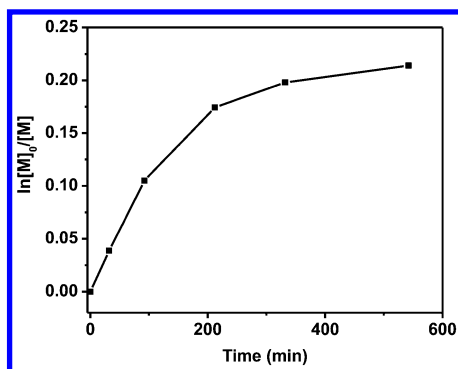


Figure 6. Kinetic plot for the ATRP of monomer 1.

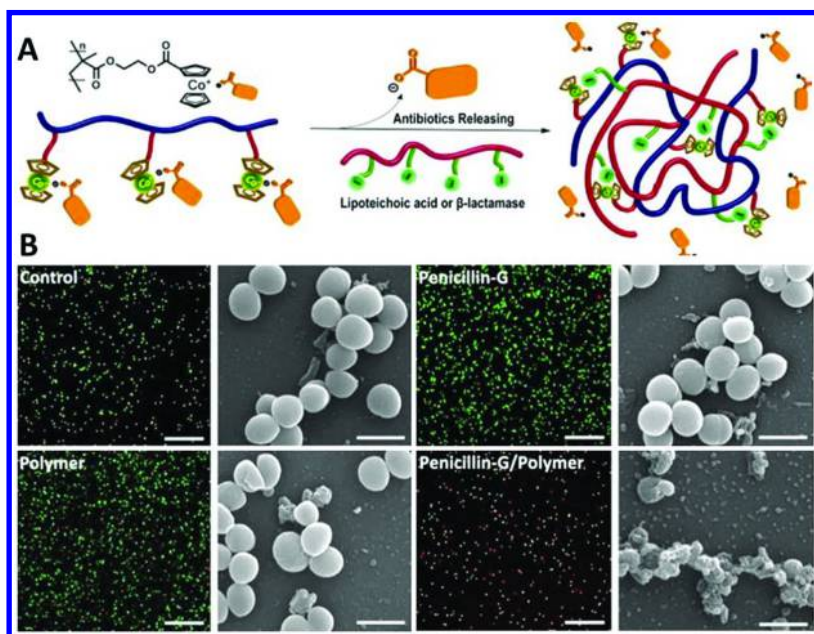


Figure 7. (A) Metallopolymer-antibiotic bioconjugates and the release of antibiotics, and (B) CSLM images and SEM images of HA-MRSA cells incubated respectively in the presence of control solution, 5.6 μ M penicillin-G (2 μ g/mL), 1 μ M Cl⁻-paired cationic cobaltocenium-containing polymers (12.5 μ g/mL), and penicillin-G–metallopolymer bioconjugate (5.6 μ M penicillin-G and 1 μ M metallopolymer). CSLM imaging employed BacLight live/dead stain (green indicates live cells, red indicates dead cells). Scale bars in confocal images, 50 μ m; scale bar in SEM images, 1 μ m. Adapted with permission from reference (28). Copyright 2014 American Chemical Society.

Biomedical Application of Cobaltocenium-Containing Polymers

As mentioned above, the amphiphilicity of these cobaltocenium-containing polymers can be tuned upon counterion exchange with the aid of tetrabutylammonium salts. It was found that the hydrophilic cobaltocenium-containing polymers paired with halide anion (Cl^- , Br^- , and I^-) exhibit synergistic effects against methicillin-resistant *Staphylococcus aureus* (MRSA) by efficiently inhibiting activity of β -lactamase and effectively lysing bacterial cells (28). As demonstrated by the nitrocefin assay, a mixture of halide-paired polymers and nitrocefin in a solution of β -lactamase did not result in appreciable hydrolysis of nitrocefin, while direct mixture of nitrocefin and β -lactamase resulted in significant hydrolysis. The reason for the protection of nitrocefin-like β -lactam antibiotic may be due to the complexation between cationic cobaltocenium moieties and carboxylate anion in antibiotics (Figure 7A).

Similarly, this study can be extended to different conventional β -lactam antibiotics, such as penicillin-G, amoxicillin, ampicillin, and cefazolin. Interestingly, our model studies showed the conjugated antibiotics can be released upon interaction with the negative charged cell wall. As shown in the confocal scanning laser microscopy (CSLM) and scanning electron microscopy (SEM) images (Figure 7B), these bioconjugates showed significantly enhanced antibacterial activities than the corresponding antibiotics. Meanwhile, the metallopolymers themselves also showed efficient inhibition against MRSA at higher concentrations. More importantly, these cationic metallopolymers showed negligible hemolytic effects on red blood cells, although they exhibited excellent abilities to lyse microbial cells.

Conclusions

Using direct controlled polymerization and post-polymerization modification methods, we synthesized a series of cobaltocenium-containing homopolymers, block copolymers and polymer brushes. These cobaltocenium-containing polymers can undergo facile counterion exchange, which could enable a switch of polymers from hydrophobicity to hydrophilicity. These polymers could serve as templating precursors for making different cobalt-based nanomaterials. Furthermore, hydrophilic cobaltocenium-containing polymers could find promising biomedical applications such as antimicrobial agents. In the context of synthetic chemistry, new design of polymer compositions, topologies and functions such as dendrimer and hydrogel would be worthy for exploration. Meanwhile, counterion-dependent properties of these polymers should be further investigated. Future work should also pay more attention to biomedical applications of these cationic metallocenium-containing polymers.

Acknowledgments

Financial support from the National Science Foundation (CHE-1151479) is acknowledged.

References

1. Whittell, G. R.; Hager, M. D.; Schubert, U. S.; Manners, I. *Nat. Mater.* **2011**, *10*, 176–188.
2. Eloi, J.-C.; Chabanne, L.; Whittell, G. R.; Manners, I. *Mater. Today* **2008**, *11*, 28–36.
3. Hardy, C. G.; Zhang, J.; Yan, Y.; Ren, L.; Tang, C. *Prog. Polym. Sci.* **2014**, *39*, 1742–1796.
4. Cui, C.; Heilmann-Brohl, J.; Sánchez Perucha, A.; Thomson, M. D.; Roskos, H. G.; Wagner, M.; Jäkle, F. *Macromolecules* **2010**, *43*, 5256–5261.
5. Abd-El-Aziz, A. S.; Strohm, E. A. *Polymer* **2012**, *53*, 4879–4921.
6. Hardy, C. G.; Ren, L.; Tamboue, T. C.; Tang, C. *J. Polym. Sci., Part A: Polym. Chem.* **2011**, *49*, 1409–1420.
7. Qiu, H.; Gilroy, J. B.; Manners, I. *Chem. Commun.* **2013**, *49*, 42–44.
8. Gilroy, J. B.; Patra, S. K.; Mitchels, J. M.; Winnik, M. A.; Manners, I. *Angew. Chem., Int. Ed.* **2011**, *50*, 5851–5855.
9. Sheats, J. E.; Rausch, M. D. *J. Org. Chem.* **1970**, *35*, 3245–3249.
10. Matyjaszewski, K.; Tsarevsky, N. V. *J. Am. Chem. Soc.* **2014**, *136*, 6513–6533.
11. Matyjaszewski, K. *Macromolecules* **2012**, *45*, 4015–4039.
12. Treat, N. J.; Sprafke, H.; Kramer, J. W.; Clark, P. G.; Barton, B. E.; Read de Alaniz, J.; Fors, B. P.; Hawker, C. J. *J. Am. Chem. Soc.* **2014**, *136*, 16096–16101.
13. Hawker, C. J.; Wooley, K. L. *Science* **2005**, *309*, 1200–1205.
14. Moad, G.; Rizzardo, E.; Thang, S. H. *Aust. J. Chem.* **2005**, *58*, 379–410.
15. Chiefari, J.; Chong, Y. K.; Ercole, F.; Krstina, J.; Jeffery, J.; Le, T. P. T.; Mayadunne, R. T. A.; Meijs, G. F.; Moad, C. L.; Moad, G.; Rizzardo, E.; Thang, S. H. *Macromolecules* **1998**, *31*, 5559–5562.
16. Schrock, R. R. *Acc. Chem. Res.* **1990**, *23*, 158–165.
17. Bielawski, C. W.; Grubbs, R. H. *Prog. Polym. Sci.* **2007**, *32*, 1–29.
18. Hardy, C. G.; Ren, L.; Zhang, J.; Tang, C. *Isr. J. Chem.* **2012**, *52*, 230–245.
19. Mayer, U. F. J.; Gilroy, J. B.; O’Hare, D.; Manners, I. *J. Am. Chem. Soc.* **2009**, *131*, 10382–10383.
20. Mayer, U. F. J.; Charmant, J. P. H.; Rae, J.; Manners, I. *Organometallics* **2008**, *27*, 1524–1533.
21. Yan, Y.; Zhang, J.; Qiao, Y.; Tang, C. *Macromol. Rapid Commun.* **2014**, *35*, 254–259.
22. Rapakousiou, A.; Mouche, C.; Duttine, M.; Ruiz, J.; Astruc, D. *Eur. J. Inorg. Chem.* **2012**, *2012*, 5071–5077.
23. Wildschek, M.; Rieker, C.; Jaitner, P.; Schottenberger, H.; Eberhard Schwarzhans, K. *J. Org. Chem.* **1990**, *396*, 355–361.
24. Vanicek, S.; Kopacka, H.; Wurst, K.; Müller, T.; Schottenberger, H.; Bildstein, B. *Organometallics* **2014**, *33*, 1152–1156.
25. Ren, L.; Hardy, C. G.; Tang, S.; Doxie, D. B.; Hamidi, N.; Tang, C. *Macromolecules* **2010**, *43*, 9304–9310.
26. Zhang, J.; Ren, L.; Hardy, C. G.; Tang, C. *Macromolecules* **2012**, *45*, 6857–6863.

27. Moad, G.; Rizzardo, E.; Thang, S. H. *Aust. J. Chem.* **2009**, *62*, 1402–1472.
28. Zhang, J.; Chen, Y. P.; Miller, K. P.; Ganewatta, M. S.; Bam, M.; Yan, Y.; Nagarkatti, M.; Decho, A. W.; Tang, C. *J. Am. Chem. Soc.* **2014**, *136*, 4873–4876.
29. Vougioukalakis, G. C.; Grubbs, R. H. *Chem. Rev.* **2009**, *110*, 1746–1787.
30. Ren, L.; Zhang, J.; Bai, X.; Hardy, C. G.; Shimizu, K. D.; Tang, C. *Chem. Sci.* **2012**, *3*, 580–583.
31. Ren, L.; Zhang, J.; Hardy, C. G.; Ma, S.; Tang, C. *Macromol. Rapid Commun.* **2012**, *33*, 510–516.
32. Zhang, J.; Yan, Y.; Chance, M. W.; Chen, J.; Hayat, J.; Ma, S.; Tang, C. *Angew. Chem., Int. Ed.* **2013**, *52*, 13387–13391.
33. Zhang, J.; Pellechia, P. J.; Hayat, J.; Hardy, C. G.; Tang, C. *Macromolecules* **2013**, *46*, 1618–1624.
34. Matyjaszewski, K.; Xia, J. *Chem. Rev.* **2001**, *101*, 2921–2990.
35. Matyjaszewski, K.; Xia, J. Fundamentals of Atom Transfer Radical Polymerization. In *Handbook of Radical Polymerization*; John Wiley & Sons, Inc.: 2003; pp 523–628.
36. Ren, L.; Hardy, C. G.; Tang, C. *J. Am. Chem. Soc.* **2010**, *132*, 8874–8875.
37. Ren, L.; Zhang, J.; Hardy, C. G.; Doxie, D.; Fleming, B.; Tang, C. *Macromolecules* **2012**, *45*, 2267–2275.

Chapter 3

Unprecedented Control over the Acrylate and Acrylamide Polymerization in Aqueous and Organic Media

Athina Anastasaki,¹ Vasiliki Nikolaou,¹ Fehaid Alsubaie,¹
Alexandre Simula,¹ Christopher Waldron,¹ Danielle J. Lloyd,¹
Jamie Godfrey,¹ Gabit Nurumbetov,¹ Qiang Zhang,¹ Paul Wilson,^{1,2}
Kristian Kempe,^{1,2} and David M. Haddleton^{1,2,*}

¹Chemistry Department, University of Warwick, Library road, CV4 7AL,
Coventry, United Kingdom

²Monash Institute of Pharmaceutical Sciences, Monash University,
Parksville, VIC 3052, Australia

*E-mail: D.M.Haddleton@warwick.ac.uk

During recent years we have witnessed the rapid development and understanding of controlled radical polymerization (CRP) methods. The scope of copper-mediated living radical polymerization in particular, has paved the way for the synthesis of a new generation of synthetic precision materials. Several versatile, simple and inexpensive methods have been employed for the synthesis of sequence-controlled multiblock copolymers in a one-pot polymerization reaction at ambient temperature or below. Careful optimization of the reaction conditions allows for monomer sequence and the chain length to be varied upon demand, furnishing complex compositions in a matter of minutes/hours. Perhaps more importantly, these techniques can be utilized for the rapid synthesis of narrow dispersed diblock and triblock copolymers, which are routinely requested for various applications *e.g.* self-assembly. The potential and the limitations of these methods are presented and discussed.

A major challenge for polymer chemistry is to approach the complexity of biological macromolecules *via* synthetic methods. Even though using radical polymerization we will be unable to mimic the structural perfection of natural analogues, getting closer towards this goal would represent a significant breakthrough. This requires the development of polymerization techniques which can accomplish precise molecular weight, narrow molecular weight distributions and high end-group fidelity.

Although the use of copper metals was initially reported by Matyjaszewski (1, 2), single electron transfer living radical polymerization (SET-LRP) received further attention in 2006 when Percec (3) and co-workers, allowed access to the “ultrafast” synthesis of “ultrahigh” molecular weight polymers from functional monomers containing electron withdrawing groups (mainly acrylates) at ambient temperature or below. Alkyl halide initiators and *N*-containing aliphatic ligands, previously employed by atom transfer living radical polymerization (ATRP) (4–7) are utilized for the polymerization while Cu(0) (in the form of powder (8–11) or wire (12)) is the proposed activator. Currently there is a debate in the literature (13, 14) regarding the mechanism of CRP in the presence of Cu(0), however, this will not be the focus of this current contribution. However, what is not under debate is that Cu(0)-mediated living radical polymerisation has received significant attention over the past few years due to its relative simplicity (15), mild conditions (3), relative tolerance to air (12, 16–19), simple removal and re-use of the catalyst (20) and relatively fast polymerization rates (3), providing access to a wide range of materials for various diverse applications. In all cases, quantitative or near quantitative end-group fidelity is maintained throughout the polymerization, even at full monomer conversion (21).

This high end-group fidelity has been further highlighted by Whittaker *et al.* in 2011 (22) who reported the facile synthesis of high-order multiblock copolymers at ambient temperature, where each block is composed of a very small number of repeat units (ideally 2 monomer units). The method involves no purification between the successive block formation steps as each iteration is taken to full monomer conversion. More importantly, under optimized conditions, minimal loss of end-group fidelity is detected and a well-defined hexablock copolymer ($\bar{D} \sim 1.20$) is presented (Figure 1). The same technique was subsequently utilized to synthesize multiblock star copolymers involving a core first approach from a multifunctional initiator (23). However, expanding the scope to a decablock copolymer proved to be problematic with significantly higher dispersities ($\bar{D} \sim 1.7$) being reported, suggesting that the limitations of the system had been reached (24). Higher molecular weight multiblocks were also obtained by Whittaker and Haddleton, although the system had to be further optimized in terms of deactivator (CuBr₂) and ligand (Me₆-Tren) concentrations (25). In the latter case, the authors faced difficulties in achieving full conversion prior to next monomer addition in order to maintain an acceptable polymerization rate. Thus, the development of a more versatile polymerization technique, capable of multiple chain extensions and perhaps of a larger diversity of monomers without the aforementioned limitations became a necessity.

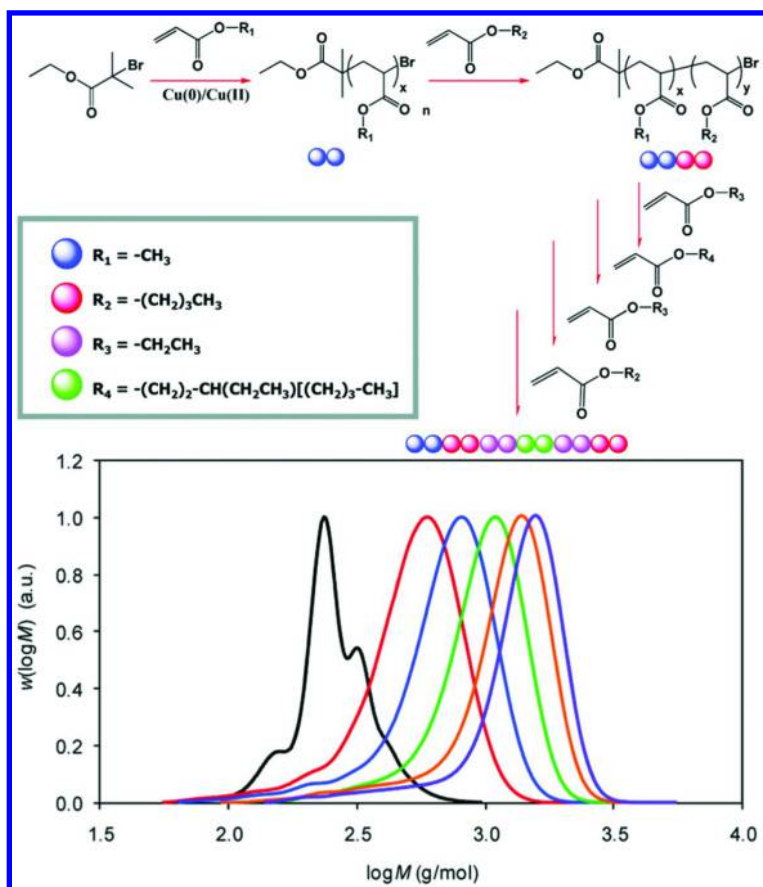


Figure 1. Schematic representation of the synthesis of multiblock copolymers by sequential addition of monomers without intermediate purification (top) and molecular weight distributions of multiblock homopolymer obtained by Cu(0) -mediated living polymerization via iterative chain extensions (bottom). Reproduced with permission from reference (22). Copyright 2011 ACS.

Recently, there has been continued effort to expand the scope of traditional CRP methods through strategies that would regulate the activation and deactivation step *via* external stimuli, including photochemical (26), pressure (27) and electrochemical (28). Of the various stimuli employed, light presents most of the attractive characteristics due to its inherent properties (*e.g.* environmentally benign natural resource, widely available, non-invasive etc.) (29). With respect to photochemical control, many groups have independently contributed to the field, demonstrating sophisticated systems that allow not only for the control over the molecular weight distributions but also for spatiotemporal control upon demand (30–35).

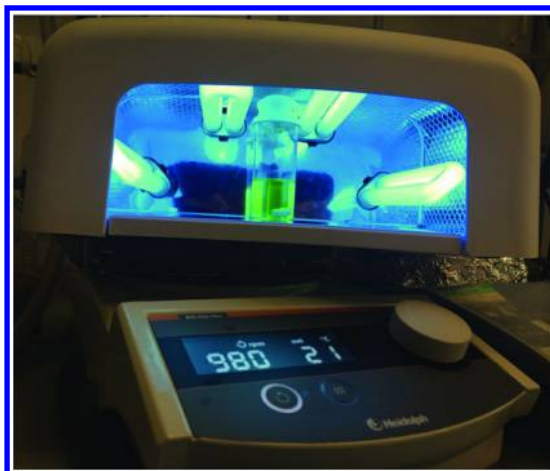


Figure 2. Typical set up for the photo-induced polymerization of MA in a commercially available UV nail lamp. Reproduced with permission from reference (37). Copyright 2013 ACS.

In 2014 Haddleton and co-workers fortuitously (36, 37) discovered a photoinduced living radical polymerization of acrylates in the absence of any conventional photoinitiator or dye sensitizer. The polymerization was even realized in “British sunlight” and the rate was significantly enhanced upon UV irradiation ($\lambda \sim 360$ nm). In the presence of ppm concentrations of CuBr_2 and an aliphatic tertiary amine ligand ($\text{Me}_6\text{-Tren}$), a high polymerization rate was observed (95% conversion obtained in just 80 min), yielding well-controlled poly(acrylates) ($\bar{D} \sim 1.05$) with very high end-group fidelity, as illustrated by both ^1H NMR and MALDI-ToF-MS ($\sim 99\%$). This exceptional end-group fidelity was further demonstrated by *in situ* chain extensions and block copolymerizations without any purification steps between the iterative chain extensions. A large number of monomers were found to be compatible with this polymerization system, including poly(ethylene glycol) methyl ether acrylate (PEGA_{480}), *tert*-butyl acrylate, glycidyl and solketal acrylate (SA) (38). Altering the solvent from dimethyl sulfoxide (DMSO) to isopropanol (IPA) or toluene/methanol mixtures allows for the polymerization of more hydrophobic monomers, including lauryl and octadecyl acrylate (38). The versatility of this technique was further exemplified by polymerization of methyl acrylate (MA) with various chain lengths ($\text{DP}_n = 25\text{-}800$) while hydroxyl- and *vic*-diol-functional initiators gave rise to equally controlled polymerizations. Importantly, and in collaboration with Junkers, Haddleton also reported the photoinduced copper-mediated polymerization of MA in a tubular photo-flow reactor as well as in a glass-chip based microreactor with excellent control obtained in both cases while 90% conversion was achieved within 20 minutes (39). Moreover, almost no polymerization is observed in the absence of light, conferring temporal control and paving the way for additional applications whereby precise spatiotemporal “on/off” control and resolution is desirable. One of the most interesting aspect

of this discovery is that the UV source is a “nail lamp” which can be purchased from multiple commercial vendors (*e.g.* Amazon, eBay) at low cost (~£10 each) (Figure 2).

Since the end-group fidelity obtained by the photoinduced polymerization is very high, the polymerization allows for the preparation of multiblock copolymers under benign reaction conditions (40, 41). Upon carefully optimized conditions, including varying [CuBr₂], [Me₆-Tren] and [monomer], a well-defined dodecablock multiblock copolymer with narrow molecular weight distribution ($\mathcal{D} < 1.20$) was obtained, while HR-ESI-MS confirmed the existence of the halogen at the end of the polymer chains, thus indicating high level of livingness (Figure 3).

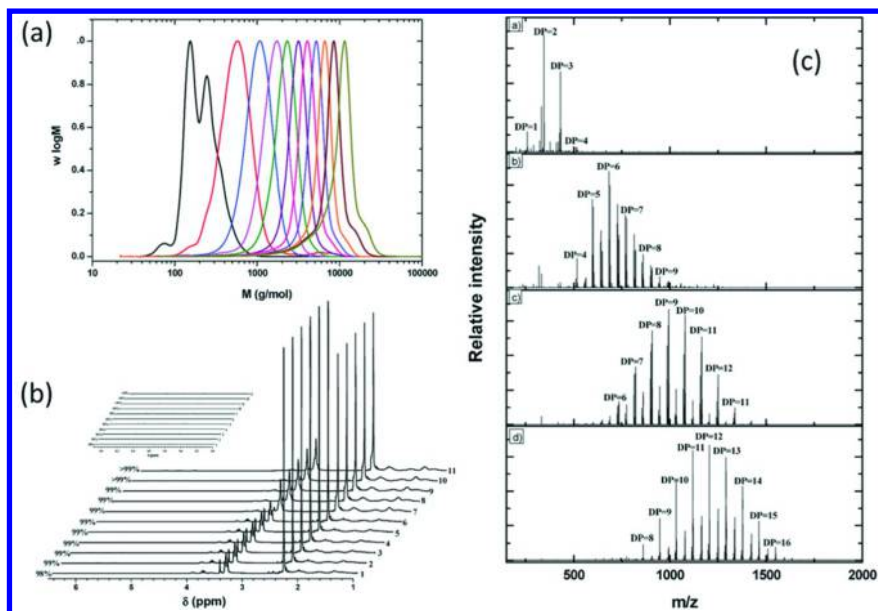


Figure 3. (a) Molecular weight distributions by CHCl₃ SEC, (b) ¹H NMR in CDCl₃ (c) HR-ESI-MS for successive cycles during the synthesis of multiblock homopolymers (DP_n=3 per block) in DMSO at ambient temperature. Reproduced with permission from reference (40). Copyright 2014 RSC.

Having optimized the reaction conditions utilizing MA, these can be applied to construct more complex microstructures. In order to do this, a family of monomers were employed, including MA, ethyl acrylate (EA), ethylene glycol methyl ether acrylate (EGA) and a protected functional monomer; (SA). Despite the incorporation of different monomers, the final dispersity of the undecablock polymer was not compromised ($\mathcal{D} < 1.20$) whilst quantitative conversions were attained throughout all the iterative monomer additions. To the best of our knowledge, 12 blocks is the largest number of blocks reported to date, obtained *via* a copper-mediated approach. It should be noted that quantitative conversion upon each monomer addition is crucial for the integrity of the multiblock copolymers. If, for example, the conversion is not quantitative (*e.g.* 95%) a gradient copolymer

will be obtained at the end of the previous block, compromising the precision of the targeted composition. More importantly, when the sequence of the monomers is alternated they were found to support propagation with equal efficiency, thus enabling the manipulation of the monomer composition upon demand (Figure 4).

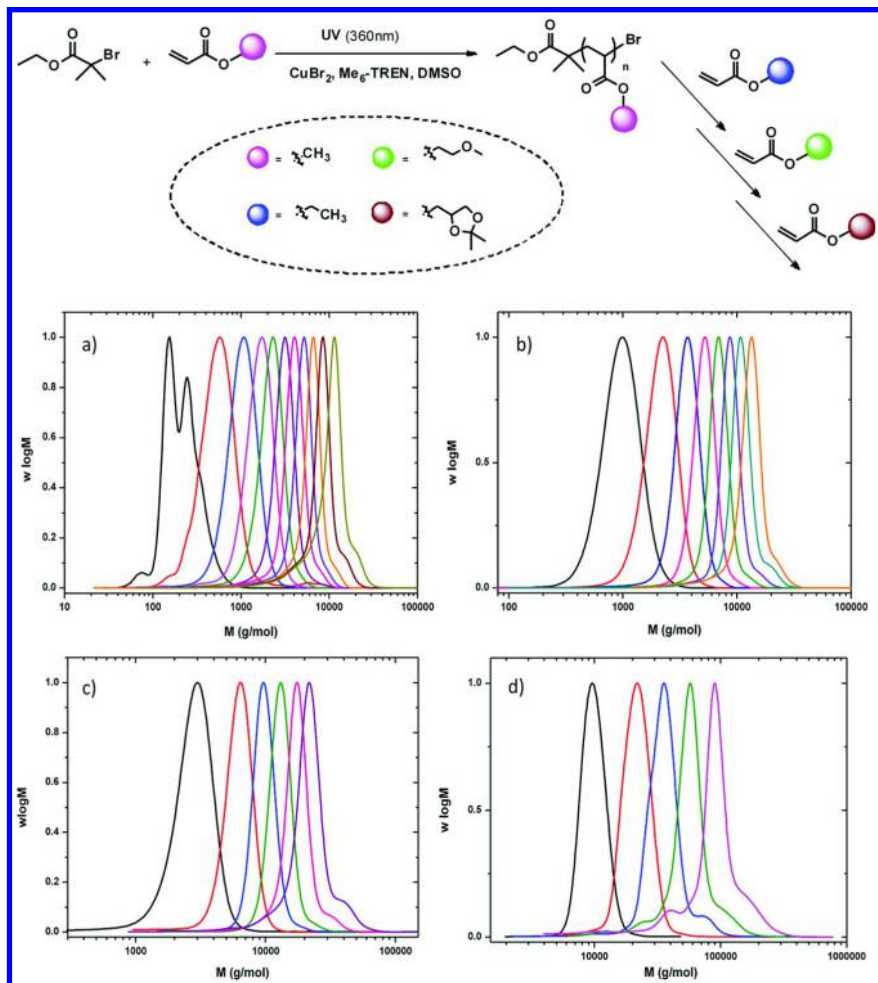


Figure 4. Molecular weight distributions for successive cycles during the synthesis of (a) an undecablock copolymer ($DP_n=3$ per block); (b) an octablock copolymer ($DP_n=10$ per block); (c) a hexablock copolymer ($DP_n=25$ per block); (d) a pentablock copolymer ($DP_n=100$ per block) in DMSO at ambient temperature. Monomers were alternated during the synthesis. Reproduced with permission from reference (40). Copyright 2014 RSC.

Although synthesis of low molecular weight multiblock copolymers is already a significant breakthrough and can be considered as a proof of concept, higher molecular weight polymers also display a wide range of interesting physicochemical properties, including self-assembly and phase separation into highly ordered structures (42–44). Diblock and triblock amphiphilic copolymers in particular are routinely utilized for the preparation of micelles and vesicles and thus the facile, rapid and one-pot access to these type of structures is desirable. Thus, it would be interesting to expand this photomediated technique to include higher molecular weight structures. Upon minor optimization of the reaction conditions, a well-defined hexablock copolymer was obtained (~ 100 kDa) with relatively narrow molecular weight distribution ($D \sim 1.30$) (the pentablock multiblock copolymer presented a D of 1.21) (Figure 4). Such high molecular weight multiblock copolymers were reported in the literature for the first time, paving the way for the synthesis of a new class of functional materials. Junkers and co-workers also reported a well-defined decablock copolymer ($M_n = 8.500$ g.mol⁻¹) utilizing a similar photo-initiated copper-mediated radical polymerization protocol (41). Good correlation between the theoretical and the experimental values as well as narrow dispersities ($D \sim 1.1$ -1.17) were achieved throughout the chain extensions as evident by ¹H NMR and SEC.

Telechelic block copolymers (45) are also of interest for the polymer community as they provide access to a wide range of architectures, including triblock copolymers, higher order self-assembled structures (46, 47) *etc.* Crucially, the reactivity of the α and ω end-group can be exploited for post polymerization modification, resulting in the preparation of functional materials (48). Moreover, the utility of bi-functional initiators provides significant advantages over the monofunctional analogues as one can add two blocks upon each monomer addition (apart from the first block which results in a homopolymer assuming that the bi-functional initiator is a small molecule and not a telechelic macroinitiator).

Herein, we take the opportunity to present some preliminary data of the synthesis of multiblock copolymers growing from both ends of a bi-functional initiator (Figure 5). Utilizing ethylene bis(2-bromoisobutyrate) (EbBiB), a well-defined heptablock copolymer can be obtained with narrow molecular weight distribution ($D \sim 1.16$) while the conversion was kept >99% between the iterative chain extensions. Moreover, an excellent correlation between the experimental molecular weight and the theoretical values is observed, further confirming the controlled/living character of the polymerisation. Four different monomers were successfully incorporated along the polymer backbone, introducing the desired functionality in the resulting multiblock copolymer. More details about these telechelic multiblock copolymers will be more thoroughly discussed in a subsequent publication. Although this photoinduced polymerization is compatible with many different functional groups and solvents, it is best suited to acrylic monomers as methacrylates and styrene present significantly slower polymerization rates and broader dispersity values (37).

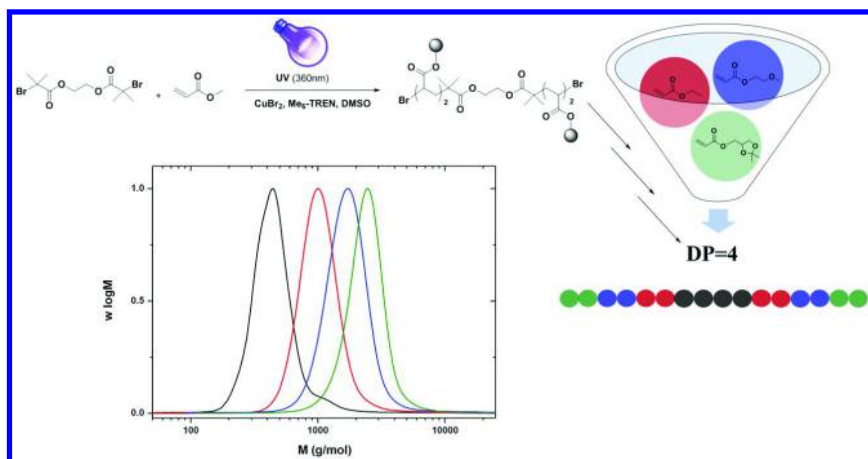


Figure 5. Schematic representation and SEC of a heptablock copolymer obtained via the photoinduced living radical polymerization utilizing a bifunctional initiator. The detailed procedure followed for the synthesis is identical to reference (40).

For applications where acrylamide-based monomers are desired, copper-mediated living radical polymerization (*e.g.* ATRP) has been proven to be problematic (49), although other polymerization techniques (*e.g.* reversible addition fragmentation polymerization (RAFT) (50, 51)) have already successfully demonstrated the synthesis of highly complex structures consisting of acrylamides (52–55). When ATRP is employed for the polymerization of acrylamides in aqueous media, loss of control is typically unavoidable (49) due to rapid activation and propagation unless a high ratio of Cu(II) salts is added to mediate an effective deactivation (56). Alternatively, several organic co-solvents (*e.g.* dimethylformamide (DMF), alcohols) have often been employed to improve control over the molecular weight distributions (57–65), although long reaction times and moderate conversions compromise the polymerizations. In the very few attempts that acrylamides were successfully polymerized by ATRP (66), very long reaction times (~20 h) were required in order to obtain narrow dispersed polymers ($\mathcal{D} = 1.11\text{--}1.29$) while the conversions reported were moderate (18.5–56%). Finally, only relatively low molecular weight ($M_n=4000\text{--}7000\text{ g}\cdot\text{mol}^{-1}$) polymers could be obtained.

Recently, Haddleton *et al.* were able to address this limitation by introducing a new technique (Figure 6) that enables the rapid and well-controlled polymerizations of both acrylamides and acrylates in water without any additional co-solvents or salts (67). The key step of this new approach is to allow full disproportionation of CuBr/Me₆-Tren (Tris[2-(dimethylamino)ethyl]amine) to Cu(0) powder and CuBr₂ in water prior to addition of monomer and initiator (Figure 6).

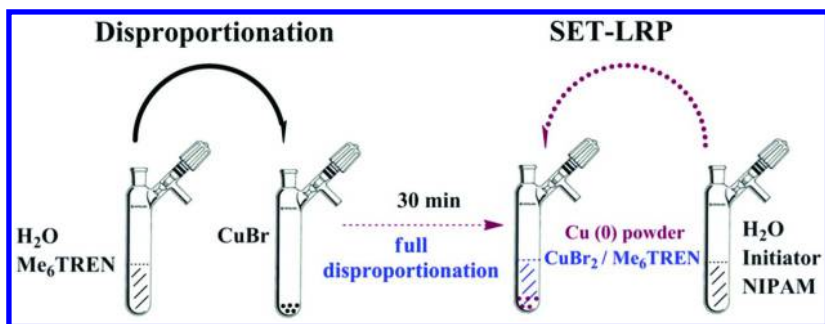


Figure 6. Schematic Representation of Cu(0)-mediated living radical polymerization via prior disproportionation of CuBr/Me₆-Tren in water, followed by the addition of the initiator and the monomer. Reproduced with permission from reference (67). Copyright 2013 ACS.

A wide range of acrylamides (67, 68) and acrylates (67) were successfully polymerized by this technique, including *N*-isopropylacrylamide (NIPAM), *N,N*-dimethylacrylamide (DMA), *N*-acryloylmorpholine (NAM), poly(ethylene glycol) acrylate (PEGA₄₈₀), 2-hydroxyethyl acrylate (HEA) and even an acrylamide glycol monomer. The polymerizations were performed at ambient temperature or below (ice bath) with quantitative conversions attained in minutes (typically < 30 min) while more importantly, all polymers presented controlled chain length and narrow molecular weight distributions ($\bar{D} \sim 1.10$). The Cu(0)-mediated polymerization of NIPAM was investigated thoroughly and upon careful optimization of the ratio between the catalyst and the ligand, a range of molecular weights were synthesized ($DP_n = 8-320$). In order to assess the end-group fidelity chain extension of poly(NIPAM) was initially attempted at ambient temperature. However, the conversion of the diblock copolymer only reached 87% with the SEC revealing a bimodal peak, suggesting premature termination events. In order to verify this, high-resolution ¹H NMR and MALDI-ToF MS were conducted, both showing that quantitative hydrolysis was occurring, yielding OH-terminated polymers (55). In order to circumvent this, the chain extensions were subsequently performed in an ice bath, whereby SEC revealed a complete shift in the chromatograms even after 3 chain extensions with a final dispersity of 1.13. Finally, the robustness of the system was further demonstrated by performing the reaction in PBS buffer (67), blood serum (69) and a even a range of alcoholic beverages (70) (Figure 7). Remarkably, none of the aforementioned “special” and “complex” solvents adversely affected the controlled nature of the polymerization, yielding well-defined polymers with narrow molecular weight distributions ($\bar{D} = 1.1-1.3$).

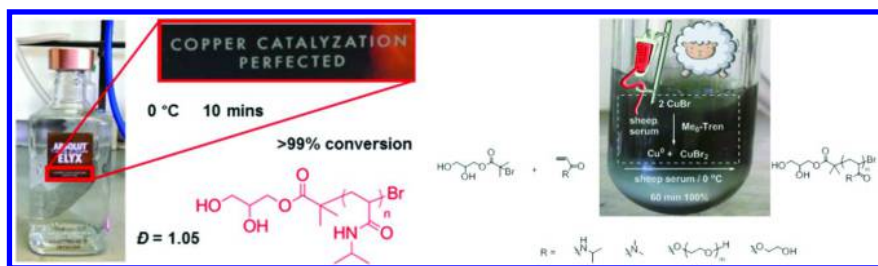


Figure 7. Cu(0)-mediated living radical polymerization of various acrylamides and acrylate monomers in vodka and blood serum. Reproduced with permission from references (69) and (70). Copyright 2013/14 RSC.

Since it was shown that ice bath cooling was sufficient to suppress hydrolysis effectively, and thus improve the end-group fidelity, the authors were interested in utilizing water as the solvent for the preparation of multiblock copolymers of various acrylamides (71). Performing the polymerizations at ambient temperature or below is advantageous not only to suppress termination but also to provide compatibility with biological systems. Following homopolymerization of NIPAM, in accordance with the aforementioned procedure (Figure 6) full conversion was attained within 1 h (by ^1H NMR), after which a deoxygenated solution of NIPAM was injected *in situ*. Chain extension was allowed to proceed for 4 h (100%, $D = 1.07$) before a second aliquot of NIPAM was again injected in the reaction mixture. After an additional period of 5.5 h the vinyl groups were completely consumed and a well-defined triblock homopolymer was obtained. However, any attempts to chain extend the triblock further proved unsuccessful, as indicated by the absence of a shift in the SEC (Figure 8).

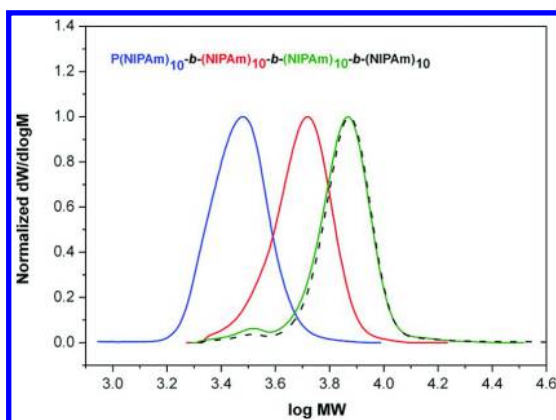


Figure 8. SEC of multiblock homopolymers prepared by sequential addition of NIPAM via aqueous Cu(0)-mediated living radical polymerization (prior optimization). Reproduced with permission from reference (71). Copyright 2015 RSC.

This inability to chain extend further was attributed to the loss of the end-group, most likely due to unavoidable hydrolysis. It was hypothesized that hydrolysis should occur in a larger extent when the monomer concentration was depleting. Thus, we decided to proceed to the next aliquot addition when the monomer conversion was $>95\%$ and preferentially less than 100% (we envisaged that under these conditions propagation should occur faster than hydrolysis). The homopolymerization of NIPAM was carried out and after 11 minutes the conversion reached 99% ($D = 1.06$), at which point the polymerization was stopped. This process was repeated for each chain extension until a well-defined nonablock poly(NIPAM) was obtained, with a final dispersity of 1.08 (Figure 9). However, subsequent chain extensions were unsuccessful. A plot of $M_{n,exp}$ and $M_{w,exp}$ versus number of cycles reveals that the molecular weight continuously deviates from the theoretical value, suggesting accumulated termination (probably bimolecular) which is hidden by SEC due to the small differences in MWt. Alternatively, apart from loss of the end-group functionality, the polymerization may also stop due to an irreversible shift of the equilibrium towards dormant species, caused by the accumulated termination.

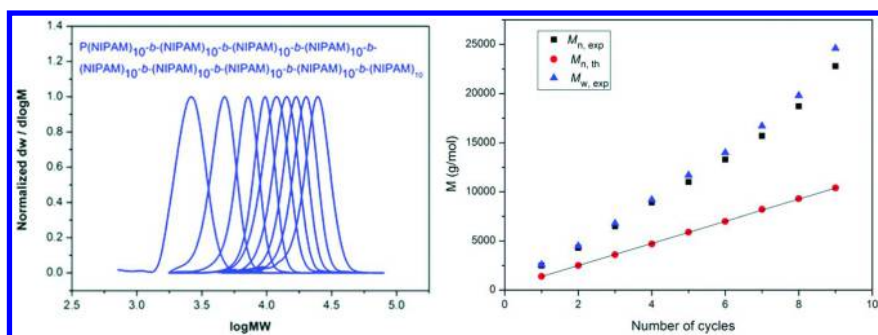


Figure 9. Evolution of the poly(NIPAM) multiblock homopolymer by SEC (left) and relative increase in molecular weight as a function of cycles (right). Reproduced with permission from reference (71). Copyright 2015 RSC.

The ability to vary monomer sequences is highly desirable as they can potentially tune the properties of the targeted material upon demand. So far, only multiblocks consisting of acrylates have been reported by copper-mediated living radical polymerization and although the dispersity values were narrow in most cases, extremely long reaction times (up to 48 h per block) proved to be a limitation (24, 72, 73). However, the authors utilized three commercially available acrylamide monomers and managed to synthesize a well-defined hexablock copolymer P(NIPAM)₁₀-b-P(DMA)₁₀-b-P(HEAA)₁₀-b-P(NIPAM)₁₀-b-P(HEAA)₁₀-b-P(DMA)₁₀ with a final dispersity of 1.11 within a total reaction time of 3 h (Figure 10).

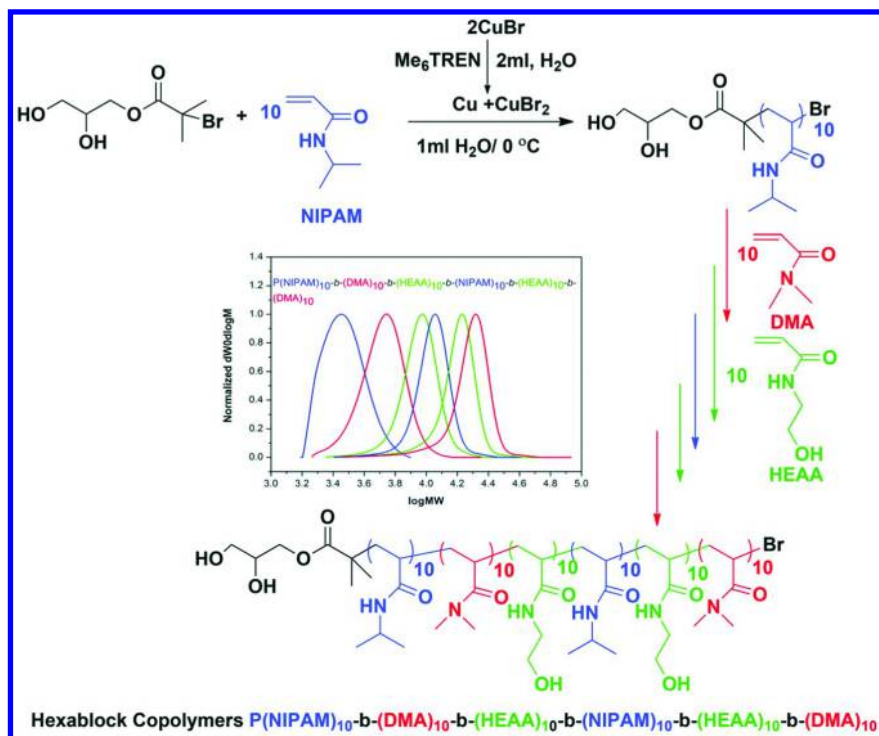


Figure 10. Schematic representation and SEC of multiblock copolymer composed of NIPAM, DMA and HEAA via Cu(0)-mediated living radical polymerization below room temperature. Reproduced with permission from reference (71). Copyright 2015 RSC.

Subsequently, Haddleton *et al* were interested in studying the effect of the structure of the monomer in these chain extensions. A detailed study revealed that NIPAM was less susceptible to termination (mainly defined as hydrolysis) in comparison with HEAA, which was capable of more chain extensions than DMA or *N,N*-diethyl acrylamide (DEA) (71). Thus, aqueous Cu(0)-mediated living radical polymerization is strongly affected by the structure of the monomers, perhaps due to faster hydrolysis depending on the monomer or due to complex formation between monomer and the catalyst. Nevertheless, for applications where more monomers are desired, even demanding monomers under these reaction conditions (*e.g.* DEA) can be successfully incorporated along the polymer backbone, yielding a pentablock copolymer with $D = 1.16$ with a final conversion of 98%. Remarkably, such complex structures can be obtained in a matter of 2-3 h (Figure 11).

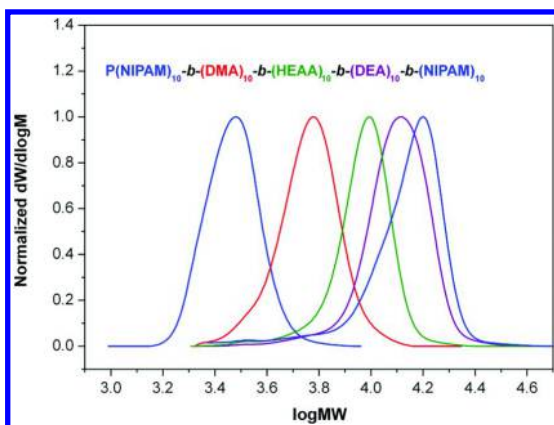


Figure 11. SEC of multiblock copolymer composed of 4 different monomers obtained via aqueous Cu(0)-mediated living radical polymerization. The detailed procedure for the synthesis of this multiblock is identical to reference (71).

Finally, for applications where higher molecular weight polymers are desired, a well-defined triblock copolymer was obtained with final $M_n > 40000 \text{ g mol}^{-1}$, $\bar{D} = 1.14$ and final conversion = 90% (Figure 12). Thus, chain length has a detrimental effect on the number of chain extensions that a system can undergo, highlighting the limitations of the current system. Nevertheless, the synthesis of such high molecular weight triblock copolymers without any purification steps required between the iterative additions remains remarkable.

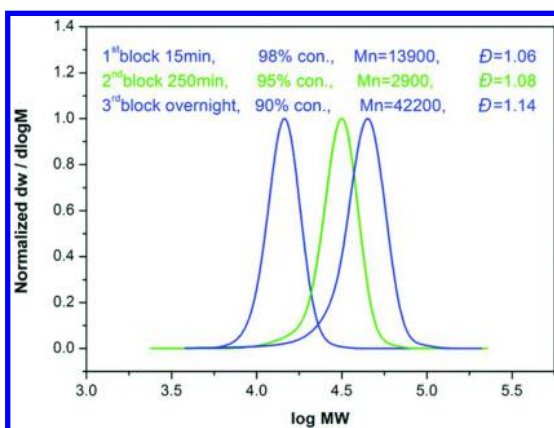


Figure 12. SEC of $P(\text{NIPAM})_{100}\text{-}P(\text{HEAA})_{100}\text{-}P(\text{NIPAM})_{100}$ prepared via aqueous Cu(0)-mediated living radical polymerization. Reproduced with permission from reference (71). Copyright 2015 RSC

In summary, research over the last 1-2 years has expanded the scope of living radical polymerization. This has led to the discovery of novel, versatile polymerization systems that yield well-defined polymers (typically with $D < 1.1$), even at quantitative conversions in extremely short period of times. Both the light-induced and the aqueous Cu(0)-mediated polymerization can provide access to complex structures (e.g. multiblock copolymers), paving the way for the facile synthesis of a new class of functional materials with potential applications both in biological and polymer field.

References

1. Matyjaszewski, K.; Coca, S.; Gaynor, S. G.; Wei, M.; Woodworth, B. E. *Macromolecules* **1997**, *30*, 7348–7350.
2. Matyjaszewski, K.; Coca, S.; Gaynor, S. G.; Greszta, D.; Patten, T. E.; Wang, J.; Xia, J. WO9718247; US Patent 8,807,937, September 15, 1998.
3. Percec, V.; Guliashvili, T.; Ladislaw, J. S.; Wistrand, A.; Stjerndahl, A.; Sienkowska, M. J.; Monteiro, M. J.; Sahoo, S. *J. Am. Chem. Soc.* **2006**, *128*, 14156–14165.
4. Matyjaszewski, K.; Xia, J. *Chem. Rev.* **2001**, *101*, 2921–2990.
5. Pintauer, T.; Matyjaszewski, K. *Chem. Soc. Rev.* **2008**, *37*, 1087–1097.
6. Matyjaszewski, K. *Macromolecules* **2012**, *45*, 4015–4039.
7. Kato, M.; Kamigaito, M.; Sawamoto, M.; Higashimura, T. *Macromolecules* **1995**, *28*, 1721–1723.
8. Lligadas, G.; Percec, V. *J. Polym. Sci., Part A: Polym. Chem.* **2007**, *45*, 4684–4695.
9. Lligadas, G.; Percec, V. *J. Polym. Sci., Part A: Polym. Chem.* **2008**, *46*, 2745–2754.
10. Lligadas, G.; Ladislaw, J. S.; Guliashvili, T.; Percec, V. *J. Polym. Sci., Part A: Polym. Chem.* **2008**, *46*, 278–288.
11. Lligadas, G.; Percec, V. *J. Polym. Sci., Part A: Polym. Chem.* **2008**, *46*, 3174–3181.
12. Jiang, X.; Rosen, B. M.; Percec, V. *J. Polym. Sci., Part A: Polym. Chem.* **2010**, *48*, 2716–2721.
13. Konkolewicz, D.; Krys, P.; Góis, J. R.; Mendonça, P. V.; Zhong, M.; Wang, Y.; Gennaro, A.; Isse, A. A.; Fantin, M.; Matyjaszewski, K. *Macromolecules* **2014**, *47*, 560–570.
14. Konkolewicz, D.; Wang, Y.; Krys, P.; Zhong, M.; Isse, A. A.; Gennaro, A.; Matyjaszewski, K. *Polym. Chem.* **2014**, *5*, 4396–4417.
15. Rosen, B. M.; Percec, V. *Chem. Rev.* **2009**, *109*, 5069–5119.
16. Nguyen, N. H.; Leng, X.; Sun, H.-J.; Percec, V. *J. Polym. Sci., Part A: Polym. Chem.* **2013**, *51*, 3110–3122.
17. Nguyen, N. H.; Percec, V. *J. Polym. Sci., Part A: Polym. Chem.* **2011**, *49*, 4756–4765.
18. Fleischmann, S.; Percec, V. *J. Polym. Sci., Part A: Polym. Chem.* **2010**, *48*, 2243–2250.

19. Fleischmann, S.; Rosen, B. M.; Percec, V. *J. Polym. Sci., Part A: Polym. Chem.* **2010**, *48*, 1190–1196.
20. Chan, N.; Cunningham, M. F.; Hutchinson, R. A. *J. Polym. Sci., Part A: Polym. Chem.* **2013**, *51*, 3081–3096.
21. Nguyen, N. H.; Levere, M. E.; Percec, V. *J. Polym. Sci., Part A: Polym. Chem.* **2012**, *50*, 860–873.
22. Soeriyadi, A. H.; Boyer, C.; Nyström, F.; Zetterlund, P. B.; Whittaker, M. R. *J. Am. Chem. Soc.* **2011**, *133*, 11128–11131.
23. Boyer, C.; Derveaux, A.; Zetterlund, P. B.; Whittaker, M. R. *Polym. Chem.* **2012**, *3*, 117–123.
24. Boyer, C.; Soeriyadi, A. H.; Zetterlund, P. B.; Whittaker, M. R. *Macromolecules* **2011**, *44*, 8028–8033.
25. Anastasaki, A.; Waldron, C.; Wilson, P.; Boyer, C.; Zetterlund, P. B.; Whittaker, M. R.; Haddleton, D. *ACS Macro Lett.* **2013**, *2*, 896–900.
26. Tanabe, M.; Vandermeulen, G. W. M.; Chan, W. Y.; Cyr, P. W.; Vanderark, L.; Rider, D. A.; Manners, I. *Nat. Mater.* **2006**, *5*, 467–470.
27. Rzayev, J.; Penelle, J. *Macromolecules* **2002**, *35*, 1489–1490.
28. Magenau, A. J. D.; Strandwitz, N. C.; Gennaro, A.; Matyjaszewski, K. *Science* **2011**, *332*, 81–84.
29. Leibfarth, F. A.; Mattson, K. M.; Fors, B. P.; Collins, H. A.; Hawker, C. J. *Angew. Chem., Int. Ed.* **2013**, *52*, 199–210.
30. Xu, J.; Jung, K.; Atme, A.; Shanmugam, S.; Boyer, C. *J. Am. Chem. Soc.* **2014**, *136*, 5508–5519.
31. Xu, J.; Jung, K.; Boyer, C. *Macromolecules* **2014**, *47*, 4217–4229.
32. Mosnáček, J.; Ilčíková, M. *Macromolecules* **2012**, *45*, 5859–5865.
33. Fors, B. P.; Hawker, C. J. *Angew. Chem., Int. Ed.* **2012**, *51*, 8850–8853.
34. Konkolewicz, D.; Schröder, K.; Buback, J.; Bernhard, S.; Matyjaszewski, K. *ACS Macro Lett.* **2012**, *1*, 1219–1223.
35. Ribelli, T. G.; Konkolewicz, D.; Bernhard, S.; Matyjaszewski, K. *J. Am. Chem. Soc.* **2014**, *136*, 13303–13312.
36. Burns, J. A.; Houben, C.; Anastasaki, A.; Waldron, C.; Lapkin, A. A.; Haddleton, D. M. *Polym. Chem.* **2013**, *4*, 4809–4813.
37. Anastasaki, A.; Nikolaou, V.; Zhang, Q.; Burns, J.; Samanta, S. R.; Waldron, C.; Haddleton, A. J.; McHale, R.; Fox, D.; Percec, V.; Wilson, P.; Haddleton, D. M. *J. Am. Chem. Soc.* **2013**, *136*, 1141–1149.
38. Anastasaki, A.; Nikolaou, V.; Simula, A.; Godfrey, J.; Li, M.; Nurumbetov, G.; Wilson, P.; Haddleton, D. M. *Macromolecules* **2014**, *47*, 3852–3859.
39. Wenn, B.; Conradi, M.; Carreiras, A. D.; Haddleton, D. M.; Junkers, T. *Polym. Chem.* **2014**, *5*, 3053–3060.
40. Anastasaki, A.; Nikolaou, V.; Pappas, G. S.; Zhang, Q.; Wan, C.; Wilson, P.; Davis, T. P.; Whittaker, M. R.; Haddleton, D. M. *Chem. Sci.* **2014**, *5*, 3536–3542.
41. Chuang, Y.-M.; Ethirajan, A.; Junkers, T. *ACS Macro Lett.* **2014**, *3*, 732–737.
42. Moughton, A. O.; Hillmyer, M. A.; Lodge, T. P. *Macromolecules* **2011**, *45*, 2–19.

43. Pasparakis, G.; Krasnogor, N.; Cronin, L.; Davis, B. G.; Alexander, C. *Chem. Soc. Rev.* **2010**, *39*, 286–300.
44. Rodríguez-Hernández, J.; Chécot, F.; Gnanou, Y.; Lecommandoux, S. *Prog. Polym. Sci.* **2005**, *30*, 691–724.
45. Boutevin, B. In *New Polymer Materials*; Springer: Berlin, Heidelberg, 1990; Vol. 94, pp 69–105.
46. Grumelard, J.; Taubert, A.; Meier, W. *Chem. Commun.* **2004**, *13*, 1462–1463.
47. Blanazs, A.; Armes, S. P.; Ryan, A. J. *Macromol. Rapid Commun.* **2009**, *30*, 267–277.
48. Simula, A.; Nurumbetov, G.; Anastasaki, A.; Wilson, P.; Haddleton, D. M. *Eur. Polym. J.* **2015**, *62*, 294–303.
49. Rademacher, J. T.; Baum, M.; Pallack, M. E.; Brittain, W. J.; Simonsick, W. J. *Macromolecules* **1999**, *33*, 284–288.
50. Chiefari, J.; Chong, Y. K.; Ercole, F.; Krstina, J.; Jeffery, J.; Le, T. P. T.; Mayadunne, R. T. A.; Meijs, G. F.; Moad, C. L.; Moad, G. *Macromolecules* **1998**, *31*, 5559–5562.
51. Moad, G.; Rizzardo, E.; Thang, S. H. *Aust. J. Chem.* **2012**, *65*, 985–1076.
52. Gody, G.; Maschmeyer, T.; Zetterlund, P. B.; Perrier, S. *Nat. Commun.* **2013**, *4*, 2505.
53. Gody, G.; Maschmeyer, T.; Zetterlund, P. B.; Perrier, S. *Macromolecules* **2014**, *47*, 639–649.
54. Gody, G.; Maschmeyer, T.; Zetterlund, P. B.; Perrier, S. *Macromolecules* **2014**, *47*, 3451–3460.
55. Zetterlund, P. B.; Gody, G.; Perrier, S. *Macromol. Theory Simul.* **2014**, *5*, 331–339.
56. Pierre-Eric, M.; Nathalie, C. M.; Alexander, B.; Müller, A. H. E. In *Controlled/Living Radical Polymerization: Progress in ATRP*; American Chemical Society: 2009; Vol. 1023, pp 127–137.
57. Masci, G.; Giacomelli, L.; Crescenzi, V. *Macromol. Rapid Commun.* **2004**, *25*, 559–564.
58. Xia, Y.; Yin, X.; Burke, N. A. D.; Stöver, H. D. H. *Macromolecules* **2005**, *38*, 5937–5943.
59. Xia, Y.; Burke, N. A. D.; Stöver, H. D. H. *Macromolecules* **2006**, *39*, 2275–2283.
60. Duan, Q.; Miura, Y.; Narumi, A.; Shen, X.; Sato, S.-I.; Satoh, T.; Kakuchi, T. *J. Polym. Sci., Part A: Polym. Chem.* **2006**, *44*, 1117–1124.
61. Akiyama, H.; Tamaoki, N. *Macromolecules* **2007**, *40*, 5129–5132.
62. Appel, E. A.; del Barrio, J.; Loh, X. J.; Dyson, J.; Scherman, O. A. *J. Polym. Sci., Part A: Polym. Chem.* **2012**, *50*, 181–186.
63. Bontempo, D.; Li, R. C.; Ly, T.; Brubaker, C. E.; Maynard, H. D. *Chem. Commun.* **2005**, *37*, 4702–4704.
64. Feng, C.; Shen, Z.; Li, Y.; Gu, L.; Zhang, Y.; Lu, G.; Huang, X. *J. Polym. Sci., Part A: Polym. Chem.* **2009**, *47*, 1811–1824.
65. Tang, X. D.; Liang, X. C.; Yang, Q.; Fan, X. H.; Shen, Z. H.; Zhou, Q. F. *J. Polym. Sci., Part A: Polym. Chem.* **2009**, *47*, 4420–4427.

66. Teodorescu, M.; Matyjaszewski*, K. *Macromol. Rapid Commun.* **2000**, *21*, 190–194.
67. Zhang, Q.; Wilson, P.; Li, Z.; McHale, R.; Godfrey, J.; Anastasaki, A.; Waldron, C.; Haddleton, D. M. *J. Am. Chem. Soc.* **2013**, *135*, 7355–7363.
68. Anastasaki, A.; Haddleton, A. J.; Zhang, Q.; Simula, A.; Droesbeke, M.; Wilson, P.; Haddleton, D. M. *Macromol. Rapid Commun.* **2014**, *35*, 965–970.
69. Zhang, Q.; Li, Z.; Wilson, P.; Haddleton, D. M. *Chem. Commun.* **2013**, *49*, 6608–6610.
70. Waldron, C.; Zhang, Q.; Li, Z.; Nikolaou, V.; Nurumbetov, G.; Godfrey, J.; McHale, R.; Yilmaz, G.; Randev, R. K.; Girault, M.; McEwan, K.; Haddleton, D. M.; Droesbeke, M.; Haddleton, A. J.; Wilson, P.; Simula, A.; Collins, J.; Lloyd, D. J.; Burns, J. A.; Summers, C.; Houben, C.; Anastasaki, A.; Li, M.; Becer, C. R.; Kiviaho, J. K.; Risangud, N. *Polym. Chem.* **2014**, *5*, 57–61.
71. Alsubaie, F.; Anastasaki, A.; Wilson, P.; Haddleton, D. M. *Polym. Chem.* **2015**, *6*, 406–417.
72. Zhang, Q.; Collins, J.; Anastasaki, A.; Wallis, R.; Mitchell, D. A.; Becer, C. R.; Haddleton, D. M. *Angew. Chem., Int. Ed.* **2013**, *52*, 4435–4439.
73. Zhang, Q.; Anastasaki, A.; Li, G.-Z.; Haddleton, A. J.; Wilson, P.; Haddleton, D. M. *Polym. Chem.* **2014**, *5*, 3876–3883.

Chapter 4

Controlled Synthesis of Ethylene-Vinyl Acetate Based Copolymers by Organometallic Mediated Radical Polymerization

Jérémy Demarteau, Anthony Kermagoret, Christine Jérôme,
Christophe Detrembleur, and Antoine Debuigne*

Center for Education and Research on Macromolecules (CERM),
Department of Chemistry, University of Liege (ULg), Sart-Tilman, B6A,
4000 Liege, Belgium

*E-mail: adebuigne@ulg.ac.be

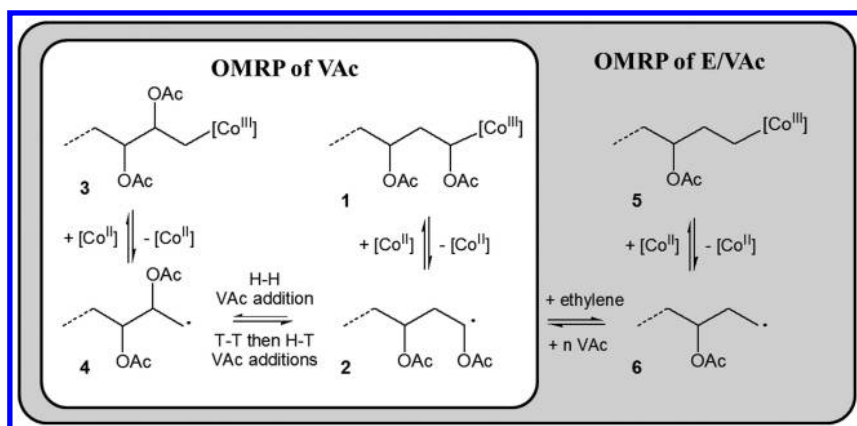
The controlled radical copolymerization of ethylene (E) and vinyl acetate (VAc) is further investigated by organometallic-mediated radical polymerization (OMRP) using $\text{Co}(\text{acac})_2$ as controlling agent at ethylene pressure up to 100 bar. The effect of ethylene pressure on kinetics, level of control and copolymer composition, is discussed. Ethylene-Vinyl Acetate copolymers (EVAs) with low dispersities and ethylene content reaching 57 mol% are notably reported. This work also successfully addresses the precision design of EVA-containing block copolymers, i.e. PVAc-*block*-EVA. In this case, the order of the synthesis of the blocks is a key parameter. The “PVAc-first” strategy is by far more practical and efficient.

Introduction

Progress made in controlled radical polymerization (CRP) in recent years is simply impressive regarding the level of understanding of the mechanisms, the increasing precision and complexity of the polymer structures achievable as well as their involvement in a wide array of applications. Such advances might leave the impression that challenges in CRP may soon be missing or confined to its industrialization and that all vinyl polymers can be produced in a controlled fashion. However, considerable efforts still need to be expended to control the

radical polymerization of unsubstituted olefins like ethylene and to mediate their copolymerization with polar vinyl monomers (1). In this perspective, the synthesis of polyethylene (PE) with low dispersity has been recently reported by radical addition fragmentation chain transfer (RAFT) polymerization but the molar mass did not exceed 2000 g/mol (2). On the other hand, the successful copolymerization of α -olefins with acrylates has been reported by various CRP methods (3–11) although the ethylene content in the final copolymers is low. Ethylene-vinyl acetate (EVA) copolymer is another valuable polymer produced on an industrial scale. Hardness, tensile strength and toughness of the latter can be adjusted by tuning its composition allowing to cover a large range of applications including adhesives, paints, automotive equipments, etc. (12–14) The synthesis of well-defined EVAs and their incorporation in more complex architectures are thus highly desirable in order to further expand the scope of this polymer. The ethylene-vinyl acetate copolymerization has been notably investigated by coordination-insertion polymerization but only a few percent of VAc was introduced in the backbone (15–17). Low VAc content EVAs (<10 mol% of VAc) have also been produced by RAFT, the molar masses and dispersities of the latter below 2500 g/mol and being around 1.6, respectively (2). Interestingly, EVA copolymers with higher VAc content (up to 50 mol%) have been prepared by iodide-mediated radical polymerization (18). Nevertheless, the level of control of the polymerization is far from perfect as assessed by the relatively high dispersity of the resulting EVAs ($D > 1.8$). To date, best results have been achieved using organometallic complexes as mediating species of the radical E/VAc copolymerization (19), as developed hereafter.

Organometallic-mediated radical polymerization (OMRP) relies on the reversible deactivation of the growing radical species by a metal complex (20–23). In this case, the equilibrium between dormant and active species can be adjusted by changing the metal center (23–25) and/or ligands (26–28). As a result, a quite large range of vinyl monomers is now covered by OMRP including difficult non conjugated monomers. For example, *bis*(acetylacetonato)cobalt(II) ($\text{Co}(\text{acac})_2$) offers an unequalled control of the radical polymerization of N-vinyl amides (29), N-vinylimidazolium (30, 31) and vinyl acetate (32–34). In the latter case, the controlled polymerization of VAc occurs at low temperature (40 °C) thanks to the weakness of the cobalt-carbon bond (33). In contrast to other CRP systems (35, 36), it has been shown that the OMRP of VAc (Scheme 1) is not altered by the formation of a more reactive primary radical (4) resulting from the inverted monomer insertion by head-to-head addition (34). In this case, the regular (1) and the inverted (3) dormant species reactivate at similar rates. The possible cleavage of the primary carbon-cobalt bond in 3 was a strong incentive to evaluate the copolymerization of VAc with ethylene by OMRP, expecting a good activation of the dormant species 5 having a terminal ethylene-cobalt moiety. As a result, EVAs with low dispersities were produced at 40 °C in the presence of $\text{Co}(\text{acac})_2$ and their ethylene content increased with the ethylene pressure (19). For example, about 50 mol% of ethylene was reached at 50 bar. Interestingly, varying the ethylene pressure during the polymerization allowed to produce block-like EVA copolymers associating ethylene rich and ethylene poor segments (19).



Scheme 1. Organometallic-mediated radical polymerization : Head-to-head addition in the VAc polymerization (white area) and E/VAc copolymerization (shaded area).

In this work, we further investigate the controlled copolymerization of ethylene and vinyl acetate by OMRP and pursue our macromolecular engineering efforts targeting novel well-defined EVA-based copolymers. Compared to our previous work (19), higher ethylene pressure (100 bar) is used for the OMRP of E/VAc and we evaluate the influence of this parameter on the kinetics, level of control of the copolymerization and copolymer composition. For the first time, we also address the precision design of EVA-containing “real” block copolymers by OMRP, i.e. PVAc-*block*-EVA. In this case, the order of the synthesis of the blocks is shown to be critical for the complete chain extension and the preparation of well-defined block copolymers.

Experimental Section

Methods

All manipulations were performed using Schlenk techniques under argon. The organocobalt initiator ($R\text{-Co}(\text{acac})_2$) was prepared as described previously (33) and stored as a CH_2Cl_2 solution at $-20\text{ }^\circ\text{C}$ under argon. VAc conversion and polymer composition were determined by ^1H NMR in CDCl_3 at 250 MHz. Molar mass (M_n) and dispersity (\mathcal{D}) of the polymers were determined by size-exclusion chromatography (SEC) in THF relative to poly(styrene) (PS) standards at $45\text{ }^\circ\text{C}$ (flow rate: 0.7 mL/min) with a Malvern chromatograph equipped with Agilent columns (two PL-gels $5\text{ }\mu\text{m}$ columns, 10^3 and $10^2\text{ }\text{\AA}$). Polymerizations were quenched with TEMPO. Polymerizations at 40 bar of ethylene were pursued in a 30 mL stainless-steel autoclave and polymerizations at 100 bar were conducted into a 24 mL high-pressure stainless-steel autoclave equipped with a compressor.

Procedures

Synthesis of EVA Copolymers

A solution of VAc (4.9 mL, 5.3×10^{-2} mol) containing the organocobalt initiator (5.3×10^{-4} mol) was transferred into the autoclave using a cannula ($[\text{VAc}]/[\text{R-Co}(\text{acac})_2] = 100$). The autoclave was pressurized to 40 bar of ethylene and heated at 40 °C. The pressure was maintained manually during the polymerization and the reaction mixture was stirred magnetically at 500 revolutions per minute (rpm). Every 2 h during 12 h, ethylene was removed and an aliquot was picked out of the medium to determine the VAc conversion and the molecular parameters of the EVA_{40 bar}. The same procedure was repeated at 100 bar for the synthesis of EVA_{100 bar}, all other conditions being equal (40 °C, $[\text{VAc}]/[\text{R-Co}(\text{acac})_2] = 100$, Table 1 and Figures 1 and 2). The composition of the EVAs are plotted versus the ethylene pressure in Figure 3.

*Synthesis of PVAc-*b*-EVA Copolymers*

VAc (10 mL, 1.1×10^{-1} mol) was placed under inert atmosphere in a Schlenk tube containing the organocobalt initiator (1.1×10^{-3} mol) and the polymerization occurred for 6 h at 40 °C leading to the PVAc first block (conversion = 50%, $M_{n, \text{SEC PVAc}} = 7300 \text{ g mol}^{-1}$, $\bar{D} = 1.08$). Then, VAc (4.9 mL, 5.3×10^{-2} mol) was introduced into another Schlenk tube containing the above mentioned PVAc-Co(acac)₂ macroinitiator (5.3×10^{-4} mol) and the solution was transferred into the autoclave using a cannula ($[\text{VAc}]/[\text{PVAc-Co}(\text{acac})_2] = 100$). The autoclave was pressurized to 40 bar of ethylene and heated at 40 °C. The pressure was maintained manually during the polymerization and the reaction mixture was stirred magnetically at 500 rpm. Aliquots were picked out of the medium to determine the VAc conversion and the molecular parameters of the PVAc-*b*-EVA_{40bar}. The same procedure was repeated at 100 bar for the synthesis of PVAc-*b*-EVA_{100 bar}, all other conditions being equal (40 °C, $[\text{VAc}]/[\text{PVAc-Co}(\text{acac})_2] = 100$, same PVAc-Co(acac)₂). (See Figure 4.)

*Synthesis of EVA-*b*-PVAc copolymers*

A solution of VAc (3 mL, 3.3×10^{-2} mol) containing the organocobalt initiator (3.3×10^{-4} mol) was transferred under inert atmosphere into the autoclave using a cannula. The autoclave was then pressurized to 100 bar of ethylene and heated at 40 °C. The pressure was maintained manually during the polymerization and the reaction mixture was stirred magnetically at 500 rpm. After 12 h, ethylene was removed and an aliquot was picked out of the medium to determine the VAc conversion and the EVA molecular parameters. For the synthesis of the second block, to the medium containing EVA-Co(acac)₂ was added VAc (1 mL, 1.1×10^{-2}

mol) in order to compensate the consumed VAc before heating at 40 °C for 12 h. The experiment was repeated but the PVAc block was synthesized in the presence of V-70 (20 mg, 6.6×10^{-5} mol or 50 mg, 1.7×10^{-4} mol, corresponding to 20 mol% or 50 mol% compared to the organocobalt initiator, respectively) dissolved in 1 mL of VAc. (See Figure 5.)

Results and Discussion

Statistical EVA Copolymers

Commercially available EVAs are composed of ethylene and vinyl acetate units distributed randomly along the copolymer backbone. They are mainly produced by free radical polymerization under harsh experimental conditions, i.e. high pressure and elevated temperature, leading to ill-defined polymers with high molar mass dispersities and branching. By contrast, the EVA copolymers prepared in our group at moderate temperature (40 °C) by Co(acac)₂-mediated radical copolymerization, exhibit predictable molar masses, low dispersities and low degree of branching (19). In this former work, the radical character of the process has been demonstrated by electron spin resonance (ESR) experiments using a tert-butyl nitron as a spin trap (19). Importantly, the ethylene molar fraction of the EVAs has been tuned from about 0.15 to 0.50 by varying the ethylene pressure from 10 to 50 bar while keeping a good control of the copolymerization (19). Unfortunately, due to technical limitations of the reactors, ethylene pressures higher than 50 bar could not be tested at that time.

Since then, the acquisition of a new reactor permits us to perform similar organometallic-mediated E/VAc radical copolymerizations up to 100 bar of ethylene pressure (P_{ethylene}). In theory, such an increase of P_{ethylene} is supposed to further enrich the copolymer in ethylene. In order to highlight the effect of the P_{ethylene} on the course of the polymerization, the OMRP of E/VAc has been conducted at 40 bar and 100 bar, all other parameters being constant (Table 1). In this case, a low molecular weight cobalt(III) adduct (R-Co(acac)₂) (33), which mimics a PVAc-Co(acac)₂ dormant species and contains less than four vinyl acetate units on average, is used to initiate the copolymerizations at 40 °C and the [VAc]/[R-Co(acac)₂] was fixed to 100. In practice, the alkyl-cobalt initiator is dissolved in VAc under inert atmosphere followed by ethylene pressurization and heating. The setup is designed to maintain a constant ethylene pressure all along the polymerization. It has been possible to make regular withdrawals for the kinetics carried out at 40 bar but not for the experiments performed at 100 bar. In the latter case, repeated depressurization/pressurization cycles between points caused loss of VAc which sometimes rendered the data not reliable. For this reason, several copolymerizations have been carried out at 100 bar and stopped at different times in order to build the kinetic curve.

Table 1. Ethylene-vinyl acetate copolymerization by OMRP^a

Entry	P_{ethylene} (bar)	Time (h)	conv. VAc ^b (%)	M_n ^c (g mol ⁻¹)	\bar{D} ^c	F_{ethylene} ^b
1	40	1	21	3300	1.14	0.40
		2	29	4100	1.13	0.40
		4	38	5100	1.17	0.42
		6	50	5900	1.20	0.43
		8	60	6300	1.25	0.40
		10	69	6900	1.29	0.43
		12	77	7800	1.27	0.43
2	100	24	85	8800	1.48	0.43
		2	11	2800	1.18	0.59
		4	17	3500	1.18	0.55
		7	20	4200	1.19	0.55
		12	22	5000	1.22	0.57

^a Conditions : 40 °C, [VAc]/[R-Co(acac)₂] = 100. ^b Measured by ¹H NMR in CDCl₃.

^c Determined by SEC in THF with a PS calibration.

From the kinetics point of view, no induction period is observed at 40 and 100 bar, as expected for polymerizations initiated with a preformed alkyl-cobalt(III) species (Figure 1). Indeed, heating the E/VAc/R-Co(acac)₂ mixture at 40 °C induces the homolytic cleavage of the Co-C bond of the organo-cobalt releasing the initiating radical and the Co(acac)₂ mediating species at the early stage of the polymerization. A quite linear time dependence of the $\ln[M]_0/[M]$ function appears in Figure 1 for both experiments suggesting that the number of radicals in the medium is constant throughout the copolymerization. However, the copolymerization rate is about four times slower at 100 bar compared to the one at 40 bar. Indeed, after 12 h, the VAc conversion reaches 77% and 22% at 40 and 100 bar, respectively (Table 1). A decrease of the polymerization rate was also observed in our previous study (19) when P_{ethylene} was increased from 10 to 50 bar. This trend was explained by the higher concentration of ethylene in the mixture at higher P_{ethylene} , by the higher stability of the terminal ethylene-cobalt dormant chains compared to the VAc-cobalt ones and by the lower propagation rate constant of ethylene compared to VAc. A slight accumulation of Co(acac)₂ deactivator in the medium resulting from some irreversible termination reactions may also account for the lower polymerization rates observed at higher ethylene pressures.

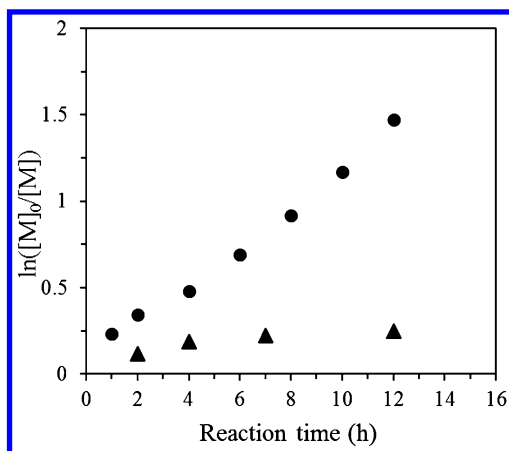


Figure 1. Time dependence of $\ln([M]_0/[M])$ for the ethylene/VAc copolymerization initiated at 40 °C by $R\text{-Co}(\text{acac})_2$ at 40 bar (●) and 100 bar (▲) of ethylene ($[\text{VAc}]/[\text{R-Co}(\text{acac})_2] = 100$).

Next, molar masses (M_n) and dispersities (\mathcal{D}) of the EVAs collected at different polymerization times at 40 and 100 bar of ethylene have been measured by size exclusion chromatography (SEC). Data are plotted as a function of the VAc conversion in Figure 2. Whatever the ethylene pressure, the molar masses increase with the monomer conversion, which demonstrates the controlled character of the copolymerizations. As a result of a slower kinetics at high P_{ethylene} , the final conversion and M_n of the last copolymer is lower at 100 bar compared to 40 bar. Nevertheless, for a given conversion, e.g. 20%, the molar masses of EVA_{40 bar} and EVA_{100 bar} are approximately in the same range (3200 and 4100 g/mol, respectively). On the other hand, the dispersity of EVA_{40 bar} remains as low as 1.2-1.3 at least up to 80% of VAc conversion and it only broadens to 1.5 at 85%. Well-defined EVA ($\mathcal{D} \sim 1.2$) are also produced at 100 bar, so significantly above the ethylene pressure investigated so far (see ref (19)).

Next, the composition of the copolymers has been determined by ^1H NMR through relative intensities between signals corresponding to the $-\text{CH}(\text{OAc})$ -proton of the VAc units ($\delta = 4.9$ ppm) and to the $-\text{CH}_2-$ protons of ethylene units ($\delta = 1.55\text{-}1.20$ ppm) (spectrum not shown, see ref (19) for detailed assignments). As a rule, the ethylene molar fraction in EVAs does not vary much along the polymerizations because the ethylene pressure is maintained constant (Figure 2). As expected, increasing the pressure from 40 to 100 bar raises the ethylene content in the copolymer from 43 to 55 mol%. A third copolymerization carried out at 75 bar leads to intermediate composition, e.g. 51 mol% of ethylene. These values as well as data from Kermagoret and coworkers (19) are reported on Figure 3 which illustrates the evolution of ethylene molar fraction (F_{ethylene}) of EVA as a function of P_{ethylene} , all other experimental parameters being constant. It clearly appears that the $F_{\text{ethylene}}/P_{\text{ethylene}}$ dependence deviates from linearity around 50 bar. Above this value, significant increase of the ethylene pressure only causes moderate enrichment of EVA in ethylene. Based on previous studies

on the solubility of ethylene in organic solvent, it is reasonable to assume that the ethylene content in VAc increases in parallel with P_{ethylene} (37). However, E/VAc reactivity ratios, which are in favor of VAc at low temperature ($< 80\text{ }^{\circ}\text{C}$) and at a P_{ethylene} of 100 bar, might account for the observed ceiling of the ethylene molar fraction in the copolymer (38, 39).

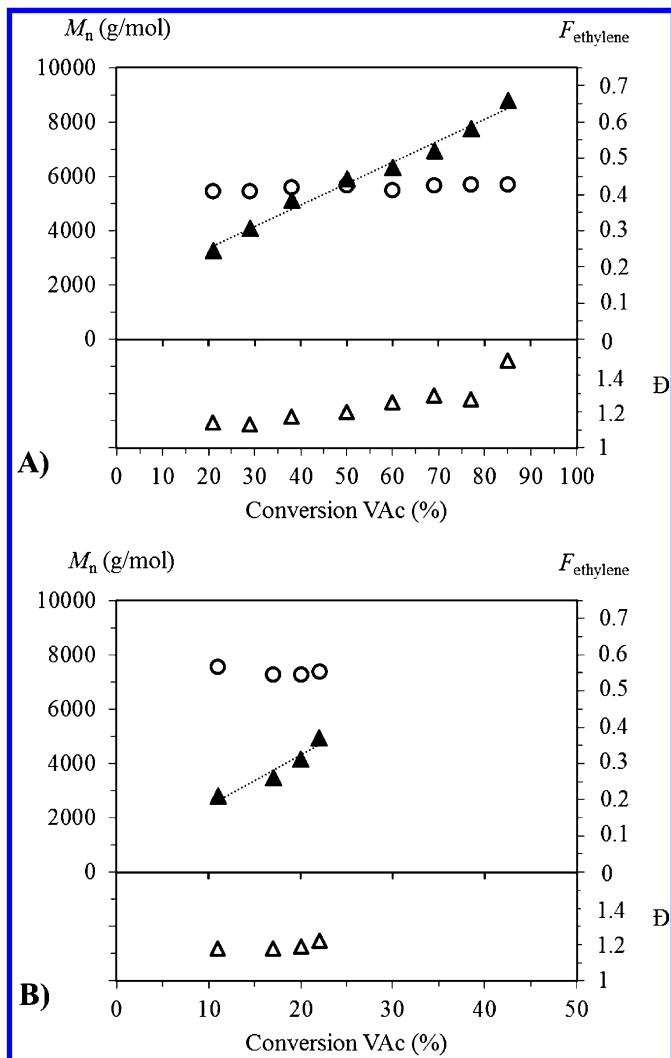


Figure 2. Dependence of M_n (▲), \bar{D} (▲) and ethylene molar fraction (○) for the ethylene/VAc copolymerizations initiated at 40 °C by R-Co(acac)₂ at 40 bar (upper graph A) and 100 bar (lower graph B) of ethylene. ($[\text{VAc}]/[\text{R-Co(acac)}_2] = 100$).

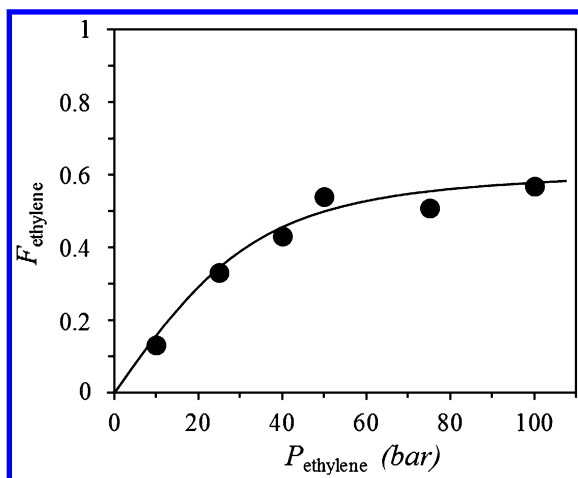


Figure 3. Evolution of the ethylene molar fraction (F_{ethylene}) in EVAs prepared by OMRP as a function of the ethylene pressure. Conditions: 40 °C, $[VAc]/[R-Co(acac)_2] = 100$. The line is drawn to guide the eyes. Data at 10, 25 and 50 bar are taken from reference (19).

EVA-Based Block Copolymers

As stated in the introduction, well-defined block-like copolymers composed of EVA sequences with different ethylene molar fractions (approximately 0.5 and 0.2, respectively) were previously synthesized by OMRP (19). Typically, the preparation of the ethylene rich segment was first carried out by E/VAc copolymerization at 50 bar followed by depressurization and subsequent copolymerization at 10 bar. Quite similar block-like copolymers were obtained by reversing the order of the block synthesis (19). Interestingly, the corresponding EVA_{50bar}-*b*-EVA_{100bar}-*b*-EVA_{50bar} and EVA_{100bar}-*b*-EVA_{50bar}-*b*-EVA_{100bar} triblocks copolymers were produced by treatment of the parent diblocks with isoprene (19), following a previously described radical coupling method (40). Although interesting, these copolymers, whose segments only differ by their composition, can not be considered as real block copolymers, a block being defined as “a portion of a polymer molecule in which the monomeric units have at least one constitutional or configurational feature absent from the adjacent portions” according to IUPAC (41).

In order to fill the gap, here, we explore the synthesis by OMRP of “real” block copolymers composed of an EVA sequence associated to a pure PVAc segment. The first approach consists in the sequential polymerization of VAc followed by E/VAc copolymerization (Figure 4). Typically, the VAc polymerization is carried out at 40 °C from R-Co(acac)₂ until 50% of conversion leading to a well-defined PVAc trapped by Co(acac)₂ (7300 g/mol, $\bar{M}_n = 1.08$) which is used as macroinitiator in the second step. For the synthesis of the EVA block, the $[VAc]/[PVAc-Co(acac)_2]$ molar ratio of the mixture is adjusted to 100 by addition of fresh VAc under inert atmosphere before pressurizing the reaction medium

with ethylene at 40 or 100 bar. Polymerization is then continued at 40 °C. Figure 4 shows SEC chromatograms of the chain extension experiments. At 40 bar, curves are shifted towards the higher molar mass side and no residual traces of the PVAc macroinitiator is detected, suggesting a successful block copolymerization. After 12 h, the VAc conversion is equal to 70% and a well defined PVAc-*b*-EVA_{40 bar} block copolymer (12700 g/mol, $\bar{D} = 1.20$) is formed. The ethylene fraction in the EVA_{40 bar} block is evaluated by ¹H NMR to 0.45, which is consistent with the composition of the statistical EVA copolymer prepared at the same P_{ethylene} (see Figure 3). The chain extension is also efficient when performed at 100 bar, as assessed by the significant shift of the chromatograms towards lower elution volume (Figure 4B). In this case, a PVAc-*b*-EVA_{100 bar} with low dispersity (1.25) is collected. At both pressures, a slight shoulder appears at the high molar mass side of the SEC peak of the final copolymers. The latter is more pronounced at 100 bar and most probably corresponds to some coupling of the copolymer chains at the end of the process. Though difficult to verify at this stage, the coupling product probably occurs between EVA chains terminated by a VAc unit which present a weaker Co-C bond compared to the ethylene terminated chains. On the other hand, radicals generated from the ethylene-terminated species, more prominent in reactions conducted at high ethylene pressure, probably exhibit a higher propensity for coupling than radical chains terminated by a vinyl acetate unit. Expectedly, the kinetics of the chain extension is slower and the ethylene content in the EVA block is higher ($F_{\text{ethylene}} = 0.55$) at 100 bar compared to 40 bar.

In a second approach, copolymers composed of PVAc and EVA segments are targeted by reversing the order of the synthesis of the blocks (Figure 5). First, a well-defined statistical EVA-Co(acac)₂ copolymer composed of 57 mol% of ethylene is formed by a 12 hours E/VAc copolymerization initiated from R-Co(acac)₂ at 40 °C and 100 bar (dotted line in Figure 5A), as described in the previous section. Then, ethylene is removed by depressurizing the reactor at room temperature, fresh VAc is added in order to adjust the [VAc]/[EVA-Co(acac)₂] ratio to 100 and the polymerization of VAc alone is continued at 40 °C. In this case, an EVA_{100 bar}-*b*-PVAc copolymer is formed but only a slight shift of the SEC curves and rather low VAc conversion (7%) are observed (Figure 5A). Such a slow polymerization of VAc might originate from accumulation of Co(acac)₂ deactivator during the synthesis of the EVA precursor as a result of some irreversible termination reactions. In order to overcome this problem, some V-70 azoinitiator (20 and 50 mol% compared to EVA-Co) is added to the medium before conducting the chain extension (Figures 5B and 5C). Radicals generated by V-70 are supposed to consume the accumulated cobalt(II) species and increase the VAc polymerization rate (32). Under these conditions, an influx of radicals is generated in the medium along the polymerization, which is known to switch the OMRP mechanism from a reversible-termination (RT) pathway to a degenerative chain transfer (DT) mode (33, 42, 43) that also offers a good control of the VAc polymerization. Comparing Figures 5A-C, addition of V-70 slightly increases the rate of the VAc polymerization, as shown by a more pronounced shift of the chromatograms after 12 h. However, the EVA-*b*-PVAc is contaminated by some unreacted EVA chains which appear as a shoulder on the low molar mass side of the main peak. These EVA dead chains most probably result from irreversible

termination reactions caused by a too large excess of radicals produced by V-70. As a confirmation, this side reaction is attenuated when decreasing the amount of V-70 from 50 to 20 mol% (compare Figures 5C and 5B). Of course, further reduction of the amount of V-70 should limit the deactivation of the macroinitiator phenomenon but it should also affect the rate of polymerization that is still low with 20-50 mol% of V-70.

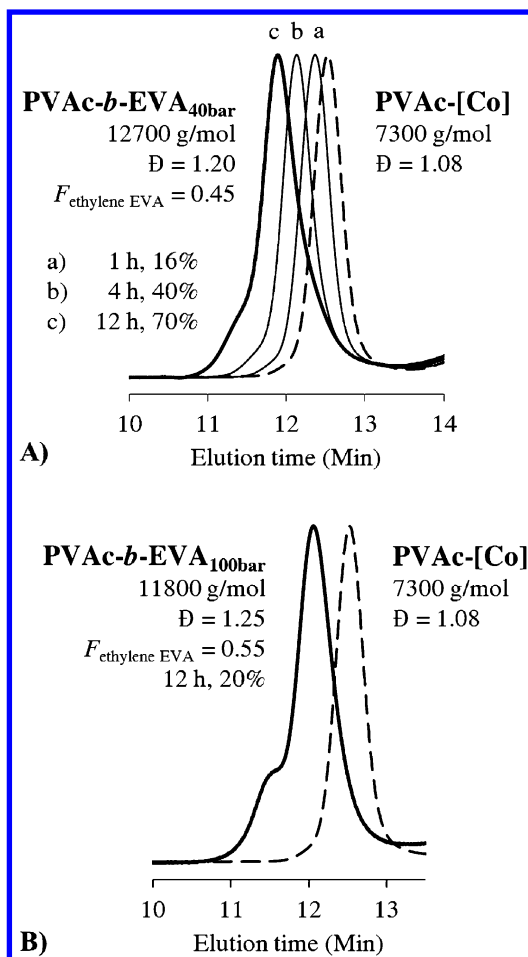


Figure 4. SEC chromatograms for PVAc-*b*-EVA block copolymers (full lines) prepared by E/VAc copolymerization initiated from a PVAc-Co(acac)₂ macroinitiator (dotted line) under 40 bar (A) or 100 bar (B) of ethylene. Conditions for PVAc-Co(acac)₂ synthesis : 40 °C, 6 h, [VAc]/[R-Co(acac)₂] = 100, VAc conv. = 50%. Chain extension conditions: 40 °C, [VAc]/[R-Co(acac)₂] = 100, P_{ethylene} = 40 or 100 bar. Percentages appearing on SEC overlays correspond to the VAc conversion during the synthesis of the EVA block.

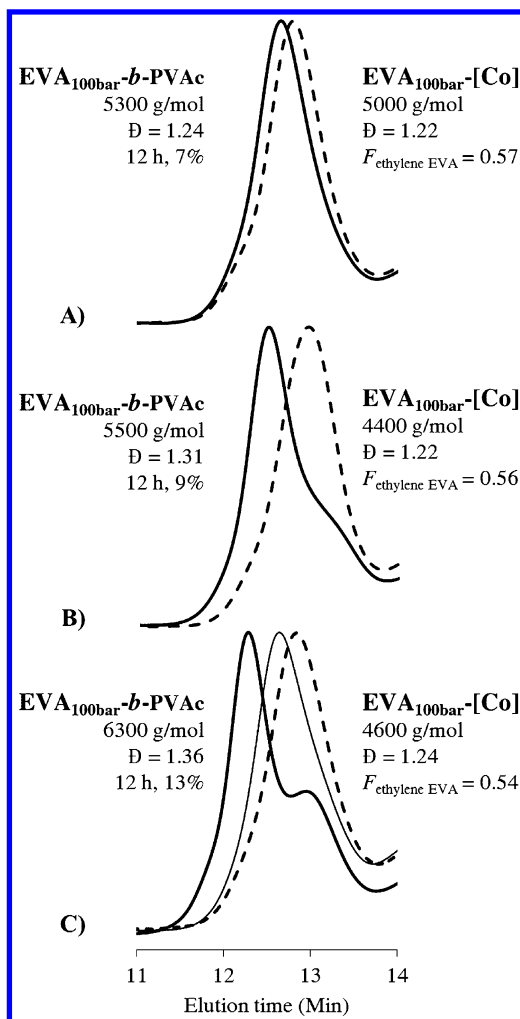


Figure 5. SEC chromatograms for the synthesis of EVA-*b*-PVAc block copolymers (bold lines) by VAc polymerization initiated from a EVA_{100 bar}-Co(acac)₂ macroinitiator (dotted line) with and without V-70 : (A) 0 mol%, (B) 20 mol%, (C) 50 mol%. Conditions for EVA-Co(acac)₂ synthesis : 40 °C, 12 h, [VAc]/[R-Co(acac)₂] = 100, 100 bar). Chain extension conditions: bulk, at 40 °C, [VAc]/[EVA_{100 bar}-Co(acac)₂] = 100. The intermediate curve in figure 5C corresponds to the EVA-*b*-PVAc produced after 6 h (4%, 5200 g/mol, Đ = 1.24). Percentages appearing on SEC overlays correspond to the VAc conversion during the synthesis of the PVAc block.

Conclusion

In this contribution, we investigated further the Co(acac)₂-mediated radical copolymerization of ethylene and vinyl acetate. We notably explored for the first time the synthesis of EVA at ethylene pressure up to 100 bar and compared it to a copolymerization performed at 40 bar. The impact of P_{ethylene} on the polymerization rate, level of control and composition of the final EVAs, was discussed. Copolymerizations occurred in a controlled manner at 40 and 100 bar leading to EVAs with quite low dispersities. Nevertheless, the polymerization was much slower at 100 bar mostly due to the lower propagation rate constant of ethylene whose concentration in the medium is higher at high P_{ethylene} . Although not linear, we emphasized a dependence of the ethylene molar fraction in the copolymer on P_{ethylene} . Ethylene rich EVAs were collected at 100 bar ($F_{\text{ethylene}} = 0.57$).

The synthesis by OMRP of EVA-containing “real” block copolymers, as opposed to the previously reported block-like copolymers (19), was also considered. In particular, we targeted copolymers composed of an EVA segment and a pure PVAc block. The effect of the order of the block synthesis was evaluated. From practical, kinetic and control point of views, the “EVA-first” approach does not compete with the “PVAc-first” strategy. Following the latter, a complete chain extension occurred from the PVAc-Co(acac)₂ precursors leading to well-defined PVAc-*b*-EVA copolymers whose composition of the second block was tunable by the ethylene pressure.

Acknowledgments

The authors are grateful to the “Fonds National de la Recherche Scientifique” (FRS-FNRS) and to the Belgian Science Policy for financial support in the frame of the Interuniversity Attraction Poles Program (P7/05)–Functional Supramolecular Systems (FS2). A.D. is also grateful for fundings from the University of Liège via the “Fonds spéciaux pour la recherche”. J.D. thanks FRIA for Ph.D. fellowship. C.D. is grateful to the FRS-FNRS for funding the MIS project “Organocobalt as clean source of radicals”. A.D. and C.D. are Research Associate and Research Director of the FRS-FNRS, respectively.

References

1. Franssen, N. M. G.; Reek, J. N. H.; de Bruin, B. *Chem. Soc. Rev.* **2013**, *42*, 5809–5832.
2. Dommanget, C.; D’Agosto, F.; Monteil, V. *Angew. Chem., Int. Ed.* **2014**, *53*, 6683–6686.
3. Liu, S.; Elyashiv, S.; Sen, A. *J. Am. Chem. Soc.* **2001**, *123*, 12738–12739.
4. Venkatesh, R.; Harrison, S.; Haddleton, D. M.; Klumperman, B. *Macromolecules* **2004**, *37*, 4406–4416.
5. Venkatesh, R.; Klumperman, B. *Macromolecules* **2004**, *37*, 1226–1233.
6. Venkatesh, R.; Vergouwen, F.; Klumperman, B. *Macromol. Chem. Phys.* **2005**, *206*, 547–552.

7. Tanaka, K.; Matyjaszewski, K. *Macromolecules* **2007**, *40*, 5255–5260.
8. Liu, S.; Gu, B.; Rowlands, H. A.; Sen, A. *Macromolecules* **2004**, *37*, 7924–7929.
9. Gu, B.; Liu, S.; Leber, J. D.; Sen, A. *Macromolecules* **2004**, *37*, 5142–5144.
10. Venkatesh, R.; Staal, B. B. P.; Klumperman, B. *Chem. Commun.* **2004**, 1554–1555.
11. Mishima, E.; Tamura, T.; Yamago, S. *Macromolecules* **2012**, *45*, 8998–9003.
12. Srivastava, S. K.; Pramanik, M.; Acharya, H. *J. Polym. Sci., Part B: Polym. Phys.* **2006**, *44*, 471–480.
13. Krieger, S.; Gohr, K.; Fichtner, T.; Rumrich, S. *Eur. Coat. J.* **2010**, 20–23.
14. Meisenheimer, H.; Zens, A. Ethylene vinyl acetate elastomers (EVM). In *Handbook of Specialty Elastomers*; CRC Press: 2008; pp 343–368.
15. Nakamura, A.; Ito, S.; Nozaki, K. *Chem. Rev.* **2009**, *109*, 5215–5244.
16. Williams, B. S.; Leatherman, M. D.; White, P. S.; Brookhart, M. *J. Am. Chem. Soc.* **2005**, *127*, 5132–5146.
17. Ito, S.; Munakata, K.; Nakamura, A.; Nozaki, K. *J. Am. Chem. Soc.* **2009**, *131*, 14606–14607.
18. Borkar, S.; Sen, A. *J. Polym. Sci., Part A: Polym. Chem.* **2005**, *43*, 3728–3736.
19. Kermagoret, A.; Debuigne, A.; Jérôme, C.; Detrembleur, C. *Nat. Chem.* **2014**, *6*, 179–187.
20. Hurtgen, M.; Detrembleur, C.; Jérôme, C.; Debuigne, A. *Polym. Rev.* **2011**, *51*, 188–213.
21. Poli, R. *Angew. Chem., Int. Ed.* **2006**, *45*, 5058–5070.
22. Allan, L. E. N.; Perry, M. R.; Shaver, M. P. *Prog. Polym. Sci.* **2012**, *37*, 127–156.
23. Debuigne, A.; Poli, R.; Jérôme, C.; Jérôme, R.; Detrembleur, C. *Prog. Polym. Sci.* **2009**, *34*, 211–239.
24. Poli, R.; Allan, L. E. N.; Shaver, M. P. *Prog. Polym. Sci.* **2014**, *39*, 1827–1845.
25. Asandei, A. D.; Moran, I. W. *J. Am. Chem. Soc.* **2004**, *126*, 15932–15933.
26. Debuigne, A.; Poli, R.; Jérôme, R.; Jérôme, C.; Detrembleur, C. *ACS Symp. Ser.* **2009**, *1024*, 131–147.
27. Peng, C.-H.; Yang, T.-Y.; Zhao, Y.; Fu, X. *Org. Biomol. Chem.* **2014**, *12*, 8580–8587.
28. Wayland, B. B.; Poszmik, G.; Mukerjee, S. L.; Fryd, M. *J. Am. Chem. Soc.* **1994**, *116*, 7943–7944.
29. Debuigne, A.; Morin, A. N.; Kermagoret, A.; Piette, Y.; Detrembleur, C.; Jérôme, C.; Poli, R. *Chem.–Eur. J.* **2012**, *18*, 12834–12844.
30. Detrembleur, C.; Debuigne, A.; Hurtgen, M.; Jérôme, C.; Pinaud, J.; Fevre, M.; Coupillaud, P.; Vignolle, J.; Taton, D. *Macromolecules* **2011**, *44*, 6397–6404.
31. Cordella, D.; Kermagoret, A.; Debuigne, A.; Riva, R.; German, I.; Isik, M.; Jerome, C.; Mecerreyes, D.; Taton, D.; Detrembleur, C. *ACS Macro Lett.* **2014**, *3*, 1276–1280.
32. Debuigne, A.; Caille, J.-R.; Detrembleur, C.; Jérôme, R. *Angew. Chem., Int. Ed.* **2005**, *44*, 3439–3442.

33. Debuigne, A.; Champouret, Y.; Jérôme, R.; Poli, R.; Detrembleur, C. *Chem.–Eur. J.* **2008**, *14*, 4046–4059.
34. Morin, A. N.; Detrembleur, C.; Jérôme, C.; De, T. P.; Poli, R.; Debuigne, A. *Macromolecules* **2013**, *46*, 4303–4312.
35. Iovu, M. C.; Matyjaszewski, K. *Macromolecules* **2003**, *36*, 9346–9354.
36. Kwak, Y.; Goto, A.; Fukuda, T.; Kobayashi, Y.; Yamago, S. *Macromolecules* **2006**, *39*, 4671–4679.
37. Grau, E.; Broyer, J.-P.; Boisson, C.; Spitz, R.; Monteil, V. *Phys. Chem. Chem. Phys.* **2010**, *12*, 11665–11669.
38. Raetzsch, M.; Schneider, W.; Musche, D. *J. Polym. Sci., Part A* **1971**, *9*, 785–790.
39. Filley, J.; McKinnon, J. T.; Wu, D. T.; Ko, G. H. *Macromolecules* **2002**, *35*, 3731–3738.
40. Debuigne, A.; Jérôme, C.; Detrembleur, C. *Angew. Chem., Int. Ed.* **2009**, *48*, 1422–1424.
41. Ring, W.; Mita, I.; Jenkins, A. D.; Bikales, N. M. *Pure Appl. Chem.* **1985**, *57*, 1427–1440.
42. Maria, S.; Kaneyoshi, H.; Matyjaszewski, K.; Poli, R. *Chem.–Eur. J.* **2007**, *13*, 2480–2492.
43. Wayland, B. B.; Peng, C.-H.; Fu, X.; Lu, Z.; Fryd, M. *Macromolecules* **2006**, *39*, 8219–8222.

Chapter 5

High-Throughput Synthesis of Thermoresponsive Poly(oligoethylene glycol acrylate) Copolymers by RAFT Polymerization

Lenny Voorhaar,¹ Kristof Van Hecke,² Gertjan Vancoillie,¹ Qilu Zhang,¹ and Richard Hoogenboom^{1,*}

¹Supramolecular Chemistry Group, Department of Organic and Macromolecular Chemistry, Ghent University, Krijgslaan 281 S4, 9000 Ghent, Belgium

²XStruct, Department of Inorganic and Physical Chemistry, Ghent University, Krijgslaan 281 S3, 9000 Ghent, Belgium

*E-mail: richard.hoogenboom@ugent.be

Thermoresponsive polymers are an interesting class of stimuli-responsive polymers because of their potential in vivo applications resulting from the easily controllable trigger. In this work, two series of statistical copolymers of di(ethylene glycol) ethyl ether acrylate with di(ethylene glycol) methyl ether acrylate and tri(ethylene glycol) methyl ether acrylate, respectively, were synthesized using high-throughput automated parallel RAFT polymerization to accurately tune the polymer phase transition temperature. Cloud point temperature determination for each copolymer was performed by parallel turbidimetry and revealed a linear relationship with copolymer composition. The crystal structure of the used chain transfer agent 2-(((butylsulfanyl)carbonothioyl) sulfanyl)propanoic acid is also reported.

Thermoresponsive polymers are among the most studied stimuli-responsive polymers due to their large potential towards *in vivo* applications and easily controllable stimulus (1, 2). This responsiveness can be expressed in multiple

ways including solid state transitions in shape memory materials (3, 4), although solution phase transitions are by far the most commonly studied. The latter is characterized by a lower critical solution temperature (LCST) when the polymer becomes insoluble upon heating of the solution, or an upper critical solution temperature (UCST) when the polymer becomes soluble upon heating. In the case of an LCST polymer solution, heating above the cloud point temperature (T_{cp}) causes the phase separation of the solution with the formation of polymer rich droplets, which usually aggregate and precipitate, in a polymer-poor solution (5, 6). The enthalpic gain originating from polymer – water interactions is in this case no longer able to compensate for its entropic loss, leading to a negative Gibbs free energy and spontaneous phase separation. The T_{cp} , i.e. the temperature where the enthalpic gain exactly compensates the entropic loss, can be tuned by various parameters including polymer concentration and ionic strength of the aqueous solution, although predominantly by the identity of the polymer structure. Increasing the hydrophilicity of the monomer will increase the enthalpic gain and therefore increase the T_{cp} , while increasing the hydrophobicity will lower the T_{cp} , making it possible to adjust the T_{cp} by careful monomer design (7).

Poly(*N*-isopropylacrylamide) (PNIPAAm) is the most studied LCST polymer due to its stable T_{cp} close to body temperature (≈ 32 °C) showing little dependence on degree of polymerization, concentration and pH (8). Recently, some other types of polymers such as poly(oligoethylene glycol (meth)acrylate)s (POEG(M)A) (9, 10) and poly(2-oxazolines) (11, 12) have been reported as alternatives of PNIPAM, showing similar thermoresponsive behavior. These polymers also show a highly tunable T_{cp} depending on the hydrophobicity and ratio of the comonomers. In the case of POEGA, polymers originated from various monomers have been reported with different T_{cp} , varying in both the length and end group of the side chains. Copolymerization of two of these monomers allows the delicate design of copolymers with T_{cp} ranging from 0 to 100 °C. In contrast to most other thermoresponsive polymers, POEGAs have a very low T_g leading to a highly reversible LCST phase transition, which can be useful in their applications. While POEGAs are more sensitive to hydrolysis than POEGMAs, it was shown that they are not cytotoxic and can therefore be considered for biomedical applications (13, 14). Examples of possible applications of POEGAs include hydrogels for drug delivery (14), thermo- and light-responsive micelles (15) and thermoresponsive polymer films (16, 17).

For the fast analysis of multiple series of statistical copolymers, high-throughput parallel synthesis is a very useful tool, since it allows for simultaneously performing many polymerizations under similar conditions (18). This technique has previously been successfully used for high-throughput parallel synthesis of polymer libraries using reversible addition–fragmentation chain transfer (RAFT) polymerization (19–21), macromolecular design via the interchange of xanthates (MADIX) (22), atom transfer radical polymerization (ATRP) (23), nitroxide mediated polymerization (NMP) (24), cationic ring-opening polymerization (CROP) (25) and Cu(0)-mediated polymerization (26).

A recent review from our group shows an overview of different thermoresponsive poly(oligo ethylene glycol acrylate)s (10). Most of the studies

reported use a combination of the very hydrophilic hydroxyethyl acrylate or oligo(ethylene glycol) methyl ether acrylate with the very hydrophobic ethylene glycol methyl ether acrylate or di(ethylene glycol) ethyl ether acrylate (eDEGA) to tune the T_{cp} . This means that only half of the available thermoresponsive oligo (ethylene glycol) acrylate monomers have currently been investigated. In an effort to fill this gap, libraries of statistical copolymers of eDEGA with di(ethylene glycol) methyl ether acrylate (mDEGA) and tri(ethylene glycol) methyl ether acrylate (mTEGA) (Figure 1), respectively, were prepared in this study using high-throughput RAFT polymerization in a Chemspeed ASW2000 parallel synthesizer. After synthesis and purification of the polymers, T_{cps} of the copolymers were measured by parallel turbidimetry. The utilized high-throughput synthesis and characterization can significantly reduce the time required to synthesize and analyze series of copolymers. The reported T_{cps} of the homopolymers of eDEGA, mDEGA and mTEGA are around 13 °C, 40 °C and 70 °C (10), respectively, so it is expected that the T_{cps} of the copolymers can be tuned within these boundaries.

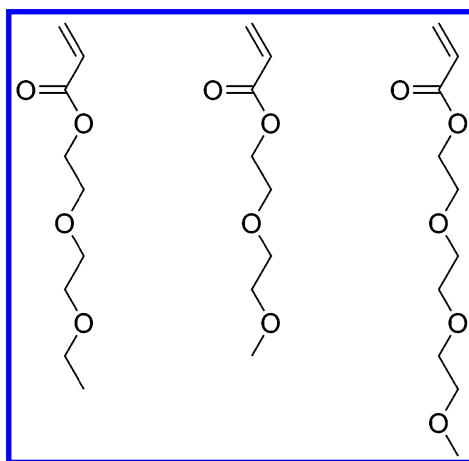


Figure 1. Chemical structures of eDEGA, mDEGA and mTEGA.

Experimental Section

Materials

Acetone (99.8%) and dichloromethane (DCM, 99.8%) were purchased from Sigma-Aldrich and used as received. *N,N*-dimethylformamide (DMF, peptide synthesis) was purchased from Biosolve and used as received. Di(ethylene glycol) ethyl ether acrylate (eDEGA) was purchased from TCI and run on a short aluminum oxide column before use. Di(ethylene glycol) methyl ether acrylate (mDEGA) and tri(ethylene glycol) methyl ether acrylate (mTEGA) were synthesized following a previously published procedure (27, 28). 2-(((Butylsulfanyl)carbonothioyl)sulfanyl)propanoic acid (PABTC) was synthesized following a previously published method (29).

2,2'-Azobis(2-methylpropionitrile) (AIBN) was purchased from Sigma and recrystallized from methanol before use.

Synthesis of Copolymers

The copolymers were synthesized via RAFT polymerization using a Chemspeed ASW2000 automated synthesizer equipped with 16 parallel reactors of 13 mL, a Huber Petite Fleur thermostat for heating/cooling, a Huber Ministat 125 for reflux and a Vacuubrand PC 3000 vacuum pump. Stock solutions of PABTC, AIBN and monomers in DMF were prepared and bubbled with argon for at least 30 minutes before being introduced into the robot system and then kept under argon atmosphere. The hood of the automated synthesizer was continuously flushed with nitrogen and the reactors were flushed with argon to ensure an inert atmosphere. Before starting the polymerizations, the reactors were degassed through ten vacuum-argon cycles. Stock solutions were transferred to the reactors using the syringe of the automated synthesizer while the reactors were kept at 10 °C. Reactions were performed using $[M]:[PABTC]:[AIBN] = 100:1:0.1$ and a total monomer concentration of 2.0 M in DMF with a total volume of 4 mL. The [eDEGA]:[mDEGA] and [eDEGA]:[mTEGA] ratios were varied with 100:0, 80:20, 60:40, 50:50, 40:60, 20:80 and 0:100. Each reaction was performed in duplicate. A $t = 0$ minutes sample was taken from each reaction for later conversion calculation. The reactors were then heated to 70 °C, which takes about 11 minutes, to start the polymerizations. During the reactions, 50 μ L samples were taken every 20 minutes and directly injected into 1.5 mL sample vials containing ~1.5 mL of acetone for GC and SEC measurements. After two hours the reactors were cooled to 10 °C to stop the reactions. The solutions were transferred to centrifuge tubes, diluted with distilled water, heated in a water bath at 80 °C and centrifuged for one minute at 7500 RPM. The water was poured off and the polymer was dissolved in cold distilled water, heated in a water bath at 80 °C and centrifuged again for one minute at 7500 RPM. The water was poured off and the polymer dissolved in dichloromethane and dried under vacuum. The mTEGA homopolymers were dialyzed against distilled water to remove all traces of monomer.

Gas Chromatography (GC)

Samples were measured with GC to determine the monomer conversions. GC was performed on an Agilent 7890A system equipped with a VWR Carrier-160 hydrogen generator and an Agilent HP-5 column of 30 m length and 0.320 mm diameter. An FID detector was used and the inlet was set to 250 °C with a split injection of ratio 25:1. Hydrogen was used as carrier gas at a flow rate of 2 mL/min. The oven temperature was increased with 20 °C/min from 50 °C to 120 °C, followed by a ramp of 50 °C/min to 300 °C. A measurement takes ~8 minutes and the large number of samples from the robot were measured overnight using the autosampler.

Size Exclusion Chromatography (SEC)

SEC was performed on a Agilent 1260-series HPLC system equipped with a 1260 online degasser, a 1260 ISO-pump, a 1260 automatic liquid sampler (ALS), a thermostatted column compartment (TCC) at 50 °C equipped with two PLgel 5 μm mixed-D columns and a precolumn in series, a 1260 diode array detector (DAD) and a 1260 refractive index detector (RID). The used eluent was DMA containing 50 mM of LiCl at a flow rate of 0.593 mL/min. The spectra were analyzed using the Agilent Chemstation software with the GPC add on. Molar mass and dispersity values were calculated against PMMA standards from Polymer Labs. A measurement takes ~45 minutes and samples were measured overnight or over the weekend using the autosampler of the system.

Nuclear Magnetic Resonance Spectroscopy (NMR)

NMR spectra were recorded on a Bruker Avance 300 MHz spectrometer at room temperature in deuterated solvents. The percentage of eDEGA in the purified copolymers was calculated by comparing the peaks of the CH₃-groups from both monomers at 1.20 and 3.36 ppm.

Crystal Structure Analysis

For the structure of PABTC, X-ray intensity data were collected on a Agilent Supernova Dual Source (Cu at zero) diffractometer equipped with an Atlas CCD detector using CuK α radiation ($\lambda = 1.54184 \text{ \AA}$) and ω scans. The images were interpreted and integrated with the program CrysAlisPro (Agilent Technologies) (30). Using Olex2 (31), the structure was solved by direct methods using the ShelXS structure solution program and refined by full-matrix least-squares on F² using the ShelXL program package (32). Non-hydrogen atoms were anisotropically refined and the hydrogen atoms in the riding mode and isotropic temperature factors fixed at 1.2 times U(eq) of the parent atoms (1.5 times for methyl groups and the hydroxyl group).

CCDC 1031562 contains the supplementary crystallographic data for this paper and can be obtained free of charge via www.ccdc.cam.ac.uk/conts/retrieving.html (or from the Cambridge Crystallographic Data Centre, 12, Union Road, Cambridge CB2 1EZ, UK; fax: +44-1223-336033; or deposit@ccdc.cam.ac.uk).

Crystal data for PABTC. C₈H₁₄O₂S₃, $M = 238.40$, triclinic, space group $P-1$ (No. 2), $a = 6.4754(5) \text{ \AA}$, $b = 7.0940(4) \text{ \AA}$, $c = 13.7074(6) \text{ \AA}$, $\alpha = 78.942(4)^\circ$, $\beta = 84.035(5)^\circ$, $\gamma = 68.379(6)^\circ$, $V = 574.12(7) \text{ \AA}^3$, $Z = 2$, $T = 100 \text{ K}$, $\rho_{\text{calc}} = 1.379 \text{ g cm}^{-3}$, $\mu(\text{Cu-K}\alpha) = 5.660 \text{ mm}^{-1}$, $F(000) = 252$, 5711 reflections measured, 2338 unique ($R_{\text{int}} = 0.0225$) which were used in all calculations. The final $R1$ was 0.0260 ($I > 2\sigma$) and $wR2$ was 0.0718 (all data).

Cloud Point Temperature Measurements

T_{cp} measurements were performed in 0.7 mL solutions containing 5 mg/mL of polymer in distilled water using an Avantium Crystal16 parallel crystallizer turbidimeter. The samples were heated/cooled at 1 °C/min while stirring at 700 RPM. Three heating and two cooling ramps were performed. The T_{cp} s and clearance point temperatures (T_{clear}) were determined as the temperature at 50% transmission during second and third heating and first and second cooling, respectively.

Results and Discussion

Synthesis and Crystal Structure Description of Chain Transfer Agent

The chain transfer agent (CTA) 2-(((butylsulfanyl)carbonothioyl)sulfanyl)propanoic acid (PABTC) was selected for this study because it can mediate the RAFT polymerization of many different acrylates and acrylamides (33–36), it can easily be synthesized on large scale and the purification is straightforward and efficient by recrystallization, yielding the relatively large amounts of CTA needed for high-throughput experimentation. The PABTC was synthesized by subsequently adding carbon disulfide and 2-bromopropionic acid to a basic solution of butanethiol. The crude product was purified by recrystallization from hexane to give pure PABTC in 85% yield (162 g in a single batch) (29). The 1H NMR spectrum of PABTC is shown in Figure 2, which confirms the success of the synthesis and purification. The recrystallization directly provided single crystals that were suitable for single crystal structure determination.

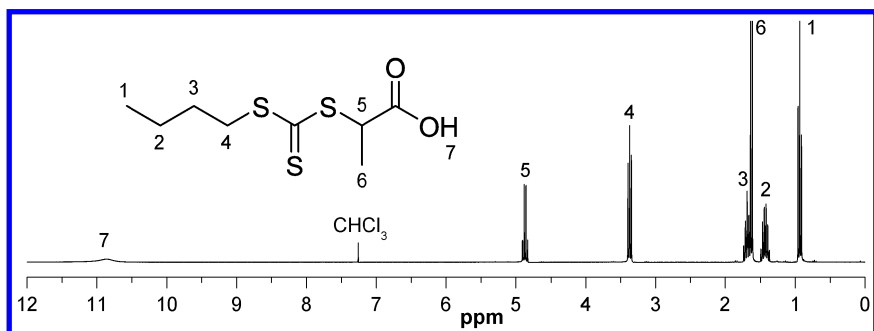


Figure 2. 1H NMR spectrum of PABTC recorded in $CDCl_3$.

The PABTC crystallized in the centro-symmetric space group $P-1$, with one PABTC molecule in the asymmetric unit (Figure 3).

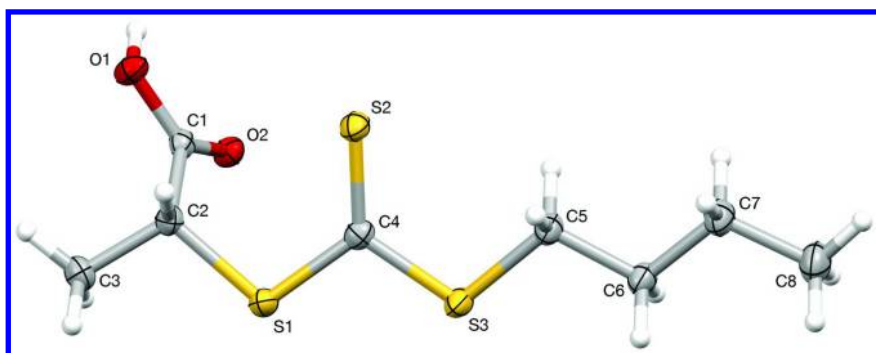


Figure 3. Asymmetric unit of the crystal structure of PABTC, showing thermal displacement ellipsoids at the 50% probability level and atom labeling scheme.

An almost perfectly planar, all-*trans*, zigzag conformation is adopted by the butyl chain and the trithiocarbonate segment, while the carboxyl group is observed in a +synclinal (+sc) position, relative to this chain direction, with a C4-S1-C2-C1 torsion angle of $64.10(11)^\circ$. In fact, for the S3-C8 chain fragment, the maximum deviation from the ideal 180° of the chain torsion angles is less than 0.6° . In addition, the S3-C3 chain fragment is also found almost perfectly *trans*-planar, with a maximum of 6.2° as the torsion angle deviation from ideal value. The +synclinal oriented carboxyl group, relative to this extended chain, can most probably be attributed to the formation of intermolecular hydrogen bonds.

The trithio central group is found almost symmetrical. The bond distances and angles in the trithio moiety are comparable to those reported for other trithio carbonate structures (37–40), found in the Cambridge Structural Database (CSD version 5.35) (41), with the S1-C4 and C4-S3 single bonds of $1.7549(14)$ Å and $1.7408(14)$ Å, respectively and a C4-S2 double bond of $1.6338(14)$ Å.

In the crystal packing, hydrogen-bonded dimeric entities are formed around inversion centers, through intermolecular hydrogen bonding of the carboxylic acid functions of two symmetry equivalent molecules, i.e. between the carbonate O(1)-H(1) and carbonate O(2) (symmetry code: (i) $-x, -y, -z$), with the O(1)-H(1) \cdots O(2) distance of $2.6216(14)$ Å. This is considered a typical feature of carboxylic acid structures. As such, these pairs of centro-symmetric dimers form cyclic structures, which can be described by the $R_2^2(8)$ motif (42). Furthermore, these dimers are connected to each other through weaker intermolecular C-H \cdots O hydrogen bonds (C(5)-H(5B) \cdots O(2) = $3.3017(17)$ Å), to form a chain of edge-fused rings, running along the [010] direction. This arrangement can be described as a molecular 1D ladder, in which the $R_2^2(8)$ rings alternate with and $R_4^4(20)$ rings, as previously observed for similar dodecyl trithio carbonates (38, 40). In this case, such a ladder is hydrogen bonded through additional hydrogen bonds (C(2)-H(2) \cdots O(1) = $3.5560(17)$ Å) to a parallel running ladder, building up 2D layers in (110) plane (Figure 4).

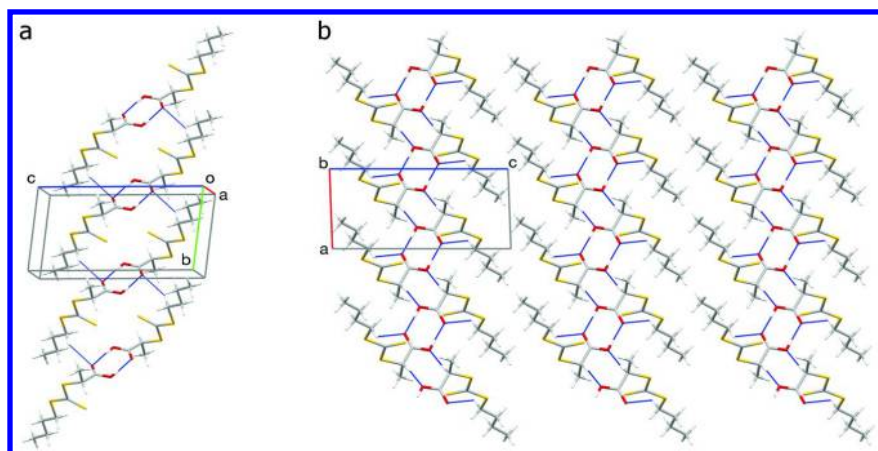


Figure 4. a: Part of the crystal structure of PABTC, showing the formation of a typical ladder, formed through hydrogen bonds, along the $[010]$ direction, containing alternating $R_2^2(8)$ and $R_4^4(20)$ rings; b: Packing diagram of the crystal structure of PABTC, along the b -axis, showing 2D layers in the (110) plane.

High-Throughput RAFT Polymerizations

Two series of copolymers of eDEGA with mDEGA and mTEGA, respectively, were synthesized via RAFT copolymerization to be able to tune the T_{cp} . Each series of copolymers was synthesized in duplicate and in parallel using an automated synthesizer. The kinetic plots for two of the polymerizations are shown in Figure 5 and Figure 6. Each polymerization shows similar pseudo-first order linear kinetics, with both monomers showing the same rate of polymerization independent of the monomer ratios. This is to be expected since the structures of the utilized monomers only differ in the side chain end-groups. Some of the reactions showed a short inhibition time, which is likely caused by small amounts of oxygen present in the system. Because of this inhibition period, small variations in the degree of polymerization of the different copolymers were detected.

Number average molar masses (M_n) determined by SEC were in good agreement with theoretical M_n with narrow dispersities. This agreement of experimental M_n with theoretical M_n does not provide conclusive information, as the molar masses are determined relative to PMMA standards, which may have different hydrodynamic volumes due to differences in solubility. Small differences between the two series of copolymers were observed by SEC measurements, which can be attributed to differences in column conditions and calibration as the experiments were performed with some time in between.

The purification of these polymers was simplified, exploiting their thermoresponsive properties by first dissolving the copolymers in cold water and subsequently centrifuging above their T_{cp} . The limitation of this procedure is that the polymers with high T_{cp} can be difficult to be precipitated upon heating, reducing the yield of the polymer samples. However, it is about a very fast

and easy method to isolate and purify large series of polymer samples, which is important for high-throughput synthesis. For the mTEGA homopolymer, which has the highest T_{cp} , it was not possible to remove all traces of unreacted monomer using this method, so these samples were purified via dialysis against water. Table 1 and Table 2 summarize the properties of the obtained copolymers. Copolymers synthesized by different monomer feed ratios are coded with numbers while both polymerizations with the same feed ratio are labeled with a or b. The percentage of eDEGA in each copolymer, determined by 1H NMR after purification, is in close agreement with the feed ratios of the comonomers for the copolymerizations. SEC characterization of the purified copolymers suggests the formation of well-defined copolymer structures with different ratios of both comonomers as indicated by the low \bar{D} ($\bar{D} < 1.2$) values.

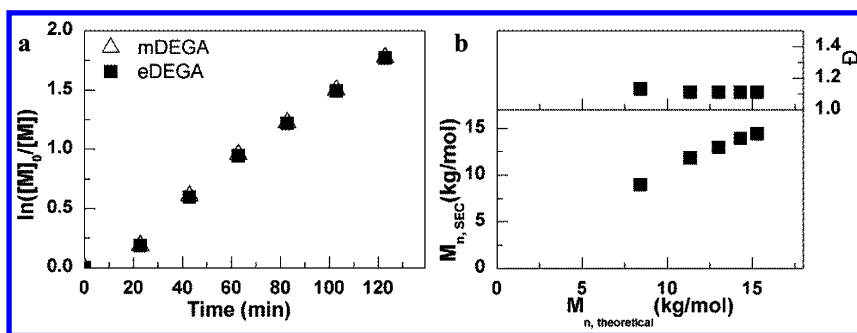


Figure 5. a: pseudo-first order kinetic plot for the RAFT copolymerization of mDEGA and eDEGA using $[mDEGA]:[eDEGA]:[PABTC]:[AIBN] = 50:50:1:0.1$, 2.0 M monomer concentration in DMF at 70 °C (polymer 4a from Table 1). b: the corresponding molar mass and dispersity vs. theoretical molar mass plot.

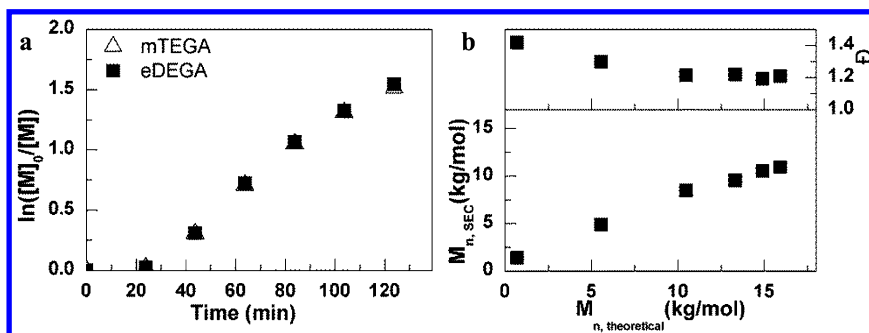


Figure 6. a: pseudo-first order kinetic plot for the RAFT copolymerization of mTEGA and eDEGA using $[mTEGA]:[eDEGA]:[PABTC]:[AIBN] = 40:60:1:0.1$, 2.0 M monomer concentration in DMF at 70 °C (polymer 15a from Table 2). b: the corresponding molar mass and dispersity vs. theoretical molar mass plot.

Table 1. Properties of the poly(eDEGA-*stat*-mDEGA) copolymers.

#	<i>DP</i> <i>eDEGA</i> (GC)	<i>DP</i> <i>mDEGA</i> (GC)	<i>mol %</i> <i>eDEGA</i> <i>theoretical</i>	<i>mol %</i> <i>eDEGA</i> (NMR)	<i>M_n</i> (g/mol, SEC)	<i>Đ</i> (SEC)	<i>T_{cp}</i> (°C)	<i>T_{clear}</i> (°C)
1a	0	84	0	0	14100	1.12	48	46
1b	0	82	0	0	16100	1.09	48	46
2a	15	61	20	22	14300	1.11	39	37
2b	17	66	20	21	15900	1.08	39	38
3a	34	51	40	40	14600	1.13	34	32
3b	33	50	40	41	16000	1.08	32	29
4a	41	42	50	50	14400	1.11	27	25
4b	42	42	50	51	15400	1.08	25	24
5a	51	34	60	60	16900	1.11	23	21
5b	49	33	60	61	15200	1.09	21	22
6a	64	16	80	84	16900	1.09	18	16
6b	66	17	80	79	15200	1.09	19	18
7a	76	0	100	100	19400	1.11	15	13
7b	81	0	100	100	14800	1.09	14	12

Cloud Point Measurements

Figure 7 and Figure 8 show the turbidity curves for all the copolymers. Three heating and two cooling ramps were performed, and the final heating ramps are shown here. In each solution a clear transition from 100% to 0% transmission is observable as well as a shift in the transition upon changing polymer compositions. Polymers containing a higher amount of the hydrophobic eDEGA show an expected lower T_{cp} .

The T_{cp} and T_{clear} values shown in Table 1 and 2 were calculated as the average temperature at 50% transmission from the last two heating and cooling ramps, respectively. While the different ramps usually lead to the same transition temperatures, in some cases a difference up to 0.4 °C was observed between the two ramps, which is within the measurement error of the experiments. Hence, all reported temperatures are rounded off to full degrees Celsius. The difference between T_{cp} and T_{clear} is around 2 °C indicating the presence of small hysteresis, which can most likely disappear or be reduced when a slower ramp is applied (43).

Table 2. Properties of the poly(eDEGA-*stat*-mTEGA) copolymers.

#	<i>DP</i> <i>eDEGA</i> (GC)	<i>DP</i> <i>mTEGA</i> (GC)	<i>mol %</i> <i>eDEGA</i> <i>theoretical</i>	<i>mol %</i> <i>eDEGA</i> (NMR)	<i>M_n</i> (g/mol, SEC)	<i>Đ</i> (SEC)	<i>T_{cp}</i> (°C)	<i>T_{clear}</i> (°C)
11a	0	63	0	0	10800	1.20	69	68
11b	0	79	0	0	12000	1.19	67	68
12a	14	54	20	23	11600	1.19	60	58
12b	15	59	20	22	12100	1.20	62	60
13a	31	46	40	41	12200	1.21	47	45
13b	30	45	40	41	11900	1.20	47	45
14a	37	37	50	50	11400	1.21	40	38
14b	38	38	50	50	11700	1.20	39	37
15a	47	31	60	66	10900	1.21	30	28
15b	48	32	60	64	11400	1.20	32	30
16a	61	15	80	79	11000	1.20	26	24
16b	65	16	80	79	11600	1.21	25	23
17a	78	0	100	100	11900	1.21	15	13
17b	80	0	100	100	11200	1.21	15	13

In some cases a small difference is observed between the two polymers with similar composition (a and b). These are generally in agreement with the corresponding variations in composition calculated from the ¹H NMR spectra, as the copolymers containing more eDEGA have slightly lower *T_{cp}*s. Other minor differences in *T_{cp}* may be explained by different degrees of polymerization, as already reported for P(mTEGA) and P(mDEGA) (44, 45).

In Figure 9 the *T_{cp}*s for both copolymer libraries are plotted against the weight percentage of eDEGA. Both plots show a linear decrease of the cloud point with the amount of eDEGA. From the linear fitting of these plots, the following general empirical formula can be determined to calculate the *T_{cp}* for a designed copolymer composition for these types of copolymers.

$$T_{cp,P(A-stat-B)} = T_{cp,PB} + (T_{cp,PA} - T_{cp,PB}) * \text{weight fraction monomer A}$$

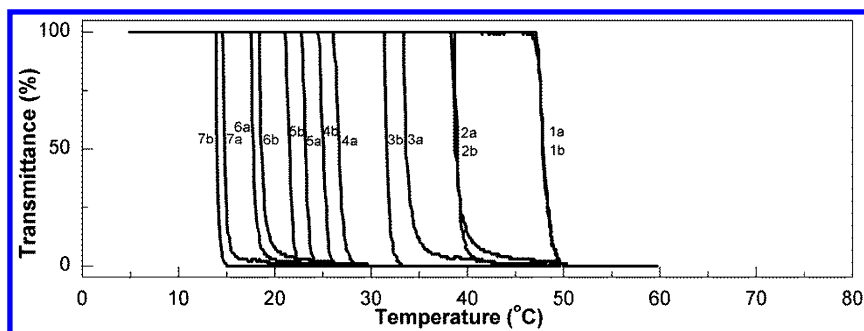


Figure 7. Transmittance versus temperature plots for poly(eDEGA-stat-mDEGA) copolymers in aqueous solutions at a concentration of 5 mg/ml.

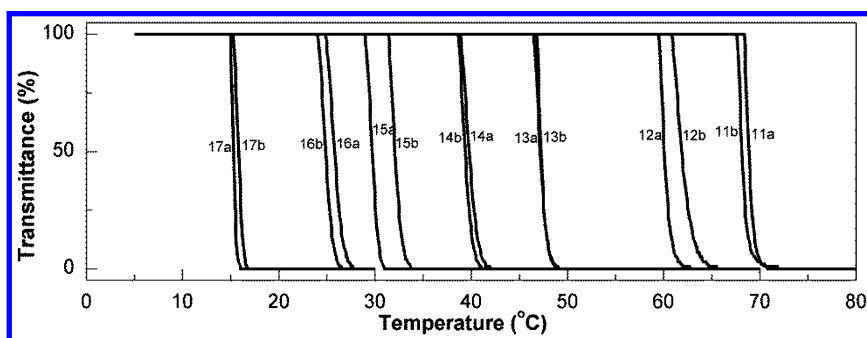


Figure 8. Transmittance versus temperature plots for poly(eDEGA-stat-mTEGA) copolymers in aqueous solutions at a concentration of 5 mg/ml.

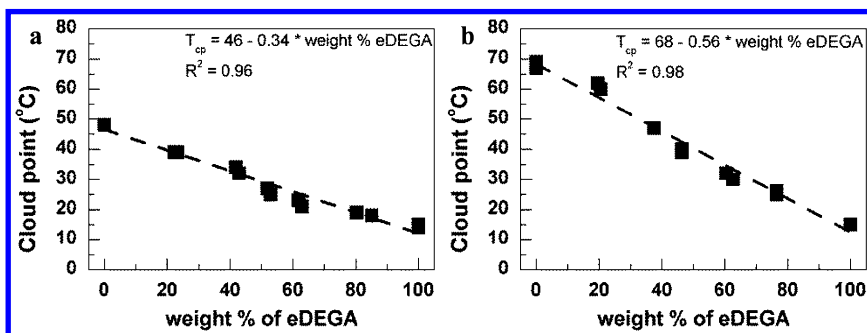


Figure 9. Cloud point temperatures for the copolymers plotted against the weight percentage of eDEGA. a: poly(eDEGA-stat-mDEGA) copolymers, b: poly(eDEGA-stat-mTEGA) copolymers.

A similar linear relationship between copolymer compositions and T_{cp} s was previously reported for gradient poly(oxazoline) copolymers, in which the gradient between the monomers was rather shallow and these polymers behaved more like random copolymers (12). While this formula is valid for both of the copolymers reported in this chapter, it cannot be generalized for all OEGA combinations. For poly(2-hydroxyethyl acrylate-*stat*-2-hydroxypropyl acrylate) (46) and poly(2-hydroxyethyl acrylate-*stat*-ethylene glycol methyl ether acrylate) (47) copolymers, an exponential relationship was found between the fraction of 2-hydroxyethyl acrylate and T_{cp} . Although these examples have a larger possible range of accessible copolymer T_{cp} s, the exponential trend makes it very difficult to accurately pin-point specific T_{cp} s in the higher temperature regime. Since the effect of an additional HEA unit on the overall T_{cp} increases with every added unit, the consequences of a polymerization error can be severe. The described linear dependencies of the used combinations allow for a far more robust and predictable thermoresponsive copolymer design across the entire accessible T_{cp} range.

Conclusion

The chain transfer agent PABTC was successfully synthesized on large scale and the crystal structure was determined. Using high-throughput RAFT polymerization we were able to synthesize two series of thermoresponsive statistical copolymers in high efficiency and reproducibility. Excellent control over polymer composition and molecular weight was shown. Cloud point temperatures determined for the obtained copolymers revealed a linear relationship with copolymer compositions. Using the general empirical relationship, the delicate design of a thermoresponsive copolymer with a desired cloud point temperature is possible, which represents a fast and easy method to synthesize low T_g polymers with any cloud point between 15 and 70 °C.

References

1. de Las Heras Alarcon, C.; Pennadam, S.; Alexander, C. *Chem. Soc. Rev.* **2005**, *34*, 276–285.
2. Schmaljohann, D. *Adv. Drug Delivery Rev.* **2006**, *58*, 1655–1670.
3. Lendlein, A.; Kelch, S. *Angew. Chem., Int. Ed.* **2002**, *41*, 2034–2057.
4. Liu, C.; Qin, H.; Mather, P. T. *J. Mater. Chem.* **2007**, *17*, 1543–1558.
5. Jeong, B.; Gutowska, A. *Trends Biotechnol.* **2002**, *20*, 305–311.
6. Gil, E. S.; Hudson, S. M. *Prog. Polym. Sci.* **2004**, *29*, 1173–1222.
7. Weber, C.; Hoogenboom, R.; Schubert, U. S. *Prog. Polym. Sci.* **2012**, *37*, 686–714.
8. Schild, H. G. *Prog. Polym. Sci.* **1992**, *17*, 163–249.
9. Lutz, J.-F. *J. Polym. Sci., Part A: Polym. Chem.* **2008**, *46*, 3459–3470.
10. Vancoillie, G.; Frank, D.; Hoogenboom, R. *Prog. Polym. Sci.* **2014**, *39*, 1074–1095.
11. Hoogenboom, R.; Thijs, H. M. L.; Jochems, M. J. H. C.; van Lankvelt, B. M.; Fijten, M. W. M.; Schubert, U. S. *Chem. Commun.* **2008**, 5758–5760.

12. Glassner, M.; Lava, K.; de la Rosa, V. R.; Hoogenboom, R. *J. Polym. Sci., Part A: Polym. Chem.* **2014**, *52*, 3118–3122.
13. Chang, C.-W.; Bays, E.; Tao, L.; Alconcel, S. N. S.; Maynard, H. D. *Chem. Commun.* **2009**, 3580–3582.
14. Kostova, B.; Momekova, D.; Petrov, P.; Momekov, G.; Toncheva-Moncheva, N.; Tsvetanov, C. B.; Lambov, N. *Polymer* **2011**, *52*, 1217–1222.
15. Jiang, X.; Lavender, C. A.; Woodcock, J. W.; Zhao, B. *Macromolecules* **2008**, *41*, 2632–2643.
16. Zhong, Q.; Adelsberger, J.; Niedermeier, M. A.; Golosova, A.; Bivigou-Koumba, A. M.; Laschewsky, A.; Funari, S. S.; Papadakis, C. M.; Müller-Buschbaum, P. *Colloid Polym. Sci.* **2013**, *291*, 1439–1451.
17. Zhong, Q.; Metwalli, E.; Rawolle, M.; Kaune, G.; Bivigou-Koumba, A. M.; Laschewsky, A.; Papadakis, C. M.; Cubitt, R.; Müller-Buschbaum, P. *Macromolecules* **2013**, *46*, 4069–4080.
18. Hoogenboom, R.; Meier, M. A. R.; Schubert, U. S. *Macromol. Rapid Commun.* **2003**, *24*, 15–32.
19. Fijten, M. W. M.; Meier, M. A. R.; Hoogenboom, R.; Schubert, U. S. *J. Polym. Sci., Part A: Polym. Chem.* **2004**, *42*, 5775–5783.
20. Becer, C. R.; Groth, A. M.; Hoogenboom, R.; Paulus, R. M.; Schubert, U. S. *QSAR Comb. Sci.* **2008**, *27*, 977–983.
21. Guerrero-Sanchez, C.; O'Brien, L.; Brackley, C.; Keddie, D. J.; Saubern, S.; Chiefari, J. *Polym. Chem.* **2013**, *4*, 1857–1862.
22. Chapon, P.; Mignaud, C.; Lizarraga, G.; Destarac, M. *Macromol. Rapid Commun.* **2003**, *24*, 87–91.
23. Zhang, H.; Fijten, M. W. M.; Hoogenboom, R.; Reinierkens, R.; Schubert, U. S. *Macromol. Rapid Commun.* **2003**, *24*, 81–86.
24. Eggenhuisen, T. M.; Becer, C. R.; Fijten, M. W. M.; Eckardt, R.; Hoogenboom, R.; Schubert, U. S. *Macromolecules* **2008**, *41*, 5132–5140.
25. Hoogenboom, R.; Fijten, M. W. M.; Meier, M. A. R.; Schubert, U. S. *Macromol. Rapid Commun.* **2003**, *24*, 92–97.
26. Voorhaar, L.; Wallyn, S.; Du Prez, F. E.; Hoogenboom, R. *Polym. Chem.* **2014**, *5*, 4268–4276.
27. Ryu, J.-H.; Roy, R.; Ventura, J.; Thayumanavan, S. *Langmuir* **2010**, *26*, 7086–7092.
28. Zhang, Q.; Vanparijs, N.; Louage, B.; De Geest, B. G.; Hoogenboom, R. *Polym. Chem.* **2014**, *5*, 1140–1144.
29. Ferguson, C. J.; Hughes, R. J.; Nguyen, D.; Pham, B. T. T.; Gilbert, R. G.; Serelis, A. K.; Such, C. H.; Hawke, B. S. *Macromolecules* **2005**, *38*, 2191–2204.
30. Agilent. *Crysalis PRO*, Version 1.171.37.31; Agilent Technologies UK Ltd.: Yarnton, Oxfordshire, England, 2014.
31. Dolomanov, O. V.; Bourhis, L. J.; Gildea, R. J.; Howard, J. A. K.; Puschmann, H. *J. Appl. Crystallogr.* **2009**, *42*, 339–341.
32. Sheldrick, G. M. *Acta Crystallogr., Sect. A* **2008**, *64*, 112–122.
33. Ferguson, C. J.; Hughes, R. J.; Pham, B. T. T.; Hawke, B. S.; Gilbert, R. G.; Serelis, A. K.; Such, C. H. *Macromolecules* **2002**, *35*, 9243–9245.

34. Rieger, J.; Zhang, W.; Stoffelbach, F. o.; Charleux, B. *Macromolecules* **2010**, *43*, 6302–6310.
35. Krieg, A.; Weber, C.; Hoogenboom, R.; Becer, C. R.; Schubert, U. S. *ACS Macro Lett.* **2012**, *1*, 776–779.
36. Heinen, J. M.; Blom, A. C. M.; Hawkett, B. S.; Warr, G. G. *J. Phys. Chem. B* **2013**, *117*, 3005–3018.
37. Zeng, G.-S.; Zou, J.-P.; Peng, Q.; Wen, Z.-H.; Zhang, A.-Q. *Acta Crystallogr., Sect. E: Struct. Rep. Online* **2008**, *64*, o2047.
38. Xiao, S.; Charpentier, P. A. *Acta Crystallogr., Sect. E: Struct. Rep. Online* **2011**, *67*, o811.
39. Moreno-Fuquen, R.; Grande, C.; Advincula, R. C.; Tenorio, J. C.; Ellena, J. *Acta Crystallogr., Sect. E: Struct. Rep. Online* **2013**, *69*, o774.
40. Zuluaga, F.; Grande, C.; Cobo, J.; Glidewell, C. *Acta Crystallogr., Sect. C: Cryst. Struct. Commun.* **2010**, *66*, o627–o630.
41. Allen, F. *Acta Crystallogr., Sect. B: Struct. Sci.* **2002**, *58*, 380–388.
42. Bernstein, J.; Davis, R. E.; Shimoni, L.; Chang, N.-L. *Angew. Chem., Int. Ed.* **1995**, *34*, 1555–1573.
43. Joseph, V. S.; Kim, S.; Zhang, Q.; Hoogenboom, R.; Hong, J.-D. *Polymer* **2013**, *54*, 4894–4901.
44. Hua, F.; Jiang, X.; Li, D.; Zhao, B. *J. Polym. Sci., Part A: Polym. Chem.* **2006**, *44*, 2454–2467.
45. Miasnikova, A.; Laschewsky, A. *J. Polym. Sci., Part A: Polym. Chem.* **2012**, *50*, 3313–3323.
46. Hoogenboom, R.; Popescu, D.; Steinhauer, W.; Keul, H.; Müller, M. *Macromol. Rapid Commun.* **2009**, *30*, 2042–2048.
47. Steinhauer, W.; Hoogenboom, R.; Keul, H.; Moeller, M. *Macromolecules* **2010**, *43*, 7041–7047.

Chapter 6

Temperature-Induced Gels from Worms Made by RAFT-Mediated Emulsion Polymerization

Zhongfan Jia and Michael J. Monteiro*

Australian Institute for Bioengineering and Nanotechnology,
The University of Queensland, Brisbane QLD 4072, Australia
*E-mail: m.monteiro@uq.edu.au

A RAFT-mediated emulsion polymerization of styrene using a thermoresponsive macro chain transfer agent (MacroCTA) was used to produce diblock copolymer spherical particles that when cooled, below the lower critical solution temperature of the thermoresponsive block, transformed into long and flexible worm structures. The MacroCTA acted as seed particles for the nucleation and polymer growth, in which the molecular weight and particle size distributions were both narrow. The worms could be cleaved to short rods of 100 nm in length using ultrasound. The temperature-induced gelation of the worms and rods (i.e., the sol-gel transition temperature) was studied as a function of the weight fraction of polymer and the concentration of salt. It was found that the addition of salt (or DPBS buffer) lowered the sol-gel transition temperature, in which less than a 2 wt% of the worm or rod could form gels at or below 37 °C. These gels could have interesting applications as scaffolds for tissue regeneration.

Introduction

Emulsion polymerization allows the synthesis of colloidal particles on the nanoscale dispersed in water. Combining the attributes of emulsion polymerization and ‘living’ radical polymerization (LRP) (1) has allowed precise control over the molecular weight and molecular weight distribution (MWD) (2–5). Recent work using reversible addition-fragmentation chain transfer (RAFT) also demonstrated that not only could the MWD be

controlled but that the size of the spherical colloidal particles could also be controlled independent of the MWD (6–10). In this case, a diblock copolymer consisting of poly(*N,N*-dimethylacrylamide) and the thermoresponsive poly(*N*-isopropylacrylamide) (PNIPAM) macro chain-transfer RAFT agent (MacroCTA) acted as seed particles for nucleation and growth. Expanding on this concept but utilizing a homopolymer PNIPAM MacroCTA in the presence of the surfactant, sodium dodecyl sulfate (SDS), our group showed that through the cooling process a wide range of structural morphologies could be formed, including spheres, worms, donuts, lamella sheets, and vesicles (11–13). This has been denoted as the temperature directed morphology transformation (TDMT) process. At a similar time, the groups of Charleux (14) and Armes (15) developed the polymerization-induced self-assembly (PISA) method to produce a variety of structures during the polymerization.

The worm structure is interesting from a biomedical perspective as it has the potential to mimic the extracellular matrix (ECM) for applications in tissue engineering and regenerative medicine (16–19). The worms must form a three-dimensional (3D) scaffold that can support cell attachment and growth, and in the case of stem cells, allow the controlled differentiation into the desired cell lines. Thermoresponsive worms have the following attributes: (i) they are readily dispersed in water below the lower critical solution temperature (LCST) and when heated above the LCST self-associate to form 3D physical gels, (ii) the gel can be disassembled within seconds by simply reducing the temperature below the LCST, and (iii) the gel can self-heal since they consist of physical and not chemical crosslinks. The worms made by our TDMT method provided a bridge between stem cells that formed into embryonic bodies (20). Through cycling the temperature above and below the LCST, the pluripotent stem cells could significantly proliferate after three passages without differentiation. The worms could also further be surface functionalized with many different orthogonal groups should the attachment of biological compounds be required (21).

However, before using such gels (from worms) as scaffolds for 3D tissue regeneration, an understanding of the sol-gel (i.e., solution-to-gel) process is first required. In this work, we studied the influence of the weight fraction of polymer worms in water and in a PBS solution (replicating conditions found in biological media) on the sol-gel at body temperature (37 °C). The worms were then subjected to ultrasound producing short rods with a similar topology as the worm. The sol-gel properties of these rods were examined, and the influence of aspect ratio determined. The transition from the sol to the gel in this system can be ascribed to the preferential inter-aggregation of the thermoresponsive blocks on different worms above the LCST to form a physical crosslinked network that is kinetically trapped before precipitation can occur (17). This is a result of the PNIPAM when heated above its LCST favoring hydrogen bonding to other PNIPAM chains over that of water.

Experimental

Materials

Unless otherwise stated, all chemicals were used as received. The solvents used were of either HPLC or AR grade; these included dichloromethane (DCM; Aldrich AR grade), dimethylformamide (DMF; Aldrich, AR grade) and tetrahydrofuran (THF; Labscan, HPLC grade). Activated basic alumina (Aldrich: Brockmann I, standard grade, ~ 150 mesh, 58 Å), Milli-Q water (Biolab, 18.2 MΩm), sodium dodecyl sulphate (SDS: Aldrich, 99 %), triethylamine (TEA; Fluka, 99%) and methyl-2-bromopropionate (MBP; Aldrich, 98%) were used as received. Styrene (STY: Aldrich, >99 %) was passed through a basic alumina column to remove inhibitor. N-isopropylacrylamide (NIPAM: Aldrich, 97 %) was recrystallized from hexane, and azobisisobutyronitrile (AIBN: Riedel-de Haen) was recrystallized from methanol twice prior to use. DPBS 14040 buffer was from Invitrogen. RAFT agent methyl 2-(butylthiocarbonothioylthio)propanoate was synthesized according previous procedure (22).

Size Exclusion Chromatography (SEC)

Size Exclusion Chromatography measurements were performed using a Waters Alliance 2690 Separations Module equipped with an auto-sampler, Differential Refractive Index (RI) detector and a Photo Diode Array (PDA) detector connected in series. HPLC grade tetrahydrofuran was used as eluent at flow rate 1 mL/min. The columns consisted of two 7.8 x 300 mm Waters linear Ultrastaygel SEC columns connected in series. Polystyrene standards were used for calibration.

Transmission Electron Microscopy (TEM)

The nanostructure appearance of the polymer latex was analyzed using a JEOL-1010 transmission electron microscope utilizing an accelerating voltage of 100 kV with spot size 6 at ambient temperature. A typical TEM grid preparation was as follows: the polymer nanostructures were diluted with Milli-Q water to approximately 0.1 wt%, and a formvar pre-coated copper TEM grid was then dipped in the solution and dried on the filter paper at 25 °C.

Scanning Electron Microscopy (SEM)

An aqueous solution of nanoworms (0.05 wt%) was dropped onto a silicon chip and allowed to dry under vacuum. It was imaged uncoated in a JEOL JSM-7800F field emission SEM at 1kV accelerating voltage. The sample was then imaged with the in-lens Upper Electron Detector (UED) with a positive bias filter that allowed the detection of both secondary and backscattered electrons for image formation. The stage was also given a negative bias, gentle beam (GB) mode, to reduce chromatic aberration and increase electron emission from the sample.

^1H Nuclear Magnetic Resonance (NMR) Spectroscopy

All NMR spectra were recorded on a Bruker DRX 500 MHz spectrometer.

Synthesis of PNIPAM₄₃-SC(=S)SC₄H₉ by RAFT Polymerization

NIPAM (15 g, 0.133 mol), RAFT agent (0.75 g, 3.0×10^{-3} mol) and AIBN (50 mg, 3.0×10^{-4} mol) were dissolved in 30 ml DMSO in a 50 ml Schlenk flask. The solution was purged with Ar for 30 min. The reaction solution was immersed in preheated oil-bath at 60 °C for 16 h. The reaction was stopped by cooling in ice-bath and exposing the solution to the air. The polymerization mixture was diluted with 500 mL of DCM and washed with Milli-Q water five times. The organic phase was dried over MgSO₄, filtered, concentrated and precipitated in diethyl ether. After filtration, the yellow powder was dried under vacuum at R.T. for 48 h. ($M_{n,SEC}=4200$ and $\bar{D}=1.08$), the repeating units was calculated based on ^1H NMR.

^1H NMR (CDCl₃, 298K, 500 MHz); 6.47 (b, -NH-C=O- of poly(NIPAM) repeating units), 3.97 (b, -NH-CH(CH₃)₂ of poly(NIPAM) repeating units), 4.62 (b, 1H, -CH-SC(=S)S-C₄H₉), 3.97 (b, -NH-CH(CH₃)₂ of poly(NIPAM) repeating units), 3.66 (b, 3H, CH₃O- RAFT residual group) 3.34 (b, 2H, -SC(=S)S-CH₂C₃H₇), 1.06-2.45 (b, methylene and methine protons of poly(NIPAM) backbone), 1.12 (b, methyl protons of poly(NIPAM) repeating units), 0.90 (b, 6H, methyl protons of RAFT residual group).

Synthesis of PNIPAM₄₃-b-PSTY₄₀ Latex by RAFT Emulsion Polymerization

Typically, a 50 ml Shlenck tube, PNIPAM-MacroCTA (0.70 g, 1.46×10^{-4} mol) and SDS (29.0 mg, 1.0×10^{-4} mol) were added in 12.5 ml Milli-Q water and stirred under ice-bath until the solid were dissolved. The solution was purged with Ar for 20 min, STY (0.70 g, 6.72×10^{-3} mol) and AIBN (2.4 mg, 1.46×10^{-5} mol) were added to the solution. After further purging with Ar for another 5 min, the reaction vessel was then immersed in 70 °C oil bath. The reaction solution turned from a clear two-phase yellow solution to a white emulsion after a few minutes. After 3.5 h, the reaction vessel was opened to the air to stop the polymerization ($M_{n,SEC}=8200$, $\bar{D}=1.09$).

Preparation of Worms by Temperature Directed Morphology Transformation (TDTM) and Rods by Sonication Cutting

A 6 mL solution of the emulsion after polymerization at 70 °C was transferred to 2 hot vials (3 mL each) with 60 μ L of toluene in each vials. These vials were sealed and shaken. The suspensions in these vials were cooled to 23 °C and kept overnight. The nanostructure was characterized by TEM to confirm the formation of worm-like nanostructures. The worms (3 mL) were diluted by adding 10 mL of Milli-Q water. This suspension was then cut by ultrasound probe (with a pulse of 15 s on and 10 s off, equivalent to one pulse cycle) for 13, 26, 39 and 52 cycles in an ice-bath at 35% amplitude (3 mm Tapered Micro Tip, VC-750 system from Sonics & Materials). At the different number of cycles, 10 μ L of solution was taken out for TEM characterization. The final rods solution was freeze-dried and redispersed in Milli-Q water and checked by TEM to confirm that the morphology did not change.

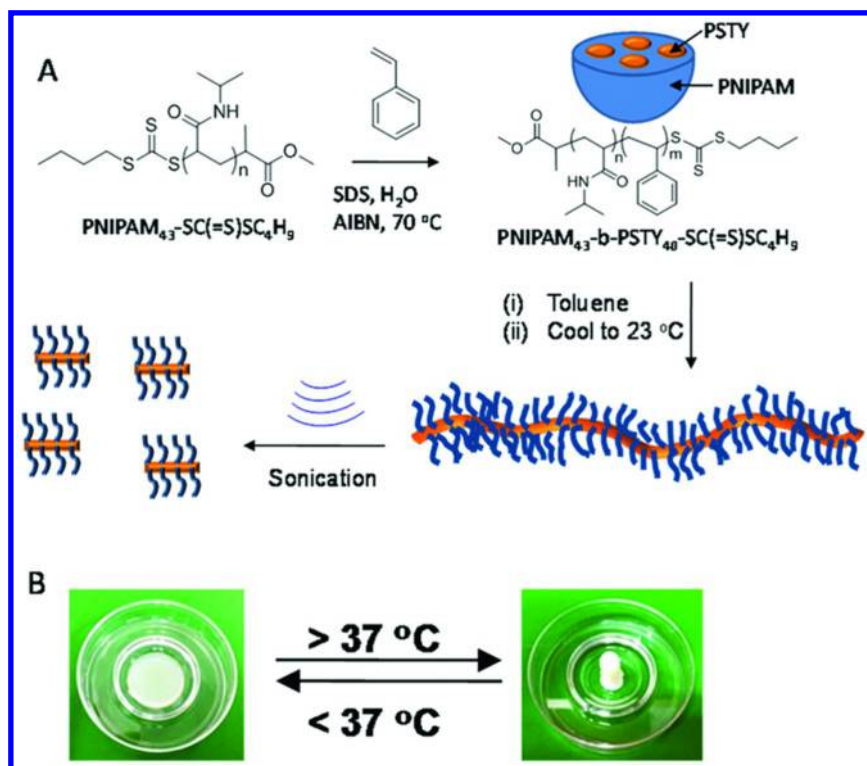
Measurement of the Gel Temperature of the Nanoworms and Nanorods

Dependence of gel temperature versus weight percentage of nanoworms and nanorods (wt %) and NaCl concentration (mM) was measured as follows: typically, to five eppendorf tubes, the freeze-dried rods (20 mg) were redispersed in five different NaCl solutions (10, 20, 50, 100, 200 mM) at 5 wt % at 22.5 °C. These tubes were capped and immersed in water bath with a temperature controller. The temperature of the water bath was steadily increased at 0.5 °C/min, and the temperature was kept constant for 1 min at each 0.5 °C increment. All five eppendorf tubes were then flipped under water to determine gel formation. We defined gel formation as no flow of the solution for 30 s. The weight fractions of the rods (wt %) and the concentration of NaCl were then decreased by the addition of more Milli-Q water and the gel temperature was remeasured according to our previous description. Dependence of gel temperature versus the weight fraction (wt %) of the worms and rods in Milli-Q water or DPBS 14040 buffer were measured as follows: typically, freeze-dried rods (10 mg) were redispersed in either Milli-Q water or DPBS 14040 buffer at 23 °C in eppendorf tubes. The tubes were then capped and immersed in water bath with temperature controller. The temperature of the water bath was steadily increased at 0.5 °C/min, and the temperature kept constant for 1 min at each 0.5 °C increment. The Eppendorf tubes were flipped under water to determine the formation of a gel. The weight fraction of the rods was then decreased by the addition of more Milli-Q water or DPBS buffer and the gel temperature was remeasured again according to the previous description.

Results and Discussion

The RAFT-mediated emulsion polymerization was carried out using a thermoresponsive MacroCTA, styrene (STY), AIBN initiator and SDS in water at 70 °C (see Scheme 1A). The MacroCTA consisted of PNIPAM₄₃-SC(=S)SC₄H₉ with a number-average molecular weight (M_n) of 4200 and a polydispersity

index (\bar{D}) of 1.08. The resulting block copolymer of PNIPAM₄₃-b-PSTY₄₀-SC(=S)SC₄H₉ after a polymerization time of 3.5 h reached a conversion of greater than 71% with a narrow MWD; that is, the M_n of 8200 was close to the theoretically calculated value and the \bar{D} was 1.09. The emulsion produce polymer particles measured at 70 °C with an average number-average diameter (D_h) of 438 nm and a variance (i.e., PDI_{DLS}) of 0.081, suggesting a relatively narrow particle size distribution. A small amount of toluene (60 μ L per 3 mL of latex solution) was then added to the latex solution and immediately cooled to 23 °C and left overnight. The addition of toluene acts as a plasticizer for the PSTY block segments, allowing block mobility. Upon cooling, the spherical polymer particles transformed through the temperature directed morphology transformation into long and flexible worms (see TEM in Figure 1A). The worm morphology in the dry state was further confirmed by SEM (Figure 1B).



Scheme 1. (A) RAFT-mediated emulsion polymerization of styrene with PNIPAM MacroCTA in water to produce thermoresponsive copolymer latex followed by TDMT to form worms and sonication to form rods, (B) Photo of the reversible sol-gel transformation with temperature.

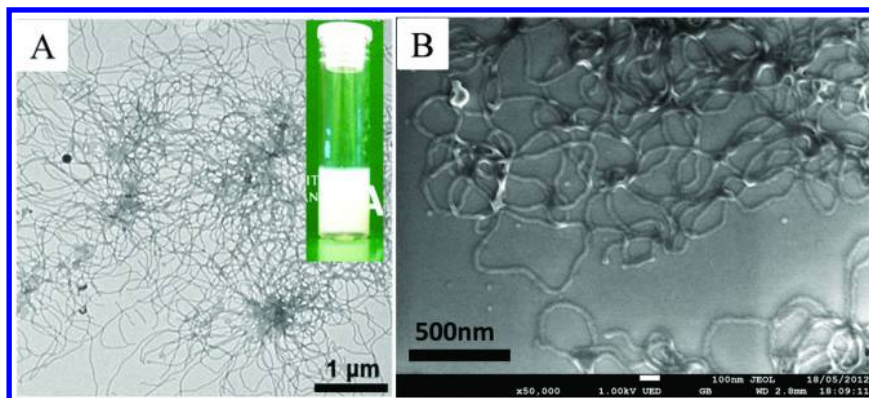


Figure 1. Worm morphology formed by cooling the PNIPAM₄₃-b-PSTY₄₀ latex solution (~8 wt %) from 70 to 23 °C (i.e., the TDMT process). (A) TEM image of worms at 0.1 wt % (inset: photo of worm latex in water at ~8 wt %), and (B) SEM image of worms at 0.05 wt %.

We then used the ultrasound method to cut worms to short rods in an ice bath with a pulse cycle of 15 s on and 10 s off. The number of cycles was varied from 13 to 52, and the TEMs in Figure 2(A-D) showed that increasing the number of cycles did not change the length of rods. It can be seen from the photo (inset in Figure 2E) that the solution became less opaque for the rod in comparison to the worms (inset in Figure 1A), and the TEMs showed that the diameter of the rods was not altered but the length decreased to approximately 100 nm. This is in agreement with the Gaussian scission model postulated by Winnik et al. (23, 24) that the limiting rod length that the worms can cut was close to 100 nm, at which length the rate of fragmentation becomes extremely slow. The rods were freeze-dried to remove all water, and then rehydrated. The TEM showed that the rod length and diameter did not change after rehydration, a similar result was also found for the worms (data not shown). This result demonstrated that the structures made by the TDMT method are stable in the dry state due to the glassy PSTY core, which kinetically traps structures in a non-equilibrium state. These kinetically trapped structures after removal of plasticizer (i.e., by freeze-drying) can be stored in either the dry or wet state for over a year.

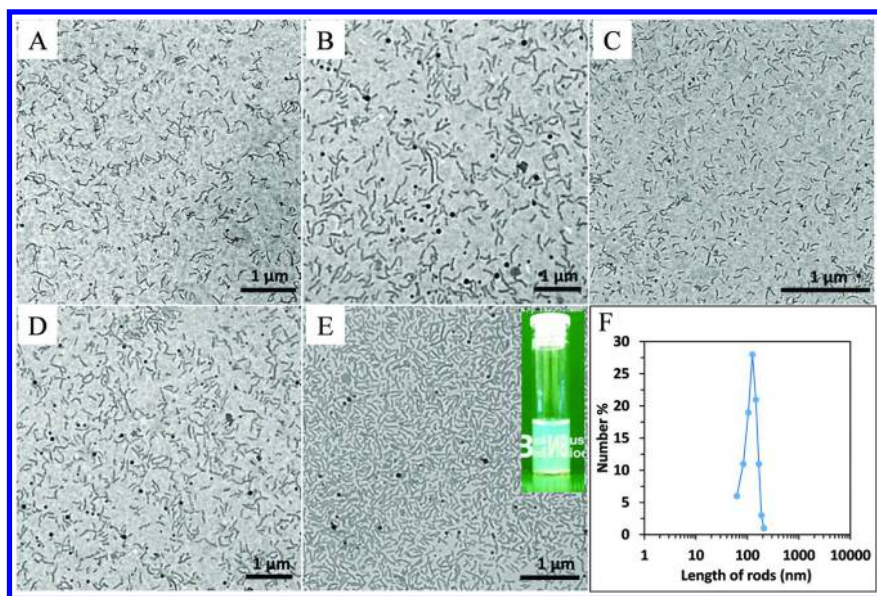


Figure 2. TEM images of rods obtained by cutting the worms with a probed ultrasound in an ice-bath with varying number of cycles (each cycle consisted of 15 s on and 10 s off). (A) 13 cycles, (B) 26 cycles, (C) 39 cycles, (D) 52 cycles and (E) Re-disperse of freeze-dried rods in water; (inset: photo of re-dispersed freeze-dried rods in water), (F) rod length distribution based on length of 100 random rods from (C).

The high solids content (or high weight fraction of polymer) of worms produced through an emulsion process is the main advantage over other self-assembly methods. Our TDMT method allows large scale production of worms in a short period of time, making such a process of industrial interest. Formation of gels through physical crosslinking not only allows a surface at which cells can bind and proliferate but can trap reagents (e.g., growth factors, inhibitors) within them that can support stem cell pluripotency or differentiation (20). The design of a gel to mimic an ECM should have a very low weight fraction, and thus the gel should consist primarily of the water (>95 wt%) (17). In addition, gels should form and be stable under physiological conditions, more specifically in the presence of buffers used in cell growth culture. Having a reversible trigger (e.g. temperature) for the sol-gel transition will have other advantages for the on-demand release of cells or other trapped nanostructures (25).

Here, we examined the influence of the weight fraction and minimum temperature for the worms and rods to undergo the transition from a sol to a gel (see Scheme 1B) in water. We also examined the effect of varying the salt, NaCl, concentration on this sol-gel transition. First, the worms and rods were freeze-dried and then re-dispersed in Milli-Q water (0.4 mL) at different concentrations of NaCl (Figure 3). The opaque solution in each NaCl concentration was immersed in a water bath, and the temperature of the water bath

increased slowly from 25 to 37 °C at a rate of 0.5 °C/min. The sol-gel transition was defined as: after inversion of the vial there was no flow of the solution for 30 s. The worms showed from Figure 3A that increasing the NaCl concentration gave a lower sol-gel transition temperature for nearly all weight fractions of polymer worms (from 1 to 5 wt%). Increasing the weight fraction of worms from 2 to 5 wt% showed that the sol-gel transition temperature decreased at high salt concentrations. Salts have been found to lower the LCST of PNIPAM through disruption of the hydrogen bonding of the amide groups to water (salting-out of the polymer) (26). This mechanism of salting-out provides a reasonable explanation for the decrease in the sol-gel-transition temperature with added salt (27). The rods on the other hand showed that the decrease in the sol-gel transition temperature with salt was not as dependent as the worms (Figure 3B). After 50 mM NaCl, the change in the sol-gel temperature was relatively constant up to a weight fraction of 4 wt%. It was observed that the gels for both the worms and the rods were weak, and would dissociate to an opaque solution upon shaking.

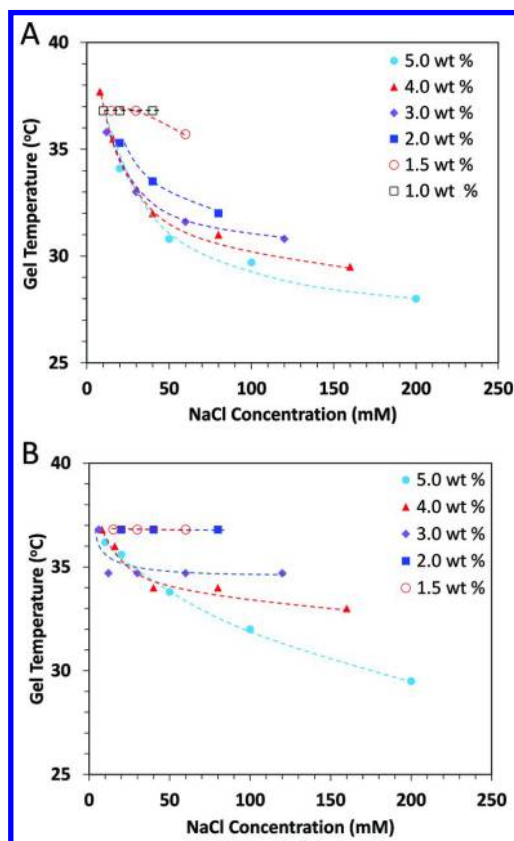


Figure 3. Influence of the concentration of NaCl on the Sol-Gel transition temperature at different weight percentage of (A) worms and (B) rods in water. Sol-Gel transition temperature was defined as the absence of flow for 30 s when the vial was turned upside-down.

The sol-gel transition temperature was next studied in both Milli-Q water and a commercially available DPBS buffer from Invitrogen™. This buffer is routinely used for culturing of stem cells. Figure 4A showed the effect of the weight fraction of the worms in water and DPBS buffer on the sol-gel transition temperature. In water (curve a), an increased wt% of worms from 9 to 15 wt% reduced the sol-gel transition temperature from 37 to 23 °C. Below 9 wt% of worms there was no observable gel formation even at high temperatures. Changing the media from Milli-Q water to buffer (curve b) resulted in a significant lowering of the weight fraction of worms to form a gel. Even at a 1.5 wt%, the worms could form a gel below 37 °C. A similar result was observed for the rods (Figure 4B). The buffer significantly reduced the weight fraction of polymer from 10 to 1.5 wt% to form a gel below 37 °C. It was observed that the worms became more viscous with an increase in the wt%; whereas, the viscosity of the rod solution was similar to that of water even at a high wt%. This suggests that the rod solution could be used to trap cells with the gel by simply increasing the temperature above the sol-gel transition temperature. In a highly viscous medium (e.g. worms at a high weight fraction) this would difficult to accomplish.

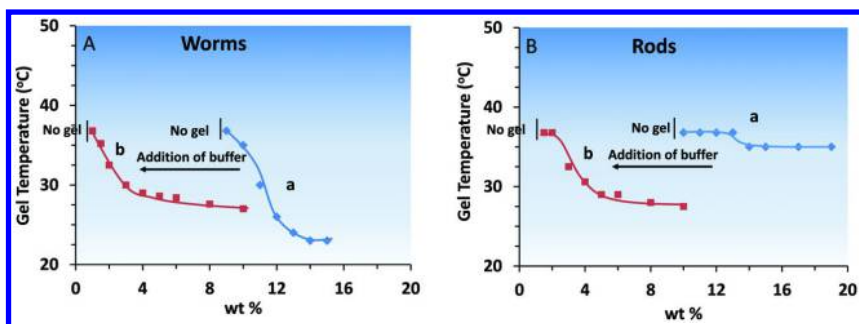


Figure 4. Influence of buffer on the Sol-Gel transition temperature over different weight fractions of polymer. (A) worms (B) rods dispersed in different aqueous media. Curve (a) Milli-Q water, and (b) commercial DPBS buffer 14040 from Invitrogen™. Sol-Gel transition temperature was defined as the absence of flow for 30 s when the vial was turned upside-down.

Conclusion

In summary, we carried out a seeded RAFT-mediated emulsion polymerization of styrene using a thermoresponsive MacroCTA seed particle. A narrow MWD of block copolymer was formed contained within monodispersed particles of 438 nm in diameter, suggesting that this RAFT polymerization provided excellent control over the MWD and particle size distribution. The addition of plasticizer and cooling from the reaction temperature of 70 to 23 °C resulted in the formation of worms. These worms consist of a PSTY core with a PNIPAM hairy layer. The worms were effectively cleaved using ultrasound to short rods of 100 nm in length. Heating the worms and rods above the LCST in pure water at greater than 9 wt% produced gels. The sol-gel transition could be

altered through the addition of salt, which lowers the LCST of PNIPAM. These gels have great potential in the tissue regeneration based on stem cell attachment, proliferation and differentiation.

Acknowledgments

M.J.M. acknowledges financial support from the ARC Discovery grant (DP140103497).

References

1. Matyjaszewski, K.; Davis, T. P. *Handbook of Radical Polymerization*; Wiley: 2002.
2. Monteiro, M. J.; Charleux, B.; van Herk, A. *Chemistry and Technology of Emulsion Polymerisation*; Wiley: 2005.
3. Monteiro, M. J. *Macromolecules* **2010**, *43*, 1159–1168.
4. Zetterlund, P. B.; Kagawa, Y.; Okubo, M. *Chem. Rev.* **2008**, *108*, 3747–3794.
5. Monteiro, M. J.; Cunningham, M. F. *Macromolecules* **2012**, *45*, 4939–4957.
6. Urbani, C. N.; Monteiro, M. J. *Macromolecules* **2009**, *42*, 3884–3886.
7. Sebakhy, K. O.; Kessel, S.; Monteiro, M. J. *Macromolecules* **2010**, *43*, 9598–9600.
8. Sebakhy, K. O.; Gavrilov, M.; Valade, D.; Jia, Z. F.; Monteiro, M. J. *Macromol. Rapid Commun.* **2014**, *35*, 193–197.
9. Perrier, S.; Takolpuckdee, P. *J. Polym. Sci., Part A: Polym. Chem.* **2005**, *43*, 5347–5393.
10. Boyer, C.; Stenzel, M. H.; Davis, T. P. *J. Polym. Sci., Part A: Polym. Chem.* **2011**, *49*, 551–595.
11. Kessel, S.; Urbani, C. N.; Monteiro, M. J. *Angew. Chem., Int. Ed.* **2011**, *50*, 8082–8085.
12. Kessel, S.; Truong, N. P.; Jia, Z.; Monteiro, M. J. *J. Polym. Sci., Part A: Polym. Chem.* **2012**, *50*, 4879–4887.
13. Jia, Z.; Truong, N. P.; Monteiro, M. J. *Polym. Chem.* **2013**, *4*, 233–236.
14. Boisse, S.; Rieger, J.; Belal, K.; Di-Cicco, A.; Beaunier, P.; Li, M. H.; Charleux, B. *Chem. Commun.* **2010**, *46*, 1950–1952.
15. Blanazs, A.; Madsen, J.; Battaglia, G.; Ryan, A. J.; Armes, S. P. *J. Am. Chem. Soc.* **2011**, *133*, 16581–16587.
16. Ma, P. X. *Adv. Drug Delivery Rev.* **2008**, *60*, 184–198.
17. Kouwer, P. H. J.; Koepf, M.; Le Sage, V. A. A.; Jaspers, M.; van Buul, A. M.; Eksteen-Akeroyd, Z. H.; Woltinge, T.; Schwartz, E.; Kitto, H. J.; Hoogenboom, R.; Picken, S. J.; Nolte, R. J. M.; Mendes, E.; Rowan, A. E. *Nature* **2013**, *493*, 651–655.
18. Geckil, H.; Xu, F.; Zhang, X. H.; Moon, S.; Demirci, U. *Nanomedicine* **2010**, *5*, 469–484.
19. Lutolf, M. P.; Hubbell, J. A. *Nat. Biotechnol.* **2005**, *23*, 47–55.
20. Chen, X. L.; Prowse, A. B. J.; Jia, Z. F.; Tellier, H.; Munro, T. P.; Gray, P. P.; Monteiro, M. J. *Biomacromolecules* **2014**, *15*, 844–855.

21. Jia, Z. F.; Bobrin, V. A.; Truong, N. P.; Gillard, M.; Monteiro, M. J. *J. Am. Chem. Soc.* **2014**, *136*, 5824–5827.
22. Truong, N. P.; Jia, Z. F.; Burges, M.; McMillan, N. A. J.; Monteiro, M. J. *Biomacromolecules* **2011**, *12*, 1876–1882.
23. Zhang, M.; Wang, M.; He, S.; Qian, J.; Saffari, A.; Lee, A.; Kumar, S.; Hassan, Y.; Guenther, A.; Scholes, G.; Winnik, M. A. *Macromolecules* **2010**, *43*, 5066–5074.
24. Guerin, G.; Wang, H.; Manners, I.; Winnik, M. A. *J. Am. Chem. Soc.* **2008**, *130*, 14763–14771.
25. Velasco, D.; Chau, M.; Therien-Aubin, H.; Kumachev, A.; Tumarkin, E.; Jia, Z.; Walker, G. C.; Monteiro, M. J.; Kumacheva, E. *Soft Matter* **2013**, *9*, 2380–2383.
26. Zhang, Y. J.; Furyk, S.; Bergbreiter, D. E.; Cremer, P. S. *J. Am. Chem. Soc.* **2005**, *127*, 14505–14510.
27. Park, T. G.; Hoffman, A. S. *Macromolecules* **1993**, *26*, 5045–5048.

Chapter 7

Worm-Like Micelles and Vesicles: Adjusting the Morphology of Self-Assembled Fructose Based Block Copolymers by Fine-Tuning the Processing Parameters

Jiacheng Zhao and Martina H. Stenzel*

Centre for Advanced Macromolecular Design (CAMD), School of Chemistry,
University of New South Wales, Sydney NSW 2052, Australia

*E-mail: m.stenzel@unsw.edu.au

The self-assembly of amphiphilic block copolymers is typically governed by parameters such as the block length. Although every block copolymer should have a morphology corresponding to the highest thermodynamic stability, the self-assembly process often traps the structures in kinetically stable non-equilibrium morphologies. This topic has been subject to a large array of studies supported by theoretical calculations. In this chapter, this knowledge has been applied to the formation of various self-assembled morphologies based on glycopolymers. The formation of nano-object with glycopolymer shells have been of immense interest for various biomedical applications. However, reports on rod-like or worm-like cylindrical micelles are limited. Here, it was illustrated how the preparation parameters such as common solvent, water injection rate and concentration affect the self-assembly of block copolymers based on 1-*O*-methacryloyl-2,3:4,5-di-*O*-isopropylidene- β -D-fructopyranose, a polymer that has recently been found to be selective to certain cancer cells.

Introduction

Glycopolymers are synthetic polymeric backbones featuring pendant and/or terminal saccharide moieties (1, 2). As oligo- and polysaccharide mimics, the properties of glycopolymers can be tailored by combination of polymeric backbones and carbohydrates groups. Due to their excellent biocompatibility and bioactivity, glycopolymers have received considerable attention in chemistry, material science and nanomedicine. The combination of properties resulting from the polymeric backbone and the carbohydrates gave rise to various uses of glycopolymers in clinical diagnostics, drug delivery systems, bioassays and affinity separations (3, 4). These potential applications have triggered great interest in the preparation of glycopolymers with various pendant carbohydrates and well-defined backbones. There are two general routes for glycopolymer synthesis: post-polymerization modification of polymer backbones with saccharide derivatives and polymerization of glycomonomers (5, 6). The commercial availability of a range of sugars provides access to a wide array of different sugar-containing monomers, and modern controlled radical polymerization techniques are capable to yield various polymer architectures with narrow molar mass distributions and a high control over the chain lengths. Thus, great efforts have been dedicated to the synthesis of glycopolymers from various polymerizable glycomonomers, which have been extensively reviewed in many recent publications (1, 7–11).

The interaction between lectins and carbohydrate can be greatly enhanced through multivalency, which is known as the cluster glycoside effect (12). Carbohydrate residues on glycopolymers, which are multivalent by definition, have great potential for their exploitation as targeted drug delivery systems (13–15). Polymeric micelles and vesicles, which are constructed by self-assembly of amphiphilic block copolymers, are regarded as one of the most promising nano-carrier systems for drug delivery (16, 17). In our recent research, we found that fructose-coated micelles express high uptake by breast cancer cells, but only negligible uptake by macrophages, which suggest excellent potential for application as drug nano-carrier for triple-negative breast cancer therapy (18). The self-assembled micelles were based on poly(3-*O*-MAFru)_n-*b*-poly(BA)_m and poly(1-*O*-MAFru)_n-*b*-poly(BA)_m. Although the size of the hydrophobic block was pushed towards a large number of repeating units, only micelles were obtained exclusively. Recent research however suggests that cylindrical micelles may enhance the circulation time of the carrier (19, 20).

Reports on glycopolymers that self-assemble into morphologies are dominated by block copolymer micelles. Non-spherical morphologies were often derived from graft copolymers resulting in structures that were coined molecular bottlebrushes (21–23). Only a small selection of reports on the preparation of cylindrical micelles is available. Amphiphilic star polymers with a glycopolymer corona are capable of forming micelles, rods and vesicle by fine-tuning the size of the hydrophilic block (24). Micelles, cylindrical micelles and polymerosomes were also obtained from N-carboxy-anhydrides (NCA) based block copolymers that were functionalized with galactose using CuAAC click reaction (25). The block length was used as a tool to

adjust the morphology similar to other reports on glycopolymers including poly(2-methacrylamido glucopyranose)–block-poly(5'-*O*-methacryloyl uridine) (26) and poly(2-(β -D-galactosyloxy)ethyl methacrylate)-block-poly(butyl acrylate) (27). A very elegant way is the simultaneous polymerization and self-assembly of the block copolymer using RAFT polymerization. The polymerization is typically carried out in a solvent that dissolves the glycopolymer macroRAFT agent and the hydrophobic monomer, but not the hydrophobic polymer. Once a critical chain length has been reached, the block copolymer starts self-assembling into glycopolymer nano-objects of various shapes (28). Despite its elegance, this technique requires careful fine-tuning of the solubility parameters and may not be suitable for all block copolymers.

While the size of both blocks determine the morphology with the highest thermodynamic stability, optimization of the processing parameters are paramount to achieve these types of aggregates in high purity. In the following chapter, we will investigate the influence of chain length of hydrophobic blocks, type of common solvent and water injection rate on the outcome using a fructose-based block copolymer that has recently been shown to be highly selective towards certain cancer cells.

Experimental Part

Materials

D-fructose (99%, Aldrich), dichloromethane (DCM; anhydrous, >99.8%, Aldrich), methacrylic anhydride (94%, Aldrich), 4-Dimethylaminopyridine (DMAP; 94%, Aldrich), sulfuric acid (95%-98%, Ajax Finechem), acetone (HPLC grade, Ajax Finechem), tetrahydrofuran (THF; anhydrous, >99.9%, Aldrich), 1,4-dioxane (anhydrous, >99.8%, Aldrich) and *N,N*-dimethylformamide (DMF; 99%, Ajax Finechem) were used as received. pyridine (99%, Ajax Finechem) was purified by reduced-pressure distillation. *n*-Butyl methacrylate (>99%, Aldrich) and methyl methacrylate (>99%, Aldrich) were passed over basic aluminum oxide to remove the inhibitor. 2,2-azobis(isobutyronitrile) (AIBN; 98%, Fluka) was recrystallized from methanol for purification. The RAFT agent 4-cyanopentanoic acid dithiobenzoate (CPADB) was synthesized according to a literature procedure (29).

Synthesis

Synthesis of Monomer

The selective protection of D-fructose was conducted according to the previously reported procedure (30). After recrystallization, 2,3:4,5-di-*O*-isopropylidene- β -D-fructopyranose of high purity was obtained. Then, into a solution of 2,3:4,5-di-*O*-isopropylidene- β -D-fructopyranose (3 g, 11.5 mmol), 4-dimethylaminopyridine (1 g) and pyridine (6 mL) in anhydrous dichloromethane (165 mL) at 0 °C methacrylic anhydride (2.2 mL) was added. After it stirring for 48 h at room temperature, the mixture was poured into ice-cold saturated

NaHCO₃ solution (165 mL), and the organic layer was separated. The aqueous layer was extracted with dichloromethane, and combined organic layers were dried using MgSO₄ and concentrated under reduced pressure. The product was further purified by flash column chromatography with ethyl acetate : hexane (1:1) as eluent. (yield: 85%). ¹H NMR (300 MHz, chloroform-*d*) δ 6.17 (dq, *J* = 1.8, 0.9 Hz, 1H), 5.62 (dd, *J* = 1.9, 1.3 Hz, 1H), 4.64 (dd, *J* = 7.9, 2.7 Hz, 1H), 4.50 (dd, *J* = 11.9, 0.6 Hz, 1H), 4.40 (dd, *J* = 2.7, 0.6 Hz, 1H), 4.27 (ddd, *J* = 7.9, 1.9, 0.8 Hz, 1H), 4.17 (dd, *J* = 11.9, 0.7 Hz, 1H), 3.96 (dd, *J* = 13.0, 1.9 Hz, 1H), 3.79 (dt, *J* = 13.0, 0.8 Hz, 1H), 1.99 (dt, *J* = 1.6, 0.8 Hz, 3H), 1.56 (s, 3H), 1.50 (s, 3H), 1.41 (s, 3H), 1.37 (s, 3H) ppm. ¹³C NMR (75 MHz, chloroform-*d*) δ 166.7, 136.0, 126.0, 109.1, 108.8, 101.6, 70.8, 70.3, 70.1, 65.0, 61.3, 26.5, 25.9, 25.4, 24.0, 18.5 ppm.

Synthesis of Poly(1-O-MAFru)-b-PMMA

In a Schlenk tube, 1-*O*-methacryloyl-2,3,4,5-di-*O*-isopropylidene-β-*D*-fructopyranose (1 g, 1.83 mmol), AIBN (0.8 mg, 4.8 × 10⁻³ mmol) and CPADB (10 mg, 0.037 mmol) were dissolved in 1,4-dioxane (4.3 mL). Then the tube was degassed by three freeze-pump-thaw cycles. The polymerization was carried out at 70 °C and stopped at 7 h by cooling the solution in ice water. The polymer solution was poured into a large excess of diethyl ether for precipitation. The viscous polymer was dried under vacuum for 24 h. The obtained polymer was then used as macro RAFT agent for the following chain extension. A typical procedure was described as follows: macro RAFT agent (100 mg, 8.6 × 10⁻³ mmol), methyl methacrylate (257 mg, 2.6 mmol), AIBN (1.7 × 10⁻³ mmol) were dissolved in 1,4-dioxane (1.5 mL). The tube was degassed by three freeze-vacuum-thaw cycles. The polymerization was carried out at 70 °C and stopped at 18 h by cooling the solution in ice water. The polymer solution was poured into a large excess of *n*-hexane for precipitation. The viscous polymer was dried under vacuum for 24 h. The deprotection of the block copolymers was carried out under acidic conditions. The polymer (80 mg) was added into 1.59 mL of TFA/H₂O (9:1 v/v) in a vial with stirring at room temperature for 30 minutes. After reaction, the polymer solution was dialyzed against deionized water for two days (MWCO 3500). The deprotected polymer was then lyophilized.

Synthesis of Poly(1-O-MAFru)-b-PBMA

The synthesis of macro RAFT agent followed the same procedure as that of Poly(1-*O*-MAFru)-*b*-PMMA. A typical procedure for the synthesis of Poly(1-*O*-MAFru)-*b*-PBMA was described as follows: macro RAFT agent (100 mg, 8.6 × 10⁻³ mmol), *n*-Butyl methacrylate (732 mg, 5.1 mmol), AIBN (1.7 × 10⁻³ mmol) were dissolved in 1,4-dioxane (1.5 mL). The tube was degassed by three freeze-vacuum-thaw cycles. The polymerization was carried out at 70 °C and stopped at 18 h by cooling the solution in ice water. The polymer solution was poured into a large excess of *n*-hexane for precipitation. The viscous polymer was dried under

vacuum for 24 h. The deprotection of the block copolymers was carried out under acidic conditions. The polymer (80 mg) was added into 1.59 mL of TFA/H₂O (9:1 v/v) in a vial with stirring at room temperature for 30 minutes. After reaction, the polymer solution was dialyzed against deionized water for two days (MWCO 3500). The deprotected polymer was then lyophilized.

Self-Assembly of Block Copolymers

A typical procedure for the preparation of micelles was described as follows: The deprotected polymer (4 mg) was dissolved in THF (0.2 mL) at first. 1.8 mL MQ water was added to the polymer solution using a syringe pump at a rate of 0.2 mL/h. Then the solution was dialysed against deionized water to remove the THF.

Analytical Methods

Nuclear Magnetic Resonance (NMR)

The conversions of polymerization were measured using a Bruker Avance III 300 spectrometer (300 MHz). All chemical shifts are recorded in ppm (δ) relative to tetramethylsilane ($\delta = 0$ ppm), referenced to the chemical shifts of residual solvent resonances (¹H). Toluene was added as standard ($\delta=2.36$ ppm). The conversion was calculated using the following equations: [Conversion (%) = $100\% - (I_{\text{monomer}} / I_{\text{std}})_{\text{after reaction}} / (I_{\text{monomer}} / I_{\text{std}})_{\text{before reaction}}$]

Size Exclusion Chromatography (SEC)

The molecular weight and polydispersity of synthesized polymers were analyzed via size exclusion chromatography (SEC). A Shimadzu modular system comprising a SIL-10AD auto-injector, DGU-12A degasser, LC-10AT pump, CTO-10A column oven and a RID-10A refractive index detector was used. A 5.0- μm bead-size guard column (50×7.8 mm) followed by four 300×7.8 mm linear columns ($500, 10^3, 10^4, \text{ and } 10^5$ Å pore size, $5 \mu\text{m}$ particle size) were employed for analysis. *N,N*-Dimethylacetamide (DMAc; HPLC grade, 0.05% w/v 2,6-di-butyl-4-methylphenol (BHT) and 0.03% w/v LiBr) with a flow rate of 1 mL/min at 50 °C was used as mobile phase. 50 μL of polymer solution with a concentration of 2 mg/mL in DMAc was used for every injection. The calibration was performed using commercially available narrow-polydispersity polystyrene standards (0.5-1000 kDa, Polymer Laboratories).

Dynamic Light Scattering (DLS)

Particle sizes (the average diameters and size distributions) were determined using a Malvern Zetaplus particle size analyser (laser, 35mW, $\lambda = 632$ nm, angle = 90°) at a polymer concentration of 1 mg/mL. Samples were prepared in

deionized water and purified from dust using a micro filter (0.45 μm) prior to the measurements.

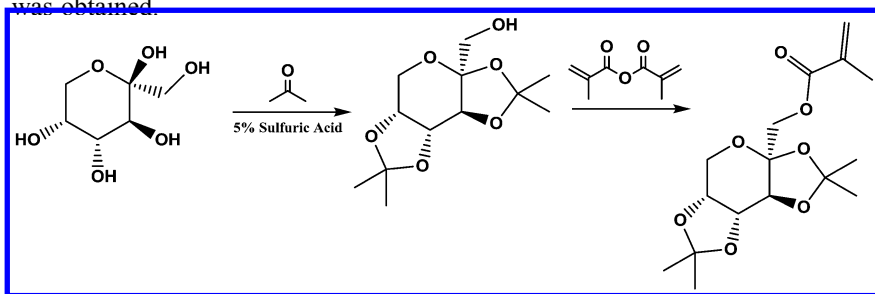
Transmission Electron Microscopy (TEM)

The TEM micrographs were obtained using a JEOL1400 transmission electron microscope comprising of a dispersive X-ray analyser and a Gatan CCD facilitating the acquisition of digital images. The measurement was conducted at an accelerating voltage of 80 kV. The samples were prepared by casting the micellar solution (1 mg/mL) onto a copper grid. The grids were dried by air and then negatively stained with uranyl acetate.

Results and Discussion

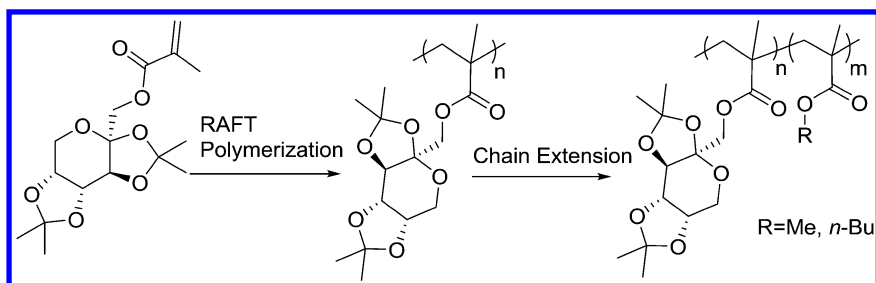
Synthesis of Block Copolymers

To obtain stereospecific functionalized glycomonomers, protective chemistry is generally employed. Fructose was selectively protected to form isopropylidene derivatives (30), followed by functionalization of the only remaining hydroxyl group with methacrylate (Scheme 1). After purification, the glycomonomer 1-*O*-methacryloyl-2,3:4,5-di-*O*-isopropylidene- β -D-fructopyranose (1-*O*-MAiPrFru) was obtained.



*Scheme 1. Synthesis of 1-*O*-methacryloyl-2,3:4,5-di-*O*-isopropylidene- β -D-fructopyranose.*

The block glycopolymers were prepared in two steps (Scheme 2). In the first step, the polymerization of 1-*O*-MAiPrFru was carried out under good control in the presence of 4-cyanopentanoic acid (CPADB). The procedure was described in detail earlier (18). The obtained homo-glycopolymer was then used as macro RAFT agent for the following chain extension with *n*-butyl methacrylate (BMA) and methyl methacrylate (MMA). By controlling the ratio of BMA or MMA to macro RAFT agent, a series of diblock glycopolymers with different hydrophobic chain lengths were synthesized, which was followed by the removal of the isopropylidene groups through acid hydrolysis.



Scheme 2. Synthesis of Macro RAFT agent and corresponding block glycopolymers based on 1-O-methacryloyl-2,3:4,5-di-O-isopropylidene-β-D-fructopyranose.

The set of block copolymers summarized in Table 1 were subsequently employed in the self-assembly study.

Table 1. Synthesis of block glycopolymers via RAFT Polymerization at 70°C in 1,4-dioxane.

<i>Glycopolymers</i>	<i>[M]:[macro CTA]:[AIBN]</i>	<i>Reaction Time (h)</i>	<i>Conversion (%) (NMR)</i>	<i>M_n (SEC)</i>	<i>PDI</i>
Poly(1- <i>O</i> -MAFru) ₃₅ - <i>b</i> -PMMA ₁₅₃	250 : 1 : 0.2	18	61	37400	1.13
Poly(1- <i>O</i> -MAFru) ₃₅ - <i>b</i> -PMMA ₁₉₂	300 : 1 : 0.2	18	64	41400	1.16
Poly(1- <i>O</i> -MAFru) ₃₅ - <i>b</i> -PMMA ₁₉₅	300 : 1 : 0.2	18	65	42800	1.18
Poly(1- <i>O</i> -MAFru) ₃₅ - <i>b</i> -PMMA ₂₆₀	400 : 1 : 0.2	18	65	48600	1.07
Poly(1- <i>O</i> -MAFru) ₃₅ - <i>b</i> -PMMA ₃₂₅	500 : 1 : 0.2	18	65	53700	1.08
Poly(1- <i>O</i> -MAFru) ₃₅ - <i>b</i> -PMMA ₃₉₆	600 : 1 : 0.2	18	66	60700	1.09
Poly(1- <i>O</i> -MAFru) ₃₅ - <i>b</i> -PBMA ₂₂₀	300 : 1 : 0.2	18	73	47500	1.16
Poly(1- <i>O</i> -MAFru) ₃₅ - <i>b</i> -PBMA ₄₃₉	600 : 1 : 0.2	18	73	64000	1.12

Morphology Control of Self-Assembled Glycopolymers

The self-assembly of highly asymmetric amphiphilic block copolymers has attracted much attention in academia because of a wide range of ordered structures it can form (31). The formation of various morphologies is primarily a result of comprise between kinetics and thermodynamics factors. The self-assembly of thermodynamically stable structures is governed by factors affecting the free

energy of the system such as copolymer composition and concentration, water content in the solution and nature of the common solvent (32, 33). However, some aggregates of thermodynamically unstable structures can be frozen during morphological transition via restricting the mobility of polymer chains. In this section, we investigated some major factors that influence the self-assembled structures via affecting the mobility of polymeric chains. It should be noted though that self-assembled aggregates will always be dynamic in nature. However, high water contents, long hydrophobic block length and high T_g of the polymers can slow down or prevent disassembly. Low concentration of micelles, as they are used in drug delivery applications, can indeed affect the efficiency (34, 35). Crosslinking of micelles is therefore recommended. In the following, the focus will be on the self-assembly process only without giving too much attention to the stability of the aggregates.

Common Solvent

The role that common solvent plays in the formation of various self-assembled morphologies has been extensively investigated (36, 37). In the process of self-assembly, the dimensions of both hydrophobic chains and hydrophilic corona are affected by the common solvent. It is worth noting that the similarity of solubility parameters (δ) between hydrophobic block and the common solvent is important in order to control the final morphologies. If the δ value of hydrophobic chain is close to that of the common solvent, the core of micelles will have a high degree of swelling and the hydrophobic chains will keep high mobility, which facilitate the morphological transition. In addition, when a good solvent for hydrophobic chains is used as the common solvent, the water contents window between the critical water content (CWC) and the point at which the morphology freezes will be broad, which provides more opportunities for morphological transitions before the structures are frozen (36).

In our research, different self-assembled morphologies of the same block glycopolymer were obtained by using different common solvents (Table 2). During self-assembly of Poly(1-*O*-MAFru)₃₅-*b*-PMMA₁₉₂, micelles and some short rods were obtained when the common solvents were DMF and dioxane. However, when THF was used as the common solvent, a mixture of micelles and worm-like structures was obtained (Figure 1). Since the δ value of PMMA ($\delta=19.3$) (38) is closer to that of THF ($\delta=18.6$) (31) than those of dioxane ($\delta=20.5$) (31) and DMF ($\delta=24.8$) (31), the hydrophobic block chains have higher mobility in THF. Furthermore, the window of water contents, in which the morphologies are still labile, is much broader in THF/water system than in dioxane/water and DMF/water systems. The higher mobility of polymeric chains during the water injection makes morphological transitions more accessible. Similar observations were made during the self-assembly of PBMA-based block glycopolymers ($\delta=18$) (38). When DMF was used as common solvent, only micelles can be observed even if the block copolymers have a relatively long PBMA block (DP=439). In contrast, THF-water solutions enabled the formation of different morphologies of various sizes because of the higher mobility of polymer

chains and the broader water contents window. The aggregates obtained using Poly(1-*O*-MAFru)₃₅-*b*-PBMA₄₃₉ can be clearly identified as vesicles (Figure 2) while the ring-shaped aggregates depicted in Figure 3 left appear to have walls thicknesses (around 100 nm) that are beyond the sizes expected for vesicle structures. Detailed analysis of the TEM micrographs, which are complemented by SEM analysis, reveal donut-like morphologies that may be the result of the formation cylindrical micelles that underwent ring-closure.

Table 2. Self-assembly of micelles prepared from different glycopolymers.

<i>Block copolymer</i>	<i>Common solvent</i>	<i>Morphology</i>	<i>Size (d.nm)</i>	<i>PDI</i>
Poly(1- <i>O</i> -MAFru) ₃₅ - <i>b</i> -PMMA ₁₉₂	THF	Micelles + Worms	36	0.16
	Dioxane	Micelles + Rods	28	0.15
	DMF	Micelles	17	0.14
Poly(1- <i>O</i> -MAFru) ₃₅ - <i>b</i> -PBMA ₂₂₀	THF	Vesicles	210	0.05
	DMF	Micelles	25	0.17
Poly(1- <i>O</i> -MAFru) ₃₅ - <i>b</i> -PBMA ₄₃₉	THF	Vesicles	592	0.06
	DMF	Micelles	33	0.17

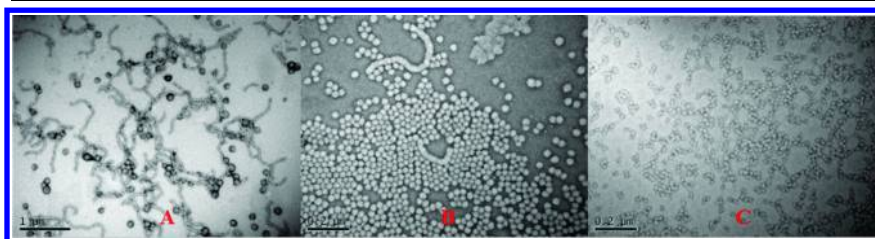


Figure 1. TEM analysis of morphologies based on Poly(1-*O*-MAFru)₃₅-*b*-PMMA₁₉₂ obtained using THF (A), 1,4-dioxane (B) and DMF (C) as common solvent.

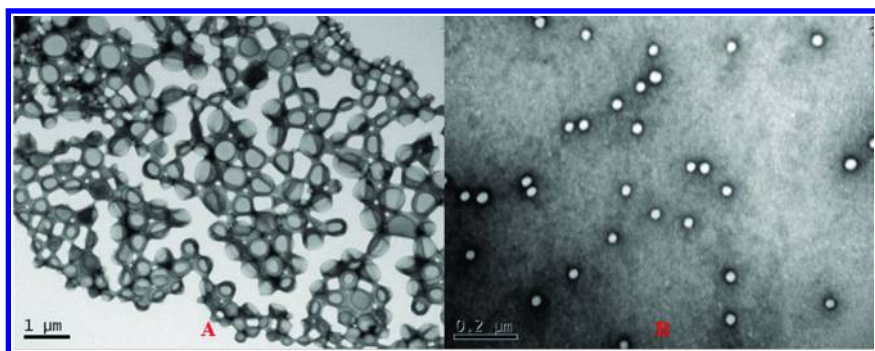


Figure 2. TEM analysis of morphologies based on Poly(1-*O*-MAFru)₃₅-*b*-PBMA₄₃₉ obtained using THF (A), and DMF (B) as common solvent.

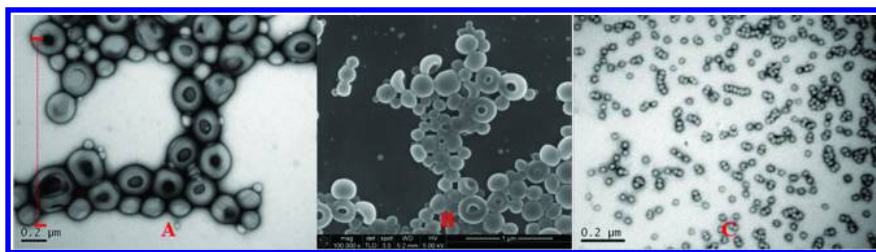


Figure 3. TEM analysis of morphologies based on Poly(1-*O*-MAFru)₃₅-*b*-PBMA₂₂₀ obtained using THF (A), and DMF (C) as common solvent; SEM analysis (B) of morphologies based on Poly(1-*O*-MAFru)₃₅-*b*-PBMA₂₂₀ obtained using THF as common solvent.

Hydrophobic Chain Length

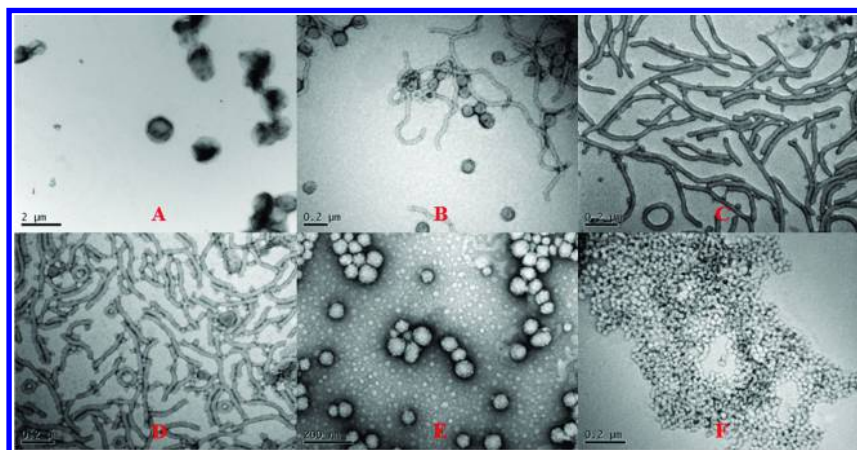
The effect of copolymer composition on self-assembled morphologies in PS-*b*-PAA system has been investigated by Eisenberg's group (32). It is found that as the percentage of the PAA block decreases, the morphologies of self-assembled aggregates transform from spheres, through cylinders and vesicles to large compound micelles (LCMs). These observations are also valid for glycopolymers. Self-assembly of block copolymer based on 2-methacrylamido glucopyranose (MAG) and 5'-*O*-methacryloyluridine (MAU) (26) led to rod-like morphologies once the hydrophobic PMAU reached a certain critical length upon which the chain stretching becomes entropically unfavourable. At this point, cylindrical micelles instead of spherical micelles are obtained to reduce the surface curvature.

However, the opposite tendency was observed when a series of fructose-based block copolymers which have the same hydrophilic block but different hydrophobic chain lengths were self-assembled (Table 3). Frequently, the morphologies can transform from spheres, through cylinders to vesicles with the increase of hydrophobic chain lengths, provided that the mobility of polymeric chains remains sufficiently high. However, this trend is only valid when the morphology is in thermodynamic equilibrium. However, the transition from one to the other morphology can succumb to kinetic control, especially when the hydrophobic blocks have a high glass transition temperature T_g . The block copolymers presented here have all T_g that are well above ambient temperatures. In addition, increasing block length will further increase T_g and lower chain mobility. The addition of water results in the formation of spherical micelles, but it also reduces the chain mobility. Compared to block copolymers with short hydrophobic chains, those with long chains tend to become frozen at very low water content already, thus limiting morphological transition. Therefore, vesicles were obtained during the self-assembly of Poly(1-*O*-MAFru)₃₅-*b*-PMMA₁₅₃, but micelles when Poly(1-*O*-MAFru)₃₅-*b*-PMMA₃₂₅ was used as copolymers (Figure 4). The latter is likely to be a kinetically trapped structure. Longer hydrophobic blocks as in the case of Poly(1-*O*-MAFru)₃₅-*b*-PMMA₃₉₆, led to a large aggregate of very small spherical structures. It is possible that the long PMMA block is

only capable to form inverse micelles, which agglomerate quickly in the aqueous media.

Table 3. Self-assembly of micelles prepared from Poly(1-*O*-MAFru)_m-*b*-PMMA_n.

<i>Block copolymer</i>	<i>PMMA (mol %)</i>	<i>Morphology</i>	<i>Size (d.nm)</i>	<i>PDI</i>
Poly(1- <i>O</i> -MAFru) ₃₅ - <i>b</i> -PMMA ₁₅₃	18.6	Vesicles	646	0.26
Poly(1- <i>O</i> -MAFru) ₃₅ - <i>b</i> -PMMA ₁₉₂	15.4	Vesicles + Worms	131	0.14
Poly(1- <i>O</i> -MAFru) ₃₅ - <i>b</i> -PMMA ₁₉₅	15.2	Long rods + Micelles	117	0.15
Poly(1- <i>O</i> -MAFru) ₃₅ - <i>b</i> -PMMA ₂₆₀	11.7	Short rods + Micelles	126	0.07
Poly(1- <i>O</i> -MAFru) ₃₅ - <i>b</i> -PMMA ₃₂₅	9.7	Micelles	45	0.15
Poly(1- <i>O</i> -MAFru) ₃₅ - <i>b</i> -PMMA ₃₉₆	8.1	Aggregated micelles	3129	0.15



*Figure 4. TEM analysis of morphologies based on Poly(1-*O*-MAFru)₃₅-*b*-PMMA₁₅₃ (A), Poly(1-*O*-MAFru)₃₅-*b*-PMMA₁₉₂ (B), Poly(1-*O*-MAFru)₃₅-*b*-PMMA₁₉₅ (C), Poly(1-*O*-MAFru)₃₅-*b*-PMMA₂₆₀ (D), Poly(1-*O*-MAFru)₃₅-*b*-PMMA₃₂₅ (E), Poly(1-*O*-MAFru)₃₅-*b*-PMMA₃₉₆ (F) obtained using THF as common solvent.*

Water Injection Rate

Finally, it was hypothesized that the water injection rate would influence the self-assembly since slow alterations to the solvent quantity are more likely to result in morphologies that are in thermodynamic equilibrium. Just as expected, an interesting trend can be seen in Table 4 and Figure 5. When water injection rates are above 0.2ml/h, the final morphologies are a mixture of vesicles and worm-like micelles with a size of around 100 nm. However, once the adding rates are below 0.2ml/h, different morphologies were obtained. When the water injection rate is 0.15ml/h, long interconnected worms and large vesicles with sizes of around 1000 nm can be observed. When the water injection rate is even lower, the self-assembly process has enough time for morphological transition and the formation of the aggregates occurs under thermodynamic control. During the sphere-rod transition, if the water injection rate is low, formed rods will have more time and opportunities to grow into long worms or networks before rearrange into vesicles. The formation of high aspect-ratio worms is energetically favourable due to the decreased number of end caps. Therefore, aspect-ratio worms, instead of vesicles, were obtained when the water injection rate was 0.1ml/h.

Table 4. Self-assembly of micelles prepared from Poly(1-*O*-MAFru)₃₅-*b*-PMMA₁₉₂ under different water injection rate using THF as common solvent.

<i>Block copolymer</i>	<i>Water injection rate</i>	<i>Morphology</i>	<i>Size (d.nm)</i>	<i>PDI</i>
Poly(1- <i>O</i> -MAFru) ₃₅ - <i>b</i> -PMMA ₁₉₂	0.10ml/h	High aspect-ratio worms	1183	0.47
	0.15ml/h	Vesicles + High aspect-ratio worms	1215	0.54
	0.20ml/h	Vesicles + Worms	232	0.13
	0.60ml/h	Vesicles + Worms	180	0.10

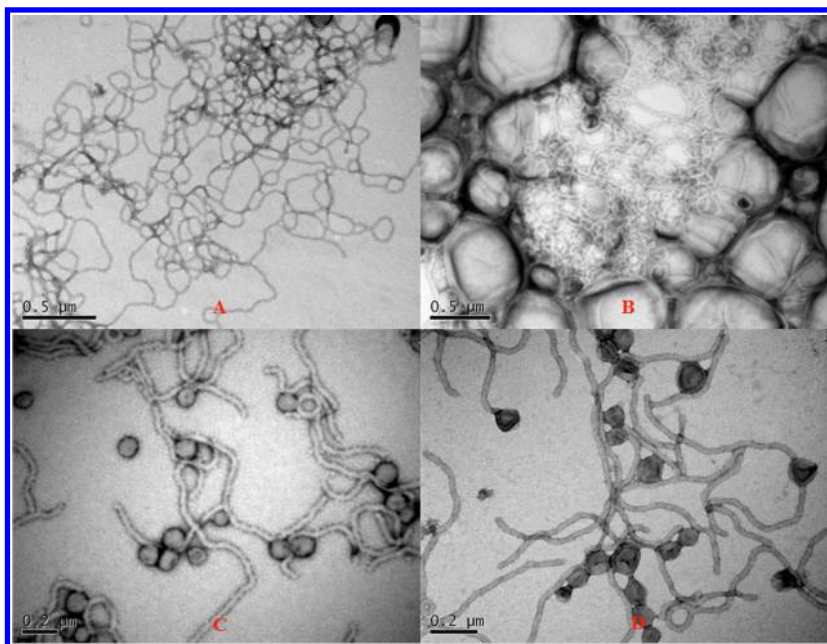


Figure 5. TEM analysis of morphologies based on Poly(1-O-MAFru)₃₅-b-PMMA₁₉₂ under different water injection rates (A: 0.1ml/h; B: 0.15ml/h; C: 0.2ml/h; D: 0.6ml/h) using THF as common solvent.

Conclusions

A great number of fructose-based block glycopolymers have been successfully synthesized via RAFT polymerization. The length and structure of chains can be well controlled thanks to modern polymerization techniques. These block glycopolymers are promising candidates to create highly ordered structures such as micelles, rods and vesicles once the processing parameters have been optimized. Due to the excellent bioactivity of glycopolymers, these fructose-coated nanoparticles can be designed to encapsulate therapeutic species for targeted drug/gene delivery. The size and structure of self-assembled aggregates can be controlled by tailoring kinetic and thermodynamic factors.

Acknowledgments

The authors would like to thank the China Scholarship Council (CSC) and the Australian Research Council (ARC) for support

References

1. Miura, Y. *Polym. J.* **2012**, *44*, 679–689.
2. Ladmiral, V.; Melia, E.; Haddleton, D. M. *Eur. Polym. J.* **2004**, *40*, 431–449.
3. Spain, S. G.; Cameron, N. R. *Polym. Chem.* **2011**, *2*, 1552–1560.
4. Ting, S. S.; Chen, G.; Stenzel, M. H. *Polym. Chem.* **2010**, *1*, 1392–1412.
5. Slavin, S.; Burns, J.; Haddleton, D. M.; Becer, C. R. *Eur. Polym. J.* **2011**, *47*, 435–446.
6. Ghadban, A.; Albertin, L. *Polymers* **2013**, *5*, 431–526.
7. Vázquez-Dorbatt, V.; Lee, J.; Lin, E. W.; Maynard, H. D. *ChemBioChem* **2012**, *13*, 2478–2487.
8. Becer, C. R. *Macromol. Rapid Commun.* **2012**, *33*, 742–752.
9. Narla, S. N.; Nie, H.; Li, Y.; Sun, X.-L. *J. Carbohydr. Chem.* **2012**, *31*, 67–92.
10. Narain, R. *Engineered carbohydrate-based materials for biomedical applications: polymers, surfaces, dendrimers, nanoparticles, and hydrogels*; John Wiley & Sons: Hoboken, 2011.
11. Spain, S. G.; Cameron, N. R. *Polym. Chem.* **2011**, *2*, 60–68.
12. Lundquist, J. J.; Toone, E. J. *Chem. Rev.* **2002**, *102*, 555–578.
13. Duncan, R. *Nat. Rev. Drug Discovery* **2003**, *2*, 347–360.
14. Satchi-Fainaro, R.; Duncan, R.; Barnes, C. M. Polymer therapeutics for cancer: current status and future challenges. In *Polymer Therapeutics II*; Springer: Heidelberg, 2006; pp 1–65.
15. Khandare, J.; Minko, T. *Prog. Polym. Sci.* **2006**, *31*, 359–397.
16. Kataoka, K.; Harada, A.; Nagasaki, Y. *Adv. Drug Delivery Rev.* **2001**, *47*, 113–131.
17. Ahmed, F.; Pakunlu, R. I.; Brannan, A.; Bates, F.; Minko, T.; Discher, D. E. *J. Controlled Release* **2006**, *116*, 150–158.
18. Zhao, J.; Babiuch, K.; Lu, H.; Dag, A.; Gottschaldt, M.; Stenzel, M. H. *Chem. Commun.* **2014**, *50*, 15928–15931.
19. Geng, Y. A. N.; Dalhaimer, P.; Cai, S.; Tsai, R.; Tewari, M.; Minko, T.; Discher, D. E. *Nat. Nanotech.* **2007**, *2*, 249–255.
20. Eliezar, J.; Scarano, W.; Boase, N.; Thurecht, K.; Stenzel, M. H. *Biomacromolecules* **2015**, *16*, 515–523.
21. Hasegawa, T.; Kondoh, S.; Matsuura, K.; Kobayashi, K. *Macromolecules* **1999**, *32*, 6595–6603.
22. Cheng, G.; Böker, A.; Zhang, M.; Krausch, G.; Müller, A. H. E. *Macromolecules* **2001**, *34*, 6883–6888.
23. Wataoka, I.; Urakawa, H.; Kobayashi, K.; Akaike, T.; Schmidt, M.; Kajiwarra, K. *Macromolecules* **1999**, *32*, 1816–1821.
24. Dai, X.-H.; Dong, C.-M. *J. Polym. Sci., Part A: Polym. Chem.* **2008**, *46*, 817–829.
25. Huang, J.; Bonduelle, C.; Thévenot, J.; Lecommandoux, S.; Heise, A. *J. Am. Chem. Soc.* **2011**, *134*, 119–122.
26. Pearson, S.; Allen, N.; Stenzel, M. H. *J. Polym. Sci., Part A: Polym. Chem.* **2009**, *47*, 1706–1723.

27. Cameron, N. R.; Spain, S. G.; Kingham, J. A.; Weck, S.; Albertin, L.; Barker, C. A.; Battaglia, G.; Smart, T.; Blanz, A. *Faraday Discuss.* **2008**, *139*, 359–368.
28. Ladmiral, V.; Semsarilar, M.; Canton, I.; Armes, S. P. *J. Am. Chem. Soc.* **2013**, *135*, 13574–13581.
29. Mitsukami, Y.; Donovan, M. S.; Lowe, A. B.; McCormick, C. L. *Macromolecules* **2001**, *34*, 2248–2256.
30. Brady, R. F., Jr. *Carbohydr. Res.* **1970**, *15*, 35–40.
31. Mai, Y.; Eisenberg, A. *Chem. Soc. Rev.* **2012**, *41*, 5969–5985.
32. Zhang, L.; Eisenberg, A. *J. Am. Chem. Soc.* **1996**, *118*, 3168–3181.
33. Zhang, L.; Eisenberg, A. *Polym. Adv. Technol.* **1998**, *9*, 677–699.
34. Kim, Y.; Pourgholami, M. H.; Morris, D. L.; Lu, H.; Stenzel, M. H. *Biomater. Sci.* **2013**, *1*, 265–275.
35. Kim, Y.; Liemawana, E. D.; Pourgholami, M. H.; Morris, D. L.; Stenzel, M. H. *Macromolecules* **2012**, *45*, 5451–5462.
36. Yu, Y.; Zhang, L.; Eisenberg, A. *Macromolecules* **1998**, *31*, 1144–1154.
37. Bhargava, P.; Zheng, J. X.; Li, P.; Quirk, R. P.; Harris, F. W.; Cheng, S. Z. *Macromolecules* **2006**, *39*, 4880–4888.
38. Motoyoshi, K.; Tajima, A.; Higuchi, T.; Yabu, H.; Shimomura, M. *Soft Matter* **2010**, *6*, 1253–1257.

Chapter 8

Synthesis of 4-Arm Polystyrene Star Polymers by Sequential Reactions

Fenja Moldenhauer and Patrick Theato*

Institute for Technical and Macromolecular Chemistry,
University of Hamburg, D-20146 Hamburg, Germany

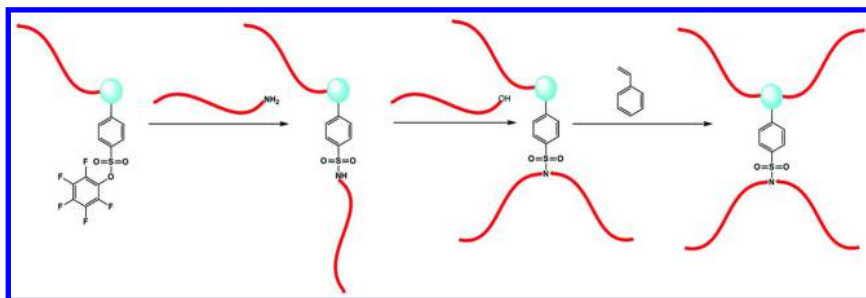
*E-mail: theato@chemie.uni-hamburg.de

We present a new synthetic route for the synthesis of 4-arm star polymers. Placing a single reactive maleimide unit at the end of a polymer chain under nitroxide-mediated polymerization conditions allows a subsequent sequential post-polymerization modification with two end-functionalized polymers. This grafting-onto approach takes advantage of the defined sequence of conjugation chemistries comprised of an ester-amine conjugation and a Mitsunobu reaction. This new route enables the linkage of amino-terminated and hydroxyl-terminated polystyrenes onto a reactive-terminated polymer chain.

Introduction

Star polymers can be described as linear chains that are connected to a central core. The resulting multiplicity of chain ends gives them unique properties in the fields of crystallinity and mechanics, which makes them highly interesting for a number of applications. In general, three synthetic strategies with different advantages and disadvantages were described in the literature (1–4). In the “core first” approach, a polyfunctional core is used to initiate the arm growth. But the initiating groups show differences in their reactivity, which usually results in an inequality of the arm length. This can be prevented in an “arm first” approach, in which the arms were synthesized via controlled polymerization techniques and then attached to the core. Even though the chain length of all arms is nearly identical, this technique can lead to an inexact number of arms. To avoid these problems, the “grafting-onto” approach gets more and more relevant. During this route, preformed arms were attached onto molecules via efficient

coupling reactions. Whether this way enables the synthesis of well-defined star polymers depends heavily on the conditions required for purification to remove unreacted arms. Furthermore, click reactions were usually used in multifunctional molecules, which do not allow the detailed analysis before the attachment of each single new arm. To tackle this problem, we investigated a sequential multicomponent reaction which allows the synthesis of well-defined polystyrene stars (Scheme 1). Besides this, the sequential approach enables the exact characterization of each intermediate. We chose a combination of an ester-amine conjugation and a Mitsunobu reaction. In this context, the design and the successful insertion of functional activated ester-containing compounds became the key step.

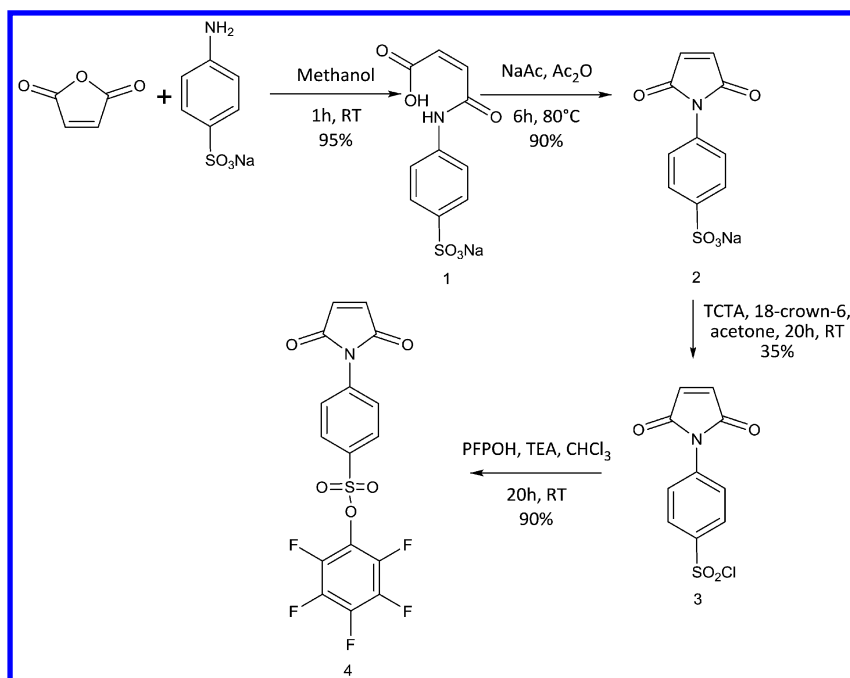


Scheme 1. Sequential post-polymerization modification for the synthesis of 4 arm polystyrene star polymers.

Results and Discussions

In our approach, we decided to use a pentafluorophenyl ester bearing maleimide. The position of this functional group in polystyrene can be well-defined as shown in our previous papers using NMP as polymerization technique (5). As illustrated in scheme 2, monomer (4) can be synthesized by using maleic anhydride and sulfanilic acid sodium salt as starting materials.

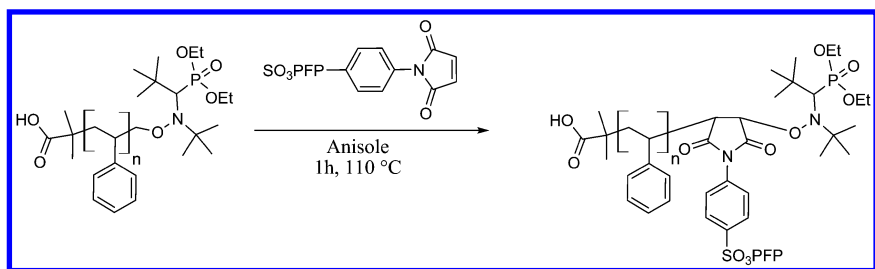
The first two steps of the synthesis of *N*-(4-sodiumsulphophenyl)-maleic acid imide (2) follow a report by Yasar *et al.* (6) The resulting sodium salt (2) could be transformed into the corresponding sulfonyl chloride (3) by using trichlorotriazine (TCTA) as chlorination agent. The reaction enabled an easy access to sulfonylchloride derivatives, yielding the pentafluorophenyl esters in a subsequent fourth reaction step in very good yields (up to 88%) (7). Different literature known synthetic pathways to yield the sulfonyl derivatives (4), such as the chlorination with thionyl chloride did not show high reproducibilities (8). Other reactions, e.g. bromination with elemental bromine and triphenylphosphine (6) or the usage of another intermediate made from trifluoromethane sulfonic acid anhydride, triphenylphosphine oxide and compound (2) did not result in the desired product (9).



Scheme 2. Four-step synthesis of N-(4-(pentafluorophenyl sulfonyl)phenyl)-maleic acid imide starting from maleic anhydride and sulfanilic acid sodium salt.

The obtained monomer **4** could be successfully inserted into the ω -chain end of a polystyrene, which was synthesized with SG1 as an initiator (scheme 3). Thereby, SG1 is a commonly used initiator for nitroxide-mediated polymerizations which carries a carboxylic acid function that can be used for post-polymerization modifications. As shown in figure 1, the $^1\text{H-NMR}$ spectra of the monomer (**4**) containing polymer show the aromatic signals of the monomer between 7.85 and 8.15 ppm. As the degree of polymerization can be determined by $^1\text{H-NMR}$, THF-GPC and MALDI-TOF measurements, one can approximate the ratio of maleimide per polymer chain. This is done by comparison of the $^1\text{H-NMR}$ integration values of the aromatic signals with the values derived from the polymer backbone signal between 0.79 and 2.09 ppm, indicating an approximate ratio of solely one (0.99) maleimides per polymer chain.

Further addition of styrene leads to the opportunity to adjust the exact position of the maleimide moiety in the chain. In this case, the maleimide-bearing polymer works as a macroinitiator leading to two PS arms with an independently adjustable chain length. Figure 2 exemplifies this for the installation of monomer (**4**) in the middle of the chain. The macroinitiator, exhibiting a molecular weight of 2100 g/mol (16 repeating units) and a PDI of 1.21, was used for the polymerization of styrene. Comparison of the $^1\text{H-NMR}$ spectra, before and after chain extension, clearly illustrates the presence of maleimide protons. The ratio of their integration values was bisected during the chain extension. The same trend can be observed by CHCl_3 -GPC (figure 2).



Scheme 3. Introduction of the new PFP-bearing monomer onto the polystyrene chain.

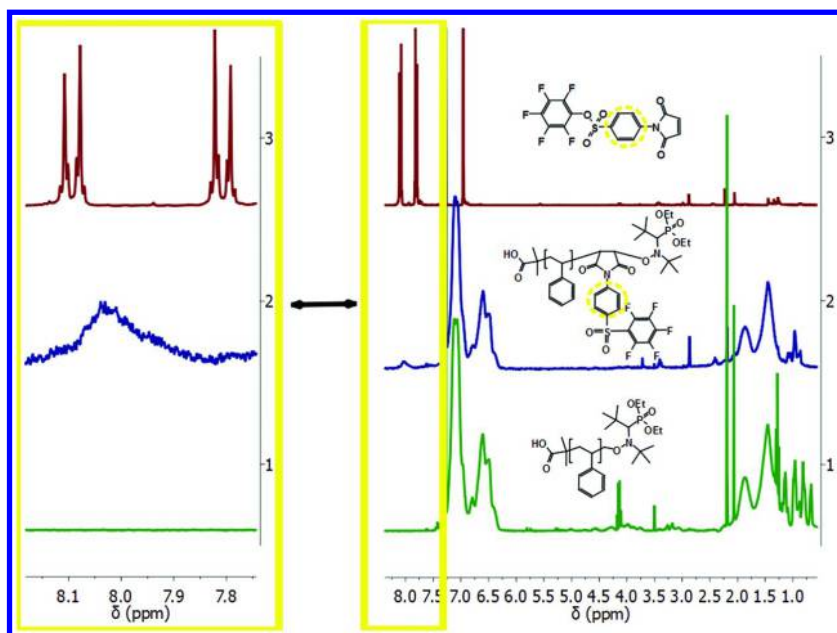


Figure 1. $^1\text{H-NMR}$ -spectra (CDCl_3) of monomer **4** (top), NMP-made PS (bottom) and PS with introduced single unit of monomer (**4**) (middle).

As clearly illustrated, the molecular weight almost doubled to 4300 g/mol (33 repeating units) while the PDI (1.34) remained low.

As highlighted in the introduction, our primary aim is not the sole chain extension and adjustment of the position of the maleimide moiety in the main chain but the synthesis of star-shaped polymers. In order to keep the system as simple as possible, we took one step backwards and started with the unextended chain. In the following, we triple-functionalized the chain ends and described these steps below.

As illustrated in scheme 4, the synthetic route can be distinguished into two pathways.

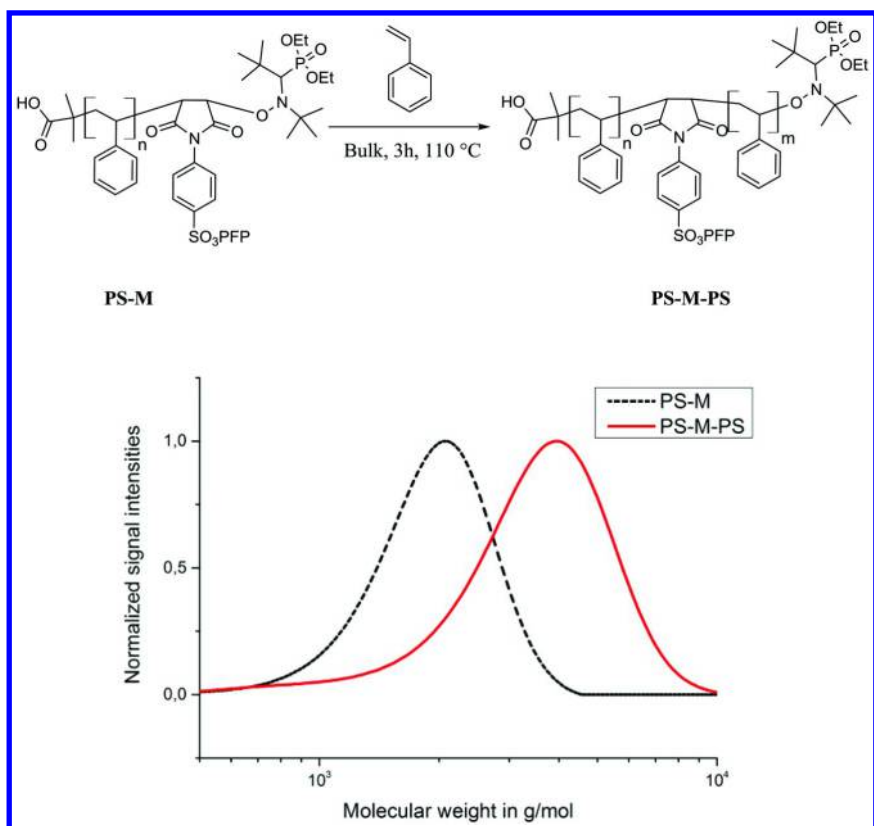
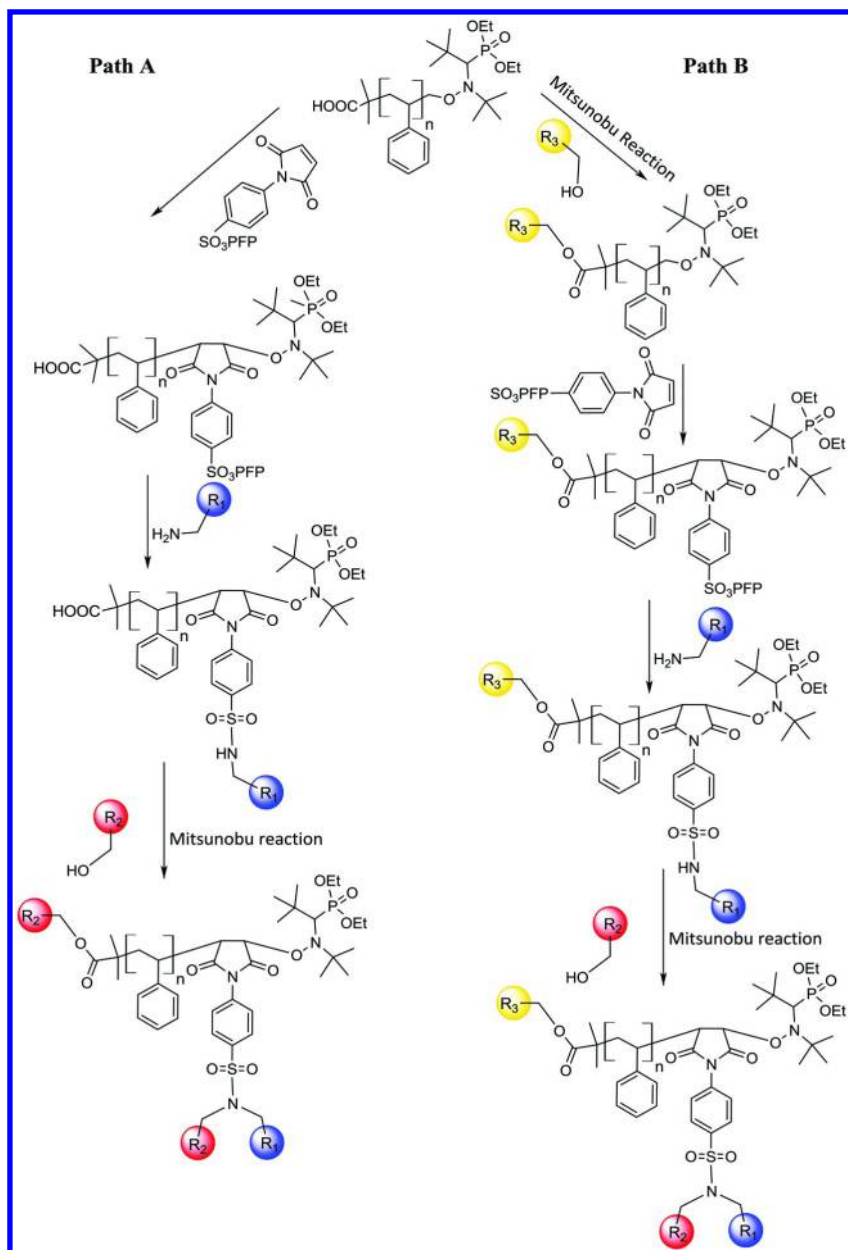


Figure 2. GPC of macroinitiator (dashed line) and the chain extended polymer (solid line) in CHCl_3 .

Path A starts with the insertion of maleimide (**4**) as already described in the previous part of this section. The first functionality can subsequently be introduced in form of an amine. Upon this reaction, the activated PFP-ester gets substituted quantitatively by an amine yielding the respective amide. Full conversion can be achieved under mild conditions with a multitude of different primary amines (**5**, **10**–**12**). The reaction can be tracked by NMR spectroscopy. The PFP-signals in all ^{19}F -NMR spectra disappeared completely, while the proton signals of the introduced amine showed up in ^1H -NMR spectra. Both observations are shown in figure 3 for the reaction with benzylamine.

The next functionality can be inserted via a Mitsunobu reaction into the unmodified NMP polystyrene. Thereby, the acid group, which was introduced with the SG1 initiator, and the secondary amine of the previous step react with an alcohol under catalysis of tetramethylazodicarboxamide (TMAD) and tri(*n*-butyl)phosphine (TBP). Proceeding in this way leads towards the functionalization of two different polymer sites with the same alcohol, at the α - and at the ω -chain end (figure 4).



Scheme 4. Overview of the introduction of up to three functionalities at the polymer chain ends.

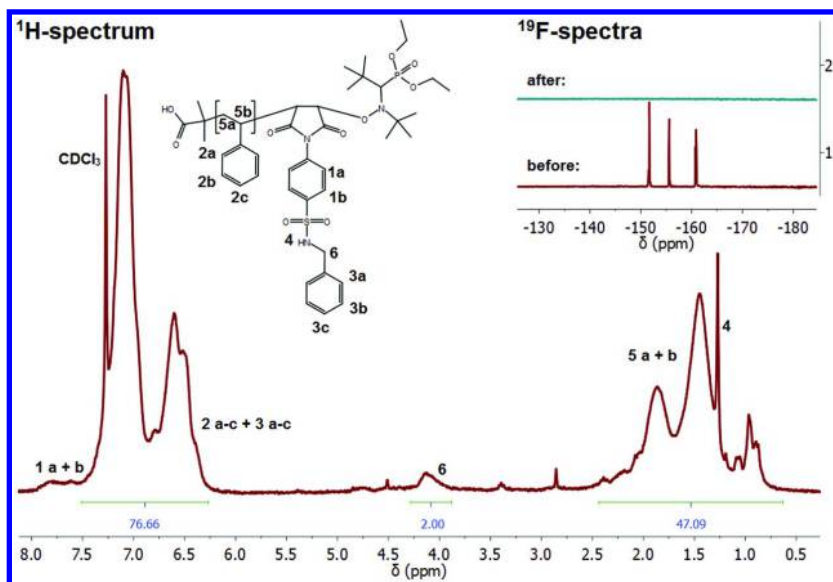


Figure 3. ¹H- and ¹⁹F-NMR spectra (CDCl₃) of the first functionalization with benzylamine.

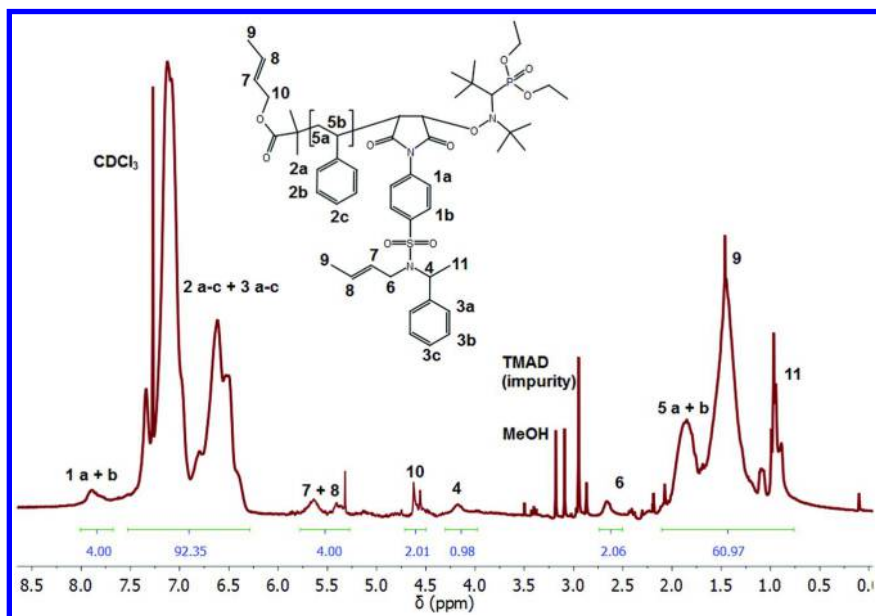


Figure 4. ¹H-NMR spectrum (CDCl₃) of a tripple chain end functionalized PS with methylbenzyl amine and but-2-enol (PSI).

The olefinic protons 7 and 8 of the inserted alcohols give rise to a signal between 5.83 and 5.31 ppm and the comparison of the integrations clearly showed, that this new functional group was installed twice per polymer chain.

In Path B, a different synthetic route is used in order to improve the number of various functionalities and to show the versatility of our post-modification approach.

Therefore, we decided to use a Mitsunobu reaction prior to the installation of the maleimide moiety in the starting polymer chain. This enabled us to change the order of functionalization as well as changing the functional groups into three different groups.

We decided to use a Mitsunobu reaction instead of an acid or base catalyzed esterification for several reasons. First of all, the Mitsunobu reaction is conducted under mild conditions. This enables the use of sensible alcohols such as unsaturated ones, which, if polymerized at high temperatures, would lead to crosslinks or cyclizations. Besides this, Mitsunobu reactions yield in much higher conversions, which is very important, due to the fact, that the separation of modified and unmodified polymers is very hard or in some cases even impossible.

To show the versatility of this reaction, we studied the modification using benzyl alcohol, 4-methyl benzyl alcohol, 2-pentanol and thiophen-2-methanol. The resulting IR-spectra (figure 5) illustrate the extinction of the carbon acid bond at 1698 cm^{-1} and the appearance of the ester bonds between 1714 and 1738 cm^{-1} .

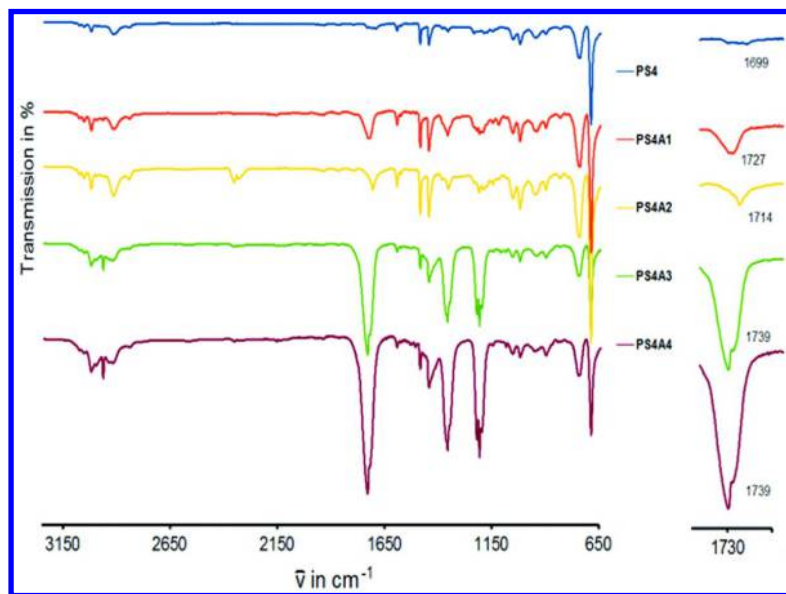


Figure 5. FT-IR-spectra before and after the first Mitsunobu reaction with benzyl alcohol, 4-methyl benzyl alcohol, 2-pentanol and thiophene-2-methanol (listed from top to bottom).

Successful modification of the polystyrene chain end by Mitsunobu was followed by insertion of maleimide (**4**) as already described above. The installation of the two functional groups is followed by substitution of the PFP-ester containing maleimide (**4**) using cyclopropylamine as the nucleophile (figure 6).

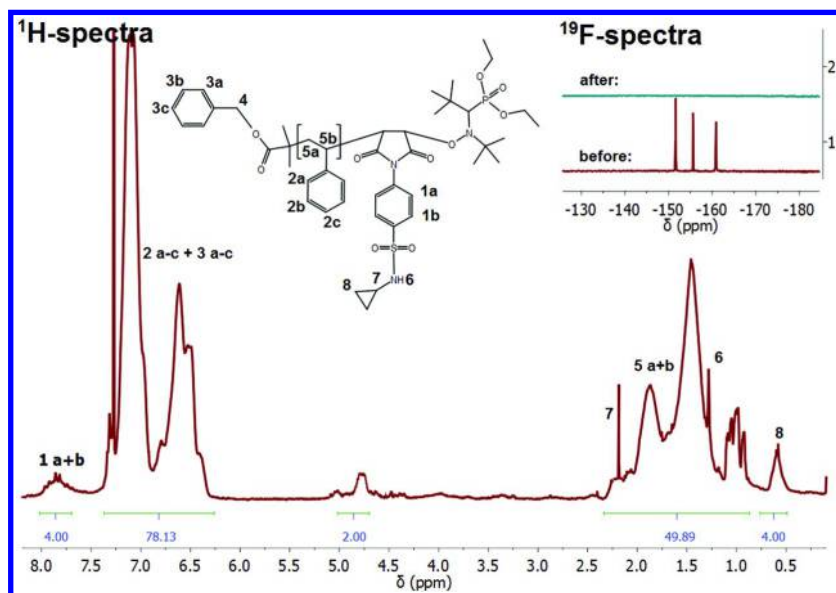


Figure 6. ^1H - and ^{19}F -NMR spectra (CDCl_3) of a double chain end functionalized PS with propyl amine and benzyl alcohol.

In the last step of Path B, the resulting secondary amine can be converted into a tertiary amine by using another hydroxyl group containing compound (figure 7). This new functionality is then again introduced by a Mitsunobu reaction.

The advantage of using path B can be summarized as the opportunity to install three different functional groups on the starting polymer material, simply by changing the order of the synthetic steps.

So far, we could show that this novel chemistry allows the introduction of two or three different functionalities at three positions at both polystyrene chain ends. According to IR and NMR, all reactions were conducted quantitatively. The obtained combinations of inserted organic groups are finally summarized in table 1.

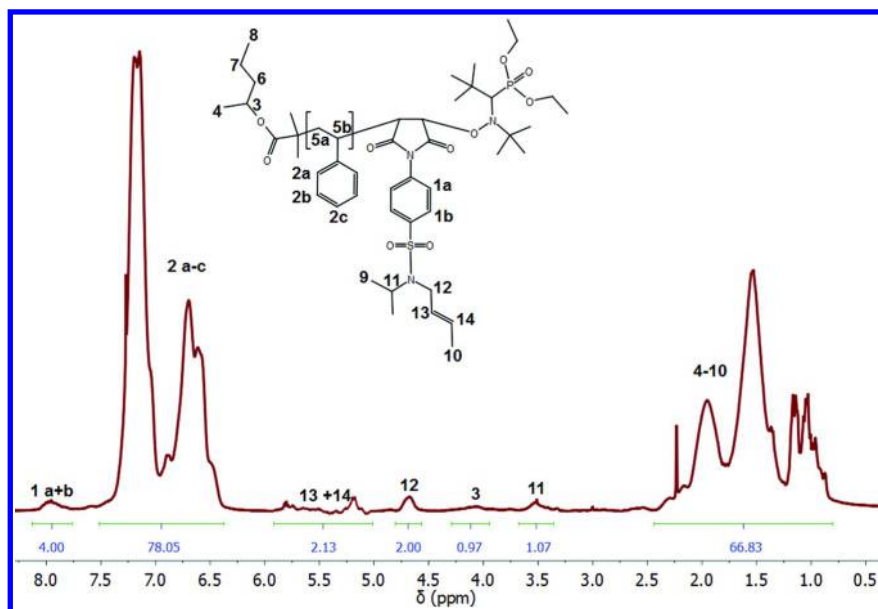


Figure 7. $^1\text{H-NMR}$ -spectrum (CDCl_3)

So far we have only used the above described synthetic pathways (path A and B) to install small organic compounds on the starting polymer material.





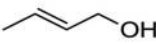
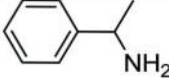
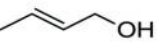
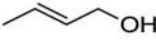
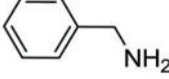
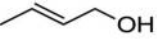
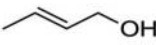
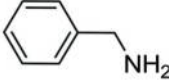
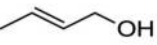
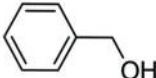
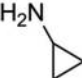
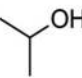
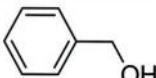
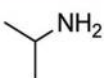
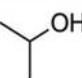

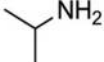
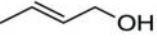
In the next step, we will use this approach to synthesize polystyrene star polymers. Therefore, NMP-made polystyrene that contains a single maleimide monomer unit (**4**) was synthesized. The molecular weight was determined via MALDI-TOF, CHCl_3 -GPC and $^1\text{H-NMR}$ to 17 repeating units ($M_n = 2500$ g/mol, PDI = 1.07). The acid end group of this polymer was esterified with *n*-hexanol to avoid a second reaction with the alcohol in a later step. Additionally, polystyrenes with amine and alcohol functionalities were needed. Both can be synthesized in ATRPs.

The alcohol functionality was directly inserted via the initiator 2-hydroxyethyl-2-bromoisobutyrate (HEBIB) (figure 8).

The use of HEBIB as initiator, bipyridine as ligand, copper(I) bromide as catalyst and styrene as monomer (5/2/1/275) leads to an alcohol capped polystyrene with a chain length of 17.7 repeating units ($M_n = 2000$ g/mol) and a PDI of 1.25. The molecular weight was detected by MALDI-TOF, CHCl_3 -GPC and $^1\text{H-NMR}$. The MALDI-TOF and the GPC-spectra are shown at the bottom of figure 8 as well.

The amine capped polystyrene could be synthesized in a three-step reaction (figure 9).

Table 1. A library of triple functionalized polymers synthesized via amination and Mitsunobu reactions at PS chain ends.

Polymer name	 R_1 /  R_2 1. Alcohol	 R_3 Amine	 R_2 2. Alcohol
PS1			
PS2			
PS3			
PS4			
PS5			
PS6			

The synthesis starts with an ATRP made polystyrene, where ethyl 2-bromo-2-methylpropanoate, bipyridine, copper(I) bromide and styrene (4.6/1.5/1/267) were used. The obtained polystyrene bromide can be treated with sodium azide to install an azide end group. In the last step, the resulting PS-azide can be applied in a Staudinger reduction to result in the polystyrene with an amine end group. While the first steps were conducted quantitatively, the Staudinger reduction gave the amine capped PS with yield of 86%. Due to a similar solubility, the following steps were conducted with the crude product. All steps towards the amino-PS can be tracked by $^1\text{H-NMR}$ -spectra, and the signal of the last styrene proton shifts from 4.47 ppm (bromide) to 3.93 ppm (azide). During the amine formation, the position of the signals was superimposed with another signal at 3.60 ppm (figure 9).

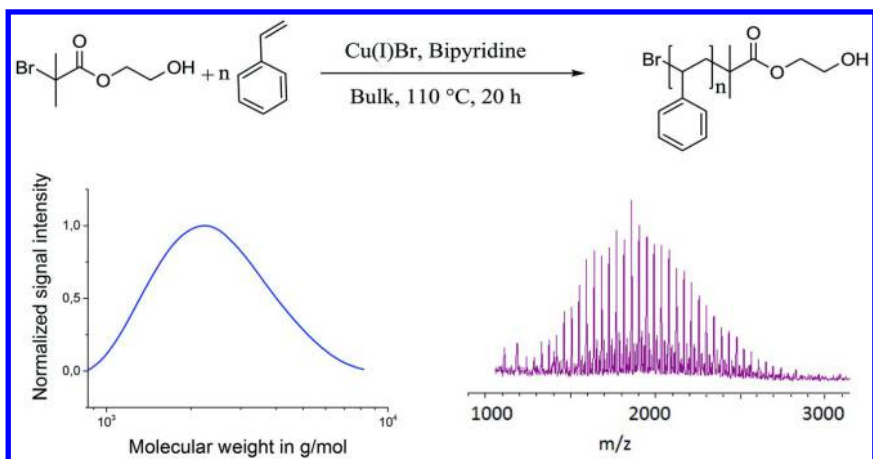


Figure 8. Synthesis of hydroxyl capped PS by use of HEBIB as initiator (top) and obtained GPC graph (bottom left) and MALDI-TOF-spectrum (bottom right).

Additionally, the transformation of the polystyrene-bromide into the polystyrene-amine could be followed by FT-IR spectroscopy (figure 10). During the azide formation, two bands at 2092 and 1682 cm^{-1} appeared, respectively, which are related to the N_3 - stretch vibration. The intensity of both bands decreased in the subsequent reduction. Consequently, new amine related peaks were observed at 2357 and 2334 cm^{-1} .

The synthesized PS-NH₂ was characterized via MALDI-TOF, CHCl₃-GPC and ¹H-NMR. It contains 21 repeating units ($M_n = 2400$ g/mol) and a PDI of 1.19.

In order to synthesize 3-arm-star-polymers, the described sequential multicomponent reaction was conducted, but this time employing polymeric agents. In the first reaction, the amine capped polystyrene reacted with the PFP-group of the maleimide moiety (**4**) to form a longer polystyrene chain. This longer chain contained a secondary amine, which was modified in a Mitsunobu reaction with the alcohol capped polystyrene. Surprisingly, the solubility of our branched PS changed dramatically. We figured out, that our linear starting polymers are soluble in acetone and the obtained stars are completely insoluble in acetone, which allowed an easy purification via precipitation.

To attach a fourth arm, the 3-arm-star polymer can be chain extended at the position of the nitroxide. Therefore, the star-polymer was used as a macroinitiator for the NMP of styrene. The reaction solution was stirred at 110 °C for 3h and the obtained polymer was purified via precipitation from chloroform into acetone.

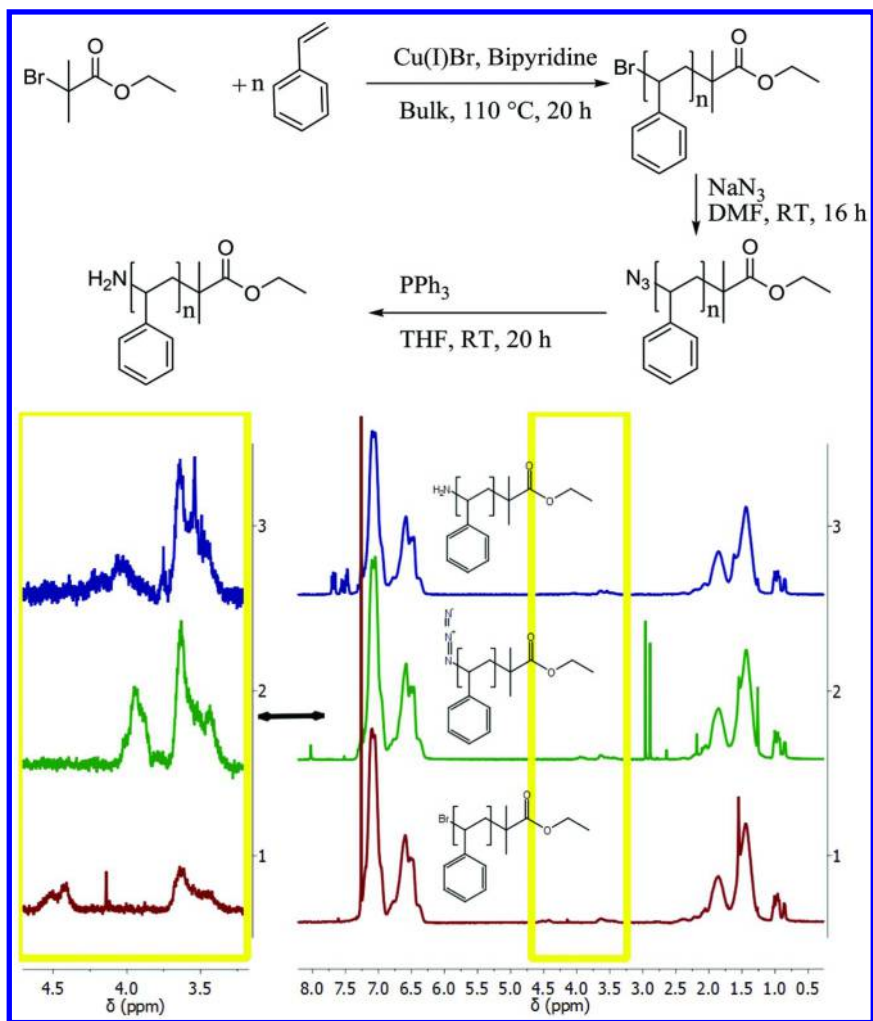


Figure 9. Three-step synthesis of PS-Amine with corresponding $^1\text{H-NMR}$ -spectra (CDCl₃).

By attachment of new arms, the molecular weights increased. This can be followed by CHCl₃-GPC and by MALDI-TOF measurements. In GPC the PS-NH₂ showed a maximum at 3200 g/mol (Figure 11, *solid line*). The PS-amine was used in excess during the amidation. Therefore, the *solid line* in figure 11 resembles the excess of the starting polymer as well as the resulting polymer chains connected via a secondary amine group (9500 g/mol). The two polymers could not be separated by precipitation due to their similar solubility. The addition of PS-OH by a Mitsunobu reaction led to a 3-arm PS-star polymer (*dashed line*), which goes along with the solubility change. A final chain extension was used to form the 4-arm-star polymer (*dash-dotted line*).

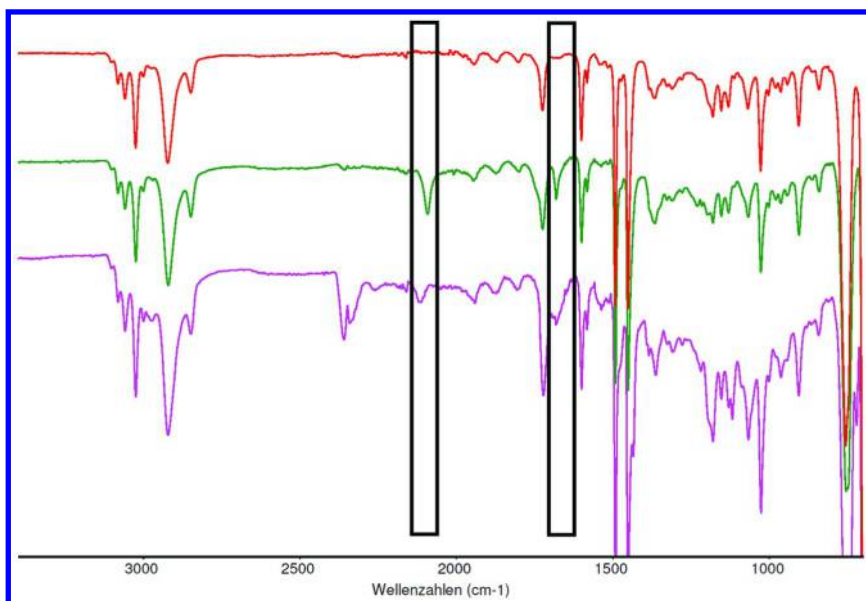


Figure 10. FT-IR-spectra of polystyrene bromide, polystyrene azide and polystyrene amine (listed from top to bottom).

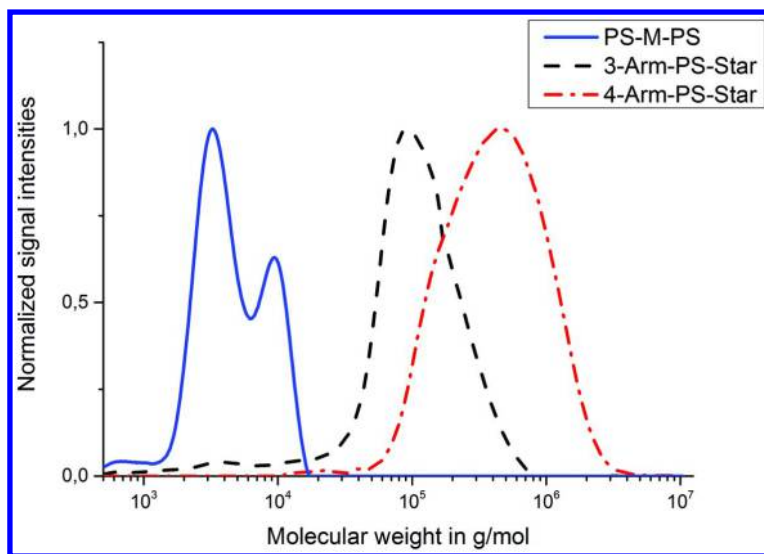


Figure 11. CHCl_3 -GPC-molecular weight distribution of mixture of excess PS-NH_2 and PS-M-PS (solid line), 3-arm (dashed line) and 4-arm star polymers (dash-dotted line).

During the star synthesis, the molecular weight increased as expected. However, the represented molecular weights are much larger than expected,

which likely is a result of the branched structure. In order to analyze the absolute molecular weight, a MALDI-TOF spectrum of the final 4-arm star polymer consisting of four PS chains was measured (Figure 12), confirming the existence of a 4-arm star architecture.

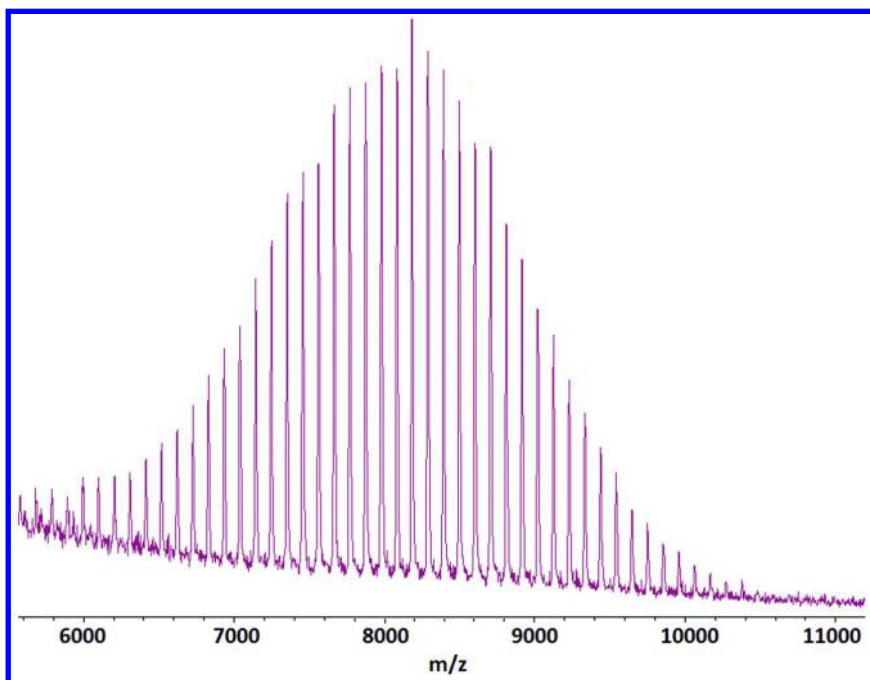


Figure 12. MALDI-TOF spectrum of a 4-arm-PS-star polymer.

Experimental Section

Materials

N,N,N',N'-Tetramethylazodicarboxamide (TMAD) was either available from TCI Europe N. V. or synthesized according to a previous report (13).

The SG1, (97%) was purchased from Arkema. Triphenylphosphine (TPP) and tributylphosphine (TBP) were available from the Sigma-Aldrich Chemicals Co., and used as received. All other chemicals were commercially available and used without further purification unless otherwise stated.

Instruments

All ^1H and ^{13}C NMR spectra were recorded on a Bruker 300 MHz FT-NMR spectrometer in deuterated solvents and chemical shifts (δ) were given in ppm with the solvent peak as internal standard. ^{19}F NMR spectra were recorded on a Bruker 188 MHz FT-NMR spectrometer in deuterated solvents. Size exclusion chromatography (SEC) was performed at room temperature in chloroform

containing 20 mL/L toluene as an internal standard at a flow rate of 1.0 mL/min. The number-average molecular weight (M_n) and molecular weight distribution (M_w/M_n) of the polymers were calculated on the basis of a polystyrene calibration. FT-IR spectra were recorded on a Thermo Scientific Nicolet 1510 (ATR) at room temperature. Elemental analysis was performed by an EuroEA Elemental Analyzer.

ESI-TOF mass spectroscopy was measured by using an Agilent 6224 which was connected online to a HPLC-setup (Agilent HPLC 1200 Series).

MALDI-TOF spectra were measured on a Bruker UltrafleXtrem in a linear and positive mode. The samples were prepared as follows: The stock solutions of silver trifluoroacetate in THF/chloroform (1:1) (1mg/mL) and dithranol in the same solvent mixture (20 mg/mL) were mixed in the ratio 1:1. 0.5 μ L of his mixture were dropped on the target plate and air dried. The polymer sample was prepared at a 2 mg/mL concentration in THF/chloroform (1:1). This solution was dropped on the dry matrix-salt-mixture and air dried as well before measuring.

Synthesis of *N*-(4-Sodiumsulfophenyl)-maleic Acid Half Imide (1)

One equivalent maleic anhydride (10.32 g, 103.1 mmol) and 0.93 equivalents sulfanilic acid sodium salt (18.74 g, 96.02 mmol) were dissolved in methanol. The solution was stirred under argon at room temperature for 1h. The resulting precipitate was filtered off and dried in vacuum at 40°C to yield a yellow powder. Yield: 26.75 g (91.22 mmol, 95%).

$^1\text{H-NMR}$ (300 MHz, DMSO-d_6) δ [ppm]: 8.60 (s, 1H, NH), 8.45 (d, $J = 8.5$ Hz, 2H), 8.04 (d, $J = 8.5$ Hz, 2H), 7.90 (s, 2H).

Synthesis of *N*-(4-Sodiumsulfophenyl)-maleic Acid Imide (2)

One equivalent of the half imide (1) (13.98 g, 47.67 mmol) and 0.3 equivalents sodium acetate (1.24 g, 15.1 mmol) were combined with 250 mL acetic anhydride. The resulting suspension was stirred at 80 °C for 6h. The reaction mixture was then cooled down and the resulting brownish precipitate was filtered off. The crude product was re-dissolved in a small portion of water and precipitated in acetone three times to remove the acetic anhydride. The reddish residue was dried in vacuum at 40°C. Yield: 11.81 g (42.91 mmol, 90%).

$^1\text{H-NMR}$ (300 MHz, DMSO-d_6) δ [ppm]: 8.40 (d, $J = 8.5$ Hz, 2H), 7.99 (d, $J = 8.5$ Hz, 2H), 7.86 (s, 2H).

IR: $\tilde{\nu}$ [cm^{-1}]: 2992 (br, C(O)-N-C(O)-stretching vibration), 2786 (s, N-C_{arom}-stretching vibration), 1871 (s, C=C-stretching vibration), 1348 (s, HC=CH-plane deformation vibration), 890 (s, S-O-stretching vibration).

Synthesis of *N*-(4-Sulfonylchloridophenyl)-maleic Acid Imide (3)

One equivalent of the sodium imide (2) (5.63 g, 20.4 mmol) and 0.06 equivalents of 18-crown-6 (300 mg, 1.13 mmol) were dissolved in 40 mL acetone. After addition of one equivalent of 2,4,6-trichlor-1,3,5-triazine (3.77 g, 20.4 mmol), the solution was stirred under reflux conditions (67 °C) for 20 h. For

purification, the solvent was first evaporated. The residue was subsequently re-dissolved in chloroform and filtered over silica. After removal of the solvent and drying under vacuum (40 °C), the title compound was obtained as a yellow powder. Yield: 1.96 g (7.15 mmol, 35%).

¹H-NMR (300 MHz, DMSO-*d*₆) δ [ppm]: 7.36 (d, *J* = 8.8 Hz, 2H), 7.07 (d, *J* = 8.8 Hz, 2H), 6.17 (s, 2H).

Synthesis of *N*-(4-(Pentafluorophenyl sulfonyl)phenyl)-maleic Acid Imide (**4**)

A solution of one equivalent (**3**) (500 mg, 1.84 mmol) and 1.1 equivalents of pentafluorophenyl (1.62 g, 8.78 mmol) in 25 mL dichloromethane was cooled down to 0 °C. Triethylamine (1.2 mL, 888 mg, 8.8 mmol, 1.1 eq.) was added slowly. The reaction mixture was allowed to warm up to room temperature while stirred overnight. The dichloromethane was washed with water (~30 mL) three times and dried over sodium sulfate afterwards. After removal of the solvent, the crude product was purified by column chromatography (SiO₂, EA/PE (1:19) → EA/PE (1:1)). The title compound was obtained as a yellow solid. Yield: 679 mg (1.62 mmol, 88%).

¹H-NMR (300 MHz, CDCl₃) δ [ppm]: 8.08 (d, *J* = 8.9 Hz, 2H), 7.80 (d, *J* = 8.9 Hz, 2H), 6.94 (s, 2H).

¹³C-NMR (300 MHz, CDCl₃) δ [ppm]: 168.6, 144.0, 142.1, 140.4, 137.8, 132.9 134.7, 129.5, 125.3

¹⁹F-NMR (200 MHz, CDCl₃) δ [ppm]: -150.47 (d, *J* = 17.9 Hz, 2F), -154.97 (t ~dd, 1F), -160.76 (dd, *J* = 22.0 Hz, 2F).

HRMS (ESI) *m/z* for C₁₆H₆F₅NO₅S: [M]⁺ calculated 419.9960; found: 419.9956.

Element (calculated in %) found in %: N (3.34) 3.34, C (45.84) 45.84, H (1.64) 1.62, S (8.55) 8.73

IR: $\tilde{\nu}$ [cm⁻¹]: 2981 (br, C(O)-N-C(O)-stretching vibration), 2787 (s, N-C_{arom}-stretching vibration), 1868 (s, C=C-stretching vibration), 1750 (m, FC_{arom}=C_{arom}F-stretching vibration), 1350 (s, HC=CH-plane deformation vibration), 901 (s, asymmetric S-O-C-stretching vibration).

Typical Procedure for Nitroxide Mediated Polymerizations of Styrene

The initiator SG1 was dissolved in prefiltered (AlOx) styrene. The resulting solution was degassed with argon and stirred at 110 °C for 3h. Subsequently, the reaction mixture was cooled down to room temperature and exposed to air to quench the polymerization. The polymer was purified by re-precipitation (acetone/MeOH) to yield a colorless solid, which was dried in vacuum at 40 °C.

Incorporation of *N*-(4-(Pentafluorophenyl sulfonyl)phenyl)-maleic Acid Imide by Polymerization

One equivalent of polystyrene (polymerized by NMP) and four equivalents (**4**) were dissolved in anisole. The mixture was degassed with argon for 10 minutes. After degassing, the reaction mixture was heated to 110 °C and stirred for 1 h.

The reaction mixture was then cooled down to room temperature and exposed to air to quench the polymerization. The polymer was purified by re-precipitation (acetone/MeOH) to yield a light yellow solid, which was dried in vacuum at 40 °C.

Typical Procedures for Post-Modification Reactions

Polymer Analogous Reaction with Amines

One equivalent of a *N*-(4-(pentafluorophenyl sulfonyl)phenyl)-maleic acid imide containing polymer was dissolved in THF. Then 1.2 equivalents of a primary amine were added. After 20 h of stirring at room temperature, the modified polymer was purified by re-precipitation (acetone/MeOH or chloroform/acetone) and dried in vacuum at 40 °C.

Mitsunobu Post-Polymerization Modification on Polymers

Typical post-polymerization modification reactions based on the Mitsunobu reaction were carried out as follows: under an argon atmosphere, tributylphosphine (0.2 eq.) was slowly added to a dry THF solution of the polymer (1 eq.), TMAD (1.5 eq.), and an alcohol (2 eq.) at room temperature. After the reaction mixture was stirred for 16 hours, it was diluted with THF and filtered. The filtrate was evaporated under vacuum and the polymer was purified by re-precipitation (acetone/MeOH or chloroform/acetone) and dried in vacuum at 40 °C.

Synthesis of 2-Hydroxy-2-bromoisobutyrate (HEBIB)

HEBIB was synthesized following reported procedures (14). 10.8 ml (20.1 g, 87.4 mmol) 2-bromoisobutyryl bromide were added dropwise to a cooled (0 °C) mixture of 80 mL (88.8 g, 1.44 mol) ethylene glycol and 12 mL (8.76 g, 86.6 mmol) triethylamine over 30 minutes. After stirring the solution at 60 °C over night, it was cooled down and diluted with 300 mL water. The product was extracted three times with 200 mL DCM. The organic phase was dried over sodium sulfate and the DCM was removed under reduced pressure to obtain the product as a colorless liquid. Yield: 15.9 g (75.2 mmol, 86%).

¹H-NMR (300 MHz, DMSO-*d*₆) δ [ppm]: 4.30 (t, 2H), 3.84 (t, 2H), 1.92 (s, 6H).

¹³C-NMR (300 MHz, DMSO-*d*₆) δ [ppm]: 171.7, 66.8 (60.1, 50.9, 32.8)

General Procedure for Atom Transfer Radical Polymerizations

Copper(I)bromide as catalyst, bipyridine as ligand and styrene were combined under an inert argon atmosphere. The solution was stirred at 110 °C overnight. The resulting suspension was cooled down to room temperature and diluted with acetone. After removing the catalyst by filtration, the polymer was purified by

precipitation (acetone/methanol, 3 times). The resulting polymer was dried in 40 °C in vacuum.

Synthesis of Hydroxy Terminated Polystyrene (PS-OH)

The synthesis of the hydroxy terminated polystyrene followed the general ATRP-procedure. Therefore, 10.8 mL (20.1 g, 87.4 mmol) 2-hydroxyethyl-2-bromoisobutyrate (HEBIB) as initiator, 32.5 mg (0.227 mmol) copper(I)bromide as ligand and 6.01 g (57.7 mmol) styrene as the monomer were used.

Synthesis of Polystyrene Bromide (PS-Br)

The synthesis of the bromide containing polystyrene followed the general ATRP-procedure: 455.6 mg (2.336 mmol) ethyl 2-bromo-2-methylpropanoate as initiator, 73.4 mg (0.512 mmol) copper(I) bromide as catalyst, 134.0 mg (0.858 mmol) bipyridin as ligand and 13.93 g (133.3 mmol) styrene as the monomer were used.

Synthesis of Azide Terminated Polystyrene (PS-N₃)

PS-Br (1.95 g) and 62.1 mg (0.948 mmol) sodium azide were dissolved in 150 mL DMF and stirred overnight. The resulting azide terminated polymer was purified by precipitation (acetone/methanol, 3 times) and dried at 40 °C in vacuum afterwards.

Synthesis of Amine Terminated Polystyrene (PS-NH₂)

The synthesis of the amine terminated polystyrene was conducted via a Staudinger reduction. For that, 1.792 g PS-N₃ were dissolved in 150 mL THF. The reaction was started with the addition of 181.3 mg (0.6912 mmol) triphenylphosphine. After 20 h in which the solution was stirred at room temperature, the product was purified by re-precipitation (acetone/methanol, 3 times) and dried at 40 °C in vacuum afterwards.

Conclusion

In conclusion, we have successfully established a new sequential post-polymerization modification protocol that allows the installation of up to three different functionalities per polystyrene chain. Our synthesis started with the insertion of a single PFP-bearing maleimide unit at the ω -chain end of a polystyrene prepared via NMP. The resulting polymer was modified by an amidation followed by a Mitsunobu reaction. In this case, the Mitsunobu reaction took place twice at both chain ends. This way, one amine and one alcohol were used for the modification. Switching the reaction order, enabled the insertion of

a third different functionality. Therefore, the α -chain end was modified with an alcohol by a Mitsunobu reaction in a first step. Afterwards, the maleimide was inserted and an amidation followed by another Mitsunobu reaction were used to introduce two further functionalities. Using this reaction order, the insertion of three different functionalities at both chain ends became possible.

During this process, the introduction of different combinations of organic moieties was conducted and the conversions of >99% were confirmed by $^1\text{H-NMR}$ and FT-IR spectroscopy.

This approach was used to synthesize 3-arm and 4-arm star polymers in the next step. First, the acid end group of the NMP-initiator SG1 was protected via a first Mitsunobu reaction using hexanol. After the insertion of the maleimide, the amidation followed by a Mitsunobu reaction took place. The required hydroxyl and amine capped polystyrenes were obtained by ATRPs before that. Coincidentally, we observed a different solubility between linear and branched polymer structures, which enabled an easy purification by precipitation. Each step of the star synthesis could be tracked by using CHCl_3 -GPC and MALDI-TOF measurements.

Acknowledgments

The authors gratefully acknowledge M. Trusch and Ch. Crist for the optimization of MALDI-TOF measurements and T. Krappitz and R. Kakuchi for fruitful discussions.

References

1. Li, Y.; Zhang, B.; Hoskins, J. N.; Grayson, S. M. *J. Polym. Sci., Part A: Polym. Chem.* **2012**, *50*, 1086–1101.
2. Gao, H.; Matyjaszewski, K. *Prog. Polym. Sci.* **2009**, *34*, 317–350.
3. Wu, Z.-M.; Liang, H.; Lu, J.; Deng, W.-L. *J. Polym. Sci., Part A: Polym. Chem.* **2010**, *48*, 3323–3330.
4. Wu, Z.; Liang, H.; Lu, J. *Macromolecules* **2010**, *43*, 5699–5705.
5. Kakuchi, R.; Zamfi, M.; Lutz, J.; Theato, P. *Macromol. Rapid Commun.* **2012**, *33*, 54–60.
6. Kahraman, M. V. *J. Appl. Polym. Sci.* **2009**, *114*, 3716–3722.
7. Blotny, G. *Tetrahedron Lett.* **2003**, *44*, 1499–1501.
8. Nilles, K.; Theato, P. *Polym. Chem.* **2011**, *2*, 376–384.
9. Caddick, S.; Wilden, J. D.; Judd, D. B. *J. Am. Chem. Soc.* **2004**, *126*, 1024–1025.
10. Kakuchi, R.; Theato, P. *Polym. Chem.* **2014**, *5*, 2320–2325.
11. Zhao, H.; Gu, W.; Kakuchi, R.; Sun, Z.; Sterner, E.; Russell, T. P.; Coughlin, E. B.; Theato, P. *ACS Macro Lett.* **2013**, *2*, 966–969.
12. Pauly, A. C.; Theato, P. *Polym. Chem.* **2012**, *3*, 1769–1782.
13. Tsunoda, T.; Otsuka, J.; Yamamiya, Y. *Chem. Lett.* **1994**, 539–542.
14. Ren, L.; Zhang, J.; Hardy, C. G.; Doxie, D.; Fleming, B.; Tang, C. *Macromolecules* **2012**, *45*, 2267–2275.

Chapter 9

Core-Shell Cylindrical Polymer Brushes with New Properties: A Mini-Review

Jun Ling^{1,*} and Axel H. E. Müller^{2,*}

¹MOE Key Laboratory of Macromolecular Synthesis and Functionalization, Department of Polymer Science and Engineering, Zhejiang University, Hangzhou 310027, China

²Institute of Organic Chemistry, Johannes Gutenberg Universität Mainz, 55099 Mainz, Germany

*E-mail: lingjun@zju.edu.cn; axel.mueller@uni-mainz.de

We report new properties and applications of polymer and hybrid materials based on the one-dimensional topology of cylindrical polymer brushes (CPBs). We review three examples of core-shell CPBs to illustrate the applications resulting from stretched backbone, dense and stretched inner layer (core) of side chains, and huge number of chain ends of the outer layer (shell).

Introduction

The properties of a polymer depend on many aspects, for instance, repeating units, composition and sequence of comonomers, molecular weight averages and distributions. Sometimes chain ends play a role as well. Topology, i.e., the geometry in which repeating units are connected, has a strong impact on the properties of polymers. In this mini-review, we summarize three unique properties derived from the topology of core-shell cylindrical polymer brushes (CPBs).

Core-shell CPBs have a molecular backbone and dense side chains consisting of di- or triblock copolymers. Due to the length of the side chains and their steric hindrance, the backbone is stretched and a CPB is a molecule with a one-dimensionally rod-like shape containing an inner (core) and an outer (shell) layer (1–3). This unique molecular conformation, which is unseen and unavailable in other materials, develops interesting properties after precise synthesis.

(1) Side Chains against Backbone

Considering the intermolecular interaction energy of 2-12 kJ/mol, a carbon-carbon covalent bond is extremely strong with an energy of 348 kJ/mol, about two orders of magnitude higher. It is amazing that a large number of interactions can organize to fight together against and finally “defeat” a single carbon-carbon bond under mild conditions. CPBs provide an ideal architecture for this “battle” since it contains a backbone and a large number of side chains. We reported controlled scissions of carbon-carbon covalent bonds in a CPB backbone caused by interactions between side chains and a substrate surface (4).

With precise design, a series of core-shell CPBs with 750 side chains was synthesized (Figure 1) and two solid substrates, i.e. negatively charged mica and neutral silicon, were used. The inner layer of the CPBs was water-soluble poly(oligoethyleneglycol methacrylate) (POEGMA) blocks with DP of 430, which contain a large amount water molecules when cast on a solid substrate. The outer layer varied between nothing ($b\text{-}[O_{430}]_{750}$) as a control, poly(2-dimethylamino)ethyl methacrylate) (PDMAEMA) segments with DP of 40 ($b\text{-}[O_{430}D_{40}]_{750}$), and its quaternized analog ($b\text{-}[O_{430}Dq_{40}]_{750}$). As soon as the aqueous CPB solution was transferred, the surface interaction between the cationic outer layer of the CPB side chains and the solid substrate determined how strong the CPB molecules could be immobilized on the surface. Here, the outer layer PDMAEMA units acted as multiple “anchors” to prevent any further movement.

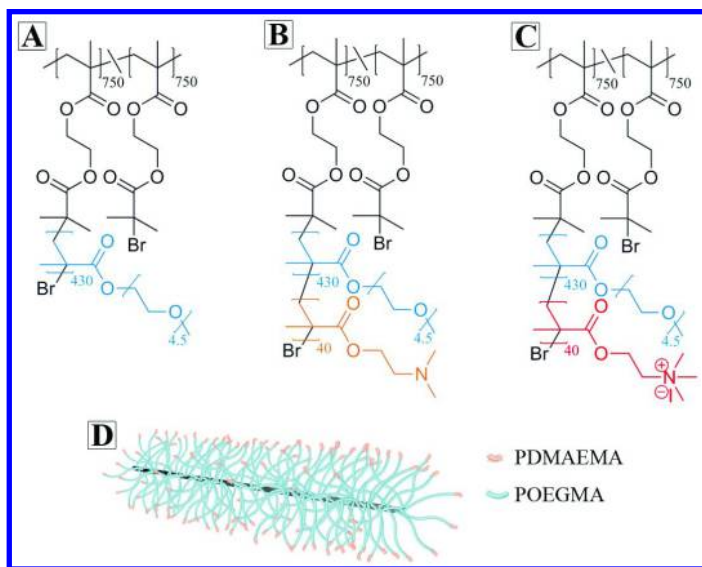


Figure 1. Chemical structures of the homopolymer CPB $b\text{-}[O_{430}]_{750}$ (A), the core-shell CPB $b\text{-}[O_{430}D_{40}]_{750}$ (B) and the core-shell CPB $b\text{-}[O_{430}Dq_{40}]_{750}$ (C) and a schematic illustration of the core-shell CPB (D). [Reproduced with permission from reference (4). Copyright 2013 American Chemical Society.] (see color insert)

Upon drying, the inner layer of CPB released water molecules, producing a huge free energy of contraction. This situation might be resolved in two ways, either by stretching along the backbone or perpendicular to it. Since the backbone is already much stretched, the former would lead to a carbon-carbon covalent bond cleavage of the backbone. The latter required to overcome the surface interactions and to make the PDMAEMA units slip on the surface, i.e. pulling the “anchors” from the surface. Thus, a direct competition of the strength of one carbon-carbon covalent bond with a number of intermolecular interactions was established based on the CPB architecture.

In fact, scissions of the CPB backbone were observed by means of atomic force microscope (AFM) when surface interaction was strong enough in all cases except those of b-[O₄₃₀]₇₅₀ on mica and b-[O₄₃₀D₄₀]₇₅₀ on silicon. Moreover, the number of CPB scissions depended exclusively on the interactions between side chains and surface. Stronger interactions resulted in more fragments (Figure 2).

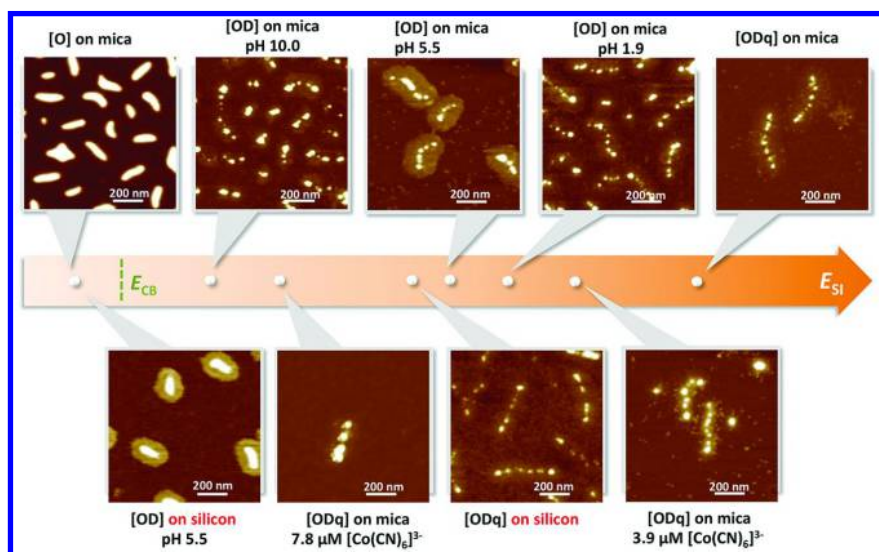


Figure 2. Dependence of scission of CPB backbones on various parameters. E_{CB} and E_{Si} stand for the energies of carbon-carbon bond, and surface interactions between side chains and substrate surface, respectively. [Reproduced with permission from reference (4). Copyright 2013 American Chemical Society.] (see color insert)

S. S. Sheiko *et al.* confined CPBs in a layer of liquid on a water or solid surface. The liquid could vary from organic solvent to bulk CPB melt with low glass transition temperature. Expansion of the liquid pushed the 3D-extended side chains into a denser 2D layer when all side chains intended to expand rather than contract in our cases, and move on surface (5–8). This confinement enhanced steric repulsion between the densely grafted side chains and resulted in scissions

of the backbone (7). Thus, backbones of homo-CPBs, ie. CPBs containing homopolymer side chains, broke in this situation, while they did not show any scission behavior in our cases. In addition, it should be mentioned that slowly increased confinement led to slow scissions and the parts randomly-ruptured from CPBs moved at the same time. It was impossible to distinguish which parts originated from one CPB molecule.

(2) Side Chains Working for the Backbone

In a CPB, both backbone and inner layer (core) of side chains are extensively stretched due to steric repulsion. The cross-section of core-shell CPB looks like concentric cylinders wrapping the backbone in the center (Figure 3). It provides an opportunity to mimic the ring-like geometry of pigments in natural light harvesting systems of bacteria and plants also known as “energy cascade” architecture (9).

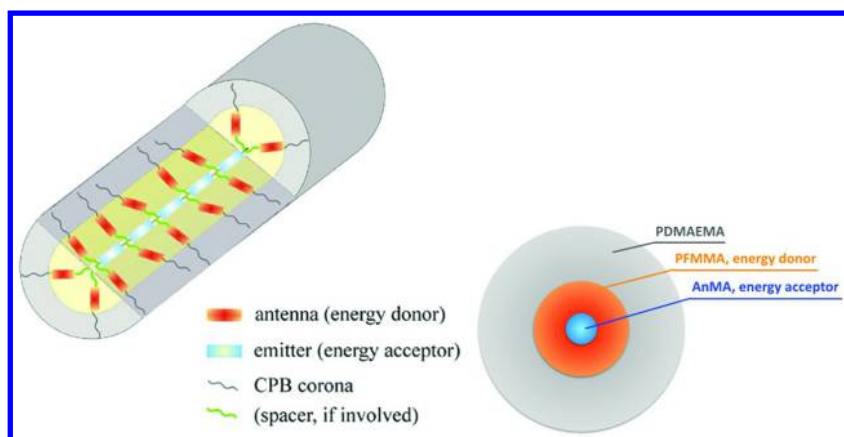


Figure 3. Illustration of nano-light harvester based on CPB topology and its cross-section. [Reproduced with permission from reference (10). Copyright 2014 Wiley-VCH Weinheim] (see color insert)

Förster resonance energy transfer (FRET) occurs when two chromophores, i.e. energy donor and acceptor, are located close to each other. The increase of donor-acceptor distance dramatically decreases FRET efficiency by $1/R$ (6). Taking advantage of the stretched inner layer of side chains in CPB, we can control the donor-acceptor distance precisely and thus their FRET efficiency.

We reported core-shell CPBs consisting of energy donors in the stretched inner layer of side chains and energy acceptors along backbone acting as a rod-like “nano-light harvesters” (10). In this geometry (Figure 3), the energy donors

(fluorene units) absorbed light acting as antenna. They transferred their excitation energy via FRET to the acceptors (anthracene units) in backbone that emitted light of their characteristic wavelength acting as emitter. FRET directed from the core layer of the CPB into the backbone, a “concentrating effect”, similar to the natural “energy cascade” (10).

Whereas the PDMAEMA shell only served the solubilization of the brush, the donor-acceptor distance was easily changeable by either physical or chemical ways. As a physical protocol, the hydrophobic inner layer expanded in organic solvent (THF) and contacted in water, which changed the distances of energy donors and acceptors. An inert PMMA spacer could be introduced between side chains and backbone to separate energy donors and acceptors. Both methods dramatically changed the efficiency of energy transfer.

(3) Crosslinking the Shell Locks Cargo in the Core

Compared with micelles, CPBs have several advantages due to their unique topology. CPBs are single molecules constructed by chemical bonds with well-defined geometry and stable sizes, differing from self-assembled micelles suffering dynamic disassembly equilibrium and uncertainty of functional core and shell layers. Moreover, most micelles are spherical, although sometimes different shapes (cylinders, vesicles) may exist. In CPBs, layers from center (backbone) to outside (shell) are clearly distinguished. Core-shell CPBs are comparable to micelles, and core-shell-corona CPBs contain more potential in carrying cargos in various layers. Taking advantages of the one-dimensional structure, our group used CPBs as template and reported hybrid nanorods with iron oxide (11), titania (12), silica (13, 14), and more.

A recent example reported the incorporation of rare-earth metal (RE) cations into the core of core-shell CPBs (15). After crosslinking the shell by silica, RE cations were “sealed” in the core and prevented from leaking out (<0.01 mmol/L RE³⁺ after 14 days in water). The synthesis protocol is shown in Figure 4C. RE cations had photoluminescent and magnetic properties, which made CPBs visible under UV-light and MRI analysis. The Gd³⁺-incorporated NPs exhibited stronger magnetic resonance imaging (MRI) contrast effects than the commercially available Gd³⁺-DTPA MRI contrast agent. The longer the backbone, i.e. the more concentrated Gd³⁺ cations, the stronger the MRI contrast (Figure 4D). It was due to the concentration effect of Gd³⁺ cations in nanoparticles.

The RE³⁺-containing silica-shelled nanoparticles had very good solubility in water and very low toxicity to living cells. With sizes of *ca.* 200 nm in length and 10-20 nm in width, CPBs could be excellent carriers to target tumor cells better than spherically shaped nanoparticles (or micelles) (16). Thus, the RE³⁺-containing nanoparticles are promising for dual-detection in early-stage tumor diagnosis and treatment, diagnosis by MRI and luminescent emission to locate tumor cells in surgery.

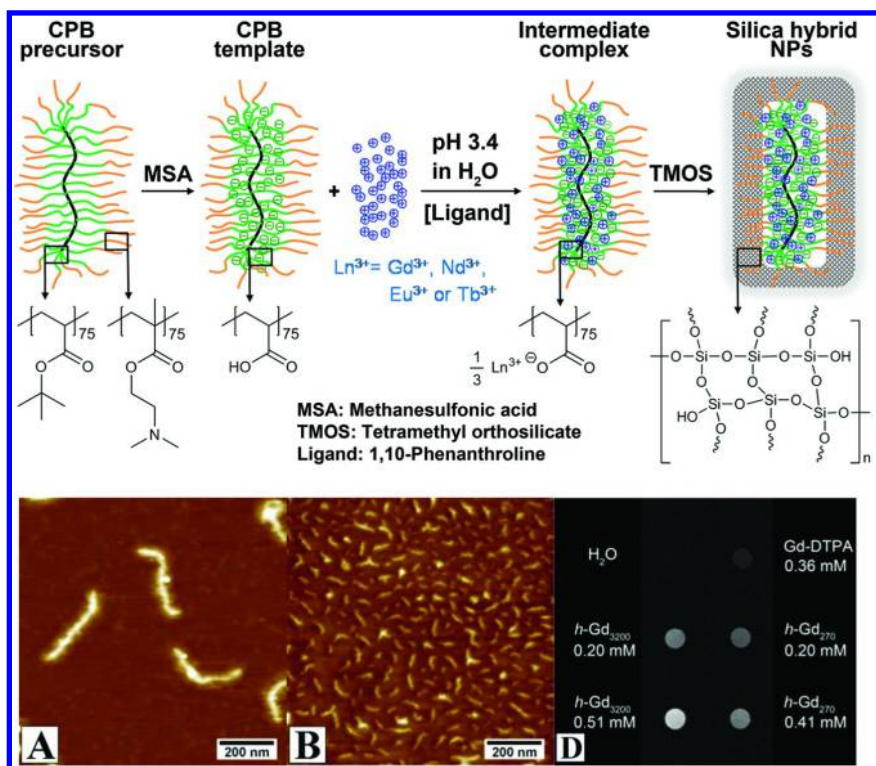


Figure 4. Preparation of well-defined rare-earth metal cations (Ln^{3+}) incorporated silica hybrid nanoparticles via the template-directed approach based on core-shell cylindrical polymer brushes (C), AFM height image of CPBs of *b*-[T₇₅D₇₅]₃₂₀₀ with long backbone (A) and *b*-[T₈₀D₇₇]₂₇₀ with short backbone (B). T₁-weighted MRI images of *h*-Gd₃₂₀₀ and *h*-Gd₂₇₀ with different Gd³⁺-concentrations using pure water and commercially available Gd-DTPA as references (D). [Reproduced with permission from reference (15). Copyright 2013 American Chemical Society.] (see color insert)

Acknowledgments

Financial support was provided by the National Natural Science Foundation of China (21374093) and the Alexander von Humboldt Foundation.

References

1. Yuan, J.; Müller, A. H. E.; Matyjaszewski, K.; Sheiko, S. S. In *Polymer Science: A Comprehensive Reference*; Müller, A. H. E., Wooley, K. L., Eds.; Elsevier: Amsterdam, 2012; Vol. 6, pp 199–264.
2. Zhang, M. F.; Müller, A. H. E. *J. Polym. Sci., Part A: Polym. Chem.* **2005**, *43*, 3461–3481.

3. Lee, H.; Pietrasik, J.; Sheiko, S. S.; Matyjaszewski, K. *Prog. Polym. Sci.* **2010**, *35*, 24–44.
4. Zheng, Z.; Müllner, M.; Ling, J.; Müller, A. H. E. *ACS Nano* **2013**, *7*, 2284–2291.
5. Sheiko, S. S.; Sun, F. C.; Randall, A.; Shirvanyants, D.; Rubinstein, M.; Lee, H.; Matyjaszewski, K. *Nature* **2006**, *440*, 191–194.
6. Lebedeva, N. V.; Sun, F. C.; Lee, H. I.; Matyjaszewski, K.; Sheiko, S. S. *J. Am. Chem. Soc.* **2008**, *130*, 4228–4229.
7. Park, I.; Shirvanyants, D.; Nese, A.; Matyjaszewski, K.; Rubinstein, M.; Sheiko, S. S. *J. Am. Chem. Soc.* **2010**, *132*, 12487–12491.
8. Park, I.; Nese, A.; Pietrasik, J.; Matyjaszewski, K.; Sheiko, S. S. *J. Mater. Chem.* **2011**, *21*, 8448–8453.
9. Mackowski, S. *J. Phys.: Condens. Matter* **2010**, *22*, 193102.
10. Ling, J.; Zheng, Z.; Köhler, A.; Müller, A. H. E. *Macromol. Rapid Commun.* **2014**, *35*, 52–55.
11. Zhang, M.; Estournès, C.; Bietsch, W.; Müller, A. H. E. *Adv. Funct. Mater.* **2004**, *14*, 871–882.
12. Müllner, M.; Lunkenbein, T.; Schieder, M.; Gröschel, A. H.; Miyajima, N.; Förtsch, M.; Breu, J.; Caruso, F.; Müller, A. H. E. *Macromolecules* **2012**, *45*, 6981–6988.
13. Yuan, J.; Xu, Y.; Walther, A.; Bolisetty, S.; Schumacher, M.; Schmalz, H.; Ballauff, M.; Müller, A. H. E. *Nat. Mater.* **2008**, *7*, 718–722.
14. Müllner, M.; Lunkenbein, T.; Breu, J.; Caruso, F.; Müller, A. H. E. *Chem. Mater.* **2012**, *24*, 1802–1810.
15. Zheng, Z.; Daniel, A.; Yu, W.; Weber, B.; Ling, J.; Müller, A. H. E. *Chem. Mater.* **2013**, *25*, 4585–4594.
16. Geng, Y.; Dalhaimer, P.; Cai, S.; Tsai, R.; Tewari, M.; Minko, T.; Discher, D. E. *Nat. Nanotechnol.* **2007**, *2*, 249–255.

Chapter 10

Recent Progress on Synthesis of Hyperbranched Polymers with Controlled Molecular Weight Distribution

Yi Shi, Robert W. Graff, and Haifeng Gao*

Department of Chemistry and Biochemistry, University of Notre Dame,
Notre Dame, Indiana 46556, United States

*E-mail: hgao@nd.edu

Hyperbranched polymers that are traditionally synthesized in a one-pot solution polymerization suffer from a poorly defined structure with broad molecular weight distribution. This paper summarizes the recent progress on one-pot synthesis of uniform hyperbranched polymers in three strategies: 1) slow addition of monomer into multifunctional core; 2) use of core molecule with higher reactivity than monomer; and 3) polymerization in confined space. A comprehensive list of literature reports using each approach is discussed in great detail, addressing both advantages and limitations. This knowledge is critical for developing new methods that can combine the advantageous features of different methods and readily produce hyperbranched polymers with low polydispersity, tunable molecular weights ($10^3 - 10^6$ g/mol) and high degrees of branching.

Introduction

Nanostructured polymers with branched architectures and multiple chain-end functionalities represent an important soft nanomaterial that can be used in a variety of applications, ranging from specialty additives, microelectronics, nanomedicines and catalysis (1–4). Among the various nanostructured polymers, hyperbranched polymers have received considerable interest due to the attractive features of one-pot synthesis, arborescent structures and a high degree of functionalities (5–7). Hyperbranched polymers are typically synthesized in

homogeneous bulk or solution systems by one-pot polymerization of either an AB_m monomer ($m \geq 2$) (7–9) or an AB^* inimer (containing *initiator* fragment B^* and *monomer* vinyl group A in one molecule) (10, 11). Although hyperbranched polymers are often considered an analog of dendrimers (4, 12), current challenge on their synthesis is the lack of structural control in the polymer product (9), which significantly limits their potential applications as advanced soft nanomaterials.

The growth of hyperbranched polymers in a continuous reaction medium is accompanied by random polymer-polymer reactions and ultimately results in polymers with extremely broad molecular weight distribution (MWD) (2, 11, 13, 14). Since the physical properties of hyperbranched polymers are critically influenced by their molecular weights and structural uniformity, it is highly desirable to develop robust synthetic methods that can regulate the MWD of the hyperbranched polymers with minimal compromise of the facile one-pot synthesis feature.

In this contribution, we present our recent progress on one-pot synthesis of uniform hyperbranched polymers using confined nanospace. Recent publications from other groups to obtain hyperbranched polymers with relatively low polydispersity are also summarized in great detail. All these methods can be classified into three categories based on different strategies (Scheme 1). The first approach uses slow addition of monomers into a dilute system containing multifunctional “core” (e.g., core dilution/slow addition, as termed by Frey) (15, 16). The second approach applies organic reactions to ensure that the reactive groups on the core polymers have higher reactivity than the groups on monomers. Both approaches are designed to achieve a mechanism of chain-growth polymerization of monomers from the “core” molecules by disfavoring the monomer-monomer reactions with respect to the monomer-core reactions. In contrast, a third approach recently developed in our group focuses on segregating the polymerization of monomers in a confined nanospace in order to decrease the polydispersity of hyperbranched polymers (Approach 3, Scheme 1). At very high conversion, there is only one hyperbranched polymer per confined loci, whose molecular weight and polydispersity are directly determined by the dimension and uniformity of the confined space.

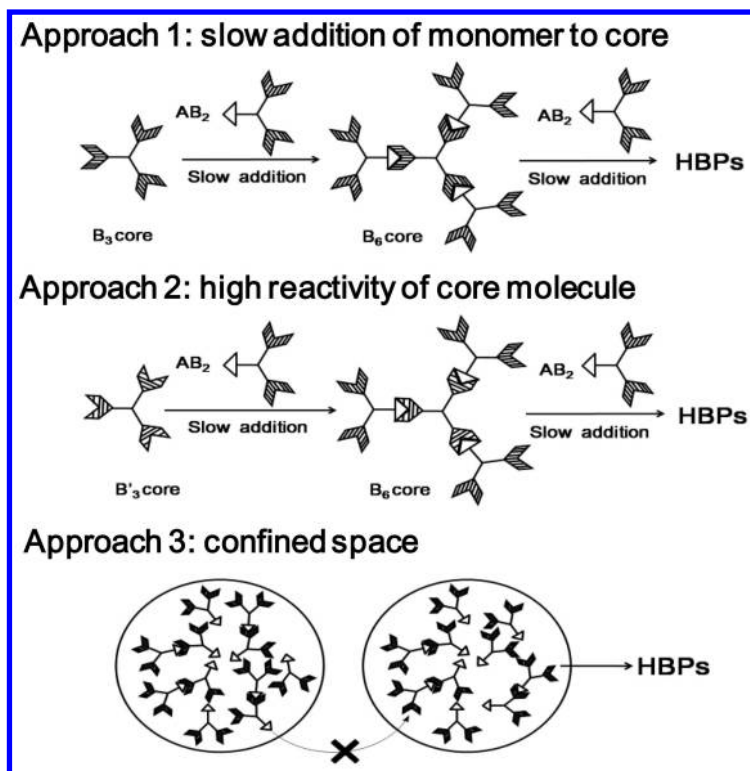
It is worth mentioning that this paper is focusing on recent progress concerning the one-pot synthesis of hyperbranched polymers with low polydispersity. Meanwhile, reports that attempted to produce hyperbranched polymers with 100% degree of branching (DB) by using special AB_2 monomers with slow reversible reaction of the first B group and fast reaction of the second B group will not be discussed. Instead, interested readers could learn more on this aspect from several recently published papers and review (17–22).

Approach 1: Slow Addition of Monomers to Multifunctional Core

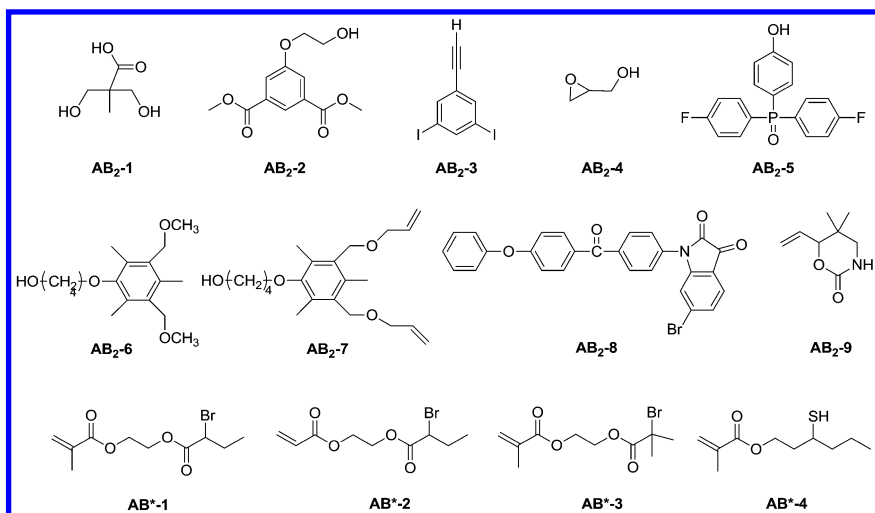
1. Use of Multifunctional Small Molecule as Core

Early work on copolymerization of AB_2 monomer with B_f ($f \geq 2$ is the number of functionality) core in a batch polymerization successfully produced

hyperbranched polymers with lower polydispersity than the products from homopolymerization of AB_2 monomers. Hult et al. (23) (entry 1, Table 1) reported the synthesis of hyperbranched aliphatic polyesters with relatively narrow MWD (ratio of weight-average molecular weight to number-average molecular weight, $M_w/M_n = 1.36-1.92$) and high DB = 0.83-0.96 when copolymerizing AB_2 monomer, 2,2-bis(hydroxymethyl) propionic acid (AB_2 -1, Scheme 2) and trifunctional B_3 molecule, 2-ethyl-2-(hydroxymethyl)-1,3-propanediol (Core-1, $R = -CH_2CH_3$, Scheme 3) in a batch reaction. Increasing the feed molar ratios of AB_2 monomer to B_3 core from 9:1 to 381:1 led to an increased polydispersity and a decreased DB. Within their studies, the production of a hyperbranched polymer with $M_w/M_n < 1.5$ required an initial feed ratio of $[AB_2]_0:[B_3]_0 \leq 45$, resulting in hyperbranched polymers with $M_n < 3.1$ kg/mol. In another study, Stainton et al. (24) (entry 2, Table 1) demonstrated that a controlled synthesis of hyperbranched aromatic polyester with $M_w/M_n = 1.65-2.79$ and DB = 0.60-0.67 via batch copolymerization of AB_2 monomer (AB_2 -2, Scheme 2) and B_3 core (Core-2, Scheme 3) with different molar ratios. An important conclusion was drawn from these early studies that the multifunctional B_f molecule could function as a “terminator core” to narrow down the MWD of the hyperbranched polymers.



Scheme 1. Illustration of three approaches to decrease the polydispersity of hyperbranched polymers (HBP).

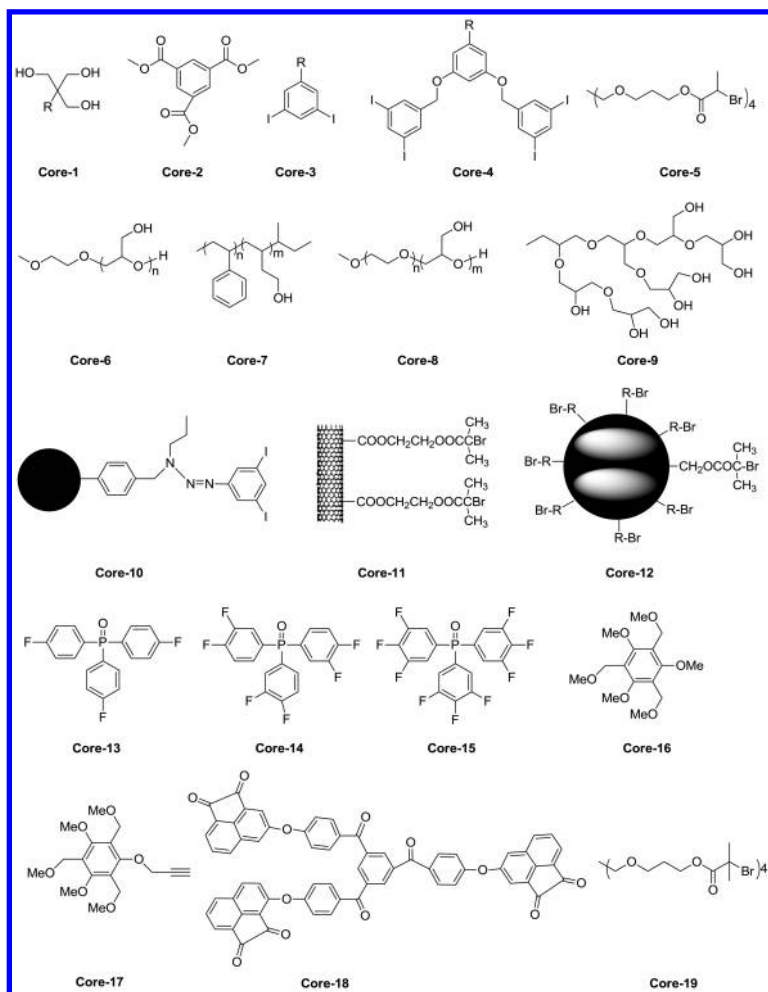


Scheme 2. Structures of AB₂ monomers and AB inimers reported in recent publications to produce hyperbranched polymers with narrow molecular weight distribution.*

Soon after these experimental results, computational calculations reported by Frey et al. (15) and Müller et al. (16) showed that the slow addition of AB_m monomers or AB* inimers into a solution of B_f cores could further decrease the polydispersity and increase the DB value of the hyperbranched polymers. In an ideal situation when the AB_m monomers only react with the B functional groups on the B_f core with complete exclusion of monomer-monomer reactions, hyperbranched polymers with $M_w/M_n = 1 + (m-1)/f$ are expected to be produced. In other words, the slow addition of AB₂ monomers into a solution of B₃ would produce a hyperbranched polymer with $M_w/M_n = 1.33$, and the use of a B₁₂ core molecule under similar strategy would produce a polymer with $M_w/M_n = 1.08$. These theoretical calculation results showed qualitative agreement to experimental results (25, 26), although high feed ratio of monomer to core in experiments broadened the MWD of the produced polymers probably due to the elevated possibility of monomer-monomer reactions. For instance, Moore et al. (25) (entry 3, Table 1) synthesized hyperbranched phenylacetylene via slow addition of AB₂-3 (Scheme 2) into a solution of Core-3 (R = -N₃Et₂, Scheme 3). To achieve a relatively low polydispersity of $M_w/M_n < 1.5$, the highest molar ratio of [AB₂-3]₀: [Core-3]₀ = 70:1 was used, producing a polymer with $M_w = 28.9$ kg/mol. The use of tetrafunctional Core-4 (R = -CH₂-O-Ph-N=N-Ph, Scheme 3) at the same feed ratio of monomer to core further decreased the $M_w/M_n = 1.2$ of the polymer product (entry 4, Table 1). In another effort, Frey et al. (26) (entry 5, Table 1) prepared hyperbranched polyglycerols (PGs) by ring opening polymerization (ROP) of glycidol (AB₂-4, Scheme 2) using 1,1,1-tris(hydroxymethyl) propane (Core-1, R = -CH₃, Scheme 3) as initiator. Slow addition of AB₂-4 into the partially deprotonated core produced hyperbranched PGs with M_n ranging from 1.2-6.4 kg/mol and $M_w/M_n = 1.13$ -1.47. Pan et al. (27) (entry 6, Table 1)

applied a tetrafunctional initiator (Core-5, Scheme 3) in the self condensing vinyl polymerization (SCVP) of inimer (AB*-1, Scheme 2) using atom transfer radical polymerization (ATRP) (13, 28–32). Within the investigation, the lowest molar ratio of $[AB^*-1]_0:[Core-5]_0 = 28$ produced hyperbranched polymers with the most uniform structure ($M_w/M_n = 2.16$).

So far, all reports that used multifunctional core molecule in either batch or semibatch polymerizations limited their initial feed ratios of monomer or inimer to core $< 100:1$, in order to obtain hyperbranched polymers with relatively low polydispersities (M_w/M_n 1.5) (22). Thus, the strategy of slow monomer addition, together with the use of multifunctional small molecules as core shows certain limitation on producing high-molecular-weight hyperbranched polymers.



Scheme 3. Structure of multifunctional cores reported in recent publications to produce hyperbranched polymers with narrow molecular weight distribution.

Table 1. Summary of the molecular weight, polydispersity and degree of branching of hyperbranched polymers ^a

Entry (ref)	AB ₂	B _f	Procedure ^b	M _n ^c (kg/mol)	M _w /M _n ^d	DB ^e
1 (23)	AB ₂ -1	Core-1	B	1.4-5.6	1.36-1.92	0.83-0.96
2 (24)	AB ₂ -2	Core-2	B	3.1-12.6	1.65-2.79	0.60-0.67
3 (25)	AB ₂ -3	Core-3	SMA	8.2-90.6 ^f	1.3-8.5	N/A
4 (25)	AB ₂ -3	Core-4	SMA	24.7 ^f	1.2	N/A
5 (26)	AB ₂ -4	Core-1	SMA	1.3-6.3	1.13-1.47	0.53-0.59
6 (27)	AB*-1	Core-5	B	107-273 ^g	2.63-4.21 ^g	N/A
7 (33)	AB ₂ -4	Core-6	SMA	1.0-4.0	1.32-1.82	0.55-0.61
8 (34)	AB ₂ -4	Core-7	SMA	N/A	1.02-1.74	N/A
9 (35)	AB ₂ -4	Core-8	SMA	N/A	1.02-1.34	N/A
10 (36)	AB ₂ -4	Core-9	SMA	4.6-24.2	1.38-1.77	0.60-0.65
11 (37)	AB ₂ -3	Core-10	B	5.0-25.0	1.10-1.50	N/A
12 (38)	AB*-2	Core-11	B	N/A	N/A	N/A
13 (39)	AB*-2	Core-12	B	18.6-29.2	1.8-2.3	N/A
14 (42)	AB ₂ -5	Core-13	B	4.5-6.7	1.62-2.28	0.56-0.61
15 (42)	AB ₂ -5	Core-14	B	4.4-7.9	1.38-1.93	0.54-0.57
16 (42)	AB ₂ -5	Core-15	B	3.3-8.1	1.25-1.55	0.55-0.57
17 (43)	AB ₂ -6	Core-16	SMA	5.4-10.1	1.46-2.58	N/A
18 (21)	AB ₂ -8	Core-18	SMA	3.5-15.6	1.12-1.56	1.0
19 (44)	AB*-2	Core-19	B	11.1-18.1 ^g	1.10-1.91 ^g	N/A
20 (45)	AB ₂ -9	N/A	B	1.4-2.0	1.30-1.50	0.61-0.81

^a N/A represents not available data in the original paper. ^b B represents a batch polymerization with all the monomers and core molecules added at time zero; SMA represents the slow monomer addition to a solution of core. ^c Range of number-average molecular weight (M_n, unless otherwise stated) reported in the original paper. ^d Range of molecular weight distribution (M_w/M_n) reported in the original paper. ^e Range of degree of branching (DB) reported in the original paper. ^f Weight-average molecular weight (M_w) ^g Number-average molecular weight (M_n) and molecular weight distribution (M_w/M_n) detected by SEC with MALLS.

2. Use of Multifunctional Polymer as Core

Frey et al. (33) reported both theoretical calculation and experimental results to study the preparation of hyperbranched graft copolymers (HGCs) via slow addition of AB_m monomers into a polymeric macroinitiator core. A general equation was derived to determine the polydispersity of the HGCs as PD_{HGC} = PD_f + (m-1)/f, where PD_f is the polydispersity of the polymeric core and f is

the average functionality of core. To verify the theoretical predication, a series of linear PG-*graft*-hyperbranched PG (linPG-*g*-hbPG) HGCs ($M_n = 1.0\text{--}4.0$ kg/mol, entry 7, Table 1) were synthesized by grafting polymerization of glycidol monomer from linear PG cores (Core-6, linPG1 with $M_w/M_n = 1.21$ and $f = 9$; linPG2 with $M_w/M_n = 1.25$ and $f = 17$, Scheme 3) using the slow monomer addition technique. The polydispersity results ($M_w/M_n = 1.32$ or 1.39 , respectively) of the HGCs confirmed the trend in calculation when the initial molar ratio of AB₂₋₄ to the OH groups in B_f core was 1:1. Increasing the molar ratio of [AB₂₋₄]₀: [OH]₀ = 3 in both cases increased the M_w/M_n values to 1.74 and 1.82, respectively, due to the high viscosity and occasional precipitation of growing polymers from the reaction mixture. The produced HGCs were further characterized by ¹³C NMR to determine the DB = 0.55–0.61. In another example (34, 35), the same group developed a convenient multi-step strategy for preparation of amphiphilic (entry 8, Table 1)/double-hydrophilic (entry 9, Table 1) linear-*b*-HGC block copolymer using a multifunctional block copolymer ($M_w/M_n < 1.2$) as core. The molecular weights of the linear-*b*-HGC increased with the molar ratios of monomer (AB₂₋₄, Scheme 2) to polymer core (Core-7 and 8, Scheme 3). When a low-molecular-weight hyperbranched PG (Core-9, $M_n = 500$ or 1000 g/mol, Scheme 3) was used as the core initiator (entry 10, Table 1), a hyperbranched product with molecular weight up to $M_n = 24.0$ kg/mol and $M_w/M_n = 1.3 - 1.8$ was synthesized using slow addition of glycidol monomer (36). The DB of the resulting hyperbranched PGs varied from 0.60 to 0.63, which was close to the theoretical limit of 0.67 using slow monomer addition procedure.

3. Growth of Hyperbranched Polymers from Insoluble Support

Moore et al. (37) (entry 11, Table 1) reported the polymerization of AB₂₋₃ (Scheme 2) in presence of a diiodophenyl (B₂) initiator linked to a solid support (Core-10, Scheme 3). The resulting hyperbranched polymers showed well-controlled molecular weight ($M_n = 5\text{--}25$ kg/mol) and relatively narrow MWD ($M_w/M_n = 1.1\text{--}1.5$ versus > 2.5 for the soluble polymer). The solid-support demonstrated function of inhibiting the intramolecular cyclizations between focal points and peripheral groups, in addition to the simplified purification process. However, the self-polymerization of AB₂ monomer was not suppressed and the yield of hyperbranched polymer was low.

The SCVP of AB*₂-2 inimer (Scheme 2) in the presence of a multiwalled carbon nanotube modified with ATRP initiators (MWNT-Br, Core-11, Scheme 3) was reported by Hong and Pan (entry 12, Table 1) (38). The resulting nanotubes with a hyperbranched polymer shell showed good dispersibility in THF and CHCl₃ although no DB and polydispersity values were determined. The same group also reported the synthesis of hyperbranched polymers (entry 13, Table 1) grafted on the exterior surface of mesoporous silica nanoparticles (MSNs) (Core-12, Scheme 3) by surface-initiated ATRP of AB*₂-2 (Scheme 2) (39). It was found that the molecular weights of the hyperbranched polymers after cleavage from the MSN increased from $M_n = 18.6$ to 29.2 kg/mol when the initial weight ratio of AB*₂ to Core-12 changed from 30 to 125. Size exclusion chromatography (SEC) traces of

the hyperbranched polymers showed multimodal peaks with broad MWD ($M_w/M_n = 1.80-2.30$).

Approach 2: Different Reactivity of Core and Monomer

1. Using High Core Reactivity To Decrease Polydispersity

Different from using slow monomer addition strategy to favor the monomer-polymer reaction, increasing the reactivity of the core molecules with respect to monomers could also decrease the polydispersity of the resulting product (40, 41). Fossum (42) reported the first study on synthesis of hyperbranched poly(arylene ether phosphine oxide) polymers using batch polymerization of AB_2 -5 (Scheme 2) in the presence of a series of core molecules (Core-13, 14 and 15, Scheme 3) with different reactivities. The most active core Core-15 provided the greatest control over MWD ($M_w/M_n < 1.55$) with $DB = 0.55-0.57$ (entry 16, Table 1).

High core reactivity combined with slow monomer addition was recently applied by Ramakrishnan et al. (entry 17, Table 1) to synthesize polyethers, in which B'_3 core molecules (Core-16 and Core-17, Scheme 3) with electron donating methoxy groups were more active to acid catalyzed trans-etherification than the AB_2 monomers (AB_2 -6 and AB_2 -7, Scheme 2) (43). Results showed that increasing the molar fraction of the B'_3 core in the initial formula decreased both polydispersity and molecular weight of the polymers. Within their investigation, a molar fraction of B'_3 core $\geq 10\%$ produced hyperbranched polymer with $M_w/M_n < 1.5$, but molecular weight $M_n < 5.4$ kg/mol.

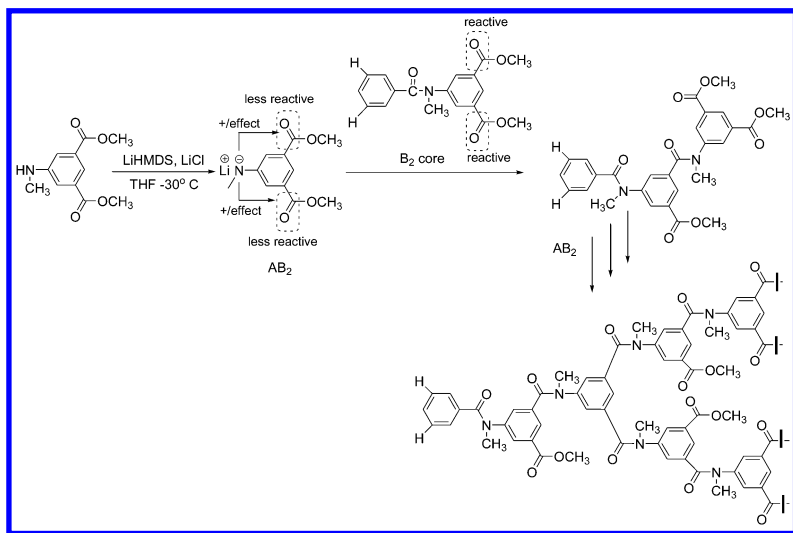
To synthesize hyperbranched polymers with both low polydispersity and high DB, a recent report applied super-electrophilic arylation with slow monomer addition strategy (entry 18, Table 1). A B'_6 core with higher reactivity of acenaphthenequinone groups (Core-18, Scheme 3) was used to reduce the polydispersity of polymers in polymerization of AB_2 -8 (Scheme 2) containing lower reactivity of isatin groups (21). To achieve a polydispersity of $M_w/M_n < 1.5$, the highest molar ratio of monomer to core = 30:1 was used, producing a polymer with $M_n = 12.1$ kg/mol and multimodal SEC distribution. The strategy of using high-reactivity multifunctional core (Core-19, Scheme 3) was also applied in the ATRP-SCVP of inimers (AB^*-2 , Scheme 2) to synthesize hyperbranched polymers with low polydispersity (entry 19, Table 1) (44). Within the studies, an optimal feed ratio of AB^*-2 to B'_4 core $\leq 40:1$ was used to produce polymer with $M_w/M_n < 1.5$, limiting the value of $M_n \leq 13.6$ kg/mol.

2. Consecutive Activation of Functional Groups on Core Polymer

As discussed above, the use of B'_f core molecule with higher reactivity of B' than B group in AB_2 monomer fosters the fast consumption of core molecules, which mimics the initial stage of chain-growth polymerization with fast initiation. However, after the complete reaction of B' with A groups, the surface B groups on the produced 1st generation hyperbranched polymer share the same reactivity with the B groups on monomers, diminishing the advantage of faster reaction in the core than monomer. To demonstrate a true chain-growth mechanism in

the hyperbranched polymer synthesis, a consecutive activation of the B groups on polymer to B' is necessary. Following this logic, Suzuki et al. (45) (entry 20, Table 1) synthesized hyperbranched polyamine polymers using palladium-catalyzed ROP of cyclic carbamate (AB₂-9, Scheme 2). In this study, free amine initiator (phenylamine) or polymer could react with monomer but cyclic carbamate monomer wouldn't undergo self-polymerization, resulting in a chain-growth type polymerization. The resulting hyperbranched polymers had narrow MWD ($M_w/M_n < 1.5$) and low molecular weight ($M_n = 1.4\text{--}2.0$ kg/mol).

Very recently, Yokozawa and co-workers (46) synthesized hyperbranched polymers by exploiting the change of substituent group reactivities in monomer and polymer using a well designed condensation polymerization. As shown in Scheme 4, the amide anion deactivated the ester groups in the AB₂ monomer and favored the reaction with the ester groups in the B'₂ core. Meanwhile, the amidation reaction formed neutral amide linkage that activated the ester groups in the polymer for further reaction with AB₂ monomers, leading to a chain-growth condensation polymerization. The produced polymers showed molecular weight $M_n = 2\text{--}40$ kg/mol based on Matrix-Assisted Laser Desorption/Ionization Mass Spec with low $M_w/M_n \leq 1.13$. However, the DBs of the hyperbranched polymers were about 0.5 since the two B' groups on a terminal unit in the polymer shared equal reactivity, as shown in Scheme 4.



Scheme 4. Deactivation of diester AB₂ monomer by amine deprotonation and reaction with active core molecule.

Approach 3: Polymerization in Confined Space

In contrast to the first two approaches that use slow monomer addition, and/or multifunctional core with potentially higher reactivity to disfavor random monomer-monomer and polymer-polymer reactions, the third approach applies confined space as a nanoreactor to regulate the polymer polydispersity. By

segregating the step-growth polymerization of monomers within discrete micelles, the monomers within a confined space can react/polymerize with each other completely, while there is no inter-space reaction. At very high conversion, there is only one hyperbranched polymer per micelle, whose size, molecular weight, and polydispersity will be closely dependent on the size and uniformity of the confined space.

Very recently, our group reported the first synthesis of uniform hyperbranched polymers in a micelle-based confined space using a one-pot ATRP of AB* inimers (AB*-3, Scheme 2) in microemulsion (Figure 1A) (47). Stopping the reaction at complete vinyl conversion (> 98% based on NMR analysis) produced one hyperbranched polymer molecule per polymer latex, which showed a uniform hydrodynamic size of $D_h = 36$ nm after purification in THF. As compared to the polymer product from a solution polymerization of AB*-3, the hyperbranched polymer from microemulsion polymerization had a much narrower MWD ($M_w/M_n = 1.24$) and higher molecular weight as shown in Figure 1B. In this situation, the molecular weight of the hyperbranched polymer is directly determined by the micelle size in the microemulsion. Tuning the micelle size from 10 to 50 nm by varying the formulation conditions could significantly change the molecular weights of the polymers from 10^5 to 10^7 g/mol without any deterioration of the polydispersity.

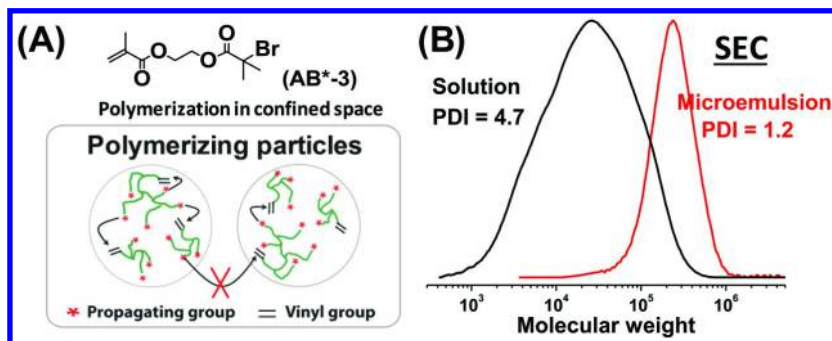


Figure 1. (A). Polymerization of AB*-3 inimer in a microemulsion; (B). SEC traces of hyperbranched polymers from microemulsion and a control solution polymerizations, based on linear PMMA standards in THF. (Adapted with permission from reference (47). Copyright 2012 American Chemical Society.)

In a later work, Jiang et al. synthesized branched vinyl polymers via conducting a radical copolymerization of monomer with chain transfer monomer (3-mercaptohexyl methacrylate, AB*-4, Scheme 2) in an aqueous (micro)emulsion system, although the hydrodynamic sizes of the micelles and nanoparticles were not reported (48). The effect of confined space on the structural control of the branched polymers turned out to be moderate. For instance, the solution polymerization of styrene and AB*-4 at a molar ratio of $[\text{styrene}]_0:[\text{AB}^*-4]_0 = 100:2$ resulted in polymers with $M_w/M_n = 10$. Further increasing the molar ratio to 100:3 produced insoluble gel. As comparison,

the emulsion copolymerization at significantly higher fraction of chain transfer monomer ($[\text{styrene}]_0:[\text{AB}^*-4]_0 = 100:25$) produced soluble branched polymers without gelation and lower polydispersity ($M_w/M_n = 5.37$).

Conclusion and Outlook

In summary, three strategies have been reported with attempts to obtain hyperbranched polymer with low polydispersity: 1) slow addition of monomer into multifunctional polymer core; 2) use of core molecule with higher reactivity than monomer; and 3) polymerization in confined space. Each method exhibits ability to improve the structural control of hyperbranched polymer with advantage and limitation. The first two methods allow solution-based polymerizations that are easy setup and carryout. However, it could be tedious to carefully adjust the monomer addition rate to be slow and synthetically challenging to identify a set of core-monomer pair with different reactivities. In addition, most reactions using these two strategies applied a molar ratio of monomer to core less than 100 in order to exclude the monomer-monomer reactions, which further limits the molecular weights of the hyperbranched polymers. In contrast, the use of confined space allows facile syntheses of hyperbranched polymers with both uniform structure (low polydispersity) and high molecular weights ($> 10^5$ g/mol) with minimum limitation on the monomer compositions. However, the polymerization is often required to reach very high conversion and the formulation to construct confined nanospace, e.g. micelles, could be delicate. Future synthetic methods that can produce hyperbranched polymers with low polydispersity, tunable molecular weights ($10^3 - 10^6$ g/mol) and high DB without the need of complicated reaction setup will be highly desirable, which in part is currently under investigation in our research group.

Acknowledgments

The authors thank the ARO YIP award (W911NF-14-1-0227) and ACS Petroleum Research Fund (PRF #54298-DN17) for financial support. H. G. thanks the startup support from the University of Notre Dame and the Center for Sustainable Energy at Notre Dame.

References

1. Burchard, W. *Adv. Polym. Sci.* **1999**, *143*, 113–194.
2. Hawker, C. J.; Fréchet, J. M. J.; Grubbs, R. B.; Dao, J. *J. Am. Chem. Soc.* **1995**, *117*, 10763–10764.
3. Kim, Y. H. *J. Polym. Sci., Part A: Polym. Chem.* **1998**, *36*, 1685–1698.
4. Grayson, S. M.; Fréchet, J. M. J. *Chem. Rev.* **2001**, *101*, 3819–3867.
5. Schoemer, M.; Schuell, C.; Frey, H. *J. Polym. Sci., Part A: Polym. Chem.* **2013**, *51*, 995–1019.
6. Jikei, M.; Kakimoto, M.-A. *Prog. Polym. Sci.* **2001**, *26*, 1233–1285.
7. Gao, C.; Yan, D. *Prog. Polym. Sci.* **2004**, *29*, 183–275.

8. Schaeffgen, J. R.; Flory, P. J. *J. Am. Chem. Soc.* **1948**, *70*, 2709–2718.
9. Voit, B. I.; Lederer, A. *Chem. Rev.* **2009**, *109*, 5924–5973.
10. Fréchet, J. M. J.; Henmi, M.; Gitsov, I.; Aoshima, S.; Leduc, M. R.; Grubbs, R. B. *Science* **1995**, *269*, 1080–1083.
11. Müller, A. H. E.; Yan, D.; Wulkow, M. *Macromolecules* **1997**, *30*, 7015–7023.
12. Tomalia, D. A. *Prog. Polym. Sci.* **2005**, *30*, 294–324.
13. Gaynor, S. G.; Edelman, S.; Matyjaszewski, K. *Macromolecules* **1996**, *29*, 1079–1081.
14. Simon, P. F. W.; Radke, W.; Müller, A. H. E. *Macromol. Rapid Commun.* **1997**, *18*, 865–873.
15. Radke, W.; Litvinenko, G.; Müller, A. H. E. *Macromolecules* **1998**, *31*, 239–248.
16. Hanselmann, R.; Hölter, D.; Frey, H. *Macromolecules* **1998**, *31*, 3790–3801.
17. Maier, G.; Zech, C.; Voit, B.; Komber, H. *Macromol. Chem. Phys.* **1998**, *199*, 2655–2664.
18. Segawa, Y.; Higashihara, T.; Ueda, M. *Polym. Chem.* **2013**, *4*, 1208–1215.
19. Chatterjee, S.; Ramakrishnan, S. *ACS Macro Lett.* **2012**, *1*, 593–598.
20. Liu, N.; Vignolle, J.; Vincent, J.-M.; Robert, F.; Landais, Y.; Cramail, H.; Taton, D. *Macromolecules* **2014**, *47*, 1532–1542.
21. Chen, J.-Y.; Smet, M.; Zhang, J.-C.; Shao, W.-K.; Li, X.; Zhang, K.; Fu, Y.; Jiao, Y.-H.; Sun, T.; Dehaen, W.; Liu, F.-C.; Han, E.-H. *Polym. Chem.* **2014**, *5*, 2401–2410.
22. Segawa, Y.; Higashihara, T.; Ueda, M. *Polym. Chem.* **2013**, *4*, 1746–1759.
23. Malmstroem, E.; Johansson, M.; Hult, A. *Macromolecules* **1995**, *28*, 1698–1703.
24. Feast, W. J.; Stainton, N. M. *J. Mater. Chem.* **1995**, *5*, 405–411.
25. Bharathi, P.; Moore, J. S. *Macromolecules* **2000**, *33*, 3212–3218.
26. Sunder, A.; Hanselmann, R.; Frey, H.; Mülhaupt, R. *Macromolecules* **1999**, *32*, 4240–4246.
27. Hong, C.-y.; Pan, C.-y.; Huang, Y.; Xu, Z.-d. *Polymer* **2001**, *42*, 6733–6740.
28. Wang, J. S.; Matyjaszewski, K. *J. Am. Chem. Soc.* **1995**, *117*, 5614–5615.
29. Matyjaszewski, K.; Gaynor, S. G. *Macromolecules* **1997**, *30*, 7042–7049.
30. Matyjaszewski, K.; Gaynor, S. G.; Kulfan, A.; Podwika, M. *Macromolecules* **1997**, *30*, 5192–5194.
31. Matyjaszewski, K.; Gaynor, S. G.; Müller, A. H. E. *Macromolecules* **1997**, *30*, 7034–7041.
32. Gaynor, S. G.; Qiu, J.; Matyjaszewski, K. *Macromolecules* **1998**, *31*, 5951–5954.
33. Schüll, C.; Rabbel, H.; Schmid, F.; Frey, H. *Macromolecules* **2013**, *46*, 5823–5830.
34. Barriau, E.; García Marcos, A.; Kautz, H.; Frey, H. *Macromol. Rapid Commun.* **2005**, *26*, 862–867.
35. Wurm, F.; Nieberle, J.; Frey, H. *Macromolecules* **2008**, *41*, 1184–1188.
36. Wilms, D.; Wurm, F.; Nieberle, J.; Böhm, P.; Kemmer-Jonas, U.; Frey, H. *Macromolecules* **2009**, *42*, 3230–3236.
37. Bharathi, P.; Moore, J. S. *J. Am. Chem. Soc.* **1997**, *119*, 3391–3392.

38. Hong, C.-Y.; You, Y.-Z.; Wu, D.; Liu, Y.; Pan, C.-Y. *Macromolecules* **2005**, *38*, 2606–2611.
39. Li, X.; Hong, C.-Y.; Pan, C.-Y. *Polymer* **2010**, *51*, 92–99.
40. Cheng, K. C.; Wang, L. Y. *Macromolecules* **2002**, *35*, 5657–5664.
41. Zhou, Z.; Jia, Z.; Yan, D. *Polymer* **2012**, *53*, 3386–3391.
42. Bernal, D. P.; Bedrossian, L.; Collins, K.; Fossum, E. *Macromolecules* **2003**, *36*, 333–338.
43. Roy, R. K.; Ramakrishnan, S. *Macromolecules* **2011**, *44*, 8398–8406.
44. Hong, C.-Y.; Pan, C.-Y. *Polymer* **2001**, *42*, 9385–9391.
45. Suzuki, M.; Yoshida, S.; Shiraga, K.; Saegusa, T. *Macromolecules* **1998**, *31*, 1716–1719.
46. Ohta, Y.; Fujii, S.; Yokoyama, A.; Furuyama, T.; Uchiyama, M.; Yokozawa, T. *Angew. Chem., Int. Ed.* **2009**, *48*, 5942–5945.
47. Min, K.; Gao, H. F. *J. Am. Chem. Soc.* **2012**, *134*, 15680–15683.
48. Jiang, Q.; Huang, W.; Yang, H.; Xue, X.; Jiang, B.; Zhang, D.; Fang, J.; Chen, J.; Yang, Y.; Zhai, G.; Kong, L.; Guo, J. *Polym. Chem.* **2014**, *5*, 1863–1873.

Chapter 11

Synthesis of Star Polymers with Epoxide-Containing Highly Branched Cores by Low-Catalyst Concentration Atom Transfer Radical Polymerization and Post-Polymerization Modifications

Shannon R. Woodruff and Nicolay V. Tsarevsky*

Department of Chemistry, 3215 Daniel Avenue, and Center for Drug Discovery, Design, and Delivery in Dedman College, Southern Methodist University, Dallas, Texas 75275

*E-mail: nvt@smu.edu

Star polymers were synthesized by atom transfer radical polymerization (ATRP) using a “core first” approach. Multibrominated, highly branched functional polymers were first synthesized by copolymerizing an epoxide-containing monomer, glycidyl methacrylate (GMA), with divinyl crosslinkers, ethylene glycol dimethacrylate or the reductively degradable bis(2-methacryloyloxyethyl) disulfide, in the presence of an efficient chain transfer agent, CBr_4 . Multiple alkyl bromide chain end groups were present in the branched polymers, which were successfully used as multifunctional macroinitiators, from which both polyacrylate- and polymethacrylate-type arms were grown under low catalyst concentration ATRP conditions. Due to the ability of epoxides to reduce Cu^{II} to Cu^{I} complexes, the low catalyst-concentration ATRP chain extensions were performed in the absence of any externally added reducing agents. The cores of the obtained stars, contained numerous epoxide functionalities, originating from GMA, and were efficiently modified using reactions with a variety of tertiary aliphatic amines to afford star polymers with hydrophilic, cationic cores. Ring-opening of the oxirane rings in polyGMA with a pyridine derivative, nicotinamide, in

the presence of acetone and a base, was also explored to afford polymers with fluorescent groups.

Introduction

Star polymers are a class of materials in which several linear polymer chains are connected at a central point, referred to as a core (1). They are very interesting for a number of applications, partially due to higher degrees of chain-end functionality as compared to their linear analogues (2). Synthetic methods for producing star polymers typically fall into one of three categories (3, 4) termed “core first (5),” “coupling onto (6),” or “arm first (7, 8)” approaches.

Arguably the simplest and most efficient of these methods for synthesizing star polymers is the “core first” approach. In this method, a multifunctional initiator is used as a core structure, from which chains can be grown by a variety of polymerization methods. These multifunctional initiators can range from small molecules to high molecular weight macroinitiators. Varying the architectures of the cores is an easy way to tailor the properties of the resulting stars.

A robust and widely-used polymerization technique used to form the arms of star polymers is atom transfer radical polymerization (ATRP) (9–13), which allows for the synthesis of polymers with well-defined architectures, controlled molecular weights, and exceptional chain-end functionality. ATRP enables the controlled growth of macroradicals via a dynamic equilibrium between these active propagating species and alkyl halide-type dormant species, which relies on halogen exchange mediated by a redox-active transition metal catalyst. Importantly, the chain-end functionalities are retained in the produced polymers and are available for further chain extension reactions, e.g., synthesis of stars with segmented copolymer arms. Recently, low-catalyst concentration ATRP techniques were developed, which eliminate the need for extensive purification, allow for synthesis of high molecular weight polymers, and simplify reaction procedures (13–15). These low-catalyst techniques rely on the use of reducing agents, which are able to continuously regenerate the lower oxidation state activator species (e.g., Cu^I complex) by reducing the higher oxidation state deactivator (e.g., Cu^{II} halide complex) that would normally accumulate in the system due to irreversible radical termination reactions (13, 16).

Branched (including hyperbranched) polymers are highly sought after for their advantages in a number of applications as compared to their linear analogues (17–22). Due to this significant interest, various methods have been developed for their synthesis, including both step- and chain-growth processes.

One of the more popular methods for preparing (hyper)branched polymers is self-condensing vinyl polymerization (SCVP), where compounds containing both an initiating and a polymerizable group in the same molecule (*inimers*) are used (23, 24). However, methods utilizing SCVP are often elaborate as the synthesis of *inimers* is typically a multistep process, which may also involve numerous purifications (25). It has been recently demonstrated that *inimers* can be formed *in situ* in polymerization mixtures from carboxylate monomers via exchange

reactions with “ligands” attached to hypervalent iodine centers (26), but such approaches have limited applicability.

Another important group of techniques for synthesizing (hyper)branched polymers involves the radical copolymerization of monovinyl monomers with di- or multivinyl crosslinkers in the presence of reagents capable of limiting the length of the polymer chains and therefore - the number of pendant vinyl groups per macromolecule, each of which originates from incorporation of a crosslinker unit into the growing chain. As a result, the gelation point is delayed and (hyper)branched polymers are formed at relatively high monomer conversions. Additives that have been successfully employed include reagents capable of reversibly deactivating the propagating radicals (27, 28), large amounts of radical sources (initiators) (29–32), and chain transfer agents (33–38). Of these, the last methodology demonstrates particularly good utility as it involves less purification and the use of inexpensive, commercially available reagents. Moreover, it allows for the synthesis of multifunctional highly branched polymers in which functional groups can be placed at several different loci, namely the chain-ends, the branching points, and the polymeric backbone. The chain-end functionalities originate from the transfer agent, those at the branching points are introduced with the crosslinker, and the backbone functionalities are derived from the monomer(s). If the chain-end functionalities are able to initiate polymerization, the highly branched polymers can serve as multifunctional macroinitiators in chain-extension reactions with a plethora of monomers to afford star copolymers with functional highly branched cores (37, 38). Of particular interest are highly branched macroinitiators that can also serve as “universal” precursors of functional materials, due to the presence of numerous reactive backbone functionalities able to undergo many useful post-polymerization chemical modifications. One robust functional group that is widely used for a number of chemical transformations is the epoxide. Epoxides are easily reacted with a variety of nucleophiles (39–43), as well as oxidants (44) or reducing agents (45, 46), to afford useful transformation products that can drastically change the properties of the original material. Some of these transformations have been demonstrated in polymers with great synthetic utility, including synthesis of polymers with pendant azide groups (47) and polymers functionalized via thiol “click” reactions (48).

The utilization of highly-functional (hyper)branched polymers as cores for star polymer synthesis via low-catalyst concentration ATRP, along with various transformations of the epoxide-containing cores, is discussed in this work.

Experimental Procedures

Materials

The polymerization inhibitor was removed from glycidyl methacrylate (GMA, 97 %, Aldrich) by passing the neat monomer through a short column of neutral alumina. The same procedure was used to purify ethylene glycol dimethacrylate (EGDMA, 98 %, Alfa Aesar), methyl methacrylate (MMA, 99 %, Aldrich), and methyl acrylate (MA, 99 %, Aldrich), but using basic alumina. Tris(2-pyridylmethyl)amine (TPMA) was a product of ATRP Solutions and

was recrystallized from diethyl ether. Azobisisobutyronitrile (AIBN, 98 %, Aldrich) was recrystallized from ethanol. Bis(2-methacryloyloxyethyl) disulfide ((MAOE)₂S₂) was synthesized as described in the literature (49). All other reagents, CBr₄ (98 %, Acros), CuBr₂ (99 %, Aldrich), *N,N'*-dimethylethanolamine (DMEA, 99 %, Acros), *N*-methyldiethanolamine (MDEA, 99 %, Acros), triethanolamine (TEAM, 98 %, Sigma), *N,N'*-dimethylpropargylamine (DMPA, 97 %, Aldrich), nicotinamide (>98 %, Aldrich), tetramethylsilane (TMS, >99.9 %, Aldrich), and the solvents: anisole (PhOMe; 99%, Aldrich), *N,N*-dimethylformamide (DMF; >99.8 %, EMD), acetone (99.5 %, EMD), methanol (MeOH; 99.8 %, EMD), tetrahydrofuran (THF; 99%, Fisher), CDCl₃ (99.8 % D, Cambridge Isotope), and DMSO-*d*₆ (99.9 % D, Cambridge Isotope) were used as received.

Analyses

Monomer conversions were determined by ¹H NMR spectroscopy on a Bruker Avance DRX 400 spectrometer operating at 400 MHz. Apparent molecular weights (*M*_{n,app}) were determined by size exclusion chromatography (SEC) using linear poly(methyl methacrylate) standards on a Tosoh EcoSEC HLC-8320 system equipped with a series of 4 columns (TSK gel guard Super HZ-L, Super HZM-M, Super HZM-N, and Super HZ2000) with THF as the eluent (0.35 mL min⁻¹, 40 °C). Part of the samples withdrawn from the reaction mixtures were diluted with THF, filtered through 0.2 μm PTFE Acrodisc filters, and the obtained solutions were directly injected into the SEC without purification.

Synthetic Procedures

Highly Branched polyGMA Macroinitiator (hb-polyGMA-Br_x)

GMA (6.0 mL, 45 mmol), EGDMA (426 μL, 2.25 mmol, 5 mol % vs. GMA), AIBN (0.0372 g, 227 μmol), CBr₄ (2.2464 g, 6.8 mmol, 30 eq. vs. AIBN), and PhOMe (6 mL) were added to a 25-mL round-bottom flask equipped with a magnetic stir bar. The flask was capped with a rubber septum (pre-washed with acetone and dried), and the solution was deoxygenated by bubbling with nitrogen for 45 min while cooling the reaction flask in an ice bath. The flask was then immersed in an oil bath set at 60 °C. Samples were taken periodically and analyzed. Final polymer was isolated by diluting the reaction mixture with acetone (ca. 1 : 1 by volume) and precipitation in diethyl ether. The polymer was redissolved in a minimal amount of chloroform and treated dropwise with a 10 % (v/v) solution of Br₂ in chloroform until a slight yellow-orange color remained, indicating complete conversion of any remaining alkenyl groups. The polymer was then finally purified by reprecipitation in diethyl ether followed by drying *in vacuo*.

This same procedure was used for all hb-polyGMA-Br_x syntheses, with variation in EGDMA amounts (10 and 15 mol % relative to GMA) or use of (MAOE)₂S₂ (569 μL, 2.25 mmol, 5 mol % relative to GMA). For reactions with 10 or 15 mol % of EDGMA vs. GMA, a higher amount of CBr₄ (40 eq. vs. to AIBN) was also used to delay gelation.

Chain Extension of hb-polyGMA-Br_x Macroinitiator with MMA under Low-Catalyst Concentration ATRP Conditions Using No External Reducing Agent

The macroinitiator, hb-polyGMA-Br_x, with $M_{n,app} = 8,500 \text{ g mol}^{-1}$ was synthesized (using 5 % EGDMA relative to GMA) and purified by the method described above. CuBr₂ (0.8 mg, 3.75 μmol) and TPMA (3.37 mg, 11.3 μmol) were weighed in a 50-mL round bottom flask and dissolved with DMF (1 mL). Dry macroinitiator (10.0 mg, 97.6 μmol Br as determined by elemental analysis) was weighed and added to the flask and diluted with PhOMe (7 mL). The targeted degree of polymerization ($DP_{n,targ}$, which is the concentration ratio of monomer to initiating alkyl halide groups) of MMA was 780. After adding a magnetic stir bar, the test tube was capped with a rubber septum (pre-washed with acetone and dried) and sealed. The resulting solution was cooled in an ice bath and deoxygenated by bubbling with nitrogen for 60 minutes. The reaction flask was then immersed in an oil bath set at 65 °C. Samples were taken at timed intervals. Part of the sample was diluted with CDCl₃ and analyzed by NMR to determine monomer conversion and the rest was diluted with THF and analyzed by SEC. Shift of the polymer peak over time verified efficient chain extension with MMA. Final polymer was purified by precipitation in diethyl ether and drying *in vacuo*. Other experiments were also carried out, in which the amount of MMA (i.e., $DP_{n,targ}$) was varied, or using MA as the monomer.

Modification of polyGMA with Different Tertiary Amines

Linear polyGMA was synthesized using low-catalyst concentration ATRP without external reducing agent ($DP_{n,targ} = 200$) as previously reported (50). Dried polyGMA (100 mg, 70.3 μmol epoxide groups) was weighed into a small test tube equipped with a magnetic stir bar and dissolved with 0.5 mL DMSO-*d*₆. In a separate test tube, the amine (1.2 eq. relative to epoxide) and concentrated HCl (1 eq. relative to acid) were mixed thoroughly. Once mixed, 0.25 mL DMSO-*d*₆ was added and the entire contents transferred to the test tube containing polyGMA. DMSO-*d*₆ (0.25 mL) was used to wash out the amine/acid test tube and added to the reaction vessel. The test tube was capped with a rubber septum (pre-washed with acetone and dried) and immersed in an oil bath set at 60 °C. Samples were taken at timed intervals, diluted with DMSO-*d*₆, and analyzed by NMR to determine reaction progress. The final polymers were then purified by precipitation in acetone, followed by redissolving in water, dialysis in water (MWCO = 2,000 Da) to remove any excess amine, and lyophilization. Polymers modified with TEAM were treated with a small amount of sodium acetate to enhance water solubility. This same procedure was used for all modifications of star copolymers with epoxide-containing cores.

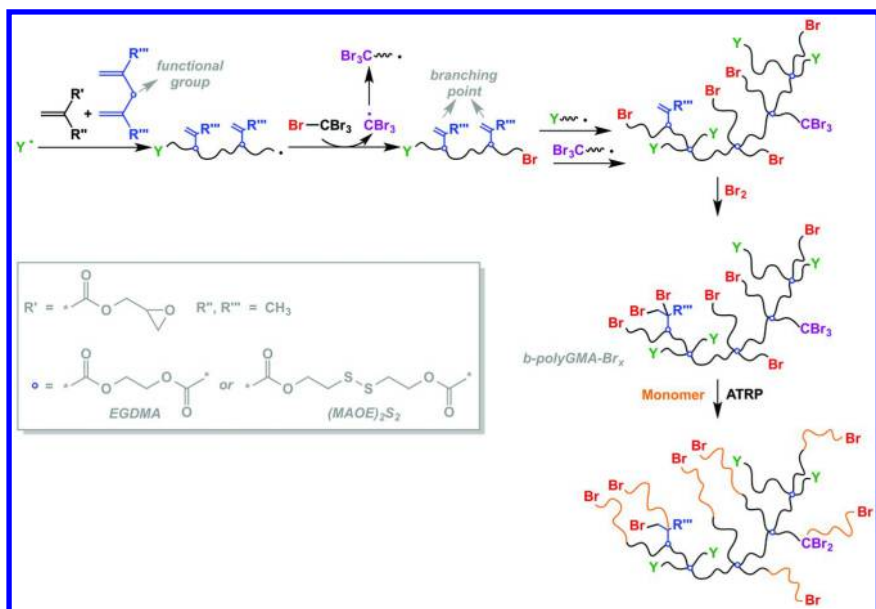
Nicotinamide (0.2442 g, 2 mmol) was weighed in a 10-mL round bottom flask equipped with a magnetic stir bar. Concentrated HCl (66.8 μ L, 0.8 mmol) was then added, followed by DMSO- d_6 (4 mL). Once the reagents were fully dissolved, polyGMA was added (0.1137 g, 0.8 mmol of epoxide groups). The polymer dissolved within ca. 1 min in the reaction mixture. The flask was then capped with a rubber septum (pre-washed with acetone and dried) and placed in an oil bath set at 70 °C. Samples were taken at timed intervals, diluted with DMSO- d_6 , and analyzed by NMR to determine the reaction progress. Once complete disappearance of epoxide peaks was observed (2.5 h), the reaction flask was removed from the heating bath. Acetone (1 mL) and solid NaOH (0.1 g) were added to the mixture, which was left to stir at room temperature for 1 h. After 1 h, concentrated HCl (0.2 mL) was slowly added. The final polymer was then used, directly from the reaction vessel as an “ink” on filter paper to demonstrate its fluorescence under UV light.

Synthesis of Star Polymers from Highly-Functional Multibrominated Branched Cores

Synthesis of Highly Branched Epoxide-Containing Polymers

Star polymers with highly branched cores are an interesting class of materials that have not been explored systematically, but are of significant interest (4), and the synthesis of such materials is the subject of this work. As mentioned, in addition to the increased chain-end functionality of (hyper)branched polymers, it is useful to include pendant reactive functionalities along the interconnected polymer chains. This would allow, after post-polymerization modifications, for the introduction of groups, including such that would otherwise be difficult to incorporate during the polymerization due to incompatibility with the reaction components. For this purpose, the epoxide functional group was chosen as it provides a robust library of chemical transformations.

Glycidyl methacrylate (GMA) was chosen as the monomer for the synthesis of branched epoxide-containing polymers because of the pendant epoxide functionality. This was copolymerized with ethylene glycol dimethacrylate (EGDMA) in the presence of a radical initiator, e.g., azobisisobutyronitrile (AIBN), and an efficient chain transfer agent, CBr₄, to afford highly-branched polymers with multiple bromine chain ends and useful pendant epoxide functionalities, as shown in Scheme 1. (Bio)degradable analogues of these polymers were also made by replacing EGDMA with bis(2-methacryloyloxyethyl) disulfide ((MAOE)₂S₂), introducing an easily-cleavable disulfide group at the branching points of the polymer.



Scheme 1. Synthesis of highly branched epoxide-containing polymers and their use as cores for growth of star blockcopolymer arms via ATRP.

The degree of branching of the polymers can be controlled by altering the amount of crosslinker in the polymerizing system and it can reach very high values. However, in order to delay the gelation up to acceptably high conversions, the systems employing large amounts of crosslinker require fast transfer, i.e., high concentrations of efficient chain transfer agents. Figure 1a shows that the kinetics of the polymerizations were not significantly affected by the amount of crosslinker present, but as Figure 1b demonstrates, the increased amount of crosslinker in the systems led to the formation of more and more branched polymers as judged from the width of the molecular weight distributions (M_w/M_n). For instance, as the amount of EGDMA increased from 5 to 10 to 15 mol % relative to GMA, the molecular weight distribution dispersity of polymers obtained at similar conversions (ca. 65 – 68 %) increases gradually from 22 to 28. For all reactions, as the polymerizations progressed, the degree of branching and the dispersity increased significantly, as Figure 1c demonstrates for the case employing 5 mol % EGDMA. Eventually, crosslinking occurred at high conversions and in order to isolate soluble branched polymers, the reactions were stopped at moderately high conversions (typically below 70 %). The branched polymers synthesized with the disulfide-containing crosslinker had narrower molecular weight distributions than those in which the same amount of EGDMA was used at similar conversions. It is known that disulfides, although markedly less efficient than CBr₄, can participate in transfer reactions with polymethacrylate radicals, and the decreased degree of branching (reflected by decreased molecular weight distribution dispersity) can plausibly be attributed to the presence of an additional transfer agent in these systems (51).

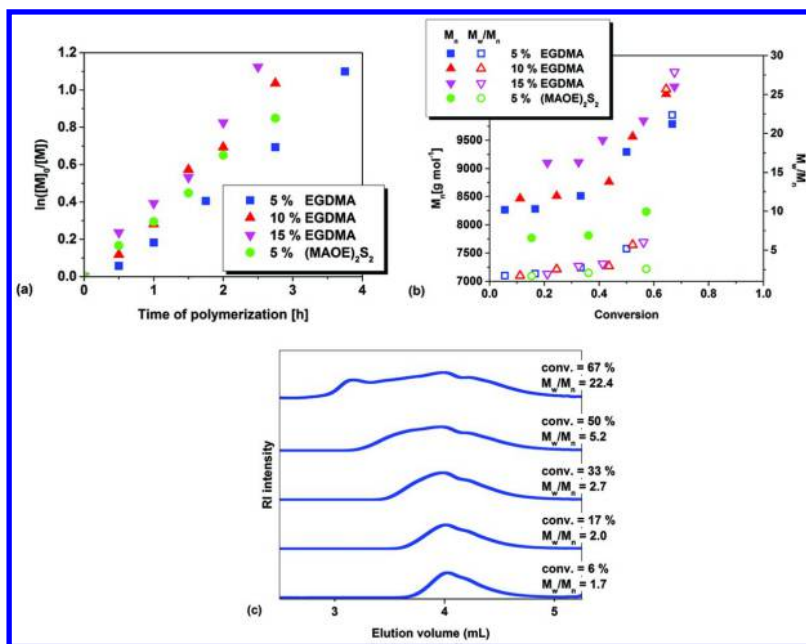


Figure 1. a) Kinetics and b) evolution of apparent molecular weights and molecular weight distribution dispersities (M_w/M_n) with monomer conversion for the synthesis of multibrominated highly branched poly(glycidyl methacrylate) (hb-polyGMA-Br_x) obtained with the use of a chain-transfer agent under the following conditions: $[GMA]_0/[EGDMA \text{ or } (MAOE)_2S_2]_0/[AIBN]_0/[CBr_4]_0 = 1/0.05 \text{ or } 0.1 \text{ or } 0.15/0.005/0.15 \text{ or } 0.2 \text{ or } 0.2$; $[GMA]_0 = 3.78 \text{ M}$ in anisole at 65 °C. c) SEC traces for the conditions utilizing 5 mol % EGDMA.

Since divinyl crosslinkers were used in the syntheses, some of the interconnected chains contained a certain amount of unreacted pendant vinyl functionalities (38), which could lead to crosslinking of the materials upon prolonged storage or during subsequent chemical modifications. Thus, after initial purification of the polymers via precipitation in diethyl ether, precautions were taken to remove any remaining pendant vinyl groups. This was done by dissolving the polymers in a minimal amount of chloroform and treating the polymer solution with a 10 % (v/v) solution of Br₂ in chloroform until slight yellow-orange coloration remained, indicating that the alkenyl groups were fully brominated. Final purification by precipitation in diethyl ether was carried out, followed by drying *in vacuo*.

The polymers containing the disulfide functionality at the branching points are of interest due to the easy cleavage of that group in the presence of reducing agents including bio-relevant reducing agents such as glutathione (52, 53). As Figure 2 shows, the reductive degradation could easily be accomplished by using tributylphosphine (Bu₃P), an efficient disulfide cleavage agent (54–56).

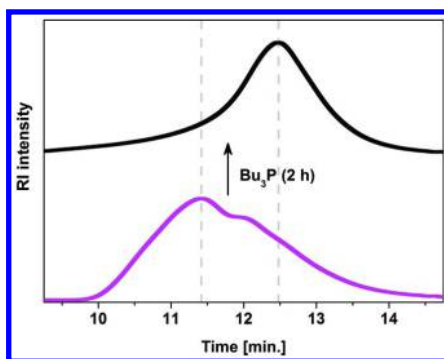


Figure 2. SEC traces of (bio)degradable disulfide-containing hb-polyGMA-Br_x before (bottom) and after (top) treatment with Bu₃P (10 μL added to a solution of 1 mg polymer in 1 mL THF, 2 h). The polymer was synthesized using the following conditions: [GMA]₀ / [(MAOE)₂S₂]₀ / [AIBN]₀ / [CBr₄]₀ = 1 / 0.05 / 0.005 / 0.15; [GMA]₀ = 3.78 M in anisole at 65 °C, stopping at monomer conversion of 57 %, M_w/M_n = 2.58.

Chain Extension of hb-polyGMA-Br_x via Low-Catalyst Concentration ATRP

The polymers synthesized in the previous section, hb-polyGMA-Br_x, were employed as multifunctional initiators for the low-catalyst concentration ATRP of (meth)acrylates to form star copolymers via the “core first” approach. It should be noted (Scheme 1) that the branched polymers contained three different types of alkyl bromide functionalities: ω-bromine-capped polymethacrylate chains, –CBr₃ end groups originating from chains initiated by the CBr₃• radical (a product of the bromine transfer from CBr₄ to the macroradicals), and vicinal bromine atoms that were introduced by the reaction of Br₂ with pendant double bonds. Of these, the tertiary alkyl bromide groups, as well as one of the bromines from –CBr₃ groups, can initiate ATRP. However, the primary alkyl bromide formed in the addition of Br₂ to the pendant double bonds and the backbone dibromomethylene groups are much less likely to initiate polymerization. Elemental analysis revealed that the highly branched polymer (obtained using a reaction with 5 mol % of EGDMA) contained 7.8 wt % of Br, which roughly corresponded to one bromine atom for every 7 GMA units. In the following discussion, the reported targeted degrees of polymerization are based on the molar ratio of monomer to the total bromine content of the branched macroinitiators due to inability to determine what fraction of the bromine atoms were actually able to initiate polymerization.

It was recently demonstrated that epoxides can act as reducing agents in low-catalyst concentration ATRP reactions (Scheme 2) (50, 57), and in the chain extension reactions reported here, the epoxides present in the macroinitiator served to regenerate the lower oxidation state metal complex (activator) via reduction of the higher oxidation state deactivator.

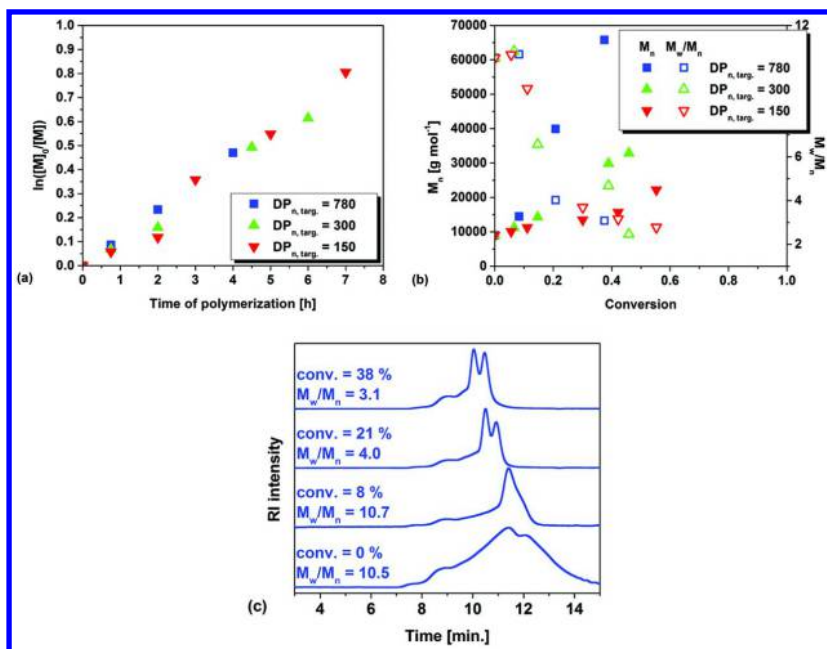


Figure 3. a) Kinetics and b) evolution of apparent molecular weights and molecular weight distribution dispersities with monomer conversion in the low-catalyst ATRP of MMA initiated by *hb*-polyGMA-Br_x in anisole/DMF at 65 °C. $[MMA]_0 / [Br \text{ from } hb\text{-polyGMA-Br}_x]_0 / [CuBr_2]_0 / [TPMA]_0 = 780 \text{ or } 300 \text{ or } 150 / 1 / 0.03 / 0.09$; $[MMA]_0 = 4.69 \text{ M}$. c) SEC traces for polymerization with $DP_{n,targ} = 780$.

At first, the modifications of linear polyGMA were carried out in order to optimize the reaction conditions. Several tertiary amines, namely DMEA, MDEA, TEAM, and DMPA (Scheme 3), were used to convert the pendant epoxide groups of polyGMA to quaternary ammonium salts. The targeted product of the ring-opening was a β -hydroxyethylammonium salt. To form this efficiently, both an amine and a proton source are needed, the former being responsible for opening the epoxide ring, and the latter being used to protonate the produced alkoxide anion. In this work, a mixture of free and protonated amine was used, which was formed by mixing amine (1.2 eq. vs. epoxide) and a proton source, e.g., HCl, (1 eq. vs. epoxide). When this preformed mixture reacts with the epoxide, the excess of free amine opens the ring, while the protonated amine transfers a proton and is converted to free amine, which can continue the reaction with another epoxide group. It is essential to react the acid with the amine before adding to the polymers to prevent free acid-catalyzed intra- and interchain crosslinking between epoxide groups.

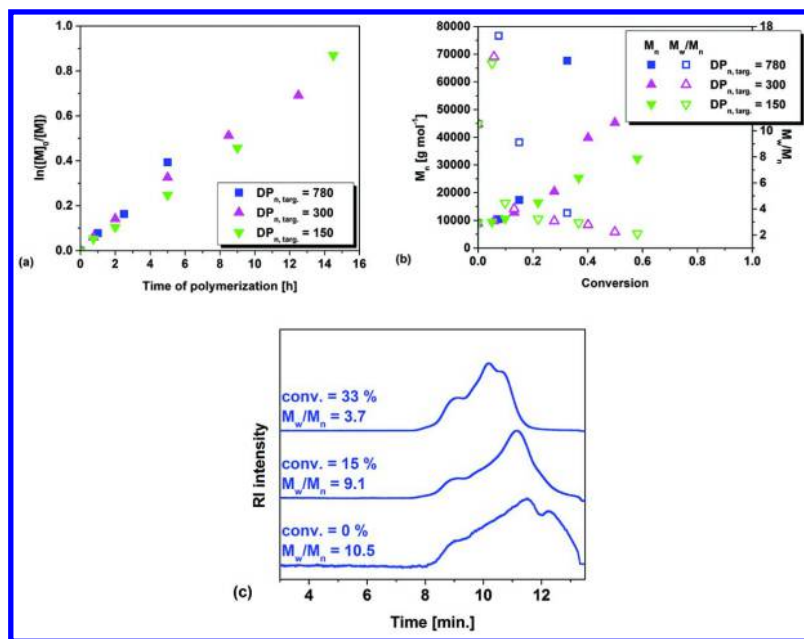
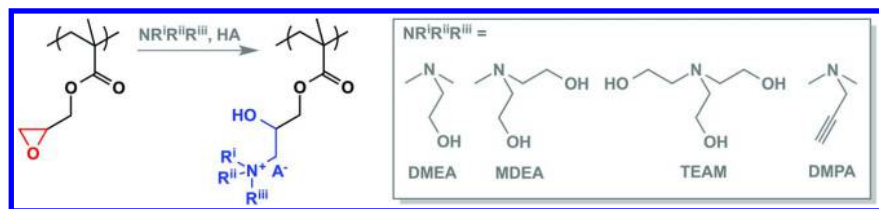


Figure 4. a) Kinetics and b) evolution of apparent molecular weights and molecular weight distribution dispersities with monomer conversion in the low-catalyst ATRP of MA initiated by *hb*-polyGMA-Br_x in anisole/DMF at 65 °C. $[MA]_0 / [Br \text{ from } hb\text{-polyGMA-Br}_x]_0 / [CuBr_2]_0 / [TPMA]_0 = 780 \text{ or } 300 \text{ or } 150 / 1 / 0.03 / 0.09$; $[MA]_0 = 4.69 \text{ M}$. c) SEC traces for polymerization with $DP_{n,targ} = 780$.



Scheme 3. Transformation of an epoxide functionality to a quaternary ammonium salt

The kinetics of the transformation reactions were monitored by NMR spectroscopy, by tracking the disappearance of the peaks corresponding to the three epoxide protons (denoted by “e” in Figure 5). In the NMR spectrum of the sample taken after 0.25 h, three peaks were observed at 2.6, 2.9, and 3.7

ppm, which respectively corresponded to the methyl, aminomethylene, and hydroxymethylene protons of the partially protonated amine (i.e., mixture of DMEA and DMEA.HCl). The peaks shifted upfield as the reaction proceeded, because the ratio of protonated to free amine decreased from the original value of ca. 1:0.2. (The chemical shifts of the corresponding protons of the free, non-protonated, amine in DMSO are 2.1, 2.3, and 3.4 ppm.) When all the epoxide groups are consumed, only 0.2 eq. of free amine (relative to the original epoxide) should be left in the reaction mixture, which is why the peaks not only shifted upfield but also decreased in intensity.

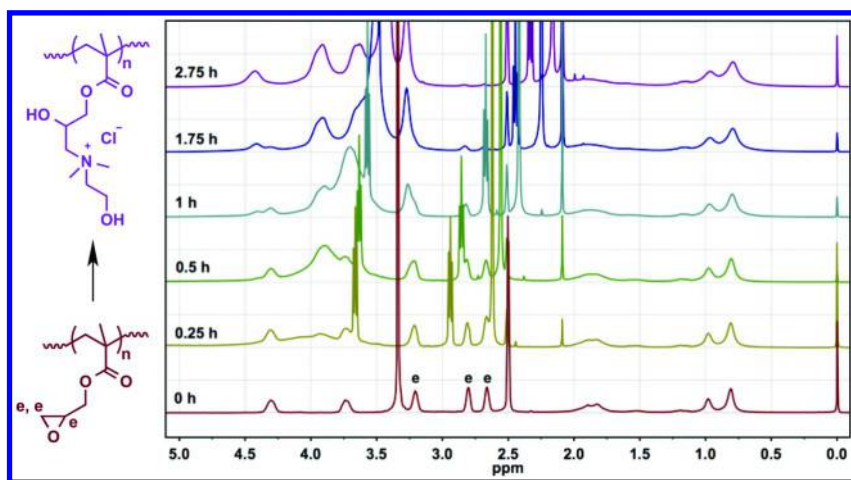


Figure 5. Evolution of NMR spectra of the reaction between DMEA and polyGMA in DMSO- d_6 at 60 °C. Reaction conditions: $[DMEA]_0 / [HCl]_0 / [epoxide]_0 = 1.2 / 1 / 1$; $[polyGMA]_0 = 4.17$ mM.

The resulting polymers were purified by precipitation in acetone, followed by redissolving in water, dialysis in water (MWCO = 2,000 Da) to remove any excess amine, and lyophilization.

As shown in Figure 6, the reactions between each tertiary amine and the epoxides were fairly rapid and virtually complete consumption of epoxides was observed in all cases. The ring opening with the most sterically hindered amine, TEAM, was the slowest and took more than a day to complete, while the next less-hindered amine, MDEA, reacted within 8 h. The transformations involving the two dimethylamines (DMEA and DMPA) were faster (completing in 3 to 6 h).

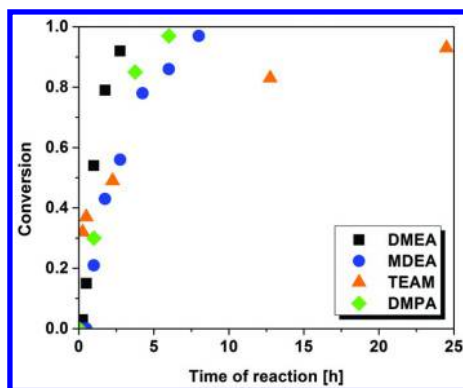
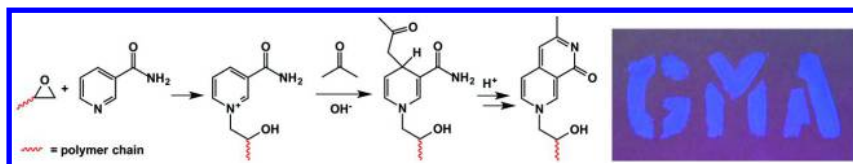


Figure 6. Kinetics of epoxide transformations with different tertiary amines and polyGMA in DMSO- d_6 at 60 °C. Reaction conditions: $[amine]_0 / [HCl]_0 / [epoxide]_0 = 1.2 / 1 / 1$; $[polyGMA]_0 = 4.17$ mM.

The choice of tertiary aminoalcohols (DMEA, MDEA, TEAM) was made to ensure water solubility of the final polymers. An interesting phenomenon that was observed was the low water solubility of the TEAM-modified polymer. This is projected to be due to intermolecular hydrogen bonding between the abundant hydroxyl groups present in each repeat unit. The addition of salts, such as sodium acetate, (the anion of which competes with the hydroxyl groups for the formation of hydrogen bonds) allowed for enhanced solubility in water. A propargyl-functionalized tertiary amine (DMPA) was also used, as the terminal alkyne moiety is interesting in its utility for “click” reactions involving 1,3-dipolar cycloadditions with azides (60–64) or thiol-yne reactions (65). This is useful for introducing other functional groups, chain-end functionalized polymers, or dyes to the polymer backbone.

One other interesting transformation is the reaction of the epoxide functionalities with a pyridine derivative, nicotinamide (see the first reaction step in Scheme 4). The alkylation of the pyridine ring is an efficient reaction as shown by NMR studies (Figure 7), and was completed in less than 3 hours under the conditions specified.



Scheme 4. Synthesis of fluorescent polymer via reaction of polyGMA with nicotinamide and acetone and an example of its use as a fluorescent “ink.”

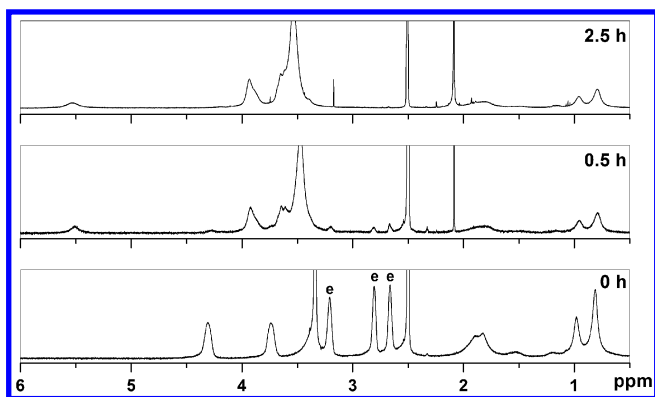


Figure 7. Evolution of NMR spectra of alkylation of nicotinamide by polyGMA in DMSO- d_6 at 70 °C. $[epoxide]_0 / [nicotinamide]_0 / [pTsOH]_0 = 1 / 2.5 / 1$; $[polyGMA]_0 = 2.08 \text{ mM}$

The resulting pyridinium salts react with acetone and other ketones with α -methylene groups in basic solutions, yielding, after acidification, a product that is highly fluorescent (66). The proposed reaction mechanism (67) is shown in Scheme 4, along with a photograph demonstrating the intense fluorescence of the obtained functional polymer, which was used as an “ink” on paper. The reaction of *N*-alkyl pyridinium salts derived from nicotinamide with acetone is very sensitive and has found analytical applications for the determination of small amounts of epoxides in biological samples (68).

Core Modifications of Star Block Copolymers with Epoxide-Containing Branched Cores

The optimized modification reactions described above were applied to the epoxide-containing highly branched core precursors or stars with branched cores. By modifying the core of star polymers to become hydrophilic, while the arms remain hydrophobic, polymers with interesting solution behavior and other physical properties can be formed (69). Similar ratios of amine and acid to epoxide functionality, which were roughly estimated by NMR, were used as in experiments with linear polyGMA. Figure 8 shows the change of the NMR spectra from hb-polyGMA-Br_x to the product of its chain extension with MMA (short arms in order to be able to see the epoxide protons in the NMR spectra), to star copolymers with hydrophilic cores formed by epoxide reaction with DMEA.

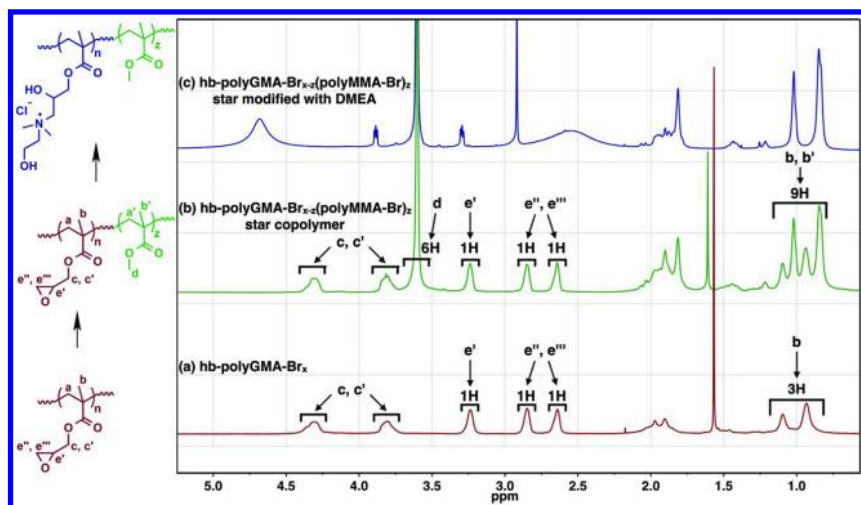


Figure 8. NMR spectra demonstrating transformation of a) *hb-polyGMA-Br_x* macroinitiator to b) *hb-polyGMA-Br_{x-z}(polyMMA-Br)_z* star copolymer to c) *hb-polyGMA-Br_{x-z}(polyMMA-Br)_z* star modified with DMEA. Relative integrals are shown, demonstrating growth of polyMMA arms from the macroinitiator. Low-catalyst ATRP of MMA was initiated by *hb-polyGMA-Br_x* in anisole/DMF at 65 °C and stopped at 65 % monomer conversion. $[MMA]_0 / [Br \text{ from } hb\text{-polyGMA-Br}_x]_0 / [CuBr_2]_0 / [TPMA]_0 = 257 / 1 / 0.03 / 0.09$; $[MMA]_0 = 4.69 \text{ M}$.

The presence of polyMMA arms in the star copolymer (Figure 8b) is evident by the appearance of methyl ester protons and also by the relative increase of the polymethacrylate backbone protons relative to the epoxide protons. By integrating the protons corresponding to MMA units and comparing them to those corresponding to GMA units, the ratio of the two building blocks in the star copolymer was determined as approximately 2:1, a value consistent with estimates based on MMA conversion from the synthesis of the star polymer (65 %) and SEC data for the original macroinitiator ($M_{n,app} = 8,500 \text{ g mol}^{-1}$). The resulting star polymer was modified with amine (DMEA) and purified as previously described.

Conclusions

The “core first” approach was used to synthesize star copolymers using a highly branched, multibrominated epoxide-containing macroinitiator via low-catalyst concentration ATRP. The highly branched core structures were first synthesized by copolymerizing glycidyl methacrylate (GMA) with divinyl crosslinkers, ethylene glycol dimethacrylate or the (bio)degradable bis(2-methacryloyloxyethyl) disulfide, in the presence of CBr_4 . In synthesizing these structures, sufficiently large amounts of CBr_4 were used to ensure that a high monomer conversions were reached before macroscopic gelation occurred.

The amount of crosslinker determined the degree of branching and in some experiments was as high as 15 mol % relative to the monomer, GMA. CBr_4 was not only used as an agent for chain transfer, but also as a source of bromine chain-ends in the resulting branched polymers, which could be used as initiating sites for ATRP. The epoxide functionalities in the branched macroinitiator served as intrinsic reducing agents, which are required to reduce Cu^{II} to Cu^{I} complexes and therefore enable the low-catalyst concentration ATRP technique to be utilized. Due to the very small amount of catalyst used in the ATRP reactions, an insignificant amount of epoxide groups were reacted, leaving the rest for use in modification reactions. Transformations of the epoxide groups in polyGMA to quaternary ammonium salts were also carried out using a variety of tertiary amines, namely *N,N'*-dimethylethanolamine, *N*-methyldiethanolamine, triethanolamine, and *N,N'*-dimethylpropargylamine. A pyridine derivative, nicotinamide, was also used to afford highly fluorescent materials. Modifications of the epoxides in the star cores were accomplished as well, providing a straightforward synthetic approach to star polymers with hydrophobic arms and cationic, hydrophilic cores. Unlike primary and secondary amines, the products of the reaction of tertiary amines and epoxides, ammonium salts, are not able to open more epoxide rings and therefore tertiary amines are much less likely to cause crosslinking than their primary or secondary analogues.

Acknowledgments

Financial support from the National Science Foundation (CHE-1111929) and Southern Methodist University (start-up funds to NVT) is gratefully acknowledged.

References

1. Hawker, C. J. *Angew. Chem., Int. Ed. Engl.* **1995**, *34*, 1456–1459.
2. Aloorkar, N. H.; Kulkarni, A. S.; Patil, R. A.; Ingale, D. J. *Int. J. Pharm. Sci. Nanotechnol.* **2012**, *5*, 1675–1684.
3. Hadjichristidis, N.; Pitsikalis, M.; Pispas, S.; Iatrou, H. *Chem. Rev.* **2001**, *101*, 3747–3792.
4. Matyjaszewski, K. *Polym. Int.* **2003**, *52*, 1559–1565.
5. Matyjaszewski, K.; Miller, P. J.; Pyun, J.; Kickelbick, G.; Diamanti, S. *Macromolecules* **1999**, *32*, 6526–6535.
6. Gao, H.; Matyjaszewski, K. *Macromolecules* **2006**, *39*, 4960–4965.
7. Gao, H.; Ohno, S.; Matyjaszewski, K. *J. Am. Chem. Soc.* **2006**, *128*, 15111–15113.
8. Gao, H.; Matyjaszewski, K. *Prog. Polym. Sci.* **2009**, *34*, 317–350.
9. Matyjaszewski, K.; Xia, J. *Chem. Rev.* **2001**, *101*, 2921–2990.
10. Ouchi, M.; Terashima, T.; Sawamoto, M. *Chem. Rev.* **2009**, *109*, 4963–5050.
11. Matyjaszewski, K.; Tsarevsky, N. V. *Nature Chem.* **2009**, *1*, 276–288.
12. Tsarevsky, N. V.; Matyjaszewski, K. In *Fundamentals of Controlled/Living Radical Polymerization*; Tsarevsky, N. V., Sumerlin, B. S., Eds.; RSC

Polymer Chemistry Series; Royal Society of Chemistry: Cambridge, 2013; pp 287–357.

13. Matyjaszewski, K.; Tsarevsky, N. V. *J. Am. Chem. Soc.* **2014**, *136*, 6513–6533.
14. Jakubowski, W.; Matyjaszewski, K. *Macromolecules* **2005**, *38*, 4139–4146.
15. Matyjaszewski, K.; Jakubowski, W.; Min, K.; Tang, W.; Huang, J.; Braunecker, W. A.; Tsarevsky, N. V. *Proc. Natl. Acad. Sci. U.S.A.* **2006**, *103*, 15309–15314.
16. Tsarevsky, N. V.; Matyjaszewski, K. *J. Polym. Sci., Part A: Polym. Chem.* **2006**, *44*, 5098–5112.
17. *Star and Hyperbranched Polymers*; Mishra, M., Kobayashi, S., Eds.; Marcel Dekker Inc.: 1999.
18. Jikei, M.; Kakimoto, M.-A. *Prog. Polym. Sci.* **2001**, *26*, 1233–1285.
19. Bolton, D. H.; Wooley, K. L. *J. Polym. Sci., Part A: Polym. Chem.* **2002**, *40*, 823–835.
20. Yates, C. R.; Hayes, W. *Eur. Polym. J.* **2004**, *40*, 1257–1281.
21. Voit, B. I.; Lederer, A. *Chem. Rev.* **2009**, *109*, 5924–5973.
22. Voit, B.; Komber, H.; Lederer, A. In *Synthesis of Polymers New Structures and Methods*; Schlüter, D. A., Hawker, C. J., Sakamoto, J., Eds.; Wiley-VCH Verlag GmbH & Co. KGaA: 2013; pp 701–740.
23. Fréchet, J. M. J.; Henmi, M.; Gitsov, I.; Aoshima, S.; Leduc, M. R.; Grubbs, R. B. *Science* **1995**, *269*, 1080–1083.
24. Hawker, C. J.; Fréchet, J. M. J.; Grubbs, R. B.; Dao, J. *J. Am. Chem. Soc.* **1995**, *117*, 10763–10764.
25. Gao, C.; Yan, D. *Prog. Polym. Sci.* **2004**, *29*, 183–275.
26. Han, H.; Tsarevsky, N. V. *Polym. Chem.* **2012**, *3*, 1910–1917.
27. Isaure, F.; Cormack, P. A. G.; Graham, S.; Sherrington, D. C.; Armes, S. P.; Bütün, V. *Chem. Commun.* **2004**, 1138–1139.
28. Li, Y.; Armes, S. P. *Macromolecules* **2005**, *38*, 8155–8162.
29. Sato, T.; Sato, N.; Seno, M.; Hirano, T. *J. Polym. Sci., Part A: Polym. Chem.* **2003**, *41*, 3038–3047.
30. Sato, T.; Miyagi, T.; Hirano, T.; Seno, M. *Polym. Int.* **2004**, *53*, 1503–1511.
31. Sato, T.; Nakamura, T.; Seno, M.; Hirano, T. *Polymer* **2006**, *47*, 4630–4637.
32. Han, H.; Tsarevsky, N. V. *Chem. Sci.* **2014**, *5*, 4599–4609.
33. Chen, H.; Ishizu, K.; Fukutomi, T.; Kakurai, T. *J. Polym. Sci., Polym. Chem. Ed.* **1984**, *22*, 2123–2130.
34. Chen, H.; Won, Y. M.; Ishizu, K.; Fukutomi, T. *Polym. J.* **1985**, *17*, 687–692.
35. O'Brien, N.; McKee, A.; Sherrington, D. C.; Slark, A. T.; Titterton, A. *Polymer* **2000**, *41*, 6027–6031.
36. Costello, P. A.; Martin, I. K.; Slark, A. T.; Sherrington, D. C.; Titterton, A. *Polymer* **2002**, *43*, 245–254.
37. Popescu, D.-L.; Tsarevsky, N. V. *Aust. J. Chem.* **2012**, *65*, 28.
38. Popescu, D.-L.; Tsarevsky, N. V. *Macromol. Rapid Commun.* **2012**, *33*, 869–875.
39. Parker, R. E.; Isaacs, N. S. *Chem. Rev.* **1959**, *59*, 737–799.
40. Rao, A. S.; Paknikar, S. K.; Kirtane, J. G. *Tetrahedron* **1983**, *39*, 2323–2367.
41. Gorzynski Smith, J. *Synthesis* **1984**, 629–656.

42. Whalen, D. L. In *Advances in Physical Organic Chemistry*; Elsevier, 2005; Vol. 40, pp. 247–298.
43. Padwa, A.; Murphree, S. S. *Arkivoc* **2006**, 6–33.
44. Antoniotti, S.; Duñach, E. *Synthesis* **2003**, 2753–2762.
45. Wong, H. N. C.; Fok, C. C. M.; Wong, T. *Heterocycles* **1987**, *26*, 1345.
46. Larock, R. C. In *Comprehensive Organic Transformations*, 2nd ed.; Wiley-VCH: New York, 1999; pp 1019–1027
47. Tsarevsky, N. V.; Bencherif, S. A.; Matyjaszewski, K. *Macromolecules* **2007**, *40*, 4439.
48. De, S.; Khan, A. *Chem. Commun.* **2012**, *48*, 3130–3132.
49. Tsarevsky, N. V.; Matyjaszewski, K. *Macromolecules* **2005**, *38*, 3087–3092.
50. Woodruff, S. R.; Davis, B. J.; Tsarevsky, N. V. *Macromol. Rapid Commun.* **2014**, *35*, 186–192.
51. Brandrup, J.; Immergut, E. H.; Grulke, E. A. *Polymer Handbook*; Wiley: New York, 1999.
52. Szajewski, R. P.; Whitesides, G. M. *J. Am. Chem. Soc.* **1980**, *102*, 2011–2026.
53. Schafer, S. Q.; Buettner, G. R. *Free Radical Biol. Med.* **2001**, *30*, 1191–1212.
54. Humphrey, R. E.; Potter, J. L. *Anal. Chem.* **1965**, *37*, 164–165.
55. Tsarevsky, N. V.; Matyjaszewski, K. *Macromolecules* **2005**, *38*, 3087–3092.
56. Tsarevsky, N. V.; Huang, J.; Matyjaszewski, K. *J. Polym. Sci., Part A: Polym. Chem.* **2009**, *47*, 6839–6851.
57. McLeod, D. C.; Tsarevsky, N. V. *Polym. Int.* **2014**, *63*, 868–875.
58. Tang, W.; Kwak, Y.; Braunecker, W.; Tsarevsky, N. V.; Coote, M. L.; Matyjaszewski, K. *J. Am. Chem. Soc.* **2008**, *130*, 10702–10713.
59. Hoover, M. F. *J. Macromol. Sci., Part A - Chem.* **1970**, *4*, 1327–1418.
60. Kolb, H. C.; Finn, M. G.; Sharpless, K. B. *Angew. Chem., Int. Ed.* **2001**, *40*, 2004–2021.
61. Fournier, D.; Hoogenboom, R.; Schubert, U. S. *Chem. Soc. Rev.* **2007**, *36*, 1369–1380.
62. Lutz, J.-F. *Angew. Chem., Int. Ed.* **2007**, *46*, 1018–1025.
63. Binder, W. H.; Sachsenhofer, R. *Macromol. Rapid Commun.* **2007**, *28*, 15–54.
64. Sumerlin, B. S.; Vogt, A. P. *Macromolecules* **2010**, *43*, 1–13.
65. Lowe, A. B. *Polymer* **2014**, *55*, 5517–5549.
66. Nakamura, H.; Tamura, Z. *Anal. Chem.* **1978**, *50*, 2047–2051.
67. Sano, A.; Asabe, Y.; Suzuki, M.; Takitani, S. *Bunseki Kagaku* **1983**, *32*, E93–E100.
68. Nelis, H. J. C. F.; Sinsheimer, J. E. *Anal. Biochem.* **1981**, *115*, 151–157.
69. Kanaoka, S.; Sawamoto, M.; Higashimura, T. *Macromolecules* **1993**, *26*, 254–259.

Chapter 12

Living Radical Polymerization from Colloidally-Templated Nanopatterned Surface

Peng-Fei Cao, Edward Foster, Al de Leon, and Rigoberto Advincula*

Department of Macromolecular Science and Engineering, Case Western Reserve University, Cleveland, Ohio 44106, United States

*E-mail: rca41@case.edu

A facile approach of creating well-defined patterned polymer brushes was developed. Herein, different techniques, such as 2D colloidal sphere templating, electrodeposition of a macroinitiator, surface initiated polymerization (SIP), and “click” reaction were utilized and discussed. Controlled radical polymerization (CRP), such as atomic transfer radical polymerization (ATRP) and reversible-addition chain transfer radical (RAFT), are mainly used for SIP for well-controlled polymer brush architecture, adjustable polymer film thickness, and possible block copolymer formations. The modifiable terminal groups of the polymers after CRP provided an opportunity to “graft onto” the nanopatterned surface *via* a “click” reaction. In this section, our recent work about “polymer brush on a colloidal nano-patterned conducting substrate” are demonstrated in detail, which includes the design, methodologies, and related results.

Background

Electro-Grafting

“Electro-grafting” has been used to describe an electrochemical reaction where an organic material binds to an electrode *i.e.* a conducting substrate. Based on the mechanism of electropolymerization of conducting polymers, polymerization starts with the formation of oligomers in solution initiated by the applied potential

(1, 2). The next general step is the deposition onto a conducting surface or electrode. This step involves nucleation, growth, and additional chemical reactions under solid state conditions (3). Potentiostatic, and potentiodynamic techniques can be used to create and monitor the electro-grafting process. As an example, potentiodynamic (e.g. cyclic voltammetry (CV)) experiments provide information on the growth rate of conducting polymers. The increase in current with each cycle of a potentiodynamic diagram is directly proportional to the increase in the amount of rechargeable redox sites on a surface (4). Further evidence of successful electro-grafting comes from monitoring the amount of mass deposited on the substrate. For example, the mass changes can be measured using electrochemical quartz crystal microbalance measurements (EC-QCM), where potential step techniques and CV have been coupled to the QCM technique.

Compared with other well studied methods for surface modification such as silanization and phosphonation of oxidized surfaces, and self-assembly of thiols on Au surfaces and other metal surface, “electro-grafting” exhibits great advantages. For example, silanes and thiols require specific surface for it to be adsorbed. In the case of electroactive monomers, on the other hand, many types of conducting or electrode surfaces (metals, carbon, metal oxides, etc.) can be readily coated *via* electro-grafting. Our group have used linear polymer, dendrimer, and star-like copolymer to form the conjugated polymer network film on the conducting surface *via* electro-grafting (5–7).

Another important application of “electro-grafting” is that they can be synthesized to incorporate a variety of functional groups. One area of recent interest is the ability to perform surface initiated polymerization (SIP) to grow polymer brushes from a variety of functional groups tethered to a surface. Polymer brushes are polymer coatings consisting of polymeric chains that are end-tethered to surface. At high grafting densities, steric repulsion leads to stretching and brush conformations (8).

Polymer Brushes Grafted to Electropolymerized Surface

“Grafting to” approach means to tether the prefabricated polymers (with a reactive end-group) using covalent bond formation *i.e.* chemisorption on a bare or pre-functionalized substrate (Figure 1A) (9). For example, the polymer can be grafted to a substrate that is pre-functionalized with silane, thiol, or electro-grafted molecules. For the latter, the covalent bond is formed through the chemical reaction of the terminal group of the linear polymer and the complimentary functional groups of the electroactive units. The linear polymer could be synthesized by different methods, which will be discussed in greater detail in the next section.

Although experimentally facile, the “grafting to” approach has limitations. One of which includes the difficulty in producing thick and dense polymer brushes because its formation is greatly hindered by steric repulsion between polymer chains.

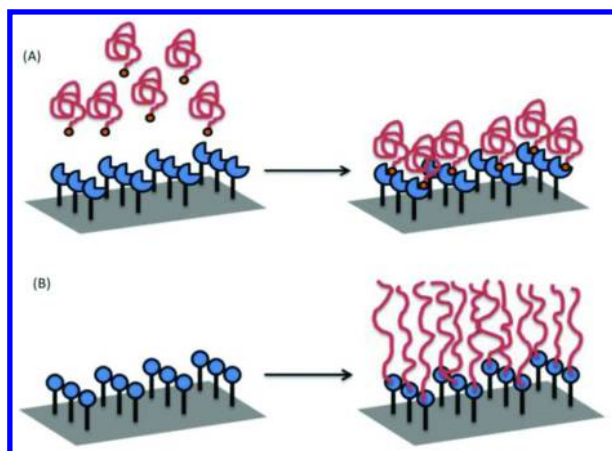


Figure 1. (A). Scheme for the preparation of polymer brushes via chemisorption reaction of end-functionalized polymers with complementary functional groups at the substrate surface (“Grafting-to” approach). (B) Synthetic strategies for the preparation of polymer brushes grown via SIP technique (“Grafting-from” approach).

Polymer Brushes Grafted from Electropolymerized Surface

To minimize the steric repulsion problem of the “grafting to” approach, monomers can be introduced to the functionalized surface directly. In this approach (Figure 1B), the polymer is directly grown from the surface which has been functionalized with an initiator or a chain transfer agent (CTA) (10). Controlled polymerization techniques are of great interest because it enables the control of thickness, composition, and architecture of polymer brushes (11). Most of the polymer brushes produced by the “grafting from” approach use surface-initiated (SI) controlled radical polymerization techniques. There are several methods of controlled radical polymerization techniques that can be extended to the fabrication of polymer brush. Reversible-addition chain transfer radical (RAFT) polymerization and atomic transfer radical polymerization (ATRP) are the mostly commonly used.

“Graft from” via Reversible-Addition Chain Transfer Radical Polymerization

Reversible-addition fragmentation chain transfer (RAFT) polymerization is based on reversible chain transfer and has been used to prepare polymer brushes via SIP (12). An early example of SI-RAFT polymerization was reported by Baum *et al.*, who prepared poly(methyl methacrylate) (PMMA), polystyrene (PS), and poly(N,N dimethylacrylamide) (PDMA) brushes from azo-functionalized surfaces in the presence of a chain transfer agent (CTA) 2-phenylprop-2-yl dithiobenzoate and a free-radical initiator (2,2'-azoisobutyronitrile (AIBN)) (13).

Recently, some researchers have used conductive surfaces with electro-grafted materials containing RAFT-CTA to perform SI-RAFT. For example, our group has reported the synthesis of homopolymer and block copolymer brush from electro-deposited polythiophene-derivative on a tin oxide-coated (ITO) glass and gold (Au) electrode (Figure 2) (14). The successful polymerization of a diblock copolymer brush confirms that a conventional SI-RAFT procedure can be done with the polythiophene macroinitiator film. Also, by using SI-RAFT polymerization from electro-grafted initiator, electrochemically cross-linked surface grafted poly(N-vinylcarbazole) (PVK) brushes can serve as the hole transport layers for photovoltaic device applications (15). The performance of the photovoltaic device is comparable to that based on poly(3,4-ethylene dioxithiophene):poly(styrene sulfonate) PEDOT:PSS. Aside from this, we also found that the electro-grafted material has strong adhesion to ITO, which could possibly allow long-term stability against acid dopants and oxygen.

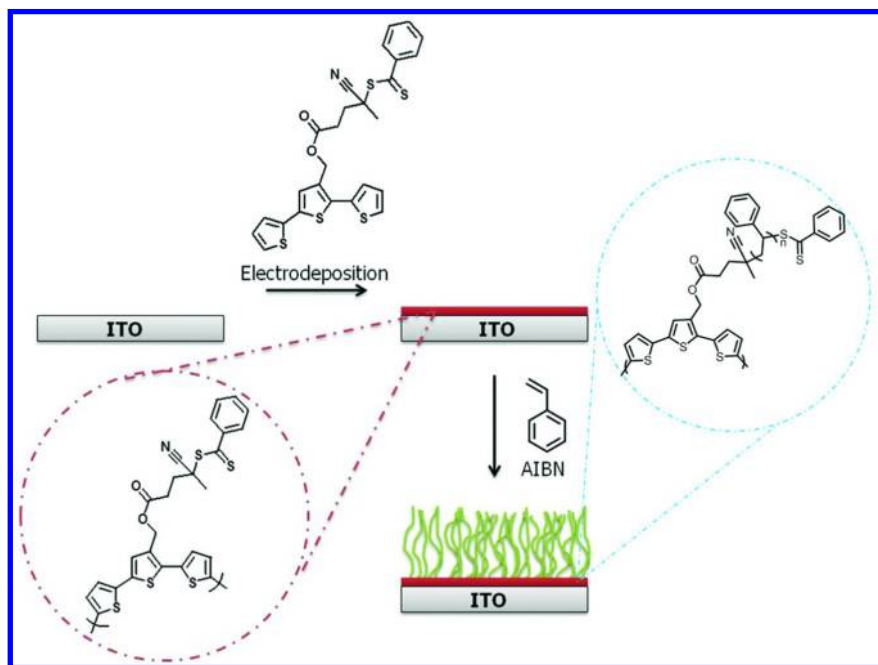


Figure 2. General route for preparing polymer brushes from an electro-grafted polythiophene with RAFT-CTA. Partially reproduced with permission from ref (14). Copyright (2011) American Chemical Society.

Analogous to the above examples, direct electro-grafting of well-defined dendritic linear polymers, which was synthesized *via* RAFT polymerization technique, has also been done. For example, our group has synthesized dendritic CTAs possessing a single dithioester moiety at the focal point, where RAFT polymerization could be carried out (16). This was done in order to attach PS and PMMA chains of controlled lengths to an ITO or Au electrode. To provide

electrochemical functionality, the dendritic CTAs were designed to contain carbazole moieties at the periphery of the structures. Although not illustrated in the study, it should be possible to grow another polymer after PS or PMMA. This is brought about by the living nature of the polymerization process.

“Graft from” via Atom Transfer Radical Polymerization

Another important type of living radical polymerization technique that has been employed to produce polymer brushes is atom transfer radical polymerization (ATRP). The process of ATRP relies on the “reversible redox activation of a dormant alkyl halide terminated polymer chain end by a halogen transfer to a transition metal complex” (17). The formal homolytic cleavage of the carbon-halogen bond, creates a free carbon radical at the end of polymer chain. This step is based on a single electron transfer from the transition metal complex to the halogen atom, leading to the oxidation of the transition metal complex.

Similar as SI-RAFT polymerization, SI-ATRP has also been extended to grow polymer brush from similar materials. Huang and coworkers were the first to report the SI-ATRP by grafting polyacrylamide brushes from halogenated terminated initiators attached to silica particles (18). The SI-ATRP has also been successfully used by Sedjo *et al.* to prepare PS brushes from a functionalized silica substrate using Cu(II)Br₂/bipyridine (bpy) agent (19, 20). The SI-ATRP on a conducting surface by electro-chemical reaction was also demonstrated although there were fewer reports compared with SI-RAFT. For example, Matrab *et al.* reported the preparation of PMMA, poly(n-butyl acrylate), and PS brushes at the surface of steel electrodes that were modified by the electrochemical reduction of a brominated aryl diazonium salt (21).

Surface Patterning

Colloidal Templating

The ability to pattern surfaces on the micro- and nanoscale is the basis of a wide range of applications including microelectronics, photonic structures, microfluidics, biosensors, and surface science (22). Examples of patterning techniques are photolithographic process, microcontact printing (μ CP), electron-beam (e-beam) lithography, and scanning probe lithography (23, 24). Template surface patterning techniques aided by colloidal templating is specifically interesting for the conducting surface.

It is well-known that colloidal particles made out of SiO₂ or polystyrene (PS) can self-assemble into periodic two- or three-dimensional structures (25). Electro-grafting onto 2D colloiddally templated surfaces consists of three steps (Figure 3a). Firstly, an ordered colloidal crystal is deposited onto an electrode (Figure 3b). Then the monomer is electro-grafted into the interstitial spaces of the colloids. Lastly, the sacrificial template is removed to reveal a microporous inverse opal structure composed of the electro-grafted material. An example of this methodology was demonstrated by Knoll *et al.*, who used colloidal

templating to fabricate ordered honeycomb shaped polyaniline (PANI) and its copolymers with poly(acrylic acid) and poly(styrene sulfonate) (Figure 3c and d) (26). The inverse opal PANI films exhibited high quality patterns, and remained electroactive in buffer solutions at neutral pH, demonstrating that these films are good candidates for biosensing applications.

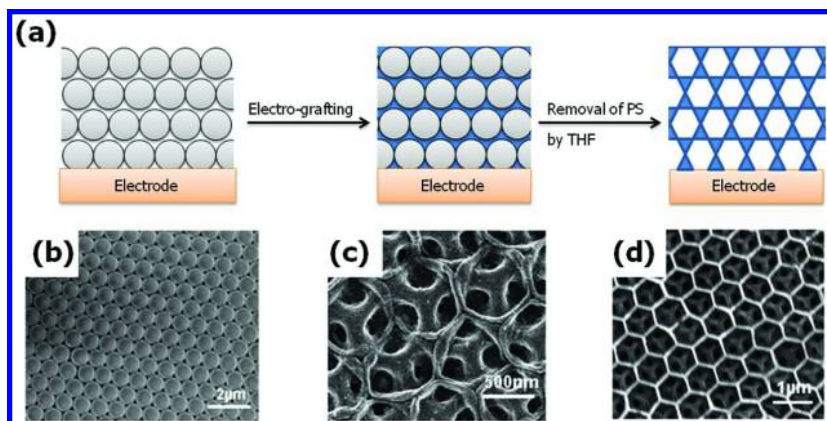


Figure 3. (a) Schematic illustration of the procedure used for fabricating PANI inverse opal microstructures via electropolymerization within a PS colloidal crystal on top of a gold electrode. SEM-images of the (b) colloidally templated gold surface and (c and d) PANI inverse opals with two different magnifications. Reprinted with permission from ref (26). Copyright (2005) American Chemical Society.

Fabrication Method

Colloidal Template-Assisted Electropolymerization

Based on the concept discussed, our group has also demonstrated electrochemical patterning of polypyrrole arrays using single-layered colloidal templates on the pyrolytic graphite (HOPG) surface as shown in Figure 4 (27). More specifically, a mixture of PS nanoparticles (1 wt%) and spreading agent (sodium n-dodecylsulfate, SDS, 34.7mM) was dispersed by sonication for 10-15 mins. It was then transferred on the HOPG substrate by slowly withdrawing the substrate from the solution (LB-like technique). In a three-electrode cell, the electrochemical synthesis was carried out with the PS latex beads array/HOPG substrate as the working electrode. Electroactive pyrrole monomers (0.05 mol/L) and its aldehyde derivate (0.05 mol/L) were used to electrodeposite around the PS template. The PS template array was then removed by dissolving with toluene to get a well-ordered 2-D porous array on HOPG.

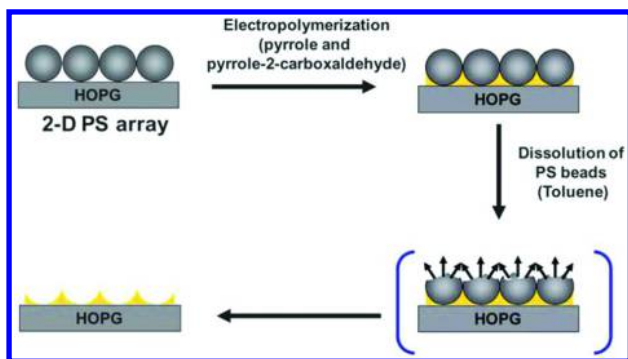


Figure 4. Procedure involved in creating an asymmetrically functionalized microporous film consisting of Ppy/Ppy-CHO. The third cartoon means that the PS beads is being dissolved by toluene. Reprinted with permission from ref (27). Copyright (2011) Royal Society of Chemistry.

We have also developed a sensor capable of differentiating chiral molecules *via* molecularly imprinted polymers (MIP) in combination with colloidal templating (28). More specifically, the electro-grafted polythiophene MIP film was fabricated to differentiate a prohibited drug (–)-norephedrine (1R, 2S) from its diastereomer (+)-norephedrine (1S, 2S) (28). The new assembly of electropolymerized MIP film demonstrated a much higher sensing response when templated than the conventional flat MIP film.

Backfilling of the void spaces on the colloiddally templated surface has also been performed as shown in Figure 5 (29). A binary composition of highly ordered 2-D conducting polymer pores was fabricated by template-directed electro-grafting followed by SAM formation of 1-octadecanethiol (1-ODT). The backfilling of the inside cavities by the SAM approach resulted in a 2-D binary patterned chemistry. The surface morphology changes depicted by AFM images confirm the backfilling of the cavities.

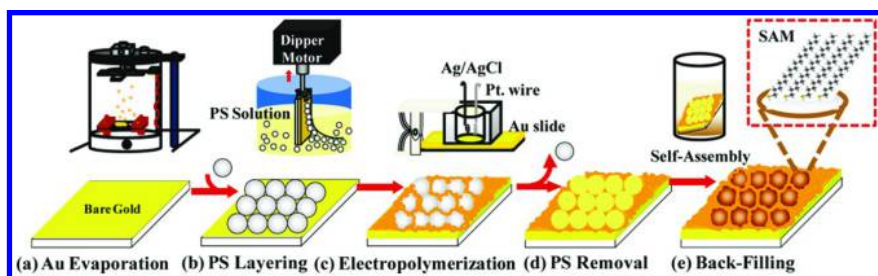


Figure 5. Fabrication of highly ordered monolayer colloidal crystals and inverse patterned colloidal crystals of conducting polymer film. Reprinted with permission from ref (29). Copyright (2011) American Chemical Society.

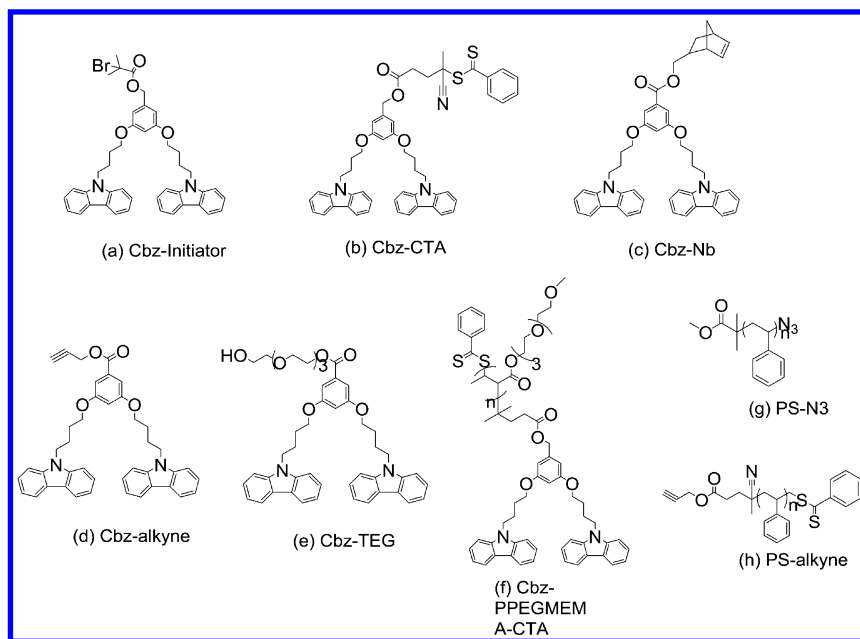


Figure 6. Structure of (a) 3,5-bis(4-(9H-carbazol-9-yl)butoxy)benzyl 2-bromo-2-methylpropanoate (Cbz-Initiator), (b) 3,5-bis(4-(9H-carbazol-9-yl)butoxy)benzyl 4-cyano-4-phenylcarbonothioylthio pentanoate (Cbz-CTA), and (c) Bicyclo[2.2.1]hept-5-en-2-ylmethyl 3,5-Bis-(4-(9H-carbazol-9-yl)butoxy)benzoate (Cbz-Nb), (d) prop-2-ynyl 3,5-bis(4-(9H-carbazol-9-yl)butoxy)benzoate (Cbz-Alkyne), (e) 2-(2-(2-(2-hydroxy)ethoxy)ethoxy)ethyl-3(4-(9H-carbazol-9-yl)butoxy)-5-(4-(9Hcarbazol-9yl)butoxy)) benzoate (Cbz-TEG), (f) electroactive dendritic-linear PPEGMEMA (Cbz-PPEGMEMA-CTA) molecule, (g) linear PS with terminal azide functional group (PS-N₃) and, (h) linear PS with terminal alkyne functional group (PS-Alkyne).

Colloidally Templated Polymer Brush via Living Radical Polymerization – “Grafting from” Approach

Instead of 1-octadecanethiol (1-ODT) for SAM formation on the Au substrate as discussed before, we also demonstrated the backfilling with an ATRP-initiator contained molecule, 11-(2-bromo-2-methylpropionyloxy) undecyltrichlorosilane or Si-Br. The subsequent SI-ATRP of N-isopropylacrylamide (NIPAM) from the ATRP initiator on the colloidally template surfaces was performed (30).

A series of electroactive initiators were also synthesized as shown in Figure 6, which includes ATRP initiator, RAFT initiator, and ring-opening metathesis polymerization (ROMP) initiator (31). The procedure for the stepwise formation of patterned polymer brush surface was illustrated in Figure 7. Similar to our previous discussion, a monolayer of polystyrene sub-microspheres particles were deposited on a conducting substrate (ITO) using the so-called Langmuir-Blodgett

(LB)-like technique. The electro-grafting of the electroactive initiator was achieved *via* chronoamperometry using an applied constant potential of 1.3 V for 3 mins. After removing the PS nanoparticles, surface initiated polymerization *via* ATRP, RAFT, or ROMP was performed to grow a polymer brush on a patterned substrate. The void spaces are free of polymer brush and further functionalization is possible, i.e. ATRP-silane initiator can be self-assembled on the void space, and another polymer brush can be grown from it. The binary brush system *via* a combination of SI-RAFT and SI-ATRP was also demonstrated in this work (31).

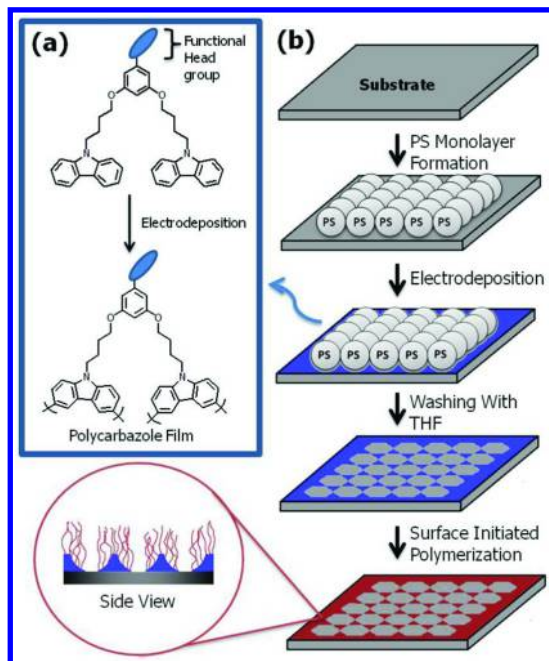


Figure 7. (a) General structure of the electro-active functional initiators before and after electro-deposition forming the polycarbazole network. (b) Fabrication of a highly ordered monolayer of colloidal crystals (500 nm diameter PS microspheres), inverse colloidal arrays, and patterned polymer brushes via SIP. Reprinted with permission from ref (31). Copyright (2012) Royal Society of Chemistry.

Colloidally Templated Polymer Brush via Living Radical Polymerization – “Grafting to” Approach

In this approach, the polymer is firstly synthesized *via* living radical polymerization, and then the end-group of the polymer is replaced with a functional group that can react with the complimentary group of the electro-grafted polymer. We tried the electro-deposition of a series of first-generation dendrons (chemical structure is shown in Figure 6) on to colloidal template substrate as

shown in Figure 8. The first route focus on the electrodeposition of electro-active molecule (G1Cbz-alkyne). Afterward, linear polystyrene molecules containing an azide (PS-N₃) was grafted onto *via* the CuAAC reaction. For route 2, G1Cbz-TEG was firstly electrodeposited on the colloidal patterned surface, and then an azide containing thiol was grafted on the Au substrate after removing the PS nanoparticles. Subsequently, a PS-alkyne was grafted to the surface *via* the CuAAC reaction. Herein linear polymers with molecular weight 2,000 to 4,000 was utilized for “click” reaction. Lastly, route 3 shows the direct attachment of the electroactive linear polymer *via* electro-grafting onto colloiddally template surface.

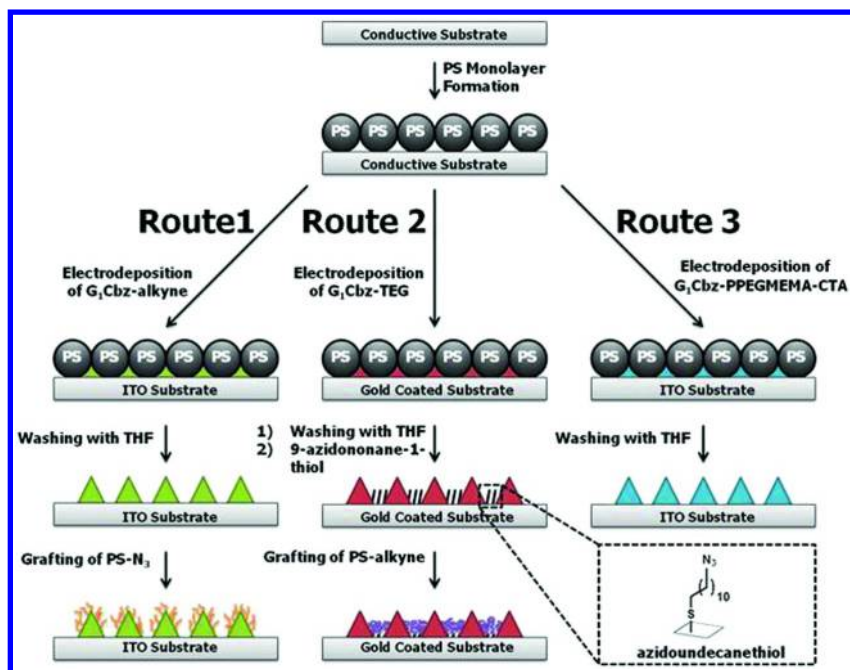


Figure 8. Fabrication of highly ordered of colloidal arrays via “grafting to” strategy. Reprinted with permission from ref (33). Copyright (2012) Elsevier.

The “grafting to” approach on colloidal template surface relies on the preparation of polymers having either a terminal azide (PS-N₃) or alkyne (PS-alkyne) functional group that can react sequentially by “click” reaction. The reactive polystyrene was polymerized *via* ATRP primarily to ensure that the polymer is monodispersed. The precursor PS-Br molecule was synthesized *via* ATRP using styrene and methyl 2-bromo-2-methylpropionate (MBMP) along with CuBr/ N,N,N',N'',N''-pentamethyldiethylenetriamine (PMDETA) as the catalyst system. Afterward, sodium azide (NaN₃) was added to replace the terminal bromide to azide group.

Results and Discussion

Colloidal Template-Assisted Nanopatterning on Conducting Substrate

Following the methodology as shown in Figure 4, a well-ordered 2-D porous array on HOPG ($d_{\text{pore}} = 210 \text{ nm}$) with a constant distance ($D_1 = 155\text{-}160 \text{ nm}$) was established as shown in Figure 9. The thickness of the thin Ppy/Ppy-CHO film was found to be around 25-26 nm (t_1), and the height of each protruded ring around each pore is about 35-38 nm (t_2). A longer electro-grafting time (350 s) will render a thicker Ppy/Ppy-CHO film. Moreover, various porous opening shapes, such as honeycomb, flat ring-shape, and hollow shell structure were made possible by varying the current density (27).

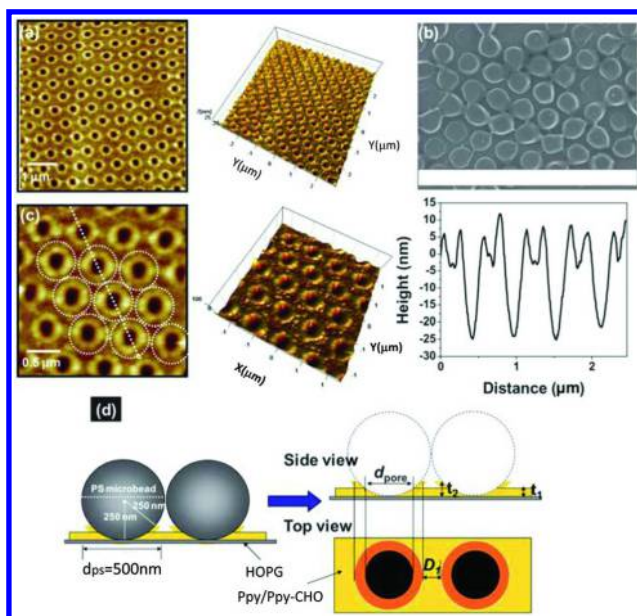


Figure 9. (a) AFM (2-D and 3-D) and (b) SEM images of the hexagonal porous structured Ppy/Ppy-CHO polymeric film after electrochemical deposition in 0.5 M KCl and 50 mM py/50 mM py-CHO for 250 s and the extraction of the PS-m template, (c) zoom-in AFM image (2-D and 3-D) and line profilometry, and (d) dimension of the micropores array measured from the AFM image. Reprinted with permission from ref (27). Copyright (2011) Royal Society of Chemistry.

A binary composition on the 2-D ordered substrate can be fabricated by backfilling the inside of cavities. The success of the self-assembly was confirmed by the Atomic Force Microscopy (AFM) and X-ray Photoelectron Spectroscopy (XPS) (29). The change in the surface morphology (shown in the AFM images) confirmed the backfilling of the cavities with the 1-ODT molecules. More specifically, the line profiles of the cavities showed increase in the height and decrease in the peak to baseline distance.

Colloidally Templated Polymer Brush via Living Radical Polymerization – “Grafting from” Approach

Instead of 1-ODT, silane functionalized ATRP initiator (Si-Br, chemical structure is shown in Figure 10) can be used to backfill the inside cavities of the inverse colloidal crystals of conducting polymer network due to the chemical bonding of silane to ITO substrate. The AFM topography images (Figure 10b and Figure 10c), along with the decrease of the peak-to-baseline height in the AFM line (Figure 10d), evidenced the successful backfilling of the Si-Br. The height difference before and after Si-Br SAM immobilization (1.8 nm) into the cavities is equivalent to the theoretical length of the molecule as modeled by Spartan. Poly(*n*-isopropylacrylamide) (PNIPAM) brush was then grown from the inner cavities for 15 mins. Similarly, the AFM topography images was utilized to monitor the growth of the PNIPAM brush, which was evidenced by the decrease in peak-to-baseline height. XPS was also used to verify the adsorption of the Si-Br and the PNIPAM brush. The presence of the bromine peak evidenced the immobilization of Si-Br, and the increase in signal of the elements (C, N, O) confirmed the growth of the PNIPAM brush.

A series of carbazole-based electroactive initiators (chemical structure is shown in Figure 6) were also electrodeposited on the PS patterned conducting substrate as demonstrated in Figure 7. The UV-vis spectrum of the electrodeposited film after removal of the PS, with peaks centered at 430 and >800nm, reveals the signature peaks of a typical cross-linked polycarbazole network film on ITO. The result is consistent with our group’s previous studies on conjugated polymer network (CPN) formation (7, 32). SI-ATRP of poly(methyl methacrylate) (PMMA) was done from the inverse colloidal Cbz-initiator arrays to create a highly ordered patterned polymer brush films. From the AFM topography image as shown in Figure 11, the morphology has changed from the hexagonal array to a relatively hemispherical void with a more granular appearance on the periphery of the patterned area. The AFM line profiles before and after brush growth exhibit an increase in the patterned film thickness from $10.5 \text{ nm} \pm 0.7 \text{ nm}$ to $25.3 \pm 1.6 \text{ nm}$. In addition, the high resolution XPS scan also confirmed the successful polymerization of the MMA (31). Moreover, the backfilling of the ATRP-silane initiator and the subsequent growth of polymer brush in the cavities were also demonstrated and confirmed by the AFM.

Colloidally Templated Polymer Brush via Living Radical Polymerization – “Grafting to” Approach

Polymer brush synthesized by controlled radical polymerization could also be “grafted to” the nanopatterned surface *via* a CuAAC reaction as demonstrated in Figure 8. The “grafting to” approach on colloidally templated surfaces relies on the preparation of polymers having either a terminal azide (PS-N₃) or a terminal alkyne (PS-alkyne) functional group that can react to its complimentary functional group on the surface. ATRP was employed for controlled living radical polymerization to enable monodispersed samples. The precursor PS-Br molecule was synthesized *via* ATRP using styrene and methyl 2-bromo-2-methylpropionate

(MBMP), along with CuBr/N,N,N',N'',N''-pentamethyldiethylenetriamine (PMDETA) as the catalyst system. The molecular weight (M_n) and polydispersity index (PDI) of the PS-Br was measured by GPC. RAFT polymerization was employed to synthesize the PS-alkyne. In the case of the PS-alkyne, no further modification was required because the “clickable” terminal alkyne was still present after polymerization. In the case of the PS-Br molecule additional steps were required to create the azido functional group for “click” reaction.

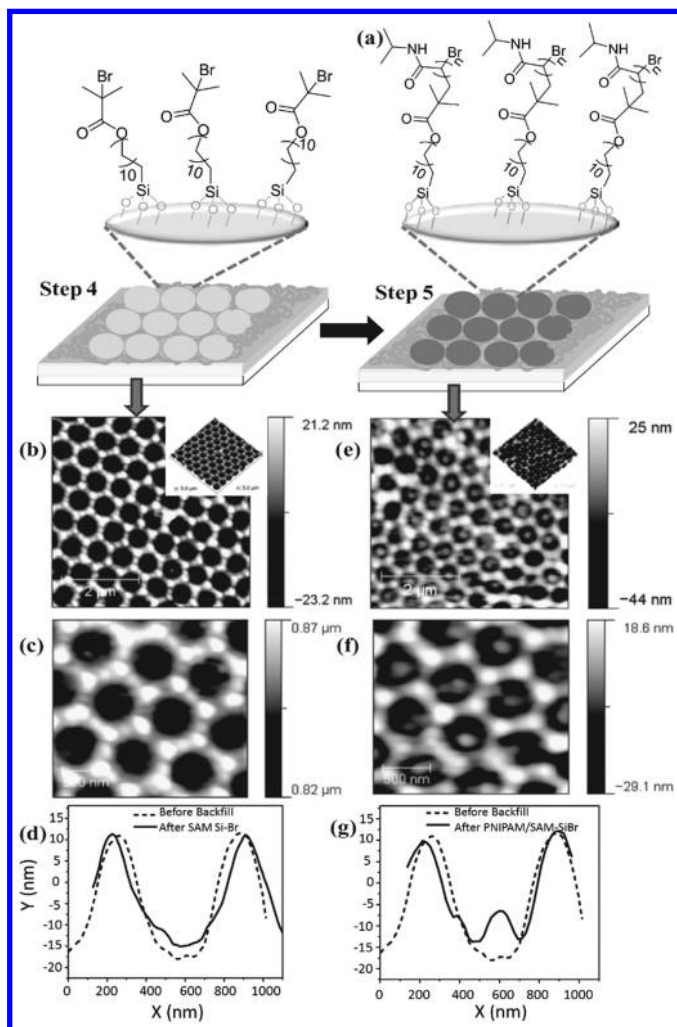


Figure 10. (a) Fabrication scheme of backfilling the inside cavities with silane SAM (ATRP-initiator) and polymer brush (PNIPAM). Low (b, e) and high (c, f) magnification AFM (in tapping mode) topography 2D images (3D on inset) of backfilled (b, c) Si-Br SAM and (e, f) pNIPAM brush. AFM line profile analysis of (d) Si-Br SAM and (g) pNIPAM brush versus bare ITO surface (before backfilling). Reprinted with permission from ref (30). Copyright (2011) Wiley.

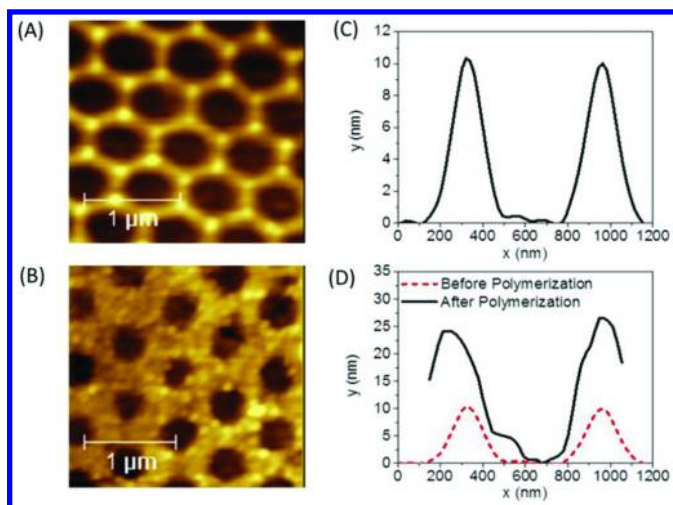


Figure 11. AFM topography 2D images ($2.5 \times 2.5 \mu\text{m}$): (A) after electrodeposition of Cbz-initiator and washing of PS microsphere (inverse colloidal Cbz-initiator arrays), and (B) after 1hr polymerization of MMA. Line profile analysis: (C) single PS microsphere, (D) cavity after electrodeposition of Cbz-Initiator and PS removal, and (D) before and after SIP of MMA. Reprinted with permission from ref (31). Copyright (2012) Royal Society of Chemistry.

As shown in route 1 of Figure 8, the PS- N_3 was grafted onto the inverse colloidal Cbz-alkyne arrays. From the AFM topography image, the morphology has changed from the hexagonal array (Figure 12 I(a)), to a relatively hemispherical void with a more granular appearance on the periphery of the patterned area (Figure 12 A(b)) (33). The increase in the film thickness (from $9.2 \pm 0.8 \text{ nm}$ to $13.4 \pm 1.8 \text{ nm}$) as measured by AFM validated the successful grafting of the polymer brush. Attenuated total reflectance infrared spectroscopy (ATR-IR) also confirmed the presence of the polymer brush. The formation of the laterally patterned binary composite surface is illustrated in Figure 8, Route 2. The inverse colloidal Cbz-TEG polymer array was firstly created on the Au substrates, and subsequent backfilling the cavities of the inverse colloidal Cbz-TEG arrays by azidoundecanethiol allowed a “clickable” terminal groups. This step was then followed by grafting PS-alkyne to the azidoundecanethiol SAM's *via* CuAAC reaction. AFM topography images (Figure 12II. a-c) and line profiles (Figure 12II. d-f), confirmed the success of the various stages of film development. The adsorption of azidoundecanethiol into the inner holes was clearly seen in the AFM topography image (Figure 12II. b). Changes in surface morphology were also evident after grafting the PS-Alkyne into the cavities of the Cbz-TEG arrays *via* the CuAAC reaction (Figure 12II. c).

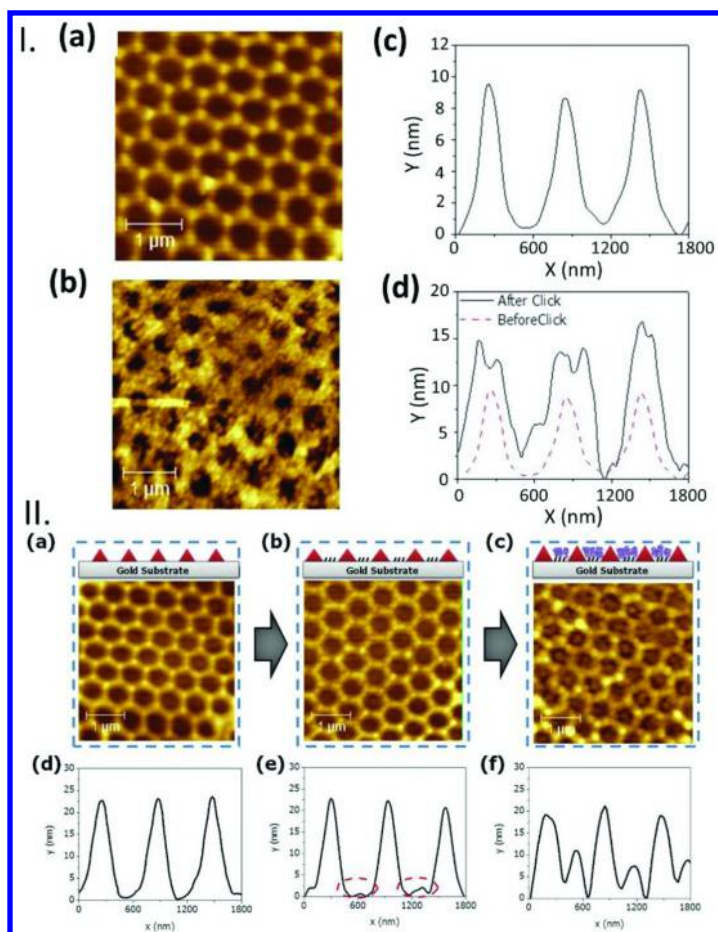


Figure 12. I. AFM topography 2D images ($4 \times 4 \mu\text{m}$): (a) after electrodeposition of Cbz-Alkyne and dissolution of PS microspheres (inverse colloidal Cbz-alkyne arrays), (b) after grafting PS-N3. Line profile analysis of (c) cavities after electrodeposition of Cbz-alkyne and PS microspheres removal, and (d) Cbz-Alkyne arrays before and after CuAAC reaction with PS-N3. II. AFM topography 2D images ($4 \times 4 \mu\text{m}$): (a) inverse colloidal Cbz-TEG array, (b) after backfilling cavities with azidoundecanethiol, and (c) after grafting PS-Alkyne via CuAAC reaction to azidoundecanethiol. Line profile analysis: (d) inverse colloidal Cbz-TEG array, (e) after backfilling cavities with azidoundecanethiol, and (f) after grafting PS-Alkyne via CuAAC reaction to azidoundecanethiol. Reprinted with permission from ref (33). Copyright (2012) Elsevier.

Conclusion

In conclusion, a facile approach of creating well-defined patterned polymer brushes by combining the techniques of 2D colloidal templating, electrodeposition of a macroinitiator, SIP *via* ATRP, RAFT polymerization, and “click” reaction was demonstrated. A non-photolithographic electrochemical patterning of polypyrrole arrays using single-layered colloidal templates on the pyrolytic graphite (HOPG) was firstly developed. Electrodeposition of the electroactive initiators or clickable macromolecules render a nanopatterned surface that allowed for further functionalization. Further functionalization includes “grafting from” *via* SI-controlled radical polymerization and “grafting to” *via* CuAAC reaction. The binary brush system on a nanopatterned surface was also made possible by backfilling the cavities with another initiator or functional groups. AFM was proved to be a very useful tool to monitor the morphology and thickness changes of the nanopatterned polymer brush system.

In the future, it should be possible to focus on both the formation of more complex polymer brush systems (block copolymers, mixed brushes, etc.) and the electro-optical properties of the underlying conjugated polymer and CPN films. Another future route is the incorporation of binary biological arrays, *e.g.* controlled or tunable absorption of various molecules into the templated Cbz-PPEGMEMA-CTA cavities with proteins or other biological macromolecules. Applications are being targeted for dual responsive sensors, stimuli-responsive wetting properties, photonic crystals, diffraction gates, surface-enhanced Raman scattering, and the tethering of biological receptors on the conducting substrate.

References

1. Diaz, A. F.; Kanazawa, K. K.; Gardini, G. P. *J. Chem. Soc., Chem. Commun.* **1979**, 635–636.
2. Genies, E. M.; Bidan, G.; Diaz, A. F. *J. Electroanal. Chem. Interfacial Electrochem.* **1983**, *149*, 101–113.
3. Gorelikov, I.; Kumacheva, E. *Chem. Mater.* **2004**, *16*, 4122–4127.
4. Mrozek, M. F.; Xie, Y.; Weaver, M. J. *Anal. Chem.* **2001**, *73*, 5953–5960.
5. Taranekar, P.; Baba, A.; Fulghum, T. M.; Advincula, R. *Macromolecules* **2005**, *38*, 3679–3687.
6. Taranekar, P.; Fulghum, T.; Patton, D.; Ponnappati, R.; Clyde, G.; Advincula, R. *J. Am. Chem. Soc.* **2007**, *129*, 12537–12548.
7. Cao, P.-F.; Felipe, M. J.; Advincula, R. C. *Macromol. Chem. Phys.* **2013**, *214*, 386–395.
8. Zhao, B.; Brittain, W. J. *Prog. Polym. Sci.* **2000**, *25*, 677–710.
9. Tsukruk, V. V. *Prog. Polym. Sci.* **1997**, *22*, 247–311.
10. Radhakrishnan, B.; Ranjan, R.; Brittain, W. J. *Soft Matter* **2006**, *2*, 386–396.
11. Braunecker, W. A.; Matyjaszewski, K. *Prog. Polym. Sci.* **2008**, *33*, 165.
12. Perrier, S.; Takolpuckdee, P. *J. Polym. Sci., Part A: Polym. Chem.* **2005**, *43*, 5347–5393.
13. Baum, M.; Brittain, W. J. *Macromolecules* **2002**, *35*, 610–615.

14. Grande, C. D.; Tria, M. C.; Jiang, G.; Ponnampati, R.; Advincula, R. *Macromolecules* **2011**, *44*, 966–975.
15. Tria, M. C.; Liao, K.-S.; Alley, N.; Curran, S.; Advincula, R. *J. Mater. Chem.* **2011**, *21*, 10261–10264.
16. Patton, D. L.; Taranekar, P.; Fulghum, T.; Advincula, R. *Macromolecules* **2008**, *41*, 6703–6713.
17. Tsarevsky, N. V.; Matyjaszewski, K. *Chem. Rev.* **2007**, *107*, 2270–2299.
18. Huang, X.; Wirth, M. J. *Anal. Chem.* **1997**, *69*, 4577–4580.
19. Sedjo, R. A.; Mirous, B. K.; Brittain, W. J. *Macromolecules* **2000**, *33*, 1492–1493.
20. Wang, Y.-P.; Pei, X.-W.; He, X.-Y.; Lei, Z.-Q. *Eur. Polym. J.* **2005**, *41*, 737–741.
21. Matrab, T.; Chehimi, M. M.; Perruchot, C.; Adenier, A.; Guillez, A.; Save, M.; Charleux, B.; Cabet-Deliry, E.; Pinson, J. *Langmuir* **2005**, *21*, 4686–4694.
22. Heinze, J.; Frontana-Uribe, B. A.; Ludwigs, S. *Chem. Rev.* **2010**, *110*, 4724–4771.
23. Ofir, Y.; Moran, I. W.; Subramani, C.; Carter, K. R.; Rotello, V. M. *Adv. Mater.* **2010**, *22*, 3608–3614.
24. del Campo, A.; Arzt, E. *Chem. Rev.* **2008**, *108*, 911–945.
25. Braun, P. V.; Wiltzius, P. *Curr. Opin. Colloid Interface Sci.* **2002**, *7*, 116–123.
26. Tian, S.; Wang, J.; Jonas, U.; Knoll, W. *Chem. Mater.* **2005**, *17*, 5726–5730.
27. Park, J. Y.; Dutta, P.; Advincula, R. *Soft Matter* **2011**, *7*, 3775–3779.
28. Pernites, R. B.; Venkata, S. K.; Tiu, B. D. B.; Yago, A. C. C.; Advincula, R. C. *Small* **2012**, *8*, 1669–1674.
29. Pernites, R. B.; Felipe, M. J. L.; Foster, E. L.; Advincula, R. C. *ACS Appl. Mater. Interfaces* **2011**, *3*, 817–827.
30. Pernites, R. B.; Foster, E. L.; Felipe, M. J. L.; Robinson, M.; Advincula, R. C. *Adv. Mater.* **2011**, *23*, 1287–1292.
31. Foster, E. L.; Tria, M. C. R.; Pernites, R. B.; Addison, S. J.; Advincula, R. C. *Soft Matter* **2012**, *8*, 353–359.
32. Kaewtong, C.; Jiang, G.; Park, Y.; Fulghum, T.; Baba, A.; Pulpoka, B.; Advincula, R. *Chem. Mater.* **2008**, *20*, 4915–4924.
33. Foster, E. L.; Bunha, A.; Advincula, R. *Polymer* **2012**, *53*, 3124–3134.

Chapter 13

RAFT Polymerization on Particle Surfaces: Same Goal, Different Strategies

Lei Wang, Junting Li, Yang Zheng, Yucheng Huang, Yali Qiao, and
Brian C. Benicewicz*

Department of Chemistry and Biochemistry, University of South Carolina,
Room 232, 541 Main Street, Columbia, South Carolina 29208

*E-mail: benice@sc.edu

Reversible addition-fragmentation chain transfer (RAFT) polymerization is an important technique for surface functionalization of nanoparticles. It provides a powerful toolbox to tune the properties of composites. The RAFT agent, 4-cyanopentanoic acid dithiobenzoate (CPDB), was anchored on silica nanoparticles via surface silane chemistry with different graft densities. Methacrylic acid (MAA) and 6-azidohexyl methacrylate (AHMA) were polymerized on nanoparticles in a controlled manner via the RAFT technique. A variety of polyMAA (PMAA) and polyAHMA (PAHMA) brushes with different polymer chain lengths and low PDIs (<1.2) were prepared. The nanoparticles were characterized by FTIR, TGA, ¹H NMR and TEM. Postfunctionalization of the surface attached polymers was conducted using bio-functional groups and the resulting polymer nanocomposites may have important biomedical applications.

Introduction

Polymer grafted nanoparticles are important materials and have found applications in chemosensors, biomedical devices, optoelectronics, coatings and dielectrics (1–4). Surface functionalization is a key step in the preparation of polymer grafted nanoparticles (5). The development of nanoparticle surface functionalization strategies has evolved in several stages (Figure 1)

(6): (1) The early stage of simple small molecule modification to alter the hydrophobic/hydrophilic properties of nanoparticles or to further introduce other functional groups; (2) Surface modification with a single population of polymer brushes to introduce new properties to the composites and enhance the matrix compatibility; (3) Functionalization with bimodal polymer brushes to further enhance the compatibility in matrices by independently controlling the entropic/enthalpic interactions; (4) Modification with mixed bimodal brushes to introduce different polymer and property varieties on particles; (5) Modification with multimodal brushes with integrated functionalities on nanoparticles to meet specific applications in complicated systems (6). This process “from the simple to the advanced” allows researchers to understand the nature of surface functionalization and choose appropriate tools to build a variety of architectures on particle surfaces.

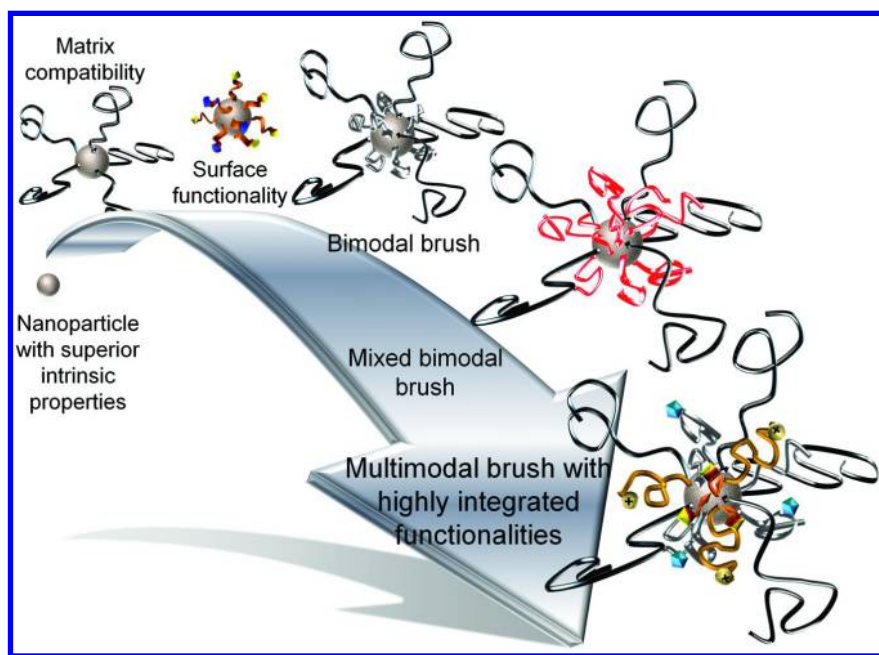


Figure 1. The development of surface functionalization of nanoparticles: from the simple to the advanced. Reproduced with permission from Reference (6). Copyright (2014). American Chemical Society.

The preparation of polymer grafted nanoparticles via surface functionalization is usually conducted using both “grafting to” and “grafting from” strategies. In the “grafting to” approach, free polymers diffuse to the particles and couple with the functional groups on the particle surfaces. It usually provides a relatively low graft density because of the steric hindrance between the previously attached

and free polymer brushes during the diffusion process. A variety of polymers, such as polydimethylsiloxane (PDMS) and poly(glycidyl methacrylate) (PGMA) have been coated on nanoparticles (7–10). In the “grafting from” strategy, polymers are prepared from the surface of nanoparticles. High graft densities can be attained by avoiding the steric limitations of diffusing chains. Controlled radical polymerizations (CRP), including nitroxide-mediated polymerization (NMP) (11), atom transfer radical polymerization (ATRP) (12) and reversible addition-fragmentation chain transfer (RAFT) (13) polymerization, have been widely utilized to prepare polymer grafted nanoparticles via the “grafting from” technique.

The RAFT technique uses a degenerative chain transfer method to control polymerization, rather than employing a persistent radical in the system as in NMP and ATRP (13). One of unique features of the RAFT technique is its applicability to functional monomers, such as vinyl acetate (14) and N-vinyl pyrrolidone (15). It has been successfully applied in mediating polymerizations of a variety of monomers under mild conditions with controllable molecular weights, narrow polydispersity and sophisticated architectures. Surface-initiated (SI) RAFT polymerization has been used to grow a variety of polymer shells on different substrate nanoparticles. The properties of the composites can be tailored by choosing different substrate-shell combinations. The SI-RAFT technique can thus be used to affect the dispersion of nanoparticles in small molecule or polymer matrices which would further influence the properties. In this paper, we discuss the RAFT polymerization on particle surfaces to develop polymer-grafted nanoparticles with desired properties.

Poly(carboxylic acids) are significant water soluble polymers with pH responsive properties. They are protonated in low pH environments and deprotonate in high pH systems. Thus, they have been used widely to conjugate other ion moieties to introduce new functionalities. In addition, they have been employed to couple with hydroxyl or amine based functionalities via covalent bonds. Based on these characteristics, carboxylic acid functionalized nanoparticles have been used in the drug delivery fields (16, 17). Thus, we are motivated to develop poly(carboxylic acid) grafted nanoparticles for delivery application. In the first part of this paper, we review our recent work on polyacid grafted particles. In the second part, we report an alternate strategy to achieve the same goal as our previous work. In addition, we report the post-functionalization of poly(carboxylic acid) grafted nanoparticles for applications in aqueous media.

Cyclodextrin is an effective molecule to capture the signal molecules known as acylated homoserine lactones (AHLs), which are released by bacteria in their quorum sensing (QS) process (18). QS allows bacteria to communicate with each other and thus makes bacteria much more resistant to antibiotics compared to individual bacteria. Thus, we were motivated to prepare cyclodextrin grafted nanoparticles to bind AHLs, lower their concentration and finally shut down QS. Cyclodextrin grafted nanoparticles could be very important in capturing signal molecules in biofilms, in which bacteria are protected by extracellular polymeric secretions (EPS). Free cyclodextrin will be blocked by the sticky EPS barrier before accessing bacterial cells whereas nanoparticles can penetrate the biofilm's EPS.

Experimental

Materials

All chemicals were purchased from Fisher or Sigma Aldrich and used as-received unless otherwise stated. Trimethylsilyldiazomethane (2.0 M in hexanes) and 4-cyanopentanoic acid dithiobenzoate (CPDB) were purchased from TCI and Strem Chemical Inc., respectively. RAFT agent CPDB coated silica nanoparticles were prepared based on previous literature (19). 3-Aminopropyldimethylethoxysilane was obtained from Gelest and used as-received. NBD based fluorescent dye was prepared according to the literature (20). Methacrylic acid (99.5%, Acros) was purified by passing through an activated neutral alumina column. AIBN was purified via recrystallization from methanol before use. The beta-lactam antibiotic penicillin-G was obtained from Sigma-Aldrich Inc. and used for all experiments.

Instrumentation

The ^1H NMR characterization was conducted using a Varian Mercury spectrometer 300/400 using CD_3OD or CDCl_3 as the solvent. Gel permeation chromatography (GPC) was conducted using a Waters PL-GPC-120 with a 515 HPLC pump, a 2410 refractive index detector, and three Styragel columns (the columns consisted of HR1, HR3 and HR4 with their corresponding effective molecular weight ranges of 100-5000, 500-30000, and 5000-500000, respectively) to characterize the molecular weights and PDI's. THF was employed as the eluent at 30 °C and a flow rate of 1.0 mL/min. Calibration was conducted using poly(methyl methacrylate) or polystyrene standards obtained from Polymer Laboratories. Samples were processed by filtration through microfilters with a pore size of 0.2 μm before analysis. Infrared spectra were recorded with a PerkinElmer Spectrum 100 spectrometer. TEM imaging was conducted using a Hitachi 8000 transmission electron microscope with an operating voltage of 200 kV. Samples were prepared by dropping sample solutions on the carbon-coated copper grids and subsequent drying in a fume hood before characterization. TGA characterization was conducted using a TA Instruments Q5000 with a heating rate of 10°C/min from 25°C to 800°C~1000°C under nitrogen flow.

Synthesis of 1-Azido-6-hydroxyhexane

1-Chlorohexanol (6.83g, 0.05 mol) and sodium azide (6.50g, 0.10 mol) were dissolved in 50 ml water. The resulting solution was stirred at 80 °C for 12 h. The cooled solution went through extraction with diethyl ether (3×50 mL), drying with anhydrous sodium sulfate and followed by filtration. After removal of the solvent, a colorless liquid was obtained and dried under vacuum to constant weight (yield, 6.00g, 84%). ^1H NMR (300 MHz, CDCl_3): δ (ppm) 1.40 (m, 4H, CH_2), 1.51-1.64 (m, 4H, CH_2), 3.24 (t, 2H, CH_2N_3), 3.66 (t, 2H, CH_2O).

Synthesis of 6-Azidoethyl Methacrylate (AHMA)

1-Azido-6-hydroxyhexane (7.34 g, 51 mmol), methacrylic acid (3.87 g, 45 mmol), 4-(dimethylamino)pyridine (DMAP) (1.84 g, 15 mmol) were dissolved in 100 mL methylene chloride and the resulting solution was cooled in an ice bath. A methylene chloride solution (50 mL) of dicyclohexylcarbodiimide (DCC) (10.32 g, 50 mmol) was then added slowly. The resulting solution was then transferred to room temperature and followed by overnight stirring. After removal of the precipitate and solvent, the crude compound was purified via silica gel column chromatography (hexane : ethyl acetate = 10:1). A colorless liquid was obtained and dried under vacuum to constant weight (yield: 5.91 g, 62.2%). ¹H NMR (300 MHz, CDCl₃): δ (ppm) 1.40 (m, 4H, CH₂), 1.55-1.70 (m, 4H, CH₂), 1.95 (s, 3H, CH₃C), 3.24 (t, 2H, CH₂N₃), 4.16 (t, 2H, CH₂O), 5.54 (s, 1H, =CH), 6.12 (s, 1H, =CH). ¹³C NMR (400 MHz, CDCl₃): 18.75, 26.04, 26.86, 28.98, 29.28, 51.6, 64.93, 125.78, 136.60, 167.90.

Surface-Initiated RAFT Polymerization of AHMA

AHMA (0.536 g, 2.54 mmol), CPDB immobilized silica nanoparticles (93.05 mg, 0.23 groups/nm²) and dry THF (2.5 mL) were added to an appropriate size Schlenk tube. The solution was sonicated until all the particles were dissolved in solution. Initiator V-70 (0.102 mL, 5 mM) was then added to the above solution. The resulting solution was degassed by four freeze-pump-thaw cycles followed by back filling with nitrogen. The tube was then placed in an oil bath of 40 °C and quenched in ice water at the desired time.

Preparation of Dye-Labeled Poly(β -CD) Grafted Silica Nanoparticles

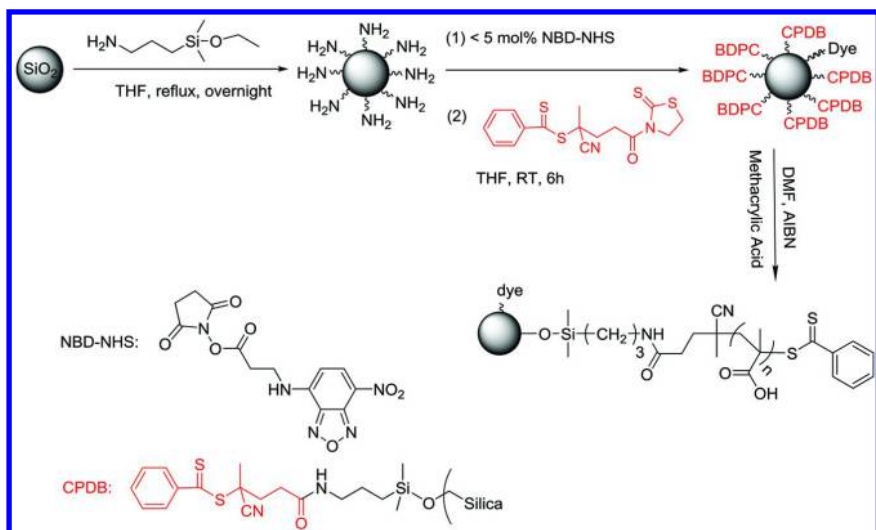
A DMF solution of β -CD (3.711 g, 3.27 mmol), N,N'-dicyclohexylcarbodiimide (DCC, 0.54 g, 2.616 mmol) and 4-dimethylaminopyridine (DMAP, 26.6 mg, 0.218 mmol) were added to a 10 mL dry DMF solution of dye-labeled poly(methacrylic acid) grafted silica nanoparticles (252 mg). The reaction was stirred at room temperature overnight. Then the reaction solution was poured into 200 mL ethyl ether followed by centrifugation at 3000 rpm for 5 min. The recovered particles were then redispersed in 20 mL of ethanol and subjected to a dialysis process to further remove impurities. The isolated dye-labeled poly(β -CD) grafted silica nanoparticles were finally dissolved in water for further use.

Results and Discussion

Poly(carboxylic acid) Grafted Nanoparticles

We have developed a series of poly(carboxylic acid) grafted nanoparticles for drug delivery applications via SI-RAFT (19, 21, 22). The first synthetic strategy is shown in Scheme 1 (19). Essentially, it contains the preparation of RAFT agent (CPDB) coated nanoparticles with dye labeling and the

variety of polymer brush grafted particles with different chain lengths and densities were synthesized in a controlled manner. Figure 2 shows the ^1H NMR results that confirmed the structure of the poly(carboxylic acid) grafted silica nanoparticles.



Scheme 2. The synthesis of dye-labeled poly(carboxylic acid) grafted silica nanoparticles via direct polymerization of MAA. Reproduced with permission from Reference (19). Copyright (2013). American Chemical Society.

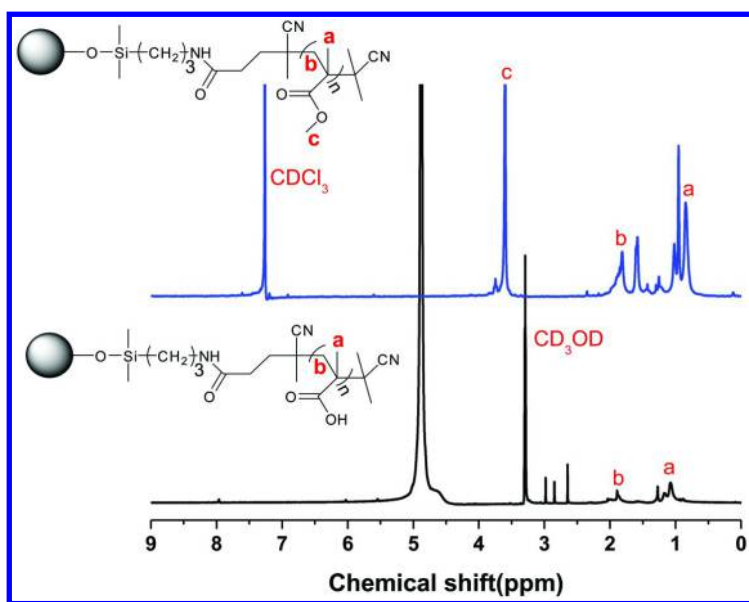


Figure 2. ^1H NMR of poly(carboxylic acid) grafted silica nanoparticles and their methylation by trimethylsilyldiazomethane. Reproduced with permission from Reference (19). Copyright (2013). American Chemical Society.

Trimethylsilyldiazomethane (TMSI) was used to methylate the acid groups on PMAA grafted particles for GPC analysis in an organic solvent. The poly(carboxylic acid) grafted silica nanoparticles with dye-labelling were yellow in DMSO and showed the strong fluorescence under UV radiation (Figure 3) (19). The as-synthesized nanoparticles had a average diameter of 30 nm as shown in the TEM image (Figure 4) (19).

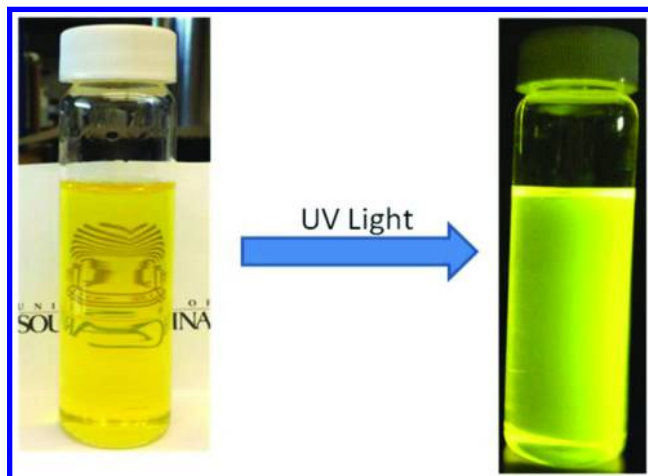


Figure 3. Images of dye-labeled poly(carboxylic acid) grafted silica nanoparticles under UV radiation in DMSO. Reproduced with permission from Reference (19). Copyright (2013). American Chemical Society.

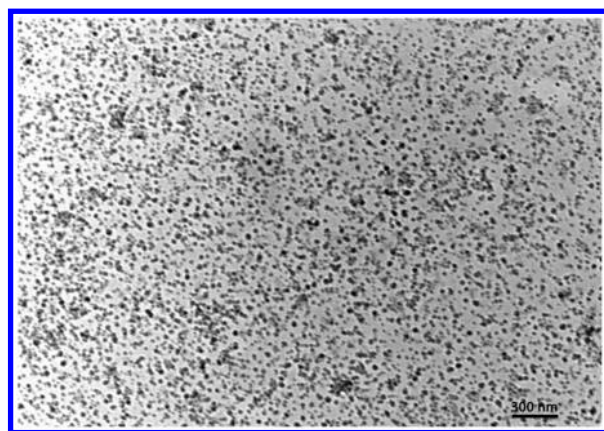
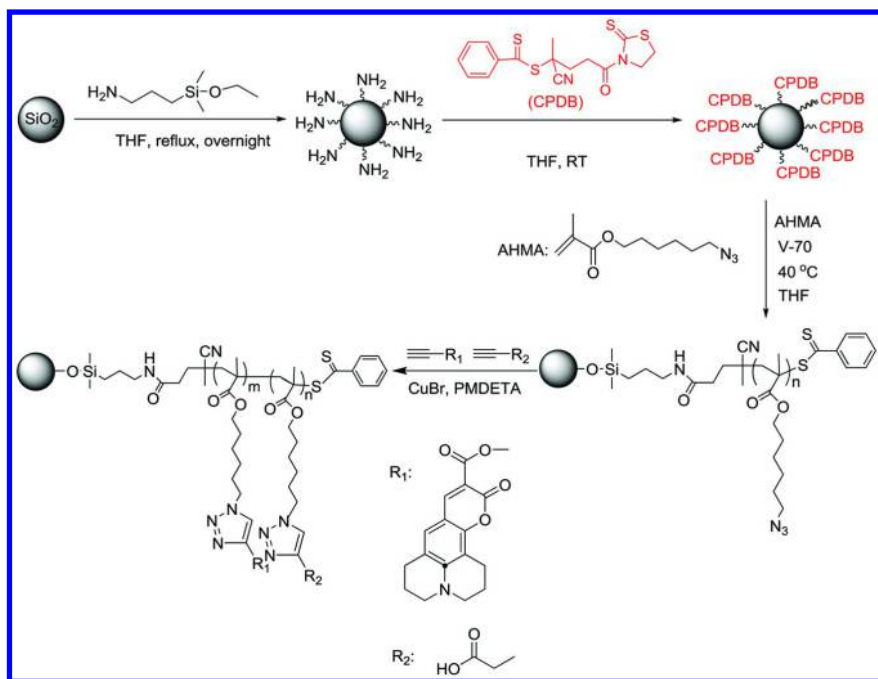


Figure 4. TEM of dye-labeled poly(carboxylic acid) grafted silica nanoparticles. Size bar = 300 nm. Reproduced with permission from Reference (19). Copyright (2013). American Chemical Society.

Alternate Strategy for Dye-Labeled Poly(carboxylic acid) Grafted Nanoparticles

An alternate synthetic strategy was developed to prepare the dye-labeled poly(carboxylic acid) grafted nanoparticles, as shown in Scheme 3. Essentially, it was based on the “one-pot” click reactions between the PAHMA grafted silica nanoparticles and alkyne functionalized molecules (alkyne based coumarin 343 fluorescent dye and 4-pentynoic acid). Thus, fluorescent dye molecules and carboxylic acids were incorporated onto the PAHMA grafted nanoparticles sequentially. The PAHMA grafted silica nanoparticles were synthesized by surface-initiated RAFT polymerization of AHMA on CPDB coated silica nanoparticles, which were synthesized by the reaction between activated CPDB and amino-functionalized silica nanoparticles (Scheme 3). The graft density of CPDB coated nanoparticles can be determined by their Uv-vis absorption at 305 nm.



Scheme 3. Synthesis of dye-labeled poly(carboxylic acid) grafted silica nanoparticles.

The surface-initiated RAFT polymerization of AHMA was conducted with a ratio between reactants of ($[\text{AHMA}]/[\text{CPDB}]/[\text{V-70}] = 500:1:0.1$) at 40 °C in THF. A variety of PAHMA grafted silica nanoparticles with different graft densities and chain lengths were prepared, as shown in Table 1. The molecular weights of these surface attached PAHMA varied from 12,000 to 28,000 g/mol and the PDIs were generally lower than 1.2. The graft densities were 0.23 – 0.42 chains/nm². The

IR spectra showed that the as-synthesized PAHMA grafted nanoparticles have a peak around 2100 cm^{-1} ascribed to the azide moiety and a peak around 1065 cm^{-1} ascribed to the silica. The loading of the dye molecules and the amount of carboxylic acids can be controlled by using PAHMA grafted nanoparticles with different graft densities and chain lengths, and the feed ratio between the dyes and 4-pentynoic acid.

Table 1. Surface-initiated RAFT polymerization of AHMA on particles^a

Entry	M_n , GPC (g/mol)	PDI	Graft Density (chains/ nm^2)
1	27280	1.37	0.42
2	21310	1.17	0.33
3	28050	1.16	0.24
4	12350	1.12	0.23
5	27060	1.10	0.23

^a Note: For all the polymerizations, ($[\text{AHMA}]/[\text{CPDB}]/[\text{V-70}] = 500:1:0.1$) and the reaction temperature was 40 °C. The surface attached polymers were cleaved by hydrofluoric acid (HF) before GPC analysis.

The “click” reaction was conducted between the as-synthesized PAHMA grafted nanoparticles and alkyne functionalized molecules with a ratio of 1:1.2 between $-\text{N}_3$ and the alkyne groups. The amount of alkyne functionalized coumarin 343 accounted for 1 mol % ~ 10 mol % of the alkyne moieties. The CuBr and PMDETA were 0.1 equivalent compared to $-\text{N}_3$. After the approximately 10 h reaction between $-\text{N}_3$ and alkyne functionalized coumarin 343, 4-pentynoic acid was added to the reaction solution. IR spectroscopy was used to monitor the progress of the “click” reaction. After 24 - 48 hours, the reaction was completed, which was confirmed by the disappearance of the azide peak around 2100 cm^{-1} as shown in Figure 5.

We recently investigated the antimicrobial application of the poly(carboxylic acid) grafted nanoparticles when conjugated with antibiotics (21). The nanoparticle-penicillin G (PenG) complex demonstrated much higher activities than free PenG on killing both gram positive and gram negative bacteria. The complexes showed significantly high activities over antibiotic-resistant bacteria such as methicillin-resistant *S. aureus* (MRSA), as shown in Figure 6.

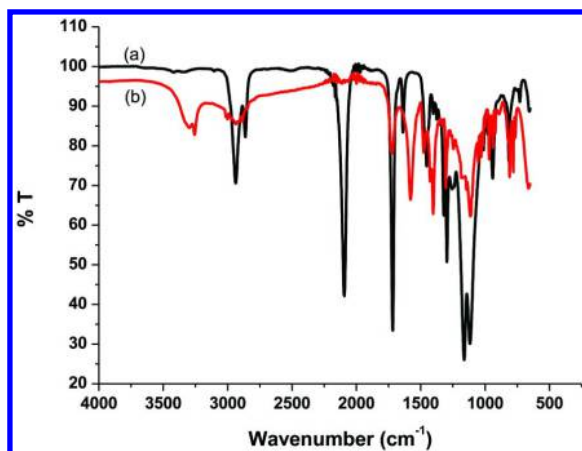


Figure 5. IR spectra of PAHMA grafted nanoparticles (a) before and (b) after “click” reaction.

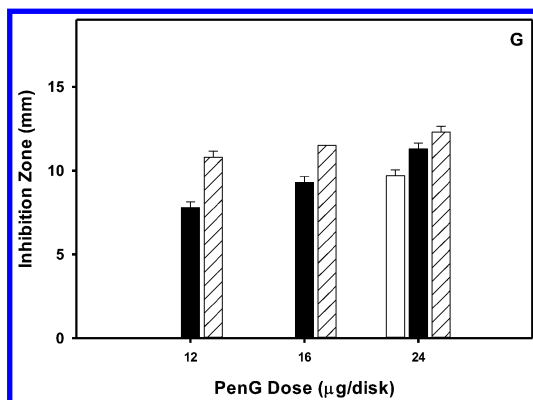


Figure 6. Disk-diffusion assays using community-associated MRSA (CA-MRSA): Antimicrobial activity of free Penicillin G (white), Penicillin G-complexed to the monolayer carboxylic acids coated silica nanoparticles (black), and PenG-complexed to poly(carboxylic acid) grafted silica nanoparticles (hatched). The same doses of penicillin G were used in the different groups. Please note that the free Penicillin G was tested at all doses, but the inhibition zone at 12 and 16 μg/disk was ~ 0 mm, and thus does not display in the figure. Reproduced with permission from Reference (21). Copyright (2014). Royal Society of Chemistry.

We also have prepared the poly(carboxylic acid) brushes on $\text{SiO}_2/\text{Fe}_3\text{O}_4$ magnetic nanoparticles via the direct SI-RAFT of methacrylic acid (22). As shown in Figure 7, the polymer grafted magnetic particles can be collected by a magnet and then redispersed in solution via sonication. The poly(carboxylic acid) grafted magnetic nanoparticles were used recyclably to kill bacteria which can prevent the nano-based pollution to biological environments (22).

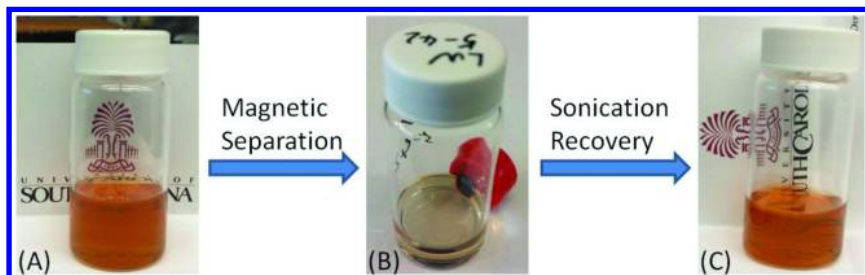


Figure 7. Poly(carboxylic acid) grafted $\text{SiO}_2/\text{Fe}_3\text{O}_4$ magnetic nanoparticles in dimethylformamide (DMF): (A) Normal state; (B) Under magnetic field; (C) Sonication-recovery and 14 days later. Reproduced with permission from Reference (22). Copyright (2015). Royal Society of Chemistry.

Cyclodextrin (CD) Grafted Nanoparticles

Polymer grafted silica nanoparticles containing β -CD side groups were prepared via the condensation reaction between the grafted poly(carboxylic acid) and the hydroxyl groups on β -CD. The carboxylic acid loading on dye-labeled poly(carboxylic acid) grafted silica nanoparticles can be controlled by tailoring the length of the surface grafted poly(carboxylic acid) brushes as well as the graft densities. The TGA data showed that the surface polymer supported chains with multiple β -CD accounted for 61.7% by weight for particles having a poly(carboxylic acid) brush density of 0.18 chains/ nm^2 and molecular weight of 54,900 mol/g (Figure 8). The β -CD side chain based polymer grafted nanoparticles showed strong fluorescence under UV light even after multiple-step surface chemical modifications (Figure 9). The polycyclodextrin grafted nanoparticles can be used to trap the signal molecule AHLs in the bacterial quorum sensing (QS) process.

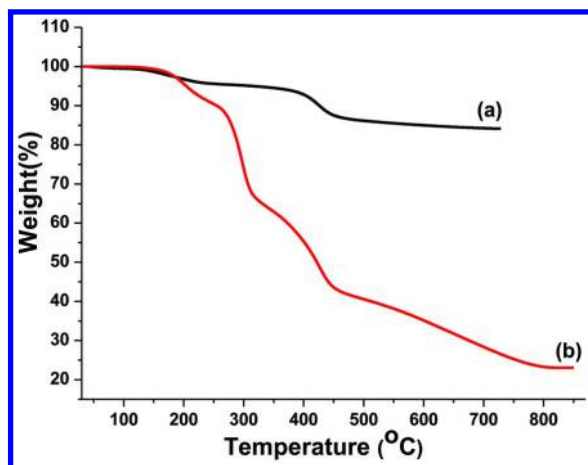


Figure 8. TGA of (a) dye-labeled poly(methacrylic acid) grafted silica nanoparticles; (b) dye-labeled poly(β -CD) grafted silica nanoparticles.

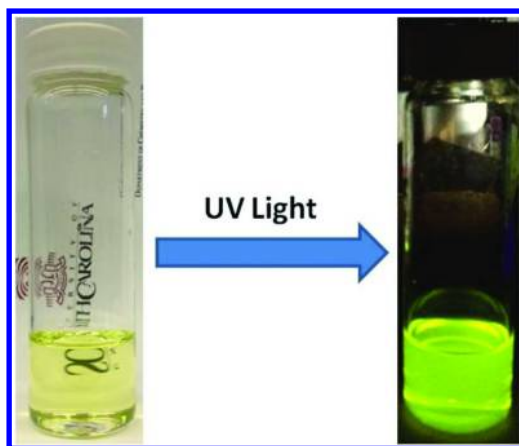


Figure 9. Photograph of dye-labeled poly(β -CD) grafted silica nanoparticles in DMSO.

Conclusions

Surface functionalization is critical in the preparation of polymer grafted nanoparticles. RAFT polymerization is a significant technique in the surface functionalization of nanoparticles with polymers. A RAFT agent was anchored on nanoparticles through surface silane chemistry and the graft densities were controllably adjusted by the reaction conditions. A variety of poly(carboxylic acid) and poly(AHMA) grafted nanoparticles were prepared with different chain lengths and graft densities in a controlled manner, using several different synthetic strategies. Poly(carboxylic acid) grafted particles had excellent dispersion in water and are important platforms for further bio-molecule conjugation/attachment via covalent or non-covalent linkages. Poly(AHMA) grafted particles are also convenient platforms for postfunctionalization via the alkyne-azide click reaction. Cyclodextrin grafted nanoparticles were prepared based on the synthetic strategy of postfunctionalization. This strategy may find broad relevance in biomedical applications.

Acknowledgments

The authors would like to gratefully acknowledge Prof. Alan W. Decho at the University of South Carolina for useful discussions and the support from NSF (BME-1032579).

References

1. Zou, H.; Wu, S.; Shen, J. *Chem. Rev.* **2008**, *108*, 3893–3957.
2. Pothayee, N.; Pothayee, N.; Jain, N.; Hu, N.; Balasubramaniam, S.; Johnson, L.; Davis, R.; Sriranganathan, N.; Riffle, J. *Chem. Mater.* **2012**, *24*, 2056–2063.
3. Qiao, Y.; Islam, M. S.; Wang, L.; Yan, Y.; Zhang, J.; Benicewicz, B. C.; Ploehn, H.; Tang, C. *Chem. Mater.* **2014**, *26*, 5319–5326.
4. Li, Y.; Wang, L.; Natarajan, B.; Tao, P.; Benicewicz, B. C.; Ullal, C.; Schadler, L. S. *RSC Adv.* **2015**, *5*, 14788–14795.
5. Li, J.; Wang, L.; Benicewicz, B. C. *Langmuir* **2013**, *29*, 11547–11553.
6. Li, Y.; Krentz, T. M.; Wang, L.; Benicewicz, B. C.; Schadler, L. S. *ACS Appl. Mater. Interfaces.* **2014**, *6*, 6005–6021.
7. Tao, P.; Li, Y.; Siegel, R. W.; Schadler, L. S. *J. Mater. Chem. C.* **2013**, *1*, 86–94.
8. Li, Y.; Tao, P.; Viswanath, A.; Benicewicz, B. C.; Schadler, L. S. *Langmuir* **2013**, *29*, 1211–1220.
9. Tao, P.; Li, Y.; Rungta, A.; Viswanath, A.; Gao, J.; Benicewicz, B.; Siegel, R.; Schadler, L. *J. Mater. Chem.* **2011**, *21*, 18623–18629.
10. Tao, P.; Viswanath, A.; Schadler, L.; Benicewicz, B.; Siegel, R. *ACS Appl. Mater. Interfaces* **2011**, *3*, 3638–3645.
11. Hawker, C. J.; Bosman, A. W.; Harth, E. *Chem. Rev.* **2001**, *101*, 3661–3688.
12. Matyjaszewski, K.; Xia, J. *Chem. Rev.* **2001**, *101*, 2921–2990.

13. Barner-Kowollik, C. In *Handbook of RAFT Polymerization*; Barner-Kowollik, C., Ed.; Wiley-VCH: Weinheim, Germany, 2008, pp 1–4.
14. Schmitt, J.; Blanchard, N.; Poly, J. *Polym. Chem.* **2011**, *2*, 2231–2238.
15. Guinaudeau, A.; Mazières, S.; Wilson, D. J.; Destarac, M. *Polym. Chem.* **2012**, *3*, 81–84.
16. Fuqua, C.; Parsek, M. R.; Greenberg, E. P. *Annu. Rev. Genet.* **2003**, *35*, 439–468.
17. Cash, B. M.; Wang, L.; Benicewicz, B. C. *J. Polym. Sci., Part A: Polym. Chem.* **2012**, *50*, 2533–2540.
18. Pothayee, N.; Pothayee, N.; Jain, N.; Hu, N.; Balasubramaniam, S.; Johnson, L.; Davis, R.; Sriranganathan, N.; Riffle, J. *Chem. Mater.* **2012**, *24*, 2056–2063.
19. Wang, L.; Benicewicz, B. *ACS Macro Lett.* **2013**, *2*, 173–176.
20. Mayer, T. G.; Weingart, R.; Münstermann, F.; Kawada, T.; Kurzchalia, T.; Schmidt, R. R. *Eur. J. Org. Chem.* **1999**, *10*, 2563–2571.
21. Wang, L.; Chen, Y. P.; Miller, K. P.; Cash, B. M.; Jones, S.; Glenn, S.; Benicewicz, B. C.; Decho, A. W. *Chem. Commun.* **2014**, *50*, 12030–12033.
22. Wang, L.; Cole, M.; Li, J.; Zheng, Y.; Chen, Y. P.; Miller, K. P.; Decho, A. W.; Benicewicz, B. C. *Polym. Chem.* **2015**, *6*, 248–255.

Chapter 14

One-Pot RAFT Synthesis of Triphenylphosphine-Functionalized Amphiphilic Core-Shell Polymers and Application as Catalytic Nanoreactors in Aqueous Biphasic Hydroformylation

Rinaldo Poli,^{*,1} Si Chen,¹ Xuwei Zhang,² Andrés Cardozo,³ Muriel Lansalot,² Franck D'Agosto,² Bernadette Charleux,² Eric Manoury,¹ Florence Gayet,¹ Carine Julcour,³ Jean-François Blanco,³ Laurie Barthe,³ and Henri Delmas³

¹CNRS, Laboratoire de Chimie de Coordination, Toulouse, 31077, France

²CNRS, Chemistry, Catalysis, Polymers & Processes (C2P2), Villeurbanne, 69616, France

³CNRS, Laboratoire de Génie Chimique, Toulouse, 31030, France

*E-mail: rinaldo.poli@lcc-toulouse.fr

Controlled radical polymerization has recently been used to develop polymers engineered for applications as catalytic nanoreactors. In this contribution, we present the joint development, in our laboratories, of core-cross-linked micelles (CCM) for application under aqueous biphasic conditions through the micellar approach, using triphenylphosphine (TPP) as polymer-anchored ligand and rhodium as catalytic metal for the hydroformylation of 1-octene as a model α -olefin. The polymers were synthesized by a one-pot convergent approach using RAFT as controlling method in water, making use of the polymerization-induced self-assembly (PISA) principle. The article will also show the polymer properties in terms of size, polydispersity, swelling, metal coordination and exchange, and interpenetration. It will also illustrate our initial catalytic studies with focus on the effect of the polymer architecture (ligand nature, ligand density, core size, nature of cross-linking)

and of the stirring rate on the catalytic performance (turnover frequency) and catalyst leaching.

Introduction

Controlled radical polymerization, through the wide choice of monomers and polymerization mechanisms, has made it possible to design and synthesize quite complex functionalized macromolecular architectures that seemed out of reach until recently (1). Among a variety of different applications, the area of catalytic nanoreactors is quite recent and rapidly expanding (2–4). This relies on the catalyst confinement in a specific part of the macromolecule which provides a special environment and properties to the catalytic site (affinity for the reaction substrate, size selectivity, site confinement, etc.) while other parts of the macromolecule are responsible for the nanoreactor compatibility with the reaction medium (homogeneous dispersion, response to stimuli such as heat, pH, magnetic fields etc.). Notable examples of this approach are provided by the site confinement principle in multistep cascade processes with non-interpenetrable polymers (5), the development of shell-cross-linked versions of self-assembled catalytic micelles (6), of thermoresponsive phosphine-containing microgels (7, 8), and of shape-selective catalytic nanogels built using molecular imprinting (9, 10). Most of these catalytic nanoreactors were used under homogeneous conditions. Catalyst recovery and recycling has been implemented, in most cases, by ultrafiltration, precipitation, or by thermoregulation.

Efficient catalyst recovery and recycling is a topic of great interest in industrial homogeneous catalysis, particularly when expensive metals and/or ligand systems are used. Among various approaches, the aqueous biphasic protocol is a most attractive one because of the simplicity of the necessary equipment and operating procedures (11). Perhaps the most successful industrial application of the aqueous biphasic approach is the Rhone-Poulenc/Ruhrchemie hydroformylation of propene (12). This involves total confinement of the Rh catalyst in the aqueous phase through coordination with triphenylphosphine trisulfonate (TPPTS). The catalytic transformation occurs homogeneously in the aqueous phase because propene has a low but sufficient solubility in this phase. Hence, the process is not too negatively affected by mass transport limitations. However, it is unfortunately inefficient for higher α -olefins because these are insufficiently soluble in water. This is a general problem in aqueous biphasic catalysis: the organic substrate must have sufficient solubility in water if the catalyst is totally confined in this phase, or the catalyst must have a slight solubility in the organic phase (this is sometimes achieved by use of phase transfer co-catalysts), or finally the reaction occurs only at the interface, in which case the interfacial area can be increased by using surfactants or other additives.

One approach that has attracted considerable attention is micellar catalysis, where the catalyst is anchored to the hydrophobic part of a surfactant molecule that self-assembles into micelles. Amphiphilic diblock copolymers have also been

used for this purpose. The resulting core-functionalized micelles can function as catalytic nanoreactors under aqueous biphasic conditions and many applications have been described (13–18). However, as attractive as it seems, this approach suffers from two major obstacles that limit large scale industrial implementation: because of their dynamic nature, extensive swelling of the micelles can lead to the formation of stable emulsions and to the loss of the free surfactants, even when the critical micelle concentration (CMC) is very low (19–24). Thus, the resulting catalyst leaching, even if low, may be intolerable for large scale production given the cost of the catalytic system. An example is the micellar 1-octene hydroformylation with a rhodium complex anchored to a poly(norbornene)-based amphiphilic diblock copolymer with $CMC = 2.2 \cdot 10^{-6}$ M. The turnover frequency (TOF) of this system was excellent but the loss of catalyst in the organic product phase (9 ppm) was also high (25).

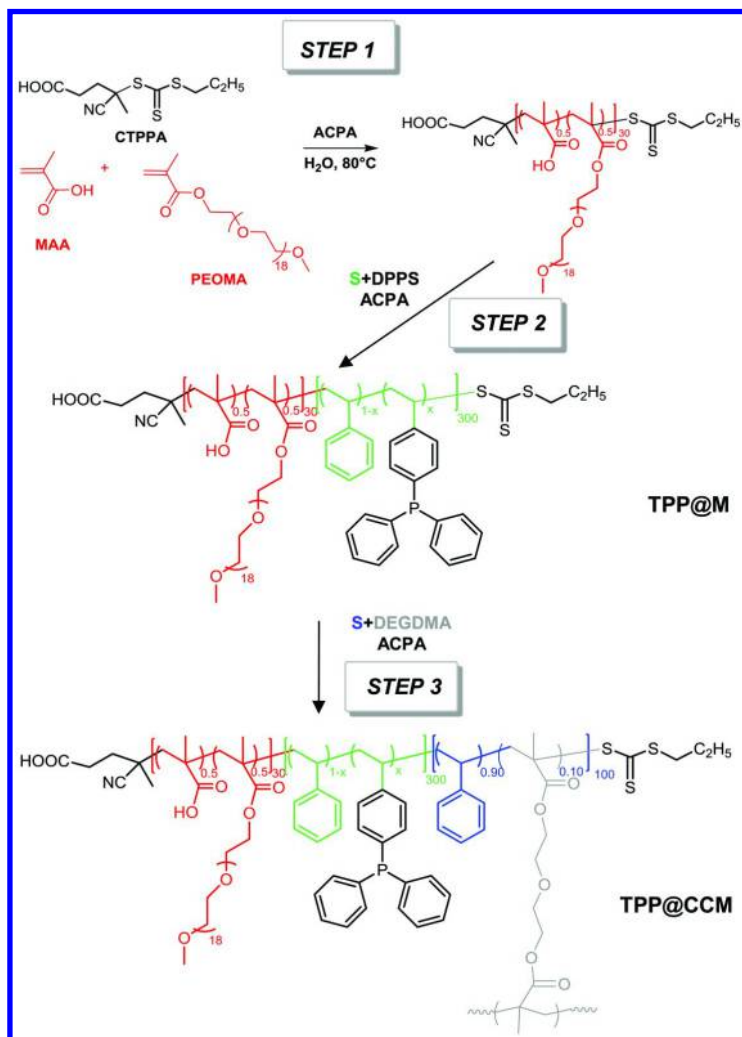
In order to avoid the stable emulsion formation and free surfactant losses, we have recently introduced a new approach consisting of cross-linking amphiphilic block copolymer micelles at the core to generate unimolecular nano-objects. We shall refer to these polymers as core-cross-linked micelles (CCM). The synthetic method leading to our first prototype polymer as well as a few structural variations, its first application to aqueous biphasic catalysis, and its potential for further development, are outlined in this article.

Results and Discussion

Polymer Synthesis

The envisaged catalytic application of our first exploratory study was 1-octene hydroformylation, the homogeneous version of which may be carried out by a triphenylphosphine (TPP) rhodium complex in toluene at high temperatures (80–100°C). Therefore, we considered that a CCM with a polystyrene (PS) core might be suitable. For the hydrophilic shell, several possibilities are available but we initially selected a 1:1 copolymer built with methacrylic acid (MAA) and poly(ethylene oxide) methyl ether methacrylate (PEOMA), since latexes of self-assembled P(MAA-*co*-PEOMA)-*b*-PS block copolymer nano-objects had already been developed in one of our laboratories with good control over the molecular mass and micelle size (26, 27). This synthetic protocol is based on a convergent one-pot polymerization in water using reversible addition-fragmentation chain transfer (RAFT) radical polymerization as the controlling method, whereby following the controlled growth of the hydrosoluble block, chain extension with the hydrophobic monomer in water leads to polymerization-induced self-assembly (PISA) (28, 29). Our polymer synthesis has two main changes relative to previous contributions: *i*) we have used a comonomer mixture of styrene and the ligand-functionalized monomer, 4-diphenylphosphinostyrene (DPPS) in the second step; *ii*) the synthesis was completed with a third step where all chain in the self-assembled micelles were covalently linked together using a cross-linking agent.

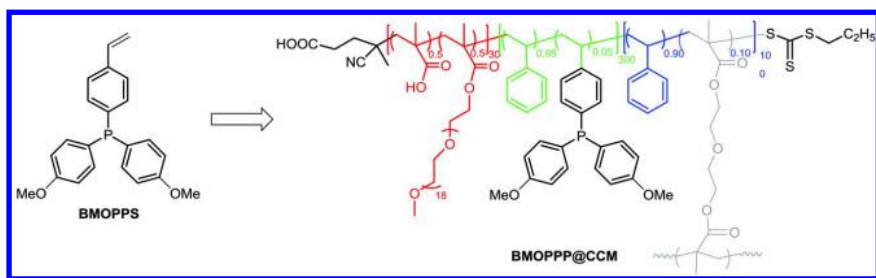
Our synthesis in its original version is summarized in Scheme 1 (30). The initial chain transfer agent (CTA) is the trithiocarbonate compound 4-cyano-4-(thiothiopropylsulfanyl)pentanoic acid (CTPPA) and the homogeneous aqueous process statistically copolymerizing MAA and PEOMA is initiated by the water-soluble initiator 4,4'-azobis(4-cyanopentanoic acid) (ACPA). The monomer/CTA ratio was set to 30 to yield hydrosoluble copolymers containing on average 15 MAA and 15 PEOMA monomer units.



Scheme 1. Synthesis of the core-cross-linked micelles functionalized with triphenylphosphine (TPP@CCM).

The second step involved an S-DPPS mixture. In the initial synthesis, 300 monomers per chain were used, with a 10% molar fraction of DPPS (*i.e.* $x = 0.1$ in Scheme 1) (30), but other polymers containing different DPPS molar fractions (5 and 25%) or different degrees of polymerization (500 hydrophobic monomers per chain) have also subsequently been generated (31). Use of a greater fraction of DPPS did not lead to well-formed CCMs because of the limited solubility of this monomer (a solid) in liquid styrene, which acts as carrier through the water phase for diffusion into the forming micelles. However, targeting CCMs with a greater degree of phosphine functionality is not necessary for the catalytic application as will be shown below. Finally, cross-linking in the third step was accomplished by addition of 10 equivalents of diethylene glycol dimethacrylate (DEGDMA) per chain, diluted with additional styrene (90 equiv per chain) to avoid macrogelation. The efficiency of the cross-linking step was confirmed by DOSY NMR in THF- D_8 (a good solvent for all polymer components): no population with a faster diffusion coefficient than the CCM, as would be expected for the non-cross-linked arms, could be detected.

CCM particles functionalized with a different ligand, bis(*p*-methoxyphenyl)phenylphosphine (BMOPPP) were also developed (32). The BMOPPP@CCM particles have the same basic structure as the reference TPP@CCM, with degrees of polymerization of 30 for the hydrophilic chains (15 MAA and 15 PEOMA monomer units), 300 for the hydrophobic chains and 100 for the inner cross-linked core (S/DEGDMA = 90:10). The phosphine was introduced via the new comonomer 4-[bis(*p*-methoxyphenyl)phosphino]styrene (BPMOPPS), see Scheme 2. Only a CCM with a 5% molar amount of BMOPPP in the PS flexible chains was obtained. Greater fractions of BPMOPPS, which is less soluble than DPPS in styrene, did not lead to well-formed particles.



Scheme 2. Incorporation of BMOPPS to obtain BMOPPP@CCM, by the same strategy shown in Scheme 1.

A slightly different architecture was also obtained for the TPP-functionalized polymer by carrying out the same synthesis, with the same molar amounts of each monomer and transfer agent, but incorporating DPPS and DEGDMA at the same time. This could not be done immediately after step 1 because of macrogel formation. However, after a short chain extension of the hydrophilic macroRAFT agent obtained in step 1 with styrene (ca. 50 units) and micelle self-assembly, all monomers could be added together in step 3 leading to the formation of a nanogel latex, TPP@NG, see Figure 1.

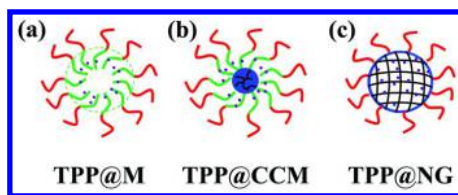


Figure 1. Topological difference between three functionalized amphiphilic nano-objects: (a) self-assembled micelles (TPP@M); (b) core-cross-linked micelles (TPP@CCM); (c) nanogel (TPP@NG).

The final polymers were obtained as stable colloidal suspensions of spherical nanoparticles, the diameters of which are a little under 100 nm as shown by transmission electron microscopy (TEM), see Figure 2. This is also consistent with the size measurements by dynamic light scattering (DLS) which gave diameters in the 70-100 nm range depending on the batch and on the DPPS content, with a narrow size distribution (PDI < 0.2). After drying and redissolving in THF, which is a good solvent for both shell and core components, the CCM particles expanded by a factor of a little more than 2 in diameter (ca. 10 in volume), whereas the NG particles expanded by a smaller factor (ca. 2 in volume), the size distributions remaining narrow.

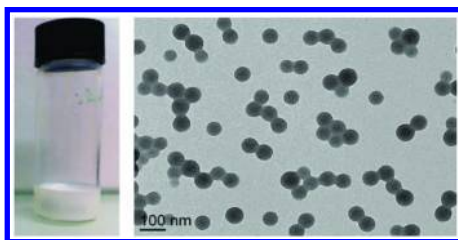


Figure 2. Photograph of a TPP@CCM latex (left) and transmission electron micrograph of the TPP@CCM particles (right).

Particle Swelling and Metal Coordination

Swelling studies were carried out for the reference 10% TPP@CCM latex with the purpose of learning about the facility with which different molecules can cross the water layer and the particle hydrophilic shell to reach the hydrophobic core. This is an essential point in terms of mass transport, during catalysis, of the reagents toward the catalytic sites and of the products back toward the bulk organic phase. NMR spectroscopy was a valuable tool for these investigations.

The ^1H NMR spectrum of the pristine latex, after dilution with D_2O , only revealed the resonance of the shell PEO side chain protons. No signal was evident neither for the polystyrene core nor for the shell main backbone chain protons, see Figure 3a, indicating that all these moieties have restricted mobility. In addition, no resonance could be observed for the core TPP functions in the

^3P NMR spectrum. Addition of organic compounds that are not miscible with water (chloroform, toluene, 1-octene, *n*-nonanal) to this suspension, however, led to interesting changes. A first visual effect was the rapid (few seconds) disappearance of the organic layer upon vigorous stirring, provided that the added amount was small and the compound is a good solvent for the polystyrene core (e.g. chloroform, toluene), accompanied by a corresponding volume increase for the aqueous phase. The incorporation of the organic compound in the particle core was confirmed by ^1H (Figure 3) and ^3P NMR, which now revealed all the expected core and shell resonances. Rough integration of the polymer and the added compound resonances also allowed quantifying the amount of incorporated solvent molecules: ca. 2000 (CHCl_3), ca. 800 (toluene), and ca. 150 (*n*-nonanal) molecules per polymer chain, respectively.

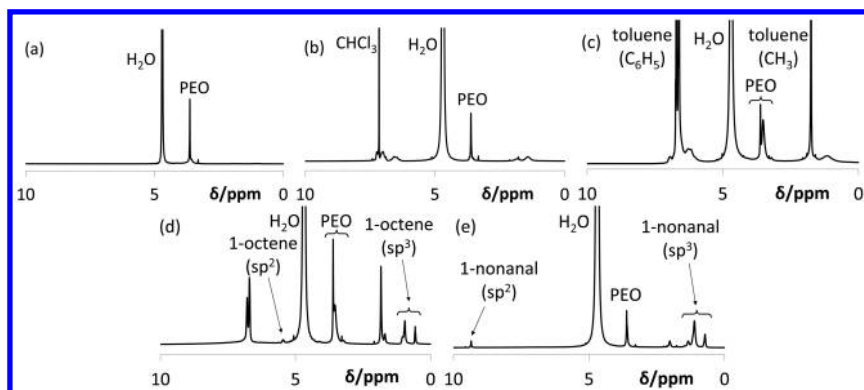


Figure 3. ^1H NMR spectra of the 10% TPP@CCM in D_2O . (a) Pristine latex; (b) saturated with chloroform; (c) saturated with toluene; (d) saturated with 1-octene/toluene (1:1); (e) saturated with *n*-nonanal.

1-Octene did not lead to any notable particle swelling at room temperature. However, it could be transported into the particle core when added as a 1:1 mixture with toluene (ca. 100 molecules of 1-octene and ca. 500 of toluene per chain). 1-Octene was also able to penetrate and swell the particle core when added as a pure phase at higher temperatures: after prolonged heating at 90°C , DLS showed a significant diameter increase in the presence of a 1-octene phase (from 70 to 100 nm) relative to the same latex heated in the absence of 1-octene. This experiment also revealed the stability of the colloidal suspension upon prolonged heating (50 h). A peculiar feature of these spectra is the splitting of the PEO resonances (the major methylene proton resonance at δ 3.6 and the minor methyl proton resonance of the methyl ether chain end at δ 3.3) upon inclusion of certain swelling solvents. This effect is particularly visible for the toluene swollen sample, but is also present for the samples swollen with toluene/1-octene and with *n*-nonanal. This phenomenon is interpreted as the result of partial folding back of the PEO chains into the polymer core under the compatibilizing effect of the swelling solvent. Strangely, this effect is not seen for the chloroform-swollen sample, even though chloroform is a good solvent for PEO.

The particles could also be easily loaded with the desired hydroformylation pre-catalyst, $[\text{Rh}(\text{acac})(\text{CO})_2]$ (acac = acetylacetonato). Transport of this molecule into the particle core is slower than that of small solvent molecules. Indeed, when a small amount of a toluene or CHCl_3 solution of the rhodium complex was offered to the pristine latex, the solvent quickly swelled the particles and the complex precipitated as a crystalline solid. However, treating a pre-swollen latex with a solution of the complex in the same solvent resulted in a slow (ca. 30 min) exchange with full incorporation of the metal complex into the polymer core, as signaled by the complete transfer of the orange-yellow color of the metal complex from the organic phase to the latex phase. ^{31}P NMR spectroscopy is a good tool to investigate this coordination process, since the resonance of the free (non-coordinated) TPP at δ -6.4 moves to δ 47.5 upon coordination of the Rh complex (doublet with $J_{\text{PRh}} = 175$ Hz), see Figure 4, in good agreement with the resonance reported for the equivalent molecular compound $[\text{Rh}(\text{acac})(\text{CO})(\text{TPP})]$ ($\delta = 47.5$ ppm, $J_{\text{PRh}} = 179.7$ Hz) (33).

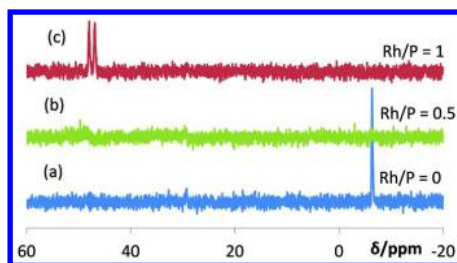


Figure 4. $^{31}\text{P}\{^1\text{H}\}$ NMR spectra of the 10% TPP@CCM swollen with chloroform in D_2O . (a) Pristine latex; (b) after treatment with 0.5 equiv Rh per P atom; (c) after treatment with 1.0 equiv of Rh per P atom. Adapted with permission from ref. (30). Copyright 2014 Wiley-VCH.

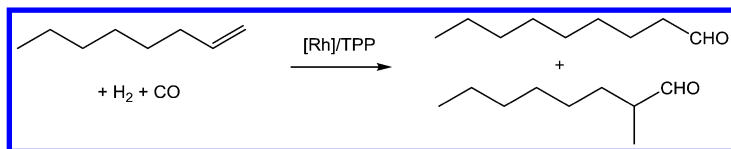
When only 50% of the P atoms are coordinated to Rh, however, no resonance is visible in the spectrum (Figure 4b). This phenomenon is related to the known rapid ligand exchange for this complex between free and coordinated TPP, which happens to be in the coalescence region at room temperature (34). This phenomenon turned out to be useful for our studies of metal mobility and particle interpenetration, as will be shown later.

All the above described swelling and Rh coordination behavior has also been evidenced for the BMOPPP@CCM (32) and TPP@NG polymers, although the latter product, prepared more recently, has so far been investigated in less extensive details.

Hydroformylation Catalysis

All the basic properties required for biphasic catalysis by the micellar strategy are reunited in the CCM and NG ligand-functionalized polymers: they give

stable colloidal solutions upon prolonged heating at the temperatures required for catalysis (90°C); they allow rapid transport of organic molecules across the hydrophilic shell in and out of the particle core, including the reaction model substrate (1-octene) and the hydroformylation products (mainly *n*-nonanal); and they lead to incorporation and coordination of the pre-catalyst. The sought catalyzed transformation is shown in Scheme 3.



Scheme 3. Hydroformylation of 1-octene, yielding the linear (l) *n*-nonanal and the branched (b) 2-methyloctanal products.

It should be mentioned that, once $[\text{Rh}(\text{acac})(\text{CO})_2]$ is coordinated to the polymer-linked TPP, as shown in the previous section, the resulting $[\text{Rh}(\text{acac})(\text{CO})(\text{TPP}@ \text{nano-object})]$ complex does not yet correspond to the active form of the hydroformylation catalyst. According to well established investigations for the molecular TPP system (35), the active form is a hydride species of formula $[\text{RhH}(\text{CO})_{4-n}(\text{TPP})_n]$, which forms *in situ* in the presence of the syngas reagent (1:1 CO/H₂ mixture).

Using the three different latexes (TPP@M, TPP@CCM and TPP@NG) for the 1-octene hydroformylation under standard biphasic conditions yielded the results shown in Table 1. The 1-octene substrate was introduced as a solution in *n*-decane, chosen as substrate carrier phase in order to closely simulate the running conditions of a continuous flow production plant, while allowing the gas-chromatographic determination of the hydroformylation products. Each run gave essentially quantitative 1-octene conversion in 2-3 h with excellent selectivity for the expected hydroformylation products (>90%). An example of the reaction kinetics, obtained by monitoring the gas consumption, is shown in Figure 5. The only observed by-products were internal octenes generated by catalytic isomerization, as is typical for this type of catalyst. The linear to branched (l/b) product ratios are greater and the catalytic activities (as measured by the initial turnover frequency) are lower than typically observed for homogeneous phase runs with free TPP under the same [Rh] and [TPP] conditions, as already reported for experiments carried out with polymer-supported TPP under homogeneous conditions (36, 37). These TOFs are close to those obtained with similar macroligands (TPP-functionalized linear or star PS built by atom transfer radical polymerization) under homogeneous conditions in toluene solution (38, 39). The Rh leaching results (last column of Table 1) will be commented more in detail below.

Table 1. Results of the aqueous biphasic hydroformylation of 1-octene by [Rh(acac)(CO)(nano-object)] latex.^a

Run	Nano-object	(l/b)	TOF/h ⁻¹	[Rh]/ppm
1	10% TPP@CCM ^b	5.0	628	1.8
1-R	10% TPP@CCM ^b	3.4	782	2.5
2	10% TPP@CCM ^c	-	13	0.1
3	10% TPP@M	3.8	560	7.2
4	10% TPP@CCM	5.0	441	2.0
5	10% TPP@NG	3.6	378	0.6

^a Standard conditions: [1-octene]_{org} = 1.1 M in *n*-decanal, [P]/[Rh] = 4, V_{org}/V_{aq} = 3:1, [1-octene]/[Rh] = 500, T = 363 K, P_{syngas} = 20 bar (CO/H₂ = 1:1), ω = 1200 rpm. The data are taken in part from ref. (30) and (31). ^b Standard conditions except for a more diluted latex phase (V_{org}/V_{aq} = 2:1). ^c [Sulfoxantphos]/[Rh] = 5.

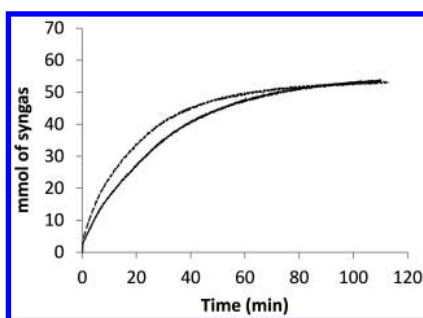


Figure 5. Monitoring of the syngas consumption for runs 1 (plain line) and 1-R (dashed line). Run 1-R was conducted with the recovered aqueous phase from run 1 after standing in air for 5 days. Adapted with permission from ref. (30). Copyright 2014 Wiley-VCH.

A most remarkable observation is that the recovered catalyst phase from run 1, after removal of the organic product phase, storage in air for 5 days, and reinjection into the reactor with a fresh substrate charge, gave rise to undiminished activity (run 1-R in Table 1) (30). This is in stark contrast with the known fragility of the TPP-supported molecular catalyst, which needs to be protected from air under a syngas atmosphere to avoid rapid deactivation. Thus, a remarkable protecting effect of catalyst by the polymer scaffold is demonstrated.

A question concerns the possible action of the nano-objects as a surfactant, simply yielding a more efficient interfacial catalysis by increasing the water/organic interface area, rather than by the micellar principle. This is excluded by the observation of a very low activity under the same conditions in the presence of sulfoxantphos (run 2), which is a water soluble chelating diphosphine ligand with a greater binding ability for rhodium than TPP. Thus, sulfoxantphos keeps

the Rh active site in the water phase while the 1-octene substrate remains in the organic phase and in the CCM core. In case of an interfacial effect, the catalytic activity should be high as observed in the presence of other surfactants (40–42). Note also that the experiment run in the presence of sulfoxantphos yields almost no measurable Rh leaching, giving a first indication that the Rh loss is related to the placement of the metal inside the polymer scaffold.

A comparison of efficiencies between the three types of nano-objects (TPP@M, TPP@CCM and TPP@NG) is shown in runs 3–5. The most interesting comparison concerns the activity (TOF) and catalyst leaching. Loosening up the polymer network on going from the NG to the CCM and to the M particle is expected to facilitate the substrate access to the catalytic site and indeed the TOF increases in this order. However, the difference between the three initial TOF values is relatively small (increase by 50% on going from NG to M). On the other hand, leaching dramatically increases in the same order. Thus, one of the anticipated results at the project outset, namely that cross-linking amphiphilic polymers into a unimolecular version of a micelle would lead to reduced catalyst losses, is validated.

Although the best polymer architecture appears to be that of the TPP@NG, the effect of structural and operating parameters on catalysis has been investigated so far with the 10% TPP@CCM particles (31). A few recycles were carried out under the standard conditions (footnote *a* of Table 1), without removing the aqueous phase from the autoclave, the major interest in this experiment being to follow the trend of the Rh leaching in subsequent runs. The organic phase was siphoned out of the autoclave at the end of each run and replaced with a fresh substrate charge, while keeping the catalyst at all times under a protective syngas atmosphere. The TOF and *l/b* values did not vary very much and the Rh leaching slightly decreased after the first two runs, suggesting the presence of slight amounts of a more lipophilic fraction in the original latex, but then remained constant beyond the second recycle at the level of about 1.7 ppm. This demonstrates the presence of an intrinsic catalyst loss but does not prove whether this occurs by Rh extraction from the CCM or by transfer of the entire TPP@CCM into the organic phase. The latter hypothesis, however, was supported by DLS measurements: the recovered organic phases showed the presence of particles, the dimension of which correspond to those expected for swollen latex particles.

Control experiments run with TPP@CCM in *n*-decanal/water, without Rh coordination and without 1-octene and syngas but under the same conditions of the catalysis (warming for 2.5 h at 90 °C with stirring at 1200 rpm) confirmed the transfer of particles to the organic phase (DLS measurement, Figure 6), although the amount of particles was not sufficient to induce significant turbidity (*cf.* Figure 2, left). Interestingly, the size of the particles measured by DLS in the organic phase depended on the delay of the measurement after the end of the treatment: $D_z = 283$ nm, PDI = 0.33 immediately after cooling; $D_z = 186$ nm, PDI = 0.10 after one week standing at room temperature, see Figure 6. The size distribution measured immediately is very broad and extends to diameters well beyond the maximum value expected for swelling individual particles, as suggested by the particle size in THF solution (*vide supra*). This indicates the occurrence of particle agglomeration. However, these agglomerates are slowly

redispersed upon standing at room temperature. When the same experiment was carried out at room temperature, on the other hand, no transfer was observed. Unfortunately, the DLS signal does not carry quantitative information, thus the solubility of the TPP@CCM in *n*-decanal cannot be estimated and compared with the Rh loss observed during catalysis.

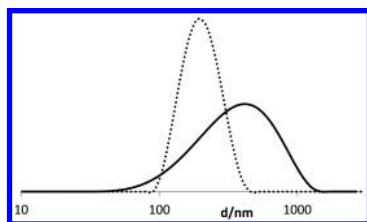


Figure 6. DLS analysis of the recovered organic phase after stirring the TPP@CCM with 1-decanal for 2.5 h at 90°C. The measurements were carried out at r.t. immediately (plain line) and one week (dotted line) after the end of the experiment. Adapted with permission from ref. (31). Copyright 2015 Elsevier.

Another interesting result is provided by the effect of the stirring rate (31). This experiment was initially run with the intention of probing the effect of mass transport on the catalytic efficiency. However, the most interesting observation is that a stirring rate increase by 33% leads to a leaching increase by 450% (6.5 ppm at 1400 rpm; 11.6 ppm at 1600 rpm)! This observation, in combination with the above DLS evidence of particle transfer to the organic phase, suggests that higher stirring rates somehow increase the polymer lipophilicity.

DLS gives again useful information on this phenomenon. The recovered organic phases shows a different particle size distribution as a function of stirring rate, see Figure 7. Again, the DLS signal unfortunately does not carry quantitative information for correlation with the Rh leaching. However, the DLS measurement shows that the particle size distribution is displaced toward greater dimensions for higher stirring rates. In addition, a bimodal distribution is observed for the phase recovered from the experiment at the highest stirring speed. Although additional studies need to be carried out to better understand this phenomenon, we tentatively propose that stirring induces interparticle cross-linking and that the agglomerated polymer particles are more lipophilic and hence are transferred more extensively toward the organic phase. Considering the nature of the active catalyst as $[\text{RhH}(\text{CO})_{4-n}(\text{TPP})_n]$, the species with $n = 1$ may be prevalent at high CO pressure and indeed this is considered as the most active form of the catalyst (35) but other species with $n > 1$ may also be present, especially at high P/Rh ratios. While these species may preferentially form with implication of different TPP functions within the same CCM (chelation or cross-linking different arms within the same particle), the possible implication of TPP ligands from arms belonging to different cores can lead to bigger particle aggregates. Interparticle cross-linking can obviously occur only if the polymer particles are

able to interpenetrate. The occurrence of such interpenetration was confirmed by additional experiments, as shown in the next section.

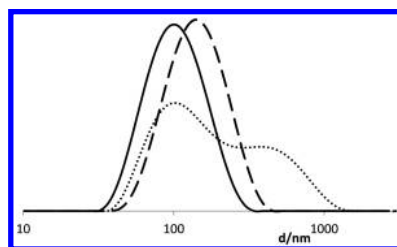


Figure 7. DLS analysis of the recovered organic phases after the catalytic runs at different stirring speeds. 1200 rpm: plain line. 1400 rpm: dashed line. 1600 rpm: dotted line. The measurements were carried out at r.t. ca. 1 year after the catalytic experiments. Adapted with permission from ref. (31). Copyright 2015 Elsevier.

Additional catalytic experiments were carried out with polymer particles containing longer hydrophobic P(S-co-DPPS) blocks or a different density of TPP ligands in the core (31). The results of the catalysis with a 10% TPP@CCM polymer having a degree of polymerization of 500 rather than 300 for the linear hydrophobic arms were essentially identical with those of the standard CCM, indicating that the core size has no significant effect on catalysis. The TPP density in the core, on the other hand, had a greater effect: the TOF was greater for a 5% TPP@CCM and smaller for a 25% TPP@CCM. It is important to keep in mind that all these runs were carried out with the same total amounts of TPP and Rh catalyst, relative volumes of the aqueous and organic phases, and [1-octene]:[TPP]:[Rh] ratios. However, the concentrations of TPP and Rh in the particle cores were different and the observed TOF trend is in line with known effects of the local TPP concentration. Finally, the experiment run with the 5% BMOPPP@CCM, showed similar catalytic activity and (I/b) as the corresponding 5% TPP@CCM, but a much greater Rh leaching (4.5 vs. 1.8 ppm) (32).

CCM Interpenetration

There are two pieces of evidence in favor of TPP@CCM particle interpenetration. The first one comes from the same experiment discussed above (Figure 6) with the detection of particles transferred to the organic phase by DLS, except that the rhodium complex was also present at the same concentration as in the catalytic experiment. At a TPP/Rh ratio of 4, that there are free TPP ligands available to replace CO and yield a bis-TPP complex, analogous to the known molecular compound $[\text{Rh}(\text{acac})(\text{TPP})_2]$ (43). It is also known from previous studies on the molecular complex that while replacement of the first CO ligand by TPP in $[\text{Rh}(\text{acac})(\text{CO})_2]$ is fast at r.t., replacement of the second one requires heat. Thus, the partially rhodium-loaded $[\text{Rh}(\text{acac})(\text{CO})(\text{TPP@CCM})]$ latex was heated at 90°C for 2.5 h in presence of decanal, like the Rh-free sample

discussed above. The recovered organic phase, once again transparent and colorless indicating that transfer of the polymer to the organic phase could not be extensive, gave the DLS response shown in Figure 8.

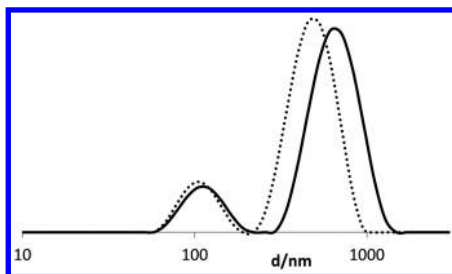


Figure 8. DLS analysis of the recovered organic phase after stirring the [Rh(acac)(CO)(TPP@CCM)] solution (TPP/Rh = 4) with 1-decanal for 2.5 h at 90°C. The measurements were carried out at r.t. immediately (plain line) and one week (dotted line) after the end of the experiment. Adapted with permission from ref. (31). Copyright 2015 Elsevier.

This time, contrary to the experiment run in the absence of Rh complex (see above, Figure 6), the measurement revealed a bimodal size distribution the minor component of which, centered at ca. 100 nm, corresponds to the size of the free TPP@CCM (the difference relative to Figure 6 may be related to a lower propensity of the particles to swell when incorporating the Rh complex relative to the Rh-free particles) while the major component, centered at ca. 650 nm, corresponds to agglomerated particles. Repeating the measurement after 1 week yielded slightly smaller particles, again because of the presumed slow release of swelling solvent after cooling, but the bimodal size distribution persists indicating that the interparticle cross-linking is irreversible. Like for the same experiment in the absence of Rh complex, no particles were transferred to the organic phase upon prolonged stirring at room temperature. In addition, prolonged heating of the latex at the reflux temperature resulted in precipitation of the polymer as an orange solid, which could no longer be dispersed in the aqueous phase. Quite evidently, the presence of rhodium favors aggregation, a phenomenon accentuated by heating and stirring, and the resulting aggregated particles appear to be extracted into the organic phase more readily than the non-aggregated CCMs.

A second and independent observation not only confirmed interpenetration of the CCM particles but also showed that this is a very rapid and reversible process. As shown in Figure 4, the swollen [Rh(acac)(CO)(TPP@CCM)] exhibits no ^{31}P signal when the Rh/P ratio is 0.5. We have therefore interrogated the system, with the help of ^{31}P NMR spectroscopy, about the rate at which a rhodium complex can migrate from the core of one nano-object to another. This was realized by mixing equimolar amounts of two solutions, one containing TPP@CCM (no Rh coordination) and the other one containing [Rh(acac)(CO)-(TPP@CCM)] (100% Rh coordination). The mixture should in principle initially display both resonances of free and Rh-coordinated TPP (Figure 4). Subsequently, these

resonances should disappear upon full equilibration. In fact, by measuring the ^{31}P NMR spectrum of TPP@CCM solutions charged with different Rh/P ratios, we have found a detectable, albeit broader, resonance for free TPP (at low Rh/P ratios, < ca. 0.4) or for Rh-coordinated TPP (at high Rh/TPP ratios, > ca. 0.6). Therefore, the exchange could in principle be monitored during most of the reaction, with full disappearance of all resonances only toward the very end. But in reality this experiment led, no matter how fast the ^{31}P spectrum could be recorded after mixing, to a silent spectrum showing a very rapid and complete equilibration.

It is unconceivable that such a fast interparticle Rh migration results from departure of the Rh complex from one core and subsequent penetration into a second one via one of the bulk phases (either the aqueous or the organic one), because this exchange rate is much faster than the rate at which the $[\text{Rh}(\text{acac})(\text{CO})_2]$ pre-catalyst is incorporated into the polymer core in the first place. Hence, the only reasonable explanation is that the particles are able to reversibly interpenetrate and exchange the rhodium complexes from a TPP ligand in the first core to one in the second core via a fast associative process, as also observed for the intraparticle TPP ligand exchange. The interpenetration must be reversible, because the DLS shows stability of the particle dimensions, even upon warming in the absence of Rh or swelling solvents for several hours (*vide supra*).

This proposition was confirmed by repeating the experiment at pH 13.6, under which conditions the MAA units are deprotonated and negative charge accumulates on the nano-object surface. ^{31}P NMR spectroscopy shows that the swollen TPP@CCM (0% Rh) and the fully loaded $[\text{Rh}(\text{acac})(\text{CO})(\text{TPP@CCM})]$ (100% Rh) latexes are stable (resonances observed at the same position as at the natural pH, not changing with time). Coulombic repulsion should in principle hamper the particle interpenetration. Indeed, upon mixing equimolar amounts of the two latexes, both resonances were now clearly seen. These resonances decreased simultaneously in intensity only very slowly, not completely disappearing even after 10 h at r.t.

Conclusions and Outlook

We have developed the first ligand-functionalized core-cross-linked micelles (CCM) as well as nanogel versions of them (NG) that function as macroligands for industrially relevant catalysis operating through the micellar principle under aqueous biphasic conditions. The efficiency of these unimolecular micelles as catalytic nanoreactors has been shown using the industrially relevant hydroformylation of a higher α -olefin, 1-octene, as a test reaction yielding turnover frequencies and l/b ratio comparable to those of related homogeneous systems. However, the catalyst phase could be easily separated from the organic product phase and recycled. A remarkable protecting effect of the active catalyst by the polymer scaffold has also been demonstrated. Catalyst leaching was reduced relative to the non-cross-linked micelles having the same chemical constitution, particularly for the NG version of the nanoreactors, but residual catalyst loss still occurs. Our investigations of performance as a function of several parameters

have shown that leaching is related to transport of the product-swollen particles to the organic phase, a phenomenon which appears, at least for the CCM, to be facilitated by agglomeration following particle interpenetration. This phenomenon is accentuated by heating and stirring. Through room temperature NMR investigations on the swollen nanoreactors, we have indeed revealed that particle interpenetration is, at least for the CCM, rapid and reversible, allowing very rapid exchange of the metal complexes between different nanoreactor cores.

Numerous avenues are now open for further explorations. It will be of interest to establish whether the agglomeration phenomenon depends on the polymer architecture (CCM vs. NG) and whether heating and stirring rate have the same effect for the TPP@NG macroligands as for TPP@CCM. New polymers with a different chemical environment in the core and/or in the shell may be developed aiming at a better catalyst confinement in the aqueous phase. Other pre-catalysts can be incorporated into these nanoreactors and applied to other catalytic reactions. Finally new polymers can be developed with incorporation of other ligand-functionalized monomers for fine tuning of catalysis.

Abbreviations

ACPA	4,4'-azobis(4-cyanopentanoic acid)
CCM	Core-cross-linked micelle
CMC	Critical micelle concentration
CTPPA	4-cyano-4-(thiothiopropylsulfanyl)pentanoic acid
DEGDMA	Diethylene glycol dimethacrylate
DLS	Dynamic light scattering
DPPS	4-diphenylphosphinostyrene
MAA	Methacrylic acid
PEOMA	Poly(ethylene oxide) methyl ether methacrylate
PISA	Polymerization-induced self-assembly
RAFT	Reversible Addition-Fragmentation Chain Transfer
TEM	Transmission electron microscopy
TPP	Triphenylphosphine
TPPTS	Tripheylphosphine Trisulfonate

Acknowledgments

We thank the Agence Nationale de la Recherche (ANR) for financial support under the Biphase nanocat Project (ANR-11-BS07-025-01). Additional support from the Centre National de la Recherche Scientifique (CNRS) and from the Institut Universitaire de France (IUF) is also gratefully acknowledged.

References

1. Matyjaszewski, K.; Gnanou, Y.; Leibler, L. *Macromolecular Engineering: Precise Synthesis, Materials Properties, Applications*; Wiley-VCH Verlag GmbH: 2007.

- Welsch, N.; Ballauff, M.; Lu, Y. *Adv. Polym. Sci.* **2010**, *234*, 129–163.
- Lu, A.; O'Reilly, R. K. *Curr. Opin. Biotechnol.* **2013**, *24*, 639–645.
- Terashima, T. In *Encyclopedia of Polymer Science and Technology*, 4th ed.; Mark, H. F., Ed.; John Wiley & Sons, Inc.: 2013; DOI: 10.1002/0471440264.pst0471440590.
- Chi, Y. G.; Scroggins, S. T.; Fréchet, J. M. J. *J. Am. Chem. Soc.* **2008**, *130*, 6322–6323.
- Levins, A. D.; Wang, X. F.; Moughton, A. O.; Skey, J.; O'Reilly, R. K. *Macromolecules* **2008**, *41*, 2998–3006.
- Terashima, T.; Ouchi, M.; Ando, T.; Sawamoto, M. *J. Polym. Sci., Polym. Chem.* **2010**, *48*, 373–379.
- Terashima, T.; Ouchi, M.; Ando, T.; Sawamoto, M. *Polym. J.* **2011**, *43*, 770–777.
- Resmini, M. *Anal. Bioanal. Chem.* **2012**, *402*, 3021–3026.
- Resmini, M.; Flavin, K.; Carboni, D. *Mol. Imprinting* **2012**, *325*, 307–342.
- Cornils, B. *Org. Process Res. Dev.* **1998**, *2*, 121–127.
- Kohlpaintner, C. W.; Fischer, R. W.; Cornils, B. *Appl. Catal., A* **2001**, *221*, 219–225.
- Oehme, G. *Appl. Homogeneous Catal. Organomet. Compd. (2nd Ed.)* **2002**, *2*, 835–841.
- Nuyken, O.; Weberskirch, R.; Kotre, T.; Schoenfelder, D.; Woerndle, A. *Polym. Mater. Org. Synth. Catal.* **2003**, 277–304.
- Reinsborough, V. C. *Interfacial Catal.* **2003**, 377–390.
- Kotre, T.; Zarka, M. T.; Krause, J. O.; Buchmeiser, M. R.; Weberskirch, R.; Nuyken, O. *Macromol. Symp.* **2004**, *217*, 203–214.
- Khan, M. N. *Micellar Catalysis*; CRC Press: 2006.
- Zhang, J.; Meng, X. G.; Zeng, X. C.; Yu, X. Q. *Coord. Chem. Rev.* **2009**, *253*, 2166–2177.
- Chen, H.; Li, Y. Z.; Chen, J. R.; Cheng, P. M.; He, Y. E.; Li, H. J. *J. Mol. Catal. A* **1999**, *149*, 1–6.
- Yang, C.; Bi, X. Y.; Mao, Z. S. *J. Mol. Catal. A* **2002**, *187*, 35–46.
- Li, M.; Li, Y. Z.; Chen, H.; He, Y. E.; Li, X. J. *J. Mol. Catal. A* **2003**, *194*, 13–17.
- Liu, X.; Kong, F.; Zheng, X.; Jin, Z. *Catal. Commun.* **2003**, *4*, 129–133.
- Desset, S. L.; Cole-Hamilton, D. J.; Foster, D. F. *Chem. Commun.* **2007**, 1933–1935.
- Zarka, M. T.; Bortenschlager, M.; Wurst, K.; Nuyken, O.; Weberskirch, R. *Organometallics* **2004**, *23*, 4817–4820.
- Pawar, G. M.; Weckesser, J.; Blechert, S.; Buchmeiser, M. R. *Beilstein J. Org. Chem.* **2010**, *6* (28), DOI: 10.3762/bjoc.6.28.
- Zhang, W. J.; D'Agosto, F.; Boyron, O.; Rieger, J.; Charleux, B. *Macromolecules* **2011**, *44*, 7584–7593.
- Zhang, W. J.; D'Agosto, F.; Boyron, O.; Rieger, J.; Charleux, B. *Macromolecules* **2012**, *45*, 4075–4084.
- Charleux, B.; Delaittre, G.; Rieger, J.; D'Agosto, F. *Macromolecules* **2012**, *45*, 6753–6765.
- Warren, N. J.; Armes, S. P. *J. Am. Chem. Soc.* **2014**, *136*, 10174–10185.

30. Zhang, X.; Cardozo, A. F.; Chen, S.; Zhang, W.; Julcour, C.; Lansalot, M.; Blanco, J.-F.; Gayet, F.; Delmas, H.; Charleux, B.; Manoury, E.; D'Agosto, F.; Poli, R. *Chem. Eur. J.* **2014**, *20*, 15505–15517.
31. Cardozo, A. F.; Julcour, C.; Barthe, L.; Blanco, J.-F.; Chen, S.; Gayet, F.; Manoury, E.; Zhang, X.; Lansalot, M.; Charleux, B.; D'Agosto, F.; Poli, R.; Delmas, H. *J. Catal.* **2015**, *324*, 1–8.
32. Chen, S.; Cardozo, A. F.; Julcour, C.; Blanco, J.-F.; Barthe, L.; Gayet, F.; Charleux, B.; Lansalot, M.; D'Agosto, F.; Delmas, H.; Manoury, E.; Poli, R. *Polymer*, submitted.
33. Bonati, F.; Wilkinson, G. *J. Chem. Soc.* **1964**, 3156–3160.
34. Kwaskowska-Cheć, E.; Trzeciak, A. M.; Ziolkowski, J. J. *React. Kinet. Catal. Lett.* **1984**, *26*, 21–24.
35. *Rhodium Catalyzed Hydroformylation*; van Leeuwen, P. W. N. M., Claver, C., Eds.; Kluwer: Dordrecht, 2000; Vol. 22.
36. Imyanitov, N. S.; Tupitsyn, S. B. *Petrol. Chem.* **1993**, *33*, 423–429.
37. Tupitsyn, S. B.; Imyanitov, N. S. *Petrol. Chem.* **1996**, *36*, 249–255.
38. Cardozo, A. F.; Manoury, E.; Julcour, C.; Blanco, J.-F.; Delmas, H.; Gayet, F.; Poli, R. *ChemCatChem* **2013**, *5*, 1161–1169.
39. Cardozo, A. F.; Manoury, E.; Julcour, C.; Blanco, J.-F.; Delmas, H.; Gayet, F.; Poli, R. *Dalton Trans.* **2013**, *42*, 9148–9156.
40. Desset, S. L.; Reader, S. W.; Cole-Hamilton, D. J. *Green Chem.* **2009**, *11*, 630–637.
41. Nowothnick, H.; Rost, A.; Hamerla, T.; Schomacker, R.; Muller, C.; Vogt, D. *Catal. Sci. Technol.* **2013**, *3*, 600–605.
42. Hamerla, T.; Rost, A.; Kasaka, Y.; Schomacker, R. *ChemCatChem* **2013**, *5*, 1854–1862.
43. Barlex, D. M.; Hacker, M. J.; Kemmitt, R. D. W. *J. Organomet. Chem.* **1972**, *43*, 425–430.

Chapter 15

RAFT Copolymerization of Thioglycosidic Glycomonomers with NiPAm and Subsequent Immobilization onto Gold Nanoparticles

C. von der Ehe,^{1,2,3} F. Kretschmer,^{1,2} C. Weber,^{1,2} S. Crotty,^{1,2}
S. Stumpf,^{1,2} S. Hoepfner,^{1,2} M. Gottschaldt,^{1,2}
and U. S. Schubert^{1,2,3,*}

¹Laboratory of Organic and Macromolecular Chemistry (IOMC), Friedrich Schiller University Jena, Humboldtstraße 10, 07743 Jena, Germany

²Jena Center for Soft Matter (JCSM), Friedrich Schiller University Jena, Philosophenweg 7, 07743 Jena, Germany

³Dutch Polymer Institute (DPI), P.O. Box 902, 5600 AX Eindhoven, The Netherlands

*E-mail: ulrich.schubert@uni-jena.de

The synthesis of a new acetyl-protected *S*-glycosidic mannose glycomonomer is reported as well as the copolymerization with *N*-isopropyl acrylamide *via* reversible addition fragmentation chain transfer (RAFT) polymerization. The glycopolymers were deprotected and analyzed *via* ¹H NMR spectroscopy, size exclusion chromatography, elemental analysis, FT-IR spectroscopy as well as asymmetric flow field-flow fractionation (AF4) coupled with multi-angle laser light scattering (MALLS). Turbidimetric studies revealed the thermoresponsive properties of the glycopolymers. Subsequent immobilization onto gold nanoparticles was achieved without cleavage of the RAFT endgroup, leading to stable glycosylated nanoparticles, which were investigated towards their protein recognition capabilities, revealing that the mannosylated nanoparticles were able to detect the lectin Concanavalin A at very low concentrations.

Introduction

Glycopolymers have attracted significant scientific interest in the last decades because of their ability to interact with natural occurring proteins (lectins). This enables synthetic glycopolymers to mimic the role that saccharides on cell-surfaces play in many biological processes (1). In order to optimize their properties as receptor mimics, the investigation of these materials is often facilitated by their immobilization, *e.g.* on microarrays (2–4). In particular gold nanoparticles (GNPs) with surface-immobilized glycopolymers are very promising for the detection of such interactions due to the surface plasmon resonance of gold nanoparticles (5–9). Therefore, glycopolymer-functionalized gold nanoparticles have shown to be very efficient sensors: An immobilized mannose glycopolymer, *e.g.*, was able to detect Concanavalin A (ConA) (6). A glycopolymer carrying *O*-glycosidic bound *N*-acetyl glucosamine was used for the detection of wheat germ agglutinin (WGA) (8) and a lactose glycopolymer immobilized to gold nanoparticles was able to efficiently detect *ricinus communis* agglutinin (RCA) (9).

The synthesis of such GNP-immobilized glycopolymers requires a glycopolymer possessing a thiol- or thioester endgroup. Thus, the reversible addition fragmentation chain transfer (RAFT) polymerization procedure represents the ideal strategy for the design of these materials due to the chemical structure of the RAFT endgroup, which can easily be converted into a thiol endgroup.

The immobilization of such glycopolymers onto gold surfaces, like nanoparticles, has been widely studied in literature, for example using disulfide-bridged glycopolymers (9–11), glycopolymers with pendant thiol-groups (12) or glycopolymers with thiol-endgroup (13–15). However, it was also shown by Ebeling and Vana that polymers with trithiocarbonate endgroups, prepared by RAFT polymerization, can be immobilized directly onto gold nanoparticles without the necessity of endgroup transformation (16, 17). This method has, to the best of our knowledge, not been applied for glycopolymers up to now.

The successful application of immobilized glycopolymers depends also on the stability of the systems. The utilization of methacrylic glycomonomers with *O*-glycosidic linkage at the anomeric position is well-known in literature (18–20). However, *S*-glycosidic bound sugars have been shown to be more stable towards enzymatic degradation (21, 22), which would be an advantage for their later application in aqueous systems. Thioglycosidic linked glycopolymers are accessible by, *e.g.*, the post-polymerization modification of polymers *via* thiol-ene reaction (23–26). However, the difficult polymerization of alkene functional acrylate or acrylamide monomers favors their synthesis by the polymerization of glycomonomers, at least as far as radical polymerization techniques are addressed.

Therefore, we present a new mannose glycomonomer with *S*-glycosidic instead of *O*-glycosidic linkage between the sugar and the polymerizable group.

Another interesting feature of certain synthetic polymers is the ability to undergo a lower critical solution temperature (LCST) transition, which results in thermoresponsive polymers that undergo a coil-to-globule transition upon exceeding a certain temperature. Thermoresponsive glycopolymers have already

been reported in literature (27–36). In some of these reports it was shown that the interaction of the respective glycopolymer with an analyte (*e.g.* lectin) could be controlled *via* the temperature (30, 33, 36).

As a consequence, thermoresponsive glycopolymers which can bind to certain analytes (*e.g.* lectins) could be promising candidates for later applications like affinity chromatography or temperature responsive drug delivery applications.

The LCST behavior of immobilized polymers is difficult to investigate, since common techniques involve the determination of the temperature where the polymer solution becomes turbid (cloud point temperature, T_{CP}). This technique cannot be applied on GNP immobilized systems. Alternatively, the surface plasmon resonance of the GNPs can be exploited for the analysis of the LCST feature (37, 38).

In this contribution, we present new thioglycosidic-linked glucose- and mannose-bearing monomers, which were copolymerized with *N*-isopropylacrylamide (NIPAm) by RAFT polymerization and subsequently subjected to deprotection reactions. The resulting thermoresponsive glycopolymers were immobilized onto gold nanoparticles, representing - to the best of our knowledge - the first report of thermoresponsive glycopolymers immobilized on the surface of gold nanoparticles. This approach allows to investigate the LCST behavior of the immobilized glycopolymer as well as the lectin binding interaction with the same GNP sensor system.

Experimental Section

Materials and Instrumentation

All chemicals were purchased from Fluka, Sigma Aldrich or Acros Organics and were used without further purification unless otherwise stated. 2-(Butylthiocarbonothioylthio)propanoic acid (BTTCP) was kindly provided by BASF SE. 1,2,3,4,6-Penta-*O*-acetyl- α -D-mannopyranose (ManOAc) was purchased from Carbosynth, 1,2,3,4,6-penta-*O*-acetyl- β -D-glucopyranose (GlcOAc) was purchased from Alfa Aesar. 4,4'-Azobis(4-cyanovaleric acid) (ACVA) was of $\geq 98\%$ purity (Sigma Aldrich). Spectra/Por® 3 dialysis membranes with molecular weight cut off (MWCO) 3,500 g/mol were purchased from VWR. 2-Mercaptoethylacrylamide was synthesized according to a literature procedure (39).

^1H and ^{13}C and 2D nuclear magnetic resonance spectra were recorded at 298 K on a Bruker AC 300 (300 MHz) or a Bruker AC 250 (250 MHz) spectrometer, respectively. The chemical shifts are given in parts per million (ppm) and the residual solvent resonance was used as an internal standard. FT-IR spectra were recorded on an IRAffinity-1 spectrometer from Shimadzu. Elemental analyses were carried out on a CHN-932 Automat Leco instrument. Size exclusion chromatograms (SEC) were measured using an Agilent 1200 series system with a PSS GRAM 1000/30 Å (10 μm particle size) column, a G1310A pump, a G1362A refractive index detector at 40 °C with a flow rate of 1 mL/min. *N,N*-Dimethylacetamide with 0.21% LiCl was used as eluent. Matrix-assisted laser desorption ionization time-of-flight (MALDI-TOF) mass spectra were

measured on an Ultraflex III TOF/TOF mass spectrometer (Bruker Daltonics) with *trans*-2-[3-(4-*tert*-butylphenyl)-2-methyl-2-propenylidene]malononitrile (DCTB) as matrix. The instrument was equipped with a Nd:YAG laser and a collision cell. All spectra were measured in the positive reflector mode. The instrument was calibrated prior to each measurement with an external poly(methyl methacrylate) standard from PSS Polymer Standards Services GmbH in the required measurement range. The MALDI-TOF mass spectra were measured from aliquots of the reaction solutions. BioBeads® S-X1 support for size exclusion chromatography was purchased from Bio Rad, swollen in THF, which was also used as eluent.

Asymmetric flow field-flow fractionation (AF4) was performed on an AF2000 MT System (Postnova Analytics, Landsberg, Germany) coupled to an UV (PN3211, 260 nm), RI (PN3150), MALLS (PN3070, 633 nm) and DLS (ZetaSizer Nano ZS) detector. The eluent is delivered by three different pumps (tip, focus, cross-flow) and the sample is injected by an autosampler (PN5300) into the channel. The channel has a trapezoidal geometry and an overall area of 31.6 cm². The nominal height of the spacer was 500 μm and a regenerated cellulose membrane with a molar mass cut-off of 10 kDa was used as accumulation wall. All experiments were carried out at 25 °C and the eluent was degassed water containing 5 mM NaCl. For all samples, the detector flow rate was set to 0.5 mL/min and 20 μL (10 mg/mL) were injected with an injection flow rate of 0.2 mL/min for 7 min. The cross-flow was set to 2.2 mL/min and after a constant period of 5 min it was decreased under an exponential gradient (0.5) to 0 mL/min within 35 min. Afterwards the cross-flow was kept constant at 0 mL/min for at least 45 min to ensure complete elution. For calculation of the molar mass Zimm plots were used. All measurements were done in triplicate. The refractive index increment (dn/dc) of all samples was measured by manual injection of a known concentration directly into the channel without any focusing or cross-flow. The dn/dc was calculated as the average of at least three injections from the area under the RI curve (AUCRI).

TEM measurements were performed on a FEI Technai G2 20 cryo-Transmission Electron Microscope at 200 kV. 15 μL of the sample solution were blotted onto carbon coated TEM grids (Mesh 400, Quantifoil) and excess material was removed by a filter paper (Whatman No. 1) under ambient conditions. Grid cleaning was performed by argon plasma treatment for 30 seconds prior to the preparation of the solutions. The samples were allowed to dry prior to the transfer to the microscope. After the sample solution was blotted onto the grid it was placed upside down onto a drop of uranyl acetate (1 wt%) for 30 minutes. A filter paper was used to remove excess material and the grid was dried for some minutes under ambient conditions.

UV-Vis spectra were recorded on a SPECORD® 250 UV-Vis spectrometer from Analytik Jena in 1 cm quartz cuvettes using the peltier temperature-controlled 8-cell changer. Measurements were performed at 25.0 °C unless stated otherwise. Turbidimetry was measured using a Crystal 16 from Avantium Technologies, connected to a chiller (Julabo FP 40) using a wavelength of 500 nm and a heating ramp of 1 K min⁻¹. Unless otherwise stated, cloud point temperatures (T_{CP}) are reported for 50% transmittance of the second heating run for a solution containing

5 mg/mL polymer in 1 mM *tris*(hydroxymethyl)aminomethane (TRIS)-buffered saline (TBS) buffer.

Glycomonomer Synthesis

General Procedure

2-Mercaptoethylacrylamide was dissolved in anhydrous dichloromethane (50 mL/g) and degassed by purging with nitrogen for 15 min. Peracetylated monosaccharide (1 equivalent) was added and the solution was cooled in an ice-water bath. Boron trifluoride diethyl etherate (48%) was slowly added (5 mL/h) to this solution. Subsequent to stirring at room temperature for 24 h the solution was washed with aqueous NaHCO₃ solution and brine, dried over anhydrous sodium sulfate and the solvent was evaporated under reduced pressure. The monomer was purified by column chromatography on silica gel (ethylacetate:hexane 3:1).

ManMAm

5.7 g (39.3 mmol) 2-Mercaptoethylacrylamide were reacted with 15.4 g (39.5 mmol) ManOAc and 26 mL boron trifluoride diethyl etherate (48%) according to the general procedure. $R_f = 0.47$ (ethylacetate:hexane 3:1). Yield: 3.11 g (17%).

¹H NMR (300 MHz, CDCl₃, δ): 1.96-2.15 (m, 15H, -CH₃), 2.75-2.93 (m, 2H, -CH₂-S-), 3.44-3.69 (m, 2H, -CH₂-NHCO), 4.09-4.14 (m, 1H, H6), 4.25-4.41 (m, 2H, H6, H4), 5.20-5.35 (m, 5H, H1,H2,H3,H5, C=CH₂), 5.70 (s, 1H, C=CH₂), 6.36 (s, 1H, NHCO). ¹³C NMR (75 MHz, CDCl₃, δ): 18.6, 20.6, 20.7, 20.9, 31.8, 39.0, 62.6, 66.3, 71.0, 82.7, 119.9, 139.8, 168.4, 169.7, 169.8, 169.9, 170.5. Elemental analysis: Calculated for C₂₀H₂₉NO₁₀S: C 50.52%, H 6.15%, N 2.95%, S 6.74%; Found: C 50.34%, H 6.41%, N 2.85%, S 6.35%.

GlcMAm

5.2 g (35.8 mmol) 2-Mercaptoethylacrylamide were reacted with 14.0 g (35.9 mmol) GlcOAc and 14 mL boron trifluoride diethyl etherate (48%) according to the general procedure. $R_f = 0.53$ (ethylacetate:hexane 3:1). Yield: 3.73 g (22%).

¹H NMR (300 MHz, CDCl₃, δ): 1.95-2.06 (m, 15H, -CH₃), 2.76-2.99 (m, 2H, -CH₂-S-), 3.37-3.68 (m, 2H, -CH₂-NHCO), 3.70-3.76 (m, 1H, H5), 4.08-4.24 (m, 2H, H6), 4.53 (d, ³J = 10.0 Hz, 1H, H1), 4.99-5.08 (m, 2H, H3, H4), 5.22 (t, ³J = 9.36 Hz, 1H, H2), 5.33 (s, 1H, C=CH₂), 5.71 (s, 1H, C=CH₂), 6.39 (s, 1H, NHCO). ¹³C NMR (75 MHz, CDCl₃, δ): 19.0, 21.0, 21.1, 31.0, 39.4, 62.4, 68.6, 70.1, 74.1, 76.4, 84.2, 120.1, 168.8, 169.9, 169.9, 170.5, 171.0. Elemental analysis: Calculated for C₂₀H₂₉NO₁₀S: C 50.52%, H 6.15%, N 2.95%, S 6.74%; Found: C 50.68%, H 6.25%, N 2.99%, S 6.70%.

RAFT Polymerization Reactions

General Procedure for RAFT Polymerization

The monomers as well as BTTCP and ACVA were dissolved in DMF ([monomer] = 2 mol/L) and the mixture was degassed by purging with argon for 1.5 h. After removal of an aliquot for conversion analysis the polymerization mixture was stirred at 80 °C for 15 h. Another aliquot (100 μ L) was removed for conversion analysis by ^1H NMR spectroscopy, using the integral of the isopropyl proton signal at 4 ppm as internal standard. The polymer was purified by precipitation into diethyl ether (PNiPAm) or a mixture of *n*-hexane and *tert*-butylmethyl ether 1:4 (glycopolymers), collected by filtration and dried under reduced pressure.

PNiPAm-1

4.0 g NiPAm (35.5 mmol) were polymerized according to the general procedure ([M]:[I]:[ACVA]=200:1:0.1). Conversion: 94%, yield: 3.63 g (91%).

AF4-MALLS: $\text{dn/dc} = 0.180 \pm 0.0012$ mL/g, $M_n = 16,600 \pm 800$ g/mol, $M_w = 18,400 \pm 700$ g/mol, PDI = 1.11.

SEC: $M_n = 26,300$ g/mol, $M_w = 33,000$ g/mol, PDI = 1.26.

PManAc-1

1.286 mg (11.36 mmol) NiPAm and 600 mg (0.63 mmol) **ManMAM** were polymerized according to the general procedure ([M]:[CTA]:[AVCA]=200:1:0.1). Conversion_{NiPAm}: 91%, conversion_{ManMAM}: 98%. Yield: 1.63 g (86%).

SEC: $M_n = 31,800$ g/mol, $M_w = 37,900$ g/mol, PDI = 1.19.

PGlcAc-1

2.142 mg (18.93 mmol) NiPAm and 1.000 mg (2.10 mmol) **GlcMAM** were polymerized according to the general procedure ([M]:[CTA]:[AVCA]=200:1:0.1). Conversion_{NiPAm}: 88%, conversion_{GlcMAM}: 93%. Yield: 2.51 g (80%).

SEC: $M_n = 33,000$ g/mol, $M_w = 36,800$ g/mol, PDI = 1.12.

Kinetic Investigation

For kinetic investigation of the copolymerization reactions, the same general procedure was applied with [M]:[CTA]:[AVCA]=200:1:0.1. Hydroquinone dimethyl ether (HDME) was added as internal standard (30 mol% of monomer) and samples were taken periodically with a degassed syringe for analysis by SEC and ^1H NMR spectroscopy. For integration of the signals in the ^1H NMR

spectra, the peak at 6.2 ppm corresponding to two double bond protons of NiPAM was used for determination of the NiPAM conversion, whereas the double bond signal at 5.7 ppm was used to determine the glycomonomer conversion, using the HDME signal at 6.85 ppm as internal standard.

PGlcAc-2

128.5 mg (1.14 mmol) NiPAM and 60 mg (126 μ mol) **GlcMAM** 94.53 μ L DMF were polymerized according to the general procedure [M]:[CTA]:[AVCA]=25:1:0.1. Conversion_{NiPAM}: 94%, conversion_{GlcMAM}: 100%. The polymer was purified by preparative size exclusion chromatography (BioBeads® column S-X1, eluent: THF) followed by precipitation into 15 mL of *n*-hexane and subsequently dried under reduced pressure. Yield: 95 mg (50%).

MALDI-TOF MS (matrix: DCTB): $M_n = 3,110$ g/mol, $M_w = 3,530$ g/mol, PDI = 1.13.

SEC: $M_n = 7,400$ g/mol, $M_w = 8,560$ g/mol, PDI = 1.16.

PManAc-2

201 mg (1.78 mmol) NiPAM and 94 mg (198 μ mol) **GlcMAM** were polymerized according to the general procedure [M]:[CTA]:[AVCA]=25:1:0.1. Conversion_{NiPAM}: 96%, conversion_{ManMAM}: 100%. The polymer was purified by preparative size exclusion chromatography (BioBeads® column S-X1, eluent: THF) followed by precipitation into 20 mL of *n*-hexane and subsequently dried under reduced pressure. Yield: 186 mg (63%).

MALDI-TOF MS (matrix: DCTB): $M_n = 2,860$ g/mol, $M_w = 3,210$ g/mol, PDI = 1.12.

SEC: $M_n = 6,000$ g/mol, $M_w = 6,770$ g/mol, PDI = 1.13.

Glycopolymer Deprotection

General Procedure for Glycopolymer Deprotection

The protected glycopolymer was dissolved in anhydrous methanol (4 mg/mL) and sodium methoxide solution (0.5 M in methanol) were added. After the solution was stirred for 2 h at room temperature, the mixture was neutralized with 1 M hydrochloric acid. The polymerization mixtures with [M]:[CTA]=200 were subjected to dialysis against deionized water (MWCO 3,500 g/mol). The polymerization mixtures with [M]:[CTA]=25 were purified by evaporation of the solvent, taking up the residue in ethanol, followed by filtration in order to remove the salt. After evaporation of the solvent the residue was re-dissolved in deionized water. Finally, all polymers were lyophilized.

PManOH-1

1,462 mg **PManAc-1** were deprotected with 1.6 mL sodium methoxide solution (0.5 M in methanol) according to the general procedure. Yield: 1.22 g (95%).

Elemental analysis: C 55.70%, H 9.38%, N 9.75%, S 1.90%.

AF4-MALLS: $dn/dc = 0.182 \pm 0.0015$ mL/g, $M_n = 18,700 \pm 130$ g/mol, $M_w = 22,200 \pm 300$ g/mol, PDI = 1.19.

SEC: $M_n = 31,100$ g/mol, $M_w = 41,700$ g/mol, PDI = 1.34.

PGlcOH-1

2,207 mg **PGlcAc-1** were deprotected with 2.35 mL sodium methoxide solution (0.5 M in methanol) according to the general procedure. Yield: 1.59 g (82%).

Elemental analysis: C 53.92%, H 9.07%, N 9.61%, S 1.77%.

AF4-MALLS: $dn/dc = 0.181 \pm 0.0017$ mL/g, $M_n = 16,300 \pm 1,000$ g/mol, $M_w = 20,000 \pm 500$ g/mol, PDI = 1.23.

SEC: $M_n = 31,700$ g/mol, $M_w = 41,500$ g/mol, PDI = 1.31.

PManOH-2

160 mg **PManAc-2** were deprotected with 170 μ L sodium methoxide solution (0.5 M in methanol) according to the general procedure. Yield: 145 mg (99%).

Elemental analysis: C 52.47%, H 8.51%, N 8.76%, S 4.02%.

MALDI-TOF MS (matrix: DCTB): $M_n = 2,650$ g/mol, $M_w = 2,760$ g/mol, PDI = 1.04.

SEC: $M_n = 6,730$ g/mol, $M_w = 7,840$ g/mol, PDI = 1.16.

PGlcOH-2

61 mg **PGlcAc-2** were deprotected with 65 μ L sodium methoxide solution (0.5 M in methanol) according to the general procedure. Yield: 45 mg (96%).

Elemental analysis: C 51.51%, H 8.43%, N 8.42%, S 3.48%.

MALDI-TOF MS (matrix: DCTB): $M_n = 3,180$ g/mol, $M_w = 3,320$ g/mol, PDI = 1.05.

SEC: $M_n = 8,770$ g/mol, $M_w = 10,100$ g/mol, PDI = 1.15.

Synthesis of Citrate Stabilized Gold Nanoparticles

The particles were synthesized as reported previously (40). Shortly, in a 250 mL round bottom flask 200 mL of a $\text{HAuCl}_4 \times 3\text{H}_2\text{O}$ (1 mM) solution was heated to 100 °C. 1 mL of a sodium citrate solution (0.78 M) was added at once while stirring under reflux. The color of the solution turned red after approximately 30 seconds, and heating was continued for 30 minutes. Subsequently, 1 mL of the citrate stabilized nanoparticles were centrifuged in a plastic vial at 5000 rpm for 90 min and 950 μL of the supernatant solution were removed. Afterwards 950 μL of distilled water were added and the particles were redispersed by simple shaking and short ultrasonication.

Immobilization of Glycopolymers onto Nanoparticles and Lectin Interaction

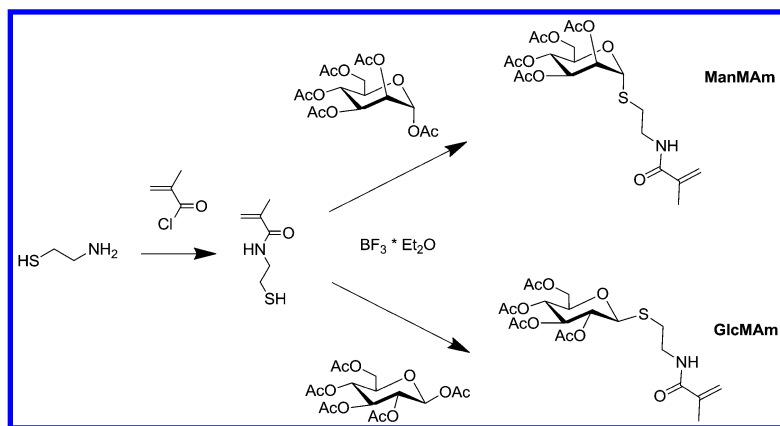
10 μL of polymer solution (1 mg/mL) were added to 1 mL of the obtained gold nanoparticle solution and incubated at room temperature for 1 h.

For the lectin interaction experiments, 200 μL of the functionalized nanoparticle solution (without centrifugation and re-dispersion) were diluted with 600 μL deionized water and 190 μL of TRIS buffered saline (pH 7.4, 5mM TRIS, 26 mM NaCl, 0.5 mM KCl) containing 5 mM Ca^{2+} , 5 mM Mn^{2+} and 5 mM Mg^{2+} (final gold concentration 40 $\mu\text{g}/\text{mL}$, final polymer concentration 2 $\mu\text{g}/\text{mL}$). Subsequently, ConA solution (0.1 mg/mL in TRIS buffered saline) was added to nanoparticle solution and the changes were monitored by UV-Vis spectroscopy.

Results and Discussion

Synthesis of Glycomonomer

S-Linked mannose and glucose bearing glycomonomers, **GlcMam** and **ManMam**, were synthesized as outlined in Scheme 1. First, 2-aminoethanethiol was reacted with methacryloylchloride to yield 2-mercaptoethylmethacrylamide (39). This compound was used as building block towards glycomonomers, exemplarily presented for glucose and mannose in this work. The obtained monomer with the nucleophilic thiol-group can react with peracetylated monosaccharides in a substitution reaction selectively at the anomeric position, retaining the α - or β -anomeric structure. The methacrylamide is less susceptible to side reactions (Michael addition), which immediately occurred for the acrylamide analogue monomer. 2-Mercaptoethylmethacrylamide only underwent Michael addition (polymerization) after extended storage time. Glycomonomer synthesis from this monomer was performed with peracetylated α -D-mannose and β -D-glucose, respectively, according to Scheme 1.



Scheme 1. Schematic representation of the glycomonomer synthesis.

The ^1H NMR spectra of the two purified monomers are depicted in Figure A1 (Appendix), proving the assumed structure of the two glycomonomers. The signals of the double bond protons could be clearly distinguished from the sugar ring protons *via* the heteronuclear single quantum coherence (HSQC) NMR spectrum (^1H , ^{13}C), depicted in Figure A2 and Figure A3, respectively (Appendix).

Synthesis of Glycopolymers by RAFT Polymerization

The protected glycomonomers were copolymerized with *N*iPAm *via* RAFT polymerization (Scheme 2), using 10 mol% of glycomonomer. BTTCP was used as chain transfer agent (CTA) and ACVA as initiator with a ratio of BTTCP:CTA of 10:1. In order to take advantage of the cluster glycoside effect by multivalent binding to biological receptors, polymers with several sugar repeating units are required. Therefore, glycopolymers with a target degree of polymerization (DP) of 200 were synthesized, controlling the chain length by the ratio of monomer to CTA ($[\text{M}]:[\text{CTA}]$).

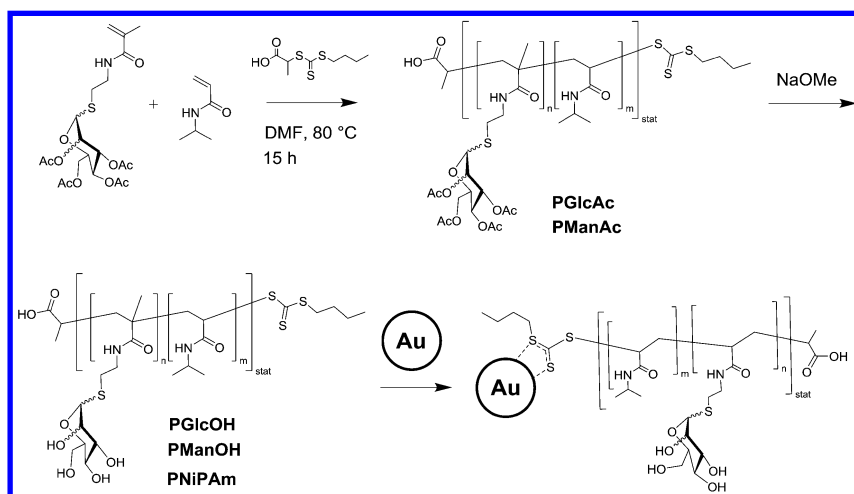
For later application of the glycopolymers (*i.e.*, immobilization) it is necessary to gain knowledge about the fate of the trithiocarbonate endgroup. Since the endgroup analysis is always easier for short polymers, glycopolymers with a target DP of 25 were also synthesized in the same way to obtain short model polymers.

The polymerizations with DP = 200 (**PManAc-1** and **PGlcAc-1**) were performed in DMF at 80 °C followed by purification *via* precipitation. Size exclusion chromatography (SEC) revealed narrow and monomodal molar mass distributions (Figure A4, Appendix) with low PDI values (PDI = 1.19 for **PManAc-1** and PDI = 1.12 for **PGlcAc-1**, respectively). However, these values as well as the molar mass values obtained by SEC alone (Table 1) are not reliable since no suitable calibration is available for the measured copolymers (see below for a discussion of the molar masses obtained from absolute methods).

Table 1. Summary of selected characterization data for the polymers synthesized by RAFT polymerization.

<i>Polymer</i>	<i>[M]:[CTA]</i>	<i>Conversion NiPAm [%]^a</i>	<i>Conversion glyco-monomer [%]^a</i>	<i>M_{n,theo} [g/mol]</i>	<i>M_n [g/mol]^b</i>	<i>PDI^b</i>
PManAc-1	200	91	98	28,090	31,800	1.19
PGlcAc-1	200	88	93	27,000	33,000	1.12
PNiPAm-1	200	94	-	21,500	26,300	1.26
PManAc-2	25	96	100	3,870	6,000	1.13
PGlcAc-2	25	94	100	3,820	7,400	1.16

^a obtained by ¹H NMR spectroscopy ^b obtained by SEC measurement



Scheme 2. Schematic representation of the glycopolymer synthesis via RAFT polymerization followed by deprotection of the sugar moieties and immobilization onto gold nanoparticles.

The conversions of the glycomonomers are slightly higher than the conversions of NiPAm, which is an indication for a slightly higher reactivity of the glycomonomer (Table 1). Therefore, the kinetics of the copolymerization reactions were studied (Figure A5, Appendix). As can be concluded from the pseudo-first order kinetic plot, the polymerization rate of the glycomonomers **ManMam** and **GlcMam** are indeed slightly higher than the polymerization rate of NiPAm. As a consequence, the statistical distribution of the glycomonomer repeating units in the final polymer chain is not strictly random but a small gradient in the monomer distribution is expected. As can be concluded from the initially linear slope of the kinetic plots (Figure A5 (left), Appendix) as well as the linear increase of the molar mass (M_n) with conversion (Figure A5 (right),

Appendix), the copolymerization is controlled up to conversions of 70%. A slight loss of control is observed for higher conversions, which can be ascribed to termination reactions, however, even for higher conversions the resulting PDI values are lower than 1.25.

The chemical structure of the copolymers was confirmed by ^1H NMR spectroscopy (Figure 1 and Figure A6, Appendix), showing the acetyl protecting groups of the sugar moieties in the protected glycopolymers **PManAc-1** and **PGlcAc-1**, respectively, as well as the signals arising from the sugar ring protons and the poly(*Ni*PAM) (*PNi*PAM) protons (the ^1H NMR spectrum of the analogue *PNi*PAM homopolymer **PNiPAm-1** is shown in Figure A7, Appendix).

Deprotection of the glycopolymers was achieved with sodium methoxide in anhydrous methanol (Scheme 2). With respect to end-group determination (see below) it is important to note that the short glycopolymers, **PManAc-2** and **PGlcAc-2**, were subjected to the same deprotection reaction as their longer analogues **PManAc-1** and **PGlcAc-1**. After purification by dialysis, the ^1H NMR spectra of the purified polymers **PManOH-1** and **PGlcOH-1** (Figure 1 and Figure A6, Appendix) reveal the disappearance of the acetyl protecting groups as well as a shift of the sugar ring protons to higher field, showing the successful deprotection of the glycopolymers. Due to this shift the signals of the sugar ring protons overlap with the isopropyl proton signal of *Ni*PAM. Therefore, a HSQC NMR spectrum (^1H , ^{13}C) was measured (Figure 1). This allows the assignment of the peaks in the region between 3 and 4 ppm (the complete spectra are depicted in Figure A8, Appendix, for **PManOH-1** and Figure A9 for **PGlcOH-1**, respectively). These spectra also reveal that the signals of the anomeric protons do not shift. Deprotection of the short glycopolymers **PGlcAc-2** and **PManAc-2** is confirmed in the same manner by ^1H NMR spectroscopy (Figure A10, Appendix).

Since the sugar proton signals in the ^1H NMR spectra overlay the methin proton signal of the isopropyl group (Figure 1 and Figure A6, Appendix), the sugar content of the glycopolymers **PManOH-1** and **PGlcOH-1** could not be determined by integration of the ^1H NMR spectra. Therefore, the sugar content was estimated by elemental analysis, using the ratio of sulfur to nitrogen content to obtain the number of sugar repeating units (in mol%), yielding 8.5 mol% mannose repeating units for **PManOH-1** and 8.0 mol% repeating units for **PGlcOH-1** (Table 2). These values are lower than expected from the monomer feed ratio, keeping in mind that the conversions of the glycomonomers were higher than the conversions of *Ni*PAM for the RAFT copolymerization reactions. The reason for this is presumably the purification step of the protected glycopolymers by precipitation in *tert*-butyl methyl ether. During this step the glycopolymer chains with a higher sugar content than 10% are more hydrophobic and more prone to dissolve in the hydrophobic precipitation medium. This results in a lowering of the average sugar content of the precipitated polymer.

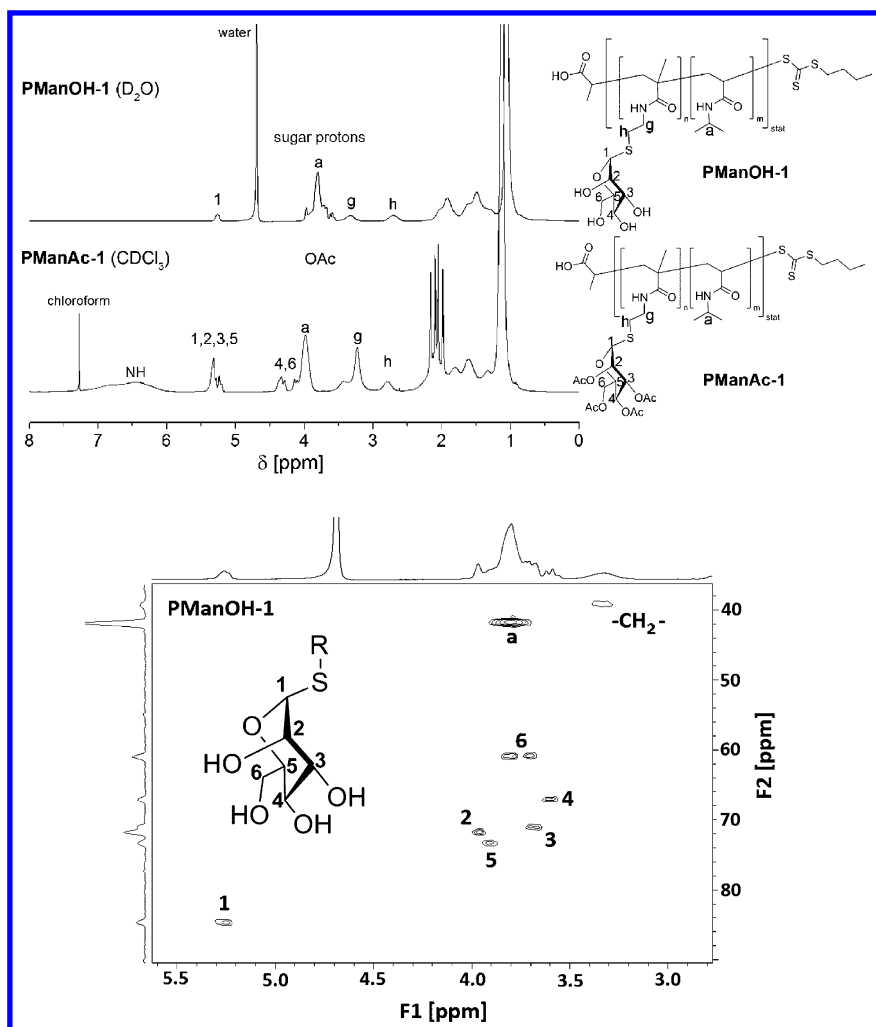


Figure 1. ^1H NMR spectra of the two glycopolymers **PManAc-1** and **PManOH-1** (top) and zoom into the HSQC NMR spectrum (^1H , ^{13}C) of the glycopolymer **PManOH-1** (bottom) showing the region of the sugar proton signals which overlap with the signal of the isopropyl methin protons of the NiPAm repeating units (300 MHz, CDCl_3 or D_2O).

Table 2. Summary of selected characterization data of the deprotected glycopolymers.

<i>Polymer</i>	<i>M_n</i> [g/mol] ^a	<i>PDI</i> ^a	<i>M_n</i> [g/mol]	<i>Sugar content</i> [mol%]	<i>Sugar DP</i> ^e	<i>T_{CP}</i> [°C]
PManOH-1	31,100	1.19 ^b	18,700 ^b	8.5 ^d	12.1	45.4
PGlcOH-1	31,700	1.23 ^b	16,300 ^b	8.0 ^d	10.0	47.4
PManOH-2	6,730	1.04 ^c	2,650 ^c	8.0 ^f	1.5	51.7
PGlcOH-2	8,770	1.05 ^c	3,180 ^c	7.6 ^f	1.7	53.0

^a obtained by SEC measurement, linear PS calibration ^b obtained by AF4-MALLS measurement ^c obtained from the MALDI-TOF mass spectra ^d determined via elemental analysis ^e calculated from the molar mass obtained by AF4-MALLS or MALDI-TOF MS and the sugar content ^f calculated from the elemental analysis and correction of the results by subtraction of the RAFT endgroup using the molar masses obtained from the MALDI-TOF mass spectra

In addition to ¹H NMR spectroscopy the successful deprotection is confirmed by the disappearance of the peak derived from the carbonyl groups of the acetyl protecting groups (1750 cm⁻¹) in the FT-IR spectrum of the deprotected glycopolymers compared to the protected precursors (Figure A11, Appendix).

The SEC traces of the deprotected glycopolymers **PGlcOH-1** and **PManOH-1** show a very small shift towards lower elution volumes compared to the protected precursors (Figure A4, Appendix), which is an indication for an increase of the hydrodynamic volume of the deprotected, more polar glycopolymer in the polar solvent of the chromatography system (*N,N*-dimethylacetamide). Also for the deprotection of the short glycopolymers **PGlcAc2** and **PManAc-2**, the analogue shift in the size exclusion chromatograms is observed (Figure A12, Appendix), indicating successful deprotection.

Since also for the determination of the molar masses of **PManOH-1** and **PGlcOH-1** by SEC no valid calibration was available, the *M_n* of these longer glycopolymers were determined by asymmetric flow field-flow fractionation (AF4) coupled to multi-angle laser light scattering (MALLS) detector (41). In the gentle characterization technique AF4 separation is achieved by a liquid cross-flow through a semipermeable membrane in a channel without any stationary phase. Together with MALLS, this technique gives access to the molar mass distribution (*M_n*, *M_w*, PDI) of the glycopolymers. The values of the sugar repeating units obtained by elemental analysis together with the molar masses obtained by the AF4-MALLS measurements were used to calculate the degree of polymerization of the glycomonomers (sugar DP), yielding 12 mannose repeating units per chain for **PManOH-1** and 10 glucose repeating units for **PGlcOH-1**, respectively (Table 2). These amounts of statistically incorporated sugar repeating units should be high enough to enable multivalent binding of one polymer chain.

The AF4 method, which could be used for the determination of the absolute molar masses of the long glycopolymer chains, cannot be applied for the short

analogues. Therefore, the short glycopolymers **PManAc-2** and **PGlcAc-2** were analyzed by MALDI-TOF mass spectrometry (Figure 2), which revealed the molar masses of **PGlcOH-2** and **PManOH-2**, for which no valid calibration was available for SEC (Table 2). Although MALDI-TOF mass spectrometry is an absolute technique for the determination of molar masses, the obtained M_n values are assumed to be lower than the real values because in MALDI-TOF mass spectrometry the smaller molecules are ionized more easily. Therefore, the real molar mass is expected to be in between the values obtained by MS and SEC (Table 2). Like for the long analogue glycopolymers, the sugar content of the short glycopolymers was estimated by elemental analysis. Here, since the polymers are much shorter, the influence of the endgroup has to be taken into account. Calculation of the sugar content, therefore, required the amount of trithiocarbonate endgroups per given amount of polymer, which is accessible *via* the molar mass obtained by mass spectrometry, revealing 8.0 mol% sugar repeating units for **PManOH-2** and 7.6 mol% sugar repeating units for **PGlcOH-2**, respectively. These values are in the same range as the values of the longer glycopolymers, which was not expected since the purification steps for the short polymers were performed differently (preparative size exclusion chromatography instead of precipitation) and should, therefore, result in higher sugar contents closer to the feed ratio of the copolymerization reactions. It has to be taken into account that the M_n values obtained by MS are expected to be slightly too low, therefore, a too high sulfur content is subtracted in the calculation step correcting the influence of the RAFT endgroup, leading to a corrected sulfur content, which is slightly lower than the real value.

A major advantage of MALDI-TOF MS is the possibility to obtain knowledge of the structure of the polymer in hand. The obtained MALDI-TOF mass spectra of the two protected glycopolymers (Figure 2) show very similar features. The main distance between two peaks corresponds to the molar mass of *Ni*PAm. Furthermore, different *PNi*PAm distributions could be observed in both cases, which correspond to the *PNi*PAm polymers with 0 to 3 protected sugar units (distance $m/z = 475.1$), which is confirmed by the comparison of calculated and measured isotopic patterns for both polymers **PManAc-2** and **PGlcAc-2** (Figure 2). In this way, MALDI-TOF mass spectrometry provides knowledge about the polymer endgroups, indicating that the carboxyl- and the trithiocarbonate endgroups are both attached to the polymer chains of all distributions found in the spectra.

The MALDI-TOF mass spectra of the deprotected glycopolymers **PGlcOH-2** and **PManOH-2** are very similar as well (Figure 3). In these spectra, different distributions are observed, all of them show the repeating unit of *Ni*PAm and are separated by an offset of 307.1, which corresponds to the molar mass of the deprotected sugar repeating unit. The peak assignment is validated by the calculated isotopic patterns, which fit to the observed isotopic patterns, as shown exemplarily for each distribution in Figure 3. Most importantly, the MALDI-TOF mass spectra of **PGlcOH-2** and **PManOH-2** show the peaks corresponding to the polymer chains with the RAFT endgroup still attached after the deprotection step. No peaks were found corresponding to a product where the trithiocarbonate endgroups were cleaved by sodium methoxide.

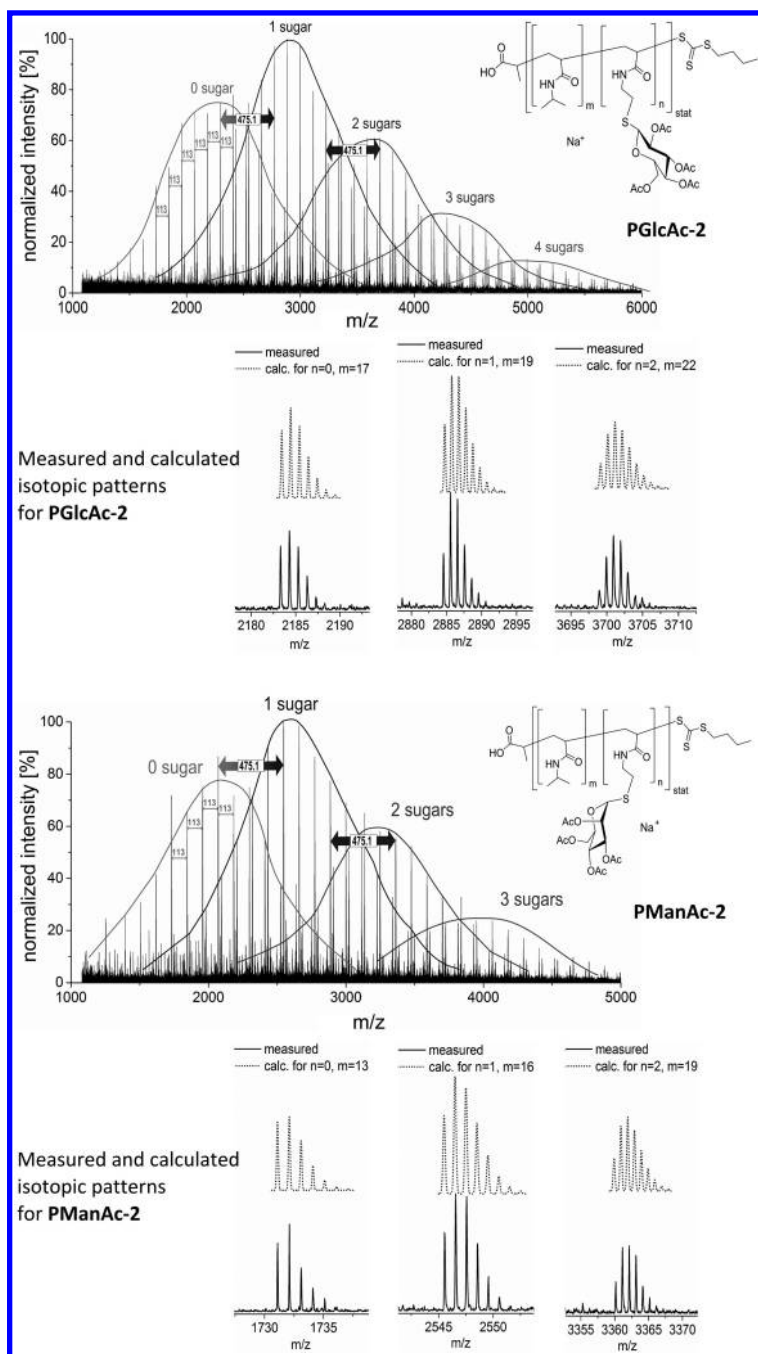


Figure 2. MALDI-TOF mass spectra of the protected glycopolymers **PGlcAc-2** (top) and **PManAc-2** (bottom, matrix DCTB) and selected isotopic patterns (right, calculated and measured).

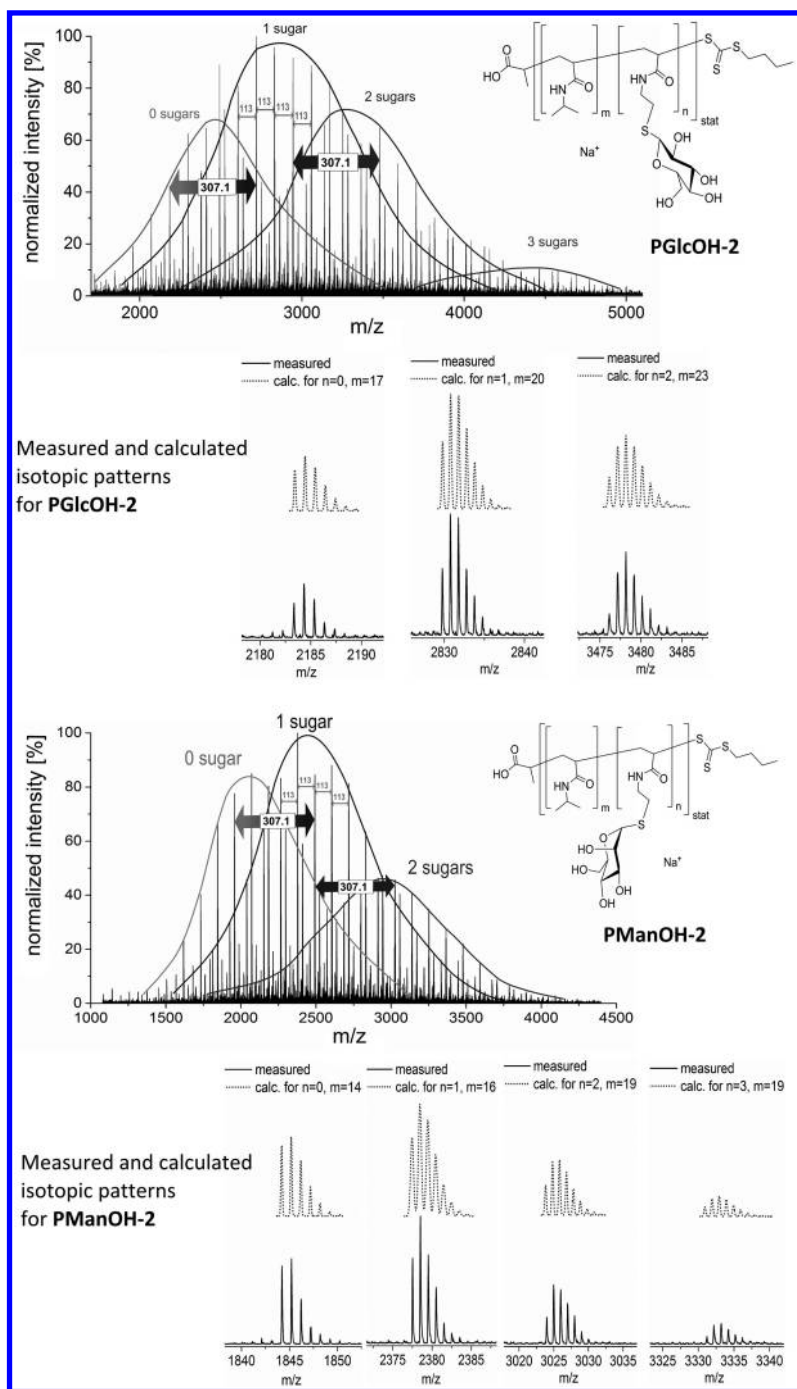


Figure 3. MALDI-TOF mass spectra of the deprotected glycopolymers **PGIcOH-2** (top) and **PManOH-2** (bottom, matrix DCTB) and selected isotopic patterns (right, calculated and measured).

These spectra in combination with the comparison of the measured and calculated isotopic patterns (Figure A13 to A20, Appendix) clearly proof the assumed structure of the synthesized glycopolymer with both endgroups, the carboxyl group and the trithiocarbonate, still attached to the polymer after deprotection. It is not possible to obtain such well resolved MALDI-TOF mass spectra for the longer analogue glycopolymers **PManOH-1** and **PGlcOH-1**, however, it can be assumed that the influence of the deprotection step and, therefore, the chemical identity of the endgroups is the same for the longer polymers.

Synthesis of Glycopolymer Coated Gold Nanoparticles

Citrate-stabilized nanoparticles for immobilization of the glycopolymers were prepared according to a literature procedure (40). Subsequently, the glycopolymers **PGlcOH-1** and **PManOH-1** as well as the NiPAm homopolymer **PNiPAm-1** were immobilized onto the surface of the gold nanoparticles (Scheme 2).

This immobilization was achieved *via* the trithiocarbonate RAFT endgroups of the polymers, as reported in literature for the direct immobilization of polymers derived from RAFT polymerization (16). The resulting polymer coated nanoparticles are stable over weeks.

Characterization of the functionalized nanoparticles by dynamic light scattering (DLS) revealed an increase of the particle diameter from 20.6 nm to 24 nm (Table 3). Additionally, the ζ -potential of the nanoparticle solutions shifted to lower negative values for the samples which were incubated with the polymers **PGlcOH-1**, **PManOH-1** and **PNiPAm-1**, respectively. This change of the ζ -potential shows that the polymers are immobilized onto the nanoparticle surface leading to replacement of the negatively charged citrate ions by non-charged polymer chains.

Table 3. DLS characterization data of the nanoparticles stabilized by the different polymers.

<i>Polymer</i>	<i>diameter [nm]</i>	<i>ζ-potential [mV]</i>	<i>λ_{max} (UV-Vis) [nm]</i>
-	20.62 ± 0.08	-45.37 ± 0.65	520.5
PManOH-1	22.92 ± 0.05	-39.0 ± 3.2	523.0
PGlcOH-1	22.45 ± 0.02	-39.27 ± 0.17	523.0
PNiPAm-1	23.79 ± 0.16	-36.17 ± 0.53	522.9

TEM imaging of a sample stained with uranylacetate (Figure 4) clearly showed the presence of the polymer shell with a thickness between 1 to 2 nm. This is in good agreement with the DLS results, which show a difference of the diameter of functionalized and unfunctionalized nanoparticles, which is in the

same order of magnitude. However, the nanoparticle diameter determined by DLS (Table 3) is slightly larger than by TEM measurement, which is ascribed to the swelling of the nanoparticles in the solvent for DLS measurement, which was also described in literature for a similar case (13).

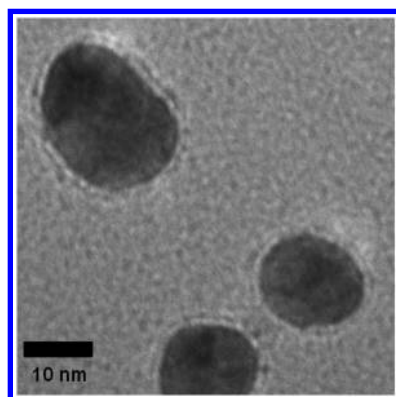


Figure 4. TEM image of gold particles coated with PManOH-1.

A further proof that the polymer is immobilized on the nanoparticle surface is the fact that the nanoparticles without polymer addition were not stable upon addition of TRIS buffered saline. This is indicated by a color change from red to blue, which shows aggregation of the particles. When gold nanoparticles are brought into close proximity the surface plasmon resonance shifts to higher wavelengths and also additional resonances arise. This is also obvious from the UV-Vis spectra, which immediately change drastically upon addition of the buffer solution to the nanoparticle solution (Figure A21, Appendix). On the other hand, the nanoparticles stabilized by **PGlcOH-1** and **PManOH-1** are stable under these conditions. A small shift of the maximum in the UV-Vis spectrum of the nanoparticles was observed upon addition of polymer (Table 3), reflecting the change in the direct environment of the gold nanoparticle surface. A higher concentration (10 fold) of polymer **PNiPAm-1** is required to stabilize the nanoparticles against addition of buffer solution. The reason for this might be the higher hydrophilic character of the glycopolymers **PGlcOH-1** and **PManOH-1**.

LCST Behavior

Since the temperature responsive behavior of the glycopolymers is of interest for potential applications, such as temperature-switchable affinity chromatography, this feature of the synthesized glycopolymers was investigated by turbidimetric studies.

The aqueous solutions of the glycopolymers display a very sharp transition from 100% to 0% transmission at 45.4 °C for **PManOH-1** and 47.4 °C for **PGlcOH-1** (Figure A22, Appendix). Furthermore, the cloud point temperatures (T_{CP}) are stable during repeated heating/cooling cycles (Figure A23, Appendix).

The increase of the transmittance upon cooling is observed approximately 2 °C lower than for the heating runs (Figure A24, Appendix). This kind of heating-cooling hysteresis of PNIPAm chains is known in literature and caused by the formation of hydrogen bonds between the amide bonds of the polymer chains, which have to be broken again upon cooling (42). Although the sugar content of **PManOH-1** is slightly higher than the sugar content of **PGlcOH-1**, the T_{CP} of the latter is slightly higher than the T_{CP} of the mannose glycopolymer. The same observations were made for the analogue shorter glycopolymers **PGlcOH-2** and **PManOH-2** (Table 2, Figure A25, Appendix). The T_{CP} s of the short glycopolymers **PManOH-2** and **PGlcOH-2** are slightly higher than the T_{CP} s of the analogue longer glycopolymers **PManOH-1** and **PGlcOH-1**, respectively (Table 2). This can be explained by the lower DP of these polymers. The lower chain length results in a more pronounced influence of the hydrophilic carboxylic endgroup compared to the longer polymers.

T_{CP} determination *via* turbidimetry relies on the decrease in transmittance that occurs upon phase separation of the binary polymer/water mixture upon heating. Therefore, it comes to no surprise that this method for T_{CP} determination has an inherent concentration dependence, since a lower amount of sample in the same volume cannot lead to the same turbidity simply because there is not enough material (the concentrated phase droplets) below certain concentrations. This is illustrated by the turbidity curves for solutions containing different concentrations of **PManOH-1** in Figure 5 (left), showing a decreased turbidity with decreasing concentration. Furthermore, this effect on the determined T_{CP} (Figure 5, right), which is due to the measurement technique, cannot be separated from the inherent concentration dependence. Consequently, below certain concentrations this method is not suitable for determination of cloud point temperatures. However, a method which does not rely on turbidity can be free from this concentration related limitation. As indicated earlier, the synthesized gold nanoparticles allow for determination of changes in the direct surface surrounding by change of the surface plasmon resonance detectable *via* UV-Vis spectroscopy.

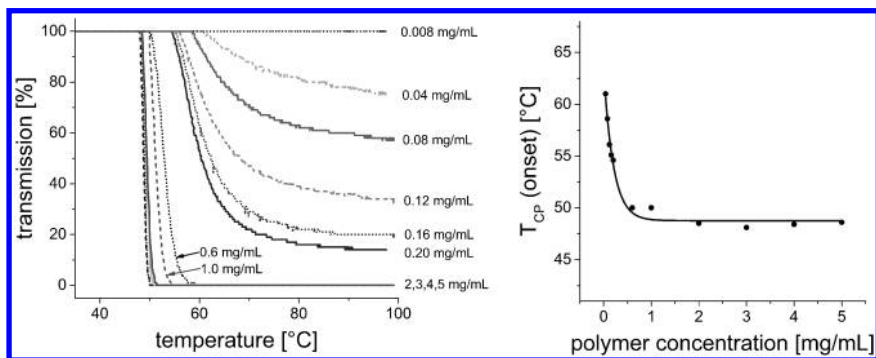


Figure 5. Turbidity curves (left) and cloud point temperatures of the glycopolymer **PManOH-1** (right, T_{CP} defined here as onset of transmission decrease) at different concentrations ($1\text{ K}\times\text{min}^{-1}$ in TBS).

Consequently, to evaluate if the LCST behavior of the glycopolymer **PManOH-1** is still present after immobilization onto the gold nanoparticles, UV-Vis spectra of the functionalized GNPs were measured at different temperatures. The increase of absorbance as well as the shift of the peak maximum show a significant increase above 47 °C, which can be attributed to the coil to globule transition of the glycopolymer. Interestingly, the nanoparticles do not aggregate immediately upon exceeding the coil to globule temperature. The first observation is a very pronounced and sudden increase of the wavelength of the peak maximum (λ_{max}), followed by a second increase upon further heating (Figure 6). The first increase is attributed to the coil to globule transition at the surface, which changes the surrounding of the nanoparticles. In contrast, the second increase is attributed to the aggregation of the nanoparticles, which is supported by a decrease of the peak upon introducing a 60 seconds equilibration time before each measurement (Figure 6, 3rd and 4th heating run). Furthermore, from Figure 6 it can be concluded that the coil to globule transition at the GNP surface is fully reversible upon cooling.

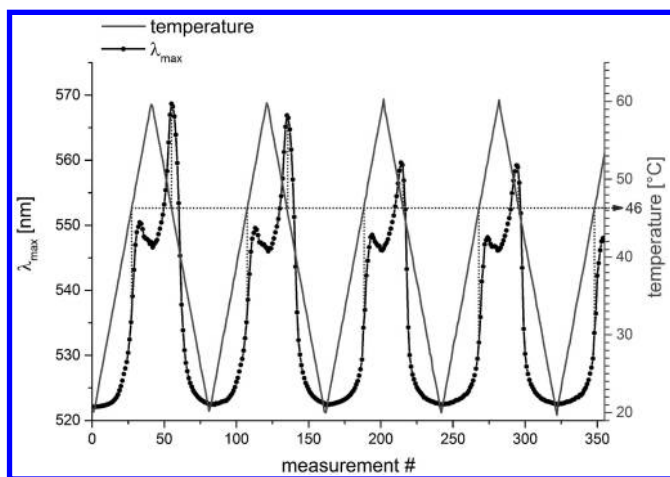


Figure 6. Change of the wavelength of the maximum in the UV-Vis spectra (λ_{max}) of the gold nanoparticles functionalized with PManOH-1 upon temperature change (polymer concentration: 2 $\mu\text{g/mL}$, gold concentration: 40 $\mu\text{g/mL}$; 1st and 2nd heating run: immediate measurement upon reaching the temperature, 3rd to 5th heating run: 60 seconds equilibration time before measurement).

These data show that the cloud point temperature of the immobilized glycopolymer is still present and can be conveniently analyzed by exploiting the surface plasmon resonance of the gold nanoparticles *via* UV-Vis spectroscopy. Another very advantageous aspect is the very low concentration, for which the determination of the coil to globule transition temperature is possible (the used polymer concentration was 2 $\mu\text{g/mL}$ and the applied gold concentration 40 $\mu\text{g/mL}$).

Lectin Interaction Experiments

In order to investigate the ability of the glycopolymer-functionalized nanoparticles to selectively recognize proteins, lectin interaction studies were performed *via* UV-Vis spectroscopy. A solution of ConA was added to a solution of gold nanoparticles (200 $\mu\text{g}_{\text{Au}}/\text{mL}$) stabilized by glycopolymer or the homopolymer, respectively. A buffer containing Mn^{2+} , Mg^{2+} and Ca^{2+} ions was used (final concentration 1 mM) because these ions are required by the used lectin to interact with carbohydrates. Upon lectin addition to the mannose glycopolymer, the nanoparticles aggregated, revealing interaction with the surface-immobilized glycopolymers. The aggregation, visible as turbidity followed by settling down of the aggregates, could be observed with the naked eye. However, for a more detailed investigation this phenomenon was followed *via* UV-Vis spectroscopy. This method is in particular suitable since the UV-Vis spectrum of the gold nanoparticles, which shows a pronounced peak due to the surface plasmon resonance, is very sensitive to the direct environment of the nanoparticle surface. A redshift of the UV-Vis spectrum could, therefore, be observed upon interaction (Figure 7 (a)). Moreover, a steady decrease of the absorbance was observed after lectin addition (Figure 7 (a)), which is caused by increasing aggregation and sedimentation of the nanoparticles. In contrast, no change of the UV-Vis absorption spectra could be observed for the particles stabilized by the glucose copolymer **PGlcOH-1** or the homopolymer **PNiPAm-1** (Figure 7 (b) and (c)), because the lectin ConA is binding specifically to α -mannose or α -glucose only. In order to study the binding interaction of ConA to the mannosylated nanoparticles in more detail, the wavelength of the peak maximum in the UV-Vis spectra is plotted against the interaction time in Figure 8. The plot clearly shows the increasing interaction of the nanoparticles stabilized with **PManOH-1** with increasing ConA concentration, whereas the peak maximum stays constant for the other polymers **PGlcOH-1** and **PNiPAm-1**. Furthermore, due to the high sensitivity of the SPR of the gold nanoparticles, these experiments could show interactions between polymer and lectin using polymer concentrations as low as 2 $\mu\text{g}/\text{mL}$.

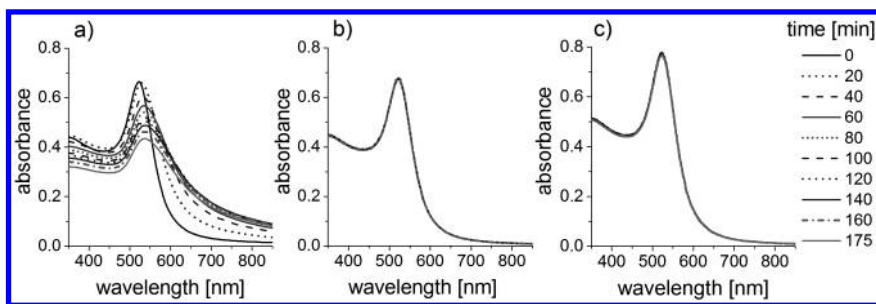


Figure 7. Overlay of the UV-Vis spectra recorded after different time intervals following lectin addition to nanoparticles stabilized by **PManOH-1** (a), **PGlcOH-1** (b) and **PNiPAm-1** (c).

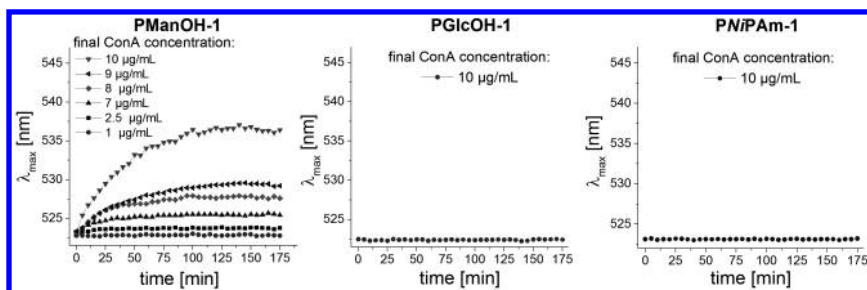


Figure 8. Change of the peak maxima of the UV-Vis spectra with time after addition of different amounts of ConA for glycopolymers stabilized by **PManOH-1** (left), **PGlcOH-1** (middle) and **PNIPAm-1** (right). The polymer concentrations were 2 $\mu\text{g/mL}$ in all cases, the gold concentration was 40 $\mu\text{g/mL}$.

As stated earlier, the LCST behavior of the immobilized glycopolymers also affects the UV-Vis spectrum and ultimately leads to aggregation of the GNPs. Therefore, the influence of the LCST transition on the binding interaction between the functionalized gold nanoparticles and the lectin cannot be studied using this system in solution. The next steps for an in-depth investigation of the influence of the LCST transition on the binding interaction will involve immobilization of the nanoparticles onto glass slides (6, 9, 11).

Conclusion

New acetyl-protected *S*-glycosidic mannose- and glucose bearing monomers were polymerized *via* reversible addition fragmentation chain transfer (RAFT) polymerization. The obtained glycopolymers were deprotected using sodium methoxide, leading to well-defined glycopolymers which were analyzed *via* ^1H NMR spectroscopy, size exclusion chromatography, MALDI-TOF mass spectrometry, AF4-MALLS, elemental analysis as well as FT-IR spectroscopy, confirming the expected polymer structure. Turbidimetric studies revealed the thermoresponsive properties of the glycopolymers with sharp coil-to-globule transitions in buffered aqueous solution. Subsequent immobilization of the glycopolymers as well as the *NiPAm* homopolymer onto gold nanoparticles was achieved without reduction of the RAFT endgroup, leading to stable glyco-nanoparticles. Subsequent spectroscopic studies showed the LCST feature of the immobilized mannose-functionalized polymer at concentrations not detectable with, *e.g.*, turbidimetry. Furthermore, the glycopolymer-functionalized gold nanoparticles were investigated towards their protein recognition capabilities, revealing binding of the mannosylated nanoparticles to the lectin Concanavalin A. Also for this study, very low polymer concentrations were sufficient, in contrast to turbidimetry, which is one of the commonly used techniques for determination of lectin interactions. However, unlike comparably sensitive methods like quartz crystal microbalance (QCM) or specialized surface plasmon resonance (SPR) devices, this method only requires a standard UV-Vis spectrophotometer.

In summary, a new mannose monomer as well as the analogue glucose monomer were synthesized and polymerized by RAFT polymerization. This synthetic strategy was shown to represent a versatile route towards well-defined thermoresponsive glycopolymers which can selectively recognize lectins.

The glycopolymer immobilized gold nanoparticles were shown to be an efficient sensor to determine LCST behavior as well as lectin interaction at very low polymer concentrations where turbidity measurements are not possible anymore.

Appendix

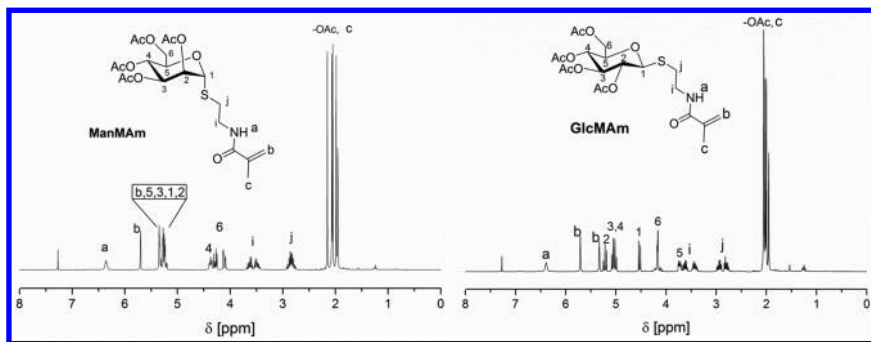


Figure A1. ^1H NMR spectra of the two glycomonomers *ManMam* (left) and *GlcMam* (right) (300 MHz, CDCl_3).

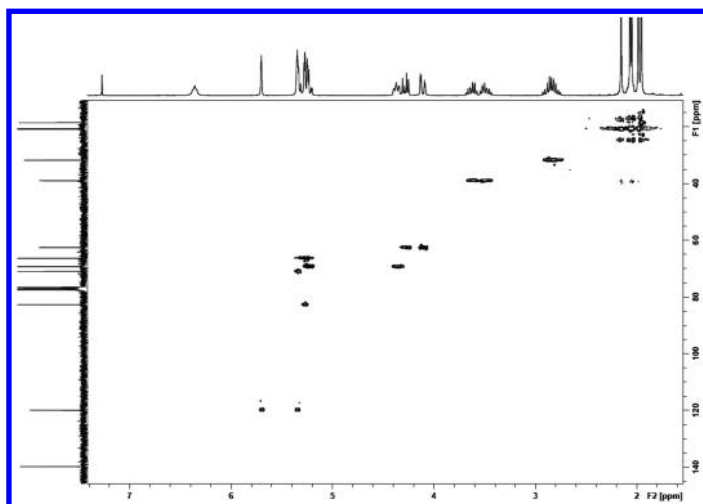


Figure A2. HSQC NMR spectrum of *ManMam* (300 MHz, CDCl_3).

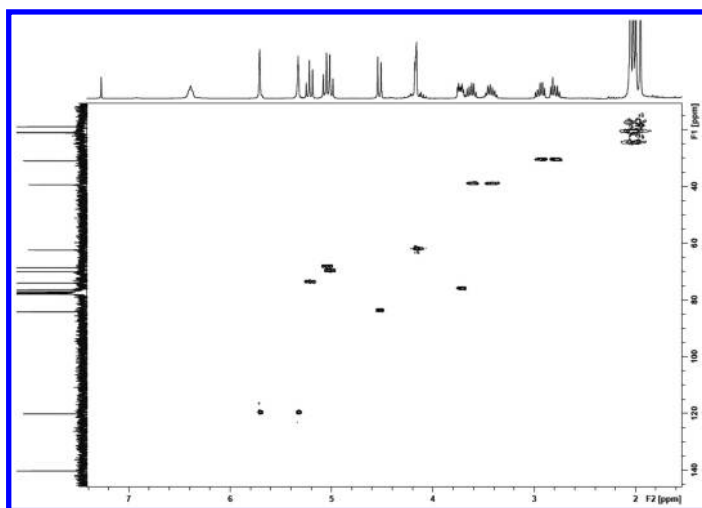


Figure A3. HSQC NMR spectrum of GlcMam (300 MHz, $CDCl_3$).

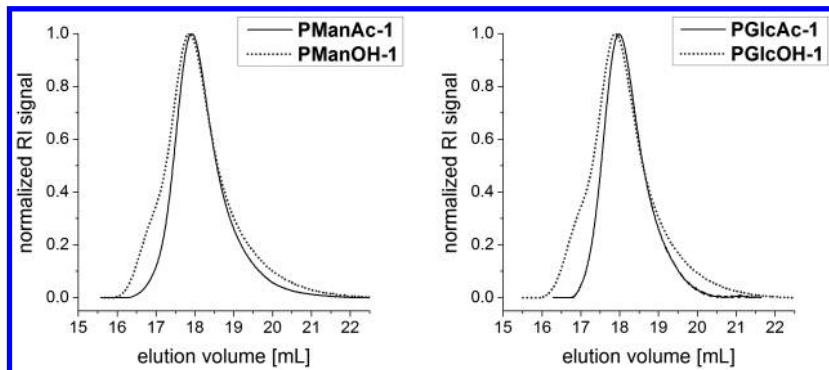


Figure A4. Overlay of the size exclusion chromatograms of selected protected and deprotected mannose carrying glycopolymers (left) and glucose carrying glycopolymers, (right) (DMAc/LiCl).

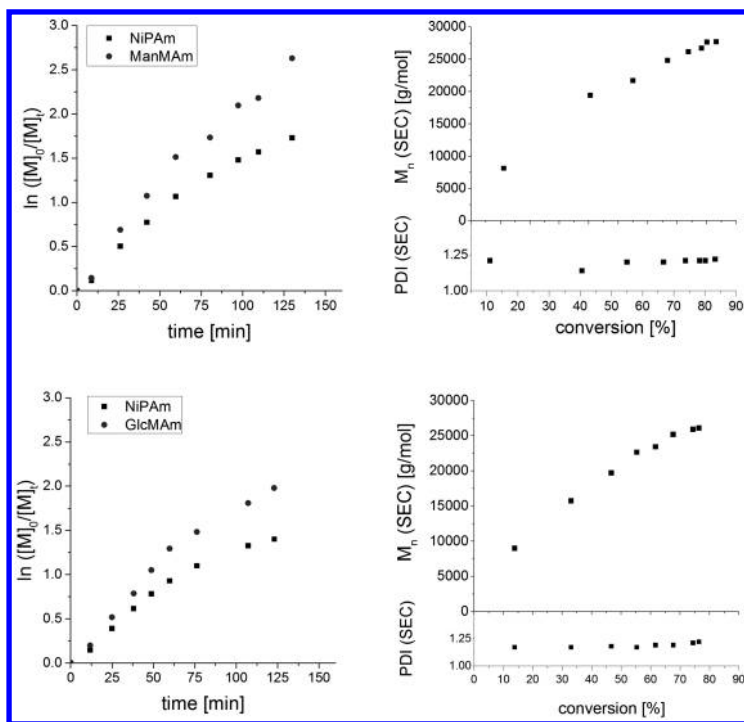


Figure A5. Pseudo-first order kinetic plot and molar mass versus conversion for the two copolymerizations of NiPAm with ManMAM (top) and GlcMAM (bottom), $([M]:[CTA]:[ACVA] = 200:1:0.1, [M] = 2 \text{ mol/L}$ in DMF, $T = 80 \text{ }^\circ\text{C}$).

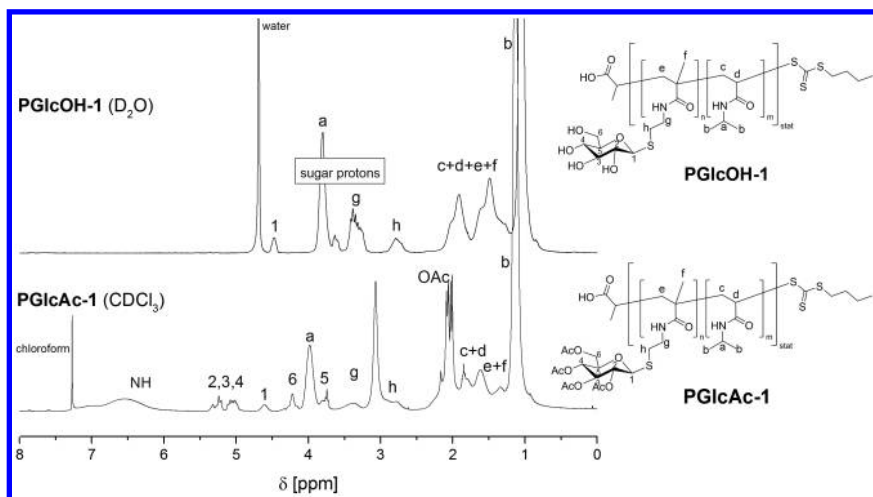


Figure A6. ^1H NMR spectra of the two glycopolymers PGlcAc-1 and PGlcOH-1 (300 MHz, CDCl_3 or D_2O).

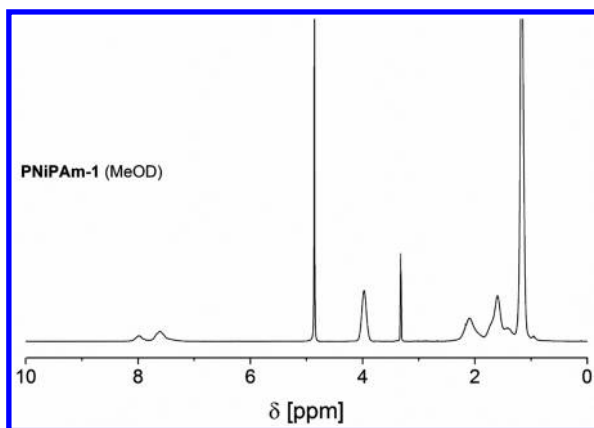


Figure A7. ^1H NMR spectrum of *PNiPAm-1* (300 MHz, MeOD).

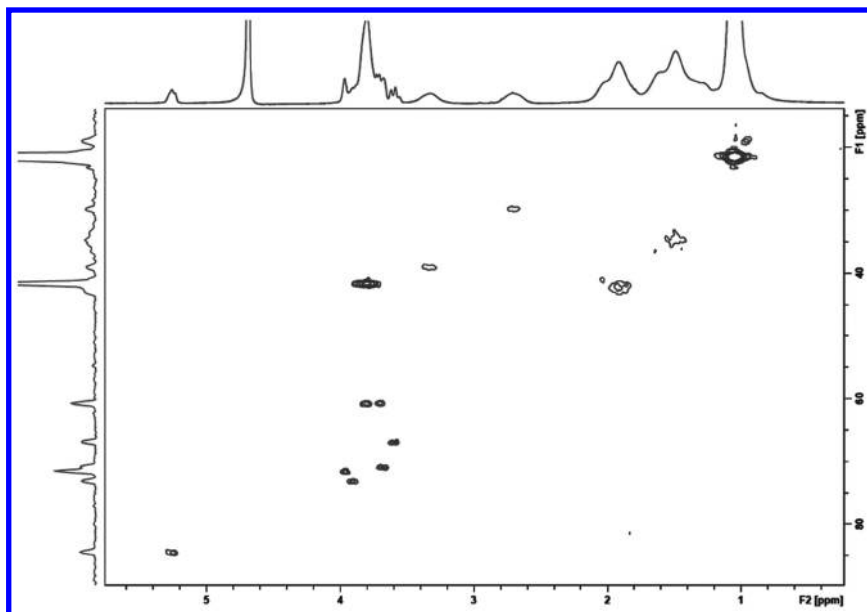


Figure A8. HSQC NMR spectrum of *PManOH-1* (300 MHz, D_2O).

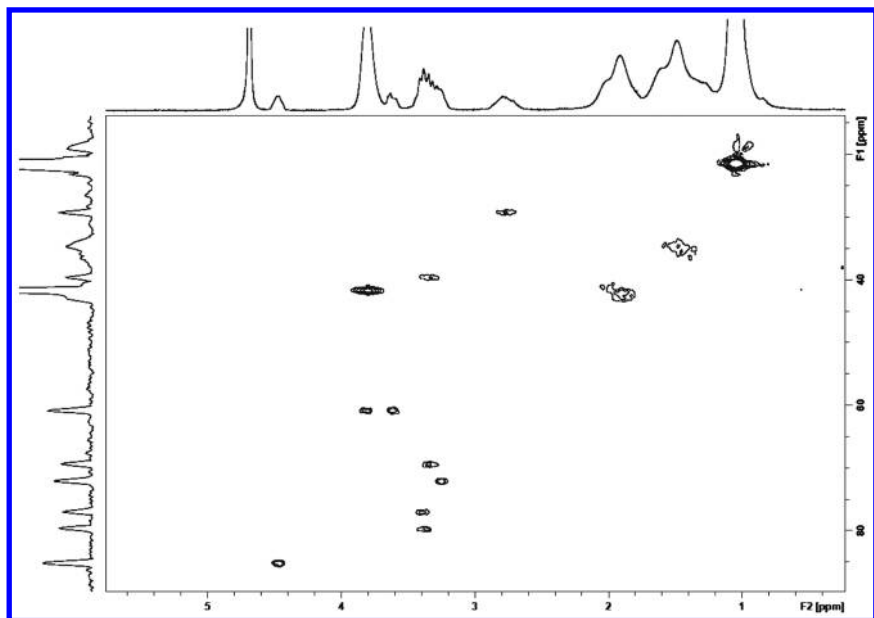


Figure A9. HSQC NMR spectrum of PGlcOH-1 (300 MHz, D₂O).

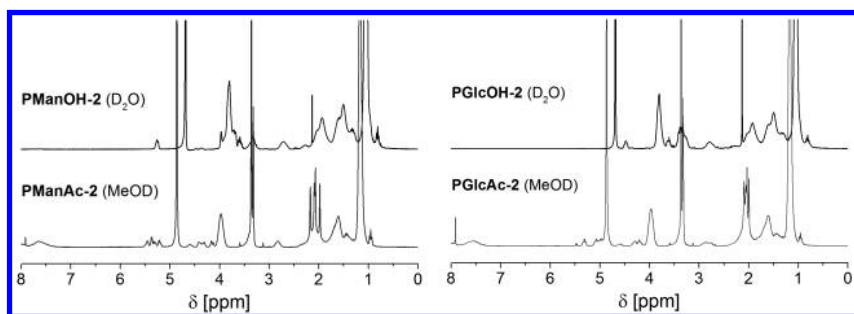


Figure A10. Overlay of ¹H NMR spectra of PManAc-2 and PManOH-2 (left) as well as PGlcAc-2 and PGlcOH-2 (right, 300 MHz, MeOD or D₂O).

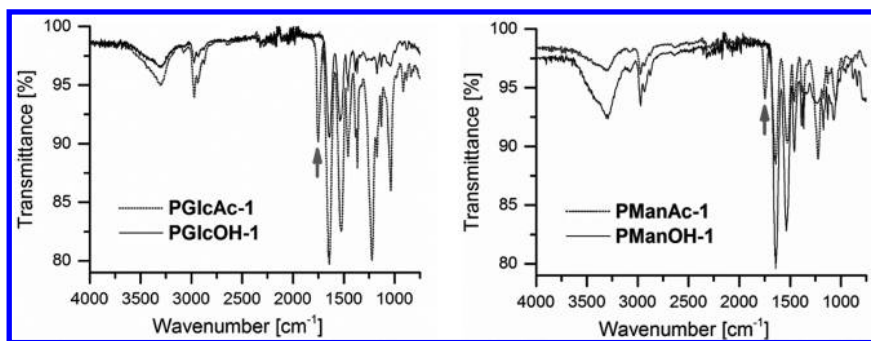


Figure A11. Overlay of the ATR FT-IR spectra of the protected and deprotected glucose glycopolymer (left) and overlay of the protected as well as the deprotected mannose glycopolymers (right).

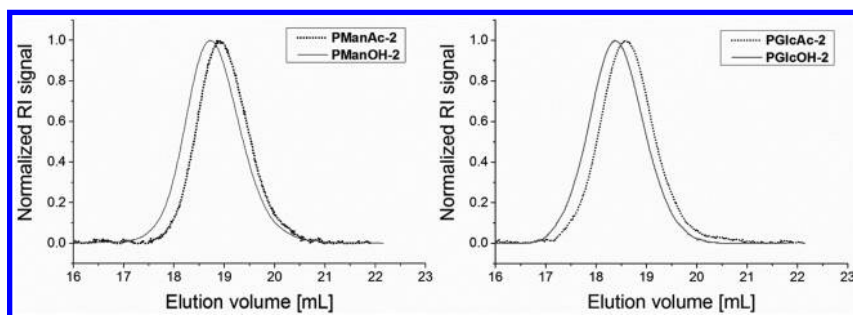


Figure A12. Overlay of the size exclusion chromatograms of *PManAc-2* and *PManOH-2* (left) as well as *PGIcAc-2* and *PGIcOH-2* (right).

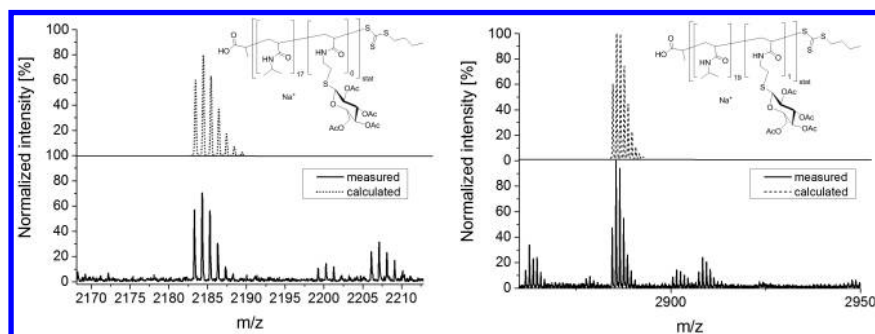


Figure A13. Overlay of the measured and calculated isotopic patterns without protected glucose repeating unit (left) and with one protected glucose repeating unit (right), calculated for $C_3H_5O_2(C_6H_{11}NO)_{17}C_5H_9S_3 + Na^+$ (left) and $C_3H_5O_2(C_{20}H_{29}NO_{10}S)_1(C_6H_{11}NO)_{19}C_5H_9S_3 + Na^+$ (right).

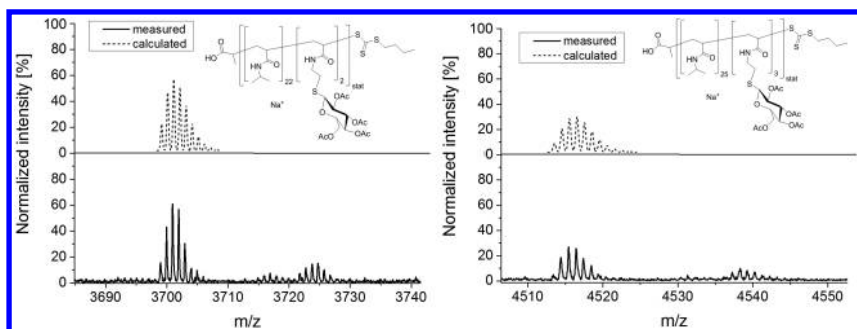


Figure A14. Overlay of the measured and calculated isotopic patterns with two protected glucose repeating units (left) and three protected glucose repeating units (right), calculated for $C_3H_5O_2(C_{20}H_{29}NO_{10}S)_2(C_6H_{11}NO)_{22}C_5H_9S_3 + Na^+$ (left) and $C_3H_5O_2(C_{20}H_{29}NO_{10}S)_3(C_6H_{11}NO)_{25}C_5H_9S_3 + Na^+$ (right).

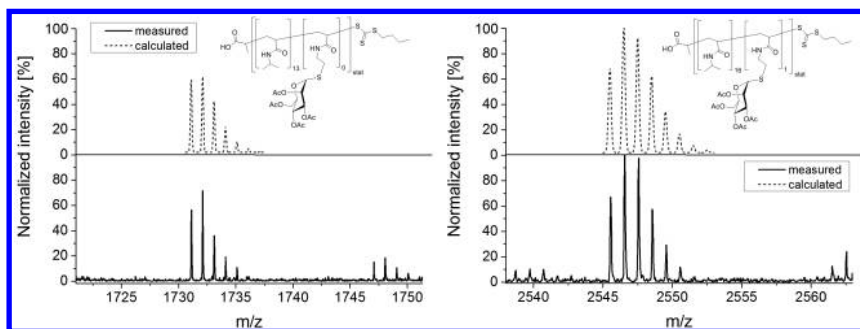


Figure A15. Overlay of the measured and calculated isotopic patterns without mannose repeating unit (left) and with one protected mannose repeating unit (right), calculated for $C_3H_5O_2(C_6H_{11}NO)_{13}C_5H_9S_3 + Na^+$ (left) and $C_3H_5O_2(C_{20}H_{29}NO_{10}S)_1(C_6H_{11}NO)_{16}C_5H_9S_3 + Na^+$ (right).

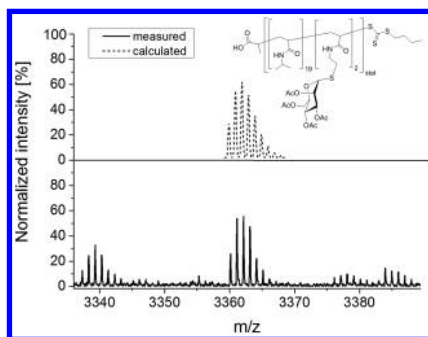


Figure A16. Overlay of the measured and calculated isotopic patterns with two protected mannose repeating units, calculated for $C_3H_5O_2(C_{20}H_{29}NO_{10}S)_2(C_6H_{11}NO)_{19}C_5H_9S_3 + Na^+$.

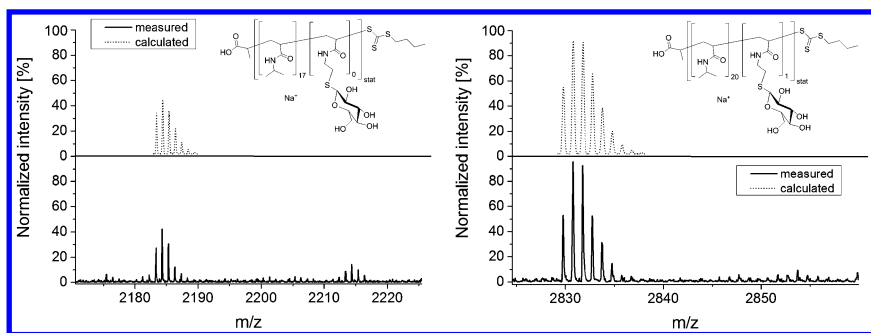


Figure A17. Overlay of the measured and calculated isotopic patterns without (left) and with one (right) glucose repeating unit. Calculated for $C_3H_5O_2(C_6H_{11}NO)_{17}C_5H_9S_3 + Na^+$ (left) and $C_3H_5O_2(C_{12}H_{21}NO_6S)(C_6H_{11}NO)_{20}C_5H_9S_3 + Na^+$ (right).

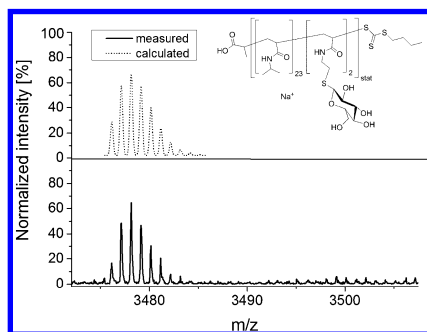


Figure A18. Overlay of the measured and calculated isotopic pattern with two repeating units of glucose, calculated for $C_3H_5O_2(C_{12}H_{21}NO_6S)_2(C_6H_{11}NO)_{23}C_5H_9S_3 + Na^+$.

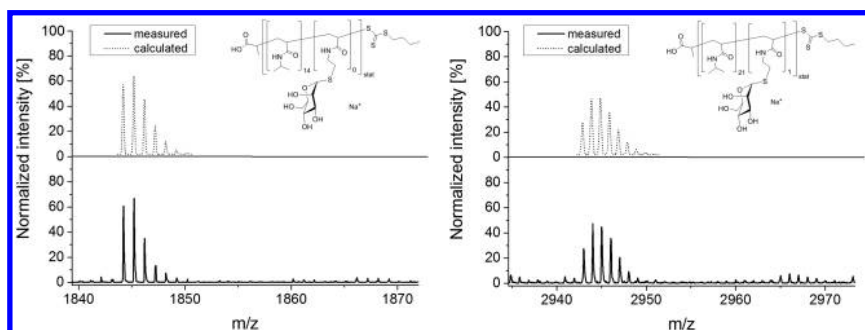


Figure A19. Overlay of the measured and calculated isotopic patterns without (left) and with one (right) deprotected mannose repeating unit, calculated for $C_3H_5O_2(C_6H_{11}NO)_{14}C_5H_9S_3 + Na^+$ (left) and $C_3H_5O_2(C_{12}H_{21}NO_6S)_1(C_6H_{11}NO)_{21}C_5H_9S_3 + Na^+$ (right).

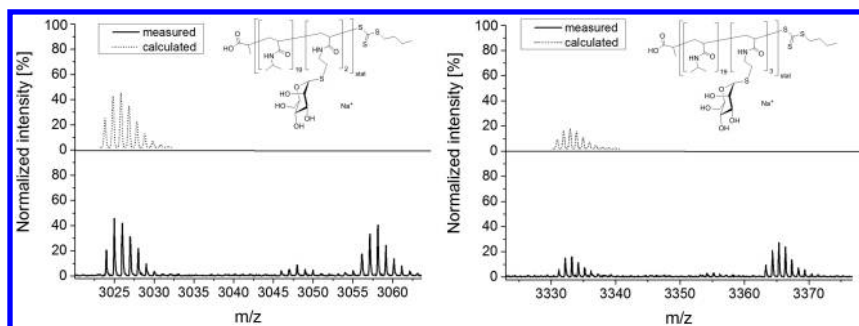


Figure A20. Overlay of the measured and calculated isotopic patterns with two (left) and three (right) deprotected mannose repeating units, calculated for $C_3H_5O_2(C_{12}H_{21}NO_6S)_2(C_6H_{11}NO)_{19}C_5H_9S_3 + Na^+$ (left) and $C_3H_5O_2(C_{12}H_{21}NO_6S)_3(C_6H_{11}NO)_{19}C_5H_9S_3 + Na^+$ (right).

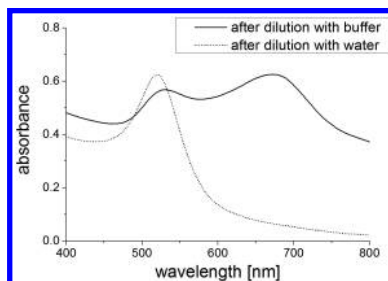


Figure A21. Overlay of UV/Vis spectra of the nanoparticle solution (same concentrations as for the lectin experiment) with and without buffer.

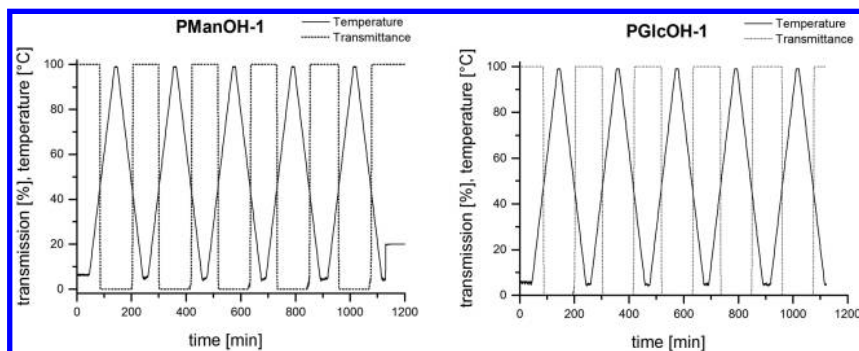


Figure A22. Turbidimetric determination of the cloud point temperatures of the two glycopolymers **PManOH-1** (left) and **PGlcOH-1** (right) (5 mg/mL in TBS).

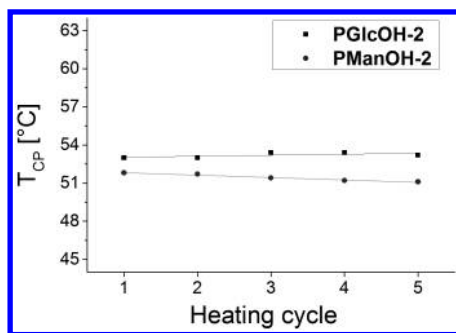


Figure A23. T_{CP} s of **PGIcOH-2** and **PManOH-2** of successive heating cycles.

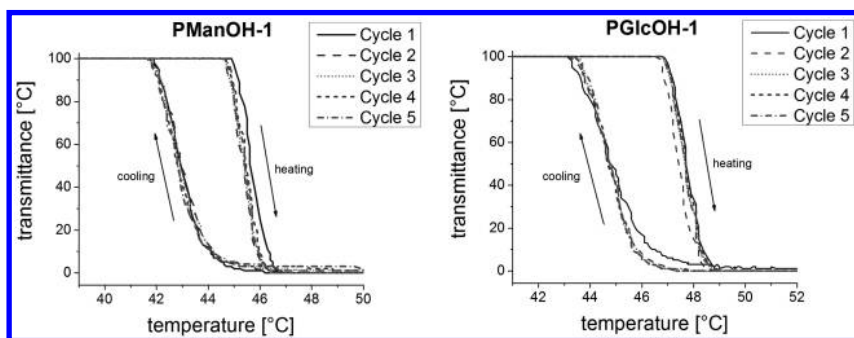


Figure A24. Transmittance plotted vs. temperature to show the heating-cooling hysteresis of the association and dissociation of the polymer chains in aqueous solution (5 mg/mL in TBS, heating rate $1 \text{ K} \times \text{min}^{-1}$).

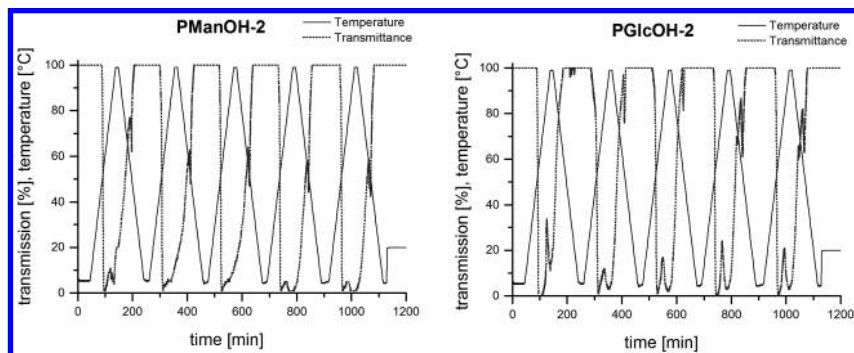


Figure A25. Turbidimetric study of aqueous solutions of **PManOH-2** (left) as well as **PGIcOH-2** (right) (5 mg/mL in TBS).

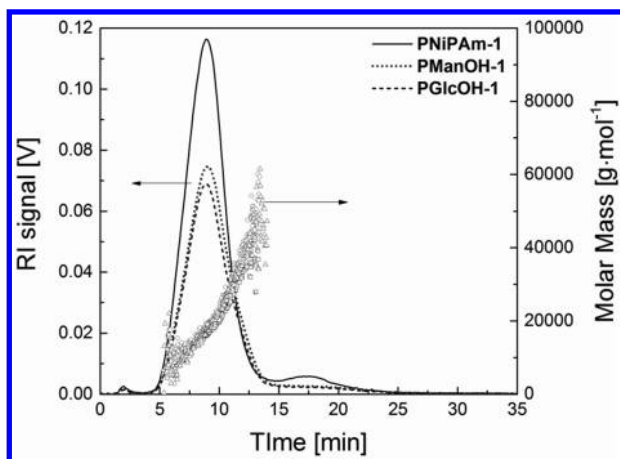


Figure A26. Overlay of the AF4-MALLS fractograms of *PNiPAm-1*, *PManOH-1* and *PGlcOH-1* with 5 mM NaCl as eluent.

Acknowledgments

This research forms part of the research program of the Dutch Polymer Institute (DPI), project #686. CW is thankful to the Carl Zeiss Foundation. Financial support from the research initiative PhoNa (Photonic nanomaterials), which is supported by the German Federal Ministry of Education and Research in the program "Spitzenforschung und Innovation in den Neuen Ländern" (support code 03IS2101A), is acknowledged. The authors also acknowledge the Thüringer Ministerium für Bildung, Wissenschaft und Kultur (grant no. B515-07008) for financial support. M. Wagner is acknowledged for the AF4 measurements. The authors also thank Bruker Daltonics for their help and support. TEM measurements were performed at the JSCM facilities, which were financed by the DFG and the European Fonds for Regional Development (EFRE).

References

- Vázquez-Dorbatt, V.; Lee, J.; Lin, E.-W.; Maynard, H. D. *ChemBioChem* **2012**, *13*, 2478–2487.
- Godula, K.; Bertozzi, C. R. *J. Am. Chem. Soc.* **2012**, *134*, 15732–15742.
- Godula, K.; Bertozzi, C. R. *J. Am. Chem. Soc.* **2010**, *132*, 9963–9965.
- Narla, S. N.; Sun, X.-L. *Lab Chip* **2012**, *12*, 1656–1663.
- Narain, R.; Housni, A.; Gody, G.; Boullanger, P.; Charreyre, M.-T.; Delair, T. *Langmuir* **2007**, *23*, 12835–12841.
- Anraku, Y.; Takahashi, Y.; Kitano, H.; Hakari, M. *Colloids Surf., B* **2007**, *57*, 61–68.
- Housni, A.; Cai, H.; Liu, S.; Pun, S. H.; Narain, R. *Langmuir* **2007**, *23*, 5056–5061.
- Kitano, H.; Nakada, H.; Mizukami, K. *Colloids Surf., B* **2008**, *61*, 17–24.

9. Mizukami, K.; Takakura, H.; Matsunaga, T.; Kitano, H. *Colloids Surf., B* **2008**, *66*, 110–118.
10. Vázquez-Dorbatt, V.; Tolstyka, Z. P.; Chang, C.-W.; Maynard, H. D. *Biomacromolecules* **2009**, *10*, 2207–2212.
11. Kitano, H.; Saito, D.; Kamada, T.; Gemmei-Ide, M. *Colloids Surf., B* **2012**, *93*, 219–225.
12. Huang, M.; Shen, Z.; Zhang, Y.; Zeng, X.; Wang, P. G. *Bioorg. Med. Chem. Lett.* **2007**, *17*, 5379–5383.
13. Toyoshima, M.; Miura, Y. *J. Polym. Sci., Part A: Polym. Chem.* **2009**, *47*, 1412–1421.
14. Spain, S. G.; Albertin, L.; Cameron, N. *Chem. Commun.* **2006**, 4198–4200.
15. Ishii, J.; Toyoshima, M.; Chikae, M.; Takamura, Y.; Miura, Y. *Bull. Chem. Soc. Jpn.* **2011**, *84*, 466–470.
16. Ebeling, B.; Vana, P. *Macromolecules* **2013**, *46*, 4862–4871.
17. Rossner, C.; Vana, P. *Angew. Chem.* **2014**, *126*, 1–5.
18. Pearson, S.; Chen, G.; Stenzel, M. H. Synthesis of Glycopolymers. In *Engineered Carbohydrate-based Materials for Biomedical Applications: Polymers, Surfaces, Dendrimers, Nanoparticles, and Hydrogels*; Narain, R., Ed.; John Wiley & Sons, Inc.: Hoboken, NJ, USA, 2011; pp 1–118.
19. Ting, S. R. S.; Min, E. H.; Escalé, P.; Save, M.; Billon, L.; Stenzel, M. H. *Macromolecules* **2009**, *42*, 9422–9434.
20. Ghadban, A.; Albertin, L. *Polymers* **2013**, *5*, 431–526.
21. Shen, H.; Byers, L. D. *Biochem. Biophys. Res. Commun.* **2007**, *362*, 717–720.
22. Wilson, J. C.; Kiefel, M. J.; Angus, D. I.; von Itzstein, M. *Org. Lett.* **1999**, *1*, 443–446.
23. Chen, G.; Amajjahe, S.; Stenzel, M. H. *Chem. Commun.* **2009**, 1198–1200.
24. Diehl, C.; Schlaad, H. *Chem. Eur. J.* **2009**, *15*, 11469–11472.
25. Diehl, C.; Schlaad, H. *Macromol. Biosci.* **2009**, *9*, 157–161.
26. Von der Ehe, C.; Czaplewska, J. A.; Gottschaldt, M.; Schubert, U. S. *Eur. Polym. J.* **2013**, *49*, 2660–2669.
27. Eissa, A. M.; Khosravi, E. *Eur. Polym. J.* **2011**, *47*, 61–69.
28. Zhang, L.; Bernard, J.; Davis, T. P.; Barner-Kowollik, C.; Stenzel, M. H. *Macromol. Rapid. Commun.* **2008**, *29*, 123–129.
29. Shinde, V. S.; Pawar, V. U. *J. Appl. Polym. Sci.* **2009**, *111*, 2607–2615.
30. Pasparakis, G.; Cockayne, A.; Alexander, C. *J. Am. Chem. Soc.* **2007**, *129*, 11014–11015.
31. Özyürek, Z.; Voit, B.; Krahl, F.; Arndt, K.-F. *e-Polymers* **2010**, *44*, 1–13.
32. Özyürek, Z.; Komber, H.; Gramm, S.; Schmaljohann, D.; Müller, A. H. E.; Voit, B. *Macromol. Chem. Phys.* **2007**, *208*, 1035–1049.
33. Min, E. H.; Ting, S. R. S.; Billon, L.; Stenzel, M. H. *J. Polym. Sci., Part A: Polym. Chem.* **2010**, *48*, 3440–3455.
34. Luo, Y.; Liu, L.; Wang, X.; Shi, H.; Lv, W.; Li, J. *Soft Matter* **2012**, *8*, 1634–1642.
35. Kumar, J.; McDowall, L.; Chen, G.; Stenzel, M. H. *Polym. Chem.* **2011**, *2*, 1879–1886.

36. Idota, N.; Ebara, M.; Kotsuchibashi, Y.; Narain, R.; Aoyagi, T. *Sci. Technol. Adv. Mater.* **2012**, *13*, 1–9.
37. Yusa, S.; Fukuda, K.; Yamamoto, T.; Iwasaki, Y.; Watanabe, A.; Akiyoshi, K.; Morishima, Y. *Langmuir* **2007**, *23*, 12842–12848.
38. Kusolkamabot, K.; Sae-ung, P.; Niamnont, N.; Wongravee, K.; Sukwattanasinitt, M.; Hoven, V. P. *Langmuir* **2013**, *29*, 12317–12327.
39. Firouzzare, M.; Wang, Q. *Talanta* **2012**, *101*, 261–266.
40. Kretschmer, F.; Mansfeld, U.; Hoepfener, S.; Hager, M. D.; Schubert, U. S. *Chem. Commun.* **2014**, *50*, 88–90.
41. Yohannes, G.; Jussila, M.; Hartonen, K.; Riekkola, M.-L. *J. Chromatogr. A* **2011**, *1218*, 4104–4116.
42. Cheng, H.; Shen, L.; Wu, C. *Macromolecules* **2006**, *39*, 2325–2329.

Chapter 16

The Drug-Initiated Method: A Convenient Approach for the Synthesis of Efficient Polymer Prodrug Nanoparticles

Simon Harrisson,¹ Andrei Maksimenko,² Duc Trung Bui,²
Didier Desmaële,² Patrick Couvreur,² and Julien Nicolas^{2,*}

¹IMRCP, UMR CNRS 5623, Univ Toulouse, 118 route de Narbonne,
F-31062 Toulouse cedex 9, France

²Institut Galien Paris-Sud, Univ Paris-Sud, UMR CNRS 8612, Faculté de
Pharmacie, 5 rue Jean-Baptiste Clément, F-92296 Châtenay-Malabry cedex,
France

*E-mail: julien.nicolas@u-psud.fr

Herein is reported the synthesis of new amphiphilic polymer prodrug nanoparticles by controlled radical polymerization (CRP) and their biological evaluation against cancer. The methodology, termed '*drug initiated*', consisted in growing a short hydrophobic polymer chain from a pre-modified hydrophilic drug under CRP conditions. It resulted in well-defined amphiphilic drug-polymer conjugates able to form self-stabilized prodrug nanoparticles with significant anticancer activity *in vitro* and *in vivo*. This was illustrated by the use of the anticancer drug gemcitabine (Gem) which was functionalized with CRP moieties for the synthesis of two different biorelevant polymer promoieties: polyisoprene and a polymethacrylate with pending squalene as a natural lipid.

Introduction

Drug-containing nanocarriers hold significant promise in nanomedicine for precisely delivering the drug to the diseased areas in the body while avoiding nonspecific cell and tissue biodistribution as well as rapid metabolization and excretion (1–4). Yet, in order to overcome the main limitations encountered with

physically encapsulated drugs (e.g., burst release, limited and hardly tunable drug payloads, etc.), the prodrug concept (5), whereby the drug is covalently linked to the nanocarriers, has been proposed for suppressing the burst release and leading to a controlled drug release (6). For instance, anticancer drugs have been covalently linked to preformed amphiphilic copolymers (7–15), leading to a sustained anticancer drug release from the nanoparticles by hydrolysis. There are also many reports on the conjugation of hydrophobic drugs to the side chain of water-soluble polymers, resulting in fully water-soluble conjugates or small aggregates (16–20).

In order to further increase their therapeutic efficiency, drug nanocarriers have continuously gained in complexity and sophistication over the years (1, 2, 21–23), reflecting recent progress, notably in polymer science due to the advent of modern polymerization techniques, including controlled radical polymerization (CRP) methods, such as nitroxide-mediated polymerization (NMP) (24–26), atom-transfer radical polymerization (ATRP) (27, 28) and reversible addition-fragmentation chain transfer (RAFT) (29, 30) polymerization. However, the more functionality assigned to the nanocarriers, the more complex they become and the more difficult their pharmaceutical development will be. Therefore, there is a crucial need in nanomedicine for simple, yet efficient concepts to give the best possible chances to eventually reach the market.

In this context, we further developed the ‘*drug-initiated*’ method (Figure 1) as an efficient and facile strategy to design polymer prodrug nanoparticles with significant *in vivo* anticancer activity (6). It consists in growing a short hydrophobic polymer chain from a hydrophilic drug under CRP conditions, resulting in amphiphilic drug-polymer conjugates able to form self-stabilized prodrug nanoparticles (31–33). This approach is flexible as it is compatible with different CRP techniques and different kinds of hydrophobic polymers. It has been illustrated by using gemcitabine (Gem), a nucleoside analogue with demonstrated activity against a wide range of solid tumors (e.g., colon, lung, pancreatic, breast, bladder and ovarian cancers) (34).

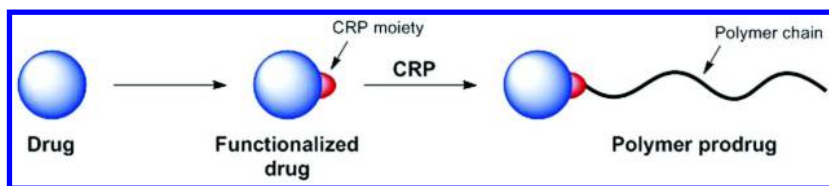


Figure 1. Synthesis of drug-polymer prodrug by the ‘*drug-initiated*’ method under controlled radical polymerization (CRP) conditions.

Experimental Part

Materials

Tetrahydrofuran (THF) was distilled from sodium/benzophenone ketyl. Dimethylformamide (DMF) and dichloromethane (DCM) were distilled from calcium hydride, under a nitrogen atmosphere. All reactions involving air- or water-sensitive compounds were routinely conducted in glassware which was flame-dried under a positive pressure of nitrogen. Gemcitabine (98%) was purchased from Sequoia Research Products Ltd. Squalene (98%), 4,4'-azobis(4-cyanopentanoic acid) (98%), 1,4-dioxane (99%), 4-cyano-4-[(dodecylsulfanylthiocarbonyl) sulfanyl] pentanoic acid (97%), methanol (99.8%) and 3-[4,5-dimethylthiazol-2-yl]-3,5-diphenyl tetrazolium bromide (MTT) were purchased from Sigma-Aldrich Chemical Co., France. Ethyl chloroformate (97%), 4-dimethylaminopyridine (99%), imidazole (99%) and tetrabutylammonium fluoride (98%) were purchased from Alfa-Aesar (A Johnson Matthey Co., France). *N*-*tert*-butyl-*N*-[1-diethylphosphono-(2,2-dimethylpropyl)] nitroxide (SG1, 85%) was obtained from Arkema (France). 2-[*N*-*tert*-butyl-*N*-(1-diethoxyphosphoryl)-2,2-di-methylpropyl]aminoxy] propionic acid (AMA-SG1) were prepared according to a previous publication (35). Gemcitabine-AMA-SG1 alkoxyamine (Gem-AMA-SG1), protected gemcitabine-RAFT agent (TBSGem-RAFT) and 1,1',2-trisnor-squalenyl methacrylate (SqMA) were prepared as reported elsewhere (31, 32). RPMI 1640 GlutaMAX I, DMEM GlutaMAX I, F12-K and fetal bovine serum were purchased from Dulbecco (Invitrogen, France). Penicillin and streptomycin solution were purchased from Lonza (Verviers, Belgium).

Synthesis

Synthesis of Gemcitabine-Polyisoprene (Gem-PI) from Gem-AMA-SG1 (31)

A stock solution was prepared comprising Gem-AMA-SG1 (180 mg, 0.031 mmol), isoprene (3.1 mL, 3.1 mmol, 100 eq) and pyridine (3.1 mL). This was divided between 4 pressure tubes (Ace Glass 8648-164) and freeze-thaw degassed. The tubes were placed in an oil bath at 115 °C and removed after 2 h (**1a**), 4 h (**1b**), 8 h (**1c**) and 16 h (**1d**) respectively. Unreacted isoprene and pyridine were removed under vacuum. Samples were characterized by SEC and NMR (Table 1). Control nanoparticles **1b'** ($M_n = 1080 \text{ g}\cdot\text{mol}^{-1}$, $D = 1.23$) and **1d'** ($M_n = 2580 \text{ g}\cdot\text{mol}^{-1}$, $D = 1.17$) were prepared from the non-functionalized SG1-based alkoxyamine as described elsewhere (31).

Table 1. Experimental Conditions for the Synthesis of Gemcitabine-Poly(Squalene Methacrylate) (Gem-PSqMA) Nanoparticles.

<i>Gem-PSqMA</i> (2)	$[SqMA]_0:[TBSGemRAFT]_0$	<i>Polym. time</i> (h)
2a	6:1	1
2b	6:1	2
2c	6:1	3
2d	6:1	3.5
2e	8:1	3
2f	10:1	3

Synthesis of Gemcitabine-Poly(squalene methacrylate) (Gem-PSqMA, 2d) (33)

SqMA (272 mg, 0.6 mmol), TBSGem-RAFT (87.4 mg, 0.1 mmol) and of 4,4'-azobis(4-cyanopentanoic acid) (2 mg, 6 μ mol) were dissolved in 1 mL of 1,4-dioxane. The mixture was degassed by 3 freeze-pump-thaw cycles and stirred at 80 °C for 3.5 h. After cooling, the polymer was precipitated in methanol 3 times to give silylated polymer (187 mg, 54% conversion) as a viscous yellow oil. The crude product was then reacted with TBAF (1 M in THF, 0.17 ml, 0.17 mmol) in 2 mL of THF for 1 h at 20 °C. The deprotected polymer was then precipitated in methanol to give a viscous yellow oil. The polymer was characterized by SEC and NMR. Gem-PSqMA **2a**, **2b**, **2c**, **2e** and **2f** with different M_n were prepared according to the experimental conditions described in Table 1. Control nanoparticles **2d'** were prepared from the non-functionalized RAFT agent as described elsewhere (33).

Analytical Methods

Nuclear Magnetic Resonance Spectroscopy (NMR)

The 1H and ^{13}C NMR spectra were recorded on Bruker Avance 300 (300 MHz and 75 MHz, respectively) or Bruker Avance 400 (400 MHz and 100 MHz, respectively) spectrometers. The ^{19}F NMR spectra were recorded on Bruker AC 200 F (188 MHz). Recognition of methyl, methylene, methine, and quaternary carbon nuclei in ^{13}C NMR spectra rests on the *J*-modulated spin-echo sequence. Mass spectra were recorded on a Bruker Esquire-LC spectrometer.

Infrared (IR) Spectroscopy

IR spectra were obtained as solid or neat liquid on a Fourier Transform Bruker Vector 22 spectrometer. Only significant absorptions are listed. Optical rotations were measured on a Perkin-Elmer 241 Polarimeter at 589 nm.

Size Exclusion Chromatography (SEC)

SEC was performed at 30 °C with two columns from Polymer Laboratories (PL-gel MIXED-D; 300 × 7.5 mm; bead diameter 5 mm; linear part 400 to 4 × 10⁵ g.mol⁻¹) and a differential refractive index detector (SpectraSystem RI-150 from Thermo Electron Corp.). The eluent was chloroform at a flow rate of 1 mL.min⁻¹ and toluene was used as a flow-rate marker. The calibration curve was based on poly(methyl methacrylate) (PMMA) standards (peak molar masses, $M_p = 625\text{--}625\,500$ g.mol⁻¹) from Polymer Laboratories. This technique allowed M_n (the number-average molar mass), M_w (the weight-average molar mass), and M_w/M_n (the dispersity, D) to be determined.

Dynamic Light Scattering (DLS) and Zeta Potential

Nanoparticle diameters (D_z) and zeta potentials (ζ) were measured by dynamic light scattering (DLS) with a Nano ZS from Malvern (173° scattering angle) at a temperature of 25 °C. The surface charge of the nanoparticles was investigated by ζ -potential (mV) measurement at 25 °C after dilution with 1 mM NaCl, using the Smoluchowski equation. Measurements were performed in triplicate following dilution of the NP suspensions in water.

Cryomicroscopy Experiments (Cryo-TEM)

The morphology of the nanoassemblies was examined by cryo-TEM. Briefly, 5 μL of the nanoparticle suspension (1 mg.mL⁻¹) was deposited on a Lacey Formvar/carbon 300 mesh copper microscopy grid (Ted Pella). Most of the drop was removed with a blotting filter paper and the residual thin film remaining within the holes was vitrified by plunging into liquid ethane. Samples were then observed using a JEOL 2100HC microscope.

Nanoparticle Formation

The nanoparticles were formed using the nanoprecipitation technique (36). A solution of the polymer prodrug (10 mg) in 0.2 mL of THF was added dropwise, under stirring (500 rpm) into 1 mL of MilliQ water. Formation of the nanoparticles occurred spontaneously. Stirring was continued for 3 min. The suspension was then transferred into a weighted round bottom flask and THF was evaporated at ambient temperature using a Rotavapor.

Biological Activity

Cell Culture

Human leukemia cell line (CCRF-CEM), murine leukemia cell line P388S, human pancreatic cancer cell line (MiaPaCa-2) and human lung carcinoma cell

line (A549) were obtained from the American Type Culture Collection. Murine leukemia cell line (L1210) was kindly provided by Dr. Lars Petter Jordheim (Université Claude Bernard Lyon I, Lyon, France). All cell lines were maintained as recommended. Briefly, A549 cells were maintained in F12-K medium. CCRF-CEM and L1210 were cultured in RPMI 1640 medium. MiaPaCa-2 cells were grown in DMEM GlutaMAX I medium supplemented with 10% heat-inactivated FBS (56 °C, 30 min), 2.5% heat-inactivated horse serum (Gibco) (56 °C, 30 min), penicillin (100 U.mL⁻¹), and streptomycin (100 µg.mL⁻¹). Cells were maintained in a humid atmosphere at 37 °C with 5% CO₂.

Cell Proliferation Assay

MTT [3-(4,5-dimethylthiazol-2-yl)-2,5-diphenyl tetrazolium bromide] was used to test cytotoxicity of the different prodrug nanoparticles. Briefly, cells (5×10^3 /well) were seeded in 96-well plates. After overnight incubation, the cells were then exposed to a series of concentrations of prodrug nanoparticles or free Gem for 72 h (incubation time was 120 h for MiaPaCa-2 cells). After drug exposure, the medium was removed and 100 µL of MTT solution (0.5 mg.mL⁻¹ in DMEM containing 10% FBS) was added to each well. The plates were incubated for 2 h at 37 °C and 100 µL of 20% SDS solution was then added to each well for 24 h at 37 °C. Absorbance was measured at 570 nm using a plate reader (Metertech Σ 960, Fisher Bioblock, Illkirch, France). The percentage of surviving cells was calculated as the absorbance ratio of treated to untreated cells. The inhibitory concentration 50% (IC₅₀) of the treatments was determined from the dose-response curve by noting the concentration at which the curve passes through the 50% inhibition level. All experiments were performed in quadruplicate to determine means and SDs.

Animals

6- to 8-week-old female athymic nude mice were purchased from Harlan Laboratory. All animals were housed in appropriate animal care facilities during the experimental period, and were handled according to the principles of laboratory animal care and legislation in force in France. All *in vivo* studies were performed in accordance with a protocol approved by the Ethical Committee of the Institut Gustave Roussy (CEEA IRCIV/IGR N° 26, registered with the French Ministry of Research).

In Vivo Anticancer Activity on Solid Tumor-Bearing Mice

The antitumor efficacy of the different prodrug nanoparticles was investigated on the human pancreatic carcinoma xenograft model MiaPaCa-2 at equimolar doses comparatively to free Gem. 200 µL of the MiaPaCa-2 cell suspension, equivalent to 1×10^7 cells, were injected subcutaneously into nude mice toward

the upper portion of the right flank, to develop a solid tumor model. Tumors were allowed to grow to a volume of $\sim 100 \text{ mm}^3$ before initiating the treatment. Tumor length and width were measured with calipers, and the tumor volume was calculated using the following equation: $V_{\text{tumor}} = \text{length} \times \text{width}^2/2$.

For Gem-PI nanoparticles, tumor-bearing nude mice were randomly divided into 6 groups of 6 each and all groups received four intravenous injections on days 0, 4, 8 and 12 in the lateral tail vein with either (i) Gem $7 \text{ mg}\cdot\text{kg}^{-1}$, (ii) Gem-PI nanoparticles (**1b**) at a Gem-equivalent dose of $7 \text{ mg}\cdot\text{kg}^{-1}$ ($3.2 \text{ mg}_{\text{Gem-PI}}\cdot\text{mL}^{-1}$), (iii) Gem-PI nanoparticles (**1d**) at a Gem-equivalent dose of $7 \text{ mg}\cdot\text{kg}^{-1}$ ($6.7 \text{ mg}_{\text{Gem-PI}}\cdot\text{mL}^{-1}$), (iv) PI nanoparticles (**1b'**, **1d'**) at an equivalent PI concentration to **1b** and **1d** (2.9 and $6.8 \text{ mg}_{\text{PI}}\cdot\text{mL}^{-1}$, respectively), (v) saline 0.9%.

For Gem-PSqMA nanoparticles, tumor-bearing nude mice were randomly divided into 4 groups of 6 each and all groups received eight intravenous injections on days 0, 4, 8, 11, 15, 18, 21 and 25 in the lateral tail vein with either (i) Gem ($3.4 \text{ mg}\cdot\text{kg}^{-1}$), (ii) Gem-PSqMA nanoparticles (**2d**, $3.4 \text{ mg}\cdot\text{kg}^{-1}$, equivalent Gem), (iii) PSqMA nanoparticles **2d'** ($77 \text{ mg}\cdot\text{kg}^{-1}$, equivalent of PSqMA in Gem-PSqMA nanoparticles **2d**) and (iv) saline 0.9%. The injected volume was $10 \mu\text{L}\cdot\text{g}^{-1}$ of body weight. The mice were monitored regularly for changes in tumor size and weight.

Immunohistochemical Analysis of Xenografts

Tumors from representative mice of each group treated with Gem-PSqMA nanoparticles **2d** and associated control experiments were excised at day 32, fixed in Finefix (Milestone, Italy), paraffin-embedded, and cut into $5\text{-}\mu\text{m}$ -thick sections. Hematoxylin-eosin-safranin (HES) staining was performed on all of the xenografts for analysis of morphology. For the evaluation of the intratumoral vascular density, anti-CD-34 (1:200; Abcam, Cambridge, UK) immunohistochemistry, detecting human endothelial cells was performed for all tumors on a large section that included the total tumor. For cell proliferation analysis, sections were incubated with Ki-67 antibody (1:200; Abcam). Cellular apoptosis was detected through terminal transferase dUTP nick end labeling (TUNEL) using Texas red-labeled nucleotide as per the manufacturer's instructions (Roche, Mannheim, Germany) and by caspase-3 staining (1:200; Abcam). In brief, the tumor biopsies were incubated with primary antibodies (1:200 dilution in blocking buffer (5% BSA)) for 1 h at room temperature. After washing (PBS), the sections were incubated with biotinylated secondary antibody (Jackson ImmunoResearch Laboratory, West Grove, PA) at room temperature for 30 min. Avidin-biotin complex and diaminobenzidine (DAB) reagent kits (Vector Laboratories, Burlingame, CA) were used according to the manufacturer's protocol to detect the secondary antibody. TUNEL, CD-34, caspase-3 or Ki-67 positive cells or nuclei were counted per view under a light microscope (Leica Microsystems GmbH, Wetzlar, Germany) at 10-times magnification. Five representative fields were chosen for counting. The average count within each region was used for statistical analysis. Necrotic fields were excluded.

Results and Discussion

Synthesis and Characterization of Gem-Based Polymer Prodrugs

Two different polymer promoieties were selected; namely polyisoprene (PI) and poly(squalene methacrylate) (PSqMA). PI was chosen as the hydrophobic polymer for its interesting properties such as chemical and enzymatic degradability (37, 38), as well as its biocompatibility (39) and its structural similarity with natural polyisoprenoids. Isoprene is the basic structural motif of naturally occurring, biocompatible terpenes (e.g., coenzyme Q10, retinol, vitamin E, etc.). We therefore considered that synthetic PI of controlled structure may also have interesting biomedical applications, especially as a nanocarrier. The second polymer promoiety is a polymethacrylate chain composed of multiple copies of pendant squalene (Sq), a lipidic precursor in the cholesterol biosynthesis widely distributed in nature. Recently, Sq has been employed as building block for the synthesis of molecular prodrugs, which self-assemble in aqueous solution to form supramolecular nanostructures (40–43). This approach has been applied to various drugs and has led to promising results *in vivo* against several pathologies (41, 44–46).

To achieve the desired polymer prodrugs (Figure 2), Gem (its solubility in water is about 15 mg.mL⁻¹ and is therefore considered hydrophilic), was derivatized with the appropriate CRP moieties. Gem-functional alkoxyamine initiator was obtained by coupling unprotected Gem to the AMA-SG1 alkoxyamine under PyBOP-linkage chemistry with 60% yield. As for the Gem-based chain transfer agent, it was obtained from the coupling of 4-cyano-4-[(dodecylsulfanylthiocarbonyl) sulfanyl] pentanoic acid to the C-4 amino group of *tert*-butyldimethylsilyl (TBS)-protected Gem by conventional acylation via the mixed anhydride pathway with 50% yield.

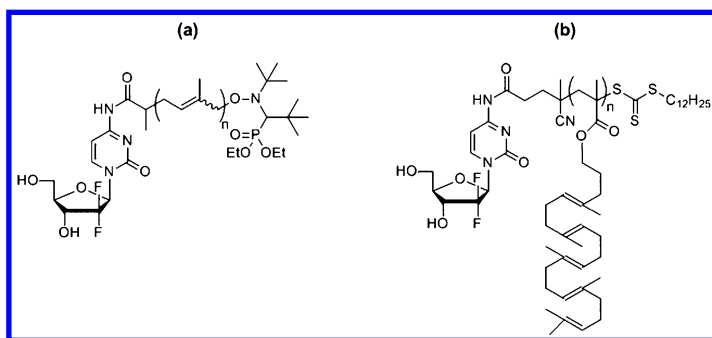


Figure 2. Structures of the gemcitabine-polyisoprene (Gem-PI, a) and gemcitabine-poly(squalene methacrylate) (Gem-PSqMA, b) polymer prodrugs described in this study.

By varying the experimental conditions (i.e., polymerization time and targeted M_n), a small library of well-defined Gem-PI (**1a–1d**) and Gem-PSqMA (**2a–2f**) polymer prodrugs exhibiting variable molar masses were prepared by NMP and

RAFT, respectively (Table 2). The Gem-PI and Gem-PSqMA structures, and the presence of Gem was confirmed through ^1H and ^{19}F NMR, and its distribution across polymer chains of all molar masses was demonstrated by SEC with RI and UV detection. Gem-PSqMA exhibited Gem drug content ranging from 2.5 to 7.2 wt.%, whereas the lower M_n Gem-PI conjugates enabled higher Gem drug contents to be obtained, from 10.5 to 31.2 wt.%. Importantly, the drug payload could easily be adjusted by changing the polymer chain length, which is possible as a result of the use of CRP methods.

Table 2. Synthesis and Characterization of Gemcitabine-Polyisoprene (Gem-PI, 1) and Gemcitabine-Poly(Squalene Methacrylate) (Gem-PSqMA, 2) Nanoparticles

Sample	M_n^a ($\text{g}\cdot\text{mol}^{-1}$)	\bar{D}^a	$DP_{n,NMR}^b$	%Gem ^c (wt.%)	D_z^d (nm)	PSD ^d
1a	840	1.35	~10	31.2	159	0.10
1b	1190	1.29	~28	22.1	137	0.10
1c	1560	1.28	~33	16.9	133	0.11
1d	2510	1.40	~47	10.5	138	0.11
2a	3720	1.18	~8	7.2	138	0.17
2b	4620	1.19	~9	6.4	142	0.11
2c	5030	1.20	~14	4.1	156	0.12
2d	5540	1.30	~14	4.2	97	0.13
2e	5950	1.27	~20	2.9	138	0.11
2f	6800	1.28	~23	2.5	122	0.13

^a Determined by size exclusion chromatography (SEC). ^b Calculated by ^1H NMR according to $DP_{n,NMR} = (M_{n,NMR} - MW_{\text{initiator}}) / MW_{\text{monomer}}$. ^c Weight fraction of Gem calculated according to $\% \text{Gem} = MW_{\text{Gem}} / (DP_{n,NMR} \times MW_{\text{monomer}})$. ^d Determined by DLS.

Self-Assembly of Gem-Based Polymer Prodrugs in Aqueous Solution

Gem-PI and Gem-PSqMA prodrug nanoparticles were obtained by self-assembly of the corresponding polymer prodrug in aqueous solution via the nanoprecipitation technique. This was performed without any additional stabilizer, likely due to the amphiphilic nature of the polymer prodrugs. Stable nanoparticles were obtained for all polymer promoieties (i.e., PI and PSqMA) and all polymer chain lengths, and their colloidal stability was assessed for a period of at least 4 weeks. Average diameters were in the range of 100–160 nm with narrow particle size distributions according to DLS measurements. Gem-PI and Gem-PSqMA nanoparticles were further characterized by cryogenic transmission electron microscopy (Cryo-TEM) and showed spherical morphologies and colloidal characteristics in good agreement with DLS data (Figure 3).

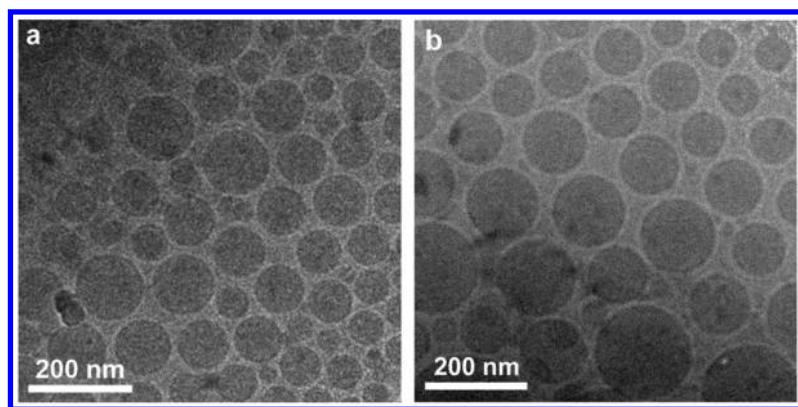


Figure 3. Cryogenic transmission electron microscopy (Cryo-TEM) of: (a) Gem-PI **1d** and (b) Gem-PSqMA **2d** nanoparticles.

Biological Evaluations of the Polymer Prodrugs in Vitro and in Vivo

The Gem-based polymer prodrug nanoparticles were then tested for their in vitro anticancer activity by measuring the half maximal inhibitory concentration (IC_{50}) of cell proliferation on four cancer cell lines: i) murine leukemia (L1210), ii) human leukemia (CCRF-CEM), iii) human pancreatic cancer (MiaPaCa-2) and iv) human lung carcinoma (A549), in order to investigate the effect of variations in chain length on the anticancer activity of these novel macromolecular prodrug nanoparticles (Table 3). Gem-PI and Gem-PSqMA prodrug nanoparticles both showed significant anticancer activity on all tested cell lines, while a control series of non-functionalized PI and PSqMA nanoparticles of similar molar masses were inactive ($IC_{50} > 10 \mu M$). Consistent with their prodrug nature, all nanoparticles showed lower cytotoxicity than free Gem (IC_{50} values for Gem were in the 36–4 nM range depending on the tested cell line) while their IC_{50} values remained however in the nanomolar range. Interestingly, for all tested cell lines, the higher the M_n of the Gem-PI prodrug, the greater the anticancer activity of the corresponding nanoparticles. This trend may be correlated with the surface hydrophobicity of the Gem-PI nanoparticles, leading to a higher rate of endocytosis due to opsonin adsorption when the PI chain length is increased, although a difference in Gem release due to a difference in M_n cannot be ruled out. No such variation was however observed with Gem-PSqMA nanoparticles, likely due to the higher M_n of the conjugates (for which the influence of the M_n could be decreased/shielded), even though the difference in terms of structure (i.e., PSqMA vs. PI) may also play a significant role. Note that control nanoparticles have also been prepared from the corresponding non-functionalized alkoxyamine and RAFT agent. They showed great colloidal stability (likely due to the presence of a carboxylic acid end functionality) and no cytotoxicity.

Table 3. Anticancer Activity of Gemcitabine-Based Polymer Prodrug Nanoparticles after 72 h of incubation (expressed as IC₅₀ ± SD in nM)^a

<i>Sample</i>	<i>MiaPaCa-2</i>	<i>L1210</i>	<i>CCRF-CEM</i>	<i>A549</i>
1a	810 ± 82	659 ± 5	232 ± 20	303 ± 8
1b	568 ± 53	358 ± 9	144 ± 1	216 ± 7
1c	169 ± 7	330 ± 18	84 ± 2	104 ± 5
1d	186 ± 11	252 ± 8	91 ± 3	87 ± 1
2a	54 ± 3	52 ± 1	63 ± 3	155 ± 5
2b	51 ± 4	58 ± 2	74 ± 1	179 ± 6
2c	76 ± 6	84 ± 2	85 ± 2	180 ± 4
2e	68 ± 5	72 ± 4	71 ± 6	180 ± 6

^a Determined by cell viability assay (MTT test).

The *in vivo* anticancer activity of these nanoparticles was then investigated against human pancreatic (MiaPaCa-2) carcinoma xenograft model in mice following intravenous injections after tumors had grown up to ~100 mm³. Gem-PI nanoparticles were injected on days 0, 4, 8, and 12 at 7 mg.kg⁻¹ Gem-equivalent dose and compared to similar injections of free Gem (7 mg.kg⁻¹) and non-functionalized PI nanoparticles of similar chain lengths (Figure 4a). Whereas untreated mice (saline 0.9%), mice treated with Gem and with non-functionalized PI nanoparticles **1b'** and **1d'** exhibited rapid tumor growth, reaching ~1350 mm³ at day 34, treatment of mice with Gem-PI nanoparticles (**1b**) at the same Gem-equivalent dose led to a considerable decrease in the tumor progression. An even higher anticancer activity was obtained with Gem-PI nanoparticles (**1d**), leading to a tumor growth inhibition as high as 72% and a tumor growth which plateaued after 23 days of treatment. Similarly to *in vitro* cytotoxicity assays, nanoparticles obtained from the higher molar mass Gem-PI conjugate (**1d**) demonstrated greater *in vivo* anticancer activity than their lower molar mass counterparts (**1b**). On the other hand, mice treated with Gem-PSqMA nanoparticles (3.4 mg.kg⁻¹, equiv. Gem, injections on days 0, 4, 8, 11, 15, 18, 21 and 25) also showed a drastic tumor growth inhibition, of about 75% at day 48, compared to untreated mice or treatment with PSqMA nanoparticles (Figure 4b).

The relative body weight loss of nude mice was also monitored throughout the treatment. Importantly, none of the Gem-based polymer prodrug nanoparticles exhibited a significant weight loss compared to free Gem (Gem total dose was 28 mg.kg⁻¹) for which a decrease up to 10% was observed. This suggests that the overall toxicity of Gem was suppressed when using the Gem-based polymer prodrug nanoparticles approach.

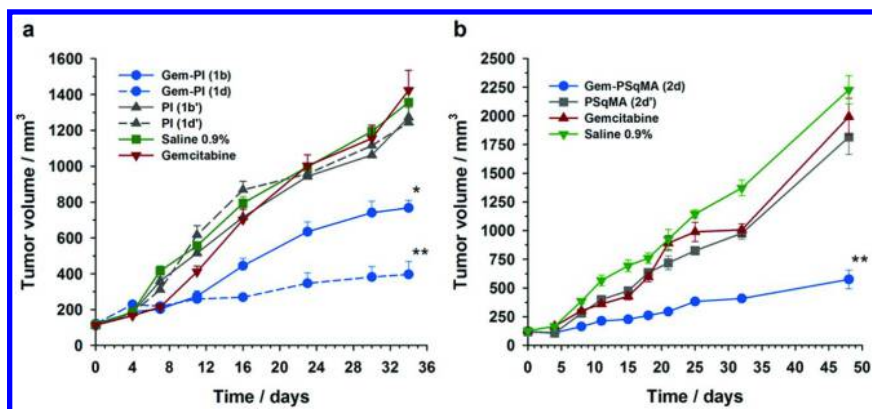


Figure 4. *In vivo* anticancer activity of Gem, Gem-based nanoparticles, saline 0.9% and control nanoparticles following intravenous treatment of mice bearing MiaPaCa-2 subcutaneous tumors: (a) Gem-PI nanoparticles and (b) Gem-PSqMA nanoparticles. The values are the mean \pm SD ($n = 6$, * $p < 0.025$, ** $p < 0.005$).

In order to have an in-depth evaluation of the therapeutic activity of the prodrug nanoparticles, immunohistochemical analysis of tumor biopsies after treatment with Gem-PSqMA nanoparticles **2d** was performed. HES staining showed enlarged cells with necrotic changes only in the case of Gem-PSqMA nanoparticle-treated tumor tissues. The TUNEL staining of tumor biopsies sections, which is a common method for detecting the DNA fragmentation resulting from apoptotic signaling cascades, was then used to assess the induction of apoptosis by the different treatments. The mean proportions of TUNEL positive cells/field for the groups treated with free Gem and the controls (saline 0.9% and PSqMA nanoparticles **2d'**) were 0.9% and 0.6%, respectively, whereas Gem-PSqMA nanoparticles reached 16.8%, demonstrating a significant induction of apoptosis (Figure 5a). Immunostaining of the active form of caspase-3 protease, which plays a central role in the execution-phase of cell apoptosis, revealed major caspase-3 activation (35.6%) exclusively for Gem-PSqMA nanoparticle-treated mice (tumors that received free Gem injections gave a mean value of 5.1% of caspase-3 positive cells/field and those tested by the control injections were as low as \sim 0.5%) (Figure 5a). Additionally, Gem-PSqMA nanoparticles caused an important decrease (about \sim 50%) of the MiaPaCa-2 tumor proliferative activity, comparatively to free Gem, as indicated by the reduced number of Ki-67-positive tumor cells, which is a cellular marker for cell proliferation (Figure 5a). Treatment with Gem-PSqMA nanoparticles exhibited mean values of 28% Ki-67 positive cells/field, which is drastically lower than values obtained with free Gem (59%), saline (55%) and PSqMA nanoparticles (57%). Finally, the antineovasculture effect of the Gem-PSqMA nanoparticles was confirmed by immunostaining of CD34. The Gem-PSqMA nanoparticles had a more pronounced suppressive effect on neovasculture compared to other treatments, with a mean value of 9.5% vessel area/field compared to 19% in the presence of free Gem, which is

in a similar range as values obtained from treatments with saline and PSqMA nanoparticles (20–22%) (Figure 5b). In summary, the Gem-PSqMA nanoparticles demonstrated a reduction in normal vasculature, together with antiproliferative and apoptotic effects.

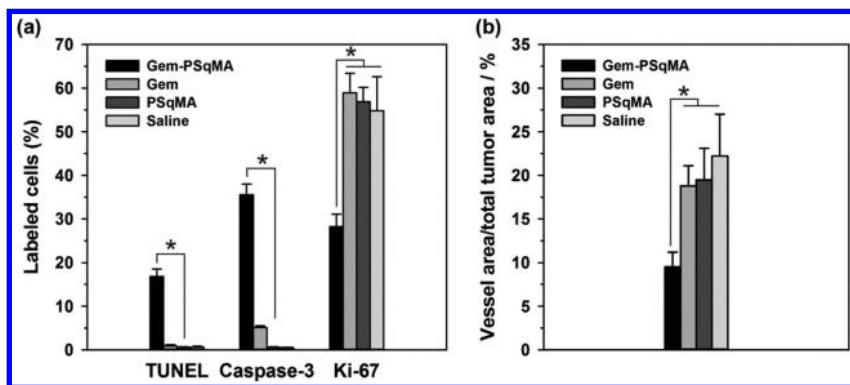


Figure 5. Immunohistochemical staining of representative tumors from each group excised at day 32 after treatment with Gem-PSqMA nanoparticles **2d** and control treatments (saline 0.9%, free Gem and PSqMA nanoparticles **2d'**): (a) quantification of the apoptotic, Ki-67 and caspase-3-positive cells in the tumor tissue sections (* $p < 0.001$); (b) percentage of the vessel area with reference to the total tumor area (* $p < 0.001$).

Conclusion

By establishing the significant in vivo anticancer activity of different Gem-based prodrug nanoparticles, we have demonstrated that the ‘drug-initiated’ method under controlled/living radical conditions, which consists of growing a short hydrophobic chain from a hydrophilic anticancer drug, is a truly robust and flexible, yet simple strategy to achieve efficient drug delivery. The simplicity of this system, solely composed of self-assembled amphiphilic drug-polymer prodrugs as building blocks, without the need for additional surfactant, is indeed a crucial advantage over other approaches, especially in the context of bench-to-bedside translation. In addition, it offers valuable benefits compared to the traditional and widely exploited ‘conjugation to’ method (i.e., when the drug is linked to a preformed polymer scaffold): (i) the efficiency of the conjugation is nearly quantitative as all the drug is retained at the chain ends; (ii) the purification of the conjugate is easier since only the unreacted monomer has to be removed as opposed to a preformed polymer and (iii) fine tuning of drug loading is achieved simply by varying the molecular weight of the polymer chain.

These findings open exciting perspectives in the biomedical field as multiple drug/polymer combinations are now worth considering and other pathologies could be treated simply by selecting suitable drugs.

Acknowledgments

The research leading to these results received funding from the European Research Council under the European Community's Seventh Framework Programme FP7/2007-2013 (Grant Agreement No. 249835). The PhD training program in France of the University of Science and Technology of Hanoi is also acknowledged for the financial support of D.T.B. CNRS and French ministry of research are also acknowledged for financial support.

References

1. Nicolas, J.; Mura, S.; Brambilla, D.; Mackiewicz, N.; Couvreur, P. *Chem. Soc. Rev.* **2013**, *42*, 1147–1235.
2. Elsabahy, M.; Wooley, K. L. *Chem. Soc. Rev.* **2012**, *41*, 2545–2561.
3. Brigger, I.; Dubernet, C.; Couvreur, P. *Adv. Drug Delivery Rev.* **2002**, *54*, 631–651.
4. Hans, M. L.; Lowman, A. M. *Curr. Opin. Solid State Mater. Sci.* **2002**, *6*, 319–327.
5. Albert, A. *Nature* **1958**, *182*, 421–423.
6. Delplace, V.; Couvreur, P.; Nicolas, J. *Polym. Chem.* **2014**, *5*, 1529–1544.
7. Bensaid, F.; Thillaye du Boullay, O.; Amgoune, A.; Pradel, C.; Harivardhan Reddy, L.; Didier, E.; Sablé, S.; Louit, G.; Bazile, D.; Bourissou, D. *Biomacromolecules* **2013**, *14*, 1189–1198.
8. Bae, Y.; Fukushima, S.; Harada, A.; Kataoka, K. *Angew. Chem., Int. Ed.* **2003**, *42*, 4640–4643.
9. Bae, Y.; Jang, W.-D.; Nishiyama, N.; Fukushima, S.; Kataoka, K. *Mol. Biosyst.* **2005**, *1*, 242–250.
10. Bae, Y.; Kataoka, K. *Adv. Drug Delivery Rev.* **2009**, *61*, 768–784.
11. Wang, Z.; Chui, W.-K.; Ho, P. C. *Pharm. Res.* **2009**, *26*, 1162–1171.
12. Wang, J.; Liu, W.; Tu, Q.; Wang, J.; Song, N.; Zhang, Y.; Nie, N.; Wang, J. *Biomacromolecules* **2010**, *12*, 228–234.
13. Huynh, V. T.; Chen, G.; Souza, P. d.; Stenzel, M. H. *Biomacromolecules* **2011**, *12*, 1738–1751.
14. Huynh, V. T.; de Souza, P.; Stenzel, M. H. *Macromolecules* **2011**, *44*, 7888–7900.
15. Huynh, V. T.; Quek, J. Y.; de Souza, P. L.; Stenzel, M. H. *Biomacromolecules* **2012**, *13*, 1010–1023.
16. Greenwald, R. B.; Choe, Y. H.; McGuire, J.; Conover, C. D. *Adv. Drug Delivery Rev.* **2003**, *55*, 217–250.
17. Minko, T.; Kopečková, P.; Pozharov, V.; Kopeček, J. *J. Controlled Release* **1998**, *54*, 223–233.
18. Thomson, A. H.; Vasey, P. A.; Murray, L. S.; Cassidy, J.; Fraier, D.; Frigerio, E.; Twelves, C. *Br. J. Cancer* **1999**, *81*, 99–107.
19. Seymour, L. W.; Ferry, D. R.; Kerr, D. J.; Rea, D.; Whitlock, M.; Poyner, R.; Boivin, C.; Hesslewood, S.; Twelves, C.; Blackie, R.; Schatzlein, A.; Jodrell, D.; Bissett, D.; Calvert, H.; Lind, M.; Robbins, A.; Burtles, S.; Duncan, R.; Cassidy, J. *Int. J. Oncol.* **2009**, *34*, 1629–1636.

20. Chen, X.; McRae, S.; Parelkar, S.; Emrick, T. *Bioconjugate Chem.* **2009**, *20*, 2331–2341.
21. Mura, S.; Nicolas, J.; Couvreur, P. *Nat. Mater.* **2013**, *12*, 991–1003.
22. Torchilin, V. P. *Adv. Drug Delivery Rev.* **2012**, *64*, 302–315.
23. Sapsford, K. E.; Algar, W. R.; Berti, L.; Gemmill, K. B.; Casey, B. J.; Oh, E.; Stewart, M. H.; Medintz, I. L. *Chem. Rev.* **2013**, *113*, 1904–2074.
24. Nicolas, J.; Guillaneuf, Y.; Lefay, C.; Bertin, D.; Gignes, D.; Charleux, B. *Prog. Polym. Sci.* **2013**, *38*, 63–235.
25. Hawker, C. J.; Bosman, A. W.; Harth, E. *Chem. Rev.* **2001**, *101*, 3661–3688.
26. Grubbs, R. B. *Polym. Rev.* **2011**, *51*, 104–137.
27. Matyjaszewski, K.; Xia, J. *Chem. Rev.* **2001**, *101*, 2921–2990.
28. Kamigaito, M.; Ando, T.; Sawamoto, M. *Chem. Rev.* **2001**, *101*, 3689–3745.
29. Perrier, S.; Takolpuckdee, P. *J. Polym. Sci., Part A: Polym. Chem.* **2005**, *43*, 5347–5393.
30. Moad, G.; Rizzardo, E.; Thang, S. H. *Aust. J. Chem.* **2009**, *62*, 1402–1472.
31. Harrisson, S.; Nicolas, J.; Maksimenko, A.; Bui, D. T.; Mougin, J.; Couvreur, P. *Angew. Chem., Int. Ed.* **2013**, *52*, 1678–1682.
32. Bui, D. T.; Maksimenko, A.; Desmaele, D.; Harrisson, S.; Vauthier, C.; Couvreur, P.; Nicolas, J. *Biomacromolecules* **2013**, *14*, 2837–2847.
33. Maksimenko, A.; Bui, D. T.; Desmaële, D.; Couvreur, P.; Nicolas, J. *Chem. Mater.* **2014**, *26*, 3606–3609.
34. Hertel, L. W.; Boder, G. B.; Kroin, J. S.; Rinzl, S. M.; Poore, G. A.; Todd, G. C.; Grindey, G. B. *Cancer Res.* **1990**, *50*, 4417–4422.
35. Harrisson, S.; Couvreur, P.; Nicolas, J. *Polym. Chem.* **2011**, *2*, 1859–1865.
36. Thioune, O.; Fessi, H.; Devissaguet, J. P.; Puisieux, F. *Int. J. Pharm.* **1997**, *146*, 233–238.
37. Cheng, C.; Qi, K.; Khoshdel, E.; Wooley, K. L. *J. Am. Chem. Soc.* **2006**, *128*, 6808–6809.
38. Watanabe, T.; Sato, S.; Honda, Y.; Kuwahara, M. *Biomacromolecules* **2003**, *4*, 321–329.
39. Yang, H.-C.; Silverman, J.; Wozniak, J. J. Low temperature heat shrinkable polymer material. U.S. Patent 4596728, 1986; U.S. Patent 4596728.
40. Couvreur, P.; Reddy, L. H.; Mangenot, S.; Poupert, J. H.; Desmaele, D.; Lepetre-Mouelhi, S.; Pili, B.; Bourgaux, C.; Amenitsch, H.; Ollivon, M. *Small* **2008**, *4*, 247–253.
41. Couvreur, P.; Stella, B.; Reddy, L. H.; Hillaireau, H.; Dubernet, C.; Desmaële, D.; Lepêtre-Mouelhi, S.; Rocco, F.; Dereuddre-Bosquet, N.; Clayette, P.; Rosilio, V.; Marsaud, V.; Renoir, J.-M.; Cattel, L. *Nano Lett.* **2006**, *6*, 2544–2548.
42. Bekkara-Aounallah, F.; Gref, R.; Othman, M.; Reddy, L. H.; Pili, B.; Allain, V.; Bourgaux, C.; Hillaireau, H.; Lepetre-Mouelhi, S.; Desmaele, D.; Nicolas, J.; Chafi, N.; Couvreur, P. *Adv. Funct. Mater.* **2008**, *18*, 3715–3725.
43. Bui, D. T.; Nicolas, J.; Maksimenko, A.; Desmaele, D.; Couvreur, P. *Chem. Commun.* **2014**.
44. Arias, J. L.; Reddy, L. H.; Othman, M.; Gillet, B.; Desmaële, D.; Zouhiri, F.; Dosio, F.; Gref, R.; Couvreur, P. *ACS Nano* **2011**, *5*, 1513–1521.

45. Desmaële, D.; Gref, R.; Couvreur, P. *J. Controlled Release* **2012**, *161*, 609–618.
46. Reddy, L. H.; Ferreira, H.; Dubernet, C.; Mouelhi, S. L.; Desmaele, D.; Rousseau, B.; Couvreur, P. *Anti-Cancer Drugs* **2008**, *19*, 999–1006.

Chapter 17

Dual Location Reduction-Responsive Degradable Nanocarriers: A New Strategy for Intracellular Anticancer Drug Delivery with Accelerated Release

**Nicky Chan, Na Re Ko, So Young An, Behnoush Khorsand,
and Jung Kwon Oh***

**Department of Chemistry and Biochemistry, Concordia University,
Montreal, Quebec, Canada H4B 1R6**

***E-mail: john.oh@concordia.ca**

Stimuli-responsive degradation (SRD) based on disulfide chemistry is highly desirable in the development of self-assembled block copolymer nanocarriers for multifunctional polymer-based drug delivery systems. In contrast to most conventional approaches involving the incorporation of disulfide linkages at single locations, an effective dual location SRD approach centers on the development of new intracellular nanocarriers having dynamic disulfide linkages in dual or multiple locations. The placement of dynamic disulfide linkages in multiple locations within a nanocarrier exhibit not only synergistically accelerated release due to dual location reduction responses, but also allows additional desirable synergistic therapeutic effects. This chapter describes three strategies to synthesize novel reduction-responsive degradable block copolymers and their self-assembled micelles that have been recently developed utilizing the dual or multi-location stimuli responsive degradation strategy. Their aqueous micellization, reduction-responsive degradation, and intracellular trafficking offer versatility in intracellular anticancer drug delivery applications.

Introduction

Polymer-based nanoscale therapeutic devices derived from self-assembly of amphiphilic block copolymers (ABP) have gained significant attention in the field of pharmaceutical science and nanotechnology. This is because self-assembled micellar nanocarriers possess a number of interesting features. They include good colloidal stability, tunable sizes with narrow size distribution, physical encapsulation of drugs without chemical modification, protection of therapeutics from possible deactivation during delivery, and passive targeting to specific organs or tissues. These features make micellar nanocarriers suitable as effective tumor-targeting delivery systems of anti-cancer therapeutics (1–5).

Micellar nanocarriers are typically assembled from well-defined ABPs possessing a hydrophilic and hydrophobic block. When the concentration of ABPs in an aqueous solution is greater than critical micellar concentration (CMC), the hydrophobic blocks begin to aggregate forming core/shell-type micelles or nanoparticles. These physically-associated micelles consist of a hydrophobic core, which enables encapsulation of biomolecules and other therapeutic or imaging agents; as well as a hydrophilic corona, which ensures colloidal stability and biocompatibility (6). The neutral hydrophilic corona can prolong blood circulation while minimizing undesired uptake by the reticuloendothelial system (RES) or mononuclear phagocyte system (MPS). The rapid growth of tumors results in new vasculatures with irregularly aligned endothelial cells as well as poor lymphatic drainage; they facilitate extravasation (enhanced permeation) and accumulation of micellar nanocarriers (retention) within tumor tissues (7–12). As a result, prolonged blood circulation leads to the enhanced permeation and retention effect (EPR) (or passive targeting) which minimizes undesired side effects and maximizes drug efficacy. As such, the physical properties and therapeutic efficiency of the desired nanocarriers are directly correlated to the chemistry and design structure of the initial ABPs.

Once conventional nanocarriers are internalized into cancer cells through endocytosis, encapsulated therapeutics are released through an uncontrolled and diffusion-limited mechanism (13). The mechanism of drug release and effective dosage can be modified by incorporation of stimuli-responsive degradation (SRD) or cleavage of dynamic covalent bonds in response to external stimuli, into the design and development of block copolymers. When triggered by the desired external stimuli, the cleavable linkages are disrupted either reversibly or irreversibly, causing a change on block copolymer structure and destabilization of the nanocarriers to provide on-demand drug delivery at the desired location and dosage. As such, SRD can be used to maximize therapeutic efficiency of encapsulated compounds while minimizing undesired side effects (14–18).

Several types of stimuli-responsive cleavable linkages have been explored, including acid-labile (19, 20), photo-cleavable groups (21–25), and polypeptides (26). In particular, materials incorporating disulfide linkages have been shown to hold great promise for tumor-targeting drug delivery applications (27–30). In reducing environments, disulfide bonds are cleaved to the corresponding thiols via disulfide-thiol exchange reactions (31, 32). In biological systems, glutathione

(GSH, a tripeptide containing cysteine) is present at elevated levels in cancer cells ($> 10 \text{ mM}$), but is present only at low concentration in extracellular milieu ($< 10 \text{ }\mu\text{M}$) (33, 34). This large redox potential difference between intracellular and extracellular compartments, as well as elevated concentrations in cancer cells makes GSH an effective intracellular trigger for reduction-responsive degradable materials. Nanocarriers which have been internalized are exposed to an elevated level of GSH, triggering cleavage of disulfide linkages, and subsequent destabilization of nanocarriers to facilitate rapid or enhanced release of encapsulated molecules. While multiple modes of stimuli-responsive degradation have been explored, a better understanding of the relationship between polymer structure and nanocarrier properties still needs to be established.

Numerous approaches have been reported for the synthesis of disulfide-containing block copolymers and their self-assembled micellar nanocarriers with reduction-responsive degradability (15). As illustrated in Figure 1, conventional reduction-responsive degradable micelles typically are assembled from ABPs with cleavable disulfide linkages (ss) in hydrophobic pendant chains (A) (35–41), in the hydrophobic main chain as multiple (B)(42–48) and single groups (C) (49–54), or at block junctions (D) (55–67). These conventional nanocarriers possess dynamic disulfide linkages positioned in only a single location within the particle structures, as in the micellar core, or at the interface between core and corona. The placement of cleavable linkages dramatically affects the colloidal properties and drug release profile of the resulting nanocarriers. When disulfide linkages are placed in the hydrophobic core (strategy A, B, and C), the cleavage of the disulfide linkages typically results in either destabilization through a change in hydrophilic/hydrophobic balance (A) or disintegration through a main chain degradation mechanism (B and C) of the block copolymers. If the cleavable linkages are placed at the interface between core and corona (D), application of an environmental trigger will lead to shedding of the hydrophilic corona and loss of colloidal stability (68). In addition, reduction-responsive prodrugs are proposed to have hydrophobic drugs conjugated to polymers or micelles through disulfide linkages that are released by the cleavage of disulfides in reducing environments (69, 70).

While a number of studies have been conducted, most studies focus on system where nanoparticles possess disulfide linkages at only one position into the nanocarrier structures. Given the apparent relationship between block copolymer structure and nanocarrier properties, a new and effective SRD strategy that centers on the development of new intracellular nanocarriers having dynamic disulfide linkages in dual or multiple locations has been recently explored. The locations are in the micellar core, in the interlayered corona, or at the interface between the hydrophobic core and corona. The placement of dynamic disulfide linkages in multiple locations within a nanocarrier was expected to yield additional desirable synergistic therapeutic effects.

This chapter describes the design and development of three novel reduction-responsive degradable block copolymers and their self-assembled micelles incorporating disulfide linkages in dual locations (Figure 2) (71–73). These micelles were designed to possess different desired properties to facilitate more efficient drug delivery after undergoing stimuli-responsive degradation at

both sites. These dual disulfide-located degradable micellar nanocarriers are summarized as:

- 1) Multi-cleavable A-ss-Bss type block copolymer with a sheddable hydrophilic corona (A) and pendant disulfide linkages in the hydrophobic core (Bss), designed as a proof-of-concept to provide accelerated release of encapsulated therapeutics.
- 2) A-ss-B-ss-B-ss-A type polylactide (PLA) triblock copolymer with cleavable disulfide linkages in the hydrophobic PLA backbone (B), and between the hydrophobic and hydrophilic junctions to synergistically enhance micellar destabilization and degradation of the hydrophobic core causing rapid drug release.
- 2) A-Bss-ss-C type triblock copolymer with pendant disulfide linkages in the crosslinkable hydrophobic interlayer (Bss), and cleavable linkages between the core (C) and extended corona (A+B) to provide both enhanced colloidal stability and drug release.

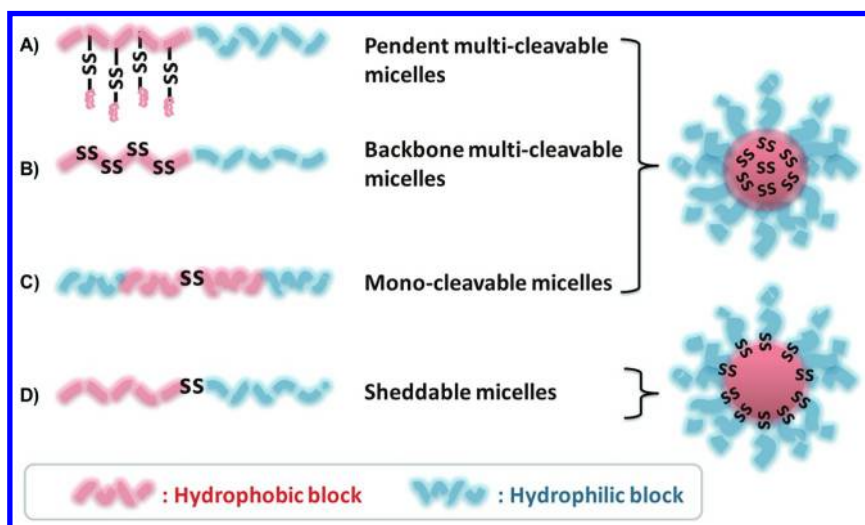


Figure 1. Schematic illustration of conventional approaches to synthesize reduction-responsive degradable block copolymer-based micellar nanocarriers having disulfide linkages in single locations. (see color insert)

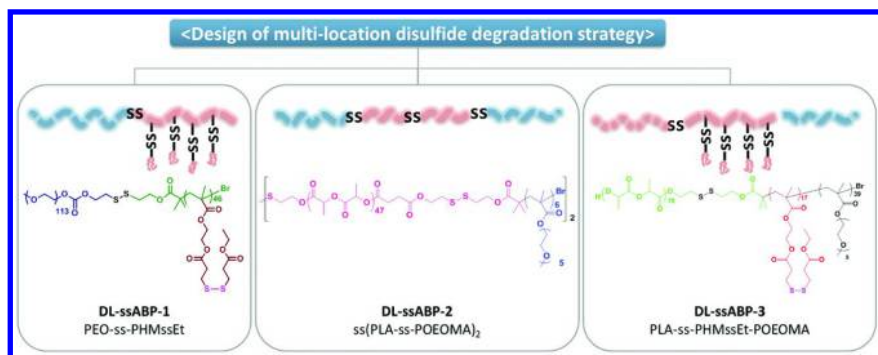


Figure 2. Schematic illustration of three reported reduction-responsive degradable block copolymers having disulfide linkages in dual locations. (see color insert)

New Dual Location Disulfide Degradable Block Copolymer Micelles

In this section, we summarize the synthesis, aqueous micellization, and degradation of three thiol-responsive degradable block copolymer micelles that have been recently developed utilizing a novel dual or multi-location stimuli responsive degradation strategy. All these micelles possess cleavable disulfide linkages in dual locations within the block copolymer structure, resulting in different desired properties in the assembled nanocarrier to enhance the therapeutic efficiency over conventional micellar drug delivery systems having stimuli-response in only a single location of the micellar structure.

Proof-of-Concept for Dual Location Stimuli-Responsive Degradation Strategy

As a proof-of-concept to demonstrate the effectiveness of a dual or multi-location stimuli-responsive degradation approach towards micellar nanocarrier design, a novel micellar system having disulfide linkages in both hydrophobic core and at the hydrophobic/hydrophilic interface has been developed (Figure 3). The dual location disulfide-containing micelles are formed from a block copolymer consisting of a hydrophilic poly(ethylene oxide) (PEO) block and a hydrophobic block having pendant disulfide linkages (PHMssEt). An additional disulfide linkage is located at the junction between the hydrophilic and hydrophobic blocks, thus forming PEO-ss-PHMssEt (DL-ssABP-1). The proposed micellar system exhibits accelerated release of encapsulated compounds upon internalization into cancer cells due to the presence of elevated levels of intracellular GSH. The highly reducing environment inside a cancer cell would cause rapid cleavage of disulfide bonds present at the interface between hydrophilic corona and hydrophobic core, leading to destabilization of the micelle and generation of water-soluble thiol-functionalized corona segments

(PEO-SH), and hydrophobic core thiol species (PHMSH with pendant SH groups and HS-Et). Hypothetically, these *in situ* generated thiols promote the cleavage of the remaining disulfide linkages in the micellar core, accelerating destabilization of the nanoparticle and thus release of encapsulated therapeutics.

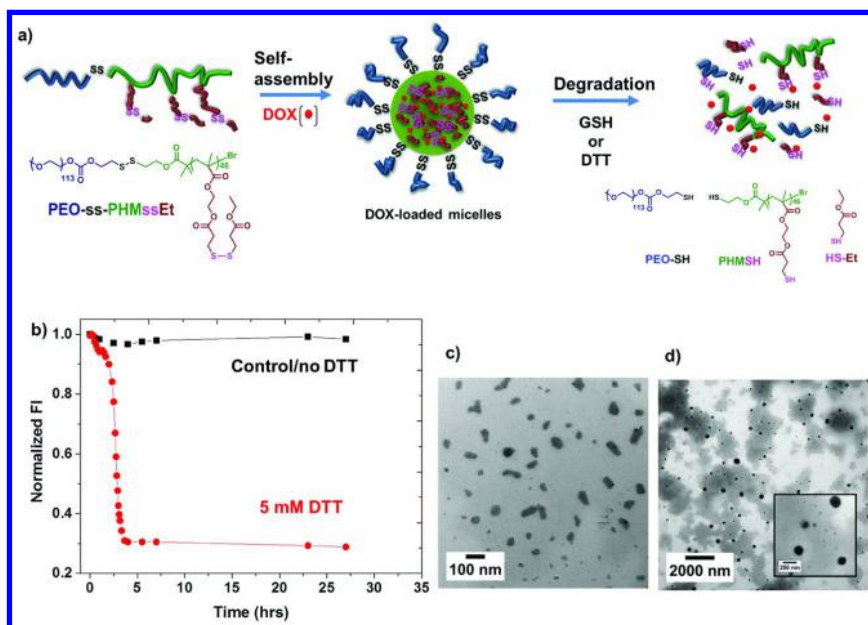


Figure 3. Design, aqueous micellization, and degradation of DL-ssABP-1 with disulfide linkages located in both hydrophobic core and interface between core/corona (a), reduction-responsive release profile of NR from NR-loaded micelles in aqueous solution (b), and TEM images of micelles in the presence of 10 mM GSH over a degradation time of $t = 0$ (c) and 24 hrs (d). Scale bar in the inset = 250 nm. Reproduced with permission from reference (71). Copyright 2013 Royal Society of Chemistry.

The block copolymer PEO-ss-PHMssEt was synthesized by atom transfer radical polymerization (ATRP) (74, 75) of a methacrylate having a pendant disulfide (HMssEt) in the presence of a PEO-ss-Br initiator (Figure 4). The synthesis of HMssEt (38) and PEO-ss-Br (61) are described in our previous publications. The well-defined PEO-ss-PHMssEt block copolymer was characterized with the molecular weight $M_n = 25$ kg/mol ($M_w/M_n < 1.1$) by gel permeation chromatography (GPC) and the degree of polymerization (DP) of PHMssEt block = 46 by ^1H NMR. Due to the amphiphilic nature, the resulting PEO-ss-PHMssEt self-assembled to form colloiddally stable micelles with a diameter = 38 nm and a monomodal size distribution at a concentration of 1.0

mg/mL, above CMC = 17 $\mu\text{g/mL}$, as measured using dynamic light scattering (DLS).

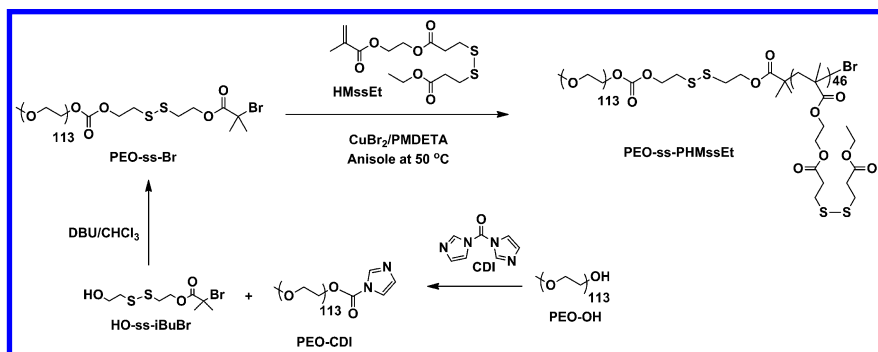


Figure 4. Our approach to synthesize well-defined DL-ssABP-1 (PEO-ss-PHMssEt).

In reductive environments, DL-ssABP-1 degrades to PEO-SH, PHMSH and SH-Et as suggested in Figure 3a. This was confirmed by the degradation of DL-ssABP-1 dissolved in *N,N*-dimethylformamide (DMF) in the presence of 5 mole equivalents of *D,L*-dithiothreitol (DTT) to disulfide linkages. The molecular weight of DL-ssABP-1 decreased significantly from $M_n = 25$ kg/mol to $M_n = 10$ kg/mol within the first 30 min. For model release kinetics in response to reductive reaction, Nile Red (NR) as a model hydrophobic drug was encapsulated in micelles through aqueous micellization resulting in fluorescent micelles. As the fluorescence of NR changes in hydrophobic (intense fluorescence) to hydrophilic (low fluorescence and low solubility) environment, the release of encapsulated NR could be monitored by measuring the change on NR fluorescence as a function of time (76, 77). As Figure 3b shows, in a control experiment with no DTT (non-reducing environment), micelle fluorescence remained unchanged over a 24 hrs period. When exposed to a reducing environment (5 mM DTT), the fluorescence intensity decreased rapidly ($> 70\%$ decrease in 4 hrs), suggesting significant degradation and cleavage of disulfide linkages in the hydrophobic core and at the hydrophilic/hydrophobic interface. The cleavage of dual location disulfide bonds was also confirmed by measuring the molecular weight of recovered polymer from colloiddally stable micelles which were exposed to DTT, where a reduction in molecular weight from $M_n = 25$ kg/mol to $M_n = 10$ kg/mol was observed. Further, the change in micelle particle size when placed in a reducing environment was also monitored using DLS and transmission electron microscopy (TEM). As shown in Figure 3c, the initial colloids formed large aggregates when exposed to DTT. The loss of the initial particle structure after 4 hrs correlates to the release of a significant population of encapsulated compounds. These results suggest that rapid reductive degradation and destabilization occurred in micelles, leading to enhanced release of encapsulated compounds.

The advantage of the proposed dual location reduction-responsive degradation strategy was evident over other systems with degradable linkages in only a single location. In particular, micellization and release kinetics of an analogous block copolymer DL-ssABP-1 with pendant disulfide linkages in hydrophobic segment, but lacking the disulfide linkage between hydrophobic and hydrophilic blocks was also investigated. Under similar reductive environments, micelles formed from DL-ssABP-1 with no disulfide linkage at the block junction exhibited only 20% release of encapsulated NR over a 25 hrs period (38), compared to over 70% release in under 4 hrs for DL-ssABP-1. When compared to other micelles with disulfide linkages between the hydrophilic/hydrophobic blocks, an enhanced release profile was also observed (55, 58).

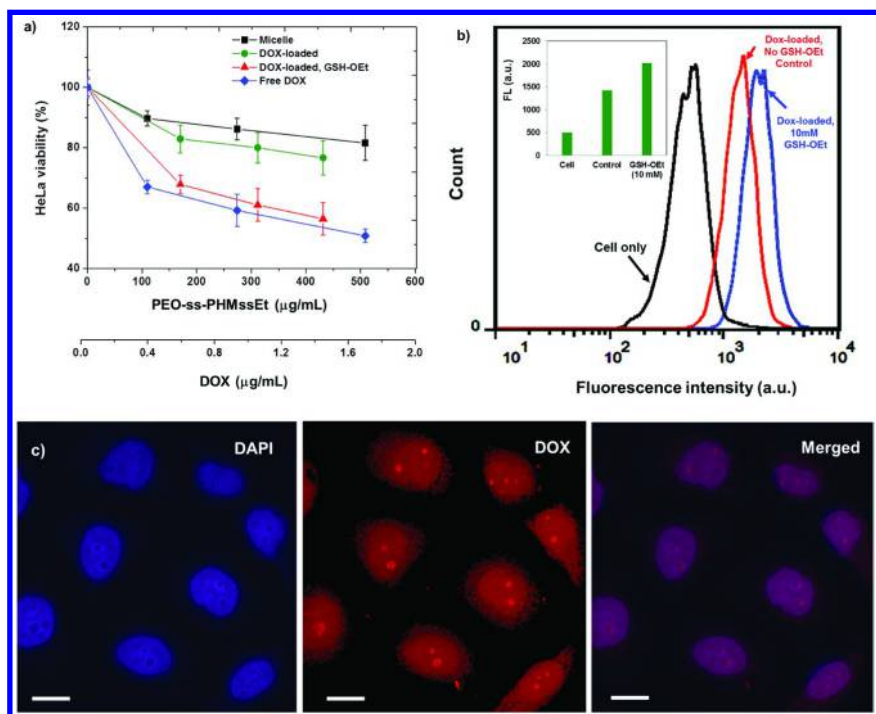


Figure 5. Viability of HeLa cells treated with and without 10 mM GSH-OEt and incubated with different amounts of free DOX and DOX-loaded micelles (a), flow cytometric histograms of HeLa cells incubated with DOX-loaded micelles for 4 hrs (b), and CLSM images (scale bar = 20 μm) of HeLa cells incubated with DOX-loaded micelles for 24 hrs (c). Reproduced with permission from reference (71). Copyright 2013 Royal Society of Chemistry. (see color insert)

The effectiveness of DL-ssABP-1 micelles as nanocarriers of anticancer drugs through redox-triggered intracellular delivery of therapeutics in response GSH was evaluated using *in vitro* cell viability studies with Doxorubicin (DOX)-loaded micelles. As shown in Figure 5a, HeLa cell viability decreased with an increasing amount of both free DOX and DOX-loaded micelles when the cells have undergone a GSH ethyl ester (GSH-OEt) pre-treatment to ensure a known equilibrium concentration of intracellular GSH. In the absence of GSH or GSH-OEt as a stimulus, the DOX-loaded micelles had comparable cell viability to empty micelles, suggesting that intracellular GSH caused rapid release of encapsulated DOX causing inhibition of cell proliferation. Cellular uptake and DOX release were further confirmed through flow cytometry (Figure 5b) and confocal laser scanning microscopy (CLSM) (Figure 5c), which both exhibit enhanced cellular fluorescence due to uptake of DOX-loaded micelles and release of encapsulated DOX.

The results show that the newly proposed dual-location disulfide degradable micellar system may have synergistically enhanced properties compared with conventional stimuli-responsive degradable micelles with cleavable linkages in only a single location. By incorporating cleavable disulfide linkages in the micellar core and at the junction between hydrophobic core and hydrophilic corona, destabilization of the micelles was accelerated and the system exhibited enhanced release of encapsulated compounds when compared to systems where degradable linkages are present only in one location.

Dual Disulfide Located Degradable Nanocarriers of PLA-Based Block Copolymers for Rapid Drug Release

The dual-location disulfide degradation design strategy was also extended to polylactide (PLA) based nanocarriers. PLAs are a class of biocompatible and biodegradable aliphatic polyesters that have been FDA-approved for clinical use (76–78). A PLA-based nanocarrier having disulfide cleavable linkages both in the micellar core and at the hydrophilic/hydrophobic interface was designed based on dual-degradable triblock copolymers (DL-ssABP-2) consisting of a hydrophobic PLA middle block and hydrophilic methacrylate blocks containing pendant oligo(ethylene oxide) (POEOMA). The copolymer possesses a disulfide linkage in the middle of PLA block and two disulfides at block junctions of PLA and POEOMA, thus forming POEOMA-ss-(PLA-ss-PLA)-ss-POEOMA triblock copolymer.

Figure 6 illustrates our approach to synthesize well-defined DL-ssABP-2 triblock copolymer by a combination of ring opening polymerization (ROP), facile coupling reactions, and ATRP. The ROP of LA initiated with 2-hydroxyethyl disulfide (ss-DOH) yielded well-controlled ss(PLA-OH)₂ with $M_n = 20$ kg/mol ($M_w/M_n = 1.1$) and DP = 94. The successful carboxylation of ss(PLA-OH)₂ with excess succinic anhydride (SA) to ss(PLA-COOH)₂ and the following esterification of ss(PLA-COOH)₂ with a double-head initiator (HO-ss-iBuBr) to ss(PLA-ss-Br)₂ were confirmed by ¹H-NMR. Lastly, the chain extension of

ss(PLA-ss-Br)₂ with OEOMA by ATRP allowed for the synthesis of well-defined DL-ssABP-2 with $M_n = 26$ kg/mol ($M_w/M_n = 1.1$) and DP of POEOMA block = 12.

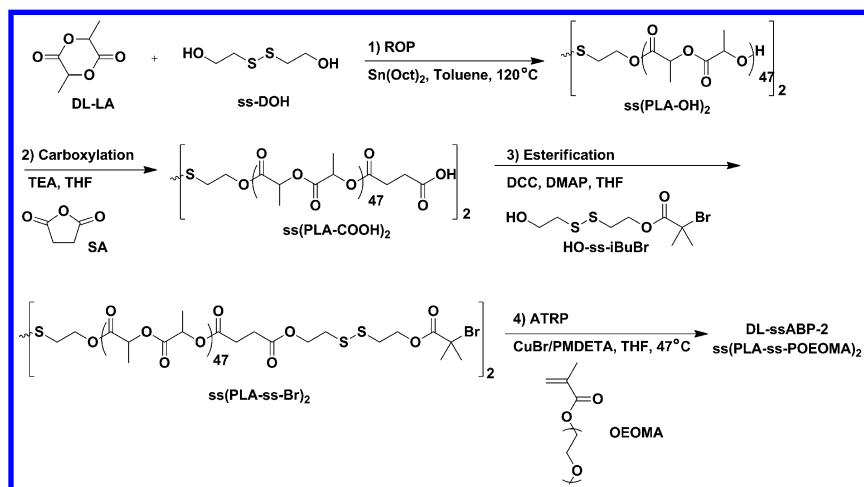


Figure 6. Our approach to synthesize DL-ssABP-2 (POEOMA-ss(PLA-ss-PLA)-ss-POEOMA) triblock copolymer by a combination of ROP, coupling reactions, and ATRP. Reproduced with permission from reference (72). Copyright 2014 American Chemical Society.

At 1.2 mg/mL concentration, above the CMC = 43 $\mu\text{g/mL}$, the DL-ssABP-2 formed self-assembled micellar aggregates in aqueous solution, with a diameter = 55 nm in aqueous solution by DLS and 30 nm in dried state by TEM images (Figure 7a). They then disassembled in 10 mM GSH (excess). As seen in Figure 7a, the micelle size increased with multimodal distribution. The occurrence of aggregation is attributed to reduction-responsive destabilization of micelles upon the cleavage of disulfide linkages in the dual locations (Figure 7b). To evaluate the enhanced release of encapsulated anticancer drugs in response to reductive environment, DOX-loaded micelles were prepared using a dialysis method at a loading level = 2.2 %. As compared in Figure 7c, the DOX release from micelles was faster in the presence of 10 mM GSH than without GSH. For example, within 5 hrs, the release reached >80 % in the presence of 10 mM GSH, while < 20% in the absence of GSH as a control. The enhanced and early burst drug release is attributed to the reductive cleavage of dually-located disulfide linkages both in micellar cores and at interfaces.

Intracellular trafficking of DOX from DOX-loaded micelles following cellular uptake was compared to HeLa cells only, as well as free DOX as controls by flow cytometry (Figure 8a) and CLSM (Figure 8b). The results suggest DOX-loaded micelles are able to deliver and release DOX into the nuclei of cancer cells. Further, *in vitro* cytotoxicity of DOX-loaded micelles was compared with

free DOX as a control using a MTT colorimetric assay. In the presence of DOX-loaded micelles, the HeLa cell viability was < 50% at 1.4 $\mu\text{g}/\text{mL}$ and further < 5% at 15 $\mu\text{g}/\text{mL}$. These results suggest the inhibition of cellular proliferation due to the effective and rapid release of DOX from DL-ssABP-2 platform, as a consequence of degradation of dual-located disulfide linkages in response to intracellular GSH inside cancer cells. These results are consistent to those obtained from flow cytometry and CLSM described above.

Interlayer-Crosslinked Micelles with Extended Sheddable Coronas

In addition to changing the drug release profile, the use of a dual or multi-location disulfide degradation strategy in the design of micellar nanocarriers can be used to incorporate other desired properties. For example, one challenge to be addressed is the colloidal stability of aggregates upon intravenous injection and dilution in the blood stream. Although block copolymer assembled micelles typically have good colloidal stability with a low CMC, drug-loaded micelles can undergo a multi-order magnitude dilution upon injection. Such a large dilution presents the micelles with local environments far below the CMC, causing micelle destabilization or dissociation, and thus premature release of encapsulated therapeutics prior to reaching the target organs or tissues. Crosslinked micelles have been proposed to address the stability issue and prevent premature micellar dissociation (79–81). The use of covalent crosslinks, however, can severely hamper the already diffusion limited release of encapsulated molecules, and thus decrease the therapeutic efficiency of drug-loaded micelles (79, 80). Using the dual location disulfide degradation strategy, novel PLA-based interlayer-crosslinked micelles (ICMs) was designed to incorporate a disulfide-crosslinked interlayer as well as a sheddable extended hydrophilic corona to provide both stability upon dilution as well as targeted and enhanced release of therapeutics at the desired sites.

As illustrated in Figure 9, well-defined triblock copolymer (DL-ssABP-3) consists of a hydrophobic and biodegradable PLA core forming block, an interlayer composed of PHMssEt to afford reversible crosslinkability, and a sheddable hydrophilic POEOMA corona (PLA-ss-PHMssEt-POEOMA). The DL-ssABP-3 undergoes aqueous self-assembly to form micellar aggregates consisting of a hydrophobic PLA-core, an interlayer of PHMssEt, and a hydrophilic POEOMA corona. Due to the presence of a disulfide linkage between the hydrophobic PLA core and the PHMssEt interlayer, the extended corona (HS-PHMSS-POEOMA) is shed upon exposure to a highly reducing environment, causing micellar destabilization and release of encapsulated compounds. In lightly reducing environments, or when a catalytic amount of reducing agents are present, the PHMssEt interlayer is crosslinked due to reductive intra- and inter-chain disulfide-thiol exchange reactions of cleaved small SH groups from HMssEt units. This enables the formation of sheddable interlayer crosslinked micelles (ICMs), providing enhanced colloidal stability upon intravenous injection, while simultaneously providing enhanced controlled release of loaded cargo in hydrophobic core.

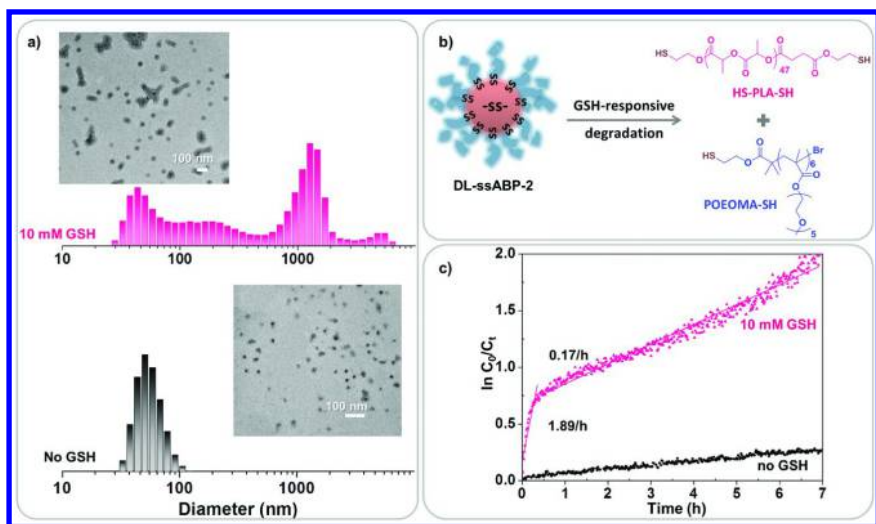


Figure 7. DLS diagrams and TEM images (a) and schematic illustration (b) of DL-ssABP-2 micelles before/after treatment with 10 mM GSH at 1.2 mg/mL, and enhanced release of DOX from DOX-loaded micelles in the absence (control) and presence of 10 mM GSH (c). Reproduced with permission from reference (72). Copyright 2014 American Chemical Society.

DL-ssABP-3 was synthesized by a combination of ROP and ATRP (Figure 10). PLA-ss-Br macroinitiator was first synthesized by ROP of LA in the presence of double-head initiator OH-ss-Br. The consecutive chain extension of the PLA-ss-Br with HMssEt and OEOMA allowed for the synthesis of well-controlled PLA-ss-PHMssEt-b-POEOMA with $M_n = 20$ kg/mol ($M_w/M_n = 1.2$) and DP = 17 for PHMssEt block and 39 for POEOMA block. At the concentration of 1.0 mg/mL (above the CMC = 4 μ g/mL), DL-ssABP-3 self-assembled to micellar aggregates with diameter ≈ 30 nm.

The formation of ICMs was conducted by slowly adding a catalytic amount of DTT stock solution to the micellar dispersion. As seen in Figure 11a, no significant change in particle size was observed after crosslinking the PHMssEt interlayer, with a diameter ≈ 30 nm as measured by DLS. To test the effect of crosslinking, a dilution study of micelles and ICM was performed. For non-crosslinked micelles, the dilution of micellar dispersion with 90% DMF by volume caused a decrease in observed diameter from 30 nm to 8.9 nm, suggesting the dissolution of micelles into single polymer chains as DMF is a good solvent to all three polymer blocks in DL-ssABP-3. However, when ICMs were mixed with the same amount of DMF, the micelle size increased from 29 nm to 96 nm. This increase in size is attributed to swelling of ICM in DMF. The results suggest that due to crosslinking of the PHMssEt interlayer with a catalytic amount of reducing agent, ICMs could withstand critical conditions such as a significant dilution in DMF or dilution in blood stream upon intravenous injection, thus improving colloidal stability of non-crosslinked micelles for drug delivery applications.

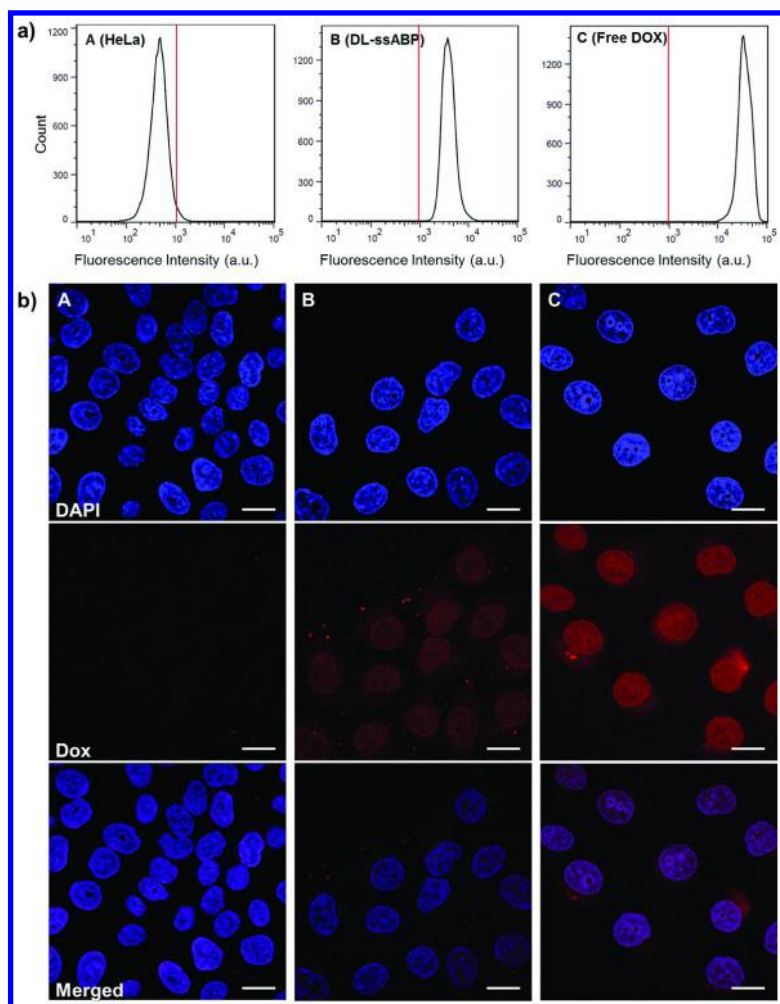


Figure 8. Flow cytometric histograms (a) and CLSM images (b) of HeLa cells only (A) and incubated with DOX-loaded DL-ssABP-2 micelles (B), and free DOX (C) for 16 hrs. Scale bar = 20 μm . Reproduced with permission from reference (72). Copyright 2014 American Chemical Society. (see color insert)

The controlled release of encapsulated NR upon disassembly of NR-loaded ICMs in response to reductive reaction was studied by monitoring change in fluorescence of a NR-loaded ICM dispersion in the absence and presence of DTT (excess, 10 mM) (Figure 11b). In the absence of DTT, no significant change in fluorescence was observed over a 90 hrs period, suggesting that encapsulated NR were securely confined in the hydrophobic PLA core. However, in the presence of excess DTT, a gradual decrease in fluorescence was observed over time due to release of encapsulated NR and subsequent quenching in a hydrophilic environment.

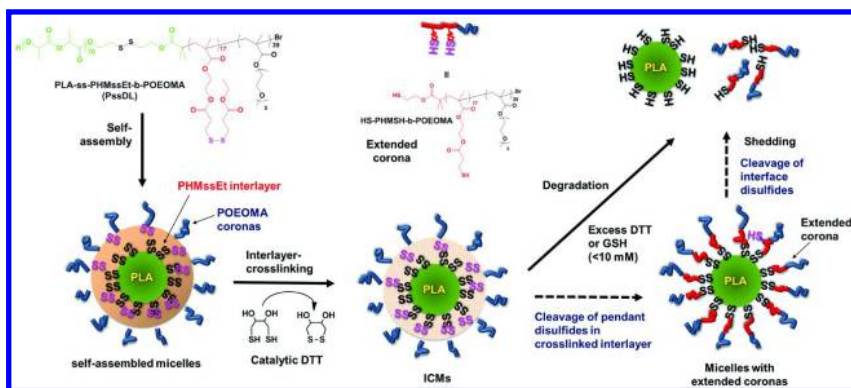


Figure 9. PLA-based ICMs for enhanced colloidal stability and shedding extended coronas for rapid release of encapsulated anticancer drugs, based on well-controlled DL-ssABP-3 triblock copolymer having multiple pendant disulfides in the interlayer and single disulfides at junctions of PHMssEt and POEOMA blocks in aqueous solution. Reproduced with permission from reference (73). Copyright 2014 Royal Society of Chemistry. (see color insert)

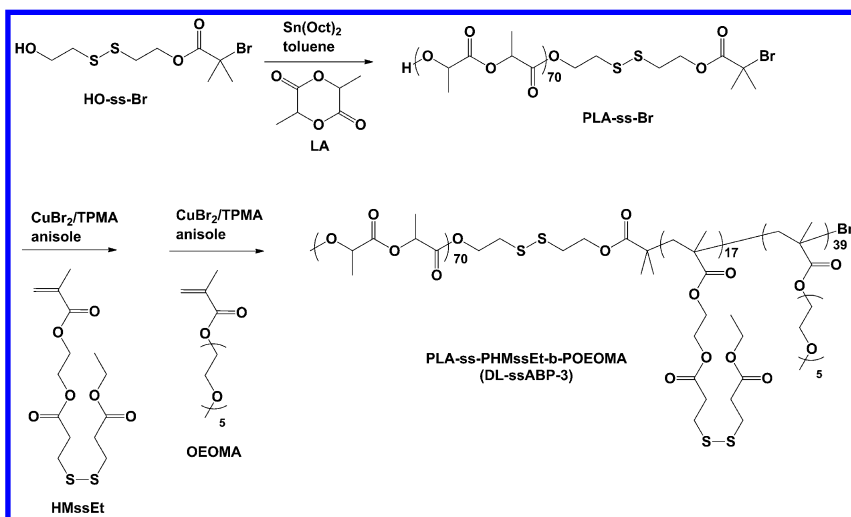


Figure 10. Our approach to synthesize DL-ssABP-3 triblock copolymer by a combination of ROP and consecutive ATRP. Reproduced with permission from reference (73). Copyright 2014 Royal Society of Chemistry.

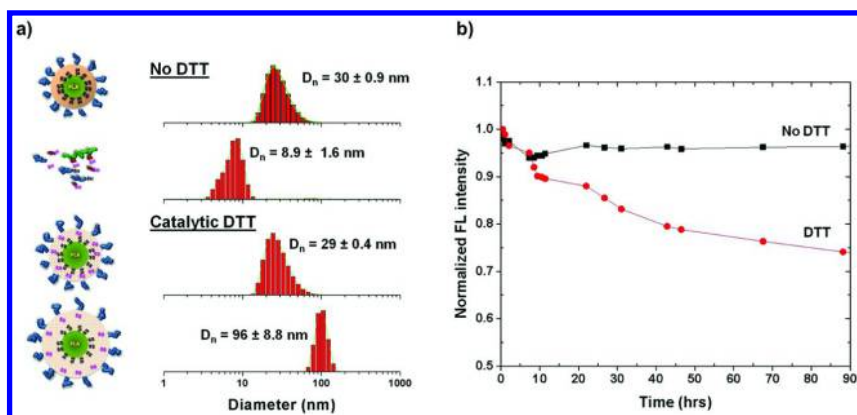


Figure 11. DLS diagrams of aqueous micellar aggregates before and after being diluted with DMF in the absence and presence of catalytic amounts of DTT (a) and reduction-responsive release profile of NR-loaded DL-ssABP-3 based interlayer-crosslinked micellar aggregates with and without excess DTT in aqueous solution (b). Reproduced with permission from reference (73).

Copyright 2014 Royal Society of Chemistry.

Further, the effectiveness of ICMs for drug delivery applications was evaluated by monitoring cell toxicity and cellular uptake of DOX-loaded ICMs. Cell viability by MTT colorimetric assay was over 90% for both empty micelles and ICMs. In the presence of DOX-loaded DL-ssABP-3 micelles, however, it decreased to $\approx 60\%$. This result, combined with results obtained from flow cytometry and CLSM suggest cellular uptake and release of encapsulated DOX causing inhibition of cell proliferation.

Summary and Outlook

Exploring an effective dual location disulfide degradation strategy, well-defined reduction-responsive degradable block copolymers and their self-assembled micellar nanocarriers incorporating disulfide linkages in dual locations have been developed. These reduction-responsive block copolymers were synthesized by a combination of well-known organic and polymer synthetic methods such as facile coupling reactions, ROP, and ATRP. Aqueous micellization through self-assembly of the block copolymers in the presence of DOX (a clinically-used anticancer drug) formed colloiddally stable micellar aggregates having disulfide linkages in dual locations as in the hydrophobic micellar cores, in the disulfide-crosslinked interlayers, and core/corona interfaces. In a reducing environment such as in the presence of GSH or DTT, the newly designed dual-location disulfide degradable micellar system exhibited rapid destabilization or disassembly and thus synergistically enhanced release properties compared with conventional reduction-responsive degradable micelles with disulfides in only a single location. The new strategy provides a better understanding of the

structure-property relationships between structure variance and stimuli-responsive degradation. The promising results can be utilized in optimizing the new design of multifunctional intracellular anticancer drug delivery nanocarriers exhibiting multiple responses of accelerated release.

Acknowledgments

This work is supported from NSERC Discovery Grant and Canada Research Chair (CRC) Award. Authors thank S. Aleksanian and A. Cunningham for their experiments done during their master program in the laboratory. JKO is entitled Tier II CRC in Nanobioscience as well as a member of Centre Québécois sur les Matériaux Fonctionnels (CQMF) funded by FQRNT.

References

1. Harada, A.; Kataoka, K. *Prog. Polym. Sci.* **2006**, *31*, 949–982.
2. Mikhail, A. S.; Allen, C. *J. Controlled Release* **2009**, *138*, 214–223.
3. Nishiyama, N.; Kataoka, K. *Adv. Polym. Sci.* **2006**, *193*, 67–101.
4. Xiong, X.-B.; Falamarzian, A.; Garg, S. M.; Lavasanifar, A. *J. Controlled Release* **2011**, *155*, 248–261.
5. Ding, J.; Chen, L.; Xiao, C.; Chen, L.; Zhuang, X.; Chen, X. *Chem. Commun.* **2014**, *50*, 11274–11290.
6. Allen, C.; Maysinger, D.; Eisenberg, A. *Colloids Surf., B* **1999**, *16*, 3–27.
7. Taurin, S.; Nehoff, H.; Greish, K. *J. Controlled Release* **2012**, *164*, 265–275.
8. Zhang, L.; Li, Y.; Yu, J. C. *J. Mater. Chem. B* **2014**, *2*, 452–470.
9. Nichols, J. W.; Bae, Y. H. *Nano Today* **2012**, *7*, 606–618.
10. Bae, Y. H.; Park, K. *J. Controlled Release* **2011**, *153*, 198–205.
11. Farokhzad, O. C.; Langer, R. *ACS Nano* **2009**, *3*, 16–20.
12. Prokop, A.; Davidson, J. M. *J. Pharm. Sci.* **2008**, *97*, 3518–3590.
13. Klinger, D.; Landfester, K. *Polymer* **2012**, *53*, 5209–5231.
14. Rijcken, C. J. F.; Soga, O.; Hennink, W. E.; van Nostrum, C. F. *J. Controlled Release* **2007**, *120*, 131–148.
15. Zhang, Q.; Ko, N. R.; Oh, J. K. *Chem. Commun.* **2012**, *48*, 7542–7552.
16. Jackson, A. W.; Fulton, D. A. *Polym. Chem.* **2013**, *4*, 31–45.
17. Wang, Y.; Xu, H.; Zhang, X. *Adv. Mater.* **2009**, *21*, 2849–2864.
18. Loomis, K.; McNeeley, K.; Bellamkonda, R. V. *Soft Matter* **2011**, *7*, 839–856.
19. Gillies, E. R.; Jonsson, T. B.; Frechet, J. M. J. *J. Am. Chem. Soc.* **2004**, *126*, 11936–11943.
20. Binauld, S.; Stenzel, M. H. *Chem. Commun.* **2013**, *49*, 2082–2102.
21. Zhao, H.; Sterner, E. S.; Coughlin, E. B.; Theato, P. *Macromolecules* **2012**, *45*, 1723–1736.
22. Sun, L.; Zhu, B.; Su, Y.; Dong, C.-M. *Polym. Chem.* **2014**, *5*, 1605–1613.

23. Bertrand, O.; Poggi, E.; Gohy, J.-F.; Fustin, C.-A. *Macromolecules* **2014**, *47*, 183–190.
24. Zhao, Y. *Macromolecules* **2012**, *45*, 3647–3657.
25. Liu, G.; Liu, W.; Dong, C.-M. *Polym. Chem.* **2013**, *4*, 3431–3443.
26. Xiong, M.-H.; Bao, Y.; Du, X.-J.; Tan, Z.-B.; Jiang, Q.; Wang, H.-X.; Zhu, Y.-H.; Wang, J. *ACS Nano* **2013**, *7*, 10636–10645.
27. Lee, M. H.; Yang, Z.; Lim, C. W.; Lee, Y. H.; Sun, D.; Kang, C.; Kim, J. S. *Chem. Rev.* **2013**, *113*, 5071–5109.
28. Cheng, R.; Feng, F.; Meng, F.; Deng, C.; Feijen, J.; Zhong, Z. *J. Controlled Release* **2011**, *152*, 2–12.
29. Wei, H.; Zhuo, R.-X.; Zhang, X.-Z. *Prog. Polym. Sci.* **2013**, *38*, 503–535.
30. Huo, M.; Yuan, J.; Tao, L.; Wei, Y. *Polym. Chem.* **2014**, *5*, 1519–1528.
31. Li, C.; Madsen, J.; Armes, S. P.; Lewis, A. L. *Angew. Chem., Int. Ed.* **2006**, *45*, 3510–3513.
32. Tsarevsky, N. V.; Matyjaszewski, K. *Macromolecules* **2005**, *38*, 3087–3092.
33. Russo, A.; DeGraff, W.; Friedman, N.; Mitchell, J. B. *Cancer Res.* **1986**, *46*, 2845–8.
34. Saito, G.; Swanson, J. A.; Lee, K.-D. *Adv. Drug Delivery Rev.* **2003**, *55*, 199–215.
35. Khorsand, B.; Lapointe, G.; Brett, C.; Oh, J. K. *Biomacromolecules* **2013**, *14*, 2103–2111.
36. Ryu, J.-H.; Roy, R.; Ventura, J.; Thayumanavan, S. *Langmuir* **2010**, *26*, 7086–7092.
37. Yuan, L.; Liu, J.; Wen, J.; Zhao, H. *Langmuir* **2012**, *28*, 11232–11240.
38. Zhang, Q.; Aleksanian, S.; Noh, S. M.; Oh, J. K. *Polym. Chem.* **2013**, *4*, 351–359.
39. Ryu, J.-H.; Chacko, R. T.; Jiwanpanich, S.; Bickerton, S.; Babu, R. P.; Thayumanavan, S. *J. Am. Chem. Soc.* **2010**, *132*, 17227–17235.
40. Li, Y.-L.; Zhu, L.; Liu, Z.; Cheng, R.; Meng, F.; Cui, J.-H.; Ji, S.-J.; Zhong, Z. *Angew. Chem., Int. Ed.* **2009**, *48*, 9914–9918.
41. Chan, N.; Yee, N.; An, S. Y.; Oh, J. K. *J. Polym. Sci., Part A: Polym. Chem.* **2014**, *52*, 2057–2067.
42. Liu, J.; Pang, Y.; Huang, W.; Zhu, Z.; Zhu, X.; Zhou, Y.; Yan, D. *Biomacromolecules* **2011**, *12*, 2407–2415.
43. Han, D.; Tong, X.; Zhao, Y. *Langmuir* **2012**, *28*, 2327–2331.
44. Nelson-Mendez, A.; Aleksanian, S.; Oh, M.; Lim, H.-S.; Oh, J. K. *Soft Matter* **2011**, *7*, 7441–7452.
45. Aleksanian, S.; Khorsand, B.; Schmidt, R.; Oh, J. K. *Polym. Chem.* **2012**, *3*, 2138–2147.
46. Fan, H.; Huang, J.; Li, Y.; Yu, J.; Chen, J. *Polymer* **2010**, *51*, 5107–5114.
47. Yu, S.; He, C.; Ding, J.; Cheng, Y.; Song, W.; Zhuang, X.; Chen, X. *Soft Matter* **2013**, *9*, 2637–2645.
48. Ding, M.; Zeng, X.; He, X.; Li, J.; Tan, H.; Fu, Q. *Biomacromolecules* **2014**, *15*, 2896–2906.
49. Ding, M.; Li, J.; He, X.; Song, N.; Tan, H.; Zhang, Y.; Zhou, L.; Gu, Q.; Deng, H.; Fu, Q. *Adv. Mater.* **2012**, *24*, 3639–3645.
50. Cunningham, A.; Oh, J. K. *Macromol. Rapid Commun.* **2013**, *34*, 163–168.

51. Liu, D.-L.; Chang, X.; Dong, C.-M. *Chem. Commun.* **2013**, *49*, 1229–1231.
52. Sun, L.; Liu, W.; Dong, C.-M. *Chem. Commun.* **2011**, *47*, 11282–11284.
53. Jiang, X.; Zhang, M.; Li, S.; Shao, W.; Zhao, Y. *Chem. Commun.* **2012**, *48*, 9906–9908.
54. Cunningham, A.; Ko, N. R.; Oh, J. K. *Colloids Surf., B* **2014**, *122*, 693–700.
55. Liu, J.; Pang, Y.; Huang, W.; Huang, X.; Meng, L.; Zhu, X.; Zhou, Y.; Yan, D. *Biomacromolecules* **2011**, *12*, 1567–1577.
56. Tang, L.-Y.; Wang, Y.-C.; Li, Y.; Du, J.-Z.; Wang, J. *Bioconjugate Chem.* **2009**, *20*, 1095–1099.
57. Klaikherd, A.; Nagamani, C.; Thayumanavan, S. *J. Am. Chem. Soc.* **2009**, *131*, 4830–4838.
58. Wen, H.-Y.; Dong, H.-Q.; Xie, W.-j.; Li, Y.-Y.; Wang, K.; Pauletti, G. M.; Shi, D.-L. *Chem. Commun.* **2011**, *47*, 3550–3552.
59. Sun, H.; Guo, B.; Li, X.; Cheng, R.; Meng, F.; Liu, H.; Zhong, Z. *Biomacromolecules* **2010**, *11*, 848–854.
60. Khorsand Sourkahi, B.; Cunningham, A.; Zhang, Q.; Oh, J. K. *Biomacromolecules* **2011**, *12*, 3819–3825.
61. Zhang, Q.; Ko, N. R.; Oh, J. K. *RSC Adv.* **2012**, *2*, 8079–8086.
62. Yuan, W.; Zou, H.; Guo, W.; Shen, T.; Ren, J. *Polym. Chem.* **2013**, *4*, 2658–2661.
63. Chen, W.; Zou, Y.; Meng, F.; Cheng, R.; Deng, C.; Feijen, J.; Zhong, Z. *Biomacromolecules* **2014**, *15*, 900–907.
64. Xuan, J.; Han, D.; Xia, H.; Zhao, Y. *Langmuir* **2014**, *30*, 410–417.
65. Tong, R.; Lu, X.; Xia, H. *Chem. Commun.* **2014**, *50*, 3575–3578.
66. Jia, L.; Cui, D.; Bignon, J.; Di Cicco, A.; Wdzieczak-Bakala, J.; Liu, J.; Li, M.-H. *Biomacromolecules* **2014**, *15*, 2206–2217.
67. Yuan, W.; Shen, T.; Wang, J.; Zou, H. *Polym. Chem.* **2014**, *5*, 3968–3971.
68. Zhang, Q.; Aleksanian, S.; Cunningham, A.; Oh, J. K. *ACS Symp. Ser.* **2012**, *1101*, 287–302.
69. Li, X.-Q.; Wen, H.-Y.; Dong, H.-Q.; Xue, W.-M.; Pauletti, G. M.; Cai, X.-J.; Xia, W.-J.; Shi, D.-L.; Li, Y.-Y. *Chem. Commun.* **2011**, *47*, 8647–8649.
70. Cheetham, A. G.; Ou, Y.-C.; Zhang, P.; Cui, H. *Chem. Commun.* **2014**, *50*, 6039–6042.
71. Chan, N.; Khorsand, B.; Aleksanian, S.; Oh, J. K. *Chem. Commun.* **2013**, *49*, 7534–7536.
72. Ko, N. R.; Oh, J. K. *Biomacromolecules* **2014**, *15*, 3180–3189.
73. Chan, N.; An, S. Y.; Oh, J. K. *Polym. Chem.* **2014**, *5*, 1637–1649.
74. Matyjaszewski, K.; Xia, J. *Chem. Rev.* **2001**, *101*, 2921–2990.
75. Kamigaito, M.; Ando, T.; Sawamoto, M. *Chem. Rev.* **2001**, *101*, 3689–3745.
76. Penczek, S.; Cypryk, M.; Duda, A.; Kubisa, P.; Slomkowski, S. *Prog. Polym. Sci.* **2007**, *32*, 247–282.
77. Uhrich, K. E.; Cannizzaro, S. M.; Langer, R. S.; Shakesheff, K. M. *Chem. Rev.* **1999**, *99*, 3181–3198.
78. Dechy-Cabaret, O.; Martin-Vaca, B.; Bourissou, D. *Chem. Rev.* **2004**, *104*, 6147–6176.
79. O'Reilly, R. K.; Joralemon, M. J.; Hawker, C. J.; Wooley, K. L. *New J. Chem.* **2007**, *31*, 718–724.

80. Talelli, M.; Rijcken, C. J. F.; Oliveira, S.; van der Meel, R.; van Bergen en Henegouwen, P. M. P.; Lammers, T.; van Nostrum, C. F.; Storm, G.; Hennink, W. E. *J. Controlled Release* **2011**, *153*, 93–102.
81. Huang, H.; Remsen, E. E.; Kowalewski, T.; Wooley, K. L. *J. Am. Chem. Soc.* **1999**, *121*, 3805–3806.

Chapter 18

Design Strategies for the Fabrication of Tailored Nanocomposites via RAFT Polymerization

Christian Rossner, Bastian Ebeling, and Philipp Vana*

Institut für Physikalische Chemie, Georg-August-Universität Göttingen,
Tammannstraße 6, D-37077 Göttingen, Germany

*E-mail: pvana@uni-goettingen.de

The formation of nanocomposites from gold nanoparticles and RAFT polymers has been investigated in detail. The binding mode of linear multifunctional RAFT polymers on the surface of two different types of nanoparticles was examined. For gold nanoparticles from citrate-reduction, multidentate binding of this type of polymer was observed, resulting in polymer loops on the nanoparticle surface. In contrast, smaller nanoparticles prepared using the two-phase Brust-Schiffrin method were shown to form cross-linked particle networks when treated with multifunctional RAFT polymers. The particle density in these superstructures was correlated with the degree of polymerization of the cross-linking macromolecules. In addition, the power of RAFT star polymers with external functional groups in the tailored assembly of gold nanoparticles was demonstrated by the controlled formation of planet-satellite nanostructures comprising both mentioned types of gold nanoparticles.

1. Introduction

The exploration of novel nanomaterials is still a vibrant field of research (1). In particular, gold nanoparticles attained huge attention because of their stability, the facile modification of their surface and their unique physical properties (2). These properties can only be preserved if nanoparticles are prevented from uncontrolled aggregation in a colloidal dispersion or matrix. This requires

sufficient nanoparticle stabilization. Moreover, the special optical features of gold nanoparticles are not only influenced by their size and shape, but also by the interparticle spatial relations (3). Therefore, to take advantage of their properties, it is necessary to 1) find ways to stabilize nanoparticles as individual units and 2) at the same time achieve control over their spatial arrangement.

Polymers are attractive candidates for fulfilling the task of nanoparticle stabilization. Due to their size (in the nm regime), polymers can form relatively thick layers when bound to a nanoparticle surface, which usually results in a large repulsive interparticle potential (4). The resulting steric stabilization of polymer-modified nanoparticles can be rationalized by a loss of configurational entropy when two nanoparticles approach each other and thus induce compression of the stabilizing polymer layer (5). In a good solvent, the stabilization of nanoparticles with macromolecules attached to their surfaces therefore increases with increasing thickness of the shielding polymer layer.

To control the spatial arrangement of nanoparticles, on the other hand, macromolecules need to be more than just large and conformationally flexible. In fact, for this function, they need to contain information that can subsequently be translated to the structure of nanoparticle arrangements. DNA is a biopolymer which is commonly known to encode polypeptide sequences and it could already be demonstrated that DNA can also be used to assemble nanoparticles in a rational and predetermined fashion (6–8).

The application of synthetic polymers to mediate the assembly of nanoparticles offers an interesting and versatile alternative to DNA. This alternative came into reach, as reversible-deactivation radical polymerization (RDRP) techniques have enabled polymer chemists to prepare macromolecules with well-defined architectures: Macromolecules with predetermined molecular weight can be produced, the distribution of functional groups among these and the polymer topology can be controlled.

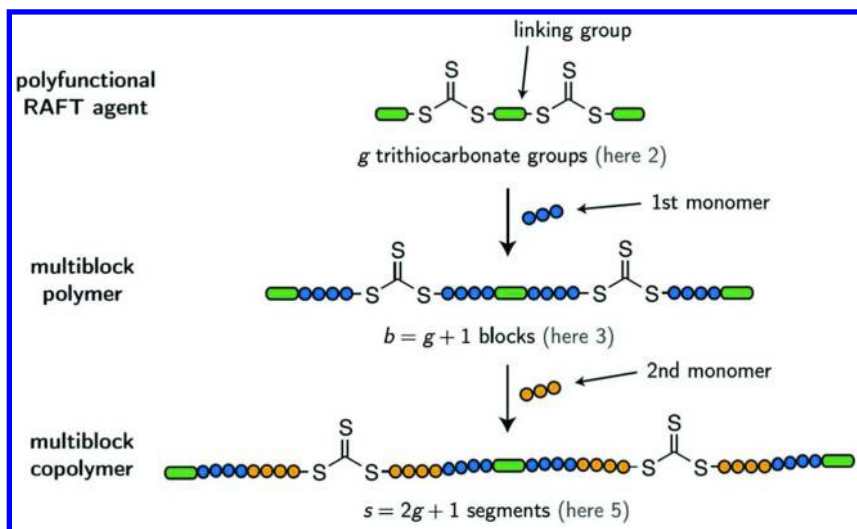
In order to guide nanoparticle-superstructure formation through the macromolecular design of synthetic polymers, the polymer-nanoparticle interactions need to be targeted. Polymers can either interact with nanoparticles via van-der-Waals forces (9) or be attached directly to their surfaces with suitable anchor groups. A variety of functional groups, such as thiols (10), disulfides (11), thioethers (12), dithiocarbonate anions (13), and terminal alkynes (14), but also functional groups inherent to RAFT polymers—like trithiocarbonates and dithioesters—have been shown to be capable to chemisorb on gold surfaces (15–17). The binding free energy of phenyldithioesters to a particular type of gold nanoparticles could be determined to be 36 kJ mol⁻¹ (17), so that especially RAFT polymers with multiples of these groups can yield stable composite materials with gold nanoparticles. Therefore, RAFT polymerization becomes an advantageous means of polymer fabrication in the realm of gold nanochemistry as opposed to other prominent reversible-deactivation radical polymerization techniques, as the RAFT groups can fulfill the dual function both of mediating the radical polymerization and providing binding sites for gold. Thus, control over the distribution of these characteristic functional groups among the synthesized macromolecules by means of macromolecular design enables the formation of made-to-measure gold-nanoparticle superstructures.

In the following, we will first discuss synthetic approaches to obtain macromolecules with desired architectures. The second part of this text will deal with the formation of nanocomposites derived from the polymers introduced before.

2. Macromolecular Design Principles

2.1. Multiblock RAFT Polymers

In multiblock RAFT polymers, several blocks made of monomeric repeating units are linearly interconnected by RAFT groups. This type of material can be obtained when cyclic (18) or linear multifunctional RAFT agents (19, 20) are employed in radical polymerizations. From the RAFT agent precursor, multiblock copolymers with alternating segments of different composition (multiblock copolymers) can thus be obtained in only two synthetic steps (see Scheme 1).



Scheme 1. Multiblock homo- and copolymers from multifunctional RAFT agents. Reproduced with permission from reference (19). Copyright (2011) MDPI AG (open access: <http://creativecommons.org/licenses/by/3.0/>)

When the resulting polymeric material is treated with a primary amine, the macromolecules are cleaved at their trithiocarbonate junctions, and the analysis of the obtained single blocks reveals that they are relatively uniform in length, that is, the RAFT mechanism results in narrow block length distributions (18, 19). A less obvious result from a detailed theoretical analysis of the underlying polymerization mechanism is that also the ideal distribution of blocks/RAFT groups among the produced macromolecules is remarkably narrow, an effect which is due to continuous redistribution of all blocks within the RAFT mechanism (21). These features enable the synthesis of relatively uniform and well-defined materials. Having in mind that the trithiocarbonate groups—which

are incorporated along the polymeric backbone—attach to gold, the blocks consisting of defined numbers of monomers can be thought of as spacers which covalently interconnect nanoparticle binding sites.

Such an incorporation of binding sites for gold into a polymer chain is an established principle (22), however, precisely tailored nanocomposites can only be obtained, when the distribution of such binding sites in macromolecules can be controlled. As has been pointed out above, multiblock RAFT polymers are very well-suited in this respect. The implications of this matter will be discussed in section 3.1.

2.2. RAFT Star Polymers

A different topology, as opposed to polymers with linear shape, are star polymers. RDRP techniques have enabled the formation of polymers of this class by the ‘core-first’ approach which circumvents significant issues associated with the coupling of preformed polymer arms. The RAFT technique is unique in this respect, as it may result in either Z-star (23) or R-star RAFT polymers (24), which differ both in the formation mechanism and the structure of the obtained products: In the Z-star approach, RAFT groups are covalently linked to a common core via their stabilizing Z groups, so that linear macroradicals undergo propagation steps in solution. Continuous interchange with the (dormant) arms of star polymer species enables the formation of star polymers with narrow molecular weight distribution. The fact that the mediating RAFT groups remain close to the core of the star does not necessarily imply that they are not efficient in mediating the polymerization (25); more important for achieving defined star polymer topologies is the appropriate choice of the leaving R group for the monomer to be polymerized (26). If the RAFT groups are joined through their reinitiating R groups to form a star-shaped chain transfer agent (R-star approach), macroradicals with star topology will inherently arise in a subsequent RAFT polymerization. Therefore, (unwanted) star–star coupling will inevitably take place in this approach. However, the fraction of star–star couples in the final material can be limited to an acceptable number, if only small amounts of radical initiator (with respect to the RAFT agent) decompose under the applied polymerization conditions. Consequently, well-defined star-shaped macromolecules with their RAFT groups being located at the exterior of the star are synthetically accessible. Owing to this feature, these macromolecules can be considered as potential linking-agents for gold nanoparticles and are arguably better defined than hyperbranched macromolecular cross-linkers (27–29), which are sometimes called ‘pseudo-star’ polymers.

3. Nanocomposites of Multifunctional RAFT Polymers

3.1. The Interaction of Linear Multiblock RAFT Polymers with Gold Nanoparticles

Once polymers of defined architecture are at hand, nanocomposite formation still depends on the specific interaction of macromolecules with nanoparticles.

As this interaction can be influenced by the type of nanoparticles as well (30) and is hard to predict *a priori*, we aimed at the experimental elucidation of the binding mode which occurs, when linear multiblock RAFT polymers are grafted to the surfaces of spherical gold nanocrystals from citrate-reduction (31) and from the two-phase Brust-Schiffrin synthesis (32). In principle conceivable results from such grafting experiments are cross-linked nanoparticle networks (Figure 1a), isolated hybrid particles with polymer loops on their surfaces (Figure 1b) and RAFT polymers attached with only one anchoring point to the gold surface (Figure 1c).

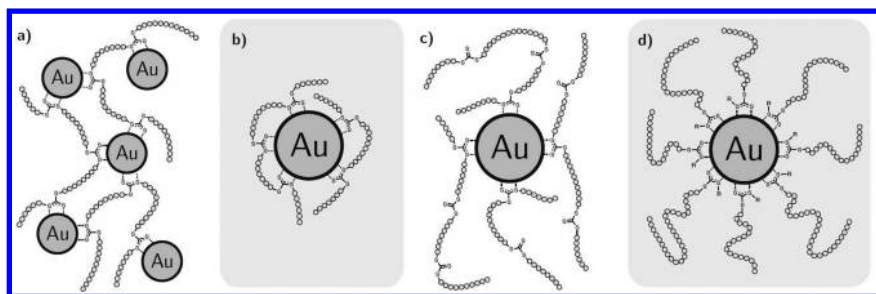


Figure 1. Possible binding modes of RAFT polymers with multiple trithiocarbonate moieties incorporated along their backbone: interconnection of particles (a); multidentate binding on the same particle resulting in polymer loops (b); and monodentate binding resulting in free trithiocarbonate groups dangling from the nanoparticle surface (c). Image (d) shows RAFT polymers containing a single trithiocarbonate group grafted to a gold nanoparticle. Adapted with permission from ref. (31). Copyright 2013 American Chemical Society.

3.1.1. Gold Nanoparticles from Citrate-Reduction

Detailed investigations of gold nanoparticles and their nanohybrids requires their reproducible fabrication. The gold-nanoparticle building blocks should be homogeneous in their size and easy to functionalize with a polymer layer. Gold nanocrystals from the citrate-reduction pioneered by Turkevich (33) fulfill these requirements. They can be produced with very low dispersities in aqueous solution and can be directly brought into contact with (water-soluble) polymers for functionalization reactions.

RAFT polymers with only a single trithiocarbonate group (which we like to refer to as ‘conventional RAFT polymers’) are expected to chemisorb on gold surfaces via this anchor site located on the ω -end of the polymeric chains (Figure 1d). Consequently, nanohybrid core-shell particles result, when such RAFT polymers are added to dispersions of gold nanoparticles with reactive surfaces. When these core-shell nanoparticles are drop-cast from colloidal dispersion on a solid substrate and the solvent is evaporated, a very useful effect occurs:

The nanohybrid particles arrange themselves regularly in two-dimensional superlattices (Figure 2, greek letters indicate samples which differ in the degree of polymerization of the conventional RAFT polymers).

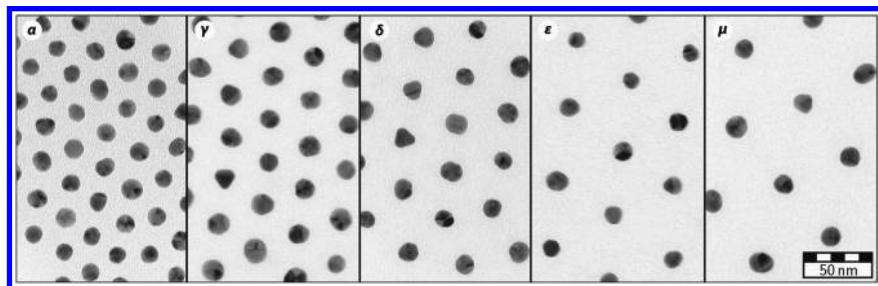


Figure 2. TEM images of self-assembled hexagonal layers of gold cores in nanohybrid particles with conventional RAFT polymers of varying degree of polymerization (increasing from left to right). Reprinted with permission from ref. (31). Copyright 2013 American Chemical Society.

The grafted conventional RAFT polymers of *N*-isopropylacrylamide (PNⁱPAAM, not directly visible on the TEM micrographs) cause distinct interparticle spacings, which strictly increase with growing molecular weight of the polymer. By measuring edge-to-edge distances of the gold cores in undistorted hexagons, reference data can be obtained and fitted to a suitable function describing this behavior. Such a function can take the form of

$$d = k \times [\bar{M}_n]^{1/l} \quad (1)$$

where the interparticle distance d is correlated with the molecular weight \bar{M}_n of the polymer, the parameter k reflecting the interparticle spacing per molar mass of the polymer and l describing the form of the increase. As the values for d and \bar{M}_n are experimentally accessible, only k and l remain as fit-parameters and are determined as $k = 6.02 \times 10^{-12}$ m and $l = 1.27$ (solid line in Figure 3). Alternatively, k can be set fixed to twice the contour length of the PNⁱPAAM chains, resulting in $k_{\text{theo}} = 2 \times 2.2 \times 10^{-12}$ m = 4.4×10^{-12} m and $l = 1.22$ (dashed line in Figure 3). In both cases, the obtained fit-curves describe the data reasonably well. Moreover, the parameter l being closer to 1 (the polymer-brush limit) than to 2 (the isolated chain limit) is indicative of relatively high grafting densities of conventional RAFT polymer on the gold-nanoparticle surfaces.

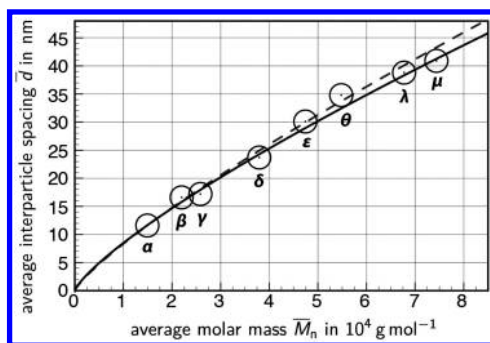


Figure 3. The molecular weight dependence of interparticle distances in conventional nanohybrids. Reprinted with permission from ref. (31). Copyright 2013 American Chemical Society.

Additionally, the data obtained from an analysis of the conventional nanohybrids can be taken as reference values for comparison with nanohybrids of multiblock RAFT polymers of NⁱPAAM with multiple trithiocarbonate groups (see above). For these nanohybrids, also no stacking of particles is observed in transmission electron microscopy, as would be expected if particles were cross-linked through multifunctional RAFT polymers. The case of nanoparticle network formation (as illustrated in Figure 1a) in this system can therefore be ruled out and it remains to be elucidated if the polymer binding is multidentate (Figure 1b) or monodentate (Figure 1c). Since the nanohybrids with multiblock RAFT polymers of NⁱPAAM also arrange in hexagonal patterns, their interparticle distances can be compared to the obtained reference (Figure 4).

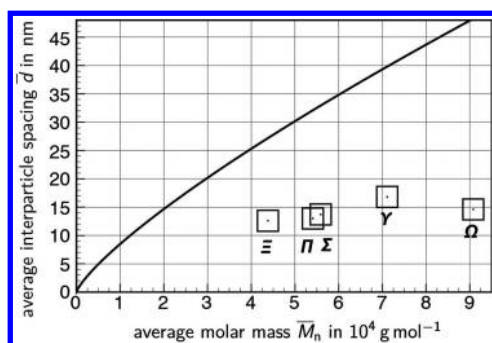


Figure 4. The molecular weight dependence of interparticle distances in nanohybrids with multiblock RAFT polymers. Reprinted with permission from ref. (31). Copyright 2013 American Chemical Society.

The data points shown in Figure 4 refer to interparticle distances in self-assembled hexagonal arrays of nanohybrids with multifunctional RAFT polymer of varying molar mass and also varying average number of trithiocarbonate groups (the average numbers of TTC groups are 3.0 in sample

Ξ, 4.5 in sample Π, 3.2 in sample Σ, 1.9 in sample Υ, and 2.0 in sample Ω, as determined by the SEC analysis of the cleavage products). It can be seen that the particle spacings are independent of molar mass and the number of trithiocarbonate groups and remain almost constant for all investigated samples. This can only be explained, if one assumes that the multifunctional RAFT polymers are wrapped around the nanoparticles, forming loops on the particle surface (Figure 1b) (34).

Because of this novel binding motif of multifunctional RAFT polymers on gold nanoparticles from citrate-reduction, it can be envisaged to prepare multiblock copolymers with a first block of functional monomer that will be exposed on the outer hybrid particle shell (and may be used for, e.g. recognition) and a second block in which monomer is used that provides solubility for the system.

3.1.2. Gold Nanoparticles from the Two-Phase Brust-Schiffrin Method

The two-phase Brust-Schiffrin synthesis permits the formation of gold nanocrystals in organic media. By employing a phase-transfer catalyst, a gold salt precursor can be transferred into an organic solvent (often toluene) and reduced in the presence or absence of additional stabilizing ligands (typically thiols). When these ligands are absent, the particles will be stabilized by a weakly chemisorbed phase-transfer catalyst (35). After washing steps that allow for the removal of remaining reduction agent, the particle surface can be functionalized by ligand exchange reactions (36). Through such reactions, nanohybrids with multifunctional RAFT polymers, which do not have to be water-soluble, can be obtained in organic media. For a sufficiently high colloidal stability, it is only necessary to use polymers that display good solubility in toluene. Polystyrene fulfills this criterion and has the additional advantage, that styrene oligomers with narrow chain length distributions can be obtained with suitable RAFT agents (37). Therefore, the degree of polymerization of styrene can be systematically varied in a wide range including very small chain lengths. We prepared several multiblock RAFT polymers of styrene with multiple trithiocarbonate groups and determined their molar mass distributions by size-exclusion chromatography and the average number of styrene units per block by NMR spectroscopy. The polymers were added to toluene dispersions of tetraoctylammonium-bromide (= phase-transfer catalyst) capped gold nanoparticles synthesized by the above described two-phase Brust-Schiffrin method and the resulting nanohybrids were analyzed by TEM and atomic force microscopy (AFM).

TEM overview images revealed well-separated spherical objects with average diameters of several hundreds of nanometers (Figure 5), which is orders of magnitude larger than the diameter of individual Brust-Schiffrin particles (approx. 4 nm). Closer inspection of individual spherical objects by taking micrographs at higher magnifications (Figure 6) reveals that they are composed of individual nanoparticles. Furthermore, the particle density in these nanoparticle networks is reduced, when multiblock polymers with larger polystyrene segments are employed in the nanoparticle-functionalization reactions.

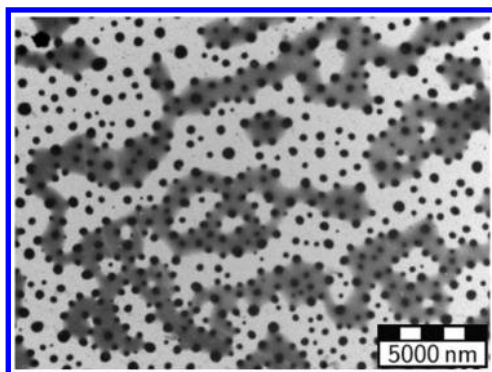


Figure 5. TEM overview image of a sample containing Brust-Schiffrin gold nanoparticles treated with multifunctional RAFT polymers of styrene. Adapted with permission from ref. (32). Copyright 2013 American Chemical Society.

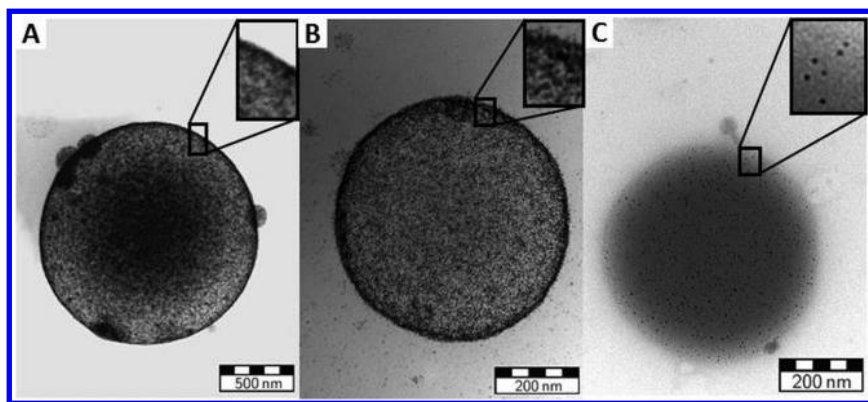


Figure 6. TEM images of spherical gold-nanoparticle assemblies with varying degree of polymerization (increasing from left to right) of the employed multiblock RAFT polymers. Adapted with permission from ref. (32). Copyright 2013 American Chemical Society.

The gold-nanoparticle superstructures were also investigated by AFM (Figure 7), in order to disclose their three-dimensional shape. This gives valuable additional information, because a preserved globular structure is indicative of nanoparticle cross-links, since neighboring particles are prevented from slipping and forming a flat monolayer when they are bonded together in a particle network (38). AFM analysis proves that these spherical objects partly preserve their globular shape after deposition, and can therefore be thought of as being made of gold nanoparticles interconnected by multifunctional RAFT polymer, that is, a gel where nanoparticles act as cross-links for macromolecules.

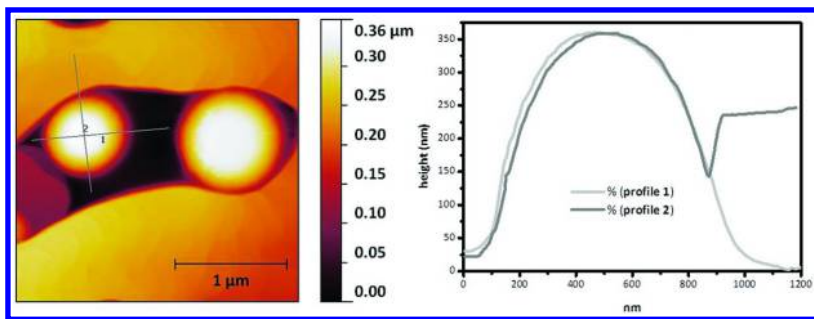


Figure 7. AFM image and corresponding height profiles of gold-nanoparticle assemblies mediated by multifunctional RAFT polymers. Adapted with permission from ref. (32). Copyright 2013 American Chemical Society.

The polymeric cross-linking species were designed to provide solubility in toluene which should result in steric stabilization of the nanocomposite superspheres. To prove that this concept had been successfully realized, nanocomposite samples were diluted with a non-solvent (in this case *iso*-propanol). After this manipulation of the environment of the nanocomposites, spherical assemblies agglomerated into chainlike structures, as evidenced by TEM (Figure 8).

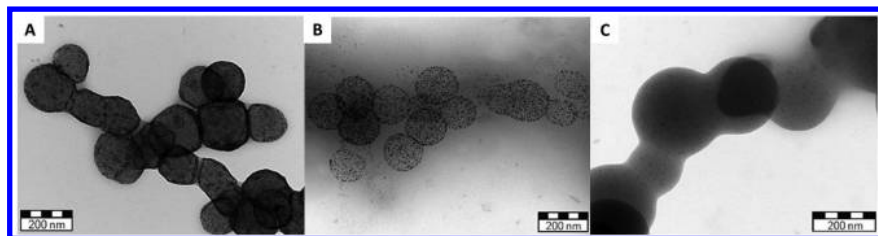


Figure 8. TEM images of chain-like agglomerates of spherical gold nanoparticle assemblies with varying degree of polymerization of the employed multiblock RAFT polymers.

This agglomeration was absent in the original colloidal solutions in toluene, indicating that the isolated spherical assemblies observed in toluene correspond to superstructures which are stabilized through solvent–polymer interactions.

3.2. The Preparation of Made-to-Order Planet-Satellite Nanostructures

Equipped with the knowledge gained from our studies that aimed at disclosing the binding motif of linear multifunctional RAFT polymers on two different types of nanoparticles (31, 32), we were able to go one step ahead and target the design of multicomponent nanoarchitectures (24). Such architectures can be achieved, when distinct domains are combined to form structured nanohybrids. A feasible approach is to use nanoparticles decorated with a polymer layer as scaffolds for the attachment of a second type of particles. For that purpose, the nanoparticle cores should remain isolated after being functionalized with a polymer. This behavior was observed, when gold nanocrystals from citrate-reduction were treated with multifunctional RAFT polymers, as presented above (31). We therefore intended to use this type of nanoparticles as core material of nanohybrids acting as scaffold structures. Linear RAFT polymers with multiple binding sites were however shown to wrap around these particles and are therefore not suited to provide binding sites exposed on the nanohybrid shell that enable the attachment of further particles. RAFT star polymers with such particle binding sites on their exterior might however lead to nanohybrids in which some of their arms do not bind to the particle surface for entropic reasons, maintaining conformational degrees of freedom.

To this end, four-arm star polymers of NiPAAM were prepared by RAFT polymerization using the R-star approach, and nanocomposites with particles from citrate-reduction were subsequently fabricated. These nanocomposites also arranged into hexagonal patterns after solvent evaporation on a solid substrate, which allowed for the evaluation of the thickness of their polymer shell from several TEM images. Representative images are shown in Figure 9.

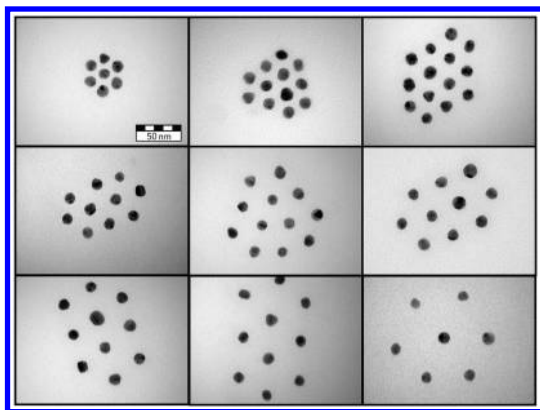


Figure 9. TEM images of self-assembled hexagonal patterns of gold cores in nanohybrid particles with RAFT star polymers of varying degree of polymerization (increasing from left to right and top to bottom). Adapted with permission from ref. (24). Copyright 2014 WILEY-VCH Verlag GmbH & Co. KGaA, Weinheim.

We intended to prove that these nanocomposites can be used as scaffolds for the formation of multicomponent nanoarchitectures. If binding sites for gold are exposed in the polymer shell of these nanohybrids, then addition of tetraoctylammonium-bromide capped Brust-Schiffirin particles should lead to the binding of these particles to the polymer layer. After Brust-Schiffirin particles had been added, linear conventional RAFT polymer of NⁱPAAM was introduced to the mixture in order to shield the hemispheres of the Brust-Schiffirin particles which are remote from the central core. The obtained multicomponent architectures are shown as exemplary images in Figure 10.

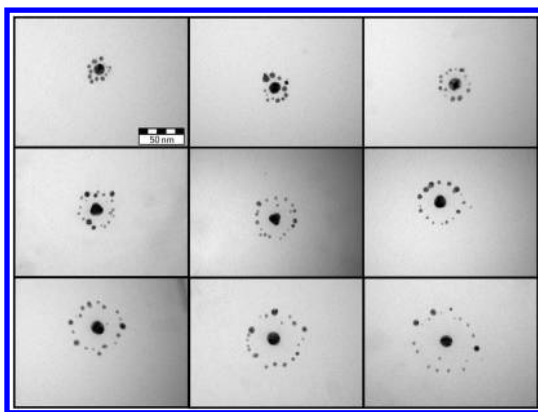


Figure 10. Planet-satellite nanostructures which are obtained from the functionalization of nanohybrid scaffolds (seen in Figure 9) with Brust-Schiffirin particles (length of the star polymers increasing from left to right and top to bottom). Adapted with permission from ref. (24). Copyright 2014 WILEY-VCH Verlag GmbH & Co. KGaA, Weinheim.

The formation of planet-satellite nanostructures results from this approach and the planet-satellite distance is a function of the molar mass of the star polymer employed. The planet-satellite distances can also be compared with edge-to-edge distances of gold cores in the hexagonal patterns shown in Figure 9. The interparticle distances in the self-assembled patterns of nanohybrid samples are always approximately two times larger than the corresponding planet-satellite distances (Figure 11). This shows that the smaller Brust-Schiffirin particles attach to the outside of the polymer layer covering the core gold nanocrystals from citrate-reduction.

4. Conclusion

RAFT polymers can be directly used as gold-nanoparticle coatings, as they inherently provide binding sites for gold. The binding of the RAFT group to gold enables high grafting densities and the formation of polymer brushes, also in grafting-to approaches.

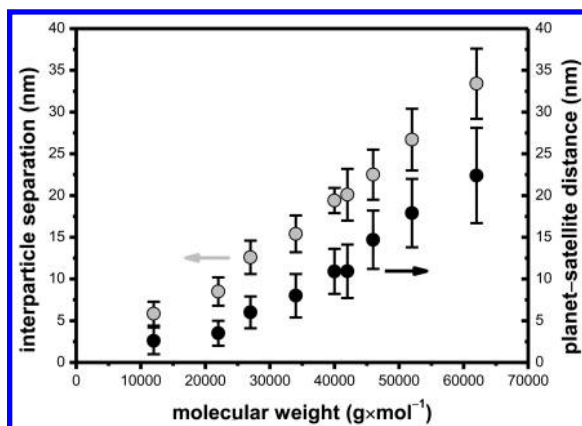


Figure 11. Interparticle distances in self-assembled hexagonal patterns of nanohybrid particles (gray circles, see Figure 9) and planet-satellite distances in the corresponding multicomponent nanostructures (black circles, see Figure 10). Reprinted with permission from ref. (24). Copyright 2014 WILEY-VCH Verlag GmbH & Co. KGaA, Weinheim.

The control over the distribution of RAFT groups among synthesized macromolecules by means of macromolecular design can lead to tailored nanocomposites. When particles from citrate-reduction are treated with multifunctional RAFT polymers, these macromolecules connect to the gold surface in a multidentate fashion, resulting in grafted polymer loops on this type of nanoparticles. In the case of nanoparticles from the two-phase Brust-Schiffrin synthesis, on the other hand, these macromolecules act as cross-linkers; the particle density in the resulting nanoparticle networks can be varied by employing polymers with different degree of polymerization. Also, RAFT star polymers can be used to interconnect different types of gold nanoparticles with defined distances, resulting in planet-satellite nanostructures.

The power of RAFT polymers to precisely arrange nanoparticles in different architectures was demonstrated for gold nanoparticles. It remains to be verified, if this concept can be extended to nanoparticles of different materials as well. This would certainly enhance the versatility and applicability of the approach. Further, this may lead to a unique combination of distinct material properties in multicomponent nanostructures with possible applications in material science.

References

- Balazs, A. C.; Emrick, T.; Russell, T. P. *Science* **2006**, *314*, 1107–1110.
- Garcia, M. A. *J. Phys. D: Appl. Phys.* **2012**, *45*, 389501.
- Karg, M.; Hellweg, T.; Mulvaney, P. *Adv. Funct. Mater.* **2011**, *21*, 4668–4676.
- Korgel, B. A.; Fullam, S.; Connolly, S.; Fitzmaurice, D. *J. Phys. Chem. B* **1998**, 8379–8388.

5. Zhang, S.; Leem, G.; Srisombat, L.-O.; Lee, T. R. *J. Am. Chem. Soc.* **2008**, *130*, 113–120.
6. Park, S. Y.; Lytton-Jean, A. K. R.; Lee, B.; Weigand, S.; Schatz, G. C.; Mirkin, C. A. *Nature* **2008**, *451*, 553–556.
7. Zhang, C.; Macfarlane, R. J.; Young, K. L.; Choi, C. H. J.; Hao, L.; Auyeung, E.; Liu, G.; Zhou, X.; Mirkin, C. A. *Nat. Mater.* **2013**, *12*, 741–746.
8. Schreiber, R.; Do, J.; Roller, E.-M.; Zhang, T.; Schüller, V. J.; Nickels, P. C.; Feldmann, J.; Liedl, T. *Nat. Nanotechnol.* **2014**, *9*, 74–78.
9. Kamps, A. C.; Sanchez-Gaytan, B. L.; Hickey, R. J.; Clarke, N.; Fryd, M.; Park, S.-J. *Langmuir* **2010**, *26*, 14345–14350.
10. Ulman, A. *Chem. Rev.* **1996**, *96*, 1533–1554.
11. Caragheorghopol, A.; Chechik, V. *Phys. Chem. Chem. Phys.* **2008**, *10*, 5029–5041.
12. Maye, M. M.; Lim, I.-I. S.; Luo, J.; Rab, Z.; Rabinovich, D.; Liu, T.; Zhong, C.-J. *J. Am. Chem. Soc.* **2005**, *127*, 1519–1529.
13. Sung, S.; Holmes, H.; Wainwright, L.; Toscani, A.; Stasiuk, G. J.; White, A. J. P.; Bell, J. D.; Wilton-Ely, J. D. E. T. *Inorg. Chem.* **2014**, *53*, 1989–2005.
14. Zhang, S.; Chandra, K. L.; Gorman, C. B. *J. Am. Chem. Soc.* **2007**, *6*, 4876–4877.
15. Duwez, A.-S.; Guillet, P.; Colard, C.; Gohy, J.-F.; Fustin, C.-A. *Macromolecules* **2006**, *39*, 2729–2731.
16. Fustin, C.-A.; Colard, C.; Filali, M.; Guillet, P.; Duwez, A.-S.; Meier, M. A. R.; Schubert, U. S.; Gohy, J.-F. *Langmuir* **2006**, *22*, 6690–6695.
17. Blakey, I.; Schiller, T. L.; Merican, Z.; Fredericks, P. M. *Langmuir* **2010**, *26*, 692–701.
18. Hong, J.; Wang, Q.; Fan, Z. *Macromol. Rapid Commun.* **2006**, *27*, 57–62.
19. Ebeling, B.; Vana, P. *Polymers* **2011**, *3*, 719–739.
20. You, Y.; Hong, C.; Pan, C. *Chem. Commun.* **2002**, 2800–2801.
21. Ebeling, B.; Eggers, M.; Vana, P. *Macromolecules* **2010**, *43*, 10283–10290.
22. Boal, A.; Ilhan, F.; DeRouchey, J.; Thurn-Albrecht, T.; Russell, T.; Rotello, V. *Nature* **2000**, *404*, 746–748.
23. Boschmann, D.; Vana, P. *Macromolecules* **2007**, *40*, 2683–2693.
24. Rossner, C.; Vana, P. *Angew. Chem., Int. Ed.* **2014**, *53*, 12639–12642.
25. Fröhlich, M. G.; Vana, P.; Zifferer, G. *Macromol. Theory Simul.* **2007**, *16*, 610–618.
26. Boschmann, D.; Mänz, M.; Pöppler, A.-C.; Sörensen, N.; Vana, P. *J. Polym. Sci., Part A: Polym. Chem.* **2008**, *46*, 7280–7286.
27. Dey, P.; Blakey, I.; Thurecht, K. J.; Fredericks, P. M. *Langmuir* **2013**, *29*, 525–533.
28. Dey, P.; Blakey, I.; Thurecht, K. J.; Fredericks, P. M. *Langmuir* **2014**, *30*, 2249–2258.
29. Dey, P.; Zhu, S.; Thurecht, K. J.; Fredericks, P. M.; Blakey, I. *J. Mater. Chem. B* **2014**, *2*, 2827–2837.
30. Hussain, I.; Brust, M.; Barauskas, J.; Cooper, A. I. *Langmuir* **2009**, *25*, 1934–1939.
31. Ebeling, B.; Vana, P. *Macromolecules* **2013**, *46*, 4862–4871.

32. Rossner, C.; Ebeling, B.; Vana, P. *ACS Macro Lett.* **2013**, *2*, 1073–1076.
33. Turkevich, J.; Stevenson, P. C.; Hillier, J. *Discuss. Faraday Soc.* **1951**, *11*, 55–75.
34. Rotzoll, R.; Vana, P. *J. Polym. Sci., Part A: Polym. Chem.* **2008**, *46*, 7656–7666.
35. Fink, J.; Kiely, C. J.; Bethell, D.; Schiffrin, D. J. *Chem. Mater.* **1998**, *10*, 922–926.
36. Zhou, J.; Beattie, D. A.; Sedev, R.; Ralston, J. *Langmuir* **2007**, *23*, 9170–9177.
37. Siau, M.; Hawke, B. S.; Perrier, S. *J. Polym., Part A: Polym. Chem.* **2012**, *50*, 187–198.
38. Lin, G.; Wang, Y.; Zhang, Q.; Zhang, X.; Ji, G.; Ba, L. *Nanoscale* **2011**, *3*, 4567–4570.

Chapter 19

Synthesis of Complexing Copolymers by RAFT and Their Use in Emulsion Polymerization To Prepare CeO₂/Polymer Hybrid Latexes

Jérôme Warnant,¹ Jérôme Garnier,^{1,2} Alex Van Herk,²
Pierre-Emmanuel Dufils,³ Jérôme Vinas,⁴
and Patrick Lacroix-Desmazes^{1,*}

¹Institut Charles Gerhardt (ICG), UMR5253 CNRS/ENSCM/UM, Ingénierie et Architectures Macromoléculaires (IAM), Ecole Nationale Supérieure de Chimie de Montpellier, 8 rue de l'École Normale, 34296 Montpellier Cedex 5, France

²Polymer Reaction Engineering Group, Eindhoven University of Technology, P.O. Box 513, 5600 MB Eindhoven, The Netherlands

³High Barrier Polymers, Solvay Specialty Polymers, Avenue de la République, 39500 Tavaux, France

⁴High Barrier Polymers, Solvay Specialty Polymers, Solvay Campus, Rue de Ransbeek 310, B-1120 Brussels, Belgium

*E-mail: patrick.lacroix-desmazes@enscm.fr

Water-soluble oligomers bearing complexing groups have been synthesized by RAFT copolymerization using various combinations of monomers such as butyl acrylate or styrene as hydrophobic monomers and acrylic acid and/or 2-acrylamido-2-methyl propane sulfonic acid or vinyl benzyl phosphonic diacid as functional hydrophilic ionogenic monomers. Then, these oligo RAFT agents have been used to modify aqueous dispersions of CeO₂ nanoparticles. The adsorption of the oligomers at the surface of the CeO₂ nanoparticles has been characterized by several complementary techniques such as UV-vis spectroscopy, taking advantage of the chromophore RAFT moiety. Finally, the modified CeO₂ nanoparticles have been involved in seeded emulsion copolymerization of styrene/methyl acrylate or vinylidene chloride/methyl acrylate. This strategy led to a very efficient

formation of CeO₂/polymer hybrid latexes, as evidenced by cryo-TEM microscopy. The correlation between the morphology of the hybrid latex particles and the composition of the oligo RAFT agents allowed us to propose mechanisms for the growth of the polymer particles. Such hybrid latexes may find applications in many areas, for instance in the elaboration of high performance nanocomposite coatings but also as templates for the preparation of functional organic or inorganic porous materials with CeO₂ or other nanoparticles evenly distributed in the porous matrix.

Introduction

Hybrid inorganic/organic latexes are of great interest for the development of innovative materials (1). In this study, we were interested in cerium oxide nanoparticles which are increasingly considered for their multiple properties in catalysis, UV-filtering and so on (2).

The preparation of hybrid inorganic/organic latexes usually requires to modify the inorganic surface in order to favor its affinity for the polymer latex. The strategy that we have been using relies on the adsorption of functional amphiphilic copolymers on the surface of the ceria nanoparticles, followed by emulsion polymerization. This strategy was recently reported by several groups (3–6). Thus, we have synthesized different water-soluble amphiphilic complexing RAFT macro-agents containing carboxylic acid, sulfonic acid or phosphonic acid groups. The interactions of these functional copolymers with the ceria nanoparticles in water have been studied by several techniques. Then, the modified ceria nanoparticles have been involved in seeded emulsion copolymerization of styrene and methyl acrylate. The correlation between the morphology of the hybrid latex particles and the composition of the RAFT oligomers allowed us to propose mechanisms for the growth of the polymer particles. Finally, this strategy was applied to the synthesis of hybrid latexes based on vinylidene chloride. Copolymers based on vinylidene chloride offer interesting performances such as a good resistance to a wide variety of solvents and an extremely low gas permeability to water vapor and oxygen (7). So, this work ultimately aims at synthesizing CeO₂/PVDC film-forming hybrid latexes to prepare transparent films with enhanced UV stability.

Experimental

Materials

Butyl acrylate (BA, Aldrich, >99%), acrylic acid (AA, Aldrich, 99%), styrene (St, Aldrich, >99%), methyl acrylate (MA, Aldrich, 99%) vinylidene chloride (VDC, Aldrich, 99%), 1,4-dioxane (Merck), dimethyl sulfoxide (DMSO, Carlo Erba) and α,α,α -trifluorotoluene (TFT, Aldrich, anhydrous 99%) were purified through inhibitor removing columns or by distillation under reduced pressure. 2-Acrylamido-2-methyl propane sulfonic acid (AMPS,

Aldrich, 99%), sodium hydride (NaH, 60% dispersion in mineral oil, Aldrich), sodium iodide (NaI, Carlo Erba Reactifs – SDS, 99%), diethyl phosphite (Fluka, >99%), vinyl benzyl chloride (mixture of meta and para isomers, Acros, 96%), silica (Carlo Erba Reactifs – SDS, 35–70 mm), trimethylsilyl bromide (TMSBr, Aldrich >97%), methanol (MeOH, Aldrich, >99.8%), hydrochloric acid (HCl, 1 M, Carlo Erba), sodium hydroxide solution (NaOH, 0.1 and 1 M, Carlo Erba), sodium pyrophosphate (TSPP, Alfa Aesar, 98%), powder of celite 545 (Carlo Erba Reactifs – SDS), sodium dodecylbenzene sulfonate (SDBS, Aldrich, 96%) acetic acid (Sigma-Aldrich, >99%), and 2,2'-azobis[N-(2-carboxyethyl)-2-methylpropionamidine] hydrate (VA-057, Wako) were used as received. 2,2'-Azobis(2-methylpropionitrile) (AIBN, Aldrich, 98%) was purified by recrystallization in methanol. Water was deionized through an ion-exchange resin (conductivity below 1 $\mu\text{S}/\text{cm}$). The commercial cerium oxide aqueous dispersion (Nanobyk-3810, 18 wt%, Byk Chemie) was dialyzed 4 times against deionized water employing Spectra/por 6 dialysis membranes (Spectrum Laboratories, MWCO 1000). The CeO_2 content of the dispersion after dialysis ranged from 10.9 to 12.3 wt%. The transfer agent, dibenzyltrithiocarbonate (DBTTC), and the phosphonated monomer, vinyl benzyl phosphonic acid diethylester (VBPDE), were synthesized according to procedures already reported (8–10).

Synthesis of the RAFT Oligomers

The oligomers were synthesized by RAFT polymerization as described elsewhere (8–10). Thus poly(BA-*co*-AA) was synthesized in 1,4-dioxane at 70°C with $[\text{DBTTC}]/[\text{AIBN}]=11$. Poly(BA-*co*-AMPS) and poly(BA-*co*-AA-*co*-AMPS) were synthesized in DMSO at 70°C with $[\text{DBTTC}]/[\text{AIBN}]=3.3$. Poly(St-*co*-VBPDE) was synthesized in trifluorotoluene at 75°C with $[\text{DBTTC}]/[\text{AIBN}]=3.3$.

Emulsion Copolymerization of Styrene and Methyl Acrylate in the Presence of Ceria Nanoparticles and RAFT Oligomers

Emulsion copolymerization of styrene and methyl acrylate was carried out in the presence of amphiphatic RAFT oligomers and cerium oxide nanoparticles according to the following procedure. The initial load containing the dialyzed cerium oxide aqueous dispersion and the RAFT oligomer diluted in deionized water, a mixture of the monomers (styrene and methyl acrylate in a 90:10 mass ratio) and an aqueous initiator solution (VA-057, 4 g/L) were bubbled separately with argon during 30 min. The initial load was introduced in a 3-neck 250 mL double-walled reactor equipped with a condenser and maintained under argon atmosphere. Continuous stirring of the medium at 250 rpm was ensured by a 6-bladed stainless steel turbine impeller, and the temperature in the reactor was controlled with a continuous flow of thermostated water delivered by a MGW Lauda M3 circulating water bath. Once the reactor had reached the temperature of 60°C, a pulse of 10 mL of the initiator solution was injected into the reaction medium and the monomer feed via a Dosimat 765 dosing pump (Metrohm) was

started and maintained for 4 h at a rate of 42 $\mu\text{L}/\text{min}$ (the emulsion polymerization process actually did not follow starved conditions and a retardation effect was noticed). Afterwards, the reactor was maintained at reaction temperature for an additional 2 h.

Emulsion Copolymerization of Vinylidene Chloride and Methyl Acrylate in the Presence of Ceria Nanoparticles and RAFT Oligomers

The emulsion copolymerization of vinylidene chloride and methyl acrylate (90:10 mass ratio) was carried out in the presence of RAFT oligomers adsorbed on the surface of cerium oxide nanoparticles according to the following typical procedure. The initial load containing the cerium oxide aqueous dispersion (14.19 g) and the poly($\text{St}_5\text{-co-VBPDA}_{12}$) RAFT oligomer (0.781 g) diluted in deionized water (95.9 g), a pre-emulsion of monomers (35.10 g of vinylidene chloride and 3.90 g of methyl acrylate, 21.50 g of water, 3.90 g of tetrasodium pyrophosphate (TSPP), 0.016 g of sodium dodecyl benzene sulfonate (SDBS)) and an initiator aqueous solution (VA-057 in water) were bubbled separately with argon for 30 min. The reaction was performed in a 300 mL stainless steel reactor (Parr Instrument Company), equipped with a stainless steel pitched blade impeller and internal pressure and temperature sensors. Oxygen was removed from the autoclave under vacuum (10^{-2} mbar). After charging the initial load with vacuum, a 3 bars nitrogen overpressure was then established in the vessel. The agitation speed was set at 250 rpm and the temperature was raised to 60°C. Using a Series III digital HPLC pump (LabAlliance), a volume of 10 mL of VA-057 initiator solution (20 g L^{-1}) was first pumped into the reactor at a rate of 4 mL min^{-1} , then a stirred pre-emulsion containing TSPP, water, SDBS, vinylidene chloride and methyl acrylate was continuously pumped into the reactor at a rate of 10.8 mL h^{-1} for 5 h. The overall reaction lasted for 6 h. The residual monomer was stripped by heating up the latex for 1 h at 60°C under reduced pressure (500 mbar).

Analyses

^1H NMR and ^{31}P NMR analyses were performed at room temperature on a Bruker 400 ultra-shield spectrometer.

SEC with DMF as eluent, calibrated with poly(methyl methacrylate) standards from Polymer Laboratories, was run with a Varian Prostar (model 210) pump at a flow rate of 0.8 mL min^{-1} using two 300 mm long, mixed-D PL-gel 5 μm columns (molecular weight range: 2×10^2 – 4×10^5 g mol^{-1} from Polymer Laboratories) thermostated at 70°C, connected to a Shodex (model RI-101) refractometer detector. Carboxylic acid AA and sulfonic acid AMPS monomer units of the copolymers were protected (reaction with trimethoxysilyl diazomethane) prior to SEC analyses. Styrenic copolymers poly(St-co-VBPDE) and vinylidene chloride copolymers poly(VDC-co-MA) were characterized with a similar equipment in THF at 1 mL min^{-1} and 35°C with polystyrene calibration ($K=14.1 \times 10^{-5}$ dL g^{-1} and $\alpha=0.7$). Mark–Houwink coefficients determined by Revillon (11) for poly(VDC-co-MA) copolymers with a 80:20 VDC:MA mass ratio were employed to exploit the data ($K=35 \times 10^{-5}$ dL g^{-1} and $\alpha=0.57$).

UV-visible spectrometric measurements were performed on Agilent 8453 and Varian Cary50 spectrometers.

Dynamic light scattering analyses were performed on a Zetasizer Nano ZS particle size analyzer (from Malvern) and on a VASCO-3 particle size analyzer (from Cordouan technologies).

CryoTEM pictures were obtained using an FEI Tecnai 20, Sphera TEM microscope (LaB 6 filament, operating voltage of 200 kV).

Results and Discussion

Synthesis of the RAFT Oligomers

We have synthesized amphiphilic copolymers by controlled radical copolymerization. The RAFT technique was used in order to control the molecular weight and the molecular weight distribution of the copolymers. Four types of copolymers were synthesized using butyl acrylate or styrene as hydrophobic monomers and AA or AMPS or a phosphonic styrenic derivative VBPDA as hydrophilic monomer units (Figure 1): poly(BA-co-AA), poly(BA-co-AMPS), poly(BA-co-AA-co-AMPS) and poly(St-co-VBPDA).

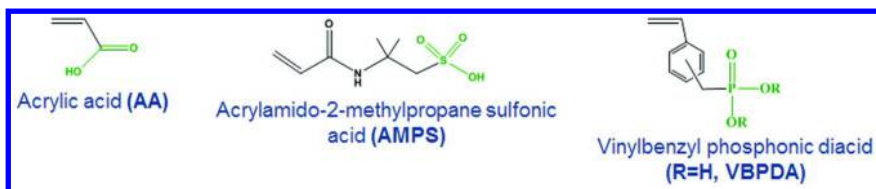


Figure 1. Structures of the hydrophilic monomer units incorporated in the RAFT oligomers.

For instance, in the case of butyl acrylate and acrylic acid, the copolymerization was performed in dioxane at 70°C using dibenzyl trithiocarbonate as the RAFT control agent (Figure 2). Low molecular weight copolymers were synthesized with a very good yield, higher than 95%. We obtained a good agreement between theoretical molecular weight $M_{n,th}$ and experimental molecular weights $M_{n,NMR}$ and the dispersity was low (Table 1). Although the molecular weights determined by SEC $M_{n,SEC}$ did not match theoretical values (as they were calculated against PMMA standards), the comparison of $M_{n,th}$ and $M_{n,SEC}$ results followed a coherent trend. When AMPS was used as comonomer, the copolymerizations were performed in similar conditions except that DMSO was used as solvent instead of dioxane.

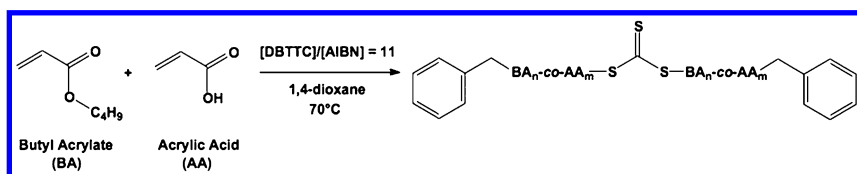


Figure 2. Synthesis of poly(BA-co-AA) RAFT oligomers.

Table 1. Characteristics of acrylic oligomers synthesized by RAFT polymerization^a

Targeted composition	X_{BA} (%)	X_{AA} (%)	X_{AMPS} (%)	$M_{n, th}$ (g.mol ⁻¹)	$M_{n, NMR}$ (g.mol ⁻¹)	Experimental composition (¹ H NMR)	$M_{n, SEC}$ (g.mol ⁻¹)	M_w/M_n
Poly(BA ₅ -co-AA ₅)	95.8	96.4	–	1260	1300	Poly(BA _{4.8} -co-AA _{4.9})	1570	1.28
Poly(BA ₅ -co-AMPS ₅)	97.8	–	76.2	1690	1750	Poly(BA _{4.9} -co-AMPS _{3.8})	2550	1.30
Poly(BA ₅ -co-AA ₅ -co-AMPS ₄)	99.3	97.5	88.2	2010	2110	Poly(BA _{5.0} -co-AA _{4.9} -co-AMPS _{3.6})	3350	1.23

^a X: monomer conversion; $M_{n, th}$: theoretical M_n ; $M_{n, NMR}$: molecular weight determined by ¹H NMR; $M_{n, SEC}$: molecular weight determined by size exclusion chromatography.

The phosphonated copolymer was synthesized in two steps: firstly, a RAFT copolymerization of styrene and VBPDE was performed, and secondly, a cleavage of the phosphoester groups was carried out to obtain the copolymer with phosphonic diacid units poly(St₅-co-VBPDA₁₂) ($M_{n, NMR}$ =3200 g.mol⁻¹) (Figure 3).

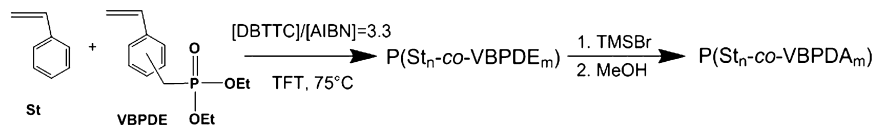


Figure 3. Synthesis of the poly(St-co-VBPDA) RAFT oligomers.

The kinetics of copolymerization were studied by ¹H NMR. The RAFT oligomer poly(AA-co-BA) was found to be a random copolymer without significant composition drift along the copolymer chain (Figure 4). This is consistent with the literature data (reactivity ratio r_{BA} =0.91 and r_{AA} =1.31) (3, 12). Random copolymers have a lower tendency to form micelles than block copolymers. Micelles were not desired in our case because it would favor secondary nucleation at the expense of the formation of hybrid particles. In the case of the copolymerization of BA and AMPS, BA reacted slightly faster than AMPS as expected from the literature data for a similar acrylamide monomer (reactivity ratio r_{BA} =0.8 and $r_{N-propyl\ acrylamide}$ =0.4) (13). Therefore, the copolymer had a gradient structure enriched in BA at the beginning of the chain (note that because we were using a trithiocarbonate RAFT agent, the copolymer had actually two branches linked by the trithiocarbonate group inside the chain). In addition, in this case, the final conversion of AMPS was limited. Therefore, the final copolymer was dialyzed in water to remove the residual AMPS monomer. The kinetics of terpolymerization of BA, AA and AMPS was not carried out, but based on the previous copolymerization experiments we may reasonably assume

that the polymer chains display a gradient structure with butyl acrylate/acrylic acid rich tails and AMPS rich center.

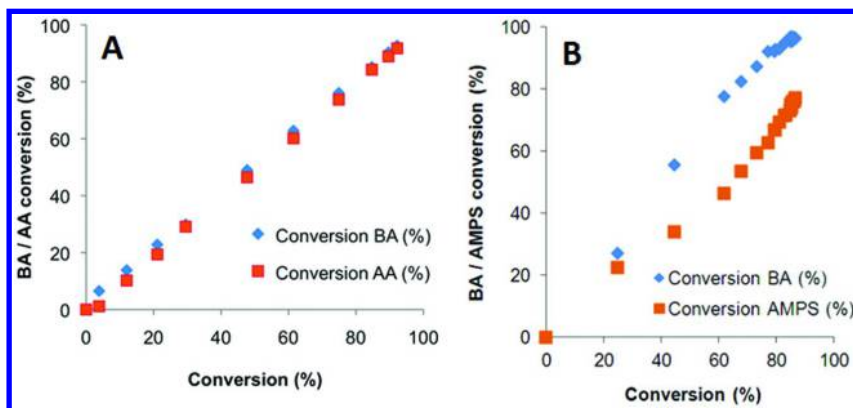


Figure 4. Kinetics of RAFT copolymerization for targeted poly(BA_5 -co- AA_5) (A) and poly(BA_5 -co- $AMPS_5$) (B) copolymers.

In the case of the copolymerization of the styrenic monomers, styrene reacted slightly faster than VBPDE (meta and para isomers), leading to a gradient copolymer (Figure 5).

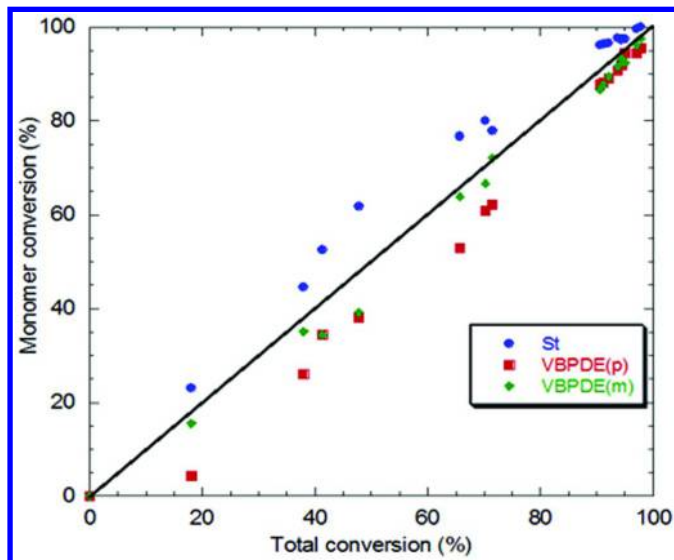


Figure 5. Kinetics of RAFT copolymerization for a targeted poly(St_5 -co- $VBPDE_{10}$) copolymer.

The structure of the poly(BA -co- AA) RAFT oligomer was also checked by mass spectrometry (MALDI-TOF). The peaks could be assigned to confirm the expected structure of the copolymer (9). In other words, the polymer chains

were dormant chains and they could be reactivated in a radical polymerization. Furthermore, this trithiocarbonate group will be useful as a chromophore probe in UV studies.

Adsorption of the RAFT Oligomers on the Ceria Nanoparticles

The ceria nanoparticles were constituted of clusters of 3 to 4 crystallites of about 3 nm size. The electrophoretic mobility of the ceria nanoparticles was found to increase (in absolute value), from $-2 \mu\text{m}\cdot\text{cm}/\text{V}\cdot\text{s}$ in the absence of copolymer to about $-8 \mu\text{m}\cdot\text{cm}/\text{V}\cdot\text{s}$ in the presence of the poly(BA-co-AA) RAFT oligomer. Furthermore, no significant variation of the particles hydrodynamic diameter ($D_{\text{CeO}_2} = 8 \pm 2 \text{ nm}$) could be noticed by light scattering after addition of the copolymer. Thus, the RAFT oligomer seemed to be adsorbed at the surface of the nanoparticles without causing colloidal stability issues.

The adsorption was further confirmed by UV-vis analyses of the serum at $\lambda=308 \text{ nm}$ (absorption peak of the chromophore trithiocarbonate group of the RAFT oligomers) after centrifugation. Figure 6 shows the concentration of the copolymer in the serum versus the concentration of the copolymer in the recipe. For poly(BA-co-AA) oligomer, about half of the copolymers was in the serum, thus the other half was adsorbed on the surface of the nanoparticles. The first objective was reached: the ceria nanoparticles have been functionalized without loss of colloidal stability. On the contrary, the same UV analysis with poly(BA-co-AMPS) revealed a very weak adsorption of this copolymer at the surface of the nanoparticles (less than 10% copolymer was adsorbed). So, these two copolymers behaved very differently in the presence of the ceria nanoparticles

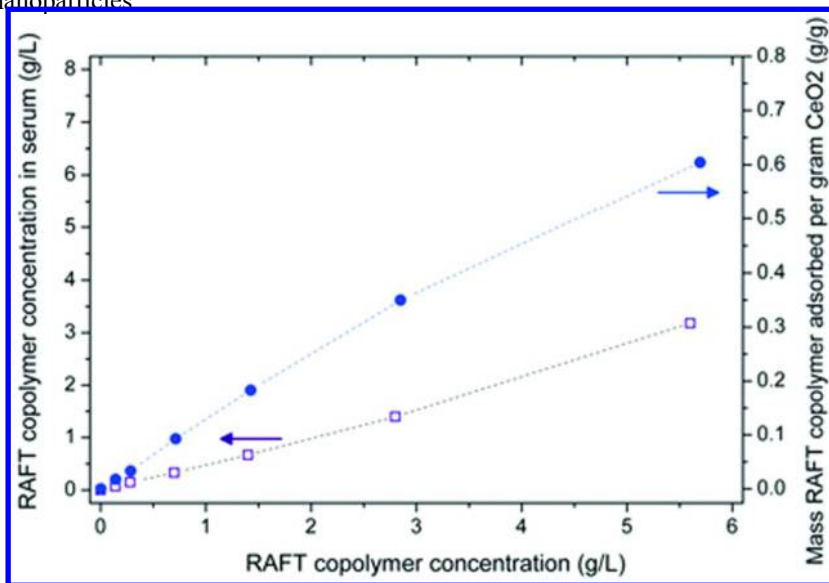


Figure 6. Adsorption of poly(BA_{4.8}-co-AA_{4.9}) RAFT oligomers at the surface of CeO₂ nanoparticles evidenced by UV-vis spectrometry.

In the case of the phosphonated copolymer, the adsorption of the copolymer was investigated by a combination of UV-vis spectroscopy and ^{31}P NMR. By this way, we could not only track the chains (by UV) but also we could track the phosphonic acid units involved in the complexation (Figure 7). Thus, after centrifugation, the average number of chains adsorbed for one nanoparticle of cerium was determined by UV analysis of the serum: up to about 100 copolymer chains could be adsorbed per CeO_2 nanoparticle. By ^{31}P NMR, without centrifugation, the attenuation of NMR signal was allocated to the reduction of the mobility of the corresponding phosphorus group complexed onto the surface of ceria nanoparticles. From this analysis, the average number of phosphonated units adsorbed for one ceria nanoparticle was determined: up to about 500 phosphonate units were adsorbed per CeO_2 nanoparticle. By combining the two previous results, we could then calculate, for the adsorbed copolymer chains, the average number of complexing groups involved in the interaction with the ceria nanoparticles (Figure 8). In this case, at low concentration of the copolymer, nine over twelve units of poly($\text{St}_5\text{-co-VBPDA}_{12}$) were involved the complexation. Thus, at low concentration, most of the copolymer chains were adsorbed and most of the phosphonic groups were in interaction with the nanoparticles. At higher concentration, the surface became crowded, and a lower fraction of the phosphonic groups of the newly adsorbed chains was able to reach the surface. Interestingly, the maximum adsorption value of phosphonates obtained here (expressed as the molar ratio between the complexing agent and cerium $N_{\text{VBPDA}}/N_{\text{Ce}}=0.17$) was very consistent with the data reported in the literature and determined by different analytical techniques (thermogravimetric and chemical analyses) (14) (Figure 8).

In summary, these two UV and ^{31}P NMR spectroscopy techniques appeared complementary to better understand how the RAFT oligomers were adsorbed at the surface of the ceria nanoparticles.

Synthesis of Hybrid Latexes CeO_2 /Poly(styrene-*co*-methyl acrylate)

The modified ceria nanoparticles have been involved in seeded emulsion copolymerization of styrene and methyl acrylate. The emulsion copolymerization was performed with a concentration of ceria nanoparticles of 4wt% versus monomers. The polymerization (solid content 12wt%) was initiated at 60°C by a zwitterionic azo initiator (VA-057) (Figure 9) with a molar ratio $[\text{VA-057}]/[\text{RAFT oligomer}]$ close to unity. Results are summarized in Table 2. For instance, when the ceria nanoparticles were modified by the poly(BA-*co*-AA) RAFT oligomer, the monomer conversion was high, close to 90% and stable latexes were obtained. The latex diameter was lower than 100nm. From the number of ceria nanoparticles and the number of latex particles, we can expect to find several ceria nanoparticles per latex particle. The different RAFT oligomers were tested and stable latexes were obtained in all cases.

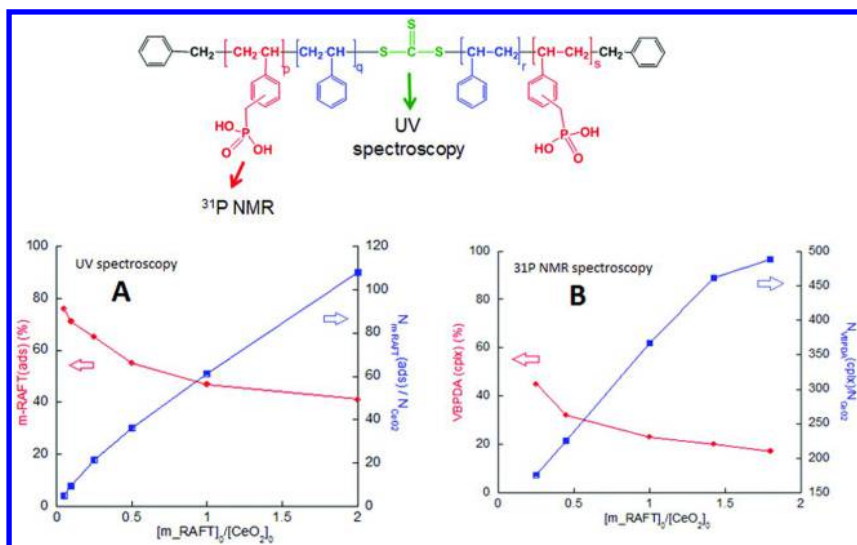


Figure 7. Adsorption of poly(St_5 -co-VBPDA $_{12}$) RAFT oligomers at the surface of CeO_2 nanoparticles evidenced by UV-vis spectrometry ($[m_RAFT]_0/[CeO_2]_0$: copolymer/ CeO_2 weight concentration ratio before centrifugation; $m_RAFT(ads) (%)$: percentage of copolymer chains adsorbed at the surface of CeO_2 nanoparticles; $N_{mRAFT(ads)}/N_{CeO_2}$: average number of copolymer chains adsorbed per CeO_2 nanoparticle) (A) and VBPDA complexation evidenced by ^{31}P NMR ($VBPDA(cplx) (%)$: percentage of complexed VBPDA units; $N_{VBPDA(cplx)}/N_{CeO_2}$: average number of VBPDA monomer units complexed at the surface of one CeO_2 nanoparticle) (B).

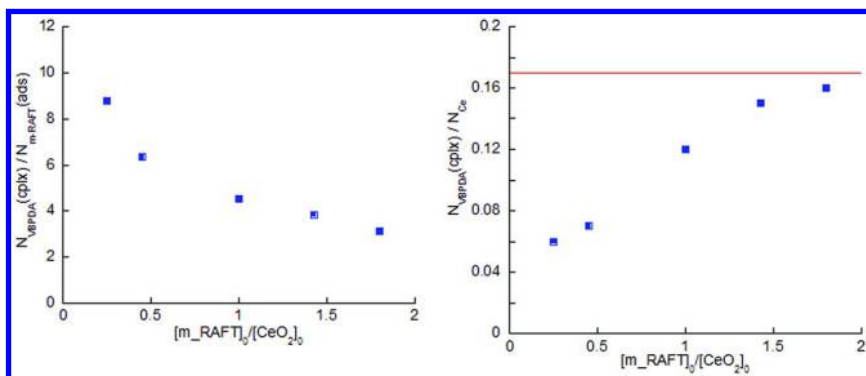


Figure 8. Combination of UV-vis spectroscopy and ^{31}P NMR to characterize the adsorption of poly(St_5 -co-VBPDA $_{12}$) RAFT oligomers at the surface of CeO_2 nanoparticles: average number of complexed VBPDA units per poly(St_5 -co-VBPDA $_{12}$) chain adsorbed at the surface of CeO_2 nanoparticles (left) and the number of VBPDA units complexed at the surface of CeO_2 nanoparticles per cerium atom (right) versus the copolymer/ CeO_2 weight concentration ratio.

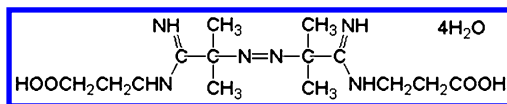


Figure 9. Structure of the azo-initiator (VA-057) used in seeded emulsion copolymerization of styrene/methyl acrylate or vinylidene chloride/methyl acrylate.

Table 2. Seeded emulsion copolymerization of styrene and methyl acrylate with CeO₂ nanoparticles in the presence of acrylic RAFT oligomers^a

RAFT oligomer composition	X_M (%)	D_P (nm)	Dispersity	$N_{CeO_2}^o$ ($\times 10^{-16}$)	N_P^f ($\times 10^{-16}$)	$N_{CeO_2}^o / N_P^f$
Poly(BA _{4.8-co} -AA _{4.9})	86.2	83	0.21	20	2.5	8.1
Poly(BA _{4.9-co} -AMPS _{3.8})	75.4	50	0.25	12	6	2.0
Poly(BA _{5.0-co} -AA _{4.9-co} -AMPS _{3.6})	84.3	48	0.19	13	8.1	1.6

^a X_M : global monomer conversion; D_P : particle diameter by light scattering; Dispersity: dispersity index of particle size by light scattering; $N_{CeO_2}^o$: initial number of CeO₂ nanoparticles; N_P^f : final number of latex particles.

Cryo-TEM was found to be necessary to avoid possible artifacts (such as heteroflocculation). Figure 10 gives an overview of the cryo-TEM results for the three types of acrylic RAFT oligomers. By using poly(BA-*co*-AA) RAFT oligomers, some hybrid latexes were indeed obtained, with a few ceria nanoparticles per latex particle. More importantly, the ceria nanoparticles did not aggregate during the polymerization. Furthermore, only hybrid latexes were formed. There was no free ceria nanoparticle in the aqueous phase. In contrast, when using the poly(BA-*co*-AMPS) RAFT oligomer, the resulting product was composed almost exclusively of free ceria nanoparticles and free polymer latex particles. Therefore, in that case, there was no formation of a hybrid latex. Finally, the poly(BA-*co*-AA-*co*-AMPS) RAFT oligomer containing both carboxylic acid and sulfonic acid groups was tested. In that case, an hybrid latex was formed containing almost exclusively only one CeO₂ nanoparticle per latex particle. Therefore, according to the composition of the RAFT oligomer, extremely different types of latexes were formed: sulfonic acid copolymers failed to produce hybrid latexes whereas carboxylic acid copolymers were able to form very efficiently hybrid latexes. Using the two functional groups together led to hybrid particles with only one CeO₂ nanoparticle per latex particle. To explain these results, we have tried to correlate the mechanism of latex formation with the composition of the RAFT oligomers.

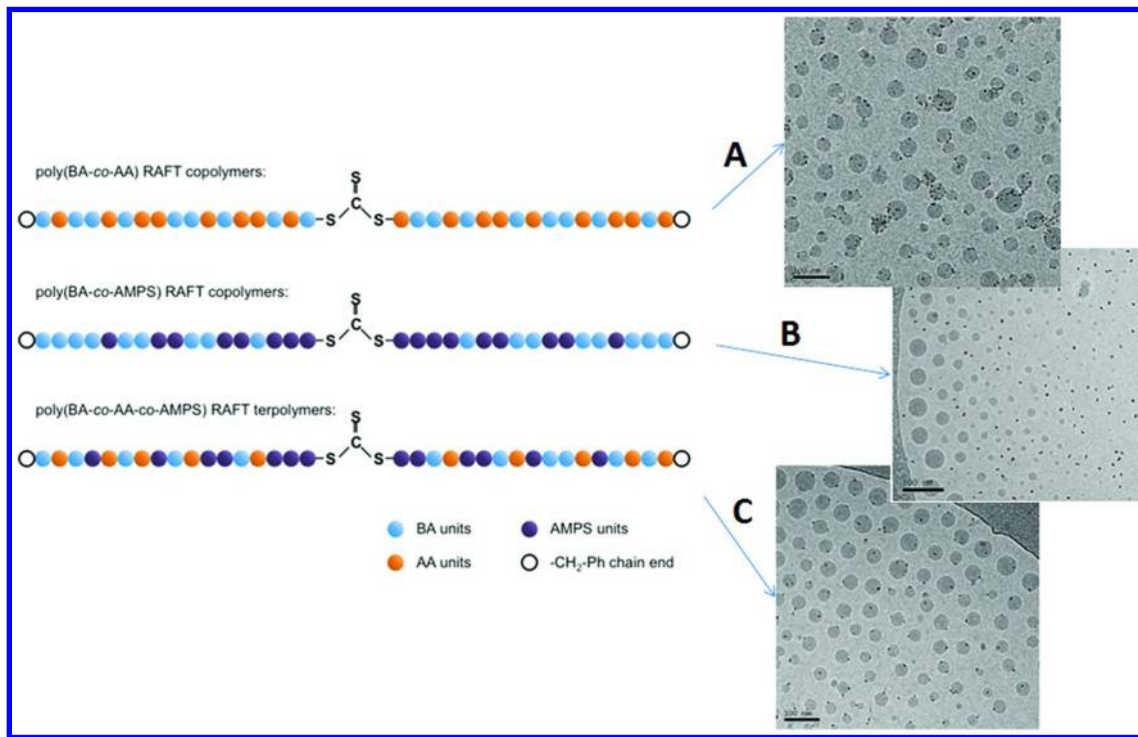


Figure 10. Schematic structures of the RAFT oligomers and cryo-TEM pictures of the resulting latexes obtained by seeded emulsion copolymerization of styrene/methyl acrylate in the presence of CeO₂ nanoparticles (4wt%) with poly(BA_{4.8}-co-AA_{4.9}) (A), poly(BA_{4.9}-co-AMPS_{3.8}) (B) and poly(BA_{5.0}-co-AA_{4.9}-co-AMPS_{3.6}) (C).

Our tentative explanation of the results is the following. In the case of the RAFT oligomers with carboxylic acid groups, poly(BA-co-AA), the copolymers were rather strongly adsorbed on the ceria nanoparticles. Some small growing hybrid particles were formed, but their colloidal stability was limited because AA was involved in the interaction with the ceria nanoparticles. Thus, some of these hybrid particles aggregated, leading to latex particles with several ceria nanoparticles per latex particle (Figure 11). Interestingly, a RAFT oligomer of higher molecular weight, poly(BA_{7.3}-co-AA_{9.8}), led to smaller particles ($D_p=56$ nm) with fewer ceria nanoparticles per latex particle ($N^{\circ}_{CeO_2}/N^{\circ}_P=2.3$), presumably due to a better colloidal stability of the small growing hybrid particles (9).

In the case of the RAFT oligomers with sulfonic acid groups, poly(BA-co-AMPS), the oligomers were not adsorbed to the ceria nanoparticles. Thus, homogeneous nucleation was favored, leading to latex particles next to free ceria nanoparticles in the aqueous phase (Figure 12).

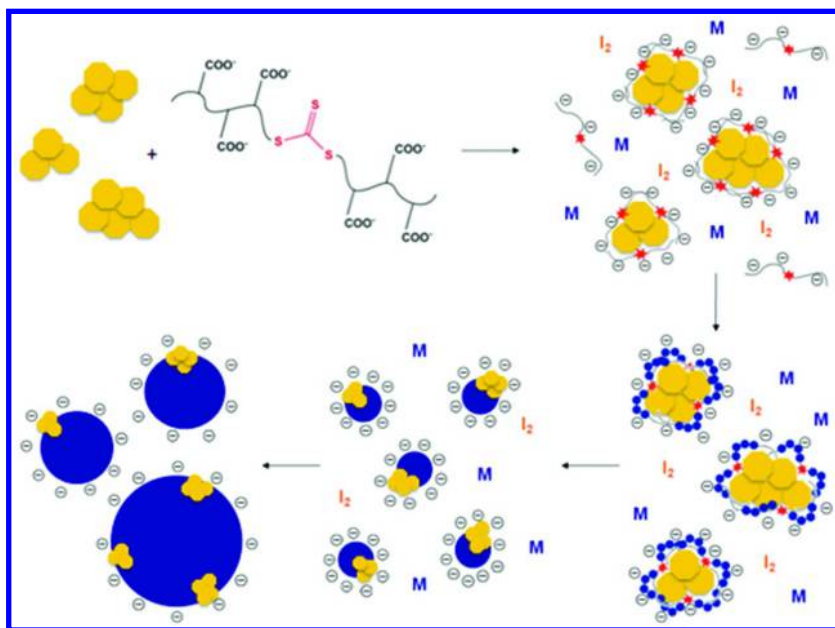


Figure 11. Mechanism of particle formation in emulsion copolymerization carried out in the presence of ceria nanoparticles and poly(BA-co-AA) RAFT oligomers.

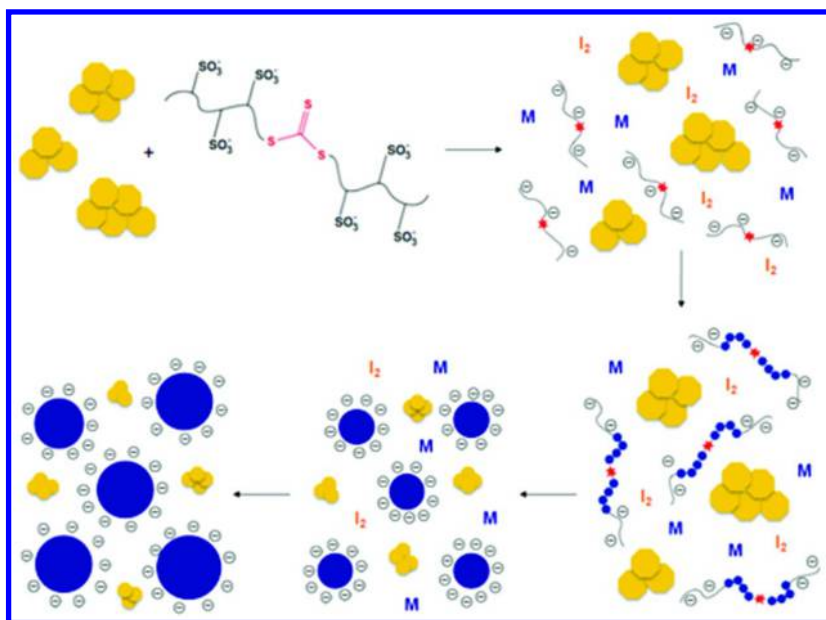


Figure 12. Mechanism of particle formation in emulsion copolymerization carried out in the presence of ceria nanoparticles and poly(BA-co-AMPS) RAFT oligomers.

Finally, in the case of the RAFT oligomer bearing both carboxylic acid and sulfonic acid groups, poly(BA-co-AA-co-AMPS), homogeneous nucleation could occur because the RAFT oligomers were mainly free in the serum. However, because of the affinity of the AA units towards ceria nanoparticles, the growing polymer chains could interact with the ceria nanoparticles, leading to hybrid particles. In addition, the sulfonic acid groups of the copolymers could impart electrostatic stabilization, so these hybrid particles could grow without loss of colloidal stability. Therefore, there was no aggregation and this was the reason why the hybrid particles contained only one CeO₂ nanoparticle per latex particle (Figure 13).

Synthesis of Hybrid Latexes CeO₂/Poly(vinylidene chloride-co-methyl acrylate) and Film Formation

The concept developed above was then applied to the emulsion copolymerization of vinylidene chloride and methyl acrylate (15). Figure 14 shows the results using the poly(BA-co-AA) and poly(St-co-VBPDA) RAFT oligomers to modify the ceria nanoparticles before performing the seeded emulsion copolymerization. In both cases, hybrid latexes were obtained with no free ceria nanoparticles in the aqueous phase, and the ceria nanoparticles did not aggregate during the polymerization.

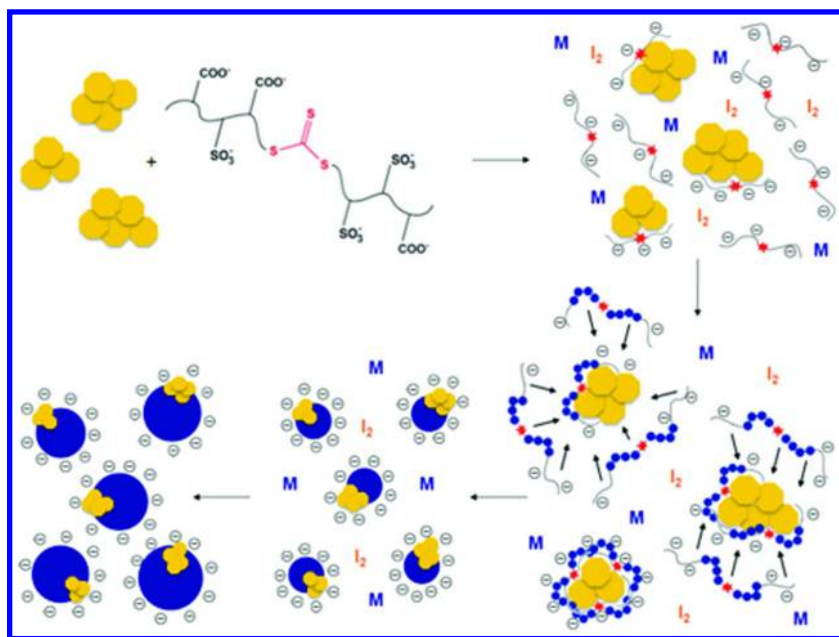


Figure 13. Mechanism of particle formation in emulsion copolymerization carried out in the presence of ceria nanoparticles and poly(BA-co-AA-co-AMPS) RAFT oligomers.

In these experiments, the molar ratio [VA-057]/[RAFT oligomer] was close to unity which is a rather high ratio if we consider typical conditions for RAFT polymerization. Indeed, our main intention was to use the RAFT oligomer as a functionalizing agent offering a possibility of chain extension rather than as a molecular weight controller. Thus, in our experimental conditions, the emulsion polymerization was primarily a conventional free radical polymerization (and not a RAFT-mediated polymerization), although the RAFT oligomer continued to polymerize during the emulsion polymerization. In fact, the dispersity value of the resulting latex, $M_w/M_n=2.0$, indicated that in spite of the co-existence of RAFT and conventional free radical polymerization, the polymerization mechanism was indeed presumably dominated by free radical polymerization.

The $\text{CeO}_2/\text{poly}(\text{VDC-co-MA})$ hybrid latex prepared with the poly(BA-co-AA) RAFT oligomer was film-coated on a poly(vinyl chloride) (PVC) support. Figure 15 shows a TEM picture of a ultramicrotomed film. The CeO_2/PVDC coating can be distinguished above the PVC + primer support. Clearly, the ceria nanoparticles were homogeneously distributed in the thickness of the PVDC film. There was no aggregation of the ceria nanoparticles during the film formation. It resulted in a transparent film as also shown in Figure 15. In addition, the resulting film showed improved UV stability (lower yellow index) compared to a reference PVDC film without CeO_2 nanoparticles. Thus, such hybrid CeO_2/PVDC latexes appear promising to elaborate transparent films with gas barrier properties and enhanced UV stability.

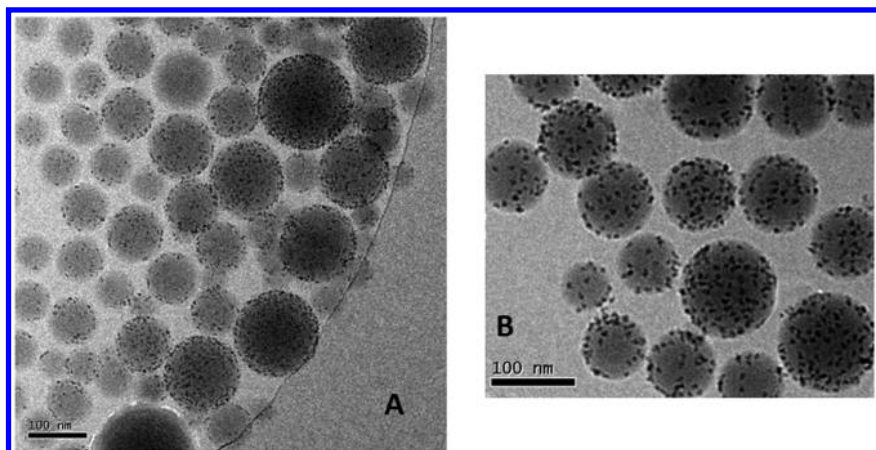


Figure 14. Cryo-TEM pictures of hybrid latexes obtained by copolymerization of vinylidene chloride/methyl acrylate in the presence of ceria nanoparticles (4wt% versus monomers) and poly(BA_{4,8}-co-AA_{4,9}) (RAFT oligomer/CeO₂ weight ratio=0.5; global monomer conversion: 86%; $D_p = 186$ nm; dispersity = 0.16; $N^{\circ}_{CeO_2} / N^{\circ}_P = 149$; $M_n = 89500$ g mol⁻¹; $M_w/M_n = 2.0$) (A) or poly(St₅-co-VBPDA₁₂) (RAFT oligomer/CeO₂ weight ratio=0.5; global monomer conversion: 98%; $D_p = 143$ nm; dispersity = 0.03; $M_n = 71500$ g mol⁻¹; $M_w/M_n = 1.9$) (B).



Figure 15. TEM picture of the section of a film prepared from a CeO₂/PVDC hybrid latex (synthesized in the presence of poly(BA_{4,8}-co-AA_{4,9}) RAFT oligomer) coated on a PVC support (A) and photography showing the transparency of the nanocomposite CeO₂/PVDC film (B).

Conclusion

Several functional RAFT oligomers have been designed and successfully used to prepare CeO₂/polymer hybrid latexes. The functional groups of the RAFT oligomers play complementary roles: carboxylic acid groups notably favor the affinity between the polymer and the ceria nanoparticles whereas sulfonic acid groups mainly contribute to the colloidal stability of the hybrid latexes. Films prepared from those hybrid latexes are transparent. Besides the elaboration of nanocomposite coatings, we are now investigating the synthesis and use of such

hybrid latexes as templates for the preparation of organic or inorganic porous materials with metal or metal oxide nanoparticles evenly distributed in the porous matrix, with possible applications as supported catalysts for instance (16).

Acknowledgments

The authors wish to thank Rinske Knoop for her experimental support on cryo-TEM observations, Byk Chemie for the supply of cerium oxide dispersions, Solvay for funding this research project, and the French Ministry of Education and Research for the ANRT grant CIFRE N°261/2008 as well as for the research grant ANR-2010-RMNP-005-05.

References

1. Bourgeat-Lami, E.; Lansalot, M. *Adv. Polym. Sci.* **2010**, *233*, 53–123.
2. Althues, H.; Henle, J.; Kaskel, S. *Chem. Soc. Rev.* **2007**, *36*, 1454–1465.
3. Nguyen, D.; Zondanos, H.; Farrugia, J.; Serelis, A.; Such, C.; Hawckett, B. *Langmuir* **2008**, *24*, 2140–2150.
4. Ali, J.; Heuts, P. A.; Hawckett, B. S.; van Herk, A. M. *Langmuir* **2009**, *25*, 10523–10533.
5. Das, P.; Zhong, W.; Claverie, J. P. *Colloid Polym. Sci.* **2011**, *289*, 1519–1533.
6. Zgheib, N.; Putaux, J. L.; Thill, A.; Bourgeat-Lami, E.; D'Agosto, F.; Lansalot, M. *Polym. Chem.* **2013**, *4*, 607–614.
7. Wessling, R. A.; Gibbs, D. S.; Obi, B. E.; Beyer, D. E.; DeLassus, P. T.; Howell, B. A. In *Kirk-Othmer Encyclopedia of Chemical Technology*, 4th ed.; Howe-Grant, M., Ed.; John Wiley & Sons Inc.: New York, 1997; Vol. 25, pp 691–745.
8. Garnier, J.; Warnant, J.; Lacroix-Desmazes, P.; Dufils, P. E.; Vinas, J.; Vanderveken, Y.; van Herk, A. M. *Macromol. Rapid Commun.* **2012**, *33*, 1388–1392.
9. Garnier, J.; Warnant, J.; Lacroix-Desmazes, P.; Dufils, P. E.; Vinas, J.; van Herk, A. M. *J. Colloid Interface Sci.* **2013**, *407*, 273–281.
10. Warnant, J.; Garnier, J.; van Herk, A. M.; Dufils, P. E.; Vinas, J.; Lacroix-Desmazes, P. *Polym. Chem.* **2013**, *4*, 5656–5663.
11. Revillon, A.; Dumont, B.; Guyot, A. *J. Polym. Sci., Part A: Polym. Chem.* **1976**, *14*, 2263–2273.
12. Vollmert, B. *Angew. Makromol. Chem.* **1968**, *3*, 1–27.
13. Oprea, S.; Dimitriu, E. *Bul. Inst. Politeh. Iasi, Sec.2: Chim. Ing. Chim.* **1980**, *26*, 71.
14. Pautrot-d'Alençon, L.; Barboux, P.; Boilot, J. P. *J. Sol-Gel Sci. Technol.* **2006**, *39*, 261–267.
15. Vinas, J.; Dufils, P. E.; Garnier, J.; Lacroix-Desmazes, P.; Van Herk, A.; Warnant, J.; Vanderveken, Y. Process for the preparation of a vinylidene chloride polymer composite. WO 2013/092588, June 27, 2013.
16. Chave, T.; Grunenwald, A.; Ayrat, A.; Lacroix-Desmazes, P.; Nikitenko, S. *I. J. Colloid Interface Sci.* **2013**, *395*, 81–84.

Chapter 20

Separation of Parent Homopolymers from Poly(ethylene oxide) and Polystyrene Based Block Copolymers by Liquid Chromatography under Limiting Conditions of Desorption—2. Studies of Samples Obtained from ATRP and NMP

Marion Rollet,^{*,1} Bérengère Pelletier,¹ Dusan Berek,²
Sébastien Maria,¹ Trang N. T. Phan,¹ and Didier Gimes^{*,1}

¹Aix Marseille Université, CNRS, Institut de Chimie Radicalaire, UMR7273,
13397 Marseille cedex 20, France

²Polymer Institute of the Slovak Academy of Sciences, Dúbravská cesta 9,
84541 Bratislava, Slovakia

*E-mail: marion.rollet@univ-amu.fr; didier.gimes@univ-amu.fr

Block copolymer synthesis often results in a complex polymer mixture containing not only the desired block copolymer macromolecules but also one or both parent homopolymers. Such complex polymer mixtures resulting from Atom Transfer Radical Polymerization (ATRP) and Nitroxide Mediated Polymerization (NMP) syntheses of PS-*b*-PEO-*b*-PS were characterized using Liquid Chromatography under Limiting Conditions of Desorption (LC LCD). The presence of PS homopolymer depends only on experimental synthesis conditions, such as the dilution of the reaction medium, the styrene/PEO molar equivalent ratio and the reaction time. Presence of residual PEO homopolymer is not only influenced by experimental synthesis conditions but also by the presence of unfunctionalized PEO in the corresponding PEO macro-initiator samples.

1. Introduction

Due to their unique self-assembly properties, block copolymers are currently the subject of intense research (1). Block copolymers have been already advantageously used in a wide range of applications, ranging from advanced nanomaterials to biocompatible drug delivery systems (2, 3). The performance of block copolymer materials highly depends on structurally-related parameters and requires both advanced polymerization techniques and powerful analytical methods. Whatever the living/controlled polymerization technique used to synthesize them, block copolymers are still complex materials that present heterogeneities in several dimensions: molar masses, chemical compositions of the different blocks, presence of residual homopolymers, and differences in architectures (4, 5). Precise characterization of such complex mixtures is of great interest not only to establish composition – properties relationships, but also to improve synthesis procedures. In this aim, different characterization techniques, such as Mass Spectrometry (MS), Nuclear Magnetic Resonance (NMR) and High Performance Liquid Chromatography (HPLC) based techniques are the subject of intense developments.

Mass Spectrometry allows determination of molar mass distribution, chemical composition and end-group functionalities of polymers. Two different ionization techniques are currently applied for polymers characterization in MS, namely Matrix Assisted Laser Desorption Ionization (MALDI) and Electro-Spray Ionization (ESI). Both of them lead to non-depolymerized and charged polymers. ESI-MS results in multi-charged macromolecules, but obtained mass spectra are often difficult to interpret because of the polymer's charge and mass distributions. Therefore, spectra are exploitable only if polymer molar mass is below 10 Kg.mol⁻¹. Although MALDI-MS does not show any molar mass limitation, it is difficult to maintain high resolution for high molar mass macromolecules and their detection can be limited. Moreover, sample preparation, especially the choice of the matrix, are still not rationalized nowadays. Several trial are necessary to find the right experimental conditions. Moreover, available matrices are often non-compatible with the different blocks of a copolymer. This is mostly true in the case of amphiphilic block copolymers like poly(ethylene oxide)-*b*-polystyrene (PEO-*b*-PS). To characterize such block copolymers by MALDI-MS, the group of Charles removed the covalent bond between PEO and PS blocks to analyze two homopolymers consisting of the constitutive initial blocks (6).

Nuclear Magnetic Resonance (NMR) is one of the most employed polymer characterization tool, particularly used due to its ability to generate highly informative spectra without any sample degradation. Solid-State NMR is preferred to liquid NMR in case of insoluble polymers and macromolecules able to self-assemble. This technique allows chemical composition information and the indirect determination of the molar mass of macromolecules in a short analysis time. However, it is not suitable to identify end-group functionalities in a long polymer chain ($M_n > 2$ Kg.mol⁻¹) or to indicate the presence of parent homopolymers in block copolymer samples. Recently, theoretical and technological improvements on Dynamic Nuclear Polarization Solid-State NMR (DNP – SSNMR) and synthesis of new polarizing agents have been enhancing

NMR sensitivity in such a way that end-group functionalities of high molar mass polymer chains can be studied (7). Nevertheless, several studies and developments of this technique are still needed to extend the scope of polymer studies.

High Performance Liquid Chromatography (HPLC) based techniques have proven to be particularly attractive and powerful methods to characterize complex polymer mixtures. Depending on interaction between the polymer sample, the stationary phase and the mobile phase, three different elution mechanisms take place in HPLC of polymers (8), which can lead to different elution procedures, namely Size Exclusion Chromatography (SEC), Liquid Adsorption Chromatography (LAC), Liquid Chromatography under Critical Conditions (LC CC) and Liquid Chromatography under Limiting Conditions of Desorption (LC LCD). The latter shows high potential even if it is not widely spread in polymer research laboratories (9).

In LC LCD, the eluent is usually a mixture of two solvents, an adsorption-preventing one (a desorli) and an adsorption-promoting one (an adsorli). Nevertheless, the eluent composition should allow desorption to prevail on adsorption for all the constituents of the complex polymer mixture. Sample injection is preceded by injection of a certain volume of solvent, which compared to eluent contains higher amount of adsorli. In the column packing, this adsorli volume forms a pore permeating zone, called a *barrier*, which is slowly eluted. Adsorbing macromolecules cannot break-through this barrier and their elution is then significantly retarded. At the same time, the non-adsorbing macromolecules elute rapidly in the exclusion mode without any influence of the barrier. Consequently, macromolecules exhibiting different adsorptivity in a complex polymer mixture can be fully separated if the number of barrier employed is optimum. Indeed, at least $n-1$ barriers will be needed to separate n polymers from a mixture, given that a barrier is expected to decelerate only one constituent of the mixture. Figure 1 illustrates LC LCD procedure applied to a blend of three polymers. In this case, two barriers are needed to separate three different sample constituents. In this figure, homopolymer A (blue) is non-adsorptive under the chromatographic conditions employed. As a consequence, A is not retained by any barrier and it elutes in the SEC mode. Homopolymer B (red) is adsorptive and it is decelerated by barrier 2 (B2). Block copolymer A-*b*-B or A-*b*-B-*b*-A (purple) is not slowed down by B2, which is not efficient enough. It breaks-through B2 and it elutes in SEC until it reaches barrier 1 (B1). Since B1 is more efficient than B2, block copolymer A-*b*-B or A-*b*-B-*b*-A is retained by B1. The retained polymers accumulate on edge of the barriers and are detected as focused peaks.

LC LCD shows several advantages including its high sample capacity, overall experimental simplicity (isocratic elution mode), and acceptable sample recovery (10).

Recently, separation of parent homopolymers from a triblock copolymers polystyrene-*b*-poly(ethylene oxide)-*b*-polystyrene PS-*b*-PEO-*b*-PS, containing 56.5 wt% PS, was achieved by LC LCD and we compared the separation ability of SEC, LC CC and LC LCD (9). These LC LCD peculiar chromatographic conditions allowed a well-efficient separation of this block copolymer from both its parent homopolymers in one single run. On the contrary, SEC analysis of this

sample exhibited too poor resolution to discriminate its parent homopolymers. Concerning LC CC, two different systems are needed to distinguish a block copolymer from both its parent homopolymers. Both PS and PEO LC CC experiments led to neither sensitive nor selective enough separations to observe both parent homopolymers contained in this studied block copolymer sample.

LC LCD chromatographic conditions for PS-*b*-PEO-*b*-PS characterization were optimized and this method can be applied to a large PEO and PS homopolymers molar masses range (11). Indeed, no upper molar mass limit was observed either for PEO homopolymers or for PS homopolymers. No lower molar mass limit concerning PS homopolymers was neither determined. On the contrary, PEO homopolymers with molar mass below than 1.5 Kg.mol⁻¹ were eluted in Size Exclusion Chromatography Assisted by Adsorption (SEC ADA) and were too slow to catch B2 and be accumulated on its edge. However, these low molar mass PEO homopolymers can still be separated from the block copolymers. On top of that, it appears that, depending on the PEO block molar mass and the PS wt% contained in the block copolymer, B2 has to be adjusted so as not to retain any block copolymer.

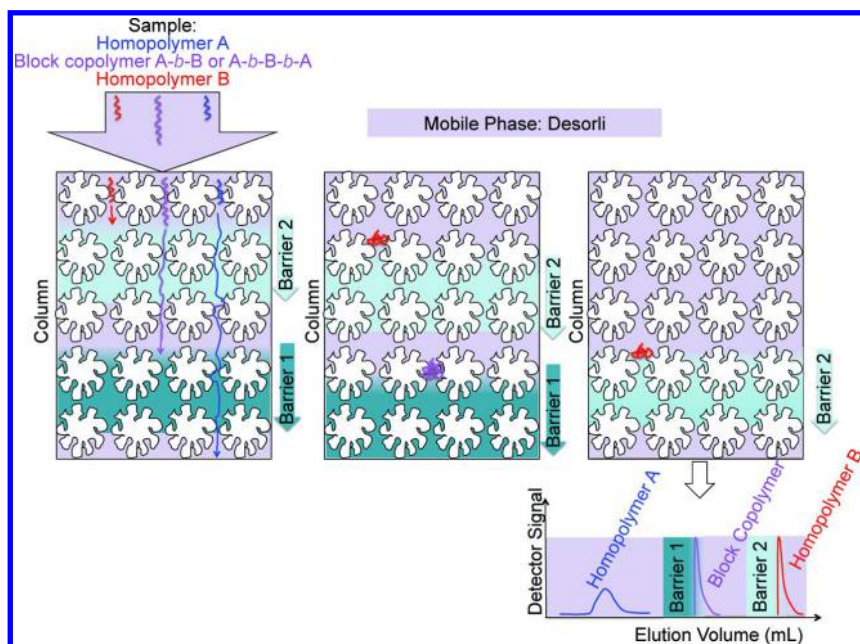


Figure 1. Principle of LC LCD applied to a blend of three polymers. (see color insert)

In this paper, we illustrate further the potential of this technique by characterizing precisely samples of PS-*b*-PEO-*b*-PS obtained from different synthesis procedures. Typically, various samples of PS-*b*-PEO-*b*-PS were synthesized using Atom Transfer Radical Polymerization (ATRP) and Nitroxide Mediated Polymerization (NMP), from the corresponding macro-initiator prepared previously. A systematic study on the experimental conditions (molar masses, bulk or solution, reaction time) has been investigated and in each case, the presence of parent homopolymers has been assessed by LC LCD.

2. Experimental Section

2.1. Materials

PEO of molar masses (M_n) 35, 20 and 10 Kg.mol⁻¹ were purchased from Sigma-Aldrich (USA). BlocBuilder MA (>99%) alkoxyamine based on the nitroxide SG1 (N-tert-butyl-N-[1-diethylphosphono-(2,2-dimethylpropyl)]nitroxide) and the 1-carboxy-1-methylethyl moiety was kindly provided by Arkema (France). Acryloyl chloride (97%), 2-bromoisobutyl bromide (98%), triethylamine (TEA) (99%), styrene (99%), N,N,N',N'',N'''-pentamethyldiethylenetriamine (99%) (PMDETA) and copper bromide (98%) were purchased from Sigma-Aldrich and were used as received. All solvents and other reagents were obtained from commercial suppliers and used without further purification.

PEO standards (0.615 to 114 Kg.mol⁻¹) and PS standards (0.682-124 Kg.mol⁻¹) were purchased from PSS (Germany) and Agilent (USA). 1-chlorobutane (CLB) of HPLC-grade was purchased from Sigma-Aldrich and was used without further purification. Dimethylformamide (DMF) of analytical grade was filtered with a 0.2 μm Nylon Alltech (USA) membrane before use. Tetrahydrofuran (THF) of analytical grade was filtered with a 0.2 μm PTFE Alltech membrane before use. DMF and THF were purchased from Carlo Erba. The mixed eluents and barriers compositions are always given in weight parts.

2.2. PS-*b*-PEO-*b*-PS Triblock Copolymer Synthesis

2.2.1. Via ATRP

ATRP made PS-*b*-PEO-*b*-PS triblock copolymers were prepared according to the chemical pathway (12) depicted on Figure 2.

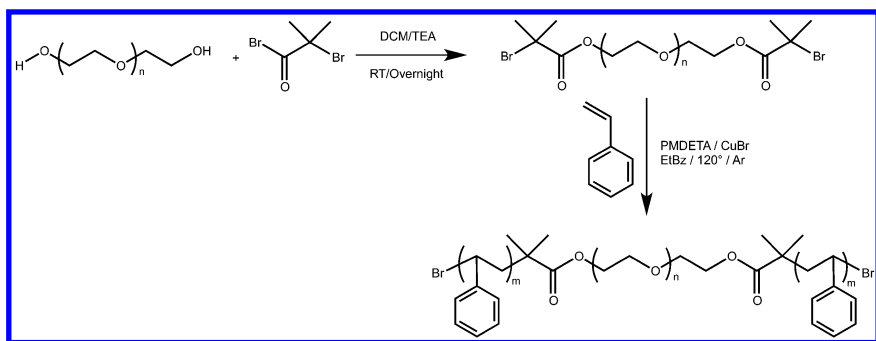


Figure 2. Synthesis procedure of PS-*b*-PEO-*b*-PS triblock copolymers by Atom Transfer Radical Polymerization (ATRP).

In a first step, difunctional PEO macro-initiator was prepared through the esterification of the hydroxyl-terminated PEO in presence of 2-bromoisobutyryl bromide. In a typical run, a three-neck round bottom flask equipped with a water-cooled condenser was charged with appropriate amount of PEO, TEA and dichloromethane (DCM). The reaction mixture was deoxygenated under stirring with argon bubbling for 30 minutes. 2-bromoisobutyryl bromide diluted in 200 mL of DCM was added dropwise at 0°C under argon. Then, the obtained reaction mixture was allowed to warm to 30°C and stirred overnight. The solution was then filtered off to remove the triethylammonium bromide, washed three times with saturated NaHCO₃ solution, then three times with distilled water, and dried over MgSO₄. DCM was removed by rotary evaporation and the PEO macro-initiator was precipitated in cold diethyl ether. The solid was recovered by filtration, washed with diethyl ether, and dried under vacuum until a constant mass was reached.

In a second step, the ATRP of styrene was performed using the PEO macro-initiator previously prepared. A three-neck round bottom flask was charged with the PEO macro-initiator, copper bromide (4 molar eq.), styrene monomer and EtBz. The system was fitted with a water-cooled condenser and the solution was degassed under stirring with argon for 30 minutes. Degassed PMDETA (2 molar eq.) was then slowly injected with a purged syringe to start the polymerization. The solution was finally allowed to heat to 120°C. At the end of the polymerization, the reaction mixture was quenched in cold water, dissolved with chloroform, and filtered through a basic alumina column. The catalyst free solution was then poured in a large excess of diethyl ether or pentane (depending on the expected copolymer composition). The solid was filtered and dried under vacuum to a constant mass.

The structures of the macro-initiator and the block copolymer were determined by ¹H NMR in CDCl₃ containing trimethylsilane as an internal reference. The esterification of the hydroxyl groups was proven by ¹H NMR spectroscopy based on the methyl proton peak of the substituted PEO ($\delta = 1.94$ ppm), and the esterification yields were estimated at 100% for all PEO macro-initiator syntheses. Nevertheless, ¹H NMR sensitivity towards end-group functionalities on polymer chains is quite low and some unfunctionalized PEO could still be present in the PEO macro-initiator samples (13).

Table 1 gathers experimental synthesis conditions and results concerning ATRP PEO macro-initiators used in the present study.

Table 1. ATRP PEO macro-initiators^a

<i>PEO Macro-initiator Kg.mol⁻¹</i>	<i>TEA Molar Equivalent</i>	<i>2-bromoisobutyryl bromide Molar Equivalent</i>	<i>Functionalization Yield Determined by ¹H NMR %</i>
A = 10	20	20	100
B = 20	40	40	100
C = 35	60	60	100

^a For all syntheses, starting PEO-(OH)₂ molar equivalent was equal to 1.

Experimental conditions for the different block copolymers synthesized by ATRP in this study are listed in the Table 2.

Table 2. PS-*b*-PEO-*b*-PS ATRP synthesis conditions^a

<i>Block Copolymer Name</i>	<i>PEO Macro-initiator Kg.mol⁻¹</i>	<i>Reaction Time min</i>	<i>Molar Eq. Sty/PEO</i>	<i>Molar Eq. Sty/EtBz</i>
ATRP1	10 (A)	60	401	1
ATRP2	10 (A)	255	401	1
ATRP3	20 (B)	100	395	0.6
ATRP4	20 (B)	150	1381	Bulk
ATRP5	20 (B)	900	1579	Bulk
ATRP6	35 (C)	900	3430	Bulk

^a All ATRP syntheses were performed by the same operator at 120°C.

2.2.2. Via NMP

NMP made PS-*b*-PEO-*b*-PS triblock copolymers were prepared according to an already described procedure (14) (cf. Figure 3).

The first step consists in an esterification reaction of the hydroxyl terminated difunctional PEO in presence of acryloyl chloride. The second step is a radical 1,2-intermolecular addition of the BlocBuilder MA on the acrylate functions of the previously modified difunctional PEO resulting in PEO macro-initiator. Then styrene polymerization is carried out to give the triblock PS-*b*-PEO-*b*-PS copolymer. Briefly, the material is precipitated in cold diethyl ether, then collected by filtration and finally dried out under vacuum.

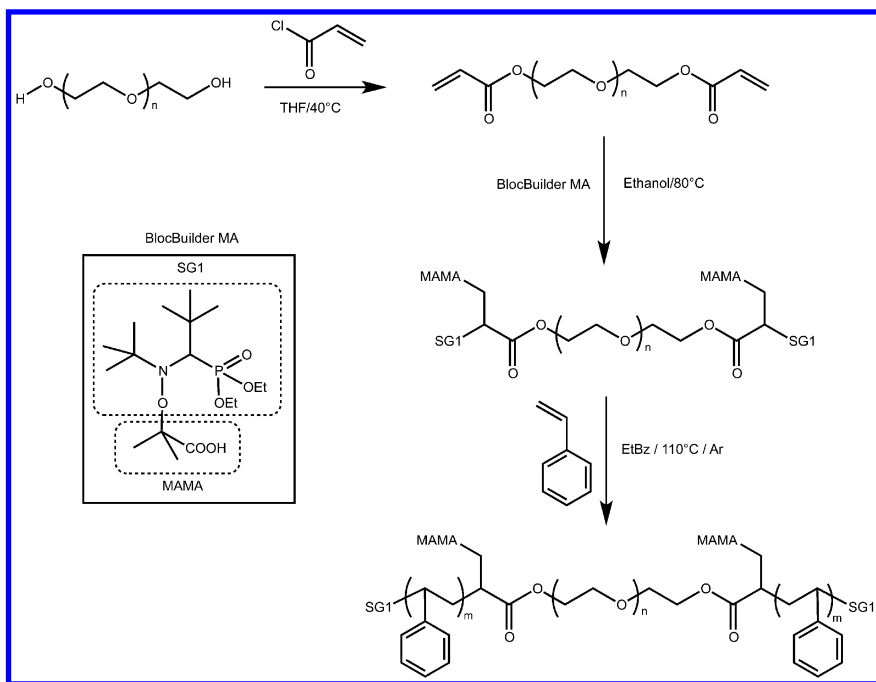


Figure 3. Synthesis procedure of PS-*b*-PEO-*b*-PS triblock copolymers by Nitroxide Mediated Polymerization (NMP).

It was already proven (13) by liquid chromatography under critical conditions (LC CC) that the esterification reaction was quantitative contrary to the radical 1,2-intermolecular addition, which leads to residual PEO-(Acrylate)₂ in the PEO macro-initiator samples. Unfortunately, this LC CC methods is not suitable for PEO with molar masses higher than 12 Kg.mol⁻¹. Therefore, ¹H NMR analyses are preferentially used to calculate the yield of PEO macro-initiator synthesis. Nevertheless, with high molar masses polymers, this technique is not sensitive enough to discriminate end-group functionalities and to highlight low amount of residual PEO-(Acrylate)₂. Consequently, even if functionalization yields are estimated at 100%, some PEO-(Acrylate)₂ could be present in PEO macro-initiator samples. Table 3 gathers the NMP PEO macro-initiators used in the present study.

Experimental conditions for the different block copolymers synthesized by NMP are listed in Table 4.

Table 3. NMP PEO macro-initiators

<i>PEO macro-initiator</i>	<i>Molar mass Kg.mol⁻¹</i>	<i>Functionalization yield of the 1,2-intermolecular radical addition of BlocBuilder determined by ¹H NMR %</i>
A'	10	86
B1'	20	91
B2'	20	64
C1' ^a	35	100
C2' ^a	35	100

^a These PEO macro-initiators were synthesized on different days.

Table 4. PS-*b*-PEO-*b*-PS NMP synthesis conditions^a

<i>Block Copolymer Name</i>	<i>PEO Macro-initiator</i>	<i>Reaction Time min</i>	<i>Molar Eq. Sty/PEO</i>	<i>Molar Eq. Sty/EtBz</i>
NMP1	10 (A')	120	402	1.8
NMP2	20 (B1')	420	786	1.6
NMP3	20 (B2')	420	785	3.1
NMP4	35 (C1')	420	1362	0.5
NMP5	35 (C1')	420	1362	0.8
NMP6	35 (C1')	420	1359	1.2
NMP7	35 (C1')	420	1362	1.9
NMP8	35 (C2')	420	1128	3.4

^a All NMP syntheses were performed by the same operator at 110°C.

2.2.3. Block Copolymers Samples

In the present work, we used only PS-*b*-PEO-*b*-PS triblock copolymers with estimated percentage of PS (based on ¹H NMR) higher than 50 wt%. They were synthesized in our laboratory by using the ATRP or NMP procedures described above. Then, from PEO-block molar mass given by the supplier and confirmed by SEC prior to use (results not shown here), each PS-block molar mass and weight percentages of PS were calculated based on ¹H NMR analysis.

In this paper, triblock copolymers are designated as PS_{XK}-*b*-PEO_{YK}-*b*-PS_{XK}; the subscripts X and Y indicate the molar mass in Kg.mol⁻¹ of each polymer part in the triblock copolymer. “K” indicates the units of molar mass. All PS-*b*-PEO-*b*-PS triblock copolymers used in this study are listed in Table 5.

Table 5. Block copolymer samples. PS wt% were determined by ¹H NMR.

<i>Synthesis Procedure</i>	<i>Block Copolymer Name</i>	<i>Block Copolymer Sample</i>	<i>PS wt %</i>
ATRP	ATRP1	PS _{6.45K} - <i>b</i> -PEO _{10K} - <i>b</i> -PS _{6.45K}	56.3
	ATRP2	PS _{16K} - <i>b</i> -PEO _{10K} - <i>b</i> -PS _{16K}	76.2
	ATRP3	PS _{10.2K} - <i>b</i> -PEO _{20K} - <i>b</i> -PS _{10.2K}	50.5
	ATRP4	PS _{12.35K} - <i>b</i> -PEO _{20K} - <i>b</i> -PS _{12.35K}	55.3
	ATRP5	PS _{79.5K} - <i>b</i> -PEO _{20K} - <i>b</i> -PS _{79.5K}	88.8
	ATRP6	PS _{46.6K} - <i>b</i> -PEO _{35K} - <i>b</i> -PS _{46.6K}	72.7
NMP	NMP1	PS _{6K} - <i>b</i> -PEO _{10K} - <i>b</i> -PS _{6K}	54.7
	NMP2	PS _{17.5K} - <i>b</i> -PEO _{20K} - <i>b</i> -PS _{17.5K}	63.7
	NMP3	PS _{24.85K} - <i>b</i> -PEO _{20K} - <i>b</i> -PS _{24.85K}	71.3
	NMP4	PS _{20K} - <i>b</i> -PEO _{35K} - <i>b</i> -PS _{20K}	54.0
	NMP5	PS _{36K} - <i>b</i> -PEO _{35K} - <i>b</i> -PS _{36K}	67.0
	NMP6	PS _{61K} - <i>b</i> -PEO _{35K} - <i>b</i> -PS _{61K}	78.0
	NMP7	PS _{27K} - <i>b</i> -PEO _{35K} - <i>b</i> -PS _{27K}	60.0
	NMP8	PS _{23K} - <i>b</i> -PEO _{35K} - <i>b</i> -PS _{23K}	56.5

From ATRP and NMP synthesis procedures, we can assume that self-initiated PS homopolymer as well as residual functionalized and non-functionalized PEO can be present in the obtained complex polymer mixtures. Moreover, it is probable that some diblock copolymer PEO-*b*-PS is also formed during these procedures.

Previously, we have demonstrated that LC LCD is a powerful tool to characterize such polymers blend (9). Indeed, we managed the separation of a PS-*b*-PEO-*b*-PS triblock copolymer, PS_{23K}-*b*-PEO_{35K}-*b*-PS_{23K} (NMP8), from both its PEO and PS parent homopolymers.

2.3. NMR Analysis

NMR experiments were performed with a Bruker Avance III 400 MHz Nanobay spectrometer. ¹H NMR spectra were recorded at 300 K with a 12.7 μs 30° pulse, a repetition time of 2 s and 64 scans.

Concerning ATRP PEO macro-initiator, the esterification of the hydroxyl groups was proven by ¹H NMR spectroscopy based on the methyl proton peak

of the substituted PEO ($\delta = 1.94$ ppm). Functionalization yields were estimated from integrations of peak corresponding to the $-\text{CH}_2-\text{CH}_2-\text{O}-$ protons of PEO chain ($\delta = 3.6\text{--}3.7$ ppm) and methyl proton peak of the substituted PEO.

For NMP PEO macro-initiator, the functionalization yields of the esterification of the hydroxyl groups were estimated from integrations of peak corresponding to the $-\text{CH}_2-\text{CH}_2-\text{O}-$ protons of PEO chain ($\delta = 3.6\text{--}3.7$ ppm) and acrylate proton peaks of the substituted PEO ($\delta = 5.8, 6.2$ and 6.4 ppm). Then, the functionalization yields of the radical 1,2-intermolecular addition of the BlocBuilder MA on PEO-(Acrylate)₂ were estimated from integrations of residual peaks corresponding to acrylate protons ($\delta = 5.8, 6.2$ and 6.4 ppm).

The ¹H NMR spectrum of the final PS-*b*-PEO-*b*-PS copolymer in CDCl₃ shows resonances ($\delta = 6.2\text{--}7.2$ ppm) corresponding to the phenyl protons of the PS blocks and peaks signals ($\delta = 3.6\text{--}3.7$ ppm) corresponding to the $-\text{CH}_2-\text{CH}_2-\text{O}-$ protons of the PEO block. The final overall average copolymer composition was thus determined from the ratio between the integrals of PS-phenyl ¹H signals and the PEO ¹H signals. Considering the molar mass value for the PEO block, ¹H NMR analysis lead to the determination of the PS block average molar mass given in Table 4.

2.4. LC LCD Analysis

LC LCD separations were performed on a Waters 600 chromatography system equipped with a Waters 600E pump, a Waters 600 controller, and a Waters 717plus autosampler. Manual Rheodyne (USA) valve with a loop of 1000 μL was employed for barrier injection. Home-packed column (7.5x300) mm that contained bare silica gel Kromasil 60 Å – 10 μm was thermostated in the Crococol oven (Polymer Laboratories/Agilent, USA). Temperature of measurements was 30°C. Mobile phase was a mixture of dimethylformamide (DMF) and 1-chlorobutane (CLB) at a composition of 40 wt.% and 60 wt.% respectively, which is noted DMF40/CLB60 in this chapter, and flow rate was set to 1 mL.min⁻¹. Samples were dissolved in eluent at concentration of 0.25 wt.% and filtered with a 0.2 μm PTFE Sodipro filter. Sample injections were done by the autosampler at a volume of 50 μL . Two barriers were employed to achieve separation of all three constituents. They are denoted Barrier 1, B1, and Barrier 2, B2. Their compositions are B1: CLB100 and B2: DMF23/CLB77, meaning that B1 is composed of 100 wt% CLB and B2 is composed of 23 wt.% DMF and 77 wt.% CLB. Accurate time delays between the injections of barriers and sample are necessary to adjust the peak retention volumes and to obtain a well-defined separation. Here, B1 is injected at 0 min, B2 is injected 2 min after B1 and the sample is injected at 3'10 min after B1. As barriers were injected manually and samples were injected with the help of an autosampler, measurements of the time delay between the start order launched on the computer and the real injection of sample into the chromatographic system were realized. Moreover, some reproducibility tests on the autosampler performance were done for every eluent and sample solvent composition in order to define right experimental conditions, which allow us to precisely respect described time delays between the injection of barriers and samples. Data recording starts with the injection of

sample. A Polymer Laboratories/Agilent, USA PL-ELS 2100 detector worked at evaporation temperature of 90°C and at nebulization temperature of 40°C. Nitrogen was used as a carrier gas at a flow rate of 1.2 mL.min⁻¹.

By applying this optimized LC LCD conditions, PEO and PS homopolymers are eluted as presented on Figure 4.

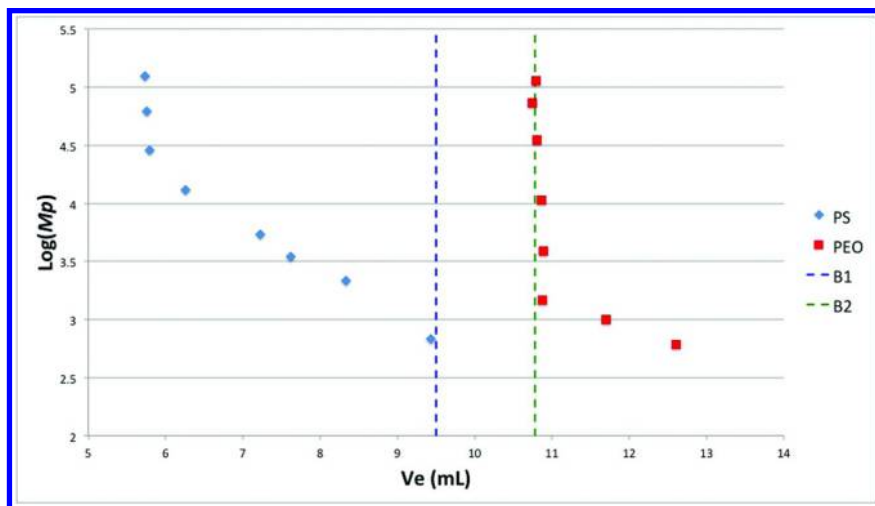


Figure 4. Log (M_p) vs Elution Volume for PS and PEO standards in LC LCD optimized conditions.

PS homopolymers are eluted in the SEC mode and molar masses higher than 28 Kg.mol⁻¹ are totally excluded from the pores of the stationary phase and are eluted at the interstitial volume of the column, which is about 5.7 mL. PEO homopolymers with molar masses between 1.5 and 115 Kg.mol⁻¹ are fully retained by B2 and elute independently of their molar mass at about 10.8 mL. PEO with molar masses lower than 1.5 Kg.mol⁻¹ are eluted in ADA SEC. They are too slow to catch B2 and accumulate on its edge but they still can be separated from the block copolymers, which elute on B1's edge at about 9.3 -9.7 mL (11).

These described chromatographic conditions were optimized for PS_{23K}-*b*-PEO_{35K}-*b*-PS_{23K} (NMP8) block copolymer and it was proven that no block copolymer was present in the PS fraction while less than 4 mol% was present in the PEO fraction (11). The presence of block copolymer in the PEO fraction can be explained by a too strong efficiency of B2. Indeed, B2 composition has to be adjusted regarding PEO block molar mass and PS wt% in the block copolymer. In case of PS_{23K}-*b*-PEO_{35K}-*b*-PS_{23K} block copolymer sample, the percentage of PS determined by ¹H NMR was 56.5 wt%. Nevertheless, this sample contains a significant amount of PS homopolymer, presuming that the real percentage of PS in the block copolymer macromolecule was overestimated. Fractionation and ¹H NMR analysis allow us to determine that, considering

measurements uncertainties, the real PS wt% of this block copolymer is 52 wt%. Therefore, these LC LCD optimized conditions, with B2 composition of DMF23/CLB77, are suitable for characterization of block copolymers containing more than 52 wt% of PS and a PEO block of 35 Kg.mol⁻¹.

It is well-known that ELS detector response is not linear according to polymer species concentration and so precise quantification of PS and PEO homopolymers is not possible. However, since the study is performed on a narrow concentration range, we assume that it is reasonable to discuss qualitatively the results by comparing peaks height and width.

3. Results and Discussion

3.1. Complex Polymer Mixtures Obtained by ATRP Procedure

Results of LC LCD separations of PS-*b*-PEO-*b*-PS copolymers, obtained by ATRP from PEO macro-initiators, are presented on Figure 5.

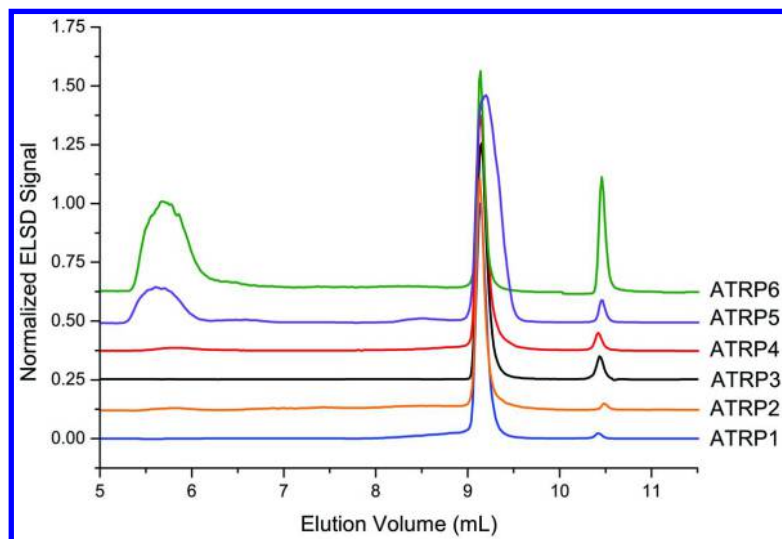


Figure 5. LC LCD Chromatograms of PS-*b*-PEO-*b*-PS synthesized by ATRP. Chromatograms were normalized on the block copolymer peak eluted at about 9.3 mL.

From Figure 5, it appears that all triblock copolymers synthesized by ATRP contain more or less residual PEO homopolymer. Moreover, block copolymers ATRP2, ATRP4, ATRP5 and ATRP6 show presence of PS homopolymers, keeping in mind that ATRP1, ATRP3 and ATRP5 were synthesized by polymerization in EtBz solution whereas ATRP2, ATRP4 and ATRP6 were synthesized in bulk.

As stated above, self-initiated PS homopolymers are present in some of the block copolymers with the following order for PS content: ATRP3=ATRP1<ATRP2<ATRP4<<ATRP5<ATRP6

ATRP1 does not contain any PS homopolymer, while ATRP2 chromatogram exhibits small traces of homopolystyrene. As the only difference is a longer reaction time for ATRP2 compared to ATRP1, 255 minutes and 60 minutes, respectively, this result is consistent with the increasing amount of self-initiated polystyrene versus time at high temperature.

Similarly, ATRP3, with a reaction time of 100 minutes, does not contain any trace of PS homopolymer. As expected, short reaction times prevent self-initiated styrene polymerization. ATRP4, made from the same macro-initiator B, but with reaction time of 150 minutes, contains traces of self-initiated PS. However, the styrene concentration was also higher for ATRP4. Indeed ATRP3 and ATRP4 were synthesized in solution and in bulk, respectively. Thus, a higher styrene concentration could also participate to increase the amount of residual styrene.

ATRP5 contains high amount of self-initiated PS homopolymer. Once again, this amount of self-initiated PS is obviously related to long reaction time (900 minutes). Then, the weight percentage of PS (88.8 PS wt%) in the block copolymer macromolecule determined from ^1H NMR analysis is probably over-estimated due to the difficulty with this technique to distinguish self-initiated PS from the PS contain in the block copolymer. However, on ATRP5 chromatogram, we can observe a small and broad peak eluted between 8.3 and 9.0 mL. This peak corresponds to block copolymer able to penetrate into B1. It could be due to a decrease of B1 efficiency with high weight percentage of PS. Therefore, weight percentage of PS in ATRP5 block copolymer is certainly rather high. We can also notice that the block copolymer peak at 9.3 mL is broader than the ones observed in the other chromatograms. Unfortunately, so far, we do not have any explanation for this phenomenon.

ATRP6 was synthesized with experimental synthesis conditions similar to ATRP5, with the same long reaction time. Thus, the amount of self-initiated PS in ATRP6 sample is relatively high.

From PEO homopolymer peaks height and width, the quantity of PEO contained in block copolymers can be classified according to the following increasing order: ATRP1 \approx ATRP2 < ATRP3 \approx ATRP4 \approx ATRP5 < ATRP6.

Clearly, the amount of residual PEO appears correlated with the macro-initiator used according to this ranking: A < B < C.

Indeed, ATRP1 and ATRP2 were synthesized from the same PEO 10 Kg.mol⁻¹ macro-initiator A and their chromatograms exhibit similar and very low amount of residual PEO homopolymer. The only difference between those samples lies on the reaction time, which were 60 and 255 minutes, respectively. Since in ATRP the initiation step is usually very fast, we can reasonably assume that residual PEO homopolymer observed is only due to an incomplete functionalization of the corresponding PEO macro-initiator.

ATRP3, ATRP4 and ATRP5 were synthesized from the same PEO 20 Kg.mol⁻¹ macro-initiator B and their chromatograms exhibit similar and low amount of residual PEO homopolymer. ATRP3 was synthesized by polymerization in solution while ATRP4 and ATRP5 were synthesized in bulk. In both cases, it seems

that PEO macro-initiator was fully efficient to initiate styrene polymerization. The amount of residual PEO homopolymer found in those samples is due to a PEO macro-initiator containing non-functionalized PEO. Moreover, we can state that PEO macro-initiator B contains more non-functionalized PEO than PEO macro-initiator A, even if both functionalization yields determined by NMR were established to 100%. Indeed, chromatograms of ATRP 1 and ATRP 2 exhibit less non-functionalized PEO than chromatograms of ATRP3, ATRP4 and ATRP5.

ATRP6 was synthesized from PEO 35 Kg.mol⁻¹ macro-initiator C. Although the experimental synthesis conditions were similar to ATRP5, the amount of residual PEO seems higher in ATRP6 sample. However, the amount of self-initiated PS in ATRP6 sample is also high. Therefore, the PS percentage determined by ¹H NMR is also overestimated and the real PS percentage of the block copolymer macromolecule could be lower than 52 wt%. As a consequence, B2 could be too efficient for this block copolymer characterization and could retained some block copolymer. Indeed, on ATRP6 chromatogram, the peak corresponding to residual PEO homopolymer is quite high although functionalization yield for PEO macro-initiator C estimated by ¹H NMR was equal to 100%. However, if we cannot totally exclude the fact that some block copolymer are retained by B2, we believe that functionalization yield determined by ¹H NMR for PEO 35 Kg.mol⁻¹ macro-initiator C is overestimated due to the lack of accuracy when comparing large vs low integral values. Indeed, functionalization yield is determined from integrations of PEO ethylene protons peak, which is intense and corresponds to 3181 protons in case of PEO 35 Kg.mol⁻¹, and methyl protons peak of the substituted PEO, which is low and attributed to 12 protons. The amount of non-functionalized PEO homopolymer in this macro-initiator is probably rather high and responsible for the intense peak observed. So, uncertainties of functionalization yield of PEO 35 Kg.mol⁻¹ determined by ¹H NMR can be important. On the contrary, PEO ethylene protons peaks for PEO 20 and 10 Kg.mol⁻¹ correspond to 1818 and 909 protons, respectively, leading to more accurate data on functionalization yields.

The presence of residual PEO is related to the functionalization rate of PEO macro-initiators, but we can also notice that this rate decreases with increasing PEO molar mass.

3.2. Complex Polymer Mixtures Obtained by NMP Procedure

Results of LC LCD separations of complex polymer mixtures obtained by NMP procedure during PS-*b*-PEO-*b*-PS syntheses are presented on Figure 6.

From Figure 6, it is obvious that all block copolymer samples synthesized by NMP contain some residual PEO homopolymer. Self-initiated PS homopolymer is also present in almost every NMP samples, except in NMP1 and NMP2 samples.

Figure 7 and 8 are focuses on PS and PEO homopolymer peaks, respectively.

From PS homopolymer peaks height and width (cf. Figure 7), the amount of PS homopolymer in block copolymers can be classified according to the following increasing order: NMP1=NMP2 < NMP4 < NMP5 < NMP6 < NMP3 < NMP7 < NMP8.

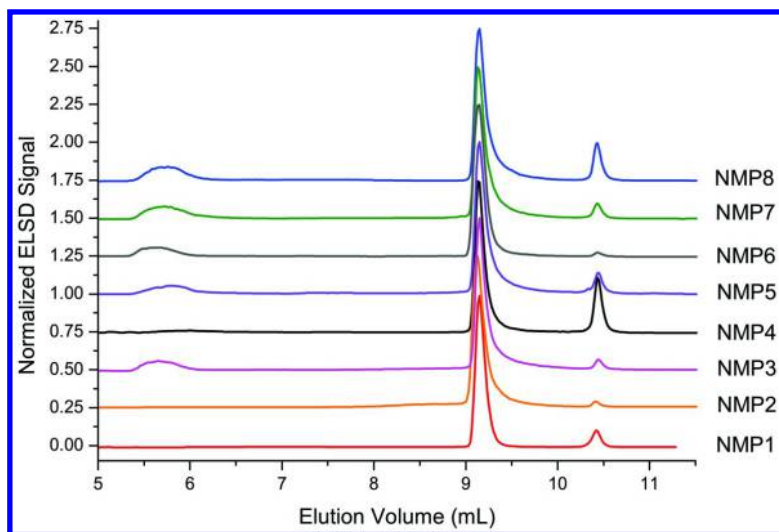


Figure 6. LC LCD Chromatograms of PS-*b*-PEO-*b*-PS synthesized by NMP. Chromatograms were normalized on the block copolymer peak eluted at about 9.3 mL.

NMP4, NMP5, NMP6, NMP7 were synthesized with Sty/PEO molar equivalent ratio about 1360. All these syntheses last 420 minutes at 110°C. The main differences between these syntheses are the Sty/EtBz molar equivalent ratio, which equal 0.5 for NMP4, 0.8 for NMP5, 1.2 for NMP6, 1.9 for NMP7. It appears that the lower is the Sty/EtBz molar equivalent ratio, the lower is the content of PS homopolymer after 420 minutes of polymerization. As expected, the more diluted is the reaction medium, the less is the amount of self-initiated PS homopolymer.

NMP8 was synthesized with Sty/PEO molar ratio equals to 1128. The reaction medium from its synthesis was concentrated since its Sty/EtBz molar equivalent ratio equals 3.4. It leads to a high content of self-initiated PS homopolymer.

NMP2 and NMP3 were both synthesized at 110°C during 420 minutes and with a Sty/PEO molar equivalent ratio equals to 785. Their Sty/EtBz molar equivalent ratios differ and equal 1.6 for NMP2 and 3.1 for NMP3. NMP3 contains a non-negligible amount of self-initiated PS homopolymer while NMP2 chromatogram does not show any traces of PS homopolymer. It confirms the previous conclusion about the dilution of the reaction medium.

Moreover, we can notice that NMP3 and NMP8 are both quite concentrated reaction medium. Their Sty/EtBz molar equivalent ratios are 3.1 and 3.4, respectively. On the other hand, NMP3 Sty/PEO molar equivalent ratio is almost 1.5 times lower than NMP8 Sty/PEO molar equivalent ratio. As NMP3 contains less PS homopolymer than NMP8, we can assume that Sty/PEO molar equivalent ratio is also a relevant parameter concerning self-initiation of styrene.

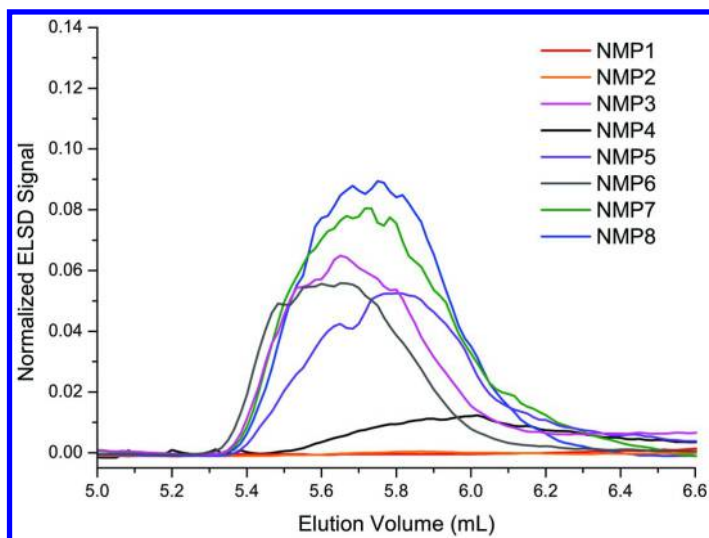


Figure 7. LC LCD Chromatograms of PS-*b*-PEO-*b*-PS synthesized by NMP. Chromatograms were normalized on the block copolymer peak eluted at about 9.3 mL and focused in the PS homopolymer elution volumes area, from 5.0 to 6.6 mL. (see color insert)

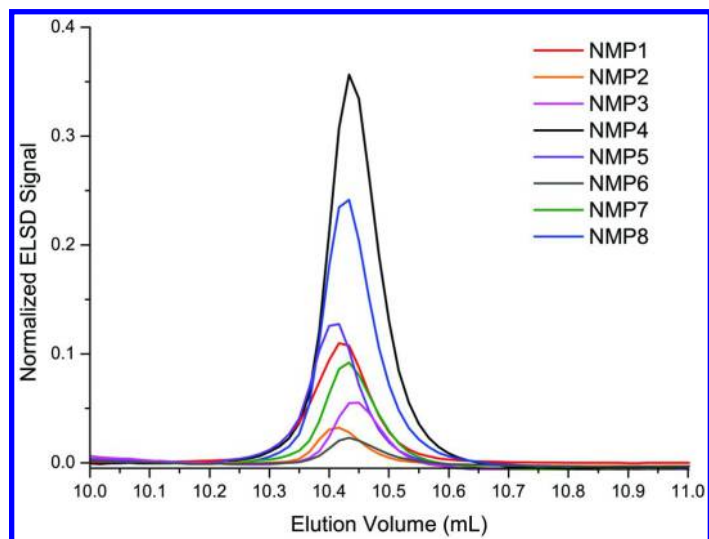


Figure 8. LC LCD Chromatograms of PS-*b*-PEO-*b*-PS synthesized by NMP. Chromatograms were normalized on the block copolymer peak eluted at about 9.3 mL and focused in the PEO homopolymer elution volumes area, from 10.0 to 11.0 mL. (see color insert)

It is confirmed by the comparison of NMP2 and NMP7. Their Sty/EtBz molar equivalent ratios are 1.6 and 1.9, respectively, and their Sty/PEO molar equivalent are 786 and 1362, respectively. NMP7 contains high amount of self-initiated PS homopolymer whereas NMP2 does not show any traces of PS homopolymer. Instead of using Sty/PEO molar equivalent ratio, we can also interpret this result thanks to the proportion of styrene. Indeed, NMP2 and NM7 reaction media were composed of 42 and 56 wt.% of styrene, respectively. Therefore, a higher proportion of styrene gives less homoPS.

NMP1 was synthesized at 110°C during 120 minutes using a 1.8 Sty/EtBz molar ratio and a 402 Sty/PEO molar ratio. In this case, no self-initiated PS was either detected.

From Figure 8, block copolymers can be classified according to the following residual PEO homopolymer amounts in increasing order: NMP2 < NMP6 < NMP3 < NMP7 < NMP1 < NMP5 < NMP8 < NMP4.

NMP4, NMP5, NMP6 and NMP7 were synthesized from the PEO 35 Kg.mol⁻¹ macro-initiator C1'. Therefore, the presence of residual PEO homopolymer is not only due to the macro-initiator itself. Experimental conditions were the same for all these block copolymers, except for the Sty/EB molar equivalent ratios, which are 1.2 for NMP6, 1.9 for NMP7, 0.8 for NMP5 and 0.5 for NMP4. At first sight, it seems that the more diluted the reaction medium, the higher the amount of residual PEO homopolymer is. However, NMP6 is more diluted than NMP7 and yet it contains less residual PEO homopolymer than the latter. It could be explained by the presence of PS homopolymer in those samples. Indeed, NMP6 contains a only low amount of PS homopolymer. Consequently, ¹H NMR estimation of the percentage of PS in the block copolymer, which is 78%, is correct. As this PS percentage is higher than 52%, B2 is well-efficient and it only retains residual PEO homopolymer. On the contrary, NMP7 contains high amount of PS homopolymer. Therefore, ¹H NMR estimation of the percentage of PS in this block copolymer, which is 60%, is probably overestimated. Then it is reasonable to think that the real percentage of PS in the block copolymer is lower than 52% and a few amount of this block copolymer could be partly retained by B2. This leads to a more intense PEO homopolymer peak than expected for NMP7 sample. Moreover, an additional effect will enhance artificially the proportion of PEO homopolymer in NMP7. Indeed, the copolymer molar mass in NMP6 sample (147 Kg.mol⁻¹) is quite high compared to the overestimated molar mass of NMP7 copolymer (89 Kg.mol⁻¹). Therefore, even if the molar ratio of non-functionalized PEO to PEO macro-initiator are the same in both sample, the intensity of PEO homopolymer peak in NMP6 should appear lower after normalization, since the weight fraction of copolymer in NMP6 would be higher than in NMP7.

NMP2 and NMP3 were synthesized in the same conditions, except for the Sty/EtBz molar equivalent ratios, which are 1.6 and 3.1, respectively. Moreover, PEO macro-initiator B2' was used for NMP3 synthesis while PEO macro-initiator B1' was used for NMP2 and their functionalization yields were 64% and 91%, respectively. Therefore, it is logical that the amount of residual PEO homopolymer is higher in NMP3 block copolymer compared to NMP2.

NMP1 was synthesized from the PEO 10 Kg.mol⁻¹ macro-initiator A', which shows a functionalization yield of 86%. Its chromatogram shows no

presence of PS homopolymer, then its percentage of PS estimated by ^1H NMR, which is 54.7%, should be close to reality. Therefore, the observed presence of PEO homopolymer in this sample probably only corresponds to unreacted PEO-(Acrylate)₂ contained in the PEO macro-initiator. Nevertheless, the amount of residual PEO homopolymer is higher in NMP1 sample compared to NMP3, although NMP1 was synthesized from a PEO macro-initiator with a lower functionalization yield. A possible explanation could be related to side-reactions, such as bimolecular termination, which would destroy alkoxyamine chain-ends during initiation step of the polymerization and would be promoted by shorter PEO macro-initiator A'. This would decrease the proportion of PEO able to initiate the polymerization in NMP1.

Because of the impact of PS homopolymer and PS percentage of the block copolymer, the influence of Sty/PEO and Sty/EtBz molar equivalent ratios on the presence of PEO homopolymer cannot be rationalized here. However, this study also highlights a certain limit of the LC LCD separation towards PS percentage of block copolymers.

4. Conclusion

With the experimental conditions employed in this study, it appears that all block PS-*b*-PEO-*b*-PS triblock copolymers synthesized *via* ATRP and NMP contain a certain amount of residual PEO and PS homopolymers.

Concerning ATRP syntheses, the observed amount of residual PEO homopolymer is, in most cases, very low. It is probably occurring from an incomplete functionalization during PEO macro-initiator synthesis. Sensitivity of LC LCD is higher than ^1H NMR sensitivity and this explains why non-functionalized PEO is not observed on the ^1H NMR spectrum of PEO macro-initiators. As expected, in some cases presence of self-initiated PS homopolymer is also observed and can be related to reaction time.

Concerning NMP syntheses, results are fairly inconclusive. However, styrene self-initiation during block copolymer synthesis could be related to experimental conditions, such as Sty/PEO molar equivalent and Sty/EtBz molar equivalent, which corresponds to the dilution of the reaction medium. Indeed, it was confirmed that the higher the proportion of styrene compared to the introduced PEO macro-initiator amount, the higher the amount of observed PS homopolymer on the chromatogram is. On the other hand, the more diluted the reaction medium, the lower the amount of self-initiated PS homopolymer in the block copolymer sample seems to be.

The presence of the PEO homopolymer peak in chromatogram of block copolymer synthesized by NMP could be related to the following features :

- Unreacted PEO-(Acrylate)₂, which is always present in the NMP during PEO macro-initiator synthesis, even when functionalization yields estimated by ^1H NMR are equal to 100%.
- Dilution of the reaction medium, and, on the contrary to the PS homopolymer case, the more diluted the reaction medium, the higher the

amount of observed residual PEO homopolymer seems to be. Therefore, dilution of the reaction medium could be optimized to minimize amount of PS and PEO homopolymers.

- Small amount of block copolymer retained by unappropriate barrier 2.

Finally, LC LCD appears as a powerful technique for characterization of complex polymer mixtures. Based on two model syntheses of PS-*b*-PEO-*b*-PS following either ATRP or NMP route, we obtained valuable information on chemical compositions of the studied samples. It has to be mentioned that these informations are difficult and almost impossible to obtain with other analytical techniques.

LC LCD is then of high interest to study synthesis procedures in order to optimize them, and to build accurate composition-properties relationships.

Further developments of this technique are currently in progress in our laboratory.

Acknowledgments

This work was done in the frame of Inter-academic Agreement on Cooperation between Centre National de la Recherche Scientifique, France and the Slovak Academy of Sciences, Slovakia, project “Synthesis, molecular characterization and purification of block copolymers”. MR, DB and DG thank Aix-Marseille University, CNRS, the Slovak Grant Agencies VEGA (project 2/0001/12) and APVV (Projects 0109-10 and 0125-011) for their financial support.

References

1. Hamley, I. W. *The physics of block copolymers*; Oxford University Press: Oxford, U.K., 1999.
2. Bang, J.; Kim, S. H.; Drockenmuller, E.; Misner, M. J.; Russell, T. P.; Hawker, C. J. *J. Am. Chem. Soc.* **2006**, *128*, 7622–7629.
3. Cheng, J.; Teply, B. A.; Sherifi, I.; Sung, J.; Luther, G.; Gu, F. X.; Levy-Nissenbaum, E.; Radovic-Moreno, A. F.; Langer, R.; Farokhzad, O. *C. Biomaterials* **2007**, *28*, 869–876.
4. Astolfi, P.; Greci, L.; Stipa, P.; Rizzoli, C.; Ysacco, C.; Rollet, M.; Autissier, L.; Tardy, A.; Guillaneuf, Y.; Gigmes, D. *Polym. Chem.* **2013**, *4*, 3694–3704.
5. Perrin, L.; Phan, T. N. T.; Querelle, S.; Deratani, A.; Bertin, D. *Macromolecules* **2008**, *41*, 6942–6951.
6. Girod, M.; Mazarin, M.; Phan, T. N. T.; Gigmes, D.; Charles, L. *J. Polym. Sci., Part A: Polym. Chem.* **2009**, *47*, 3380–3390.
7. Ouari, O.; Phan, T. N. T.; Ziarelli, F.; Casano, G.; Aussenac, F.; Thureau, P.; Gigmes, D.; Tordo, P.; Viel, S. *ACS Macrolett.* **2013**, *2*, 715–719.
8. Philipsen, H. J. A. *J. Chromatogr. A* **2004**, *1037*, 329–350.
9. Rollet, M.; Pelletier, B.; Altounian, A.; Berek, D.; Maria, S.; Beaudoin, E.; Gigmes, D. *Anal. Chem.* **2014**, *86*, 2694–2702.

10. Snauko, M.; Berek, D. *Chromatographia* **2003**, *57*, S55–S59.
11. Rollet, M.; Pelletier, B.; Altounian, A.; Berek, D.; Maria, S.; Phan, T. N. T.; Gimes, D. *J. Chromatogr. A* **2015**, *1392*, 37–47.
12. Beaudoin, E.; Phan, T. N. T.; Robinet, M.; Denoyel, R.; Davidson, P.; Bertin, D.; Bouchet, R. *Langmuir* **2013**, *29*, 10874–10880.
13. Rollet, M.; Glé, D.; Phan, T. N. T.; Guillaneuf, Y.; Bertin, D.; Gimes, D. *Macromolecules* **2012**, *45*, 7171–7178.
14. Bloch, E.; Phan, T. N. T.; Bertin, D.; Llewellyn, P.; Hornebecq, V. *Microporous Mesoporous Mater.* **2008**, *112*, 612–620.

Subject Index

A

Acrylate and acrylamide polymerization

Cu(0)-mediated living radical polymerization

prior disproportionation of

CuBr/Me₆-Tren, 37*f*

problems, 36

vodka and blood serum, 38*f*

high end-group fidelity, 30

high level of livingness, 33*f*

molecular weight distributions, 34*f*

multiblock copolymers, synthesis, 31*f*

NIPAM, DMA and HEAA via Cu(0), 40*f*

photo-induced polymerization, 32*f*

photomediated technique, expansion, 35

polymerization techniques development, 30

poly(NIPAM) multiblock homopolymer, evolution, 39*f*

SEC of multiblock homopolymers, 38*f*

summary, 42

unprecedented control, 29

well-defined triblock copolymer, 41*f*

Amphiphilic polymer prodrug

nanoparticles synthesis

analytical methods, 260

biological activity, 261

cell proliferation assay, 262

in vivo anticancer activity, 262

xenografts, immunohistochemical analysis, 263

conclusion, 269

design polymer prodrug nanoparticles, 258

introduction, 257

materials, 259

nanoparticle formation, 261

result and discussion

gem-based polymer prodrugs, 264

gemcitabine-based polymer prodrug nanoparticles, anticancer activity, 267*t*

polymer prodrugs in vitro and in vivo, 266

self-assembly of gem-based polymer prodrugs, 265

in vivo anticancer activity, 268*f*

synthesis, 259

4-Arm polystyrene star polymers synthesis

CHCl₃-GPC-molecular weight

distribution, 120*f*

experimental section

atom transfer radical polymerizations, general procedure, 124

azide terminated polystyrene (PS-N₃) and amine terminated polystyrene (PS-NH₂), 125

conclusion, 125

2-hydroxy-2-bromoisobutyrate (HEBIB), 124

instruments, 121

materials, 121

nitroxide mediated polymerizations of styrene, typical procedure, 123

N-(4-(pentafluorophenyl sulfonyl)phenyl)-maleic acid imide, 123

N-(4-sodiumsulfophenyl)-maleic acid imide and *N*-(4-sodiumsulfophenyl)-maleic acid half imide, 122

N-(4-sulfonylchloridophenyl)-maleic acid imide, 122

post-modification reactions, typical procedures, 124

FT-IR-spectra of polystyrene bromide, polystyrene azide and polystyrene amine, 120*f*

FT-IR-spectra using benzyl alcohol, 4-methyl benzyl alcohol, 2-pentanol and thiophen-2-methanol, 114*f*

GPC and chain extended polymer, 111*f*
¹H- and ¹⁹F-NMR spectra (CDCl₃), 113*f*, 115*f*

¹H-NMR spectrum (CDCl₃), 113*f*, 116*f*

¹H-NMR-spectra (CDCl₃), NMP, PS, 110*f*

hydroxyl capped PS, synthesis, 118*f*

N-(4-(pentafluorophenyl sulfonyl)phenyl)-maleic acid imide, synthesis, 109*s*

pentafluorophenyl ester bearing maleimide, use, 108

polymer chain ends, functionalities, 112*s*

PS-Amine, three-step synthesis, 119*f*

sequential post-polymerization modification, 108*s*

sequential reactions, 107

triple functionalized polymers, 117*t*

Atom transfer radical polymerization (ATRP), 327

ATRP. *See* Atom transfer radical polymerization (ATRP)

C

- CCM. *See* Core-cross-linked micelles (CCM)
- Cobaltocenium-containing monomers
ATRP
 HA-MRSA cells, 24*f*
 kinetic plot, 24*f*
 side chain cobaltocenium, block copolymer, 23*f*
 tentative direct ATRP polymerization, 23*s*
RAFT polymerization, 18
 kinetic plots, 19*f*
ROMP, 20
 kinetic plots, 21*f*
- Complexing copolymers synthesis and preparation of CeO₂/polymer hybrid latexes, 309
 analyses, 312
 conclusion, 324
 emulsion copolymerization of styrene and methyl acrylate, 311
 emulsion copolymerization of vinylidene chloride and methyl acrylate, 312
 introduction, 310
 materials, 310
 RAFT oligomers, synthesis, 311
 results and discussion
 ceria nanoparticles, 316
 ceria nanoparticles and poly(BA-*co*-AA) RAFT oligomers, 321*f*
 ceria nanoparticles and poly(BA-*co*-AA-*co*-AMPS) RAFT oligomers, 323*f*
 combination of UV-vis spectroscopy and ³¹P NMR, 318*f*
 hybrid latexes CeO₂/poly(styrene-*co*-methyl acrylate), 317
 hybrid latexes CeO₂/poly(vinylidene chloride-*co*-methyl acrylate), 322
 poly(BA₅-*co*-AA₅) and poly(BA₅-*co*-AMPS₅) copolymers, 315
 poly(St-*co*-VBPDA) RAFT oligomers, synthesis, 314
 poly(St₅-*co*-VBPDA₁₂) RAFT oligomers at the surface of CeO₂, 318*f*
 poly(St₅-*co*-VBPDE₁₀) copolymer, 315*f*
 RAFT oligomers, synthesis, 313
 RAFT oligomers and cryo-TEM pictures, structure, 320*f*

styrene and methyl acrylate with CeO₂, 319*t*

- Controlled radical polymerization (CRP), 29
- Core-cross-linked micelles (CCM), 203
- Core-shell cylindrical polymer brushes with new properties
 CPB backbones, dependence of scission, 129*f*
 crosslinking shell locks cargo in core, 131
 introduction, 127
 side chains against backbone, 128
 side chains working for backbone, 130
 template-directed approach, 132*f*
- CPBs. *See* Cylindrical polymer brushes (CPBs)
- CRP. *See* Controlled radical polymerization (CRP)
- Cylindrical polymer brushes (CPBs), 127

D

- Dual location disulfide degradable block copolymer micelles
 disulfide linkages in hydrophobic core and corona interface, 278*f*
 dual location reduction-responsive degradation strategy, advantage, 280
 proof-of-concept, 277
 synthesis fo well-defined DL-ssABP-1, 279*f*

E

- Ethylene-vinyl acetate based copolymers
 chain extension experiments, SEC chromatograms, 55
 conclusion, 59
 controlled synthesis, 47
 copolymers composed of PVAc and EVA segments, targeted, 56
 ethylene-vinyl acetate copolymerization, 52*t*
 EVA-based block copolymers, 55
 E/VAc copolymerizations, molar masses (*M_n*) and dispersities (*Đ*), 54*f*
 experimental
 methods, 49
 procedures, 50
 introduction, 47
 SEC chromatograms
 EVA-*b*-PVAc block copolymers, 58*f*

PVAc-*b*-EVA block copolymers, 57*f*
statistical EVA copolymers, 51
time dependence of $\ln[M]_0/[M]$, 53*f*
using organometallic complexes, best
result, 47
VAc polymerization and E/VAc
copolymerization, 49*s*

F

Fabrication of tailored nanocomposites,
design strategies
citrate-reduction, gold nanoparticles,
297
conclusion, 304
conventional nanohybrids, interparticle
distances, 299*f*
gold-nanoparticle superstructures, AFM,
301
interparticle distances and planet-satellite
distances, 305*f*
introduction, 293
made-to-order planet-satellite
nanostructures, 303
multiblock RAFT polymers, 295
multifunctional RAFT polymers,
nanocomposites, 296
nanohybrids with multiblock RAFT
polymers, interparticle distances, 299*f*
nanoparticle stabilization, 294
polymeric cross-linking species, 302
polymer-nanoparticle interactions,
targeted, 294
RAFT star polymers, 296
self-assembled hexagonal layers of gold
cores in nanohybrid particles, 298*f*
two-phase Brust-Schiffrin method, gold
nanoparticles, 300

H

Hyperbranched polymers, progress on
synthesis
conclusion, 145
core and monomer, different reactivity
consecutive activation of functional
groups, 142
decreased polydispersity, high core
reactivity use, 142
introduction, 135
polymerization in confined space, 143
slow addition of monomers to core

AB₂ monomers and AB inimers,
structures, 138*s*
hyperbranched polymers, 141
hyperbranched polymers (HBP),
decreased polydispersity, 137*s*
multifunctional cores, structure, 139*s*
multifunctional polymer as core, 140
multifunctional small molecule as
core, 136
uniform hyperbranched polymers, 144

I

Intracellular anticancer drug delivery with
accelerated release
DLS diagrams and TEM images, 284*f*
dual disulfide-located degradable
micellar nanocarriers, 275
effective SRD strategy, 275
flow cytometric histograms, 285*f*
interlayer-crosslinked micelles, 283
introduction, 274
new strategy, 273
PLA-based block copolymers, 281
synthesis of DL-ssABP-2
(POEOMA-ss-(PLA-ss-PLA)-
ss-POEOMA) triblock copolymer,
282*f*
PLA-based ICMs, 286*f*
SRD, multiple modes, 274
summary, 287
synthesis of DL-ssABP-3 triblock
copolymer, 286*f*

L

LC LCD. *See* Liquid chromatography
under limiting conditions of desorption
(LC LCD)
Liquid chromatography under limiting
conditions of desorption (LC LCD), 327
Living radical polymerization
atom transfer radical polymerization,
173
colloidally-templated nanopatterned
surface, 169
electro-grafted polythiophene with
RAFT-CTA, 172*f*
electro-grafting, 169
fabrication method
colloidal template surface, grafting to
approach, 178

- colloidal template-assisted electropolymerization, 174
 highly ordered monolayer colloidal crystals and inverse patterned colloidal crystals, 175*f*
 microporous film consisting of Ppy/Ppy-CHO, 175*f*
 via living radical polymerization, grafting from approach, 176
 via living radical polymerization, grafting to approach, 177
 grafted from electropolymerized surface, 171
 grafted to electropolymerized surface, 170
 results and discussion
 AFM topography 2D images (2.5 × 2.5 μm), 182*f*
 AFM topography 2D images (4 × 4 μm), 183*f*
 assisted nanopatterning on conducting substrate, 179
 backfilling inside cavities with silane SAM and polymer brush, fabrication scheme, 181*f*
 conclusion, 184
 grafting from approach, 180
 grafting to approach, 180
 surface patterning, 173
- N**
- NIPAM. *See* *N*-isopropylacrylamide (NIPAM)
N-isopropylacrylamide (NIPAM), 1
 Nitroxide mediated polymerization (NMP), 327
 NMP. *See* Nitroxide mediated polymerization (NMP)
- O**
- OMRP. *See* Organometallic-mediated radical polymerization (OMRP)
 Organometallic-mediated radical polymerization (OMRP), 47
- P**
- Periodically titanium-containing organometallic polymer
 aqueous solutions, thermoresponsive properties, 9
 conclusion, 25
 experimental materials, 11
 measurements, 12
 simultaneous polymerization, 12
 titanium-containing polymer, synthesis, 12
 triethanolamine-bearing dichloroacetamide (1), synthesis, 11
¹H NMR spectra, 8*f*
 introduction, 2
 simultaneous chain- and step-growth radical polymerization, 4
 initial feed ratio, effect, 7*f*
 M_n curves, 6*f*
 size-exclusion chromatograms, 6*f*
 time-conversion curves, 5*f*
 synthesis, 1
 titanatrane introduction, 7
 triethanolamine-bearing dichloroacetamide (1), 3
 UV-vis spectroscopy, 9*f*
- R**
- RAFT. *See* Reversible addition-fragmentation chain transfer (RAFT)
 RAFT copolymerization of thioglycosidic glycomonomers with NiPAM
 asymmetric flow field-flow fractionation (AF4), 224
 conclusion, 243
 GlcMAM, HSQC NMR spectrum, 245*f*
 glycomonomer synthesis, 225
 glycopolymer deprotection, 227
 procedure, 228
 immobilization of glycopolymers onto nanoparticles and lectin interaction, 229
 immobilization onto gold nanoparticles, 221
 introduction, 222
 ManMAM, HSQC NMR spectrum, 244*f*
 ManMAM and GlcMAM, ¹H NMR spectra, 244*f*
 materials and instrumentation, 223
 measured and calculated isotopic patterns
 two protected mannose repeating units, 250*f*
 two repeating units of glucose, 251*f*
 overlay of ATR FT-IR spectra, 249*f*

- overlay of size exclusion chromatograms, 245*f*
- PGlcAc-1 and PGlcOH-1, ¹H NMR spectra, 246*f*
- PGlcOH-1, HSQC NMR spectrum, 248*f*
- PGlcOH-2 and PManOH-2, T_{CPS}, 253*f*
- PManOH-1, HSQC NMR spectrum, 247*f*
- PManOH-1 and PGlcOH-1, cloud point temperatures, 252*f*
- PNiPAm-1, ¹H NMR spectrum, 247*f*
- PNiPAm-1, PManOH-1, and PGlcOH-1, AF4-MALLS fractograms, 254*f*
- reactions, 226
- results and discussion
- change of wavelength, 241*f*
 - chemical structure of copolymers, 232
 - conversions of glycomonomers, 231
 - deprotected glycopolymers, data, 234*t*
 - glycopolymer coated gold nanoparticles, synthesis, 238
 - LCST behavior, 239
 - lectin interaction experiments, 242
 - MALDI-TOF MS, advantage, 235
 - PGlcAc-2 and PManAc-2, MALDI-TOF MS, 236*f*
 - PGlcOH-2 and PManOH-2, MALDI-TOF MS, 237*f*
 - PManAc-1 and PManOH-1, ¹H NMR spectra, 233*f*
 - PManOH-1, turbidity curves and cloud point temperatures, 240*f*
 - by RAFT polymerization, 230
 - synthesis of glycomonomer, 229
 - UV-vis spectra, 224
- RAFT-mediated emulsion polymerization
- buffer on sol-gel transition temperature, 88
 - concentration of NaCl on sol-gel transition temperature, 87*f*
 - conclusion, 88
 - cooling PNIPAM₄₃-b-PSTY₄₀ latex solution, worm morphology, 85*f*
 - experimental
 - gel temperature of nanoworms and nanorods, measurement, 83
 - materials, 81
 - scanning electron microscopy (SEM), 82
 - size exclusion chromatography (SEC), 81
 - synthesis of PNIPAM₄₃-b-PSTY₄₀ latex, 82
 - synthesis of PNIPAM₄₃-SC(=S)SC₄H₉, 82
 - transmission electron microscopy (TEM), 81
 - worms preparation, 83
- MacroCTA, styrene (STY), AIBN initiator and SDS in water, 84*s*
- TEM images of rods, ultrasound method to cut worms, 86*f*
- thermoresponsive macro chain transfer agent (MacroCTA), 79
- worm structure, 80
- RAFT polymerization on particle surfaces
- conclusion, 200
 - cyclodextrin, 189
 - degenerative chain transfer method, 189
 - experimental
 - 6-azidoethyl methacrylate (AHMA), synthesis, 191
 - 1-azido-6-hydroxyhexane, synthesis, 190
 - dye-labeled poly(methacrylic acid) grafted silica nanoparticles, 191
 - instrumentation, 190
 - materials, 190
- grafting to and grafting from, strategies, 188
- introduction, 187
- nanoparticle surface functionalization, stages, 187
- results and discussion
- alternate strategy, 195
 - cyclodextrin (CD) grafted nanoparticles, 198
 - disk-diffusion assays using CA-MRSA, 197*f*
 - DMSO, photograph, 199*f*
 - dye-labeled poly(carboxylic acid) grafted silica nanoparticles, 192*s*
 - ¹H NMR, 193*f*
 - PAHMA grafted nanoparticles, IR spectra, 197*f*
 - poly(carboxylic acid) grafted nanoparticles, 191
 - surface-initiated RAFT polymerization, 196*t*
 - TEM image, 194*f*
 - TGA data, 199*f*
 - UV radiation in DMSO, 194*f*
 - via direct polymerization of MAA, 193*s*
- Reversible addition-fragmentation chain transfer (RAFT), 169

S

- Separation of parent homopolymers from poly(ethylene oxide) and polystyrene based block copolymers
high performance liquid chromatography (HPLC), 329
introduction, 328
LC LCD
 advantages, 329
 analysis, 337
 principle, 330*f*
liquid chromatography, 327
materials, 331
NMR analysis, 336
PEO and PS homopolymers, 338*f*
PS-*b*-PEO-*b*-PS triblock copolymers
 synthesis
 by ATRP, 332
 block copolymers samples, 335
 liquid chromatography under critical conditions (LC CC), 334
 by NMP, 333
 results and discussion
 ATRP, PS and PEO content, 340
 ATRP procedure, 339
 conclusion, 345
 NMP, PS and PEO content, 342
 NMP procedure, 341
 PEO homopolymer peaks, 343*f*
 PS homopolymer peaks, 343*f*
 Sty/PEO molar equivalent ratio, 344
Side-chain cobaltocenium-containing polymers
 biomedical application, 25
 conclusion, 25
 introduction, 15
 mono-substituted cobaltocenium, 15
 cobaltocenium-containing monomers, synthesis, 18*s*
 methods, 17*s*
SRD. *See* Stimuli-responsive degradation (SRD)
Star polymers synthesis with epoxide-containing highly branched cores
 conclusions, 164
 core modifications, 163
 experimental procedures
 analyses, 152
 hb-polyGMA-Br_x macroinitiator, chain extension, 153
 materials, 151
 polyGMA, modification, 153
 synthetic procedures, 152

- highly branched epoxide-containing polymers, 154
 divinyl crosslinkers, use, 156
 polymerizing system, altering amount of crosslinker, 155
introduction, 150
low-catalyst concentration ATRP, 157
post-polymerization modifications, 149
selected post-polymerization modifications of epoxides, 158
linear polyGMA, modifications, 159
NMR spectroscopy, 160
purified by precipitation in acetone, 161
tertiary aminoalcohols, ensure water solubility, 162
Stimuli-responsive degradation (SRD), 273

T

- Thermoresponsive poly(oligoethylene glycol acrylate) copolymers
 chain transfer agent (CTA)
 asymmetric unit of crystal structure of PABTC, 69*f*
 synthesis and crystal structure description, 68
 cloud point measurements, 72
 conclusion, 75
 copolymers plotted against weight percentage of eDEGA, 74*f*
 eDEGA, mDEGA and mTEGA, chemical structures, 65*f*
 experimental
 cloud point temperature measurements, 68
 crystal structure analysis, 67
 gas chromatography (GC), 66
 materials, 65
 nuclear magnetic resonance spectroscopy (NMR), 67
 size exclusion chromatography (SEC), 67
 synthesis of copolymers, 66
 high-throughput parallel synthesis, 64
 high-throughput RAFT polymerizations, 70
 poly(eDEGA-*stat*-mDEGA) copolymers, 72*t*
 poly(eDEGA-*stat*-mTEGA) copolymers, 73*t*
 poly(*N*-isopropylacrylamide) (PNIPAAm), 64
 RAFT polymerization, 63

mDEGA and eDEGA, 71*f*
mTEGA and eDEGA, 71*f*
transmittance vs. temperature plots
for poly(eDEGA-*stat*-mDEGA)
copolymers, 74*f*
transmittance vs. temperature plots
for poly(eDEGA-*stat*-mTEGA)
copolymers, 74*f*
TPP. *See* Triphenylphosphine (TPP)
Triphenylphosphine (TPP), 203
Triphenylphosphine-functionalized
amphiphilic core-shell polymers
abbreviations, 218
aqueous biphasic hydroformylation of
1-octene, results, 212*t*
CCM interpenetration, 215
conclusion, 217
core-cross-linked micelles with
triphenylphosphine, 206*s*
DLS analysis of recovered organic phase
[Rh(acac)(CO)(TPP@CCM)]
solution, 216*f*
TPP@CCM, 214*f*
types of nano-objects, comparison of
efficiencies, 213
final polymers, 208
¹H NMR spectra, 209*f*
hydroformylation
catalysis, 210
1-octene, 211*s*
incorporation of BMOPPS, 207*s*
introduction, 204

³¹P NMR spectroscopy, investigation of
coordination process, 210
particle swelling and metal coordination,
208
polymer synthesis, 205

W

Worm-like micelles and vesicles
block copolymers, synthesis, 96
conclusion, 103
experimental part
analytical methods, 95
materials, 93
monomer, synthesis, 93
poly(1-*O*-MAFru)-*b*-PMMA and
poly(1-*O*-MAFru)-*b*-PBMA,
synthesis, 94
fine-tuning processing parameters, 91
introduction, 92
self-assembled glycopolymers,
morphology control, 97
common solvent, 98
glycopolymers, 99*t*
hydrophobic chain length, 100
poly(1-*O*-MAFru)₃₅-*b*-PMMA₁₉₂,
102*t*
poly(1-*O*-MAFru)_{*m*}-*b*-PMMA_{*n*}, 101*t*
water injection rate, 102